

Experimental and Model-Based Study of Gas-Liquid-Solid Flows in pH-Shift Electrolyzers

Experimentelle und modellgestützte Untersuchung von
Gas-Flüssig-Fest Strömungen in pH-Shift Elektrolyseuren

Von der Fakultät für Maschinenwesen der Rheinisch-Westfälischen
Technischen Hochschule Aachen zur Erlangung des akademischen Grades
eines Doktors der Ingenieurwissenschaften genehmigte Dissertation

vorgelegt von

Jonas Tim Görtz

Berichter: Universitätsprofessor Dr.-Ing. Andreas Jupke
Universitätsprofessor Dr.-Ing. habil. Mark Hlawitschka

Tag der mündlichen Prüfung: 22.08.2025

Diese Dissertation ist auf den Internetseiten der Universitätsbibliothek online verfügbar.

Impressum

Titel: Experimental and Model-Based Study of Gas-Liquid Flows
in pH-Shift Electrolyzers

Autor: Jonas Tim Görtz

Reihe: Aachener Verfahrenstechnik – Fluidverfahrenstechnik –
Dissertationen, Band 17 (2025)

Herausgeber: Aachener Verfahrenstechnik
Forckenbeckstraße 51
52074 Aachen
+49 (0)241 8095246
Secretary.fvt@avt.rwth-aachen.de
<http://www.avt.rwth-aachen.de/AVT>

Nutzungsbedingungen:

Die Universitätsbibliothek der RWTH Aachen University räumt das unentgeltliche, räumlich unbeschränkte und zeitlich auf die Dauer des Schutzrechtes beschränkte einfache Recht ein, das Werk im Rahmen der in der Policy des Dokumentenservers „RWTH Publications“ beschriebenen Nutzungsbedingungen zu vervielfältigen. Dieses Werk bzw. Inhalt ist lizenziert unter einer Creative Commons Namensnennung 4.0 International Lizenz (Creative Commons Attribution 4.0 International).

Danksagung

Diese Dissertationsschrift ist während meiner Zeit als wissenschaftlicher Mitarbeiter am Lehrstuhl für Fluidverfahrenstechnik der Aachener Verfahrenstechnik an der RWTH Aachen University entstanden. Ich möchte mich daher bei meinem Doktorvater Univ.-Prof. Dr.-Ing. Andreas Jupke für die Ermöglichung und Betreuung der Promotion bedanken. Weiterer Dank gilt meinen Kollegen Christian Kocks, Moritz Becker, Robert Kiefel, Jan Haß, Kristina Mielke, Arne Holtz, Josia Tonn, Christian Schröder, Stephan Mushold, Andreas Biselli, Martin Leipnitz und Manuel Lück sowie meinen studentischen Hilfskräften und Abschlussarbeitern Stine Kuhlemann, Katharina Sander, Vincent Wiederhold, Matthias Arnoldi, Julian Borowec, Julian Weigele, Nikolai Witschke, See Yuan Choo und Anna-Lena David.

Abschließend möchte ich meinen Eltern, Lisa und Manfred, meinen Brüdern, Jan und Max, meiner Frau Svenja und meinen beiden Söhnen Felix und Paul danken.

Kurzfassung

Der Einsatz von elektrochemischen pH-Shift-Trenntechniken stellt eine vielversprechende Alternative für das konventionelle pH-Management durch Additive im Kontext der Kreislaufwirtschaft dar. Durch die Abkehr von fossilen Kohlenstoffquellen kommt dem pH-Management bei z.B. biotechnologischen Herstellungsprozessen sowie in Recyclingprozessen von Carbonsäuren eine zentrale Rolle zu, da während der Aufarbeitung meist wässrige Ströme prozessiert werden. Dabei werden gezielt die Eigenschaften der unterschiedlichen Säurespezies genutzt, um Trennoperationen zu ermöglichen. Zum Beispiel nutzt die elektrochemische Kristallisation die niedrigere Löslichkeit der vollständig protonierten Säurespezies, um eine reaktiv pH-Shift-Kristallisation durchzuführen.

Diese Arbeit präsentiert eine detaillierte Studie der Fluidodynamik in pH-Shift-Elektrolyseuren. Hierfür wird zunächst experimentell die Größe und Geschwindigkeit von elektrolytisch erzeugten Sauerstoff- wie Wasserstoffgasblasen vermessen sowie die örtlich aufgelöste Strömung des Elektrolyten. Hierbei kommt ein eigens für diesen Zweck entwickelter semitransparenter Elektrolyseur zum Einsatz, der neue Einblicke in die Gas-Flüssig-Strömung ermöglicht. Als Nächstes wird ein neues Euler-Lagrange-Modell für die Simulation der Fluidodynamik der Gas-Flüssig-Strömung vorgeschlagen, das die Aufweitung des Gasblasenvorhangs vor der Elektrode mittels Blasen-Blasen-Kollisionen abbilden kann. Für dieses implementierte Modell werden nachfolgend mittels einer Sensitivitätsstudie geeignete Modellparameter für z.B. Gittergröße, Widerstandsbeiwert und Kollisionsmodell ausgewählt. Mit diesen Simulationsparametern wird anschließend der neuartige Elektrolyseur simuliert und das Modell mit experimentellen Daten validiert.

Abschließend lässt sich mithilfe des Modells eine Analyse eines neuen Prototyps für die elektrochemische Kristallisation von Carbonsäuren durchführen. Hierbei lässt sich der Einfluss von unterschiedlichen Stromstärken und Elektrolytvolumenströmen auf das Strömungsprofil und die räumliche Verteilung der Gasblasen untersuchen. Des Weiteren können durch die Simulation der Anoden- und Dissoziationsreaktionen die Konzentrations-, pH- sowie Übersättigungsprofile ermittelt werden. Durch die modelltechnische Analyse lassen sich hier kritische Totzonen sowie der Einfluss unterschiedlicher Elektrodenabstände untersuchen und deren Einfluss auf die maximale lokale Übersättigung quantifizieren. Zukünftig ermöglicht die in dieser Arbeit etablierte modellgestützte Analyse die Bewertung sowie Entwicklung neuer Prototypen-Designs für die elektrochemische Kristallisation.

Summary

In the context of the circular economy, electrochemical pH shift techniques offer a promising alternative to conventional pH management methods that rely on additives. The transition away from fossil carbon sources leads to pH management playing a central role in processes such as biotechnological production and recycling processes for carboxylic acids, as aqueous streams require processing. The properties of the different acid species, which depend on the pH value, are specifically utilized to enable their separation. For example, electrochemical crystallization takes advantage of the lower solubility of the fully protonated acid species to perform reactive pH shift crystallization.

This work presents a detailed study of fluid dynamics in electrochemical separation units. For this purpose, the size and velocity of electrolytically generated oxygen and hydrogen gas bubbles and the spatially resolved, qualitative flow of the electrolyte are measured experimentally. For this purpose, a specially developed semi-transparent electrolyzer is used, which provides new insights into the gas-liquid flow. Next, based on the state of the art, a new Euler-Lagrangian model for the simulation of the fluid dynamics of the gas-liquid flow is proposed, which depicts the expansion of the gas bubble curtain through bubble-bubble collisions. For this implemented model, suitable parameters, e.g., grid size, drag coefficient, and collision model, are selected through a sensitivity study. These simulation parameters are then used to simulate the novel electrolysis apparatus, and the model is validated with experimental data.

Finally, the model can be used to analyze a new prototype for the electrochemical crystallization of carboxylic acids. Here, the influence of different current densities and electrolyte volume flows on the flow profile and spatial distribution of the gas bubbles can be investigated. Furthermore, the acid species concentration, pH, and supersaturation profiles can be determined by simulating the anodic and dissociation reactions. This model-based analysis enables the identification of dead zones and the study of different electrode-membrane gaps, quantifying their influence on the maximum local supersaturation. In the future, the model-based analysis established in this work enables the evaluation and development of new prototype designs for electrochemical crystallization.

Publications

Research items

- J. Görtz, J. Seiler, und A. Jupke, „Bubble up: Tracking down the vertical velocity of oxygen bubbles in parallel plate electrolyzers using CNN“, *International Journal of Multiphase Flow*, Bd. **177**, S. **104849**, 2024, doi: 10.1016/j.ijmultiphaseflow.2024.104849.
- J. Görtz, J. Seiler, P. Kolmer, und A. Jupke, „Raising the curtain: Bubble size measurement inside parallel plate electrolyzers“, *Chemical Engineering Science*, Bd. **286**, S. **119550**, 2024, doi: 10.1016/j.ces.2023.119550.
- N. Tenhaef, A. Hermann, M.F. Müller, J. Görtz, J. Marienhagen, M. Oldiges, W. Wiechert, M. Bott, A. Jupke, L. Hartmann, S. Herres-Pawlis, S. Noack, „From Microbial Succinic Acid Production to Polybutylene Bio-Succinate Synthesis“, *Chemie Ingenieur Technik*, Bd. **95**, Nr. **4**, S. **587–595**, 2023, doi: 10.1002/cite.202200163.
- M. Labib, J. Görtz, C. Brüsseler, N. Kallscheuer, J. Gätgens, A. Jupke, J. Marienhagen und S. Noack, „Metabolic and process engineering for microbial production of protocatechuic acid with *Corynebacterium glutamicum*“, *Biotech & Bioengineering*, Bd. **118**, Nr. **11**, S. **4414–4427**, 2021, doi: 10.1002/bit.27909.
- A. Holtz, J. Görtz, C. Kocks, M. Junker, und A. Jupke, „Automated measurement of pH-dependent solid-liquid equilibria of itaconic acid and protocatechuic acid“, *Fluid Phase Equilibria*, Bd. **532**, S. **112893**, 2021, doi: 10.1016/j.fluid.2020.112893.
- B. Weber, M. Schneider, J. Görtz, und A. Jupke, „Compartment Model for Liquid-Liquid Extraction Columns“, *Solvent Extraction and Ion Exchange*, Bd. **38**, Nr. **1**, S. **66–87**, 2020, doi: 10.1080/07366299.2019.1691137.
- C. Kocks, J. Görtz, A. Holtz, M. Gausmann, und A. Jupke, „Electrochemical Crystallization Concept for Succinic Acid Reduces Waste Salt Production“, *Chemie Ingenieur Technik*, Bd. **92**, Nr. **3**, S. **221–228**, 2020, doi: 10.1002/cite.201900088.

Patents

- M. Gausmann, J. Görtz, W. Graf von Westarp, A. Jupke, A. Becker, und T. Gries, „Method for producing a monomer from the polymer comprising the monomer“, WO2024013254A1, *World Intellectual Property Organization*, 2023.

Presentations

- J. Hass, S. Kuhleemann, J. Görtz, M. Gausmann und A. Jupke, „From Solution to Solid: Investigating the Electrochemical Crystallization of Muconic Acid for Separation from Fermentation Broth“, *Jahrestreffen der ProcessNet-Fachgruppe Kristallisation*, 2025, Winterthur, Schweiz.
- C. Kocks, J. Görtz, A. Jupke, Design and Characterization of Electrochemical pH-shift Crystallization Processes, *International Symposium on Industrial Crystallization (ISIC)*, 2023, Glasgow, Scotland.
- J. Görtz, K. Mielke, M. Gausmann, A. Jupke, „Model-Based Development of a Novel Apparatus for Electrochemically Induced Crystallization of (di-)Carboxylic Acids“, AICHE Annual Meeting: Powering the Future, 2022, Phoenix, Arizona, USA.
- M. Labib, J. Görtz, C. Brüsseler, J. Marienhagen, A. Jupke, und S. Noack, „Bio-based production of 3,4-dihydroxybenzoate from D -xylose using genetically engineered *Corynebacterium glutamicum*“, *Chemie Ingenieur Technik*, Bd. **92**, Nr. **9**, S. **1183**, 2020, doi: 10.1002/cite.202055123.
- C. Kocks, J. Görtz, A. Jupke, Experimentelle Charakterisierung eines Reaktorprototyps für die elektrochemisch induzierte pH shift Kristallisation von Bernsteinsäure, *Jahrestreffen der ProcessNet-Fachgruppe Kristallisation*, 2022, Dortmund, Deutschland.
- J. Görtz, M. Gausmann, C. Schröder, C. Kocks, A. Jupke, „Lastflexible Elektrifizierung als Schlüsseltechnologie für nachhaltige Bioraffineriekonzepte“, Keynote, *Jahrestreffen der ProcessNet-Fachgemeinschaft Prozess-, Apparate- und Anlagentechnik*, 2021, virtuelle Konferenz.
- J. Görtz, C. Kocks, M. Gausmann, A. Jupke, „Emissionsreduzierung der industriellen Biotechnologie durch elektrochemische Trennapparate“, *Jahrestreffen der ProcessNet-Fachgemeinschaft "Prozess-, Apparate- und Anlagentechnik"*, 2020, Münster (virtuelle Konferenz), Deutschland.

- C. Kocks, J. Görtz, M. Gausmann, und A. Jupke, „Electrochemically induced downstream processes for dicarboxylic acids reduce neutral salt emission“, *Chemie Ingenieur Technik*, Bd. **92**, Nr. **9**, S. **1175–1176**, 2020, doi: 10.1002/cite.202055050.

Poster-Presentation

- J. Görtz und A. Jupke, „Modell-basierte Untersuchung der lokalen Übersättigung in elektrochemischen Kristallisationsapparaten“, *Jahrestreffen der ProcessNet-Fachgruppe Kristallisation*, 2025, Winterthur, Schweiz.
- J. Haß, J. Görtz, C. Kocks, und A. Jupke, „ZeTA – Electrochemical separation technology and electrolysis cell design for the pH-shift crystallization“, *Chemie Ingenieur Technik*, Bd. **94**, Nr. **9**, S. **1355**, 2022, doi: 10.1002/cite.202255215.
- J. Görtz, C. Kocks, M. Gausmann, und A. Jupke, „Modeling of electrochemical separation processes for bio-based carboxylic acids using a finite-volume method“, *Chemie Ingenieur Technik*, Bd. **92**, Nr. **9**, S. **1300–1300**, 2020, doi: 10.1002/cite.202055118.

Contents

Kurzfassung	vii
Summary	ix
Publications	xi
Nomenclature	xix
1. Introduction	1
2. Fundamentals	5
2.1. Electrochemical pH-shift	5
2.1.1. pH-shift water electrolysis	8
2.1.2. Electrochemical pH-shift crystallization	10
2.1.3. Electrogeneration of bubbles in electrolyzers	14
2.2. Optical measurement techniques for gas-liquid flow in electrolyzer	20
2.2.1. Size determination of detached electrogenerated bubbles	20
2.2.2. Neuronal networks for image recognition	21
2.2.3. Measurement of electrolyte and bubble velocity in electrolyzers	23
2.3. Modeling of electrochemical reactors	25
2.3.1. Gas-liquid flow in electrochemical reactors	25
2.3.2. Mass transport in pH-shift electrolyzers	40
2.3.3. Coupling of fluid flow and electrochemistry	42
2.3.4. Flow characterization of ideal reactors	43
3. Experimental study of the gas-liquid flow in parallel plate electrolyzers	47
3.1. Methods	47
3.1.1. Materials, chemicals, and electrochemical stability	48
3.1.2. Experimental Setup	48
3.1.3. Bubble detection and size determination using Mask R-CNN	51
3.1.4. PTV algorithm for the measurement of the bubble velocity	53
3.1.5. PIV algorithm of the anode-membrane gap	57
3.1.6. Contact angle measurements	59

3.1.7. Operating parameters for experimental studies	61
3.2. Size distribution of oxygen bubbles	64
3.2.1. Effect of superficial electrolyte velocity	66
3.2.2. Effect of current density	67
3.2.3. Effect of measurement height	69
3.2.4. Effect of electrolyte composition	69
3.2.5. Effect of catalyst	71
3.2.6. Comparison of the two camera systems	77
3.3. Size distribution of hydrogen bubbles	78
3.4. Vertical bubble velocity of oxygen bubbles	81
3.4.1. Vertical bubble velocity for different bubble size bins	82
3.4.2. Impact of current density	84
3.4.3. Vertical bubble velocity across measuring panels	85
3.4.4. Impact of electrolyte flow velocity	87
3.5. Vertical bubble velocity of hydrogen bubbles	91
3.6. PIV measurment of anolyte flow field	94
3.6.1. Impact of current density and electrolyte flow velocity	94
3.6.2. Flow field across different viewing panels	98
3.6.3. Impact of electrode-membrane gap	99
3.7. Summary of experimental findings	103
4. Euler-Lagrange multiphase model for pH shift electrolyzers	107
4.1. Model assumptions	109
4.2. Disperse gaseous Lagrangian phase	110
4.2.1. Parcel injection	110
4.2.2. Parcel forces	112
4.2.3. Collision Model	115
4.2.4. Lagrange-Euler mapping	117
4.2.5. Interphase Coupling	118
4.3. Continuous electrolyte Euler phase	120
4.3.1. Turbulence model	122
4.3.2. Volume displacement due to bubble nucleation	123
4.3.3. Mass transfer and electrolyte composition	124
4.4. Determination of the residence time distribution	126
4.4.1. Electrolyte phase	127
4.4.2. Crystal phase	127
4.5. Simulation Setups	127
4.5.1. Electrolyte properties	127

4.5.2.	Computational domains and boundary conditions	128
4.5.3.	Simulation of the partially transparent electrolyzer	129
4.5.4.	Simulation of a novel prototype for electrochemical crystallization .	129
4.6.	Criteria for comparison of simulation results	131
5.	Evaluation of the Euler-Lagrangian model for gas-liquid flows in electrolyzers	135
5.1.	Sensitivity analysis of simulation parameters	135
5.1.1.	Influence of averaging technique	135
5.1.2.	Mesh size	136
5.1.3.	Number of bubbles per parcels	139
5.1.4.	Drag model	141
5.1.5.	Two-way vs. four-way coupling	144
5.1.6.	Sensitivity study of the collision model parameter	145
5.2.	Simulation of partially transparent electrolyzer	146
5.2.1.	No net flow configuration	146
5.2.2.	Forced flow configuration	152
5.3.	Summary of model evaluation	158
6.	Study of the gas-liquid-solid flow inside a novel electrochemical crystallizer	161
6.1.	Gas-liquid flow inside a novel prototype for the electrochemical crystallization	161
6.1.1.	Impact of superficial electrolyte velocity	163
6.1.2.	Impact of current density	164
6.1.3.	Impact of electrode-membrane gap	166
6.1.4.	Simulated residence time distribution of the electrolyte and compar- ison with experimental data	168
6.2.	Residence time distribution of the crystal phase	171
6.2.1.	Experimental measurement	172
6.2.2.	Experimental result	173
6.2.3.	Simulation result and comparison	176
6.3.	Local pH and supersaturation	177
6.3.1.	Succinic acid	177
6.3.2.	2,5-furandicarboxylic acid	181
6.3.3.	Terephthalic acid	183
6.4.	Summary of reactor study	184
7.	Conclusion and Outlook	187
7.1.	Summary of findings	187
7.2.	Future research question	189

A. Additional experimental settings and results	191
A.1. Illumination of PTV setup	191
A.2. Image results from the PIV measurement	191
B. Additional simulation settings and results	199
B.1. Mesh description	199
B.2. General Solver structure in OpenFOAM	202
B.3. Boundary conditions	203
B.4. Flow profiles of the prototypes in the xy and zy -plane	203
B.5. Miscellaneous simulation settings results	216
B.6. pH profiles of the 8 mm prototype	218
B.7. Oversaturation profiles of the 8 mm prototype	223
B.8. Comparison of experimental and simulated residence time distribution of the electrolyte	226
List of Figures	227
List of Tables	238
Bibliography	241

Nomenclature

Abbreviations

Symbol	Description
A^{-2}	Fully deprotonated acid specie
CDF_N	cumulative normal probability function
CFD	Computational fluid dynamics
CHPS	core hourse per simulated second
CNN	Convolutional neural network
FDCA	Furan-2,5-dicarboxylic acid
fps	frames per second
H_2A	Fully protonated dicarboxylic acid
HA^{-1}	Mono-deprotonated acid specie
HRHSC	high resolution high speed camera
LRHSC	low resolution high speed camera
ODE	ordinary differential equation
PDF_N	normal probability density function
PDF_T	truncated probability density function
RTD	Residence time distribution
SA	succinic acid
TA	Terephtalic acid

Latin symbols

Symbol	Description	Unit
a	Acceleration	m s^{-2}
<i>A</i>	Area	cm^2
<i>a</i>	Activity	mol L^{-1}
<i>c</i>	Concentration	mol L^{-1}
<i>D</i>	Diffusion coefficient	$\text{m}^2 \text{s}^{-1}$
<i>d</i>	Diameter	μm
D_{ax}	Axial dispersion coefficient	$\text{m}^2 \text{s}^{-1}$
\tilde{d}_{max}	Adjusted maximum diameter	m
\tilde{d}_{min}	Adjusted minimum diameter	m
e_n	Normal vector	-
$E(t)$	RTD function	-
F	force	km s^{-3}
<i>F</i>	Faraday's constant	A s mol^{-1}
<i>f</i>	Frames per second	s^{-1}
$F(t)$	Normalized outlet RTD function	-
g	Gravitational vector	m s^{-2}
<i>h</i>	Height	mm
h_{f}	Enthalpy of fusion	J mol^{-1}
<i>I</i>	Current	A
<i>i</i>	Current density	A cm^{-2}
IQR	interquartile range	m
J	Flux	$\text{m}^2 \text{s}^{-1}$
<i>k</i>	Turbulent kinetic energy	$\text{m}^2 \text{s}^{-3}$

k	Turbulent kinetic energy	$\text{m}^2 \text{s}^{-2}$
K^{\rightarrow}	forward reaction rate	$\text{mol L}^{-1} \text{s}$
k^{\rightarrow}	forward reaction rate constant	$\text{L}^2 \text{mol}^{-2} \text{s}$
K^{\leftarrow}	backward reaction rate	$\text{mol L}^{-1} \text{s}$
k^{\leftarrow}	backward reaction rate constant	$\text{L}^2 \text{mol}^{-2} \text{s}$
L	Length	m
m	mass	kg
N_{b}	Number of bubbles in domain	-
n_{p}	Number of bubbles per parcel	-
P	Pressure	Pa
$\text{p}K_{\text{a}}$	Dissociation constant	mol L^{-1}
q_0	number-based density distribution	-
q_3	volume-based density distribution	-
R	Molar gas constant	$\text{J K}^{-1} \text{mol}$
$\mathbf{S}_{\mathbf{u}, \text{Transfer}}$	Exchanged momentum	$\text{kg m}^{-2} \text{s}^2$
S	Relative supersaturation	-
s	relative size difference	-
T	Temperature	K
t	time	s
Δt	time step size	s
U	Potential	$\text{kg m}^2 \text{A}^{-1} \text{s}^3$
u	Velocity	m s^{-1}
U_0	Thermodynamic equilibrium potential	$\text{kg m}^2 \text{A}^{-1} \text{s}^3$
v	Mobility	$\text{m}^2 \text{s}^{-1}$
\dot{V}	Volume flow	$\text{m}^3 \text{s}^{-1}$

W	Electric work	$\text{kg m}^2 \text{s}^{-2}$
w	Width	mm
\mathbf{x}	position	mm
$x^*(T)$	Temperature dependent molar solubility	-
Z	Ionic strength	mol L^{-1}
z	Charge number	-
Δz	Grid size in z -direction	mm

Greek symbols

Symbol	Description	Unit
α	Phase fraction	-
β	Degree of dissociation	-
γ	Activity coefficient	-
ϵ	Turbulent energy dissipation rate	$\text{m}^2 \text{s}^{-3}$
κ	Conductivity	S m^{-1}
Λ	Angle of descend	°
μ	Viscosity	$\text{m}^2 \text{s}^{-1}$
ρ	Density	kg m^{-3}
σ	Surface tension	kg s^{-2}
ς	Variance	-
$\bar{\sigma}_\theta$	Dimensionless variance of the RTD	s
Θ	Contact angle	°
ω	Specific dissipation rate	s^{-1}
Ψ	Resistance	Ω

χ	Chemical potential	J mol^{-1}
--------	--------------------	---------------------

Subscripts

Symbol	Description
25	25th quantile
50	median (50th quantile)
75	75th quantile
a	acid
b	Bubble
c	Cell
d	number of dissociation reaction
e	educt of dissociation reaction
eff	Effective
el	Electrolyte
g	Gravitational
g	Gas
H ₂	hydrogen
k	time step iterator
kin	Kinetic
l	Liquid
m	mixed
mol	Molar
N	Norm
O ₂	oxygen
p	parcel

p1, p2	products of dissociation reaction
RI	Electrolyte resistance
sim	simulative
s	Solid
t	Turbulent
TC	target compon
vm	Virtual mass
w	Species iterator

Superscripts

Symbol	Description
0	Superficial
an	Anode
ca	Cathode
f	face
h	Horizontal
mag	Magnitude
v	Vertical

Dimensionless Numbers

Symbol	Description
Bo	Bodenstein number
Eo	Eötvös number
Re _b	Bubble Reynolds number
Re _{el}	Electrolyte Reynolds number
Sc	Schmidt number
Sh	Sherwood number

1. Introduction

As the global economy transitions towards more sustainable and environmentally friendly production and separation processes, novel process routes based on non-fossil carbon sources, as well as the development and implementation of waste-reduced, low-temperature separation processes play key roles [1, 2]. Research [3–8] into new production processes for promising (di-)carboxylic acids such as itaconic, succinic, 2,5-furandicarboxylic, and protocatechuic acid via biotechnological routes enabled the utilization of biomass as the primary carbon source for platform chemicals. However, to this day, industrial-scale biotechnological production of these acids has struggled to compete with conventional petrochemical processes. The industrial implementation of biotechnological production processes is impeded by both the high production costs and the complexity of product purification [2]. As the microorganism typically metabolizes either glucose or sucrose, the substrate of the fermentation process becomes a significant expense. In addition, fermentation processes are often subject to product inhibition, which negatively impacts yield and titer [9]. To circumvent product inhibition, a separation technique that obtains the target component from the aqueous fermentation broth during fermentation is beneficial and often referred to as *in situ* removal. Implementing an *in situ* removal further complicates an already challenging purification process that requires large amounts of pH agents and unit operation to concentrate the product [3].

Alongside biomass, the utilization of recycling streams either as a carbon source or directly for the recovery of monomers poses challenges similar to those previously described in biotechnological production routes. Here, impurities pose significant challenges for separating the target component from the aqueous solution since their concentration fluctuates and they are either unknown or not quantified. Nonetheless, the processing of polymer waste streams is a major challenge of the transition towards a more sustainable economy due to their large volume [10]. For example, alkaline hydrolysis can be utilized to recover (di-)carboxylic acids from these polymer waste streams, but it also requires large amounts of pH agents during the process [11].

Driven by the need to reduce energy consumption, minimize greenhouse gas emissions, and decrease the environmental impact of industrial activities, electrochemical processes have emerged as a promising component in achieving these goals [2]. Recent research [12–15] proposed a promising combination of either biotechnological or recycling streams with

an electrochemically driven pH-shift. Instead of using acids and bases to adjust the pH value, the pH-shift is conducted by the anodic and cathodic water-splitting reactions that create protons and hydroxide ions, respectively, altering the pH value of the exiting anolyte and catholyte. This technique avoids the common drawbacks of using pH agents, namely the generation of at least equimolar neutral salt waste and the large amount of required liquid discharge. Further, the electrochemical pH-shift can also be applied to enable *in situ* processes and, thus, decrease the amount of liquid discharge and neutral salt emissions of these processes [14]. Moreover, by lowering the pH value in the anode, the carboxylates are protonated, which reduces their solubility and ultimately leads to their crystallization within the pH-shift electrolyzers. This combined process of electrochemical pH-shift and crystallization was titled electrochemically induced crystallization [12].

With the implementation and demonstrated proof of concept of this novel technique to both biotechnological and polymer recycling processes, the technology readiness level has to be further improved. Therefore, the electrochemical process has to be transferred from batch experiments conducted in H-cells [12] into a parallel plate electrolyzer that can be operated continuously. In addition to enabling continuous operation, parallel plate electrolyzers also feature smaller inter-electrode gaps, reducing the applied voltage and, thus, power consumption. However, the design of suitable prototypes for the electrochemical pH-shift and electrochemically induced crystallization is challenging due to large concentration gradients in the system [16]. Kocks et al. [17] proposed and studied the first design for an electrolyte chamber. Yet, this design still exhibits issues like the formation of a solid blockade during continuous operation.

This thesis aims to study the gas-liquid-solid flow inside pH-shift electrolyzers and provide a validated computational fluid dynamic (CFD) based model that enables insights into the anode chamber. Ultimately, the findings can then be used to improve the design of pH-shift electrolyzers. The first chapter of the thesis presents the state of the art regarding the basic principle and physical phenomena of pH-shift electrolyzers and their implementation into a production process. Next, available optical measurement techniques for the experimental study of the gas-liquid flow inside electrolyzers are introduced, and the published results regarding the electrolyte and gaseous flows are examined. The chapter closes with an overview of modeling techniques for the gas-liquid flow, mass transport, phase coupling, and flow characterization within parallel plate electrolyzers.

Based on the state of the art presented regarding the experimental measurements of gas-liquid flow, the second chapter depicts methods and results for the experimental investigation of the gas-liquid flow inside parallel plate electrolyzers. Therefore, a tailored semi-transparent electrolyzer is developed and equipped with high-speed camera systems. Here, crucial input parameters for the CFD simulation, such as the size distribution of oxygen bubbles produced through the anode reaction, are determined alongside data for

the model validation, such as bubble velocities and electrolyte flow patterns.

The third chapter introduces the underlying assumptions and model equations for the developed Euler-Lagrangian model. It further presents the algorithms for calculating acid speciation, mass transfer, and determining the residence time distribution of the electrolyte and crystal phase. The last subsection lists the parameters and their variations for the sensitivity and simulation study of the partially transparent electrolyzer alongside a model-based analysis of the prototype proposed by Kocks et al. [17].

The results of the sensitivity analysis and the comparison of simulation results with experimental data illustrated in Chapter 3 are presented in the fifth chapter. Using sensitivity analysis and comparison of simulative and experimental results, the validity and limitations of the Euler-Lagrangian are discussed and suitable model parameters are selected. The chosen model parameters are then applied to the simulation of the prototype from Kocks et al. [17], and the resulting flow profiles, concentration gradients, and design limitations are shown in Chapter 6. Suggestions for the future design of prototypes are derived through examining the determined flow profiles.

In closing, the thesis results are summarized in the last chapter. Here, a brief summary of the experimental final is given, and the contribution to the analysis of the gas-liquid flow dynamics in parallel plate electrolyzers is critically evaluated. Furthermore, the disadvantages and advantages of the developed Euler-Lagrangian model are briefly summed up, and an outlook on possible follow-up work is given.

2. Fundamentals

This chapter introduces the basic physical principles of pH-shift electrolyzers that incorporate pH water-splitting electrolysis alongside their typical applications. Next, it presents state-of-the-art optical measurement techniques and experimental results for the study of the fluid flow within these electrochemical apparatuses. The last section of this chapter provides an in-depth review of different modeling approaches of gas-liquid flow, mass transport, and coupling with electrochemistry and the obtained results and observed phenomena.

2.1. Electrochemical pH-shift

Due to the expedited insertion of aqueous bio-based, recycling, or waste-based processes to substitute conventional, fossil-based production processes, controlling the pH value during the up-and-downstream process has gained a key role [5]. Whereas, in established solvent-based processes, the physicochemical properties of a component are mainly temperature dependent, an additional change in pH leads to the addition or subtraction of a proton from the target molecule. This so-called speciation of the target molecule leads to a complete change of physical properties enabling or disabling the possibility of, e.g., extraction or crystallization from the aqueous medium [3].

Instead of adding bases and acids to the aqueous process media, recent research [12, 13, 16–28] focused on electrochemical units that perform the pH-shift electrochemically. pH-shift electrolyzers shift the pH of the solution and target molecule's properties by employing water electrolysis, enabling a simultaneous or immediate downstream separation. Figure 2.1 shows the process concept of Gausmann and Kocks et. al [13] for inserting an electrochemical pH-shift extraction and crystallization unit into a bio-based production process for succinic acid (SA). Here, a cell-free medium from a fermentation (1) is electrochemically acidified in an anode chamber (3), and to increase the concentration of the target component, it is extracted into a solvent phase. The depleted anolyte is basified in the cathode chamber of the first cell and subsequently recycled to the bio-reactor. The extractant is fed into the cathode chamber of a second electrochemical cell, and the target component is back extracted in an alkaline aqueous phase (5). Subsequently, the concen-

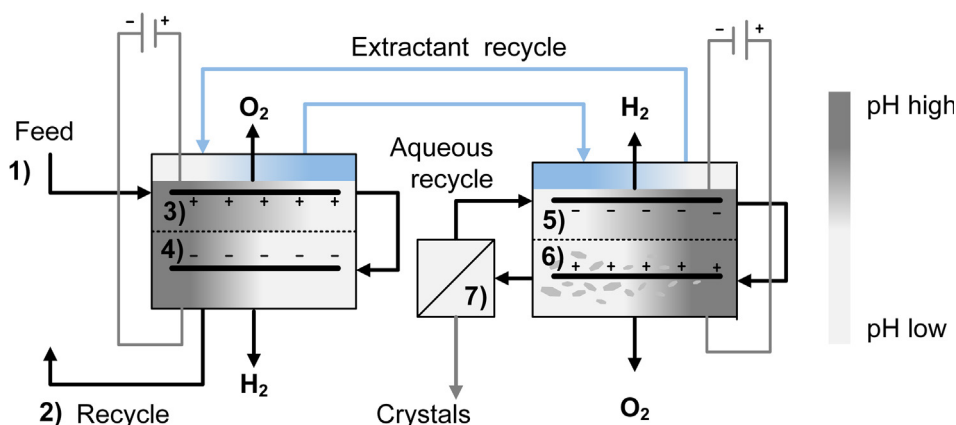


Figure 2.1.: Insertion of electrochemical pH-shift electrolyzers in a biotechnological separation process for succinic acid [13]. Reprinted from *Separation and Purification Technology*, 240, M. Gausmann, C. Kocks, M. Doeker, A. Eggert, T. Maßmann, and A. Jupke, Recovery of succinic acid by integrated multi-phase electrochemical pH-shift extraction and crystallization, 116489, Copyright 2024, with permission from Elsevier.

trated solution is fed into the anode chamber of the second electrochemical cell (6), where the second acidification takes place and the target component crystallizes. The suspension is filtered (7), and the permeate is fed back to the cathode chamber (5). By employing the electrochemical pH-shifts, the addition of bases and acids and formation of neutral salt emission can be substantially decreased by a molar ratio of up to $4 \text{ mol}_{\text{NaCl}} : 1 \text{ mol}_{\text{SA}}$ compared to a conventional route [3]. Besides emitting neutral salts, adding bases and acids also leads to the dilution the target component and further complicates the downstream process. Hence, the application of electrochemical pH-shift units can lead to a substantial decrease in pH agents and waste disposal costs [29, 30]. This decrease in auxiliary also renders the electrochemical pH-shift crystallization an energy-efficient and ecologically promising alternative to conventional processes for separating carboxylic acids. [29].

Despite the possible benefits, designing and operating electrochemical pH-shift units is challenging. Depending on the chosen separation task, e.g., electrochemical pH-shift dialysis, extraction, or crystallization, different apparatus concepts exist:

- (i) Electrodialysis setups [23–25] that consist of multiple electrode chambers shift the pH and concentrate, e.g., succinic acid, through migration. Therefore, a sufficiently large potential has to be applied to induce the migration of the negatively charged succinate ions from the cathode to the anode. In comparison to a simpler two-chamber setup (Figure 2.1), the electrochemical setup for electrodialysis requires higher voltages, bipolar, anion-exchange, and cation-exchange membranes, increasing the capital costs [23, 24].

- (ii) Andersen et al. [18–21] successfully developed an extraction process that utilized a two-chamber setup for the *in-situ* extraction of a carboxylic acid from a fermentation broth through a membrane into an organic phase.
- (iii) The same working group [26–28] also developed an electrochemical pH-shift crystallizer consisting of two chambers. Comparably to electrodialysis, the negatively charged succinate ions migrate through a membrane to the acidified anolyte and immediately crystallize on the membrane.
- (iv) Based on water-softening processes [31, 32], Kocks et al. [17] proposed a chamber design for the electrochemical pH-shift crystallization that can be integrated in a commercially available parallel plate electrolysis cell. Contrary to the previous concept, the crystals form in the proximity of the electrode.

In order to enable continuous operating and further improve electrochemical pH-shift apparatuses, the interplay of electrochemical, thermodynamic, and fluid dynamic phenomena must be understood. Depending on the physical phenomena, an electrochemical cell can be studied at different size scales, as exemplarily sketched in Figure 2.2. Usually, the multiphase fluid flow within an electrolysis cell, cell potential, conductivity, mixing, extraction, and crystallization are studied on a macro-scale. In contrast, electrochemical phenomena can be investigated on meso down to molecular scales. This thesis focuses on the investigation, description, and interplay of the phenomena on a macroscopic scale.

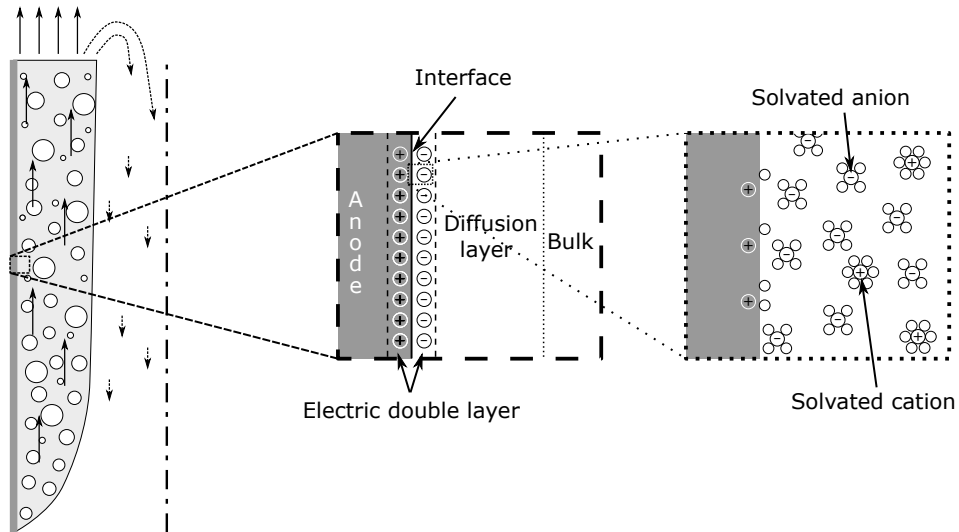


Figure 2.2.: Different physical phenomena in electrochemical parallel plate electrolyzer on macro-, meso- and molecular-scale.

To compete with the additive-based pH-shift processes, the electrochemical pH-shift apparatuses have to work efficiently. The operating costs mainly depend on the energy

costs that themselves depend on the required cell potential U_c to induce an electrochemical reaction or, equivalently, current flow I . The electric work W is defined by Ohm's Law

$$W = U_c I, \quad (2.1)$$

where U_c is the sum of the thermodynamic equilibrium potential U_0 , kinetic overpotentials Ψ_{kin} , resistance of the electrolytes Ψ_{RI} , limited mass transport to the electrodes $\Psi_{\text{transport}}$, and ohmic voltage drop of the membrane Ψ_{membrane} [33]:

$$U_c = U_0 - \Psi_{\text{kin}}^{\text{an}} - \Psi_{\text{transport}}^{\text{an}} - \Psi_{\text{RI}}^{\text{an}} - \Psi_{\text{membrane}} - \Psi_{\text{RI}}^{\text{ca}} - \Psi_{\text{transport}}^{\text{ca}} - \Psi_{\text{kin}}^{\text{ca}}. \quad (2.2)$$

Here, the superscripts indicate the contribution of the anode (an) and cathode (ca). Despite U_0 , all overpotentials and voltage drops depend on the area-specific amount of exchanged electrons characterized by the current density

$$i = \frac{I}{A_{\text{electrode}}}, \quad (2.3)$$

where $A_{\text{electrode}}$ denotes the electrode surface area most commonly given in cm^2 [33]. Whereas the reaction kinetics and mass transport overpotentials dominate for low current densities, the share of the ohmic potential drop over the electrolytes increases steadily because of Ohm's law ($\Psi_{\text{RI}} \sim i$). To minimize the resistance of the electrolyte, a sufficiently large conductivity must be ensured through the addition of conducting salts. The purposefully induced pH-shift also induces an energy penalty: U_0 depends on the electrochemical cell's pH difference between the anolyte and catholyte in the electrochemical cell. Per pH unit, an additional

$$\Delta U_0 = -0.059 \cdot \Delta \text{pH} \quad (2.4)$$

is added to the required cell voltage to perform the water-splitting reactions.

2.1.1. pH-shift water electrolysis

Water-splitting electrolysis belongs to one of the oldest yet still important electrochemical processes mainly employed for hydrogen production of hydrogen from purified water [33]. Worldwide hydrogen production is $1.4 \cdot 10^9 \text{ m}_N^3$ and one-tenth of chloralkali production [34]. The three most common electrolysis types are alkaline, proton exchange membrane electrolysis (PEM), and solid oxide, with alkaline electrolysis being the most commercially used method [35]. In contrast to the three established electrolysis processes, pH-shift water electrolysis focuses on creating a pH difference between the in- and outlet of an electrochemical cell. Here, hydrogen and oxygen are produced as a by-product instead of

being the target product. Additionally, industrial electrolysis processes usually avoid pH differences between anode and cathode chambers since they increase the thermodynamic potential U_0 (equation (2.2)) [33].

Since the two different electrolytic chambers are separated by a (cation exchange) membrane, the brutto reaction of the electrolysis [35]



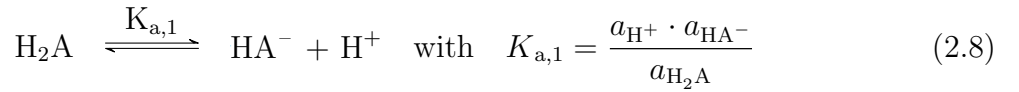
has to be split into the anodic reaction



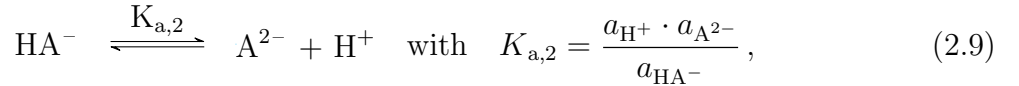
and cathodic reaction



By consuming and producing H_2 , the pH in the cathode and anode chamber is altered. This change in the pH affects the equilibrium position of the dissociation reactions of, e.g., a dicarboxylic acid A:



and



where a_w denotes the activity of species w in the electrolyte. a_w is linked to the concentration c_w by

$$a_w = \gamma_w \cdot c_w, \quad (2.10)$$

with γ_w resembling the activity coefficient of the species i . For the calculation of γ_w different semi-empirical correlation like, e.g., Debeye-Hückel [36], extended Debeye-Hückel also referred to as Davies equation [37], Pitzer [38] and electrolyte Perturbed Chain model Statistical Associating Fluid Theory (ePC-SAFT) [39, 40] are available. However, the applicability of the activity models to electrolyte solutions is limited by the ionic strength calculated by

$$Z = 0.5 \sum_w c_w z_i^2. \quad (2.11)$$

It uses the concentration of the species w , c_w , and the charge number z_i of the present ions. Out of the four previously mentioned activity models, the ePC-SAFT model is the most versatile, with a maximum ionic strength of $Z < 0.3 \text{ mol L}^{-1}$. Nonetheless, electrolyte solutions for electrochemical reactors require background electrolytes to ensure a sufficient

conductivity exceeding the validity range of all known activity models. For example, a moderate electrolyte solution containing 0.2 mol L^{-1} sodium sulfate (Na_2SO_4) already has an ionic strength of 0.6 mol L^{-1} . Though, for simplicity, the activity coefficient is regarded as equal to one, resulting in $a_i \equiv c_i$.

To reflect the present fraction of each species in comparison to the total acid concentration c_A , the degree of dissociation β_i for a dicarboxylic acid is introduced by

$$\beta_i = \frac{c_i}{c_A} \quad \text{for } i = \text{H}_2\text{A}, \text{HA}^-, \text{A}^{2-} \quad (2.12)$$

and its dependency on the pH is exemplarily shown for succinic acid with $\text{p}K_{a1,2}$ values of 4.21 and 5.64 [41], respectively, in Figure 2.3. The different equilibrium compositions in Figure 2.3 are obtained from the dissociation reactions (2.8) and (2.9). This pH-triggered change in the dissociation degrees can be utilized to shift the solid-liquid equilibrium to a species with a lower solubility and induce crystallization.

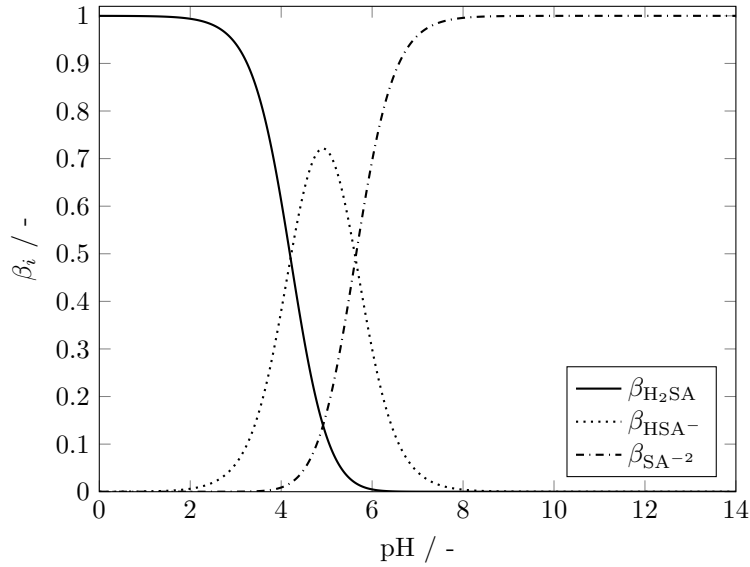


Figure 2.3.: Degrees of dissociation, $\beta_{\text{H}_2\text{SA}}$, β_{HSA^-} and $\beta_{\text{SA}^{2-}}$, of succinic acid with $\text{p}K_{a,1} = 4.21$ and $\text{p}K_{a,2} = 5.64$ [41] against the pH.

2.1.2. Electrochemical pH-shift crystallization

Crystallization processes and their various types differ in the way a change in the chemical potential between the potential of the solid χ_s and liquid χ_l phase of a component

$$\Delta\chi = \chi_s - \chi_l \quad (2.13)$$

is created. In the state of equilibrium, also referred to as solid-liquid equilibrium (SLE), $\Delta\chi_w = 0$. The chemical potential itself depends on the temperature T , pressure P , and system composition. P is usually neglected for solution crystallization due to the incompressibility of both liquid and solid phases. Cooling crystallization processes utilize the temperature dependency of the SLE that can be expressed by the semi-empirical Schröder-van-Laar equation

$$-\ln [x^*(T)] = \frac{\Delta h_f}{R} \left(\frac{1}{T} - \frac{1}{T_m} \right). \quad (2.14)$$

Here, $x^*(T)$, R , h_f , T_f denote the molar solubility for the temperature T , molar gas constant, enthalpy, and temperature of fusion, respectively. Figure 2.4 shows the molar fraction of succinic acid for temperatures between 5 and 65 °C and fitted Schröder-van-Laar equation from Apelblat and Manzurola [42]. Equation (2.14) and Figure 2.4 depict the exponential increase of the solubility with respect to the temperature: Whereas increasing the temperature by 5 K leads to a change in molar solubility of 0.002 at 10 °C, the change amounts to 0.012 at 60 °C.

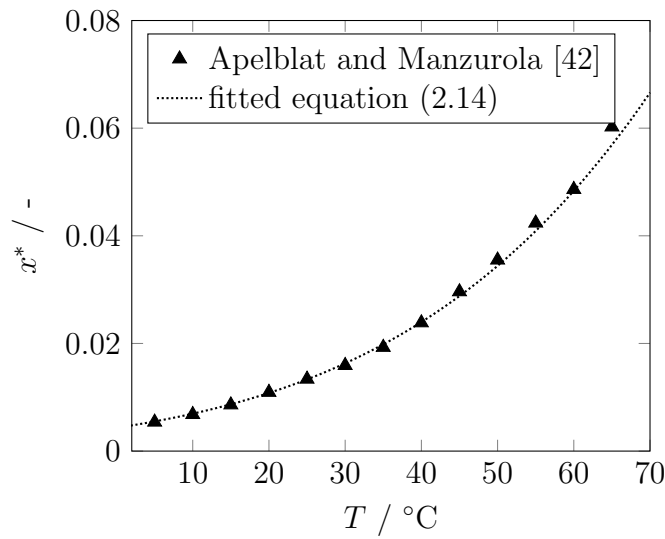


Figure 2.4.: SLE data from Apelblat and Manzurola [42] and fitted Schröder-van-Laar equation of succinic acid for different temperatures.

If the solubility component is subject to the dissociation reaction described in Section 2.1.1, the SLE of the component is also affected by the pH value of the solution. Figure 2.5 depicts the deprotonation of the acid at different pH values and as a result of the different solubility of each specie, the total amount of soluble component changes due to the speciation of the component [43]. Even though the solubility of a single species, also referred to as intrinsic solubility, is solely temperature-dependent, the speciation leads to an 'observed' increase in the total soluble amount of the component. Figure 2.5 demonstrates this effect: Up to a pH value of roughly 4.5 (I), the concentration of the fully protonated

acid species remains constant at its intrinsic solubility limit. The increase in the 'combined' solubility of all succinic acid species starts at a pH of 2.2. Here, the first dissociation reaction (2.8) shifts towards HSA^- enlarging c_{NaHSA} . In the pH range between 4.5 and 6 (**II**), NaHSA is the solubility limiting species, also correspondingly resulting in a solid state of NaHSA. The boundary pH values 4.5 and 6 exhibit local maxima due to two species being at or close to their intrinsic solubility limit. For pH values greater than 6 (**III**), the 'combined' solubility decreases until it reaches the intrinsic solubility of the sodium succinate-decahydrate of 0.0365 [43].

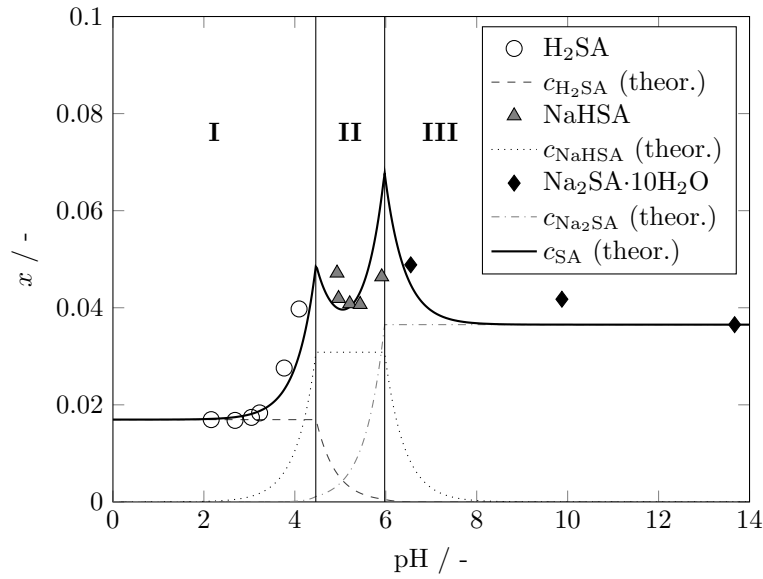


Figure 2.5.: Experimental data [43] and theoretical concentration of the different succinic acid species against different pH values at 25 °C. The black line corresponds to the total soluble amount of all succinic acid species. In the first (**I**) pH range, the protonated acid species, H_2SA , precipitates. The present solid states in equilibrium in the second (**II**) and third (**III**) pH range are NaHSA and $\text{Na}_2\text{SA} \cdot 10\text{H}_2\text{O}$, respectively. Adapted with permission from Lange et al. [43]. Copyright 2024 American Chemical Society.

Reactive or, more specifically, pH-shift crystallization exploits the different intrinsic solubilities of the different species. For example, lowering the pH from 4 to 2 decreases the solubility from 0.03 to 0.017 g g^{-1} resulting in a relative supersaturation of 43.3%. The relative supersaturation S of a component or species w is defined as

$$S = \frac{\Delta c_i}{c_w^*} = \frac{c_w - c_w^*}{c_w^*} = \frac{x_w - x_w^*}{x_w^*}, \quad (2.15)$$

c_w , and c_w^* denote the present concentration and corresponding solubility limit [44, 45]. The relative supersaturation S is a crucial process parameter defining the occurring crystallization phenomena. Except for crystal agglomeration and breakage, the nucleation, growth, and dissolution of crystals are directly linked to S [44, 46]. Here, S determines

whether and at what rate new crystal nuclei are created, and molecules diffuse to, integrate with, and disintegrate from the crystal surface. For all those mechanisms, a wide range of models with different applications and assumptions are available. For a detailed overview of these crystallization phenomena, the reader is invited to study Mullin [44] Beckmann [45] and Mersmann et al. [46].

As previously described in Section 2.1, the necessary change in pH for the crystallization is commonly achieved by adding bases and acids with their known drawbacks, namely dilution and neutral salt generation. Urbanus et al. [26, 27, 28] were the first to apply the electrochemical pH-shift crystallization to separate a bio-based carboxylic acid. They transferred different carboxylic acids from fermentation broths through the membrane in an anolyte. Due to the anodic pH water-splitting reaction, the anolyte is acidic, and thus, the carboxylic acid crystallizes due to its lower solubility. Even though the concept from Urbanus et al. [26, 27, 28] showed great potential, the crystal nucleation occurred directly on the membrane, rendering a continuous operation nearly impossible [18].

To prevent the crystal nucleation on the membrane and enable a continuous operation, Kocks et al. [12, 16, 17] transferred the concept of electrochemical pH-shift crystallization that occurs in the proximity of the electrode from water treatment and softening processes to the crystallization of carboxylic acids. During water treatment, the cathode chamber is electrochemically basified, resulting in the precipitation of poorly soluble calcium and magnesium salts. Subsequently, these precipitated salts can be separated from the liquid [31, 32]. Applying this concept to the crystallization of carboxylic acids that have a lower solubility in their protonated form at low pH values (Figure 2.5) introduces the challenge of electrode scaling. Due to the electrolysis reaction at the liquid-solid interface, the local change in pH value, and thus, S in the proximity of the electrodes is large. These gradients then lead to local crystal nucleation and scaling of the electrode [31]. Kocks et al. [16] studied the effect of bulk concentration, pH value, and i on the local nucleation H_2SA of a system also containing H_2 and $NaSO_4$. Here, they measured the metastable zone width (MSZW), which they defined as the absolute difference between the actually measured pH value at the nucleation event and the corresponding pH value of the SLE at the given concentration. A small MSZW indicates a high tendency of a crystallization system to spontaneously form crystals and/or to exhibit high local oversaturations [44]. In their work, Kocks et al. [16] demonstrated the presence of high local gradients at small i of $0.05 A cm^{-2}$. They reported MSZWs of 0.01 to 0.07 pH units in the electrolyte bulk to trigger the crystal nucleation. In comparison, conventional pH-shift processes for similar carboxylic acids, e.g. itaconic acid, can be oversaturated between 0.15 and 0.35 [47]. By increasing i , the resulted MSZW further decreased to pH differences of 0.01 to 0.04. Incorporating the findings of their MSZW measurement, Kocks et al. [17] developed a novel, specific chamber design to enable the continuous electrochemical pH-shift crystallization

inside commonly available electrolysis modules. Using this prototype, they successfully crystallized succinic acid from artificial solutions, finding operating conditions at which electrode scaling could be diminished. The works of Kocks et al. [17] and Ben Moussa et al. [48] highlight the importance and interplay of operating conditions alongside local effects on the performance of electrochemical pH-shift apparatuses. In order to study and understand the local phenomena occurring at the electrode, the gas evolution and bubble motion, has to be characterized.

2.1.3. Electrogeneration of bubbles in electrolyzers

Initially, during the electrolysis, the produced oxygen and hydrogen molecules are dissolved in water. Since the electrochemical reaction occurs directly at the electrolyte-electrode interface, the local dissolved gas concentration quickly exceeds the solubility once the current is applied. Consequently, the solution is locally super-saturated with levels up to 400 [49], ultimately leading to the nucleation of bubbles on small cavities on the electrode surface [50]. Besides the nucleation, this supersaturation also imposes a concentration overpotential η_c [51]. After a bubble nucleates on the electrode surface, it starts to grow due to the local supersaturation until it contacts bubbles that have nucleated on different cavities. Subsequently, the bubbles in contact coalesce, forming a larger bubble [52, 53]. This bubble continues to grow and coalesce with other bubbles until it finally departs from the electrode surface. For illustration, Figure 2.6 showcases the nucleation, growth, and coalescence of gas bubbles on an iridium-oxide mixed metal (IrOMM)-coated titanium electrode in a parallel plate electrolyzer. After the bubble detaches and escapes in the bulk electrode, the bubble still grows and coalesces, but with lower rates due to the lesser oversaturation and bubble density.

The final size of departing and detached bubbles d_b in the electrolyte heavily impacts the fluid flow and electrochemical properties of the electrochemical reactor and can not be predicted reliably. The dependency of the bubble size on process parameter has also been discussed accordingly in publication

Görtz, J., Seiler, J., Kolmer, P. und Jupke, A., „Raising the Curtain: Bubble Size Measurement inside Parallel Plate Electrolyzers“. *Chemical Engineering Science*, 286 (2024) [54].

It relies on a few experimental research items [55–59] that report the following influencing parameter:

(i) **The type of the produced gas molecule**

Most commonly, O_2 , H_2 , and Cl_2 are produced in gas-evolving electrochemical pro-

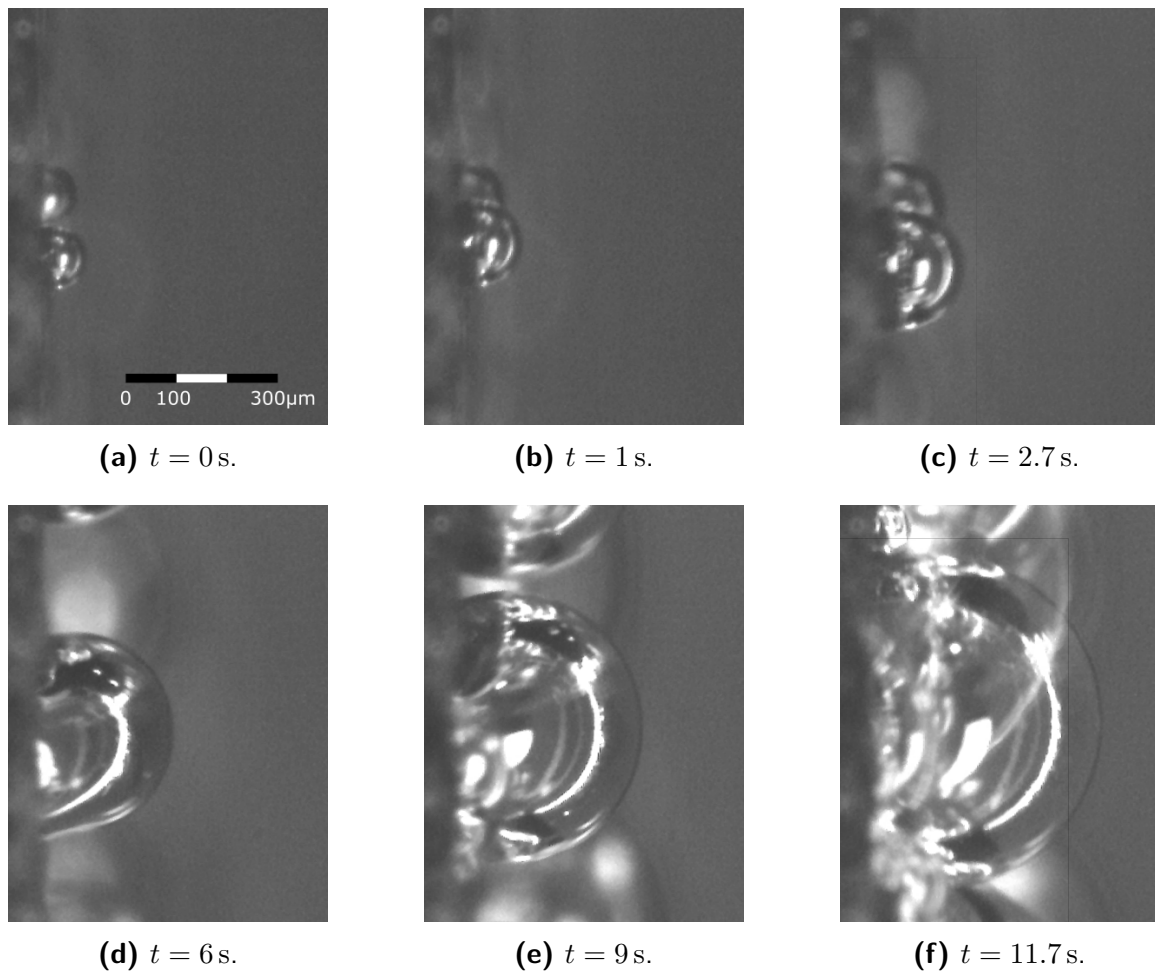


Figure 2.6.: Nucleation, growth, and coalescence of oxygen bubbles on an IrOMM-coated titanium electrode surface.

cesses and have different physicochemical properties, which affect the bubble size [55, 56].

(ii) **Electrolyte flow velocity u_{el}**

Depending on the electrolyte flow velocity, the drag force acting on the attached bubbles increases. Due to the increased drag force, the bubbles depart prematurely, making their size smaller [57, 58].

(iii) **Current density i**

The current density is directly linked to the amount of electrochemically generated gas volume and is the most defining parameter for the bubble size [58, 59]. By increasing the current density, both research groups report an increase in the average size of detached bubbles.

(iv) **Contact angle Θ**

Similar to the electrolyte flow velocity, the contact angle affects the bubble departure

and bubble size. Depending on the composition of the electrolyte, the electrode's catalyst, surface roughness, and overpotential, the contact angle varies. Vogt and Balzer [56] and Kabanow and Frumkin [60] argued that based on theoretical consideration regarding Θ , the bubble size should decrease with greater i . Nonetheless, this contradicts the previous findings concerning i and has not been experimentally proven [60, 61].

(v) **Electrolyte composition**

By changing the electrolyte composition, the cell, and over-potential at the electrode surface as well as the interfacial tension of the bubble and electrolyte is altered. Thus, this alters the contact angle of the bubble on the electrode surface [60] and coalescence frequency [61].

(vi) **Catalyst and surface structure**

Depending on the application, most plate electrodes are coated with (noble) metal catalysts. The catalyst and the surface structure created upon coating affect the number of active nucleation sides and, thus, the bubble size.

(vii) **Temperature T**

By changing the temperature, Janssen et al. [59] and Chin Kwie Joe et al. [58] reported either a slight increase or decrease in the bubble size.

(viii) **Pressure P** An increased pressure reduces the average size of attached bubbles on the electrode [59] and, thereby, also of detached bubbles.

(ix) **Coalescence and growth**

Despite all previous parameters, the size of bubbles that detach from the electrode is subject to coalescence, growth, and breakage [52, 61–65].

In contrast to d_b , the sheer amount of electrogenerated gas volume \dot{V}_g can easily be calculated by Faraday's law of electrolysis

$$\dot{V}_g = \frac{i A_{\text{electrode}}}{V_{\text{mol}} z F}, \quad (2.16)$$

with the molar gas volume V_m , Faraday's constant F and the amount of exchanged electrons (e^-) in the reaction z . From the anodic and cathodic reaction (equations (2.6) and (2.7)), it follows that twice as much hydrogen is produced compared to oxygen during the electrolysis. The following presents the impact of the electrogenerated gas due to bubble coverage on the electrode surface and electrolyte displacement.

Bubble coverage of electrodes

Figure 2.6 depicts the process of nucleation, growth, and coalescence, and the attached bubbles occupying parts of the active surface. Depending on the operating parameters, mainly i , the bubbles cover up to 60 % of the electrode surface [56]. This reduction in free electrode surface area leads to an increased effective current density that heavily affects the mass transfer, electrochemical reaction, overpotential, and, ultimately, the energy efficiency [51, 57, 66, 67]. For example, Figure 2.7 shows the bubble coverage on an IrOMM-anode inside a parallel plate electrolyzer for a moderate current density of $i = 0.01 \text{ A m}^{-2}$. A large area of the electrode is occupied by gas bubbles, with a few empty spots due to the recent departure of a bubble.

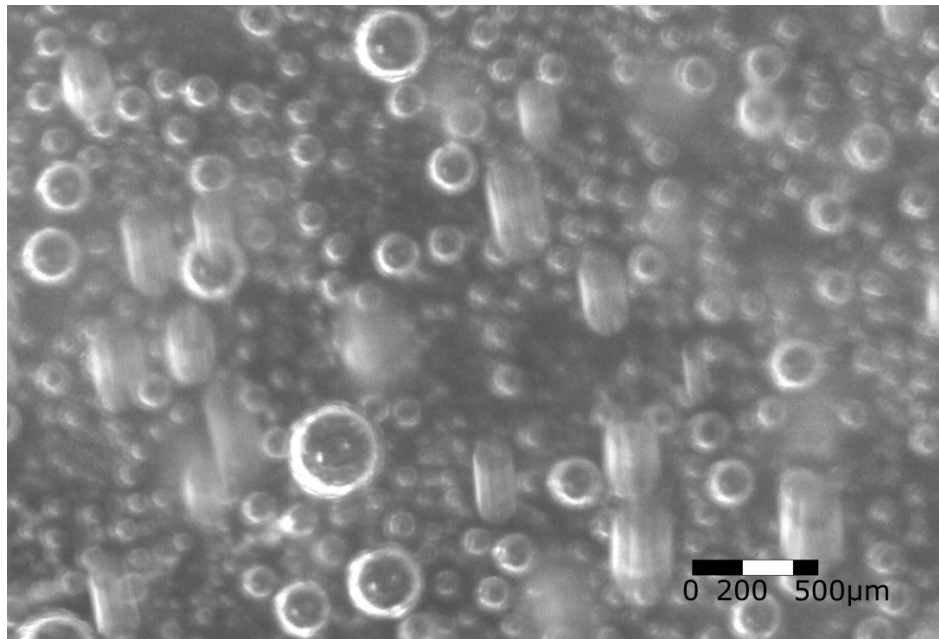


Figure 2.7.: Bubble coverage on an IrOMM-anode during electrolysis in a parallel plate electrolyzer. The oxygen bubbles in focus are attached to the electrode, whereas the bubble with motion blur are detached bubbles.

As mentioned in the previous enumeration of impact factors on the bubble size, the contact angle Θ of the electrolyte-electrode interface directly affects the bubble departure diameter and, hence, also the bubble coverage [56]. Further, the contact angle is directly linked to the bubble shape, which also influences the fluid flow at the three-phase contact line of the bubble, electrolyte, and electrode. Here, the mass transfer is enhanced by the micro-convection induced by buoyancy forces, Marangoni effects, and thermal gradients [51, 52, 64]. Nonetheless, the attached bubbles impose an additional resistance on the electrochemical system [35].

Recent research highlighted the impact of the bubble coverage by applying mechanical [68] and power ultrasound [69] to decrease the occupied surface. Through sonification, Cho

et al. [69] triggered the breakage and premature detachment of bubbles, lowering the mean bubble size from 72 μm to 17 μm . Thus, the bubble coverage was decreased, leading to an energy reduction of up to 9 %.

Bubble curtain and gas phase fraction

Initially, the different phenomena in a parallel plate electrolyzer are depicted in Figure 2.2. Here, the local distribution of bubbles is sketched on a macroscopic scale, showing an accumulation in the proximity of the electrode. Due to the continuous generation of bubbles at the electrode, a curtain-like accumulation is generated that is hence often referred to as a bubble curtain or shield [35, 70]. On vertical electrodes, the width of the bubble curtain increases from bottom to top due to the accumulation of electrogenerated bubbles that also travel upwards. Hence, the electrolyte's flow direction is commonly also chosen to be on par with the bubble travel. This same flow direction prevents a further increase in the gas phase fraction by slowing or reversing the bubble motion [35]. The shape and width of the bubble curtain are challenging to predict and are influenced by various factors, e.g., chamber geometry, i , electrolyte velocity u_{el} , and d_{b} [70].

Due to the varying gas phase fraction alongside the electrode, the distribution of i is also non-uniform. Since the gas phase fraction is the smallest at the bottom of the gas-evolving electrode, the largest current densities are also typically found there [70–74]. Greater gas-phase fractions reduce the conductivity of the gas-liquid mixture because the gas bubbles do not conduct electricity [75]. Thus, the gas-phase fraction has been of great research interest, and models were developed to describe the 'mixed' conductivity κ_{m} and gas phase fraction based on superficial velocities and vice versa:

Over the course of the last two centuries, different models have been proposed to depict the dependency of the conductivity of the gas-liquid mixture. The most commonly used models are those by Rayleigh [76], Maxwell [77], Tobias [78], Bruggeman [79] and Prager [80] that are illustrated in Figure 2.8 [75]. For moderate gas phase fraction smaller than 20 %, all models except the one from Prager [80] yield similar values for κ_{m} . Out of those four models, the correlation by Bruggeman [79] has seen frequent use and is defined by

$$\frac{\kappa_{\text{m}}}{\kappa_{\text{el}}} = (1 - \alpha_{\text{g}})^{\frac{3}{2}}, \quad (2.17)$$

where κ_{el} denotes the conductivity of the electrolyte. Employing Bruggemann's law [79], various studies [75, 81–83] researched the interplay of u_{b} with the gas phase fraction in electrochemical reactors. Measuring κ_{mixed} at different operating conditions and heights, they calculated the gas volume fraction α_{g} employing equation (2.17). Next, using the cross-sectional area A_{cross} and \dot{V}_{el} , they determined the superficial gas and electrolyte velocity

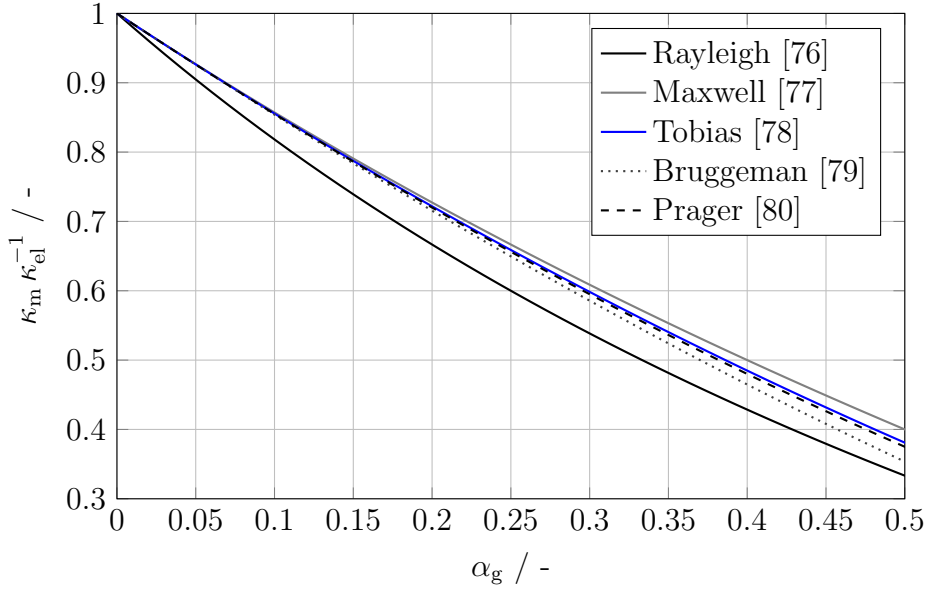


Figure 2.8.: Different models for the estimation of κ_{mixed} for the gas-liquid mixture for gas fractions between 0 and 50 %.

u_g^0 and u_{el}^0 by

$$\mathbf{u}_i^0 = \frac{\dot{V}_{el}}{A_{\text{cross}}} \text{ for } i = g, el \quad (2.18)$$

Here, \dot{V}_{el} is an adjustable process parameter, and \dot{V}_g is determined using equation 2.16. Inserting u_g^0 and u_{el}^0 in the equation

$$\mathbf{u}_b = u_g^0 + u_{el}^0 + u_{b,\text{swarm}} \quad (2.19)$$

proposed by Nicklin [84] enables the calculation of α_g based on the bubble velocity u_b and vice versa [75]. $u_{b,\text{swarm}}$ denotes the bubble swarm rise velocity due to buoyancy. Yet again, different correlations are available that correlate the swarm rise velocity to single rise velocity with the model by Richardson and Zaki [85] being one of the most common one:

$$\frac{u_{b,\text{swarm}}}{u_b} = 1 - \alpha_g^{4.65} \quad (2.20)$$

The presented Nicklin equation implies an increased liquid phase velocity due to the reduction cross-area by the gas phase. Hence, this equation adjusts for the error of superpositioning the superficial velocities of liquid and gas phases, highlighting the interplay between bubble velocity and gas phase fraction.

2.2. Optical measurement techniques for gas-liquid flow in electrolyzer

Several optical techniques have been deployed to study and measure the previously in Section 2.1.3 described impact of electrogenerated bubbles on the fluid flow and electrochemical reaction. The electrolyte flow, bubble size and velocity, and coverage have been measured by applying cameras, lasers, tracer particles, and other light sources on (partially) transparent electrolyzers. However, due to the small inter-electrode gap and housing of electrolysis cells, the application of optical flow measurement techniques in parallel plate electrolyzers is challenging and requires dedicated setups and evaluation methods. The following subsections present suitable bubble size and velocity determination methods and their results. Parts of the following sections are also reported correspondingly in the publications

Görtz, J., Seiler, J., Kolmer, P. und Jupke, A., „Raising the Curtain: Bubble Size Measurement inside Parallel Plate Electrolyzers“. *Chemical Engineering Science*, 286 (2024) [54] and

Görtz, J., Seiler, J., and Jupke, A., „Bubble up: Tracking down the Vertical Velocity of Oxygen Bubbles in Parallel Plate Electrolyzers Using CNN“. *International Journal of Multiphase Flow*, 177 (2024) [86].

2.2.1. Size determination of detached electrogenerated bubbles

As depicted in Figure 2.6, electro-generated bubbles undergo various stages until they detach into the bulk electrolyte. To measure the size at those various stages, different approaches have been presented in publications [58, 59, 87–89]. Since this thesis focuses on the macroscopic gas-electrolyte flow, this section focuses on the size distribution of detached bubbles and their influencing parameters.

Janssen and Sillen et al. [57, 59] were the first to thoroughly study the bubble size under different operating conditions. They constructed a poly-methyl methacrylate (PMMA)-cell and placed an optical-transparent vertical nickel electrode with a dimension of (3x1 cm) alongside a nickel perforated plate acting as counter-electrode. They used an inter-electrode gap of 4 mm and employed a high-speed camera with a microscope optic and a mercury lamp as a light source for image acquisition. Using their setup, they measured the size of bubbles attached to the transparent electrode and reported average sizes between 8-133 μm for O_2 and 4-32 μm for H_2 . Within a comparable scope, Chin Kwie Joe et al. [58] developed an electrochemical setup to study the size of detached O_2 , H_2 , and Cl_2 bubbles. Their setup comprises a 1.35 cm^2 thick compartment that features a 0.8 mm^2 thick and between 2 to

4 mm long wire working electrode. The material of the wire electrode is varied between nickel and coated as well as plain platinum, and the bubbles were recorded at 1.7 mm above the end of the wire with a high-speed camera. In a solution containing 4 M sodium-chlorine (NaCl) and 0.1 M hydro-chlorine (HCl) and $i = 0.1 \text{ A cm}^{-1}$, they measured an average detached bubble size of 40 μm , 55 μm , and 59 μm for H_2 , O_2 and Cl_2 , respectively.

Aside from these comprehensive studies that investigated the effect of operating parameters on the bubble size, different authors measured the bubble size alongside other aspects, e.g., flow velocities of the bubbles or electrolyte: Abdelouahed [90] measured the size of oxygen bubbles in an alkaline, lantern blade electrolysis and reported average values between 60 and 210 μm at, respectively, $i = 0.02$ and 0.2 A cm^{-1} . However, the camera's resolution and the method for the size determination are not provided. Also, utilizing a high-speed camera, Davis et al. [87] measured the size distribution of hydrogen in a membrane-less electrolyzer. For comparably low i of 0.02 A cm^{-1} , they measured an average diameter of 112 μm for H_2 bubbles using a circle detection algorithm. This circle algorithm is based on the *Circle Hough Transform* and detects spheres in an image but has trouble detecting overlapping objects [91]. Liu et al. [92] experimentally determined the size of oxygen bubbles during the electrochemical oxidation of *p*-methoxyphenol. Despite poor image quality, they applied various filters and reported the bubble size distribution following a Gaussian distribution alongside an average bubble size of 125 μm with a standard deviation of 35 μm . Cho et al. [69] measured the distribution of H_2 bubbles in a stationary electrolyte by using a set of a stainless steel and a platinum wire electrode as working and counter electrodes, respectively. They report an average size of 72 μm with a standard deviation of 21 μm . Studying the characteristics of hydrogen bubbles, Chandran et al. [93] report a decrease of the mean bubble size from 41 to 12 μm when increasing i up to 1.2 A cm^{-1} .

All of these works examined the small inter-electrode gap and relied on measuring bubbles that escaped the bubble curtain into the bulk electrolyte or measured at small i . Focusing on the escaped bubbles and image acquisition of the few millimeter-wide gap renders the bubble size determination erroneous and difficult [94]. To enhance object detection in images, neuronal networks have emerged and been shown to be superior to previously used algorithms [95].

2.2.2. Neuronal networks for image recognition

Most of the previously mentioned works on bubble sizes rely on traditional methods for image detection, and the measurement often involves manual or semi-automated techniques, which can be time-consuming and prone to human error. Further, using a filter often leads to reducing image information. Neural networks are able to learn and generalize from

large datasets, representing a novel, promising, and robust solution for the automation and improvement of this process [96].

Neural networks, particularly convolutional neural networks (CNNs), are well-suited for image recognition tasks due to their architecture mimicking the human visual system. These networks can automatically learn relevant features from raw image data through a series of convolutional and pooling layers that are exemplary depicted in Figure 2.9. For

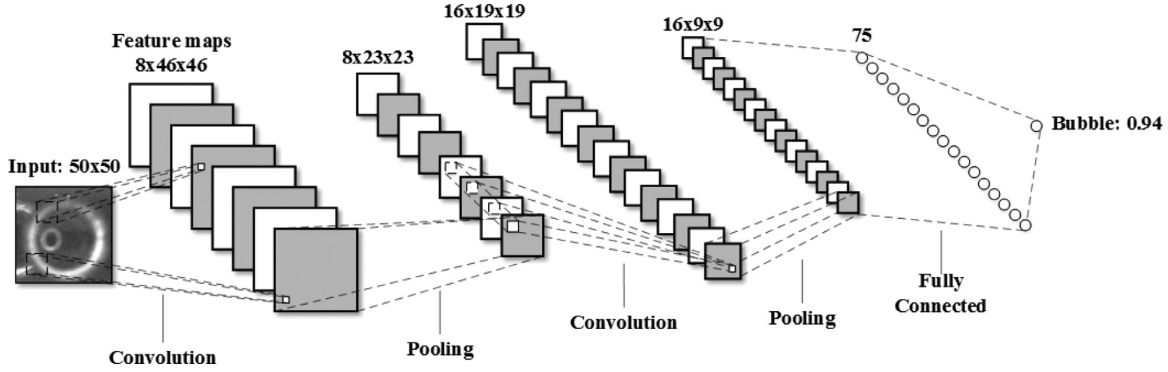


Figure 2.9.: CNN classifier architecture for the detection of bubbles in a two-phase bubbly jet used in Poletaev et al. [97]. Image is taken from Poletaev et al. [97].

image recognition, CNNs can be trained to detect objects in various conditions, including different lighting, backgrounds, and bubble sizes. This adaptability makes them highly effective for various technical and machine vision applications [96, 98].

The setup and implementation of neural networks for a specific object detection involves three basic steps:

- Data collection,
- network training, and
- validation.

A large dataset of annotated images is required to train the network effectively. When selecting the images, great care must be taken in order to prevent the over- or under-fitting of the neuronal network. Sibirtsev et al. [99, 100] examined different generalization and training strategies to either get dedicated weights for a specific purpose or obtain weights generally applicable to dispersed flows. The training process involves adjusting the network's parameters to minimize the error in object detection, which is measured by comparing the network's predictions to the ground truth annotations. Once trained, the network's performance is validated using a separate set of images that has not been used for training to ensure its accuracy and generalizability. To further improve the performance, the training and validation of the network can be repeatedly iterated by changing the pictures used for training and validation [98, 99].

Poletaev et al. [97] discussed and demonstrated the benefits of using neural networks for bubble image recognition. CNNs provide high accuracy and speed, reducing the need for manual intervention. Additionally, neural networks can handle complex and noisy images that feature overlapping objects, which are often challenging for traditional image processing techniques [95]. Recently, Sibirtsev et al. [99] published an adaptable open-source framework that is based on the Mask R-CNN algorithm [95, 101] and the implementation of Abdulla [102]. For a liquid-liquid system, Sibirtsev et al. [99] successfully generated weights for the droplet detection [99, 100] and further improved the generalizability [103].

2.2.3. Measurement of electrolyte and bubble velocity in electrolyzers

Besides influencing the local mass transfer at the electrode boundary, electrogenerated bubbles also shape the flow pattern inside electrochemical apparatuses with gas-evolving electrodes [104]. The huge density difference between the gas and electrolyte phases accelerates the bubbles, which exchange their momentum with the electrolyte based on their velocity u_b . Here, an increasing size of the gas bubble leads to greater momentum and affects on the local electrolyte velocity. Hence, both d_b and u_b define the flow, especially in the proximity of the electrodes [70, 105].

The challenges for experimental measurement of the bubble size has already been described in Section 2.2.1 and by Hreiz et al. [106]. Velocity measurements inside electrolysis cells encounter similar difficulties. Despite the small inter-electrode gap and overlapping bubbles, different authors applied different fluid flow measurement techniques to overcome these difficulties and study the bubble motion and the two-phase flow. Especially, velocity measurements of the bubble curtain and at industrial current densities of $i \geq 0.1 \text{ A cm}^{-1}$ commonly used velocimetry methods struggle or fail to measure u_b [106]:

- (i) Particle image velocimetry (PIV) involves illuminating and capturing of the flow twice within a short, distinct time frame. By dividing the images into small regions and applying cross-correlation techniques, the displacement of particles or pixels is determined and converted to velocity, providing a comprehensive velocity field of the fluid flow [107]. Boissonneau and Byrne [88] tried to apply the PIV algorithm for the measurement of u_b , but due to the presence of overlapping bubbles in the 2D-image were unsuccessful. To overcome the shortcomings of the technique, Kuroda et al. [108] utilized the cross-correlation PIV method developed by Cheng et al. [109] for u_b in areas with high bubble number densities and successfully implemented this technique in a small electrolytic cell [108]. Applying their algorithm to images taken at different current densities and inter-electrode gaps, they have measured time-averaged rising velocities between 15 and 70 mm s⁻¹. Hreiz et al. [94] have executed a study on u_b in a narrow vertical electrochemical electrolyzer applying a similar method. Prior to

exercising the PIV algorithm on taken photography, they pre-processed images and averaged them over several frames. They report average u_b between 0 and 20 mm s^{-1} that are considerably smaller lesser than the reported values from the work of Kuroda et al. [108]. Although, the time-averaging and filters used in both works lessens the reliability of the measured bubble velocity distribution, since it is affected by pre-processing parameters. In addition, the PIV algorithm does not allow for single bubble nor measuring the bubble size distribution.

- (ii) As suggested by its name, the laser Doppler velocimetry (LDV) depends on the Doppler effect to determine the velocity a particle. A laser is split into two beams that are focused on a specific position. If a particle passes the beams, it induces a fluctuation of the laser intensity. By measuring this fluctuation between the two beams, the velocity can be determined [107]. Though, the LDV-measurement inside the electrolysis cell is limited, because the bubble surfaces introduce numerous side reflections, especially at high bubble densities [94]. Despite the challenging application, Abdelouahed [90] tried to measure u_b inside an electrolysis cell by using the LDV. Unfortunately, the LDV algorithm was unable to register the increase of the velocity alongside the electrode that has been displayed by the manual tracking of single bubbles. By employing a back-scattered LDV, Boissonneau and Byrne [88] recorded the velocity of bubbles that escape the bubble curtain into the bulk and measured values for u_b between 4 and 120 mm s^{-1} . Nonetheless, their setup has not been capable of recording the (bubble) velocity close to the electrode.
- (iii) The third flow measurement technique tracks the movement of individual (tracer) particles within a fluid and is therefore referred to as particle tracking velocimetry (PTV). High-speed cameras capture sequences of images in specific time intervals, and specialized algorithms [110] identify and follow the particles over time. By analyzing the trajectories of these particles, bubbles or drops, their velocities and accelerations are calculated, offering detailed Lagrangian insights into the fluid dynamics [107]. Davis et al. [87] used an adapted PTV algorithm to examine the rising velocity alongside the bubble size of 20 hydrogen bubbles in a membraneless electrolyzer. For different bubble sizes of $d_b = 50$ up to $550 \mu\text{m}$ they determined velocity between $50 \mu\text{m}$ and 130 mm s^{-1} . By manually tracking bubbles between subsequent images, Abdelouahed et al. [111] measured velocities of oxygen bubbles of 5 up to 30 mm s^{-1} . However, they only considered small bubbles in the bulk electrolyte

Whereas the LDV method relies on lasers with a specific wavelength, PIV and PTV can work with any illumination. This flexibility regarding the employed light source makes the PTV, and especially the widely used PIV method, easily applicable [107]. Additionally,

open-source algorithms and software exist that can be applied to calculate the fluid flow from various images and videos. For example, PIVlab by Thielicke and Sonntag [112] is a MATLAB[®] App that is free of use and runs parallelized on a set of images. Numerous different PTV algorithms have been proposed in literature based on the target image quality and fluid flow. Different criteria are introduced to ensure the 'correct' tracking of particles between subsequent images [107, 110]. For example, increasing the number of consecutive frames in which a fitting trajectory for a particle has to be found dramatically increases the algorithm's accuracy. Vukasinovic et al. [110] proposed a Four-frame particle-tracking algorithm that superpositions the trajectory of a particle between two frames (k and $k+1$), an additional frame forward ($k+2$), and one frame backward ($k-1$). Thus, false detections can be minimized.

2.3. Modeling of electrochemical reactors

Like other chemical reactors, various model approaches exist to describe electrochemical reactors. Depending on the problem formulation, different model depths are available that vary from zero-dimensional, ideally mixed models [75] to spatially-resolved, three-dimensional computational fluid dynamic (CFD) models. Further, as depicted in Figure 2.2, different length scales exist, ranging from macroscopic gas-liquid flow regimes to single bubble nucleation and departure Zhang et al. [61], Van Damme et al. [113] downwards to molecular dynamic simulation [114]. Since this work focuses on the spatially resolved physical phenomena of fluid flow within the electrochemical reactor, a spatially-resolved CFD model is required, and suitable numerical models used in literature to describe the gas-liquid flow are presented in the following. Next, approaches that incorporate mass transfer and electrochemistry are introduced. Conclusively, the last subsection describes the reactor characterization using dimensionless numbers and residence time characteristics.

2.3.1. Gas-liquid flow in electrochemical reactors

For the modeling of the gas-liquid multiphase flow in electrochemical reactors, different numerical approaches have been employed to describe the fluid flow. Table 2.1 shows an overview of the different methods that have been used to model electrochemical reactors. In descending order of frequency of application for simulations, the most frequently used models are Full Euler-Euler, mixture, and disperse phase Modeling (DPM) or Euler-Lagrange. The three multiphase models differ in how the gaseous phase is described. Whereas the full Euler-Euler and Euler-Lagrangian model treat the continuous, electrolyte phase as an Eulerian Phase, the mixture model accounts for the gas phase by adjusting ρ and μ . With the assumption of incompressibility no mass transfer between phases, no reaction and

Table 2.1.: Overview of different simulation domains, multiphase models, and turbulence models for gas-liquid flows in electrochemical reactors (extended from Hreiz et al. [94]).

Authors	Simulation domain and solver	Multiphase model	Turbulence model	Electro-chemistry
Aldas [115]	2D steady	Full Euler-Euler	k- ϵ	Yes
Mat [116]	2D steady	Full Euler-Euler	No	Yes
Mat and Aldas [117]	2D steady	Full Euler-Euler	No	Yes
Aldas et al. [118]	2D steady	Full Euler-Euler	No	Yes
Charton et al. [105]	3D steady	Full Euler-Euler	k- ϵ RNG	Yes
Charton et al. [119]	3D steady	Full Euler-Euler	k- ϵ RNG	Yes
Alexiadis et al. [104]	2D transient	Full Euler-Euler	No	No
Alexiadis et al. [120]	2D transient	Full Euler-Euler	No	No
Alexiadis et al. [121]	2D transient	Full Euler-Euler	No	No
Alexiadis et al. [122]	2D transient	Full Euler-Euler	No	No
Abdelouahed et al. [123]	3D transient	Full Euler-Euler	No	No
Abdelouahed et al. [111]	3D steady	Full Euler-Euler	No	No
Wosiak et al. [67]	3D steady	Full Euler-Euler	k- ϵ	No
Liu et al. [92]	3D steady	Full Euler-Euler	k- ϵ	Yes
Dreoni et al. [124]	2D steady	Full Euler-Euler	No	No
Rodríguez and Amores [125]	2D steady	Full Euler-Euler	k- ϵ	Yes
Zhan et al. [126]	2D steady	Full Euler-Euler	Many	No
Zarghami et al. [127]	2D steady	Full Euler-Euler	RSE	No
Le Bideau et al. [128]	2D steady	Full Euler-Euler	No	No
Colli and Bisang [129]	2D steady	Euler-Electrolyte	No	Yes
Colli and Bisang [130]	2D steady	Full Euler-Euler	k- ω SST	Yes
Colli and Bisang [74]	2D transient	Full Euler-Euler	k- ϵ	Yes
Colli and Bisang [131]	2D transient	Full Euler-Euler	k- ϵ	Yes
Colli and Bisang [132]	2D transient	Full Euler-Euler	k- ω SST	Yes
Karimi-Sibaki et al. [133]	3D transient	Full Euler-Euler	Mixture	Yes
Dahlkild [134]	2D steady	Mixture	No	Yes
Wedin and Dahlkild [135]	2D steady	Mixture	No	Yes
Ipek et al. [136]	2D steady	Mixture	No	Yes
Mandin et al. [73]	2D steady	DPM	No	Yes
Hreiz et al. [106]	3D transient	DPM	No	No
Van Parys et al. [137]	3D transient	DPM	No	Yes
Rajora and Haverkort [138]	2D steady	Analytical	No	Yes
Nierhaus et al. [139]	3D steady	DNS+DPM	Yes	No

constant viscosity, the Navier-Stokes continuity and momentum equations for the Eulerian phase are written as

$$\frac{\partial \alpha_{\text{el}}}{\partial t} + \nabla \cdot (\alpha_{\text{el}} \mathbf{u}_{\text{el}}) = 0 \quad (2.21)$$

and

$$\frac{\partial (\alpha_{\text{el}} \rho_{\text{el}} \mathbf{u}_{\text{el}})}{\partial t} + \nabla \cdot (\alpha_{\text{el}} \rho_{\text{el}} \mathbf{u}_{\text{el}} \otimes \mathbf{u}_{\text{el}}) - \nabla \cdot (\alpha_{\text{el}} \boldsymbol{\tau}_{\text{eff}}) = -\alpha_{\text{el}} \nabla P + \alpha_{\text{el}} \rho_{\text{el}} \mathbf{g} + \mathbf{S}_{\mathbf{u}, \text{Transfer}}, \quad (2.22)$$

respectively [140]. Here, α_{el} refers to the volumetric electrolyte phase fraction, \mathbf{u}_{el} to the computed electrolyte velocity, ρ_{el} to the electrolyte density, \mathbf{g} to the gravitational vector, and P to the pressure field. $\boldsymbol{\tau}_{\text{eff}}$ represents the effective stress tensor and can be calculated by

$$\boldsymbol{\tau}_{\text{eff}} = \mu_{\text{eff}} [(\nabla \mathbf{u}_{\text{el}}) + (\nabla \mathbf{u}_{\text{el}}^T)] - \frac{2}{3} \mu_{\text{eff}} (\nabla \cdot \mathbf{u}_{\text{el}}) \mathbf{I} - \frac{2}{3} \rho_{\text{el}} k \mathbf{I}, \quad (2.23)$$

where μ_{eff} denotes the effective viscosity that is defined as the sum of the μ_{el} and the turbulent viscosity μ_t , k the turbulent kinetic energy, and \mathbf{I} the identity tensor. As tabulated in Table 2.1, different approaches are used for the calculation of $\boldsymbol{\tau}_{\text{eff}}$. When assuming a laminar flow, Newtonian fluid, and an incompressible flow, μ_t , k , and \mathbf{I} equal zero, and μ_{eff} can be simplified to

$$\mu_{\text{eff}} = \mu_{\text{el}} \nabla^2 \mathbf{u}_{\text{el}}. \quad (2.24)$$

To model the turbulence, Reynolds-Averaged Navier-Stokes (RANS) equations and models can be introduced. Here, the changes in flow quantities due to turbulence are decomposed into time-averaged and fluctuating components described using one of many turbulence models [140]. Common models that have been applied for the modeling of electrolyzers are the two-equation turbulence models k - ϵ and k - ω Shear Stress Transport (SST). The suitability of the latter for electrolyzers has been demonstrated by Colli and Bisang [130]. k - ω SST combines an accurate near-wall treatment with robustness in free-stream regions [140, 141]. The turbulent kinetic energy, k , and the specific dissipation rate, ω , can be calculated after Menter et al. [141] by:

$$\frac{\partial k}{\partial t} + U_i \frac{\partial k}{\partial x_i} = \frac{\tilde{P}_k}{\rho} - \beta^* k \omega + \frac{1}{\rho} \frac{\partial}{\partial x_i} \left[(\mu + \sigma_k \mu_t) \frac{\partial k}{\partial x_i} \right] \quad (2.25)$$

$$\begin{aligned} \frac{\partial \omega}{\partial t} + U_i \frac{\partial \omega}{\partial x_i} = & \alpha S^2 - \beta \omega^2 + \frac{1}{\rho} \frac{\partial}{\partial x_i} \left[(\mu + \sigma_\omega \mu_t) \frac{\partial \omega}{\partial x_i} \right] \\ & + 2(1 - F_1) \frac{\sigma_{\omega 2}}{\omega} \frac{\partial k}{\partial x_i} \frac{\partial \omega}{\partial x_i}. \end{aligned} \quad (2.26)$$

In addition, the turbulent viscosity is defined by

$$\nu_t = \frac{a_1 k}{\max(a_1 \omega, S F_2)}. \quad (2.27)$$

For the detailed blending functions and model parameters, the reader is revised to the detailed description of Menter et al. [141]. Depending on the mesh size, the turbulence model can either be fully resolved at the walls or approximated by wall functions.

Besides μ_{eff} , the disperse gas phase fraction α_g is the most defining parameter in equation (2.22) for multiphase flows [140] and reflects the disperse volume that is linked to the number of disperse particles N with a bubble volume of V_b in a unit volume V_{cell} by

$$\alpha_g = 1 - \alpha_{\text{el}} = \frac{\sum_{n=1}^N V_{b,n}}{V_{\text{cell}}}. \quad (2.28)$$

$\mathbf{S}_{\mathbf{u},\text{Transfer}}$ denotes the momentum exchange between both phases and depends on the selected disperse modeling method, acting forces and coupling mechanism. In case of an Euler-Lagrangian modeling approach, the momentum exchange is calculated for each cell by adding the exchanged momentum of all N_p particles in a volume by

$$\mathbf{S}_{\mathbf{u},\text{Transfer}} = \sum_{n=1}^{N_p} \mathbf{S}_{\mathbf{u},\text{Transfer},n}. \quad (2.29)$$

In contrast to summing each individual particle, the full Euler-Euler calculates the phase interactions and transfer terms using a representative diameter, e.g., the Sauter mean diameter. Based on the previous publications listed in Table 2.1, the most common fluid interaction forces in electrochemical reactors are the drag, gravitational, and virtual mass forces. Previous studies [126] have shown that the influence of the lift force is negligible. Depending on the bubble Reynolds number

$$\text{Re}_b = \frac{\text{Inertial forces}}{\text{Viscous forces}} = \frac{\rho_c |\mathbf{u}_b - \mathbf{u}_{\text{el}}| d_b}{\mu_{\text{el}}}, \quad (2.30)$$

and Eötvös number

$$\text{Eo} = \frac{\text{Gravitational forces}}{\text{Capillary forces}} = \frac{|\mathbf{g}| |\rho_{\text{el}} - \rho_g| d_b^2}{\sigma}, \quad (2.31)$$

different formulations of the drag force are available and listed in Table 2.2. In addition, Figure 2.11 displays the drag coefficient for various Reynolds numbers for the three most commonly utilized models for electrolyzers: Schiller and Naumann [142], Lain et al. [143], and Morsi and Alexander [144]. Since $\text{Re} \propto d_b$ and d_b is smaller than 1 mm (see section 2.2.1), the bubbles inside electrolyzers mostly maintain a spherical shape. The relation between the bubble shape and the Reynolds and Eötvös number is depicted in Figure 2.10. Within the spherical regime, the terms in Table 2.2 containing Eo can be neglected. As a result, all models except the one proposed by Lain et al. [143] and Hadamard and

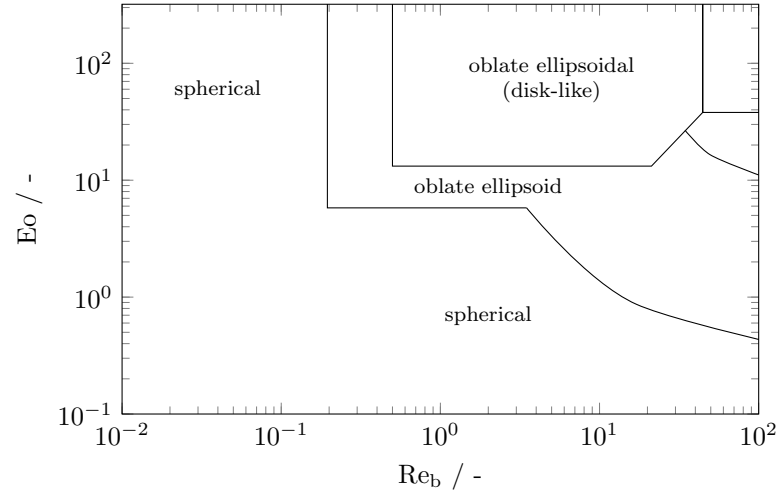


Figure 2.10.: Modified illustration of the different shape regimes of gas bubbles for different Reynolds and Eötvös numbers based on the findings of Bhaga and Weber [145].

Rybczński [146] calculate the same values for C_D for the spherical bubbles. Zhan et al. [126] analyzed the suitability of different drag models for aluminum electrolysis cells and concluded that the model by Grace et al. [147] fits the experimental data best. Nonetheless, the transfer to water-splitting electrolyzers is limited due to the large bubble size of 7 mm, and the associated bubble shape assumed in the study by Zhan et al. [126].

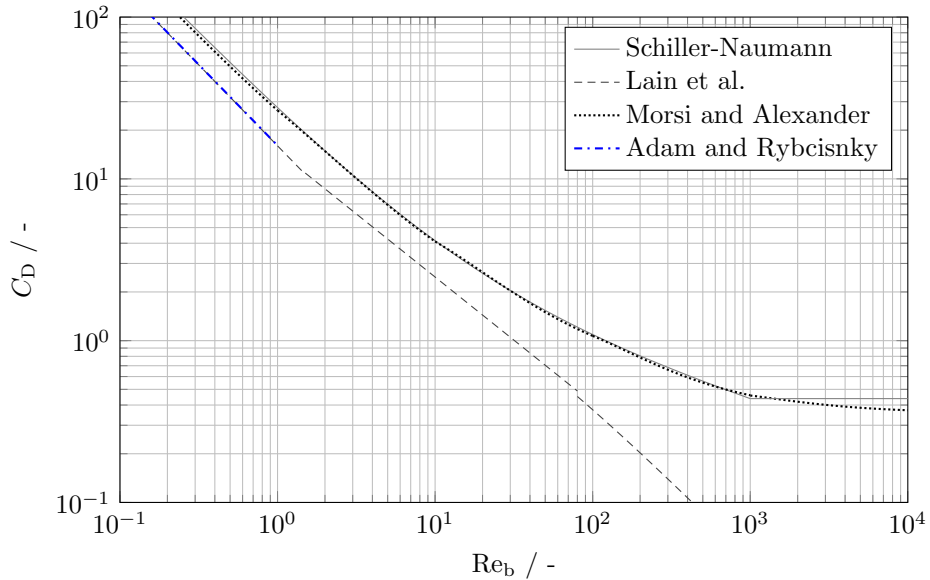


Figure 2.11.: Drag coefficient C_D as proposed by Schiller and Naumann [142], Morsi and Alexander [144] and Lain et al. [143] for different Re_b .

Contrary to the numerous drag models available to describe the fluid-fluid interactions,

Table 2.2.: Comparison of different drag coefficient correlations for spherical bubbles in the viscous region ($0 \geq Re_b \geq 1000$) that have been used for the modeling of gas-liquid flows in electrolyzers. Table is adapted from Mühlbauer et al. [148] and Sander [149].

Reference	Correlation	Related work
Rigid-bubbles		
Schiller and Naumann [142]	$C_D = \frac{24}{Re_b} (1 + 0.15Re_b^{0.687}) \quad Re_b \leq 1000$	[104, 124, 126, 127, 150]
Grace et al. [147]	$C_D = \max(C_{D,sphere}, \min(C_{D,ellipsoidal}, C_{D,cap}))$ $C_{D,sphere} = \frac{24}{Re_b} (1 + 0.15Re_b^{0.687})$	[126]
Ishii and Zuber [151]	$C_D = \max \left[\frac{24}{Re_b} (1 + 0.15Re_b^{0.687}), \min \left[\frac{2}{3}\sqrt{Eo}, \frac{8}{3} \right] \right]$	[124, 126]
Tomiyama et al. [152]	$C_D = \max \left[\frac{24}{Re_b} (1 + 0.15Re_b^{0.687}), \frac{8}{3} \frac{Eo}{Eo+4} \right]$	[126]
Morsi and Alexander [144]	$C_D = a_1 + \frac{a_2}{Re_b} + \frac{a_3}{Re_b^2}$, with $a_1, a_2, a_3 = \begin{cases} 0, 24, 0 & 0 < Re_b < 0.1 \\ 3.69, 22.73, 0.0903 & 0.1 < Re_b < 1 \\ 1.222, 29.1667, -3.8889 & 1 < Re_b < 10 \\ 0.6167, 46.50, -116.67 & 10 < Re_b < 100 \end{cases}$	[106, 124, 153]
Fluid-sphere		
Lain et al. [143]	$C_D = \begin{cases} \frac{16}{Re_b} + 14.9Re_b^{-0.78} & Re_b < 1.5 \\ 48Re_b^{-1}(1 - 2.21Re_b^{-0.5}) & 1.5 < Re_b < 80 \\ +1.86 \cdot 10^{-15}Re_b^{4.756} & 80 < Re_b < 1500 \\ 2.61 & 80 < Re_b < 1500 \end{cases}$	[129]
Hadamard and Rybczński [146]	$C_D = \frac{24}{Re_b} \left(\frac{1 + \frac{2\mu_{el}}{3\mu_b}}{1 + \frac{\mu_{el}}{\mu_b}} \right) \quad Re_b \leq 1$	[125]

the gravitational and virtual mass forces are defined by

$$\mathbf{F}_g = m_b \mathbf{g} (\rho_g - \rho_{el}) \quad (2.32)$$

and

$$\mathbf{F}_{vm} = C_{vm} \frac{m_b \rho_{el}}{\rho_g} \left(\frac{\partial (\mathbf{u}_{el} - \mathbf{u}_b)}{\partial t} \right) \quad (2.33)$$

respectively. The formulation of \mathbf{F}_{vm} corresponds to that proposed by Maxey and Riley [154] and is based on potential flow theory representing the addition of inertia due to the fluid displacement by the accelerating sphere. Depending on the bubble shape, C_{vm} varies between 0.5 and 1 [155] and equals 0.5 for spherical particles [154].

The following subsection presents the disperse phase modeling approaches Euler-Euler, Mixture, and Euler-Lagrange. For each model, the basic assumptions, coupling mechanisms, dis-, and advantages are introduced, and obtained results for electrochemical reactors are presented.

Full Euler-Euler

The full Euler-Euler approach is the most common approach for modeling the gas-liquid flow in electrolysis cells. Both liquid and gas phases are modeled as continuous phases and in addition to equations (2.21) and (2.22), a second continuity and momentum equation is solved [140]

$$\frac{\partial \alpha_g}{\partial t} + \nabla \cdot (\alpha_g \mathbf{u}_g) = 0 \quad (2.34)$$

and

$$\frac{\partial (\alpha_g \rho_g \mathbf{u}_g)}{\partial t} + \nabla \cdot (\alpha_g \rho_g \mathbf{u}_g \otimes \mathbf{u}_g) - \nabla \cdot (\alpha_g \boldsymbol{\tau}_{eff}) = -\alpha_g \nabla P + \alpha_g \rho_g \mathbf{g} + \mathbf{S}_u. \quad (2.35)$$

It has to be noted that the presented formulation of the continuity equations (2.21) and (2.34) are only valid when neglecting a mass transfer between the two phases. In addition to the momentum and continuity equation, the closing condition for the gas-liquid flow

$$\alpha_g + \alpha_{el} = 1 \quad (2.36)$$

has to be met. Without the addition of population balances, the full Euler-Euler model simply tracks the phase fraction in each cell of the computational domain without any information on the dispersed particle size. Based on the volume $V_{b,n}$ and surface $A_{b,n}$ of a

dispersed (bubbly) phase, a Sauter diameter

$$d_{3,2} = 6 \frac{\sum_{n=1}^N V_{b,n}}{\sum_{n=1}^N A_{b,n}} \quad (2.37)$$

is often specified as a constant property and then used to calculate the acting forces.

The complete Euler-Euler model is very robust and can be applied to various flow problems. Despite applying even to complex flow problems, the Euler-Euler model does not always produce the best physical results since empirical information is required to close the momentum equations [140]. For example, the value of α_g and, thereby, linked, the velocity of the entering gas volume flow \mathbf{u}_g at the electrode boundary has to be explicitly specified a priori to close the momentum equation [74, 104, 117]. Here, the chosen number is either an arbitrary value or an empirical correlation based on Faraday's law. Let alone the complexity and sensitivity of the chosen value for α_g on the fluid flow have been subject to a short communication by Alexiadis et al. [120].

Although the full Euler Euler model requires many empirical parameters that have to be specified a priori, published results using full Euler-Euler modeling were able to reproduce aspects of measured gas-liquid flows in electrolysis cells:

- The works by Alexiadis et al. [104, 121, 122] predicted the existence and transition of three different flow regimes, 'quasi-steady', 'transitional' and 'pseudo-turbulent' for parallel plate electrolyzers without a convective flow. These three flow regimes that have also been reported in experimental works [88, 118] are depicted in Figure 2.12. The transitional regime, displayed in Figure 2.12 (a), describes a segregated two-channel flow present at low current densities and larger bubbles. Due to the buoyancy forces of the gas bubbles, the electrolyte close to the electrode is accelerated, imposing high upward velocity. Due to the free surface on top, the velocity of the bubbles generates a backflow (II). By increasing i , the flow pattern changes to transitional as bubbles start to escape the bubble curtain, thus widening it. If an even greater i is applied, the two-channel flow completely breaks apart, and the bubbles start to chaotically move throughout the whole width between electrode and membrane (Figure 2.12 (c)).
- The local gas fraction predicted by full Euler-Euler models is able to depict experimental data in a 'suitable manner' [92]. The experimental validation is also challenging since measuring the gas phase fraction is already difficult, as described in Section 2.2. The excellent works by Colli and Bisang [74, 129, 130] were able to match the experimental one-dimensional and zero-dimensional data from Bisang [72] and Tobias [156]. Here, it has to be mentioned that parameters for, e.g., the bubble diameter, were adapted according to the electrolysis conditions.

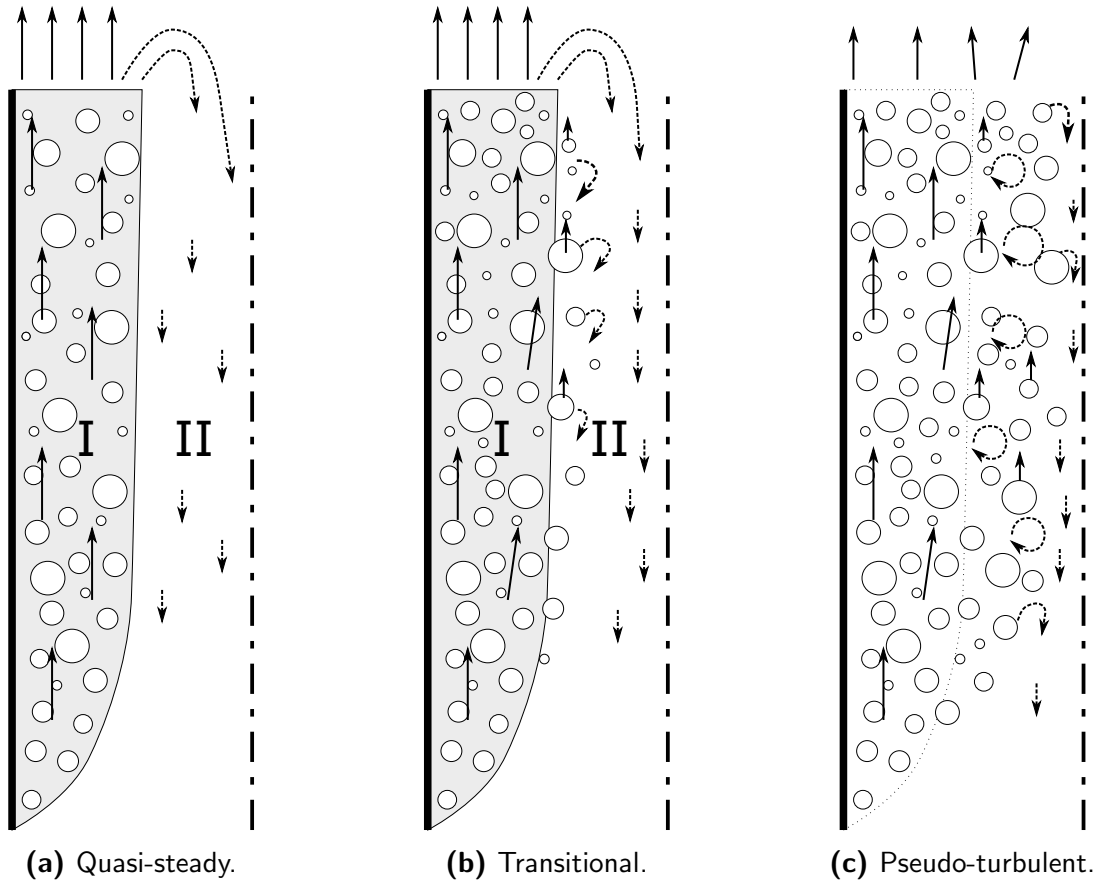


Figure 2.12.: Schematic drawing of different electrolyte flow patterns based on i under no net flow conditions based on the works of Alexiadis et al. [104, 121, 122]. The dashed vectors indicate the reflux or pseudo-turbulence of the electrolyte due to the bubble motion. Figure is taken from [86].

- In most cases, the full Euler-Euler model has struggled to predict the experimentally observed spreading of the bubble curtain [94]. As sketched in Figure 2.12, the bubble curtain width increases with greater i and over the height of the electrode. Some works, e.g. [73, 123], were unable to predict this phenomenon at all, captured the spreading solely due to numerical diffusion, or added turbulent and bubble dispersion forces and transverse migration terms.

Mixture Model

The mixture model is applicable when a strong interaction between dispersed continuous phases is assumed. In this case, the separate solving of momentum balances for each different phase is not required. Instead, a 'mixed' density ρ_m and viscosity μ_m is estimated

for the mixture based on the local gas phase fraction. For example, Dahlkild [134] defined

$$\mu_m = \mu_{el} \frac{1}{1 - \alpha_g} \quad (2.38)$$

and

$$\rho_m = \rho_{el}(1 - \alpha_g) \quad (2.39)$$

based on an empirical correlation by Ishii and Zuber [151]. Contrarily to the full Euler-Euler model, the mixture model does not require a specification of \mathbf{u}_g and α_g at the electrode surface to close the momentum balance. Next, the relative velocities of the different phases compared with the mean velocity of the mixture are calculated based on the acting forces, enabling the estimation of the velocity of the different phases. Afterwards, the continuity equations (2.21) and (2.34) are solved separately. Typical applications of the mixture model are bubble columns, fine particle suspensions, and stirred-tank reactors. Due to being applied to bubble columns, the mixture model has also been used to model gas-liquid flows in electrolyzers [134–136]. [94, 140]

Dahlkild [134] and Wedin and Dahlkild [135] introduced a mixture model for the gas-liquid flow and the electric current distribution along a gas-evolving electrode. They could predict the nonlinear decrease of current density alongside the electrode and match experiments conducted by Hine and Murakami [157]. Their results revealed a widening of the bubble curtain with greater i and increasing electrode height. Additionally, they report smaller local gas phase fractions at the electrode boundary when i is increased. The behavior of α_g agrees with the described phenomena in Figure 2.12. Additionally, they were able to match the electrolyte velocity profiles of Boissonneau and Byrne [88]. Ipek et al. [136] further developed the model, added the speciation, and pH calculation (similar to equations (2.8) and (2.9)) to the model, and applied it to the two-phase steel pickling. Nonetheless, the simulated flow and pH profile were not compared to experimental data. Although, Wedin and Dahlkild [135] demonstrated that the mixture model is a promising approach to reflect the fluid and physical phenomena within an electrolysis cell, it has yet to be used in recent years.

Euler-Lagrange

In contrast to the previous two models that model each phase as interpenetrating continua, the Euler-Lagrange models the dispersed phase as a cloud of point masses. Thereby, each point mass or parcel p resembles either a single or a group of bubbles, and their motion

within the flow field is tracked using Newton's second law of motion [158]:

$$\underbrace{n_p \frac{\pi \rho_g d_p^3}{6}}_{m_p} \underbrace{\frac{\partial \mathbf{u}_p}{\partial t}}_{a_p} = \mathbf{F}_{\text{Sum}}, \quad (2.40)$$

where a_p and m_p denote the parcel's acceleration and mass, respectively. \mathbf{F}_{Sum} sums up all forces acting on each bubble. In the case of an electrolysis cell, these are the previously introduced drag, gravitational, and virtual mass forces that arise due to the interaction with the surrounding fluid. The three forces and required dimensionless numbers are calculated based on the properties of the bubble and the local fluid motion. Using \mathbf{u}_p from equation (2.40), the change in bubble position \mathbf{x}_p for each single or group of bubbles can be obtained by

$$\int_{t_i}^{t_{i+1}} \mathbf{x}_p(t) dt = \int_{t_i}^{t_{i+1}} \mathbf{u}_p(t) dt \quad (2.41)$$

and transformed into the Euler-scheme [106, 158]

$$\mathbf{x}_p(t_{i+1}) = \mathbf{x}_p(t_i) + \mathbf{u}_p(t) \Delta t. \quad (2.42)$$

Finally, the change of momentum of all N_b bubbles ($\sum_{n=1}^N \mathbf{F}_{\text{sum},n}$) is exchanged with the continuous electrolyte phase. Based on α_b , different phase coupling mechanisms are proposed by Elghobashi [159] and depicted in Figure 2.13:

- For 'very dilute suspensions' ($\alpha_b \leq 10^{-6}$), the impact of the disperse phase on the continuous phase is entirely negligible. Hence, only the continuous flow field impacts the disperse phase through, e.g., drag forces. Since there is no back coupling of the dispersed phase, this approach is called one-way coupling.
- The modeling of 'dilute suspensions' ($10^{-6} < \alpha_b < 10^{-3}$) should include a momentum exchange between dispersed and continuous phases. This coupling mechanism is denoted as two-way coupling.
- 'Dense suspension' describes two-phase flows with $\alpha_b \geq 10^{-3}$ and demands the modeling of bubble-bubble interaction on top of the momentum coupling of disperse and continuous phase (two-way coupling). By implementing the bubble-bubble and bubble-wall collision, the so-called four-way phase coupling is completed.

In the case of electrolysis cells, the gas fraction is reported to exceed the threshold of 0.1 %, regardless of the modeling and experimental approach [117, 118, 123, 134]. Hence, simulations using the Euler-Lagrangian approach should account for the interactions between individual bubbles and fluid and bubbles. However, published studies [73, 106, 137]

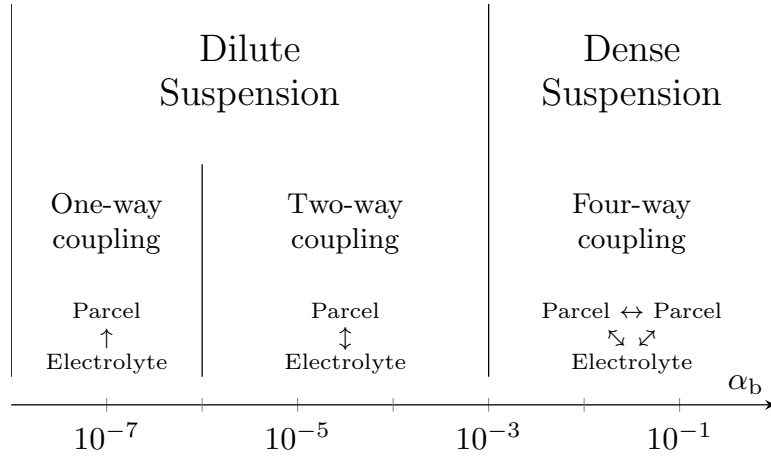


Figure 2.13.: Overview of the different phase coupling mechanisms between the Euler and Lagrangian phase. Figure is adapted with permission from Springer Nature from Elghobashi [159].

employed only two-way coupling. In order to enable four-way coupling, different models have been proposed:

Commonly, the model proposed by Cundall and Strack [160] and its alteration, e.g. [161], are used to model the four-way coupling in CFD simulation. Here, the collision is represented by a combined spring-dashpot system depicted in Figure 2.14. The model sys-

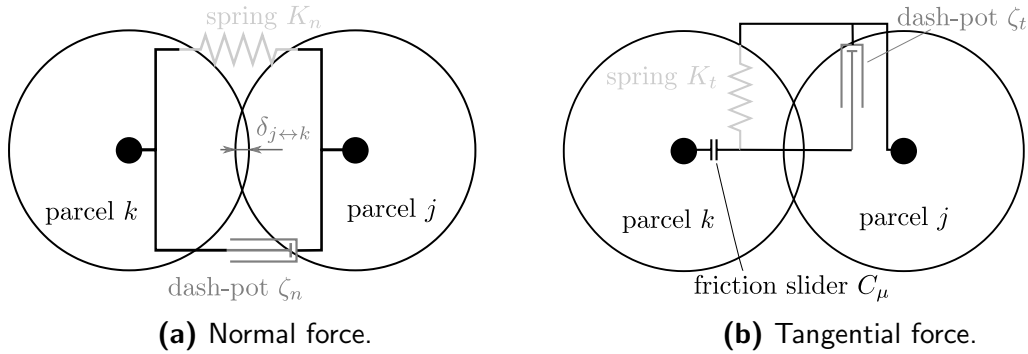


Figure 2.14.: Illustration of the used slider-dash-pot model. Figure is adapted with permission from Elsevier from Tsuji et al. [161].

tem accounts for the contact forces, stiffness, and damping that occur during the collision of parcels k and j or a parcel and a wall. The normal contact force $\mathbf{F}_{n,\text{elastic}}$ is calculated according to Hertzian contact theory:

$$\mathbf{F}_{n,\text{elastic}} = K_n \cdot \delta_{j \leftrightarrow k}^{3/2}, \quad (2.43)$$

where K_n denotes the spring constant that can be calculated by solid mechanical properties

and $\delta_{j \leftrightarrow k}$ the displacement that can simply be calculated by

$$\delta_{j \leftrightarrow k} = \frac{d_k + d_j}{2} - |\mathbf{x}_j - \mathbf{x}_k|. \quad (2.44)$$

Derived from the condition of critical damping, Cundall and Strack [160] introduced the damping during the collision \mathbf{F}_{ζ_n} by

$$\mathbf{F}_{\zeta_n} = -\zeta_n |\mathbf{u}_j - \mathbf{u}_k| \cdot \mathbf{n}_{j \leftrightarrow k}. \quad (2.45)$$

$\mathbf{n}_{j \leftrightarrow k}$ represents the normal vector between the center of the bubbles and ζ_n the damping coefficient. Lastly, tangential force \mathbf{F}_{tang} completes the model. Therefore, the slip velocity $\mathbf{u}_{j,k,\text{slip}}$ between two bubbles or bubble and wall is obtained by

$$\mathbf{u}_{j,k,\text{slip}} = |\mathbf{u}_j - \mathbf{u}_k| - (|\mathbf{u}_j - \mathbf{u}_k| \cdot \mathbf{n}_{j \leftrightarrow k}) \mathbf{n}_{j \leftrightarrow k}. \quad (2.46)$$

Depending on the quotient of $\frac{K_{\text{tang}} \delta_{j \leftrightarrow k}}{\mu_{\text{el}} |\mathbf{F}_{\text{elastic}} + \mathbf{F}_{\zeta_n}|}$, $\mathbf{u}_{j,k,\text{slip}}$ is then used to calculate \mathbf{F}_{tang} by

$$\mathbf{F}_{\text{tang}} = \begin{cases} \mu_{\text{el}} \delta_{j \leftrightarrow k} \frac{\mathbf{u}_{j,k,\text{slip}}}{|\mathbf{u}_{j,k,\text{slip}}|} & \text{if } \frac{K_{\text{tang}} \delta_{j \leftrightarrow k}}{\mu_{\text{el}} |\mathbf{F}_{\text{elastic}} + \mathbf{F}_{\zeta_n}|} > 1 \\ -K_{\text{tang}} \delta_{j \leftrightarrow k} - K_{\text{tang}} - \zeta_{\text{tang}} \mathbf{u}_{j,k,\text{slip}} & \text{if } \frac{K_{\text{tang}} \delta_{j \leftrightarrow k}}{\mu_{\text{el}} |\mathbf{F}_{\text{elastic}} + \mathbf{F}_{\zeta_n}|} \leq 1 \end{cases}, \quad (2.47)$$

where K_{tang} and ζ_{tang} denote the spring constant and damping coefficient in the tangential direction.

As the model of Cundall and Strack [160] and its derivatives have been successfully employed to reflect the collisions within granular flows in simulations, it does not apply to liquid-liquid, liquid-gas, liquid-wall, and gas-wall collisions. Both K_n and ζ_n rely on solid material properties, namely the shear and Young's Modulus, which are not defined for fluids. Additionally, light, deformable particles, like gas bubbles, experience greater deformation and shape change during a collision event. Further, the previously described models account for the kinetic energy of particles, which is negligible due to the low density of bubbles. Heitkam et al. [162] proposed a simple collision model explicitly applicable to bubble-wall and bubble-bubble collision of small gas bubbles. Analogously to the slider-dashpot model from Cundall and Strack [160], Heitkam et al. [162] introduced an elastic normal and tangential force but replaced the damping with a viscous force. Figure 2.15 depicts the equivalent network of the assumed collision of their work. Instead of direct contact, they assume that a gap with a width h_{gap} and a pressure p_{gap} exists between two colliding objects. h_{gap} represents the small fluid lamella separating the bubble from the collision object. Further, as depicted in Figure 2.15, an axisymmetric deformation and a constant spherical shape is assumed.

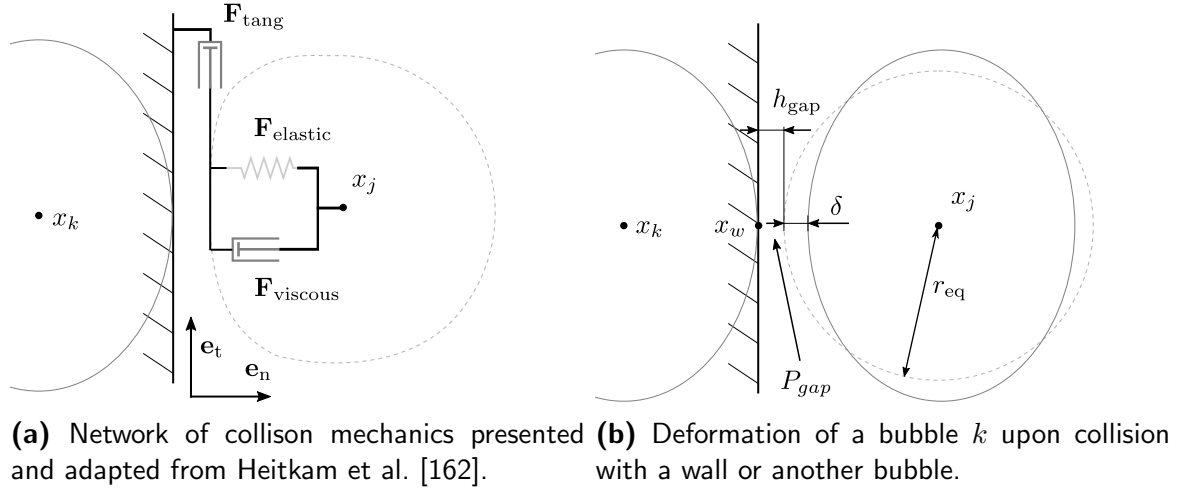


Figure 2.15.: Illustration of the used slider-dash-pot model from Heitkam et al. [162]. Adapted with permission from IOP Publishing.

Similar to the equation (2.44), Heitkam et al. [162] defined the distance deficit $\delta_{j \leftrightarrow k}^*$ for the collision between two deformed bubbles k and j by

$$\delta_{j \leftrightarrow k}^* = \frac{1}{2} \left(\frac{d_k + d_j}{2} - |\mathbf{x}_j - \mathbf{x}_k| + h_{\text{gap}} \right) \quad (2.48)$$

and the bubble-wall collision of j by

$$\delta_{j \leftrightarrow w}^* = \frac{d_j}{2} - |(\mathbf{x}_j - \mathbf{x}_w) \cdot \mathbf{e}_n| + h_{\text{gap}}, \quad (2.49)$$

where \mathbf{x}_j , \mathbf{x}_k , and \mathbf{x}_w denotes the bubble center of bubbles j and k or the nearest wall position, respectively. \mathbf{e}_n represents the normal vector from wall to bubble. As equation (2.48) indicates, the distance deficit is evenly attributed to the two bubbles in the event of a bubble-bubble collision.

Upon deformation, the elastic normal force $\mathbf{F}_{\text{elastic}}$ results from the variation of surface energy A_b and is expressed as

$$\mathbf{F}_{\text{elastic}} = \sigma \frac{dA_b}{d\delta}. \quad (2.50)$$

Here, σ denotes the surface tension of the bubble in the surrounding fluid. To describe the change in surface area, Heitkam deduced a physically motivated correlation that takes in the bubble diameter and distance deficit, enabling the calculation of $\mathbf{F}_{\text{elastic}}$:

$$\mathbf{F}_{\text{elastic}} = \sigma d_j \left[9.25 \left(\frac{2\delta_{j \leftrightarrow k|w}^*}{d_j} \right)^2 + \frac{2\delta_j}{d_j} \right]. \quad (2.51)$$

For the detailed derivation of the correlation for $\frac{dA_b}{d\delta}$, the reader is referred to publication

of Heitkam et al. [162].

To calculate the viscous normal force, the shape of the lamella has to be known [163]. For this, Heitkam et al. [162] divided the collision process into two schemes that are depicted in Figure 2.16: First, upon approaching the collision obstacle, the bubble remains spherical, and the fluid interacts with the bubble. In this regime, the fluid interacts with the bubble, and the Stokes flow between the wall and the bubble can be modeled using an expression derived by Cox and Brenner:

$$\mathbf{F}_{\text{viscous}} = -6\pi\mu_e l \mathbf{u}_j \cdot \mathbf{e}_n \frac{d_j^2}{4\delta_{j \leftrightarrow k|w}^*} \quad (2.52)$$

This force, also referred to as wall lubrication force, only occurs until the distance between

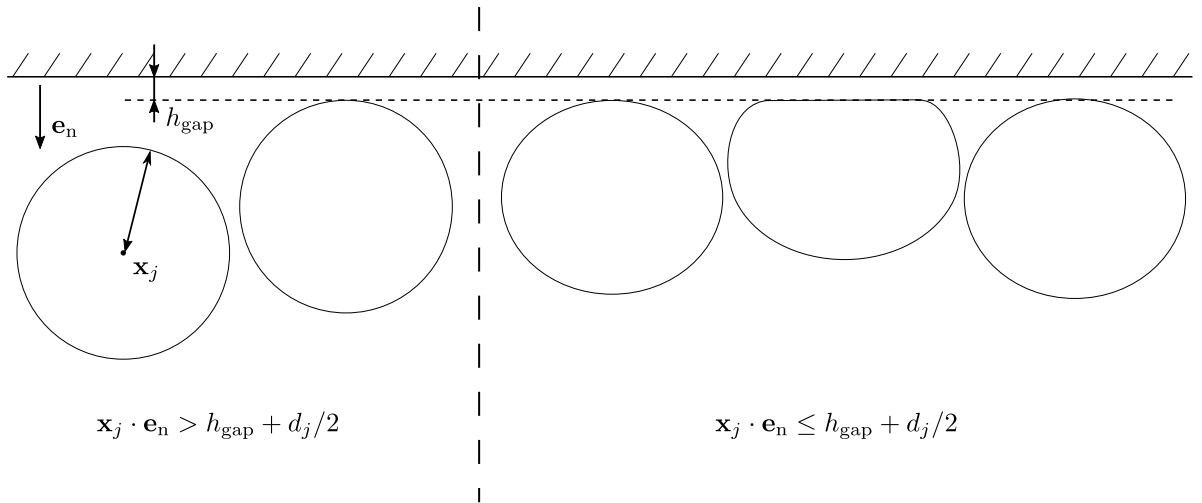


Figure 2.16.: Visualization of the simplified collision process and two validity ranges of the calculation of the viscous force after either (2.52) or (2.53) after Heitkam et al. [162]. Adapted with permission from IOP Publishing.

the center of the bubble and the wall exceeds the sum of bubble radius and fluid lamella ($\mathbf{x}_j \cdot \mathbf{e}_n > h_{\text{gap}} + d_j/2$). For the opposite case of $\mathbf{x}_j \cdot \mathbf{e}_n \leq h_{\text{gap}} + d_j/2$, Heitkam et al. [162] proposed a different viscous force that also accounts for the deformation and, hence, is valid for deformed bubbles. They assumed no-slip conditions on the bubble and obstacle surface, no influence due to tangential movement, and that the obstacle was either a planar wall or another bubble of a similar radius. During a collision, the fluid lamella is trapped and remains constant throughout the entire process. Using this simplification and an energy

balance for the kinetic energy and energy dissipation, the viscous force is deduced as

$$\mathbf{F}_{\text{viscous}} = 0.65 \mathbf{u}_j C_{bc} \mu_{el} \left(\frac{2\delta_{j \leftrightarrow k|w}^*}{d_j} + 0.0002 \right)^{-0.5} \cdot \left[4.0 \sqrt{\frac{d_j^3}{8h_{\text{gap}}}} + \frac{d_j^2}{h_{\text{gap}}} \left(-90.0 + \sqrt{8100 + 7.632 \frac{\delta_{j \leftrightarrow k|w}^*}{d_j}} \right) \right]. \quad (2.53)$$

The detailed model assumptions for the viscous force for deformed bubbles are included in the Supporting Information of Heitkam et al. [162].

Close to a wall, bubbles experience an additional friction force that completes the collision model and is sketched as \mathbf{F}_{tang} in Figure 2.15. This force can be calculated according to Goldman et al. [164] by using the distance to the wall $\delta_{j \leftrightarrow w}^*$ and fluid properties:

$$\mathbf{F}_{\text{tang}} = \frac{8}{5} \pi \mu_{el} \mathbf{u}_{j,\text{slip}} d_j \ln \left(\frac{2\delta_{j \leftrightarrow w}^*}{d_j} \right). \quad (2.54)$$

Despite α_b exceeding 0.1 %, prior works [73, 106, 137] have neglected the bubble-bubble interactions when applying the Euler-Lagrangian model to the liquid-gas flow. Compared to the Euler-Euler approach, the Euler-Lagrangian approach is computationally more intensive in most cases. Nonetheless, it offers the possibility to generate and track individual parcels alongside their trajectories and other properties, e.g., particle size [140]. Hereby, the Lagrangian approach allows the utilization of virtually any size distribution and injection pattern depicting the distribution of active sites [106, 137]. Further, the combined size and velocity tuple of a particles allows for a detailed examination of their interplay.

Using the Euler-Lagrangian model, Hreiz et al. [106] obtained a quasi-mesh-independent solution that showed good agreement with a PIV measurement they conducted. By solely considering drag and gravitational forces, they were able to model the bubble curtain spreading toward the center of the electrolyzer. Mandin et al. [73] applied the Euler-Lagrange model to match the experimental setup and results by Tobias [156]. Despite using a wide range of $0.1 \text{ mm} < d_b < 1 \text{ mm}$, they were able to reproduce aspects of the experimental data and suggested adding bubble-bubble interactions to the model. During their simulation, they observed gas phase fractions greater than 70 % that have not been experimentally reported anywhere. Mandin et al. [73] attributed this error to the possible overlapping of multiple particles when using two-way coupling.

2.3.2. Mass transport in pH-shift electrolyzers

As previously described, electrochemical reactions take place on the electrode surface. Therefore, new educts must be transported to and products away from the electrode surface

to enable a continuous reaction. When applying high current densities, this mass transport becomes the limiting factor of the reaction rate [33]. Hence, a maximal value for i is introduced as the limiting current density i_{lim} for the limiting condition at a certain cell potential. i_{lim} is a function of the concentration of the electrochemical active substance and its mass transport coefficient k_m and can be obtained by [33]

$$i_{\text{lim}} = zFk_m c. \quad (2.55)$$

From this equation, it follows that the flowing current can either be increased by raising the concentration or k_m . Usually, a change in the concentration is impracticable due to solubility and operating limits. Contrarily, k_m can be improved by mixing, forced convection, bubble-induced mixing, and optimized flow conditions by adapting the flow towards the electrode and inside the chamber [33]. The impact of the bubble-induced mixing has been studied thoroughly, e.g. [51, 72, 165], and based on experimental measurements, a semi-empirical correlation for k_m is proposed :

$$\text{Sh} = 1.38(1 - \alpha_b)^{0.5} \text{Re}^{0.5} \text{Sc}^{0.5}. \quad (2.56)$$

Here, k_m is included in the Sherwood number Sh

$$\text{Sh} = \frac{\text{Convective mass transfer rate}}{\text{Diffusive mass transfer rate}} = \frac{k_m \cdot \bar{d}_b}{D}, \quad (2.57)$$

and Sc denotes the Schmidt number

$$\text{Sc} = \frac{\text{Viscous diffusion rate}}{\text{Mass diffusion rate}} = \frac{\nu}{D}. \quad (2.58)$$

Equations (2.56) and (2.57) reflect the direct linkage of k_m to the bubble size d_b and gas phase fraction α_b . For optimizing the flow towards the electrode and inside the chamber, the previously introduced spatially resolved CFD models can be employed. Using the numerical models, different authors [89, 92, 129, 131, 132, 153, 166] conducted detailed studies of the mass transfer insight electrochemical units.

When describing or modeling the spatially dependent and/or time (t) concentration $c_w(t, \mathbf{x})$ of a species w , it can be distinguished between three different mass transport phenomena [167]:

- **Diffusion** describes the movement of particles or molecules from an area of high concentration to an area of low concentration, driven by the concentration gradient.
- **Electromigration** refers to the movement of charged particles under the influence of an external electric field due to the presence of an electric potential gradient $\nabla \Phi$.

- **Advective** mass transport involves the movement of particles or molecules with the bulk fluid flow and is directed by the velocity gradient of the fluid [33].

The Nernst-Planck equation describes mass transport of a species w and sums all three phenomena by

$$\frac{\partial c_w(t, \mathbf{x})}{\partial t} + \nabla \cdot \mathbf{J}_w = R_w, \quad (2.59)$$

where R_w denotes the change in concentration due to reaction(s) and \mathbf{J}_w the combined flux by [167]

$$\mathbf{J}_w = \underbrace{-D_w \nabla c_w}_{\text{Diffusion}} + \underbrace{c_w \mathbf{u}_{\text{el}}}_{\text{Advection}} + \underbrace{z_w F v_w c_w \nabla \Phi}_{\text{Electromigration}}. \quad (2.60)$$

Here, D_w and v_w represent the diffusion coefficient and mobility of an ionic species w , respectively. Combining the Nernst-Planck equation (2.59) with the calculated electrolyte velocity field \mathbf{u}_{el} that is obtained from solving the multiphase flow problem described in section 2.3.1 allows for the examination of concentration gradients in pH-shift electrolyzers.

2.3.3. Coupling of fluid flow and electrochemistry

Of the various authors that studied the gas-liquid flow in electrochemical reactors and are listed in Table 2.1, roughly two-thirds also modeled at least parts of the interplay of the fluid flow and mass transport, current distribution, or other electrochemical cell properties. Since the gas accumulates from bottom to top in a vertical gas-evolving electrode, the current distribution is also strongly non-uniform. However, for simplicity, different authors assumed a uniform distribution of i , resulting in an evenly distributed gas evolution alongside the electrode [104, 111, 120, 122].

Instead of a uniform volumetric gas flux, Mandin et al. [153] evaluated the gas phase fraction in the computational cells adjacent to the electrode. By using Bruggemann's law [79], the used theoretical relations in an adjacent cell k allow for the linking of $\alpha_b^k \propto \kappa_m^k \propto i^k \propto \dot{V}_g^k$. Using a similar approach, Charton et al. [105] obtained a current distribution alongside the electrode and reported an increase of about 18 %. In a magnesium electrolysis cell, Liu et al. [89] examined the impact of accounting for a non-uniform current distribution on the simulation. Their study showed that the current distribution has only little effect on the liquid velocity profile inside the cell, but also demonstrated a substantial variation of i along the electrode. Nonetheless, at the boundaries of the simulation domain, i shows a nonphysical behavior and more than doubles compared to the center area of the electrode.

Colli and Bisang [74] distributed the volumetric gas flux weighted by the local gas phase fraction at the electrode $\alpha_{b,w}$ that they calculated using a correlation proposed by Vogt et al. [55, 56, 168]. Their novel approach considers the ohmic drop in the fluid phase and

the previously described mass transport enhancement of the gas bubbles. Further, this approach matches their experimental data for the current distribution over the height exceptionally well. Here, they recorded the current distribution over height using a specially designed electrolysis setup with electrodes that was segmented into 25 sections.

Besides the effect on the distribution of generated gas, gas phase fraction, and velocity, the electrochemistry, and fluid flow coupling also enables the calculation and study of the cell voltage. By using equation (2.2) and simplification for the transport and kinetic overpotential, the model by Colli and Bisang [130] can match experimental data of cyclic voltammetry experiments using rotating disc electrodes [35] at different rpm. Using the electrochemical setup with segmented electrodes, Colli and Bisang [74] were able to predict the experimentally measured cell voltage at different u_{el}^0 and i with errors between -6 and 1 %. Their toolbox also offers the possibility of distinguishing between potentiostatic and galvanostatic control. Potentiostatic refers to the operation at a certain cell (or reference) potential, whereas a galvanostatic operation implies the variation of the cell potential to achieve a set current flow [33].

By combining the fluid flow with electrochemical laws, complex models can be set up that show great potential to, e.g., predict the spatially-resolved current distribution and cell potential of electrochemical reactors. Though, a study by Liu et al. [89] suggests that the impact of the current distribution on the gas phase fraction is relatively small, resulting in a relative change in the local gas phase fraction by 10 % at $\alpha_b = 0.06$. Additionally, they report that the velocity distribution is hardly affected. Further, as shown in Section 2.3.1, other authors were also able to reproduce experimental findings regarding the flow patterns and velocities by assuming a uniform current distribution. Hence, the complexization of the model by adding of electrochemical laws must be evaluated against the goals of each individual study.

2.3.4. Flow characterization of ideal reactors

As presented in the previous sections, the gas-liquid flow is of great importance to the performance of electrochemical reactors. Besides detailed specially resolved measurements introduced in Section 2.2.3, the flow can also be characterized by dimensionless numbers that are based on the residence time distribution (RTD). The RTD reflects the mixing inside a chemical reactor that ranges from a plug-flow reactor (PFR) with no axial mixing to an ideally mixed continuous stirred tank reactor (CSTR). Here, both PFR and CSTR represent ideal cases, and the RTD of actual reactors lies in between these boundaries. To experimentally study the RTD, two different approaches are available [169, 170]:

- (i) The pulse injection alters a tracer concentration c_0 at the input of a reactor at a distinct time t_0 and for a time interval Δt before returning to the concentration

before the start of the injection. At the outlet of the reactor, a detector measures the pulse response. The inlet concentration $c_{\text{in,pulse}}(t)$ is defined as

$$c_{\text{in,pulse}}(t) = \begin{cases} c_0 & t \leq t_0 \\ c_{\text{pulse}} & t_0 + \Delta t > t > t_0 \\ c_0 & t \geq t_0 + \Delta t \end{cases} \quad (2.61)$$

- (ii) A step injection increases the concentration of a tracer at a distinct t_0 and maintains this concentration throughout the whole RTD experiment. Usually, the experiment finishes when the measured concentration at the reactor outlet matches the one at the inlet. The concentration $c_{\text{in,step}}(t)$ during a step injection is defined by

$$c_{\text{in,step}}(t) = \begin{cases} c_0 & t \leq t_0 \\ c_{\text{step}} & t > t_0 \end{cases}. \quad (2.62)$$

When experimentally determining the RTD of a reactor, the tracer can either be a concentration of a particular substance or small tracer particles detected after passing through the outlet. In order to obtain the mean residence time \bar{t} , the dead time t_{dead} of the reactor periphery is first subtracted from the actual time t , and the monitored concentration at the outlet $c_{\text{out}}(t - t_{\text{dead}})$ is normalized by

$$F(t) = \frac{c_{\text{out}}(t - t_{\text{dead}}) - c_0}{c_{\text{step}} - c_0}. \quad (2.63)$$

Subsequently, the RTD function $E(t)$ is defined as the derivative of the normalized concentration $F(t)$

$$E(t) = \frac{dF(t)}{dt} \quad (2.64)$$

and \bar{t} can finally be obtained by [170]

$$\bar{t} = \frac{\int_0^\infty t \cdot E(t) dt}{\int_0^\infty E(t) dt}. \quad (2.65)$$

Here, through normalizing $c(t)$, the denominator in equation (2.65) is equal to one and can thus be neglected. As experimental values are taken at distinct time intervals Δt , the numerator in equation (2.65) can be approximated using a trapezoidal method for N data

points [171]:

$$\int_0^\infty t \cdot E(t) dt \approx \Delta t \left[\frac{t_0 \cdot E(t_0)}{2} + \sum_{j=1}^{N-1} t_j \cdot E(t_j) + \frac{t_N \cdot E(t_N)}{2} \right] \quad (2.66)$$

In addition to \bar{t} , the variance $\bar{\sigma}_t$ is an indicator for the spreading or width of $E(t)$ and is defined by

$$\bar{\sigma}_t = \int_0^\infty (t - \bar{t})^2 \cdot E(t) dt. \quad (2.67)$$

To compare the characteristics of the RTD for different operating conditions, e.g., flow rate, the time is normalized by

$$\theta = \frac{t}{\bar{t}}, \quad (2.68)$$

allowing the dimensionless expression of the RTD functions using θ . Further, $\bar{\sigma}_t$ can also be rewritten as

$$\bar{\sigma}_\theta = \frac{\bar{\sigma}_t}{\bar{t}}. \quad (2.69)$$

$\bar{\sigma}_\theta$ is linked to the widely used Bodenstein number (Bo) by

$$\bar{\sigma}_\theta = \frac{2}{\text{Bo}} + \frac{8}{\text{Bo}^2} \quad (2.70)$$

The Bodenstein number allows for the quantification of the axial dispersion coefficient D_{ax} based on the reactor length L_{reactor} and superficial electrolyte velocity u_{el}^0 :

$$\text{Bo} = \frac{u_{\text{el}}^0 L_{\text{reactor}}}{D_{\text{ax}}}. \quad (2.71)$$

The ideal cases of an ideally mixed CSTR and ideal PFR correspond to Bodenstein numbers of 0 and ∞ , respectively. Hence, in an ideal PFR with $\text{Bo} = \infty$, it follows from equation (2.71) that the axial dispersion coefficient D_{ax} equals zero. [170]

Exemplary, Figure 2.17 shows $F(t)$, $E(t)$, $t \cdot E(t)$, and the corresponding area for \bar{t} for experimental data. For illustration, the bottom and top x-axis show the time and corresponding dimensionless parameter θ , respectively. The $\text{Bo}=14$ indicates that the convective transport is predominant and 14 times greater than the diffusive transport, which still plays a significant role.

Kocks [172] measured \bar{t} for different pairs of u_{el}^0 and i in three prototypes with different electrode-membrane gaps. For the prototype with the smallest electrode-membrane gap of 6 mm and at u_{el}^0 of 1.4 mm s^{-1} , he reported a change in the RTD with respect to i . Between $i = 0$ and 0.01 A cm^{-1} , the electrochemical reactor performed more like a PFR. In contrast, at higher i it transitions towards a CSTR, and the RTD widens. This observation fits well with the described pattern in Figure 2.12. With greater i , the flow becomes pseudo-

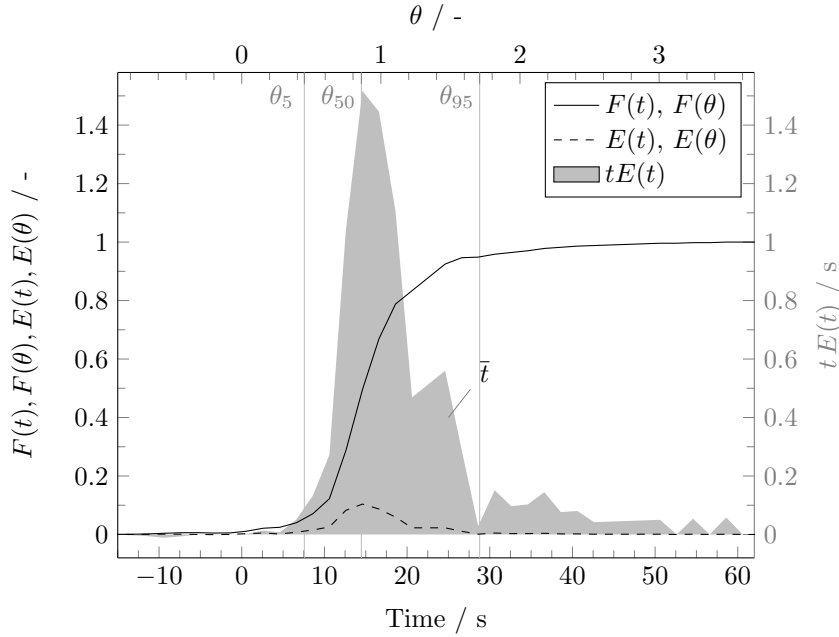


Figure 2.17.: Illustration of the normal and normalized RTD function $E(t)$, $E(\theta)$, summed RTD function $F(t)$, $F(\theta)$ and $E(t) \cdot t$ for artificial experimental data. Here, \bar{t} , $\bar{\sigma}_t$ and Bo amount 18.6 s, 7.3 s, and 14, respectively.

turbulent, increasing the mixing inside the reactor. At higher u_{el}^0 of circa 14 mm s^{-1} , the impact of the gas bubble on the RTD becomes smaller, and independent of i , the RTD leans towards an ideally mixed CSTR. The RTD of the prototype with a slightly enlarged electrode-membrane gap of 8 mm shows a similar trend. At an electrode-membrane gap of 10 mm, the reactor exhibited a large axial dispersion and showed a widened RTD. This work enables the study and selection of a distinct behavior of the axial dispersion inside an electrochemical reactor based on operating conditions.

Besides experimental studies, RTD can also be determined based on CFD simulations introduced in Section 2.3.1. Using a steady-state or transient velocity field, a fluid tracer can be modeled as either pulse or step and the response at the outlet of the computational domain can be measured. This allows for a quick 0D comparison between CFD models and experimental measurement data. Aparicio-Mauricio et al. [173] showed the potential of combining both simulation- and experimental-based RTD determination for the locating of stagnant zones inside a redox-flow battery.

3. Experimental study of the gas-liquid flow in parallel plate electrolyzers

This chapter presents the experimental study of the liquid-gas flow inside parallel plate electrolyzers. First, the implemented methods for obtaining the distribution of bubble size d_b and velocity u_b alongside the contact angle Θ and a 'mixed' velocity of bubbles and electrolyte are described. Next, the results of the size determination of oxygen and hydrogen bubbles for different u_{el}^0 , i , c_{Na^+} and electrode materials are presented alongside measured values for Θ . Subsequently, the distribution of u_b with respect to different size bins is described for different operating parameters. Next, the measured 'mixed' velocity obtained by the PIV algorithm allows a three-dimensional insight into the velocity field in the parallel plate electrolyzer. Large parts of this section are also reported in

Görtz, J., Seiler, J., Kolmer, P. und Jupke, A., „Raising the Curtain: Bubble Size Measurement inside Parallel Plate Electrolyzers“. *Chemical Engineering Science*, 286 (2024) [54] and

Görtz, J., Seiler, J., and Jupke, A., „Bubble up: Tracking down the Vertical Velocity of Oxygen Bubbles in Parallel Plate Electrolyzers Using CNN“. *International Journal of Multiphase Flow*, 177 (2024) [86].

In this thesis, instead of using a number-based density distribution q_0 as in Görtz et al. [54], the bubble size distributions are reported as volume-weighted q_3 distributions.

3.1. Methods

This section introduces the methods for studying the gas-liquid flow inside a tailored parallel plate electrolyzer. First, the chemicals and materials used are listed. Next, the novel, customized parallel plate electrolyzer is introduced, followed by the camera setups and employed lighting installation. Thereafter, the methods for the data acquisition from the raw image data are presented: A neuronal network based on the Mask R-CNN structure is trained to detect of gas bubbles, enabling the measurement of the bubble sizes and positions in images. Based on the obtained data containing tuples of size and position, a

PTV algorithm is developed to determine u_b . Additionally, the camera angle is changed, and the method for a PIV measurement of the electrode-membrane gap is introduced. Hereafter, a simplified method for determining the contact angle Θ is introduced.

3.1.1. Materials, chemicals, and electrochemical stability

Deionized water with a conductivity below $0.7 \mu\text{S cm}^{-1}$ is internally produced to prepare electrolyte solutions. Sodium sulfate (Na_2SO_4 , $\geq 99 \text{ wt}\%$) is procured from Acros Organics BKBA (Geel, Belgium), while succinic acid (H_2SA , $\geq 99 \text{ wt}\%$) and di-sodium succinic acid (Na_2SA , $\geq 96 \text{ wt}\%$) are acquired from Sigma Aldrich (St. Louis, USA). PMMA sheets are supplied by Vink König Deutschland GmbH (Gilching, Germany), and Magneto Special Anodes B.V. (Schiedam, The Netherlands) is the provider of IrOMM and RuOMM-coated and plain titanium electrodes, with no information available regarding the composition of the base material and coatings. The cathode is manufactured from a Nickel 205 (99.6 wt% Nickel) sheet and provided by Teprosa GmbH (Magdeburg, Germany). Polyamide tracer particles for the PIV measurement are acquired from LaVision[®] with a diameter of $60 \mu\text{m}$.

3.1.2. Experimental Setup

To circumvent the described limitations in section 2.2, a dedicated parallel plate is designed and manufactured. By introducing a customized electrode geometry, three viewing panels are machined into a titan sheet and later coated with IrOMM and RuOMM. The insertion of the three viewing panels allows for a spatial equalization of the bubble curtain, overcoming typical limitations when recording the inter-electrode gap, mainly due to bubble overlapping.

Figure 3.1 illustrates the cell, which is composed of two electrodes, a cation exchange membrane, sealing cords, two lids, and two electrolyte chambers. The lids and electrolyte chambers are constructed from 8 mm thick PMMA, resulting in an electrode-membrane distance of 8 mm and an electrode-electrode distance of approximately 16 mm. The custom-made electrode has three small viewing panels, each with a width of 62 mm and a height of 10 mm and the whole geometry is depicted in Figure 3.2. This electrode geometry was machined into both PMMA lids to allow the electrode to be inserted flush. Both electrolyte chambers have small strips to secure the Nafion 117 membrane from Frontis Energy (Probstzella, Germany) in place, and threads are tapped into both lids for the inlets and outlets of the electrolyte. The anode chamber and lid are transparent, while the mirrored cathode side is opaque to prevent the illumination of cathodically produced hydrogen bubbles. The active geometric area of the electrodes is 117.2 cm^2 , and the DC-power supply PSI 9000 T from EA Elektro-Automatik GmbH (Viersen, Germany) is utilized as a power supply for

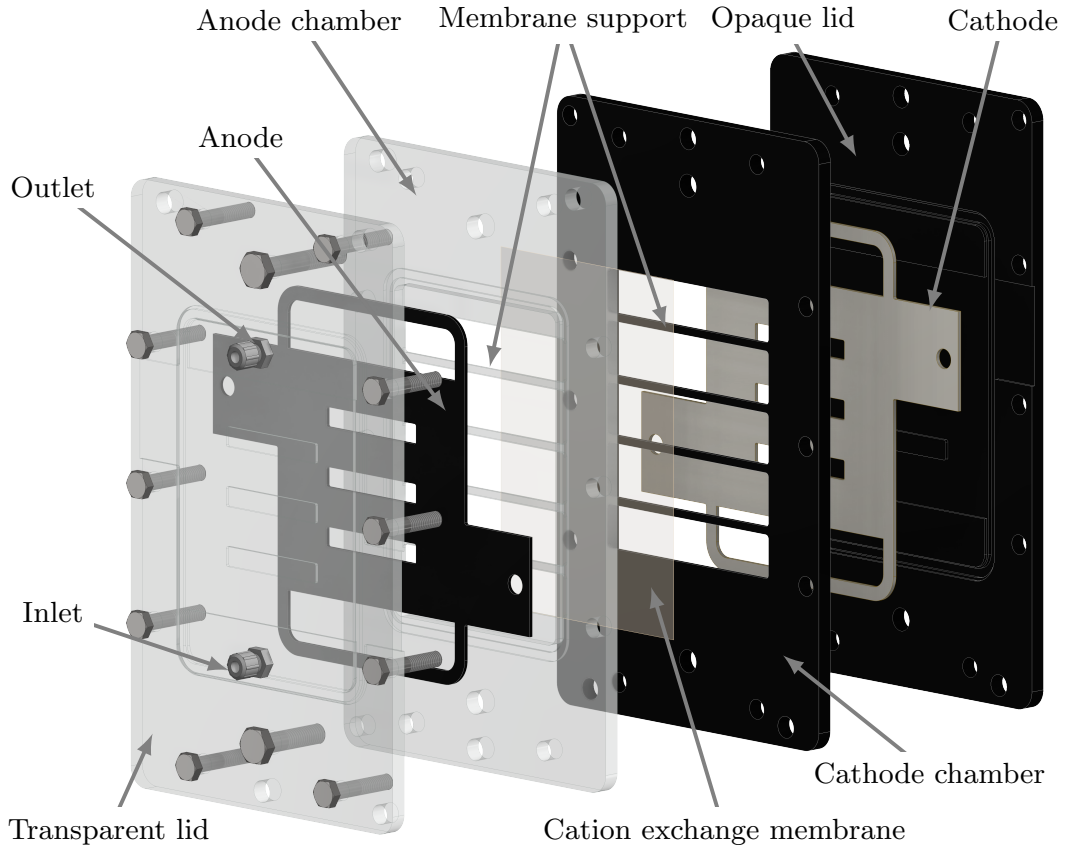


Figure 3.1.: The developed novel parallel plate electrolyzer for the study of the gas-liquid flow. It consists of two PMMA lids, two PMMA electrolyte chambers and two customized electrodes. For clarity, the sealing chords and mats are not shown. The image is taken from Görtz et al. [54].

the experiments.

Figure 3.2 (a) illustrates the movement of the electrolyte within the electrolyzer. The electrolyte is pumped from the bottom to the top of the cathode and anode chamber through the inlets and outlets located at the front and back of the electrolyzer, utilizing two MCP Standard peristaltic pumps from Cole-Parmer GmbH (Wertheim, Deutschland). As it circulates, the electrolyte passes through the three viewing panels (bottom, middle, and top) depicted in Figure 3.2 (b). The outer brim of the electrode is not in contact with the electrolyte. Instead, it is designed to apply pressure on the sealing chords and mats, thus improving the impermeability of the electrolyzer. The pH value before and during each experiment is monitored and measured by the pH meter HND-R106 from KOBOLD Messring GmbH (Hofheim am Taunus, Germany) paired with the pH electrode pHenomenal® 221 from VWR International GmbH (Langenfeld, Germany). LabView®

high-speed camera (HRHSC), XS Mini 5k, can record 5k-images but at a lower maximal framerate than the OS X 4 camera. Depending on the application, three different lenses from Kowa Optimed Deutschland GmbH (Düsseldorf, Germany) that suit 4/3" sensors were combined with the HRC. Two telecentric lenses, LM1119TC and LM1138TC, allow for magnifications of 0.5-1x and 2x, respectively. Additionally, a wide-angle lens, LM25XC, with a focal length of 25 mm was inserted to study the electrode-membrane gap. Table 3.1 tabulates the characteristics of each different camera-lens combination.

Table 3.1.: Characteristics of the camera setups used for the study of the gas-liquid flow.

Camera	LRHSC	HRHSC		
Lens	1X-WD110-1.1-NI	LM1119TC	LM1138TC	LM25XC
Sensor size	1.1"	4/3"	4/3"	4/3"
Lens type	telecentric	telecentric	telecentric	wide-angle
Magnification	1x	0.7x	2x	*
Pixel size (μm)	13.68	5	1.75	*
Field of view (mmxmm)	14x14	25.6x14.4	9x5	*
Depth of field (mm)	0.3	1.6	0.2	*
Exposure time (ms)	1.7	0.9	0.039	X
Maximum fps	3000	400	400	400

*dependent on the working distance between object and camera

3.1.3. Bubble detection and size determination using Mask R-CNN

To detect bubbles in the acquired images and subsequently measure their size, an algorithm based on the popular neuronal network architecture Mask R-CNN [101] and its implementation by Abdulla [102] is employed. Sibirtsev et al. [99, 100] further developed this algorithm to detect droplets in liquid-liquid extraction systems and published the source code publicly as a free, Python-based, open-source repository [174]. This implementation is adopted and trained using 40 experimental images. Approximately 70 bubbles were manually annotated for each image, as illustrated in Figure 3.3. To mitigate overfitting, filters like gamma-manipulation, and blurring alongside flipping, rotating, and mirroring were applied to the images. Additionally, a four-fold cross-validation technique was employed that splits the 40 images into 4 equally sized bins. In each epoch, three of the four bins are randomly selected for training, and the remaining bin is selected for validation. The resulting training and validation losses for different training epochs are displayed in Figure 3.4 and show no signs of overfitting. Since no substantial improvement was noticed after 70 epochs, the training was stopped after 80 epochs.

During each experiment, 2,000 frames are captured over the course of 10 s. Afterwards, the electrolyte is pumped out of the anode chamber to eliminate any stuck bubbles and

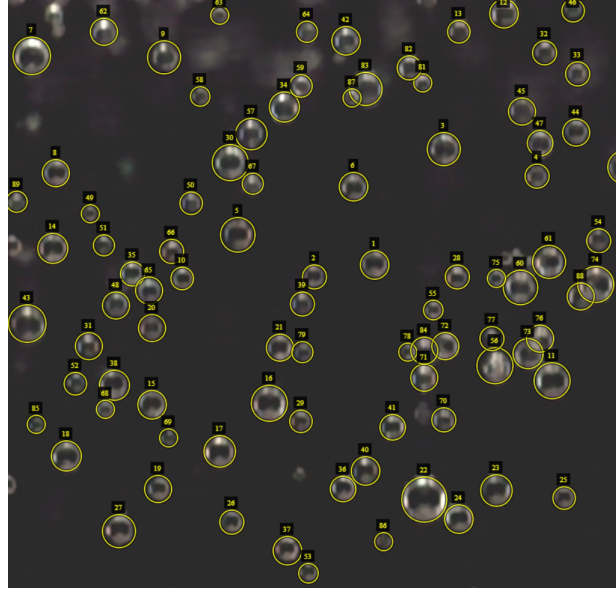


Figure 3.3.: Sample of the annotated images for the training of the CNN.

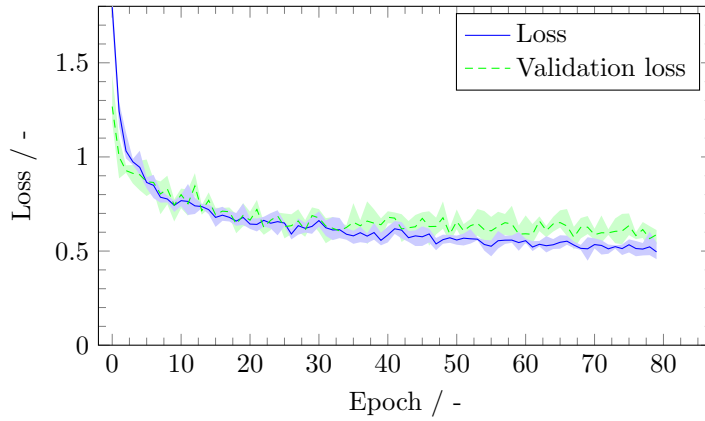


Figure 3.4.: Combined loss and validation loss of the CNN during training against the epoch number [54].

to fill the chamber with new electrolyte. Subsequently, each frame is passed to the Mask R-CNN algorithm, and for each detected bubble, the algorithm finds the bounding boxes around the object. Next, it measures the pixel width w and height H , calculates the bubble size by

$$d_b = \sqrt{wH}, \quad (3.1)$$

and stores the size alongside the center position and frame number in a list. Since the bubbles show little to no deformation, bubbles with an aspect ratio outside of $0.8 < W : H < 1.2$ are discarded. Additionally, bubbles with a bounding box that collides with the edge of the image are also removed from the list, as the bubble shape might be erroneous. The utilized optical setup exhibits a lower detection limit of roughly $27 \mu\text{m}$ and cannot capture any nano-scale bubbles [114].

Finally, the bubble size distribution can be obtained by using the stored sizes of the list. The number-based density distribution, q_0 , uses all entries, whereas the volume-based density distribution, q_3 , first weights all sizes by their corresponding volume. Independent of the type of distribution, the bubble size distribution can be plotted using a histogram or box plot diagram. To plot a histogram, the size range is divided into a calculated [175] or chosen number of size bins and the frequency or volume fraction of all bubbles belonging to a size bin in relation to the number or volume of all detected bubbles is determined. For a comprehensive comparison of different operating parameters, box plot diagrams feature the key characteristics \tilde{d}_{\min} , d_{25} , d_{50} , d_{75} , and \tilde{d}_{\max} , respectively representing the adjusted minimum, 25th, 50th, and 75th percentile, and adjusted maximum values. In this thesis, the minimal and maximum values are defined by

$$\tilde{d}_{\min} = \max(d_{\min}, d_{50} - 1.5 \cdot \text{IQR}) \quad (3.2)$$

and

$$\tilde{d}_{\max} = \min(d_{\min}, d_{50} + 1.5 \cdot \text{IQR}) \quad (3.3)$$

with IQR being the interquartile range that is defined by

$$\text{IQR} = d_{75} - d_{25} . \quad (3.4)$$

Values exceeding \tilde{d}_{\max} or falling below \tilde{d}_{\min} are regarded as outliers and will not be represented in the box plot diagram for better readability. All of the previous post-processing steps can also be applied to different evaluation frame rates by only evaluating each second, third, fifth, or tenth frame.

3.1.4. PTV algorithm for the measurement of the bubble velocity

To measure the horizontal and vertical bubble velocity, a PTV algorithm based on the four-frame, forward-backward algorithm used by Vukasinovic et al. [110] is implemented, depicted in Figure 3.5, and is described in the following: The algorithm starts by using the in the previous section 3.1.3 described object list of bubble sizes, and positions with the corresponding frame number. Next, a queue is created that stores all objects for a base frame n , the next two ($n+1$, $n+2$) and previous frame, $n-1$. Then, for each detected bubble in the base image n , the algorithm scans the one-frame forward image ($n+1$) for every bubble with a distance between the center points in between a minimum $r_{1,\min}$ and maximum radius $r_{1,\max}$. For each determined bubble pair, the sizes are compared by

$$s = \frac{|d_{b,n+1} - d_{b,n}|}{d_{b,n}} . \quad (3.5)$$

If the relative size exceeds a set threshold s_{\max} , the bubble pair is discarded. For the

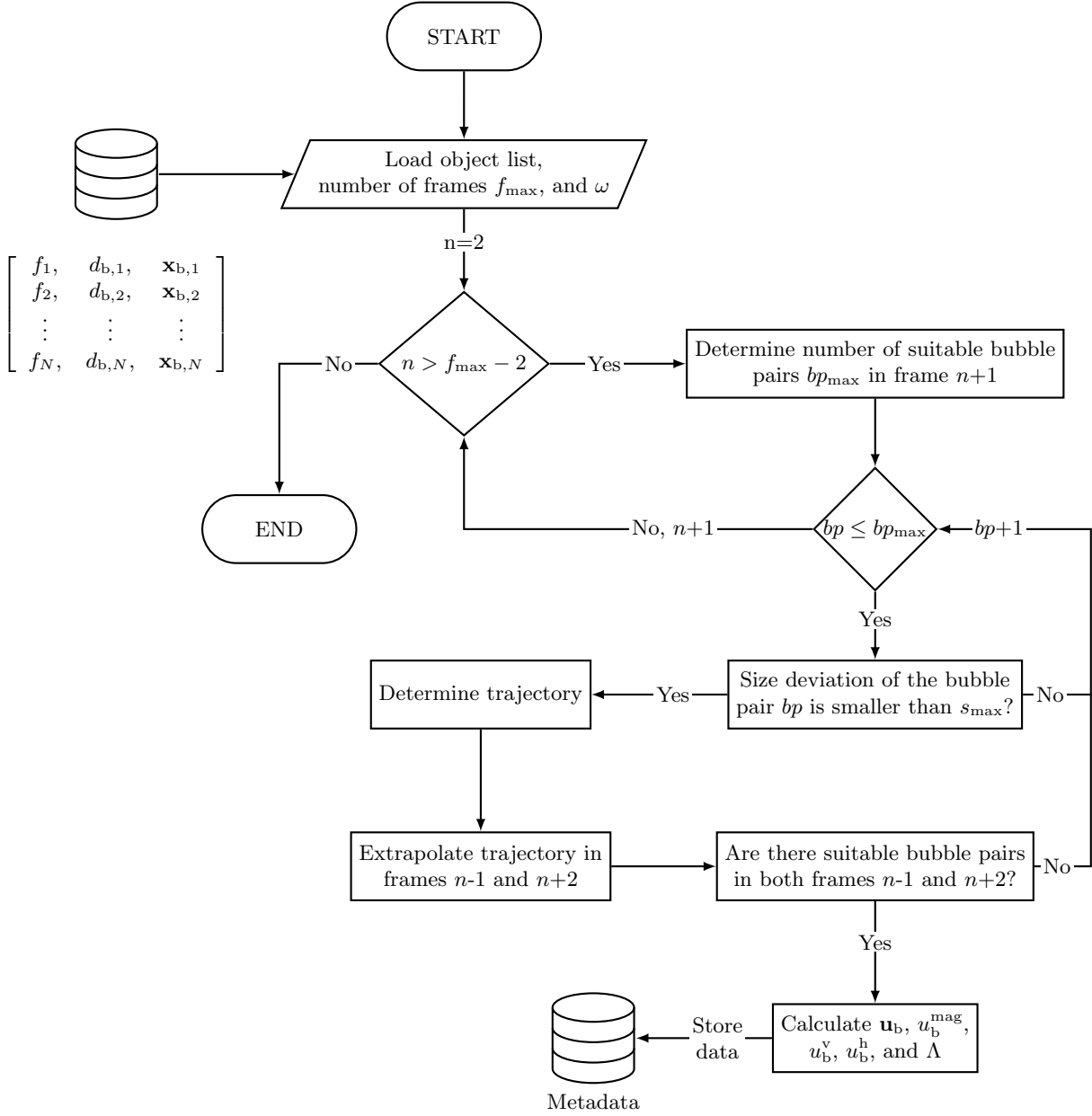


Figure 3.5.: Illustration of the developed PTV algorithm for the bubble velocity determination based on the implementation of Vukasinovic et al. [110].

remaining pairs, the trajectory is calculated by

$$\Delta \mathbf{x}_{n \rightarrow n+1} = \mathbf{x}_{b,n+1} - \mathbf{x}_{b,1} \quad (3.6)$$

and is projected into the one frame backward ($n-1$) and two frame forward ($n+2$) frame by the simple superposition of the trajectory:

$$\begin{aligned} \mathbf{x}_{b,n-1} &= \mathbf{x}_{b,n} - \Delta\mathbf{x}_{n \rightarrow n+1} \\ \mathbf{x}_{b,n+2} &= \mathbf{x}_{b,n} + 2\Delta\mathbf{x}_{n \rightarrow n+1} \end{aligned} \quad (3.7)$$

If bubbles are found in both frames $n-1$ and $n+2$ whose positions lie within a radius $r_{2,\max}$ around $\mathbf{x}_{b,n-1}$ and $\mathbf{x}_{b,n+2}$ respectively, the trajectory $\Delta\mathbf{x}_{n \rightarrow n+1}$ is converted into \mathbf{u}_b of the starting bubble by

$$\mathbf{u}_b = \Delta\mathbf{x}_{n \rightarrow n+1} \cdot f. \quad (3.8)$$

Figure 3.6 illustrates the algorithm and Figure 3.7 shows an example of a section from four

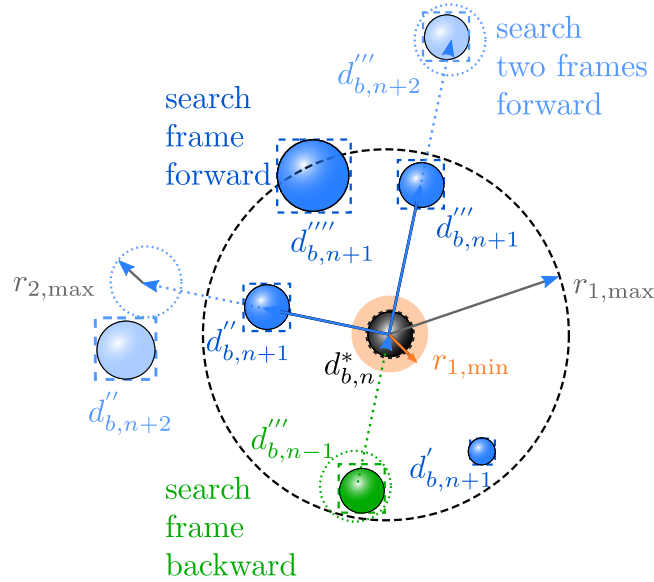


Figure 3.6.: Illustration of the further developed four-frames, forward-backward PTV algorithm from Vukasinovic et al. [110]. The indices indicate the frame number. $r_{1,\min}$ represents the threshold for the stuck particle detection and $r_{1,\max}$ for the maximal velocity. The image is taken from [86].

consecutive frames, where a bubble is tracked over the series of four frames. Additionally, the vector \mathbf{u}_b can also be split into the horizontal u_b^h , and vertical u_b^v components, as well as transferred into the velocity magnitude u^{mag} . From the relation of the velocity components, the angle of descent Λ can be obtained by

$$\Lambda = \arctan \left(\frac{u_b^h}{u_b^v} \right). \quad (3.9)$$

By this definition, $\Lambda = 0^\circ$ refers to a bubble ascending solely vertically.

After the bubble velocity and angle of descent are obtained, the algorithm creates and stores an object for each bubble. Afterwards, it proceeds and moves the base frame one

frame forward ($n+1 \rightarrow n$). Suppose trajectories are found for an object in subsequent sets of frames. In that case, the algorithm calculates the acceleration by

$$\mathbf{a} = (\mathbf{u}_{b,n} - \mathbf{u}_{b,n+1}) \cdot f \quad (3.10)$$

and stores it alongside the other values inside the bubble object. Table 3.2 stores the

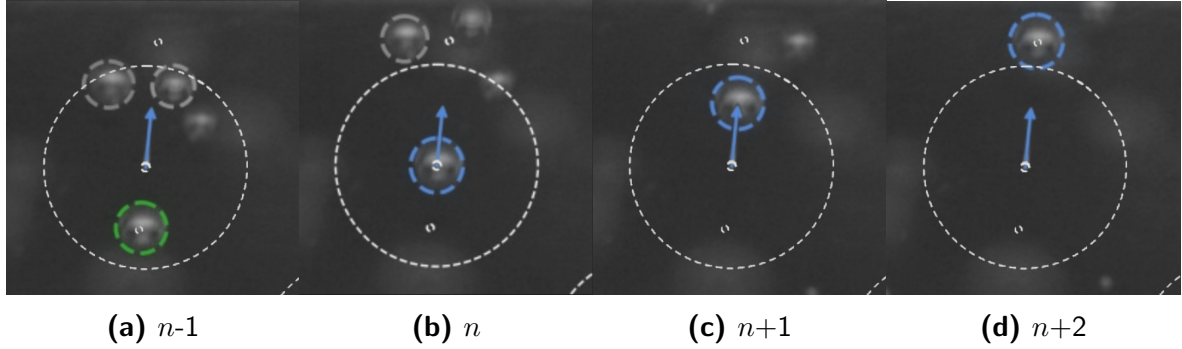


Figure 3.7.: Sample of the introduced four-frames, forward-backward PTV algorithm applied to a series of four frames. Here, for the blue bubble **(b)** in the base frame, matching bubbles in the **(a)** backwards, **(c)** forward, **(d)** and two forward frames are found. Images are taken from [86].

parameters for the four-frame, forward-backward PTV algorithm used within this thesis in pixels and their corresponding velocity for the HRHSC with a 0.7x resolution and $f = 200$.

Table 3.2.: Chosen parameter for the minimal, and maximal search radii and maximal size deviation s_{\max} for the four-frame, forward-backward PTV algorithm.

Parameter	Value	Corresponding value
s_{\max}	10 %	-
$r_{1,\min}$	5 px	5 mm s^{-1}
$r_{1,\max}$	150 px	150 mm s^{-1}
$r_{2,\max}$	8 px	8 mm s^{-1}

During each PTV measurement, a total of 2000 images are taken over 10 s. Though, only the last 500 frames are fed to the PTV algorithm since this number is sufficient to reflect the velocity distribution. Increasing the number of images did not alter the distribution. For the visualization of the velocity of different sized bubbles, all determined bubble velocities are sorted into equally 100 μm -spaced size bins regarding the complementary bubble size. Similar to the representation of the bubble sizes (section 3.1.3), the velocity can be plotted as histograms, box plot diagrams with \tilde{u}_{\min}^v , u_{25}^v , u_{50}^v , u_{75}^v , and \tilde{u}_{\max}^v and with the arithmetic mean values \bar{u}_b^v and standard deviation $\varsigma(u_b^v)$ for the different size bins.

When implementing a PTV algorithm to measure the bubble velocity based on images, errors in the measurement arise from two sources of uncertainty, namely position and accel-

eration uncertainty [176]. Position uncertainties emerge due to the influence of the particle positions on \mathbf{u}_p , as shown in equations (3.6)–(3.8). The position errors are introduced by random noise in the images, inaccuracies in the bounding boxes produced by our R-CNN algorithm, and the finite pixel size of the camera sensor. Following Feng et al. [176], the position error Γ can thus be estimated by

$$\Gamma = \sqrt{2 \cdot \mathbf{x}_{\text{error}}^2 f^2}. \quad (3.11)$$

For the values tabulated in Table 3.2, a pixel deviation results in $1.41 \text{ mm s}^{-1} \text{ px}$. For instance, for an average velocity of 40 mm s^{-1} , the resulting relative error would be 3.5 %, but it becomes larger as the velocity decreases.

Particle acceleration errors are only present if a particulate tracer is used to measure the velocity of a continuous (electrolyte) phase. Here, the error quantifies possible deviations between the velocity of the particulate tracer and the continuous phase due to the deceleration and acceleration of the tracer particles. The greater particles' momentum, the greater the error, as they cannot account for sudden changes in the velocity field of the continuous phase. Since the PTV algorithm is employed to determine the velocity of the dispersed bubble phase, this error is negligible, and we can also measure the acceleration by equation (3.10) [86, 176].

3.1.5. PIV algorithm of the anode-membrane gap

Besides the PTV algorithm, which resolves the two-dimensional bubble velocity in horizontal (x) and vertical (y) directions, the gas phase fraction and velocity in the normal yz -plane is of great importance as it captures the possible recirculation of the electrolyte and bubbles alongside the width of the bubble curtain [104]. To capture the velocity in the yz -plane, the LED bars and camera positions must be modified. In order to measure a defined area, an LED bar is placed directly onto the surface of the transparent lid on either the top or bottom viewing panel. Most of the viewing panel is masked off so that only a 5 mm wide and 10 mm height section is illuminated. The camera setup consists of the HRHSC with the LM25XC wide-angle lens, which is placed on the short side of the electrolyzer, aimed towards the electrode-membrane gap, and is used to capture images at the bottom and top positions. Figure 3.8 depicts the lighting setup and illuminated field.

The acquired raw images are evaluated as depicted in Figure 3.9. First, the images are preprocessed using a Python script. There, the images are semi-automatically corrected for a possible tilt, subsequently cropped, and optimized regarding brightness and contrast. Afterwards, all images are fed into PIVlab [112], which determines the velocity of each image. Here, the algorithm determines a velocity field for each frame based on itself and

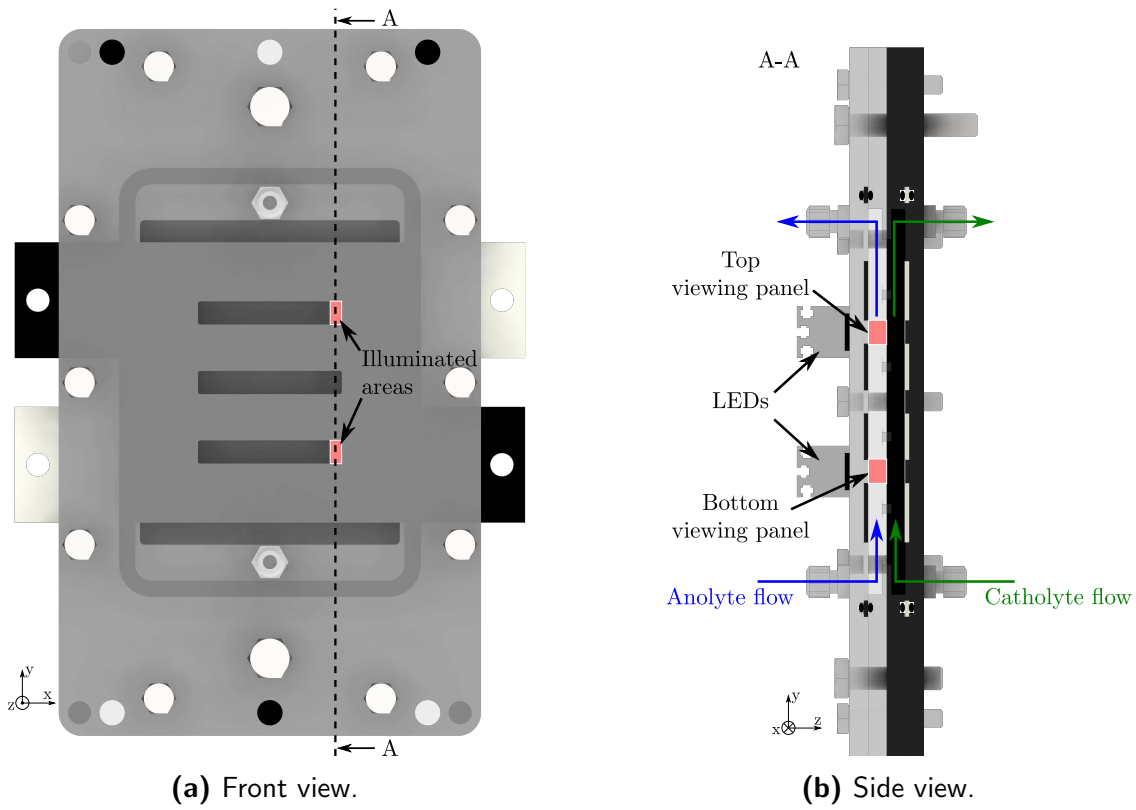


Figure 3.8.: Illustration of **(a)** the front and **(b)** side view of the modified illumination and the two viewing panels at which images are recorded for the PIV algorithm.

the following frame. Hence, $N-1$ velocity fields are obtained, averaged, and saved and the vertical velocity component along a line parallel to the z -axis (see Figure 3.37) is extracted.

As described in section 2.2.3, PIVlab is an open-source toolbox that includes a PIV algorithm for image data and is based on the work of Thielicke and Sonntag [112]. The algorithm requires multiple inputs to obtain a velocity field based on two images. The standard PIV algorithm that uses a direct Fourier transform correlation with multiple passes and deforming windows (FFT window deformation) is selected for this analysis. This FFT window deformation algorithm is known to deliver the best results in most situations [112]. The standard settings are selected for the correlation robustness as increasing the robustness did not yield any noticeable improvements but significantly increased the analysis computational time. The subpixel estimators, Gauss 2x3 and 2D Gauss, yielded similar results; thus, the Gauss 2x3 was selected. By measuring the number of pixels of the flow frame in the image, the pixel size amounts to $6.67\text{ }\mu\text{m}$. By try and error, three interrogation steps were selected with step sizes of 128, 64, and 32 px, which are depicted in Figure 3.10. A step size of 32 px corresponds to the average bubble size and further reducing the step size introduced noise into the velocity fields. Starting with a greater first interrogation value had no impact. Table 3.3 summarizes all the parameters and settings used in the PIV algorithm.

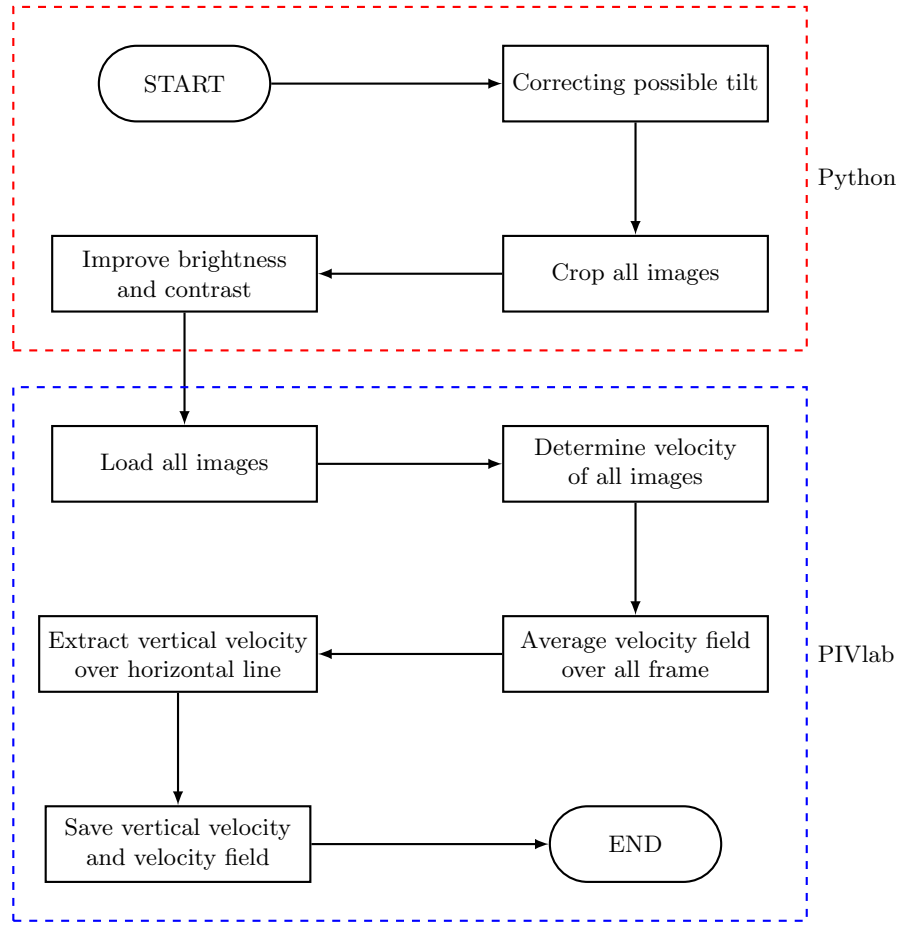


Figure 3.9.: Flow chart of the evaluation process of the raw image data in the yz-plane.

Table 3.3.: Parameters and settings of the PIV algorithm

Setting	Value		
PIV algorithm	FFT window deformation		
Subpixel estimator	Gauss 2x3 point		
Pixel size	6.67 μm		
Frame rate	200 fps		
Pixel per frame	1.33 m s^{-1}		
Pass	1 st	2 nd	3 rd
Interrogation area (px)	256	128	64
Step (px)	128	64	32

3.1.6. Contact angle measurements

To measure the contact angle of the different electrode materials and coatings, the *Contact Angle*-plugin of Marco Brugnara is used. The plugin is incorporated into the open-source software ImageJ [177] and is a commonly used tool for the precise determination of the contact angle of spherical or ellipsoid drops and bubbles [178].

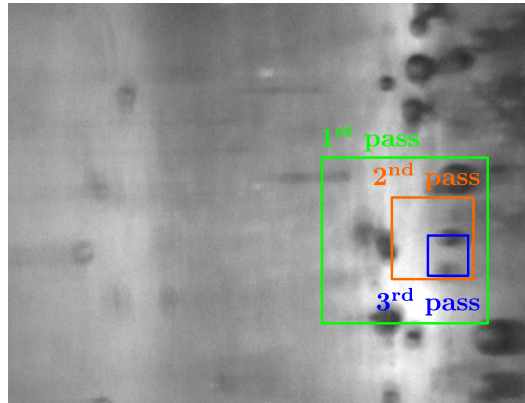


Figure 3.10.: Illustration of the three different interrogation areas used by the PIV algorithm on an exemplary image.

First, the anode and cathode were placed into an electrolyte bath at the same distance between them as in the PMMA-electrolyzer to obtain images of the nucleating bubbles on the surfaces of different electrode materials. In this simplified setup, no forced circulation can be applied, and no membrane is inserted. Using the HRHSC and LM1138TC lens (see Table 3.1), images of the adhering bubbles are obtained with a pixel size of $1.75\text{ }\mu\text{m}$. The setup is backlit by LED bar lights that are placed outside the glass container. Figure 3.11 depicts the setup, direction of view, and lighting.

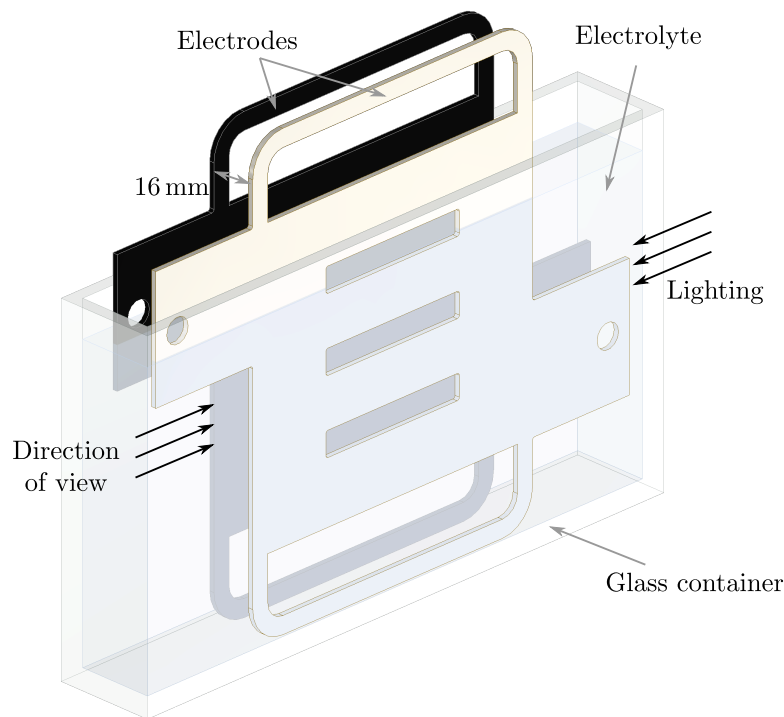


Figure 3.11.: Setup for the measurement of the contact angle.

The determination of the contact angle relies on manually selecting a baseline for the

solid-liquid interface and a minimum of three points that are used to fit either a circle or an ellipse to the bubble. In the following, the ellipse fit will be used, as the sphere approximation resulted in erroneous measurements and negative values for Θ . After the point selection, the algorithm determines the angle between the solid-liquid interface and the tangent of the bubble at the solid-liquid-gas interface. Figure 3.12 illustrates the resulting fit and contact angle for a bubble on a RuOMM-coated titanium electrode. The

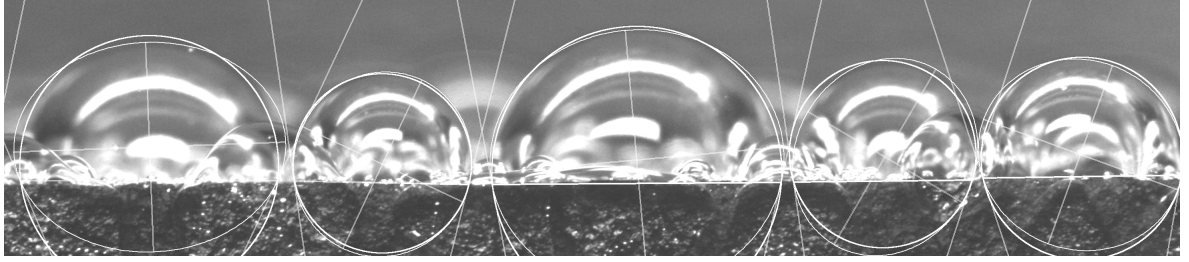


Figure 3.12.: Exemplary determination of the contact angle Θ using the *Contact Angle*-plugin of the open-source software ImageJ on a RuOMM-coated electrode.

contact angle itself Θ can be determined by the Young equation that relates the solid-liquid σ_{SL} , solid-gas σ_{SG} , and liquid-gas σ_{LG} interfacial tensions by

$$\sigma_{SG} - \sigma_{SL} - \sigma_{LG} \cos \Theta = 0. \quad (3.12)$$

This equation is usually employed to characterize the wetting behavior of drops on a solid surface, and values for Θ smaller or greater than 90° refer to a hydrophilic or hydrophobic solid surface, respectively. This definition is reversed to describe the adhesion of a gas bubble on the electrode surface within the surrounding electrolyte. Hence, the smaller the angle, the stronger gas adhesion on the electrode surface.

3.1.7. Operating parameters for experimental studies

The cathode solution contains $0.5 \text{ mol L}^{-1} \text{ Na}_2\text{SO}_4$ and $0.35 \text{ mol L}^{-1} \text{ H}_2\text{SA}$ throughout all experiments. Here, $c_{\text{H}_2\text{SA}}$ resembles the solubility limit of H_2SA [12] and the pH value of the catholyte amounts to 2.2 throughout all experiments. Based on the operating parameters studied in the work of Kocks et al. [17], the influence of different u_{el}^0 and i on the bubble size is studied at an IrOMM-coated titanium electrode. First, u_{el}^0 is varied from 0 to 18.6 mm s^{-1} in intervals of 4.65 mm s^{-1} at constant i and c_{Na^+} of 0.1 A m^{-2} and 0.3 mol L^{-1} , respectively, and the bubble size is recorded in the middle viewing panel. Here, an interval of $u_{\text{el}}^0 = 4.65 \text{ mm s}^{-1}$ corresponds to a volumetric flow rate of 250 mL min^{-1} . Next, the bubble distribution at five different current densities between 0.01 and 0.2 A m^{-2} , NNF conditions ($u_{\text{el}}^0 = 0 \text{ mm s}^{-1}$), $c_{\text{Na}^+} = 0.6 \text{ mol L}^{-1}$, and top and middle viewing panels are studied.

Subsequently, the influence of different ratios of H_2SA and Na_2SA and, thus, different pH values on the oxygen bubble size distribution are recorded at $u_{\text{el}}^0 = 9.3 \text{ mm s}^{-1}$ and $i = 0.043 \text{ A m}^{-2}$ in the middle viewing panel. The value for i is chosen to enable the same current density at the lowest concentration of Na^+ ions. Lastly, the bubble size distribution is measured for different anode materials. Therefore, the IrOMM-coated anode is replaced by a RuOMM-coated titanium and a plain titanium electrode. In addition to the bubble size, the surface composition and topology are examined for possible relations between the catalyst coating and bubble size. The surface of the electrode catalyst was analyzed using a Field Emission Scanning Electron Microscope (FESEM) from Hitachi (Tokyo, Japan). For qualitative elemental composition studies, the FESEM is combined with Energy-dispersive X-ray spectroscopy (EDS) from Bruker (Billerica, America). Additionally, the surface roughness of the electrodes was examined using the 3D-confocal laser scanning microscopy VK-X3000 from Keyence (Neu-Isenburg, Germany). For clarity, Table 3.4 displays all the different sets of operating parameters, composition, pH value, employed catalyst, and examined viewing panel that are used to study their impact on the oxygen bubble size.

Besides the size of oxygen bubbles, the experimental setup can be also be modified to quantify the size of hydrogen bubbles. Therefore, the positions of anode and cathode have to be switched in the experimental arrangement, depicted in Figure 3.1. Since the size of hydrogen bubbles has already been examined more frequently than oxygen bubbles, the investigation of the influencing variables on the bubble size is limited to i in this thesis. At NNF conditions, $c_{\text{Na}^+} = 0.6 \text{ mol L}^{-1}$ and the middle viewing panel, the hydrogen bubble size distribution is evaluated for the five previously used values (see Table 3.4) for the i . During the experiments, a nickel electrode is used as cathode. Table 3.5 shows the five different sets of experimental parameters.

At similar conditions as the previous experiments for the bubble size determination, PTV and PIV experiments were conducted with an anolyte composition of $c_{\text{Na}^+} = 0.6 \text{ mol L}^{-1}$ and $c_{\text{SA}^{2-}} = 0.3 \text{ mol L}^{-1}$. Three different values for each i and u_{el}^0 are chosen, resulting in a total of nine experiments that are tabulated in Table 3.6. For each set of operating conditions, the PTV algorithm is applied to images taken at all three viewing panels. PIV measurements of the short side of the electrolyzer were only possible at the top and bottom position since a bolt prevents the view at the middle position. In addition, to study the effect of the electrode-membrane gap on the gas-liquid flow, the PIV measurement is also conducted with a smaller thickness of the anode and cathode chamber of 6 mm.

At the beginning of each experimental study, fresh electrolyte is introduced into the anolyte and catholyte reservoir and then transferred to the anode and catholyte chamber, respectively. Following this, the specified volumetric flow rate and current density are set, and images are captured after at least ten seconds. Janssen et al. [59] showed that this time period is adequate for achieving a consistent distribution of bubble sizes and demonstrated

Table 3.4.: Varied operating parameter to study the effect of u_{el}^0 , i , c_{Na^+} , viewing panel, and electrode material on the size distribution of detached oxygen bubbles. The table is adapted from [54].

Varied parameter	u_{el}^0 (mm s ⁻¹)	i (A cm ⁻²)	c_{Na^+} (mol L ⁻¹)	$c_{\text{SA}^{2-}}$ (mol L ⁻¹)	pH (-)	Catalyst (-)	Position (-)
u_{el}^0	0	0.1	0.3	0.3	4.82	IrOMM	Middle
	4.65	0.1	0.3	0.3			
	9.3	0.1	0.3	0.3			
	13.95	0.1	0.3	0.3			
	18.6	0.1	0.3	0.3			
i	0	0.01	0.6	0.3	6.99	IrOMM	Middle
	0	0.05	0.6	0.3			
	0	0.1	0.6	0.3			
	0	0.15	0.6	0.3			
	0	0.2	0.6	0.3			
Position	0	0.01	0.6	0.3	6.99	IrOMM	Top
	0	0.05	0.6	0.3			
	0	0.1	0.6	0.3			
	0	0.15	0.6	0.3			
	0	0.2	0.6	0.3			
c_{Na^+} pH	9.3	0.043	0.05	0.3	3.69	IrOMM	Middle
	9.3	0.043	0.1	0.3	3.82		
	9.3	0.043	0.2	0.3	4.37		
	9.3	0.043	0.3	0.3	4.82		
	9.3	0.043	0.5	0.3	5.68		
Catalyst	0	0.01	0.6	0.3	6.99	RuOMM	Middle
	0	0.05	0.6	0.3			
	0	0.1	0.6	0.3			
	0	0.15	0.6	0.3			
	0	0.01	0.6	0.3	6.99	Ti	Middle
	0	0.05	0.6	0.3			
	0	0.1	0.6	0.3			

Table 3.5.: Varied operating parameter to study the effect of i on the size distribution of hydrogen bubbles with a Ni-electrode.

Varied parameter	u_{el}^0 (mm s ⁻¹)	i (A cm ⁻²)	c_{Na^+} (mol L ⁻¹)	$c_{\text{SA}^{2-}}$ (mol L ⁻¹)	pH (-)	Catalyst (-)	Position (-)
i	0	0.01	0.6	0.3	6.99	Ni	Middle
	0	0.05	0.6	0.3			
	0	0.1	0.6	0.3			
	0	0.15	0.6	0.3			
	0	0.2	0.6	0.3			

Table 3.6.: Experimental matrix for the PTV and PIV measurements inside the parallel plate electrolyzer. The anolyte consists of $c_{\text{Na}^+}=0.6 \text{ mol L}^{-1}$ and $c_{\text{SA}^{2-}}=0.3 \text{ mol L}^{-1}$. PTV measurements are carried out in all three viewing panels, whereas the PIV algorithm is only applied to images of the top and bottom viewing panel. * denotes only PTV measurement

$i \setminus u_{\text{el}}^0$	0 mm s^{-1}	10 mm s^{-1}	20 mm s^{-1}	30 mm s^{-1}
0.01 A cm^{-2}	0.01-0	0.01-10	0.01-20	
0.05 A cm^{-2}	0.05-0	0.05-10	0.05-20	
0.1 A cm^{-2}	0.1-0	0.1-10	0.1-20	0.1-30*

only a minimal temporal variation in the detached bubble size distribution with greater experimental duration.

All experiments were conducted at an ambient pressure of 1 atm and a temperature of 295 K in the electrolyte feed. Depending on the operating conditions, the temperature difference between in- and outlet is 1 to 6 K.

3.2. Size distribution of oxygen bubbles

Using the algorithm and operating conditions described in sections 3.1.3 and 3.1.7, the size distribution of the electrogenerated oxygen bubble is determined. Depending on the set of operating parameters, between 925 and 25.575 and an average of 13.406 bubbles are identified. The determined bubble sizes of each experiment follow a Gaussian distribution, and Figure 3.13 exemplary illustrates the number- (a) and volume-based (b) histograms of the bubble sizes and fitted Gaussian distributions at $i=0.15 \text{ A cm}^{-2}$, $u_{\text{el}}^0=0 \text{ mm s}^{-1}$, $c_{\text{Na}^+}=0.6 \text{ mol L}^{-1}$ and IrOMM-coated anode. Both q_0 and q_3 closely follow the Gaussian distribution with the same standard deviation $\varsigma(d_b)$ of $74 \mu\text{m}$. The weighted volume-based distribution exhibits a greater arithmetic mean $\bar{d}_{b,3}$ of $335 \mu\text{m}$ compared to $280 \mu\text{m}$ of the number-based distribution. This shift results from the increased weight of the larger bubbles and can also be observed with the values for the 25% percentiles d_{25} , the medians d_{50} , and 75% percentiles d_{75} . For both distributions, the values for \tilde{d}_{min} and \tilde{d}_{max} are limited by the IQR.

Different evaluation frame rates were studied to prevent multiple counting of a single bubble. Figure 3.14 displays the number-based box plot, and Table 3.7 shows the standard deviation, mean, min, and max value, number of detected bubbles, and outliers for different evaluation frame rates. At $i = 0.1 \text{ A cm}^{-2}$, $u_{\text{el}}^0=0 \text{ mm s}^{-1}$, $c_{\text{Na}^+}=0.6 \text{ mol L}^{-1}$ and with an IrOMM-coated titanium anode, the arithmetic means and standard deviation, remain constant independent of the evaluated frame rate and are stored in Table 3.7. Additionally, the number of detected bubbles per frame stabilizes for evaluation frame rates greater

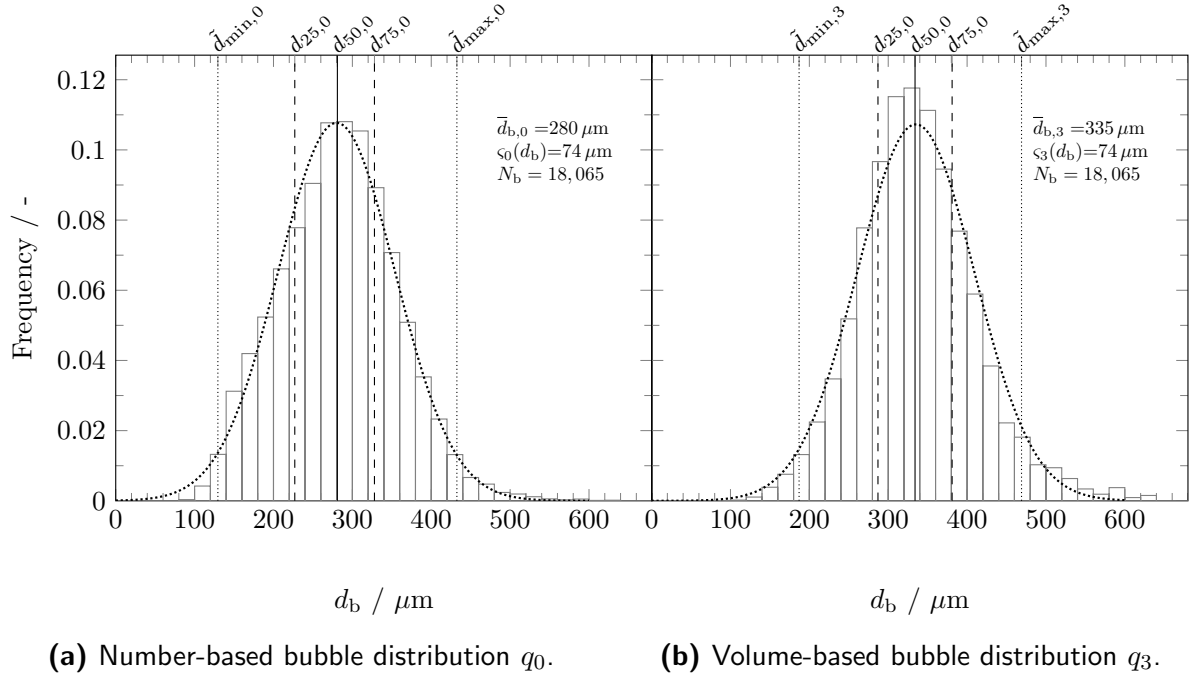


Figure 3.13.: Exemplary bubble size distribution, \tilde{d}_{\min} , d_{25} , d_{50} , d_{75} , and \tilde{d}_{\max} for an IrOMM-coated titanium anode at $i=0.15 \text{ A cm}^{-2}$, $u_{\text{el}}^0=0 \text{ mm s}^{-1}$ and $c_{\text{Na}^+}=0.6 \text{ mol L}^{-1}$.

than five. Subsequently, an evaluation frame rate of 20 fps is chosen for the following experimental results to minimize the multiple counting of bubbles and provide a sufficiently large sample size for the size distribution.

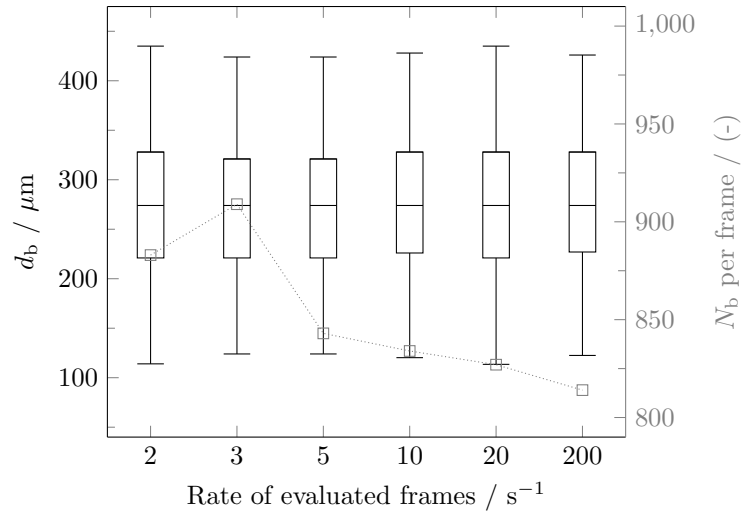


Figure 3.14.: Box plot diagram of the number-based distribution obtained with different evaluation frame rates at $i = 0.1 \text{ A cm}^{-2}$, $u_{\text{el}}^0=0 \text{ mm s}^{-1}$, $c_{\text{Na}^+}=0.6 \text{ mol L}^{-1}$ and IrOMM-coated titanium anode. The gray boxes represent the average number of detected bubbles in each frame.

Table 3.7.: $\bar{d}_{b,0}$, $\varsigma(d_{b,0})$, Min, Max, N_b and outliers for different evaluated frame rates at $i = 0.1 \text{ A cm}^{-2}$, $u_{\text{el}}^0 = 0 \text{ mm s}^{-1}$, $c_{\text{Na}^+} = 0.6 \text{ mol L}^{-1}$ and IrOMM-coated titanium anode.

Evaluated erate (fps)	Fram-	Mean (μm)	$\varsigma(d_{b,0})$ (μm)	Min (μm)	Max (μm)	N_b (-)	Outliers (-)
2		275.1	72.3	114	615	1765	2.0%
3		274.7	73.8	107	769	2728	2.8%
5		276.1	73.6	107	702	4217	3.1%
10		276.6	73.3	107	729	8336	3.2%
20		276.5	73	107	769	16535	2.4%
200		277.2	72.6	94	735	162701	3.0%

3.2.1. Effect of superficial electrolyte velocity

Figure 3.15 displays the box plots of the volume-weighted bubble size distribution at 0.1 A cm^{-2} , $c_{\text{Na}^+} = 0.3 \text{ mol L}^{-1}$, and an IrOMM-coating for different electrolyte flow velocities between 0 and 18.6 mm s^{-1} . Here, the each box plot's lower and upper boxes display 25 to

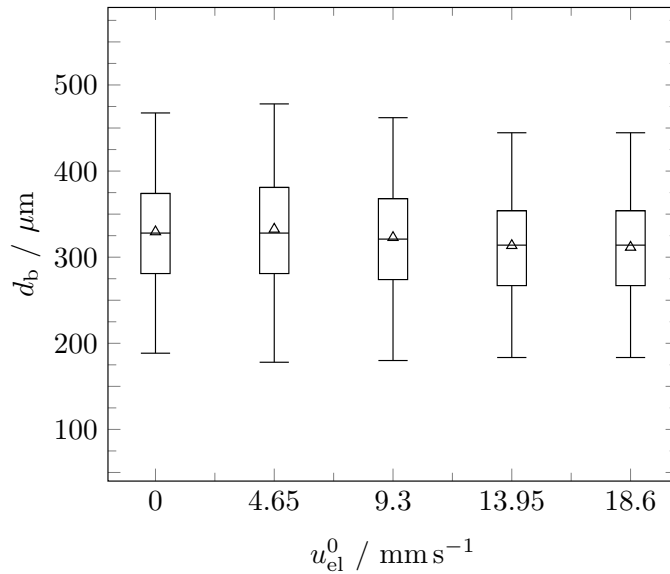


Figure 3.15.: Arithmetic mean size (\triangle) and box plot diagram of the volume-weighted size distribution of oxygen bubbles at $u_{\text{el}}^0 = 0, 4.65, 9.3, 13.95$ and 18.6 mm s^{-1} at $i = 0.1 \text{ A cm}^{-2}$, $c_{\text{Na}^+} = 0.6 \text{ mol L}^{-1}$ and an IrOMM-coated titanium anode.

50 % and 50 to 75 % fractions of the bubble sizes, respectively. Over the five experiments, 50 % of the identified weighted bubbles have sizes between $274 \pm 4 \mu\text{m}$ and $336 \pm 12 \mu\text{m}$. The horizontal line between both boxes indicates the median, $d_{50,3}$, and slightly decreases from 328 at $u_{\text{el}}^0 = 0 \text{ mm s}^{-1}$ to $314 \mu\text{m}$ at 18.6 mm s^{-1} . Analogically, the arithmetic mean that is indicated by the triangles lessens from 329 to $312 \mu\text{m}$. The IQR and the thereby linked span ($\tilde{d}_{\text{max}} - \tilde{d}_{\text{min}}$) remain almost constant at $92 \pm 5 \mu\text{m}$ and $273 \pm 16 \mu\text{m}$, respectively. Hence, the superficial electrolyte flow velocity up to a value of 18.6 mm s^{-1} affects the

width of the $q3$ distribution only marginally. [54]

The observations align with the research of Chin Kwie Joe et al. [58], which also indicated a slight decrease in the average size distribution of bubbles formed at their wire electrode with greater u_{el}^0 . In addition, Janssen et al. [59] also report that the diameter of attached oxygen bubbles decreases as the velocity of the electrolyte solution increases. By increasing u_{el}^0 , attached bubbles experience a greater drag, decreasing the nucleation time and forcing a premature departure. Nonetheless, this effect is diminished by the buoyancy-induced acceleration of the electrolyte, which dominates the local electrolyte velocity close to the electrode [88, 118]. As described in section 2.2.3, the measured bubble velocity ranges up to 100 mm s^{-1} , far exceeding the investigated values for u_{el}^0 of this thesis. Furthermore, higher electrolyte flow velocities lead to a decrease in the coalescence rate, causing an increase in smaller bubbles [57]. The results depicted in Figure 3.15 also confirm this observation, as an increased number of bubbles are identified for 18.6 mm s^{-1} (17,461) are identified compared to 14,274 at 0 mm s^{-1} . However, these findings, as well as those of Janssen et al. [59] and Chin Kwie Joe et al. [58], indicate that the impact of electrolyte velocity on bubble size distribution is only minimal. [54]

3.2.2. Effect of current density

As described in section 2.1.3, varying the current density also changes the amount of electrogenerated gas. Figure 3.16 displays the box plot diagram of the bubble size distribution for different current densities with $u_{\text{el}}^0 = 0 \text{ mm s}^{-1}$, $c_{\text{Na}^+} = 0.6 \text{ mol L}^{-1}$, and IrOMM-coated anode. Alongside \dot{V}_g , the volume-averaged arithmetic mean of the bubble size enlarges from $219 \mu\text{m}$ at 0.01 A cm^{-2} to $335 \mu\text{m}$ at 0.15 A cm^{-2} and further increases to $364 \mu\text{m}$ at 0.2 A cm^{-2} . For the same set of current densities, the span ($\tilde{d}_{\text{max}} - \tilde{d}_{\text{min}}$) changes from 263 to 282 and finally $300 \mu\text{m}$. Contrarily to the increased mean size, the IQR of the bubble size distribution remains almost constant: At 0.01 A cm^{-2} , the difference between $d_{75,3}$ and $d_{25,3}$ equals $100 \mu\text{m}$, decreases to $87 \mu\text{m}$ at 0.1 A cm^{-2} before returning to a value of $100 \mu\text{m}$.

To compare the obtained distributions, the correlation for the Sauter mean size (d_{32}) of detached oxygen bubbles at a wire electrode from the work of Chin Kwie Joe et al. [58] is appended to Figure 3.16. The measured oxygen bubbles formed at a wire electrode were significantly smaller than the reported values in this thesis. Between 0.01 and 0.2 A cm^{-2} , the difference between the volume-weighted arithmetic mean and the Sauter diameter sizes is greater than $200 \mu\text{m}$. Whereas the volume-weighted box plots display a linear increase of the arithmetic mean value with respect to i , the number-based size distribution reported in [54] exhibits an asymptotic progression similar to that of Chin Kwie Joe et al. [58]. However, the measurements are hard to compare, as the wire electrode exhibits an infinitesimal small active surface area. From the small surface area, it follows that the

flowing current, amount of generated oxygen gas and number of gas bubbles are several orders of magnitude smaller than in this study. Hence, the coalescence rate on the electrode depicted in Figure 2.6 also lessens. In addition, the contact area between the bubble and the electrode is smaller at the wire electrode of Chin Kwie Joe et al. [58] than on a plate electrode. This smaller contact area leads to a premature departure and a greater hydrodynamic drag exerted on the bubbles. In their experimental study, Abdelouahed [90] measured oxygen bubbles with an average size of roughly $120 \mu\text{m}$ at 0.1 A cm^{-2} . Though, they used a lantern blade electrode configuration in which the anode and cathode are aligned perpendicular instead of parallel.

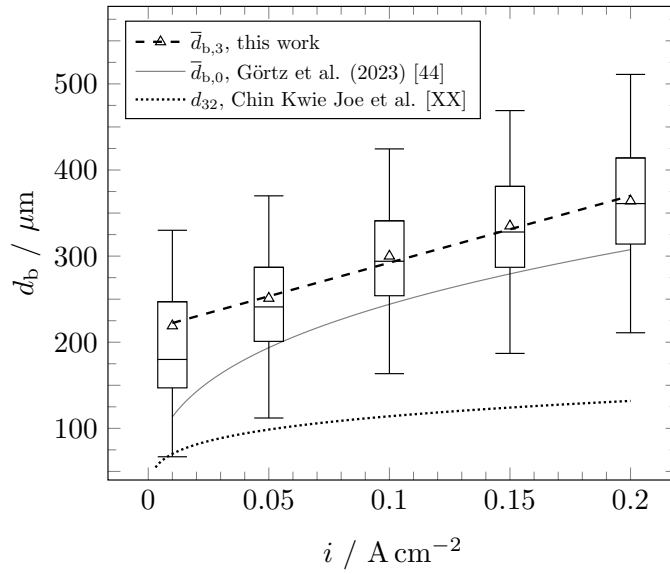


Figure 3.16.: Average oxygen bubble size and distribution for $i=0.01, 0.05, 0.1, 0.15$ and 0.2 A cm^{-2} at $u_{\text{el}}^0=0 \text{ mm s}^{-1}$, $c_{\text{Na}^+}=0.6 \text{ mol L}^{-1}$ and an IrOMM-coated titanium anode.

In good agreement with the results of this thesis, the works of Janssen et al. [59] and Chin Kwie Joe et al. [58] both show an increase in the mean size of attached and detached bubbles with greater current densities. Whereas other studies [56, 179] suggested semi-empirical models that used additional parameters, like the number of nucleation sides, bubble coverage, surface tension, and contact angle, Chin Kwie Joe et al. [58] suggested a simple power law approach to describe the correlation between the mean bubble size and i . Since parameters like the number of nucleation sides are primarily unavailable, the simple, fundamental correlation between $i \propto V_g$ is used. Further, by assuming the same number of nucleation sides and release time, the relation $V_g \propto \bar{d}_{b,0}^3 \propto \bar{d}_{b,3}$ also holds. Therefore, depending on the type of distribution, two different equations can be proposed:

$$\bar{d}_{b,0} = D_0 \sqrt[3]{i} \quad \text{and} \quad (3.13)$$

$$\bar{d}_{b,3} = D_{3,0} + D_3 i. \quad (3.14)$$

Fitting the experimental data to the number-based equation (3.13), yields $D_0 = 525.8 \mu\text{m cm}^{2/3} \text{A}^{-1/3}$ and a good coefficient of determination R^2 of 0.993. Fitting the linear increase of the volume-weighted mean size $\bar{d}_{b,3}$ to the experimental data led to values for the parameters $D_{3,0}$ and D_3 of $214.5 \mu\text{m}$ and $777.8 \mu\text{m cm}^2 \text{A}^{-1}$, respectively. Here, the coefficient of determination is smaller with $R^2 = 0.991$. Both fitted equations are added to Figure 3.16.

3.2.3. Effect of measurement height

To diminish the impact of inflow and outflow phenomena, the previous parameter variations listed in Table 3.4 were studied at the middle viewing panel. Using the same operating parameter as in the previous section 3.2.2, the volume-weighted oxygen bubble size distribution is measured at the top viewing panel. Figure 3.17 displays the determined values for $\bar{d}_{b,3}$ and $\varsigma_3(d_b)$ alongside the corresponding values for the distributions determined at the middle viewing panel. Additionally, the equation (3.14) is fitted to $\bar{d}_{b,3}$ of the top viewing panel and added to Figure 3.17. Thereby, $D_{3,0}$ and D_3 amount to $212.4 \mu\text{m}$ and $975.1 \mu\text{m cm}^2 \text{A}^{-1}$, respectively. The value $D_{3,0}$ is almost identical for the top and middle viewing panels, whereas D_3 captures the steeper increase of the average, volume-weighted bubble size with respect to i . At current densities equal to or greater than 0.05A cm^{-2} , the average oxygen bubble size is greater at the top viewing panel than at the middle one, and the difference between the top and bottom amounts to $18 \mu\text{m}$ on average. Hence, a slight increase can be noted that most likely results from further bubble growth in the supersaturated electrolyte and bubble coalescence due to the larger average residence time of the bubbles at the top viewing panel.

In contrast, $\bar{d}_{b,3}$ measured at the smallest current density of 0.01A cm^{-2} , and the middle viewing panel is $20 \mu\text{m}$ larger than the corresponding value at the top panel. At these operating conditions, the generation of oxygen gas is reduced, leading to the generation of fewer gas bubbles. Hence, the rate of bubble coalescence is relatively small compared to higher i . In conclusion, the measurement height affects the bubble size distribution and leads to a minor increase of $\bar{d}_{b,3}$. Though, this effect of the measurement height is small in lab-scale electrolyzers with an $A_{\text{electrode}}$ of around 100cm^2 like the often employed Electro MP Cell[®] from ElectroCell A/S (Tarm, Denmark).

3.2.4. Effect of electrolyte composition

The variation of the electrolyte composition leads to multiple effects: Besides the obvious change in conductivity, cell voltage, and pH value, the change also affects the contact angle [165]. Ultimately, this change in Θ also affects the bubble size distribution. The impact

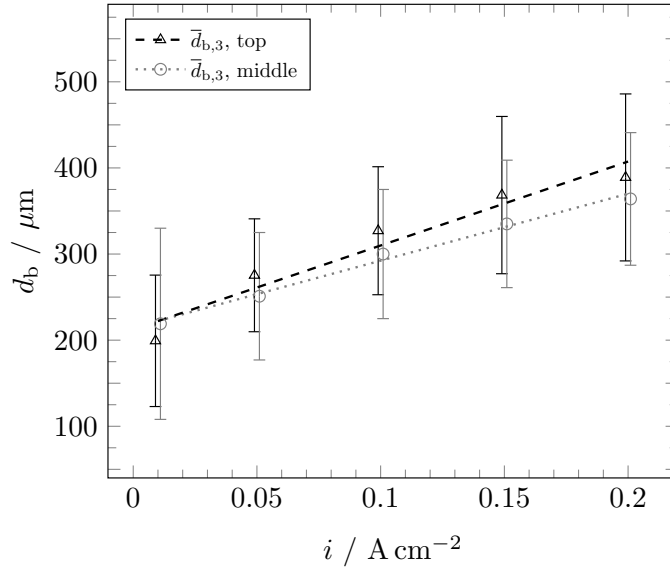


Figure 3.17.: Average, volume-weighted oxygen bubble size and distribution for $i=0.01, 0.05, 0.1, 0.15$ and 0.2 A cm^{-2} at $u_{\text{el}}^0=0 \text{ mm s}^{-1}$, $c_{\text{Na}^+}=0.6 \text{ mol L}^{-1}$, an IrOMM-coated titanium anode and the middle and top viewing panel.

of different c_{Na^+} on the volume-weighted oxygen bubble size distribution at a constant current density of $i=0.043 \text{ A cm}^{-2}$, $u_{\text{el}} = 0 \text{ mm s}^{-1}$ and a IrOMM-coated anode is depicted in Figure 3.18. The median of the volume weighted bubble size increases from $207 \mu\text{m}$ at 0.05 mol L^{-1} to $287 \mu\text{m}$ at $c_{\text{Na}^+} = 0.1 \text{ mol L}^{-1}$ and remains constant for a further increase of Na^+ -ions. Contrarily, the number-based distribution reported a parabolic behavior of the size distribution with respect to c_{Na^+} [54]. While the distributions at the medium

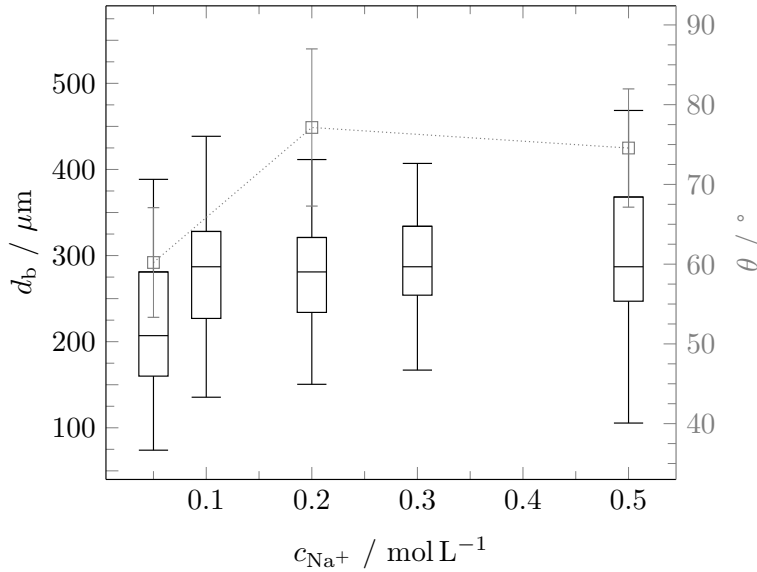


Figure 3.18.: Volume-based oxygen bubble size distribution and cell voltage for different electrolyte compositions between 0.05 and 0.5 mol L^{-1} Na^+ -ions at $i=0.15 \text{ A cm}^{-2}$, $u_{\text{el}}^0=9.3 \text{ mm s}^{-1}$ and an IrOMM-coated titanium anode.

values for $c_{\text{Na}^+}=0.1, 0.2$, and 0.3 mol L^{-1} exhibit relatively small IQRs of, on average $89 \mu\text{m}$, the smallest and largest concentrations both have an IQR of $121 \mu\text{m}$. During the experiments, the cell voltage U_c decreases from 39.5 V at 0.05 mol L^{-1} to 9.9 V at 0.5 mol L^{-1} . By using the setup described in section 3.1.6, the contact angle Θ is determined for $c_{\text{Na}^+}=0.05, 0.2$, and 0.5 mol L^{-1} at the IrOMM-coated titanium anode, and the resulting values and standard deviations are added to Figure 3.18. Here, Θ amounts $60 \pm 7^\circ$ at $c_{\text{Na}^+} = 0.05 \text{ mol L}^{-1}$ before increasing to $77 \pm 10^\circ$ and $74 \pm 7^\circ$ at $c_{\text{Na}^+} = 0.3$ and 0.5 mol L^{-1} , respectively. The small value of Θ at $c_{\text{Na}^+} = 0.05 \text{ mol L}^{-1}$ could be hinting a premature release of bubbles since the shape attributed to Θ leads to an increased drag acting on the attached bubbles. The progression of Θ shows a similar behavior as the measured bubble size distribution, suggesting a linkage between both parameters. Möller [180] theoretically derived and Kabanow and Frumkin [60] experimentally demonstrated that the bubble departure size is directly proportional to Θ . They report that with an increasing edge angle, which is inverse to the definition of Θ in this work, the maximum diameter of hydrogen bubbles decreases exponentially at a platinum and mercury electrode.

The variance of the measured values for Θ can result from the applied excessive voltage, the increased surface tension between the gas-liquid and liquid-solid interface, or the change of electrolyte concentration and pH value that is discussed by Jones and Ray [181]. In order to assign the change in bubble size at $c_{\text{Na}^+} = 0.05 \text{ mol L}^{-1}$ to any of the three aspects, additional experimental protocols must be established. For example, the cell voltage could vary by adjusting the distance between electrodes. Nonetheless, the effect of different concentrations of the conducting Na^+ -ions is small compared to the impact of i (see Section 3.2.2).

3.2.5. Effect of catalyst

As discussed in the previous sections 3.2.2 and 2.1.3, the number of nucleation sides, the composition of the catalysts, and the contact angle affect the bubble nucleation and, hence, the size distribution of detached bubbles. Figure 3.19 displays the box plots of the volume-weighted oxygen size distribution of the RuOMM-coated and plain titanium anode alongside the results from the IrOMM-coated anode for different i . Here, u_{el}^0 and c_{Na^+} were held constant at 0 mm s^{-1} and 0.6 mol L^{-1} , respectively, and the distribution is measured at the middle viewing panel. In addition, equation (3.14) is fitted to the values and plotted in dashed lines alongside the $\bar{d}_{b,3}$, which is indicated by triangles. The size distribution for RuOMM follows a similar trend for $0.05 \text{ A cm}^{-2} < i < 0.15 \text{ A cm}^{-2}$. For the RuOMM-coating, the increase with i that is indicated by the fitting parameter D_3 , amounts to $658 \mu\text{m cm}^2 \text{ A}^{-1}$ and is slightly lower than the value for IrOMM-coating. At $i=0.15 \text{ A cm}^{-2}$, the average bubble size obtained by using the RuOMM-coated titanium anode is $183 \mu\text{m}$,

almost identical to the value of $188\text{ }\mu\text{m}$ obtained with the IrOMM-coating. In addition, the IQR of both measurements equals $101\text{ }\mu\text{m}$ and $94\text{ }\mu\text{m}$, respectively, and also indicates a similar width of the size distribution. In contrast to the behavior for $i \geq 0.05\text{ A cm}^{-2}$, the behavior of IrOMM and RuOMM differs at $i = 0.01\text{ A cm}^{-2}$. Here, RuOMM exhibits a greater average size of $260\text{ }\mu\text{m}$, a larger span with an IQR of $200\text{ }\mu\text{m}$, and a maximal bubble size of $501\text{ }\mu\text{m}$ compared to the values for IrOMM, $220\text{ }\mu\text{m}$, $100\text{ }\mu\text{m}$, and $330\text{ }\mu\text{m}$. This deviation arises from the detection of a few greater bubbles that exceed a size of $350\text{ }\mu\text{m}$ and were detected during the measurement for RuOMM. This is also indicated by the mean size close to the 25th percentile and very close to the one of IrOMM. These large bubbles of the experiment using the RuOMM-coating heavily impact the volume-weighted distribution. The number-based distribution that is displayed in Görtz et al. [54] reveals an almost identical size distribution for RuOMM and IrOMM at $i=0.01\text{ A cm}^{-2}$.

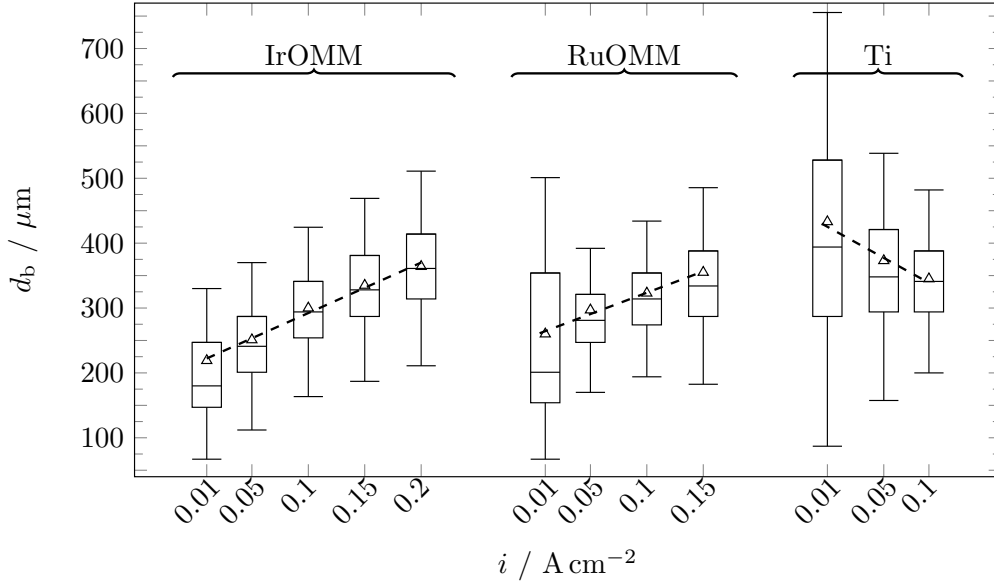


Figure 3.19.: Bubble size distribution for different anodic materials and current densities of $i=0.01, 0.05, 0.1, 0.15$ and 0.2 A cm^{-2} at $u_{\text{el}}^0=0\text{ mm s}^{-1}$ and $c_{\text{Na}^+}=0.6\text{ mol L}^{-1}$.

The size distribution obtained for the plain titanium anode exhibits an entirely different trend. Instead of increasing with i , the volume-weighted average bubble size decreases from $433\text{ }\mu\text{m}$ at $i=0.01\text{ A cm}^{-2}$ to $372\text{ }\mu\text{m}$ and $345\text{ }\mu\text{m}$ at $i=0.05$ and 0.1 A cm^{-2} , respectively. This decrease is unphysical and in contradiction to all previous experiments and literature [57–59]. Consequently, the fitted value for D_3 becomes negative, resulting in a value of $-960.7\text{ }\mu\text{m cm}^2\text{ A}^{-1}$ and $435\text{ }\mu\text{m}$ for D_0 . For the titanium anode, the size distribution at $i=0.01\text{ A cm}^{-2}$ is extremely wide. This result stems from the lowest number of detected bubbles of all measurements, 925. Despite a higher U_c , the size distribution for the titanium anode at $i=0.1\text{ A cm}^{-2}$ is close to the ones obtained using the IrOMM- and RuOMM-coating: The average size amounts to $345\text{ }\mu\text{m}$ and is only $23\text{ }\mu\text{m}$ larger than the one obtained

using the RuOMM-coated anode. In addition, $\varsigma_3(d_b)$ equals $79\text{ }\mu\text{m}$ and is within the range of RuOMM and IrOMM with $\varsigma_3(d_b)=95$ and $75\text{ }\mu\text{m}$, respectively.

The results show that measurements at low values for i exhibit a larger span of the distribution. This might arise from the volume-weighting of the distribution but also from the stochastic event of bubble coalescence on the electrode surface. As soon as one bubble leaves the nucleation side and starts to move, it consumes the other bubbles on its way up before it finally detaches from the electrode. This effect can be observed when taking images comparable to Figure 2.6. In addition, the driving force for bubble growth is reduced, leading to a longer departure time. This longer departure time also favors the formation of big bubbles that consume many tiny attached bubbles.

Further, Figure 3.19 also shows two different trends of the bubble size: The coated anodes (IrOMM and RuOMM) behave differently than the cold-rolled plain titanium electrode. This different behavior also correlates to the obtained values for the surface roughness and optical images stored in Table 3.9. Table 3.8 includes the measured values for the arithmetic average roughness R_a , maximum valley to peak height R_z , texture aspect ratio S_{tr} , arithmetic mean peak curvature S_{pc} , and developed interfacial area ratio S_{dr} for the three different catalysts. The IrOMM-coated anode has the largest values for R_a and R_z ,

Table 3.8.: Results for the surface roughness analysis of the IrOMM-, RuOMM-coated and plain titanium electrode. Table is taken from [54].

Catalyst	R_a (μm)	R_z (μm)	S_{pc} ($1/\text{mm}$)	S_{dr} (m^2m^{-2})
IrOMM	0.84	4.76	1193	0.24
RuOMM	0.61	3.9	1243	0.25
Titanium	0.46	2.74	503	0.06

followed by the RuOMM-coated anode, and the cold-rolled, plain titanium anode exhibits the smoothest surface. This difference is also visible in the microscopy pictures, FESEM images with small magnifications, and the topology map in Table 3.9. The difference between the coated and cold-rolled electrodes also manifests in the obtained values for S_{pc} and S_{dr} . The values for S_{pc} depict the curvature of the elevations on a surface, and the two coated (IrOMM and RuOMM) electrodes have comparable values and double the value of the plain titanium anode. This disparity between the coated and uncoated surfaces also becomes apparent in the FESEM images with a magnification of 70 and 1000. Here, the amount of little lumps and peaks is more significant for the coated surfaces. In addition, the coating also leads to the formation of small cracks in the surface, and these defects can act as a nucleation center. S_{dr} indicates the additionally developed interfacial area due to elevations and dips on the surface. Here, the coated anodes have similar values of 0.24 and 0.25 and exceed the value for the plain titanium anode (0.06). Again, the greater developed

interfacial area is visible in the FESEM images in Table 3.9 with high magnifications that closely depict the coated electrodes' surface and reveal the different, more regular patterns on the cold-rolled titanium surface. By using S_{dr} , the current density i can be transferred to the corrected current density

$$\tilde{i} = \frac{i}{1 + S_{\text{dr}}} . \quad (3.15)$$

By accounting for the different values of S_{dr} , the previous Figure 3.19 can be modified, and the \tilde{i} instead of i can be used as abscissa in Figure 3.20. Through this representa-

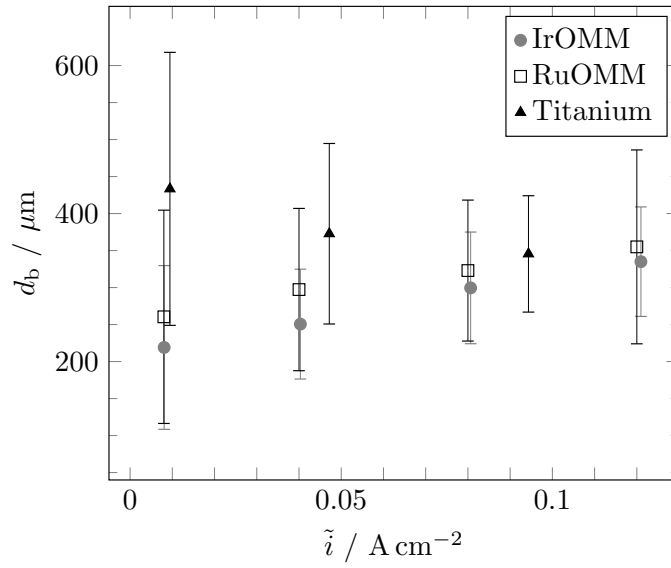
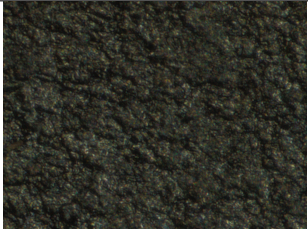
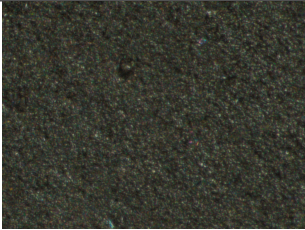
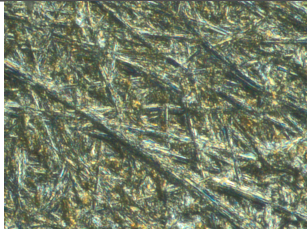
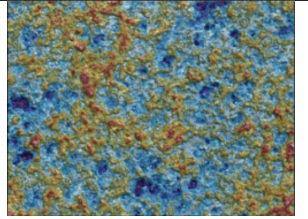
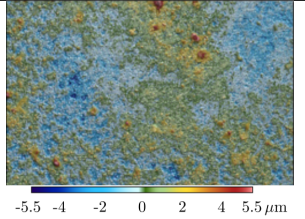
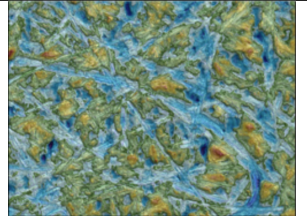
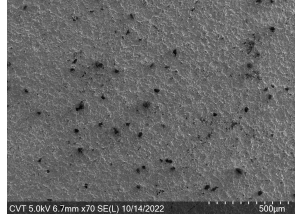
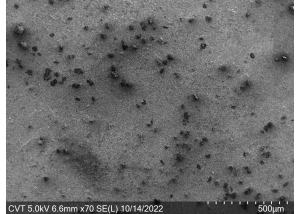
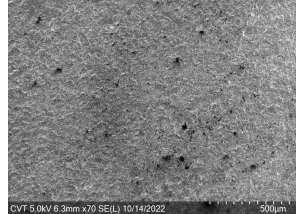
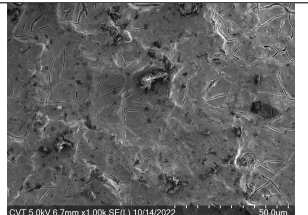
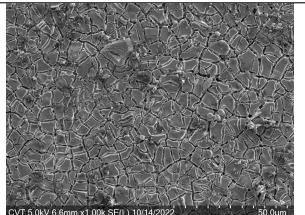
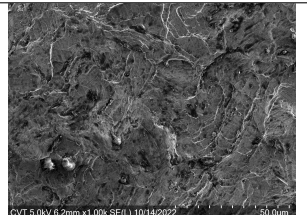
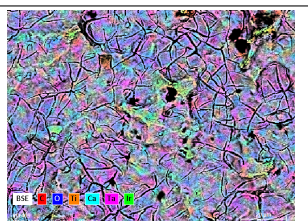

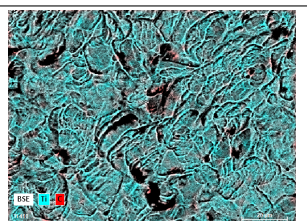
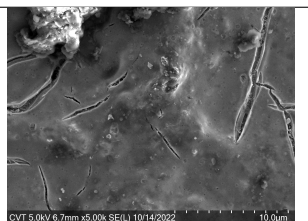
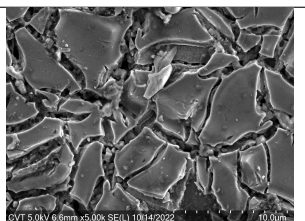
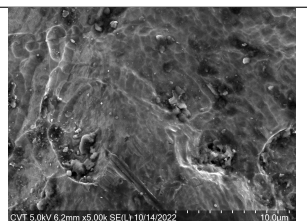
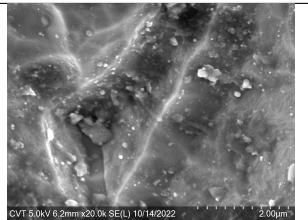
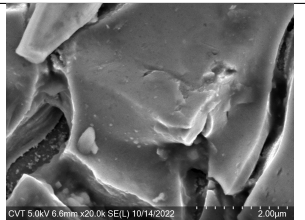
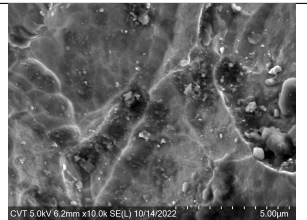


Figure 3.20.: Oxygen bubble size distribution for different anodic materials and current densities of $i=0.01, 0.05$ and 0.1 A cm^{-2} at $u_{\text{el}}^0=0 \text{ mm s}^{-1}$ and $c_{\text{Na}^+}=0.6 \text{ mol L}^{-1}$.

tion of the data, the $\bar{d}_{b,3}$ and $\varsigma_3(d_b)$ recorded for the plain titanium at $\tilde{i}=0.094 \text{ A cm}^{-2}$ appears to be in line with the values for RuOMM and IrOMM recorded in between $0.08 \text{ A cm}^{-2} < \tilde{i} < 1.21 \text{ A cm}^{-2}$. This observation highlights the importance of the surface topology and its effect on the bubble size distribution. Especially the use of uncoated electrodes in research works might introduce a different bubble behavior than coated electrodes, affecting the experimental findings.

Table 3.9.: Images from microscopy, topology measurements, FESEM, and from the EDS analysis of the three different catalyst materials IrOMM, RuOMM and plain titanium. Parts of the pictures are taken from [54].

Image type	IrOMM	RuOMM	Titanium
Microscopy image			
Topology measurement			
FESEM image with a magnification of 70			
FESEM image with a magnification of 1000.			
FESEM image with colored-results from the EDS-analysis.			
FESEM image with a magnification of 5000.			
FESEM image with a magnification of 19988.			

In addition to the additional developed interfacial area, the Θ also depends on the catalyst surface topology and composition. At $i=0.1 \text{ A cm}^{-2}$ and $c_{\text{Na}^+}=0.6 \text{ mol L}^{-1}$, the contact angle of the bubble on the three different electrode surfaces was measured in the simplified setup (Figure 3.11) and the results are depicted in Figure 3.21. The measured

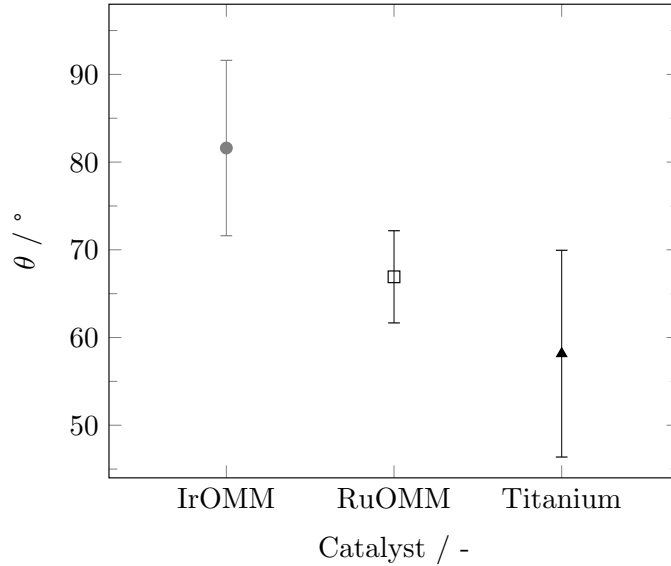


Figure 3.21.: Determined contact angle of between 20 and 40 oxygen bubbles for each of the three different electrode catalysts, IrOMM, RuOMM, and titanium. The Figure is printed with permission from [54].

values for Θ match with the average sizes plotted in Figure 3.20: The plain titanium electrode exhibits the lowest value for Θ of $58 \pm 11^\circ$, corresponding to a stronger adhesion of oxygen bubbles on the electrode surface. This accordance of Θ and \bar{d}_b matches the previously discussed larger values for $\bar{d}_{b,3}$ due to greater coalescence rates on the electrode surface, especially at smaller i . The IrOMM-coated electrode features the greatest Θ with $82 \pm 10^\circ$ out of the three catalysts and also reports the smallest $\bar{d}_{b,3}$. Hence, contact angle measurements of oxygen bubbles on the catalyst's surface can be a good qualitative indicator of the (oxygen) bubble size.

Further, the composition of the catalyst obtained by the EDS analysis is tabulated in Table 3.10. Surprisingly, the IrOMM coating largely ($\approx 40\%$) contains tantalum that is also known to form a small oxide layer and to inactivate Quelle. The normalized mass fraction of iridium is only a little above 20 % and combines with oxygen to about 40 % of the mass of the catalyst. However, the analysis also reveals an excellent coating of the titanium electrodes, as only 1 % of the mass on the surface is attributed to titanium. In contrast, the analysis of the RuOMM coating reports a normalized mass fraction of titanium of about 35 %, disclosing a large portion of uncoated areas of the titanium blank. The normalized mass fraction of the ruthenium-oxide catalyst amounts to about half of

Table 3.10.: Composition of the IrOMM-, RuOMM-coated and plain titanium electrode from Magneto[®] obtained by EDS analysis. Table is adapted from [54].

Electrode type	Element	Atomic number (-)	Net (-)	Mass (%)	Mass normalized (%)	Atom (%)	Relative Error (%)
IrOMM	Tantalum	73	8414	38.33	42.86	8.79	4.01
	Oxygen	8	9881	19.34	21.62	50.14	5.07
	Carbon	6	3197	10.2	11.41	35.23	5.62
	Calcium	20	1156	0.73	0.82	0.76	6.93
	Iridium	77	20784	19.93	22.29	4.3	3.81
	Titanium	22	1096	0.9	1.01	0.78	7.15
	Sum:			89.43	100	100	
RuOMM	Titanium	22	63669	33.2	36.43	18.31	2.89
	Oxygen	8	17722	34.58	37.94	57.06	5.21
	Ruthenium	44	23631	9.92	10.88	2.59	3.28
	Carbon	6	6479	7.77	8.52	17.08	5.12
	Silicon	14	5602	1.45	1.59	1.36	4.57
	Sodium	11	3094	1.57	1.72	1.8	7.92
	Phosphorus	15	3049	0.78	0.85	0.66	5.06
	Sulfur	16	2104	0.52	0.57	0.43	5.89
	Zinc	30	379	0.96	1.06	0.39	11.9
	Aluminum	13	578	0.16	0.18	0.16	12.68
	Sum:			91.16	100	100	
Titanium	Titanium	22	59350	93.62	95.16	83.13	4.00
	Carbon	6	1161	4.76	4.84	16.87	6.13
	Sum:			98.38	100	100	

the catalyst's mass, with the mass fraction of ruthenium being 10 %. The EDS analysis of the titanium electrode shows only the presence of titanium (95 %) and carbon (5 %). From the results of the EDS analysis, it can be argued that the presence of the uncoated, plain titanium areas leads to a decreased Θ and, hence, to a larger $\bar{d}_{b,3}$. However, further electrode samples have to be examined to draw firmer conclusions.

3.2.6. Comparison of the two camera systems

During the course of this thesis, the LRHSC with 1xWD110-1.1-NI camera system is upgraded to the HRHSC with the LM119TC lens to enable a higher resolution of the latter presented bubble velocity. During the PTV experiments with the operating condition listed in Table 3.2, three sets of operating conditions also match the previously presented operating conditions for the bubble size distribution (Table 3.4), enabling a comparison between the two camera systems. At NNF conditions, the bubble size is measured for $c_{\text{Na}^+}=0.6 \text{ mol L}^{-1}$ and $i=0.01, 0.05$ and 0.1 A cm^{-2} with both camera systems allowing for

a direct comparison of both measurements. Figure 3.22 depicts the determined values for $\bar{d}_{b,0}$ and $\varsigma_0(d_b)$. At $i=0.05 \text{ A cm}^{-2}$, the experiments using the HRHSC and LRHSC report similar average sizes $194 \mu\text{m}$ and $199 \mu\text{m}$, respectively. Whereas the measured values with the LRHSC that are discussed in section 3.2.2 show a strong dependence on i , the distributions measured with the HRHSC reflect a smaller impact of i : Here, $\bar{d}_{b,0}$ only increases from $168 \mu\text{m}$ at $i=0.01 \text{ A cm}^{-2}$ to $196 \mu\text{m}$ at $i=0.1 \text{ A cm}^{-2}$. Besides, $\varsigma_0(d_b)$ remains almost constant at $36 \pm 1 \mu\text{m}$. The measured values indicate that the trained neuronal network only detects bubbles in a certain pixel range. As the pixel size of the HRHSC is only a third of the size of the LRHSC, the detected bubble size distributions exhibit smaller $\varsigma(d_b)$, and the values of $\tilde{d}_{\text{max},0}$ stay below $300 \mu\text{m}$. Nonetheless, this error in the bubble size distribution of the HRHSC system is acceptable for the latter presented velocity measurement, as the velocity will be distributed alongside defined size bins.

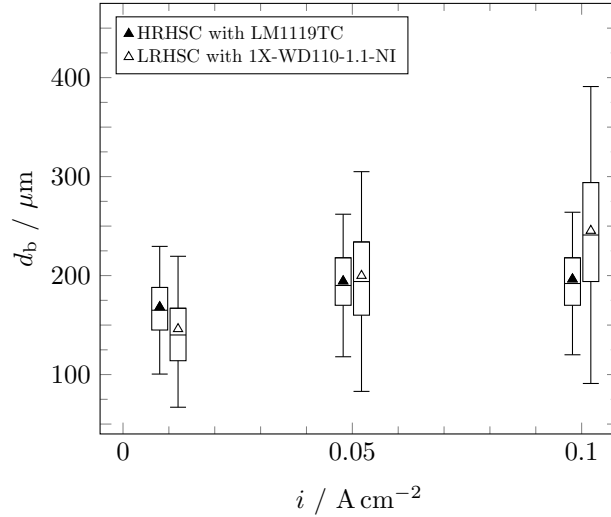


Figure 3.22.: Comparison of the size distribution at 0.01 , 0.05 and 0.1 A cm^{-2} obtained by the two camera systems HRHSC with LM1119TC and LRHSC with 1X-WD110-1.1-NI. To enhance the readability, the box plots are shifted slightly to the left and right, respectively.

3.3. Size distribution of hydrogen bubbles

By switching the position of the anode and cathode in the experimental setup, the size distributions of detached hydrogen bubbles are studied for the same five i values and operating parameters as used in section 3.2.2 for oxygen bubbles. Figure 3.23 displays the number- and volume-weighted distributions for detached hydrogen bubbles at $i=0.15 \text{ A cm}^{-2}$, $u_{\text{el}}^0=0 \text{ mm s}^{-1}$, $c_{\text{Na}^+}=0.6 \text{ mol L}^{-1}$, and a nickel cathode measured at the middle viewing panel. The number-based distribution closely resembles a Gaussian distribution with $\bar{d}_{b,0}$ and $\varsigma_0(d_b)$ amounting 126 and $34 \mu\text{m}$, respectively. Compared to the

size distribution of oxygen bubbles at the same operating conditions (see Figure 3.13), both values are more than halved, showing similar relative behavior to that reported by Janssen et al. [59] and Chin Kwie Joe et al. [58]. As a result, the number of detected bubbles, N_b , increases from 18,065 to 29,496. This increase in N_b also stems from the fact that $\dot{V}_g^{\text{H}_2}$ is twice as large as $\dot{V}_g^{\text{O}_2}$. The volume-weighted distribution, q_3 , shows a similar trend. Though, the depicted q_3 hydrogen size distribution in Figure 3.23 (b) differs from the fitted normal distribution. Here, the distribution could be better resembled by a beta distribution.

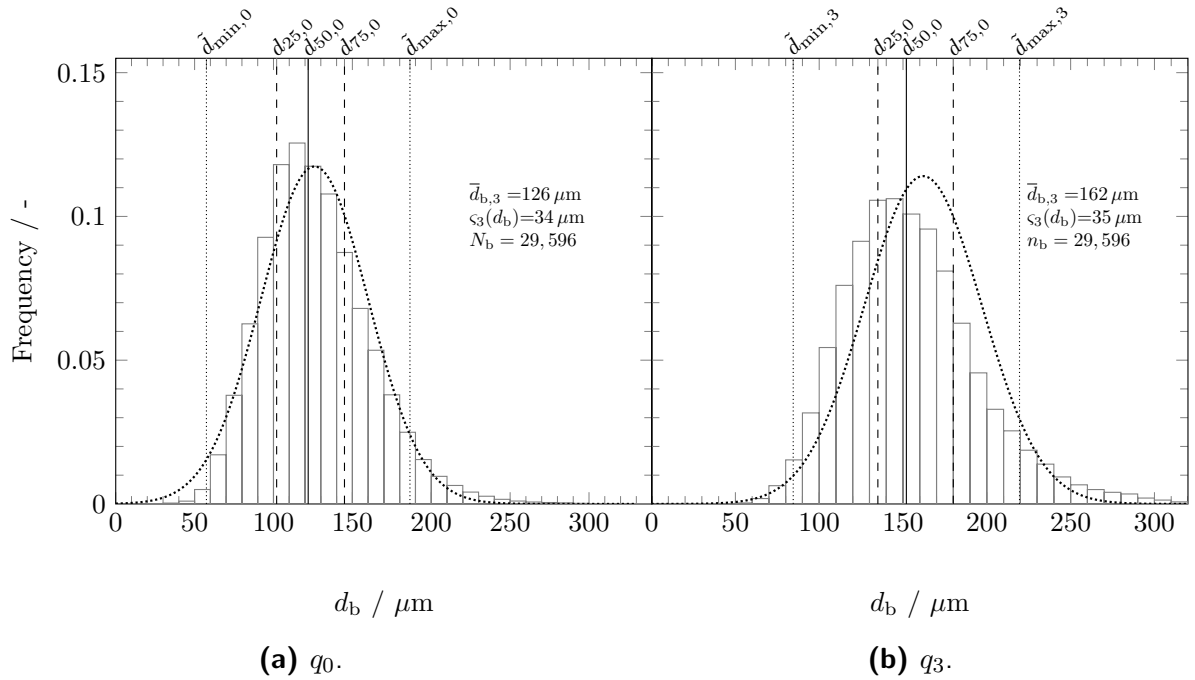


Figure 3.23.: Exemplary (a) number- and (b) volume-weighted size distributions, \tilde{d}_{\min} , d_{25} , d_{50} , d_{75} , and \tilde{d}_{\max} of detached hydrogen bubble at $i=0.15 \text{ A cm}^{-2}$, $u_{\text{el}}^0=0 \text{ mm s}^{-1}$, $c_{\text{Na}^+}=0.6 \text{ mol L}^{-1}$ and a nickel cathode.

Figure 3.24 displays the number- and volume-weighted average size and size distribution of detached hydrogen bubbles at different current densities of 0.01, 0.05, 0.1, 0.15 and 0.2 A cm^{-2} at $u_{\text{el}}^0=0 \text{ mm s}^{-1}$, $c_{\text{Na}^+}=0.6 \text{ mol L}^{-1}$, and for a nickel cathode. For reference, the average size and Sauter mean diameter of the work of Chin Kwie Joe et al. [58] are respectively added to the q_0 and q_3 depicted in Figure 3.24. The number-weighted average mean size amounts $104 \mu\text{m}$ at $i=0.01 \text{ A cm}^{-2}$ and remains relatively constant throughout the different current densities with an averaged mean value of $108 \pm 13 \mu\text{m}$. Compared to the oxygen size distribution results, the IQR is rather small, with an average of $37 \mu\text{m}$, meaning that 50 % of the bubbles around the median are within this size range. After an increase at $i=0.05$ and 0.15 A cm^{-2} to $\bar{d}_{b,0}=116$ and $126 \mu\text{m}$, respectively, the mean size falls to $92 \mu\text{m}$ at the highest value for i (0.2 A cm^{-2}). This decline results from an increased

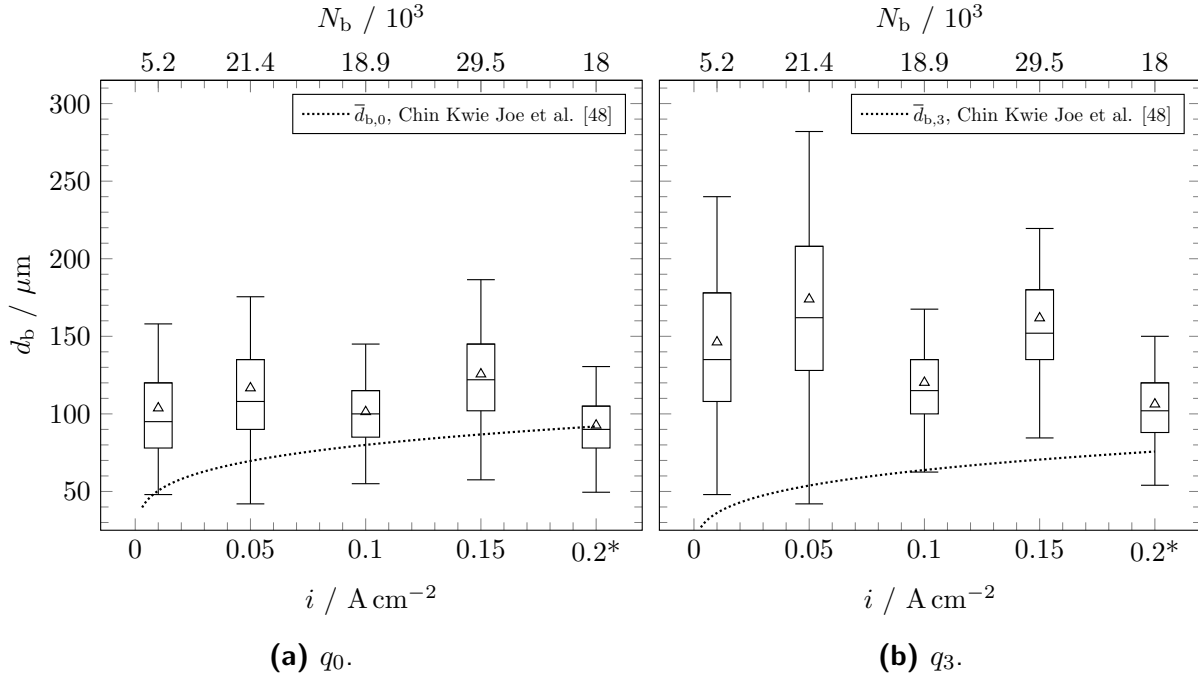


Figure 3.24.: Average **(a)** number- and **(b)** volume-weighted hydrogen bubble size and distribution for $i=0.01, 0.05, 0.1, 0.15$ and 0.2 A cm^{-2} at $u_{\text{el}}^0=0 \text{ mm s}^{-1}$, $c_{\text{Na}^+}=0.6 \text{ mol L}^{-1}$, and for a nickel cathode. (*) indicates the compromise of the experimental data due to overlapping bubbles.

bubble density at these operating conditions, rendering a large area of the image taken with the LRHSC unanalyzable. In particular, the increased chance of overlapping bubbles impairs the detection of large bubbles and favors the detection of smaller bubbles. For illustration, Figure 3.25 shows an analyzed frame at $i=0.2 \text{ A cm}^{-2}$ and the small number of detected bubbles. Further, the brightness fluctuates within the image due to the local bubble density, and the LED light is scattered.

Similar to the measurement of the size distribution of the oxygen bubbles, the number-weighted average hydrogen bubble sizes exceed those reported by Chin Kwie Joe et al. [58] by a margin of up to $100 \mu\text{m}$ at $i=0.05 \text{ A cm}^{-2}$. In contrast to the results in section 3.2.2 for the oxygen bubbles, the average size at the highest current density ($i=0.2 \text{ A cm}^{-2}$) matches the correlation of Chin Kwie Joe et al. [58]. Though, this agreement results from the previously described, flawed analysis of the taken images. In further studies, the illumination could be further fine-tuned alongside the pixel size and exposure time. In addition, dedicated training on the neuronal network would further increase the number of detected bubbles.

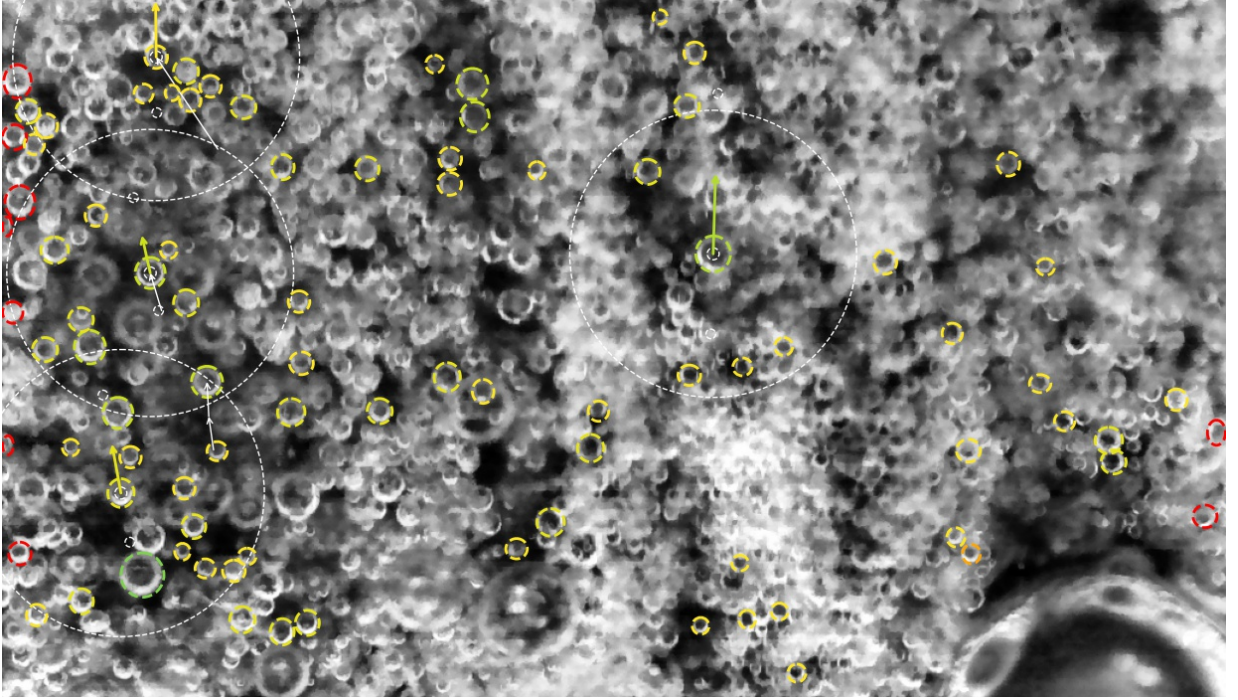


Figure 3.25.: Exemplary detection of the hydrogen bubbles at $i=0.2 \text{ A cm}^{-2}$, $u_{\text{el}}^0=0 \text{ mm s}^{-1}$, $c_{\text{Na}^+}=0.6 \text{ mol L}^{-1}$. The white circles resemble bubbles with successful velocity determination using the PTV algorithm.

3.4. Vertical bubble velocity of oxygen bubbles

Applying the in section 3.1.4 described PTV algorithm to the last 500 images of each experiment, bubble trajectories can be determined between consecutive frames. Here, the number of bubble trajectories determined by the PTV algorithm varies between 20,000 and 150,000, depending on i , u_{el}^0 , and the analyzed viewing panel. On average, each experiment yields approximately 73,000 velocity vectors. In all experiments, the vertical velocity distribution follows a Gaussian profile. For instance, Figure 3.26 presents both the measured velocity distribution and its corresponding normal distribution fit for the middle viewing panel at $i=0.1 \text{ A cm}^{-2}$ and $u_{\text{el}}^0=0 \text{ mm s}^{-1}$. The measured velocities are well-represented by a normal distribution, with the mean velocity $\bar{u}_{\text{b},0}^v$ calculated as 43.9 mm s^{-1} and the standard deviation $\varsigma_0(u_{\text{b}}^v)$ as 13.1 mm s^{-1} . Since a lower velocity threshold $r_{1,\text{min}}$ is applied, no velocities below 5 mm s^{-1} are captured. The introduction of this threshold results in an error of about 0.1 %, as estimated using the cumulative normal distribution function. By analyzing all particle objects tracked over at least five consecutive frames, we estimated the velocity change caused by positional uncertainty: The mean velocity deviation, along with the 99 % confidence interval, is calculated for each size bin and presented alongside the standard deviation in Figure 3.27. For all size bins, the maximum observed mean acceleration is less than 56 mm s^{-2} . Given the chosen frame rate and pixel

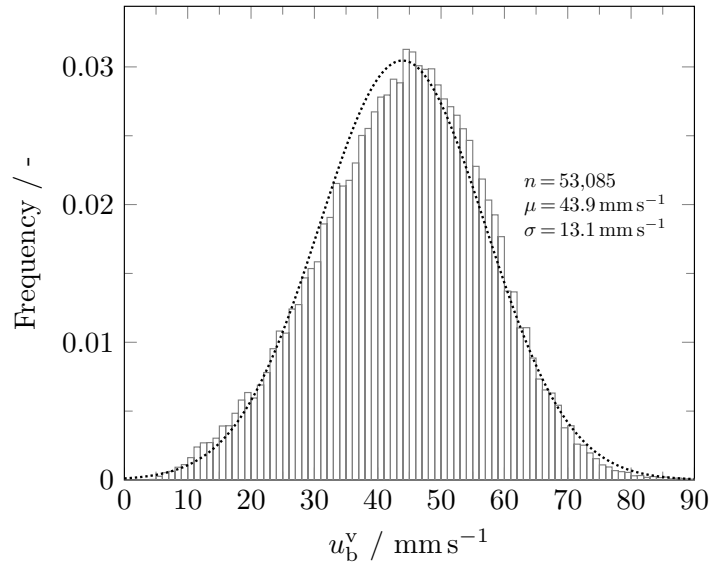


Figure 3.26.: Distribution of vertical velocity of oxygen bubbles over all sizes at $i=0.1 \text{ A cm}^{-2}$, $u_{\text{el}}^0=0 \text{ mm s}^{-1}$, $c_{\text{Na}^+}=0.6 \text{ mol L}^{-1}$, and an IrOMM-coated anode. Figure is adapted from [86].

resolution, this corresponds to a deviation of less than 0.5 pixels between the two measured trajectories. Consequently, the bubbles exhibit little to no acceleration between successive measurements. Moreover, the standard deviations show that 68% of the successive vertical velocities differ by less than ± 2 pixels. Therefore, Γ is estimated to be below 0.71 mm s^{-2} . In addition, no correlation was found between the vertical position and velocity of the bubbles, suggesting that the bubbles reached terminal vertical velocity during their ascent within the 10 mm viewing panel. [86]

3.4.1. Vertical bubble velocity for different bubble size bins

Box plots of the vertical velocities for different bubble size bins at the middle viewing panel are shown in Figure 3.28 at $i=0.1 \text{ A cm}^{-2}$ and $u_{\text{el}}^0=0 \text{ mm s}^{-1}$. The cumulative bubble size distribution is plotted on the right y -axis. For bubble size bins ranging from 130 to $310 \mu\text{m}$, sufficient velocity trajectories were recorded to calculate and display the box plot of the velocity distribution. The median velocity of the smallest bubbles, with sizes between $100 \mu\text{m}$ and $110 \mu\text{m}$, amounts to 26 mm s^{-1} , and the velocity shows logarithmic growth relative to d_b . The bin including $\bar{d}_{b,0}$ ($190\text{--}200 \mu\text{m}$) has an average vertical velocity of 44.1 mm s^{-1} , while larger bubbles with diameters exceeding $300 \mu\text{m}$ exhibit velocities up to 82 mm s^{-1} . [86]

As a reference, the terminal rising velocities of single, electrogenerated oxygen bubbles, as measured by Brandon et al. [182] and Kelsall et al. [183], are included in Figure 3.28. The $\bar{u}_{b,0}(d_b)$ determined in this study exceed those reported by Brandon et al. [182] and Kelsall et al. [183] by uniform offsets of roughly 20 and 30 mm s^{-1} , respectively. These discrepancies

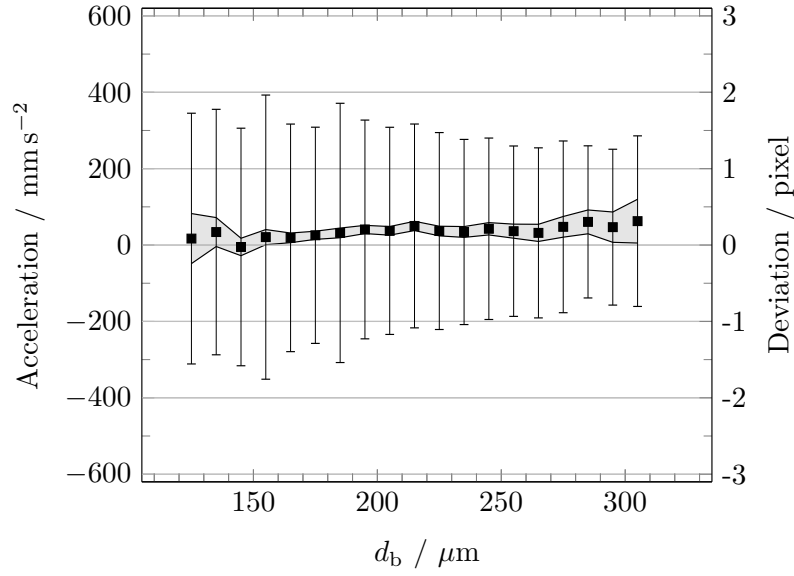


Figure 3.27.: Calculated average acceleration for each bubble size bin at the middle viewing panel for $i=0.1 \text{ A cm}^{-2}$ and $u_{\text{el}}^0=0 \text{ mm s}^{-1}$. The gray area displays the 99 % confidence interval of the average acceleration. The right y-axis indicates the deviation between two subsequent trajectories of a tracked bubble in pixels. Figure is adapted from [86].

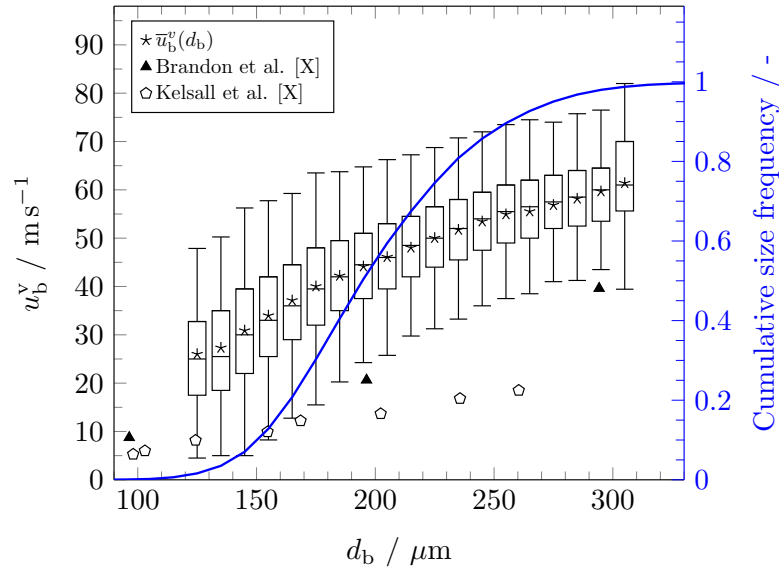


Figure 3.28.: Distribution of u_b^v for different oxygen bubble size bins and cumulative bubble size distribution (blue) at the middle viewing panel at $i=0.1 \text{ A cm}^{-2}$ and $u_{\text{el}}^0=0 \text{ mm s}^{-1}$. For comparison, terminal velocities of single oxygen bubbles, measured by Brandon et al. [182] and Kelsall et al. [183], are added. Figure is adapted from [86].

arise because, in our experiments, bubbles ascend in a swarm within the bubble curtain, while in single-bubble studies, bubbles rise individually in a stationary electrolyte. In typical single-bubble experiments, the vertical velocity increases linearly with bubble size [184]. In contrast, in a parallel plate electrolyzer, the velocity of each bubble is influenced

by the momentum of surrounding bubbles and the accelerated electrolyte. As most bubbles rise near the electrode, the electrolyte acceleration is especially high in this region. Hence, the local electrolyte velocity at the electrode is influenced by the combined momentum of the entire bubble swarm, consisting of bubbles of various sizes. This interaction leads to smaller bubbles experiencing increased velocity due to the enhanced momentum of the electrolyte, driven by larger bubbles. Conversely, the impact of the accelerated electrolyte on larger bubbles is smaller, resulting in the observed asymptotic behavior of u_b^v at larger values for d_b . [86]

The range of the velocity distribution, $\tilde{u}_{\max}^v - \tilde{u}_{\min}^v$, stays close to constant for bubble sizes between 190 μm and 300 μm at $37 \pm 3 \text{ mm s}^{-1}$. However, it broadens for both smaller bubbles ($47 \pm 3 \text{ mm s}^{-1}$) and the largest bubble size bin (43 mm s^{-1}). This broadening in the velocity distribution for the smallest and largest size bins is partially attributed to the smaller sample size, as indicated by the cumulative size frequency. Further, as the absolute difference between a single bubble's velocity and the mean velocity increases, the likelihood of bubble collisions increases, either accelerating or decelerating individual bubbles. [86]

3.4.2. Impact of current density

Figure 9 illustrates the effect of three distinct values for i , and consequently $\dot{V}_g^{\text{O}_2}$, on the measured vertical velocities of gas bubbles ranging in size from 100 to 310 μm . As to be expected, u_b^v increases with d_b at all current densities. For the lowest value for i of 0.01 A cm^{-2} , the relationship between vertical velocity and bubble size is nearly linear. However, at higher current densities — 0.05 A cm^{-2} and 0.1 A cm^{-2} — the rate of velocity increase diminishes for larger bubbles. As current density increases, the average bubble velocity rises. For bubbles sized between 120 and 130 μm at the middle viewing panel, the average vertical velocities are 18.2 mm s^{-1} , 22.2 mm s^{-1} , and 26.0 mm s^{-1} at current densities of 0.01 A cm^{-2} , 0.05 A cm^{-2} , and 0.1 A cm^{-2} , respectively. For larger bubbles between 250 and 260 μm , the differences in the average vertical velocities become more pronounced, with mean velocities of 34.2 mm s^{-1} , 48.8 mm s^{-1} , and 54.9 mm s^{-1} for the same current densities.

These findings showcase the significant dependence of u_b^v on the gas phase fraction. Notably, the average vertical velocity of bubbles with a size of 150 μm at 0.1 A cm^{-2} nearly matches that of bubbles twice the size at 0.01 A cm^{-2} . This indicates that as $\dot{V}_g^{\text{O}_2}$ increases, the local electrolyte velocity, along with the mean bubble size also enlarges. As shown and discussed in sections 3.2.2 and 3.2.6, the average bubble sizes measured with the HRHPC system at $u_{\text{el}}^0 = 0 \text{ mm s}^{-1}$ for the three different current densities grow from 182 μm at 0.01 A cm^{-2} to 196 μm at 0.05 A cm^{-2} and 205 μm at 0.1 A cm^{-2} . Thus, the representation of the average velocity of each individual bubble size counteracts the superposition

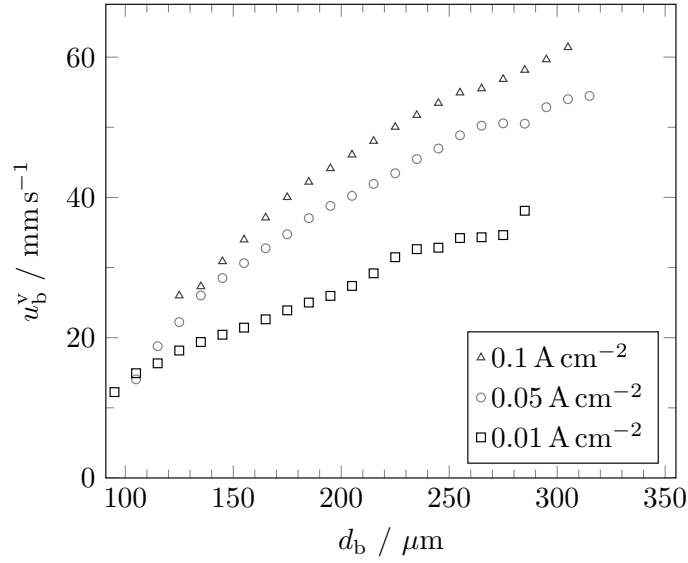


Figure 3.29.: Comparison of the average vertical velocity of oxygen bubbles at the middle viewing panels at different $i = 0.01, 0.5$ and 0.1 A cm^{-2} and $u_{\text{el}}^v = 0 \text{ mm s}^{-1}$. Figure is adapted from [86].

caused by the increasing mean bubble size. [86]

Due to the absence of large experimental works investigating the interplay of u_b , d_b , u_{el}^0 , and i , comparisons with literature are limited. The values for \bar{u}_b reported in the work of Boissonneau and Byrne [88] surpass the values presented in Figure 3.29. At $u_{\text{el}}^0 = 0 \text{ mm s}^{-1}$, they recorded mean velocities of 50 mm s^{-1} for electrogenerated hydrogen bubbles at 0.05 A cm^{-2} and 70 mm s^{-1} at 0.1 A cm^{-2} , compared to our measured mean vertical velocities of 38 mm s^{-1} and 44 mm s^{-1} for oxygen bubbles at the same current densities. However, these discrepancies are likely due to differences in experimental setups and bubble types. While our study used a membrane-separated parallel plate electrolyzer with an electrode-membrane gap of 8 mm, Boissonneau and Byrne [88] utilized a membrane-less setup with a small inter-electrode gap of 3 mm where oxygen and hydrogen bubbles could mix. As a result, this mixing altered the electrolyte flow and made it difficult to precisely report individual oxygen and hydrogen bubble diameters and velocities.

3.4.3. Vertical bubble velocity across measuring panels

By determining the bubble velocity at the three different viewing panels, the effect of increasing height and, consequently, rise in gas fraction can be studied. Figure 3.30 depicts the resulting average vertical velocities for the bottom, middle, and top panels against different bubble size bins, under conditions of $i = 0.1 \text{ A cm}^{-2}$ and $u_{\text{el}}^0 = 0 \text{ mm s}^{-1}$. For bubbles smaller than $150 \mu\text{m}$, the difference in mean bubble velocity between the viewing panels is minimal. However, as bubble size increases, the velocity differences between the bottom,

middle, and top panels become apparent: At a bubble size of $190\text{ }\mu\text{m}$, the mean velocity at the bottom panel is 39 mm s^{-1} , which is 6 mm s^{-1} lower than at the middle and top panels. For bubbles larger than $200\text{ }\mu\text{m}$, the mean velocities at the middle and top panels begin to diverge, For sizes between $290\text{ }\mu\text{m}$ and $300\text{ }\mu\text{m}$, the corresponding mean velocities at the bottom, middle, and top panels are 53 mm s^{-1} , 60 mm s^{-1} , and 70 mm s^{-1} , respectively. The relative standard deviation for each size bin decreases consistently, regardless of the viewing panel, from roughly 40 % for small bubbles to 13 % for larger bubbles. [86]

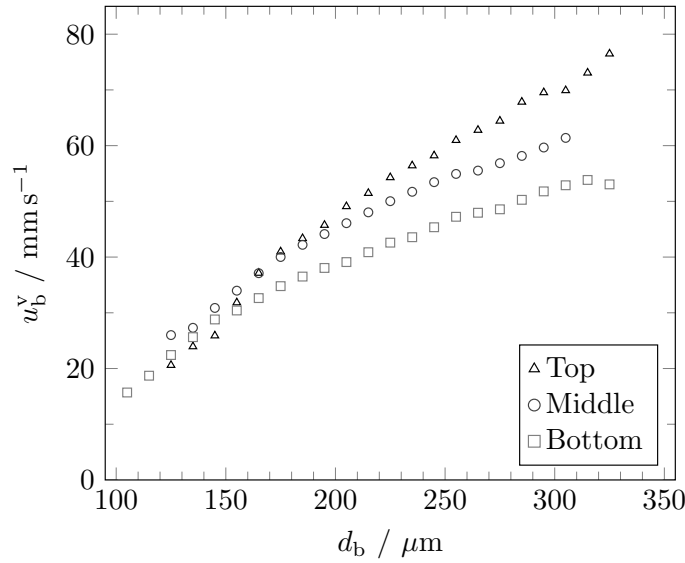


Figure 3.30.: Comparison of the average vertical velocity at the three different viewing panels, bottom, middle and top, at $i=0.1\text{ A cm}^{-2}$ and $u_{\text{el}}^v=0\text{ mm s}^{-1}$. Figure is adapted from [86].

At the lowest current density of 0.01 A cm^{-2} , the vertical velocity exhibits a linear increase with respect to bubble size, whereas greater values for i showed a more asymptotic increase. Here, at $i=0.05\text{ A cm}^{-2}$, the difference between the average values of size bins decreases with greater bubble size. The results for $i=0.01\text{ A cm}^{-2}$ are comparable to the linear correlation reported for electrogenerated hydrogen bubbles by Davis et al. [87]. They reported a linear correlation of bubble velocity and size for bubbles with sizes between 50 and $600\text{ }\mu\text{m}$ at experiments with a similar, low value for i of 0.02 A cm^{-2} . As described in the previous section 3.4.1, the increase of i and thus \dot{V}_g leads to a larger gas phase fraction and bubble collision rates that affect u_b^v of especially larger and smaller bubbles. [86]

Table 3.11 lists the average and standard deviation of both the velocity of all detected bubbles at the three viewing panels at $i=0.01$, 0.05 , and 0.1 A cm^{-2} alongside the average increase of \bar{u}_b^v of the panel with respect to the average velocity at the bottom panel. On average, the relative change of \bar{u}_b^v with respect to the value measured at the bottom viewing panel amounts to roughly +15 % at the middle and +30 % at the top panel. Thus, the linear relative increase between each viewing panel is consistent with the amount of additional

gas volume produced between the viewing panels. Here, the active electrode height at the lower edge of the bottom panel amounts to 25.5 mm and height of the active electrode segment in between the panels is 20 mm. Therefore, a relative change in active electrode height and thereby linked relative change in \dot{V}_g of roughly 44 % leads to an increase of 15 % of \bar{u}_b^v .

Table 3.11.: \bar{u}_b^v and $\varsigma_0(\bar{u}_b^v)$ for the vertical bubble velocity distribution at the three different viewing panels at $i=0.01, 0.05$ and 0.1 A cm^{-2} and $u_{el}^0=0 \text{ mm s}^{-1}$.

i Panel	0.01 A cm^{-2}	0.05 A cm^{-2}	0.1 A cm^{-2}	$\frac{\bar{u}_b^v - \bar{u}_{b, \text{Bottom}}^v}{\bar{u}_{b, \text{Bottom}}^v}$
Top	$27.6 \pm 7.5 \text{ mm s}^{-1}$	$42.8 \pm 14 \text{ mm s}^{-1}$	$49.6 \pm 16.9 \text{ mm s}^{-1}$	30.4 %
Middle	$23.5 \pm 6.4 \text{ mm s}^{-1}$	$38.5 \pm 10.5 \text{ mm s}^{-1}$	$43.9 \pm 13.1 \text{ mm s}^{-1}$	14.7 %
Bottom	$21.8 \pm 5.6 \text{ mm s}^{-1}$	$30.7 \pm 8.4 \text{ mm s}^{-1}$	$39.5 \pm 10.0 \text{ mm s}^{-1}$	-

Over the three viewing panels, the average size of all evaluated oxygen bubbles remains almost constant, with the maximum variation in average bubble size being $15 \mu\text{m}$ [86]. This small variation was also detected by the LRHSC and discussed in section 3.2.3. Therefore, it can be concluded that the observed increase in u_b^v primarily results from the rise in gas fraction and the corresponding local electrolyte acceleration along the electrode height. By limiting the comparison to bubbles within a specific size range, we eliminate the effect of bubble size on the vertical velocity across different operating conditions. The changes in Re_b , and hence the experienced drag, are solely due to local relative velocity and bubble-bubble interactions. This finding is consistent with previous studies: Boissonneau and Byrne [88] measured u_b^v in a small electrochemical cell. They report an increase of u_b^v with respect to the active electrode surface, followed by a uniform velocity above the electrode as the gas fraction and electrolyte velocity stabilize [88]. At heights comparable to the bottom and middle viewing panels of the used setup in this thesis, Abdelouahed et al. [111] reported mean velocities of 17 mm s^{-1} and 20 mm s^{-1} for oxygen bubbles with a mean size of $120 \mu\text{m}$ in a lantern blade electrode at $i=0.1 \text{ A cm}^{-2}$ and $u_{el}^0=0 \text{ mm s}^{-1}$. [86]

3.4.4. Impact of electrolyte flow velocity

By adjusting the volumetric flow rates of the peristaltic pumps, u_0^{el} is set to 10 mm s^{-1} and 20 mm s^{-1} , switching the parallel plate electrolyzer to FCF mode. Under these FCF conditions, the angle of ascend Λ of the bubble movement changes. To depict this observation, the measured values for Λ for all viewing panels are combined and presented in Figure 3.31, showing results for $i=0.1 \text{ A cm}^{-2}$ at $u_0^{el} = 0, 10$, and 20 mm s^{-1} . In this con-

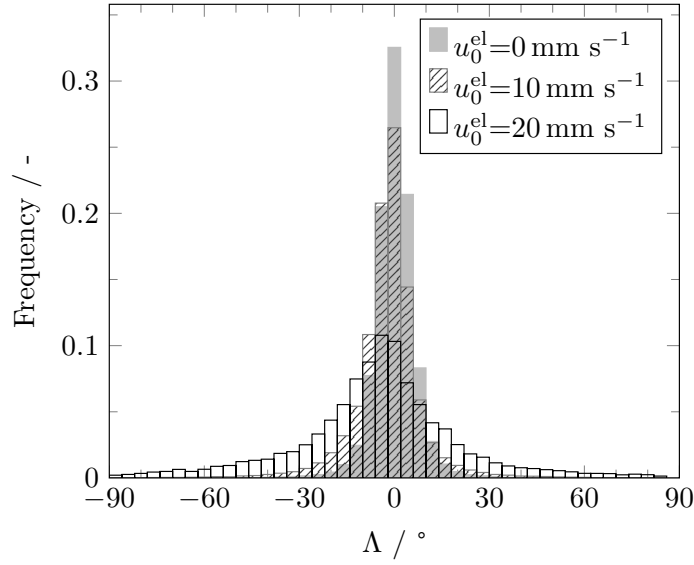


Figure 3.31.: Distribution of Λ of u_b at $u_{el}^0=0$, 10 and $u_{el}^0=20 \text{ mm s}^{-1}$. An angle of 0° corresponds to a straight vertical velocity trajectory. Figure is adapted from [86].

text, an angle of 0° represents a perfectly vertical, upward trajectory. At NNF conditions ($u_{el}^0=0 \text{ mm s}^{-1}$), most bubbles rise completely vertically, with a mean angle of -0.1° and a standard deviation of 6.5° , meaning that 95% of bubbles are having an upward trajectory within $\pm 12.8^\circ$. When u_{el}^0 is increased to 10 mm s^{-1} , the angle distribution broadens, with the standard deviation increasing to 11.4° and the mean angle slightly shifting to -1.9° and to the left. At $u_{el}^0 = 20 \text{ mm s}^{-1}$, this trend continues: the distribution of Λ widens even further, with a mean of -11° and a standard deviation of 23.7° . The observed rightward shift at $u_{el}^0 = 20 \text{ mm s}^{-1}$ also arises at lower values for i . [86]

Subsequently, the impact of different u_{el}^0 on u_b^v of different bubble sizes is evaluated. Figure 3.32 shows the box plot diagrams for the velocity distribution of three different size bins - $150\text{-}160 \mu\text{m}$, $210\text{-}220 \mu\text{m}$, and $300\text{-}310 \mu\text{m}$ - at $i=0.1 \text{ A cm}^{-2}$ for different u_{el}^0 between 0 and $u_{el}^0=30 \text{ mm s}^{-1}$. Further, \bar{u}_b^v for all evaluated trajectories is added to Figure 3.32. As discussed in Section 3.4.1, the average bubble velocity highly depends on the present size bin. At $u_{el}^0=0 \text{ mm s}^{-1}$, \bar{u}_b^v respectively amounts to 34, 48 and 61 mm s^{-1} for the three bubble size bins, $150\text{-}160 \mu\text{m}$, $210\text{-}220 \mu\text{m}$, and $300\text{-}310 \mu\text{m}$. The values for \bar{u}_b^v and $\zeta_0(u_b^v)$ remain almost unchanged when raising u_{el}^0 to 10 mm s^{-1} . By further increasing u_{el}^0 to 20 mm s^{-1} , the velocity distributions of all bubbles and the three distinct size bins decrease. For example, for bubbles with a medium size in between 210 and $220 \mu\text{m}$, \bar{u}_b^v amounts to 17.6 mm s^{-1} , which is close to the obtained value of all measured bubbles, $\bar{u}_b^v=20.4 \text{ mm s}^{-1}$. In addition, $\tilde{u}_{b,\min}$ for the two smaller bubble size bins is below the lower limit of 5 mm s^{-1} introduced by $r_{1,\min}$ of the stuck bubble detection. Hence, \bar{u}_b^v could be even below the algorithm determined value for the two size bins since bubbles between $\pm 5 \text{ mm s}^{-1}$ were discarded.

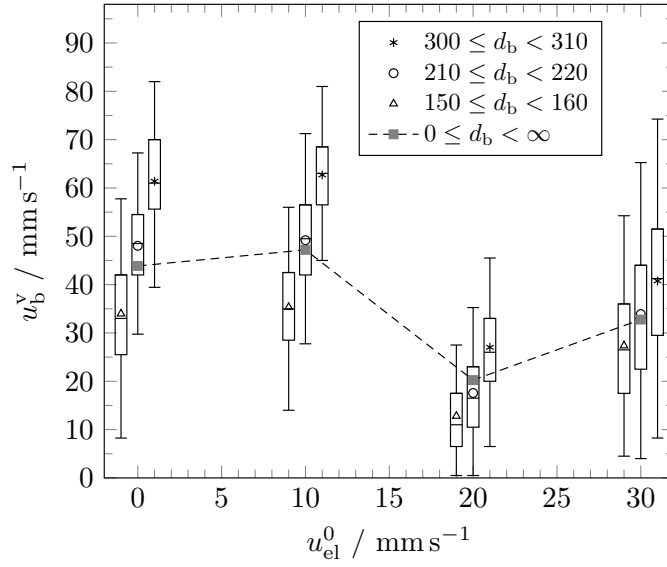


Figure 3.32.: Impact of u_{el}^0 on u_b^v of oxygen bubbles with different sizes at $i=0.1 \text{ A cm}^{-2}$. Figure is adapted from [86].

When increasing u_{el}^0 to 30 mm s^{-1} , the bubble velocity follows along: \bar{u}_b^v of all bubbles increases from 20.4 mm s^{-1} at $u_{el}^0=20 \text{ mm s}^{-1}$ to 32.8 mm s^{-1} at $u_{el}^0=30 \text{ mm s}^{-1}$. Thereby, \bar{u}_b^v and $\tilde{u}_{\max}^v - \tilde{u}_{\min}^v$ of the three size bins raises to 27.3 mm s^{-1} and 49.8 mm s^{-1} for $d_b=150\text{--}160 \text{ }\mu\text{m}$, 34 mm s^{-1} and 60.3 mm s^{-1} for $210\text{--}220 \text{ }\mu\text{m}$, and 40.8 mm s^{-1} and 66 mm s^{-1} for d_b $300\text{--}310 \text{ }\mu\text{m}$.

For u_{el}^0 up to 20 mm s^{-1} , similar effects are observed for the $i=0.05 \text{ A cm}^{-2}$. Figure 3.33 displays \bar{u}_b^v of the average size bin with $210 \text{ }\mu\text{m} < d_b < 220 \text{ }\mu\text{m}$ for $i=0.01, 0.05$, and 0.1 A cm^{-2} and $u_{el}^0=0, 10$, and 20 mm s^{-1} . For a current density of 0.05 A cm^{-2} , the decline of u_b already begins at $u_{el}^0 = 10 \text{ mm s}^{-1}$, where \bar{u}_b^v decreases from 42 mm s^{-1} at $u_{el}^0=0 \text{ mm s}^{-1}$ to 35 mm s^{-1} at $u_{el}^0=10 \text{ mm s}^{-1}$. Finally, at $u_{el}^0=20 \text{ mm s}^{-1}$, \bar{u}_b^v drops to an average of 18.5 mm s^{-1} . In contrast, at the smallest current density of $i = 0.01 \text{ A cm}^{-2}$, \bar{u}_b^v of the studied size bin stays around 27 mm s^{-1} , regardless of the value of u_{el}^0 . [86] The measured widening of the distribution of Λ alongside the first decline in \bar{u}_b^v and subsequent equality to u_{el}^0 arose from the following three factors:

- (i) **Flow pattern transition:** As suggested by Alexiadis et al. [104, 122], the flow pattern shifts from 'quasi-steady' to 'transitional' as u_{el}^0 increases. Figure 2.12 depicts these changes and the disruption of the two vertical flow regimes, causing individual bubbles to drift away from the electrode and into the bulk electrolyte. Consequently, the bubbles experience changes in relative velocity, local gas volume fraction, and drag. Inside bulk electrolyte, the acceleration due to the lower gas phase fraction is smaller, resulting in lower values for u_b^v that are closer to that of single bubble rising velocities [182, 183]. The results for $i=0.01 \text{ A cm}^{-2}$ and electrolyte velocities

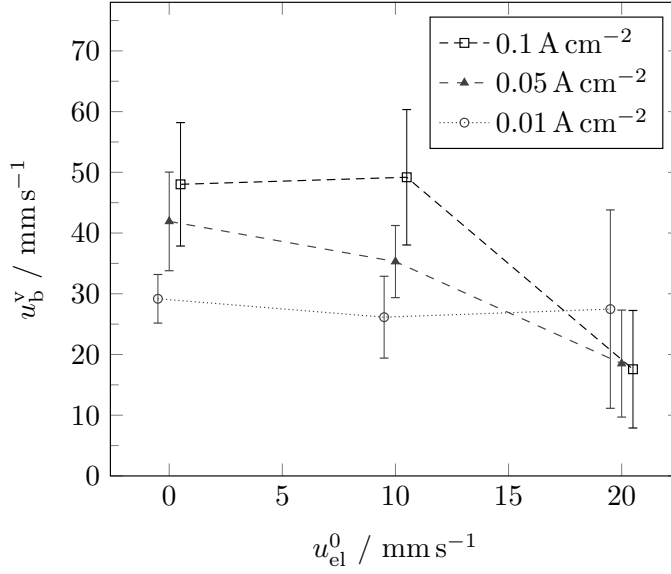


Figure 3.33.: Comparison of \bar{u}_b^v for bubbles with a size between $210 \mu\text{m} < d_b < 220 \mu\text{m}$ at $i=0.01, 0.5$, and 0.1 A cm^{-2} , and $u_{el}^0=0, 10$ and 20 mm s^{-1} . For readability, the curves for $i=0.01$ and 0.01 A cm^{-2} are slightly displaced to the right and left, respectively. Figure is adapted from [86].

of 20 and 30 mm s^{-1} show that after the breakup of the segregated flow, the average bubble size seems to align with u_{el}^0 . Further, this pattern shift depends not only on u_0^{el} but also significantly on the current density i , which explains the different behaviors observed at $i=0.01, 0.05$, and $i=0.1 \text{ A cm}^{-2}$. Overall, at $i=0.01 \text{ A cm}^{-2}$, the gas phase fraction is small. As a result, swarm effects and high electrolyte acceleration are not presented, leading to a constant \bar{u}_b^v . Solely, $\varsigma_0(u_b^v)$ increases, most likely due to velocity fluctuations induced by the forced convection. Although the Reynolds number for the continuous phase that can be calculated by using u_0^{el} and the hydraulic diameter ($d_{\text{hydraulic}} \approx 8 \text{ mm}$) amounts to 294 for $u_{el}^0=20 \text{ mm s}^{-1}$, the flow behavior near the electrode is likely pseudo-turbulent [104, 111], inducing the measured changes in velocity.

- (ii) **Peristaltic pump effects:** The use of peristaltic pumps to create forced convection results in a non-continuous electrolyte flow, causing bubbles to experience oscillations [185]. By periodically pushing-stopping-pushing the electrolyte, bubbles are also dragged back and forth, and local disturbances of the flow field are created that induce horizontal movements of the bubbles. Ultimately, this leads to the widening of the measured distribution of Λ . This horizontal movement disrupts the straight upward electrolyte flow and bubble motion near the electrode, increasing the drag force and subsequently reducing vertical bubble velocity.
- (iii) **Electrolyte backflow disturbance:** As illustrated in Figure 2.12, the rising bub-

bles generate a backflow in the bulk electrolyte at greater values for i , which enhances the electrolyte velocity near the electrode [94, 118, 122]. When larger convective electrolyte flow is applied, it disrupts this back- and circular flow within the parallel plate electrolyzer. As a result, the bubble velocity decreases, the collision rate increases, and the bubble curtain widens. Thereby, the local gas volume fraction near the electrode, further decreasing u_b^v . [86]

3.5. Vertical bubble velocity of hydrogen bubbles

By using the raw data taken for the size distribution measurements of hydrogen bubbles, u_b^v can also be determined for the hydrogen bubbles. Though, the employed LRHSC system only allows for a resolution of the determined velocity in steps of 2.74 mm s^{-1} . Figure 3.34 maps the vertical bubble velocity distribution of hydrogen bubbles at $i=0.1 \text{ A cm}^{-2}$, $u_{\text{el}}^0=0 \text{ mm s}^{-1}$, $c_{\text{Na}^+}=0.6 \text{ mol L}^{-1}$, and using nickel as cathode material. The distribution of u_b^v closely follows a Gaussian distribution and compared to the velocity distribution of oxygen bubbles (Figure 3.26), \bar{u}_b^v and $\varsigma_0(u_b^v)$ doubled to 86.5 mm s^{-1} and 30.6 mm s^{-1} , respectively. This is despite the lower value of \bar{d}_b for the analyzed hydrogen bubbles of $126 \mu\text{m}$ than the corresponding value of $196 \mu\text{m}$ for the oxygen bubbles.

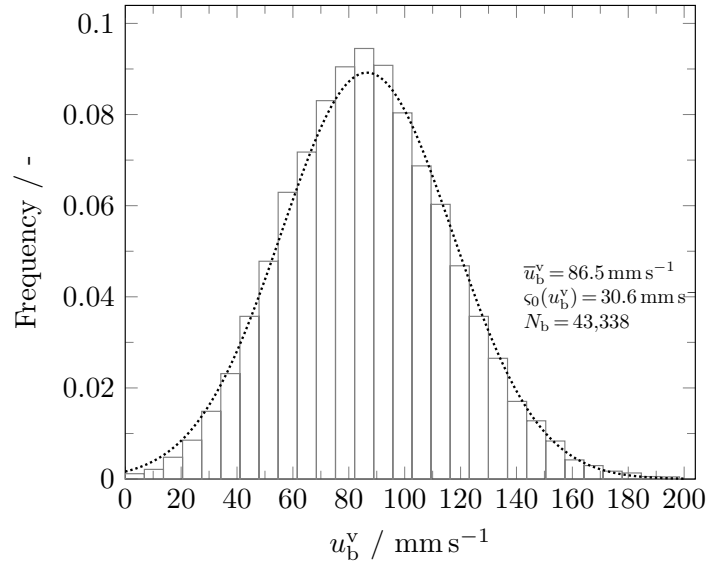


Figure 3.34.: Distribution of vertical velocity of hydrogen bubbles over all sizes at $i=0.1 \text{ A cm}^{-2}$, $u_{\text{el}}^0=0 \text{ mm s}^{-1}$, $c_{\text{Na}^+}=0.6 \text{ mol L}^{-1}$, and nickel cathode.

By sorting the vertical bubble velocity into the $10 \mu\text{m}$ -spaced size bins, \tilde{u}_{min}^v , u_{25}^v , u_{50}^v , u_{75}^v , and \tilde{u}_{max}^v can be calculated for each size bin containing at least 200 data points and Figure 3.35 depicts the resulting box plot. Further, the rising velocities of hydrogen bubbles in a membrane-less electrolyzer reported by Davis et al. [87] are added for comparison to

Figure 3.35 alongside the cumulative size-frequency on the right y-axis. The median of each

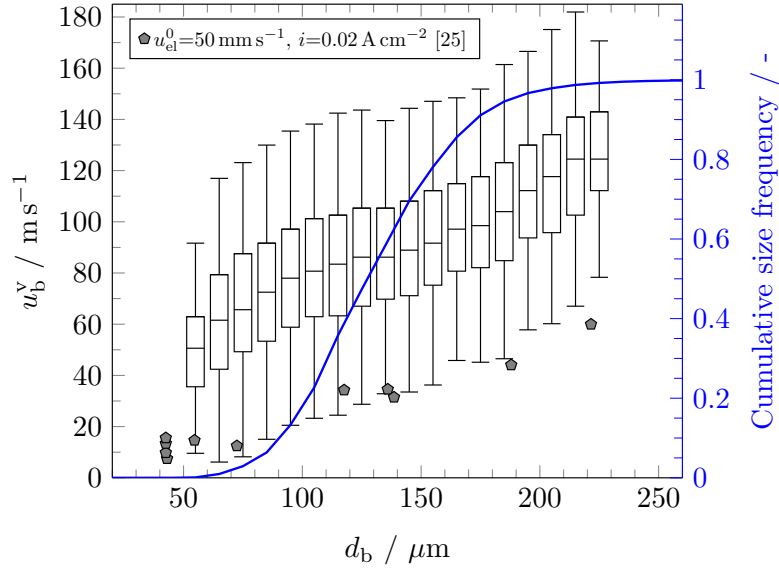


Figure 3.35.: Box plots of u_b^v for different hydrogen bubble size bins and cumulative bubble size distribution (blue) at the middle viewing panel at $i=0.1 \text{ A cm}^{-2}$ and $u_{el}^0=0 \text{ mm s}^{-1}$. For comparison, velocities of hydrogen bubbles measured by Davis et al. [87] are added.

size bin's velocity distribution increases monotonically with respect to d_b from 50.6 mm s^{-1} for d_b in between $50\text{-}60 \mu\text{m}$ to 86.2 mm s^{-1} at $120\text{;}d_b\text{;}130 \mu\text{m}$ and finally 124.5 mm s^{-1} for the largest size bin of $220\text{-}230 \mu\text{m}$. Throughout all size bins except the first, the IQR remains almost constant at a value of $37 \pm 2.1 \text{ mm s}^{-1}$, and on average, the span ($\tilde{u}_{\max}^v - \tilde{u}_{\min}^v$) amounts to $73.6 \pm 5.2 \text{ mm s}^{-1}$. Further, \bar{u}_b^v of the size bins between 90 and $170 \mu\text{m}$ that contain the majority of $\approx 72\%$ of the analyzed bubbles only show a small increase of 13.6 mm s^{-1} . Compared to the vertical velocity distribution of all oxygen bubbles at the same operating conditions (see Figure 3.26), the distribution of a single hydrogen bubble size bin exhibits a similar width and span. This broad distribution results from the higher local gas phase fraction, which is induced from the doubled \dot{V}_g of hydrogen at the same i and hereby increased bubble collision frequency.

The obtained results exceed the reported tuple of bubble velocity and size data from Davis et al. [87], who reported a linear correlation between velocity and size by an average of 69 mm s^{-1} . Though, they operated their membrane-less electrolyzer at $i=0.02 \text{ A cm}^{-2}$ and $u_{el}^0=50 \text{ mm s}^{-1}$ to prevent gas crossover. As a result, the bubble-bubble interactions are limited, and a local acceleration of the electrolyte is prevented. Boissonneau and Byrne [88] measured the lumped velocity of hydrogen and oxygen bubbles along with that of the electrolyte. At $u_{el}^0=0 \text{ mm s}^{-1}$ and $i=0.1 \text{ A cm}^{-2}$, they reported velocities of about 80 mm s^{-1} that match the presented value for \bar{u}_b^v in Figure 3.34. Though, their experimental setup consisted of a membrane-less electrolyzer with a small inter-electrode gap of 3 mm that

most likely led to a mixing of the oxygen and hydrogen bubbles.

Next, to study the effect of \dot{V}_g on the \bar{u}_b^v of the different size bins, i is varied to 0.01 and 0.05 A cm⁻². Figure 3.36 depicts the resulting average velocities of each size bin for the two operating conditions alongside the previously shown values at $i=0.1$ A cm⁻². At

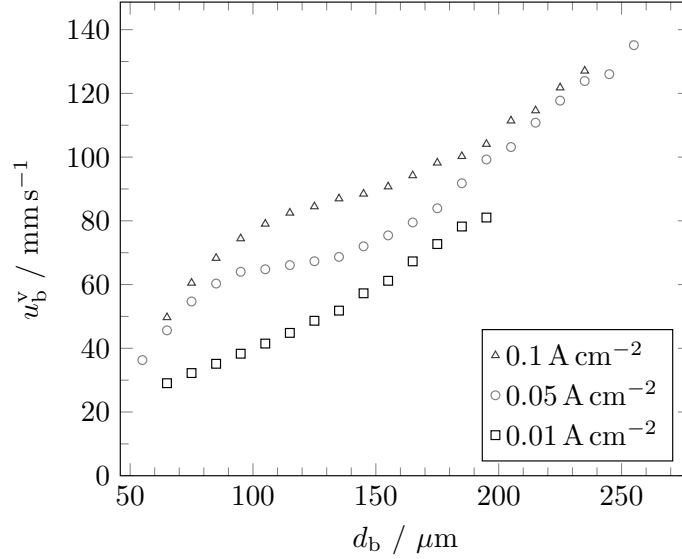


Figure 3.36.: Comparison of the average vertical velocity of hydrogen bubbles at the middle viewing panels at different $i = 0.01, 0.5$ and 0.1 A cm^{-2} and $u_{el}^0 = 0 \text{ mm s}^{-1}$.

$i=0.05 \text{ A cm}^{-2}$, the progression of \bar{u}_b^v with respect to d_b is similar to that obtained for $i=0.1 \text{ A cm}^{-2}$. The gradient of the vertical velocity can be divided into three different sections: First, \bar{u}_b^v increases linearly from 36.3 mm s^{-1} for $d_b = 55 \pm 5 \mu\text{m}$ to 60.3 mm s^{-1} for bubbles with sizes between 80 and 90 μm . Subsequently, \bar{u}_b^v remains almost constant for $90 < d_b < 140 \mu\text{m}$ and shows only a slight increase from 64 mm s^{-1} to 72 mm s^{-1} . Again, as previously discussed for $i=0.1 \text{ A cm}^{-2}$, this size range accounts for 62.5 % of successfully analyzed bubbles. After this plateau, \bar{u}_b^v increases linearly again with a slope of roughly $0.6 \text{ mm s}^{-1} \mu\text{m}$. In contrast, the slope of \bar{u}_b^v against d_b at $i=0.01 \text{ A cm}^{-2}$ remains linear with a gradient of $0.41 \text{ mm s}^{-1} \mu\text{m}$, which represents the data with an R^2 of 0.987. This linear correlation matches the findings from Davis et al. [87], who measured the relation between u_b and d_b at $i=0.02 \text{ A cm}^{-2}$ and reported an increase of $0.25 \text{ mm s}^{-1} \mu\text{m}$. As previously discussed, this different behavior at low current densities results from the lower gas phase fraction and thereby correlates lower acceleration of electrolyte and bubble-bubble interactions.

3.6. PIV measurment of anolyte flow field

To qualitatively measure the flow field between electrode and membrane, a PIV algorithm was applied on images taken of the xz -plane of the custom made electrolyzer. The examination of the 'mixed' electrolyte-bubble flow in this plane allows for a 3-dimensional discussion of the flow field and comparison with simulation data. Further, it enables the examination of the bubble curtain behavior at different operating conditions and the top and bottom viewing panel. Through the described setup in section 3.1.5 and the small illuminated area, a few limitations described in the fundamentals section 2.2.3 can be circumvented. Though, the PIV algorithm determines a 'mixed' velocity, u_m^v that is composed by both the movement of bubbles and tracer particles.

Exemplary, Figure 3.37 depicts the local values for u_m^v , the direction of the velocity and streamlines for $i=0.1 \text{ A cm}^{-2}$, $u_{el}^0=0 \text{ mm s}^{-1}$ at the top viewing panel averaged over 1 s. The color code of u_m^v is displayed on the right side and dark blue corresponds to a negative (downward) value of -20 mm s^{-1} whereas red represents the maximal upward vertical velocity of 26 mm s^{-1} . This figure perfectly illustrates the presence of the two flow regimes as described in section 2.12 that consists of on the one hand an area close to the electrode with an upward velocity and on the other hand area with a downward flow outside the bubble curtain. The circulation between both flow regimes is indicated by the calculated yellow streamlines. For better comparison of different operating conditions, the white poly-line is introduced that ranges from the electrode ($D_{E \rightarrow M}=0$) to the membrane on the right edge. The circulation of the electrolyte originates from bubbles ascending, reaching the electrolyte-air interface at the top of the electrolyzer and inducing a downward flow when the bubble escape into the gas headspace. In addition, Figure 3.37 also shows the raw image data of the bubble-electrolyte flow used as the basis for the PIV algorithm.

3.6.1. Impact of current density and electrolyte flow velocity

The extracted values of u_m^v along the white poly-line displayed in Figure 3.37 are plotted in Figure 3.38 (a) alongside the corresponding curves for $i=0.01$ and 0.05 A cm^{-2} at $u_{el}^0=0 \text{ mm s}^{-1}$. Here, the width of the bubble curtain and first flow regime can be determined by the range of $D_{E \rightarrow M}$ in which u_m^v is positive. A negative value for u_m^v indicates the second flow regime where a downward flow is induced by the rising bubbles of the first regime. For each of the three values of i , the width of the bubble curtain is about 3 mm and is independent of i . For both $i=0.05$ and 0.1 A cm^{-2} , u_m^v amounts to roughly 25 mm s^{-1} in between the electrode surface and 1 mm into the electrolyte. Afterwards, u_m^v decreases until it becomes negative at $D_{E \rightarrow M}=3 \text{ mm}$. At $D_{E \rightarrow M} \approx 5.5 \text{ mm}$, u_m^v reaches its minima of -10.3 mm s^{-1} and -16.5 mm s^{-1} for $i=0.05$ and 0.1 A cm^{-2} , respectively. By

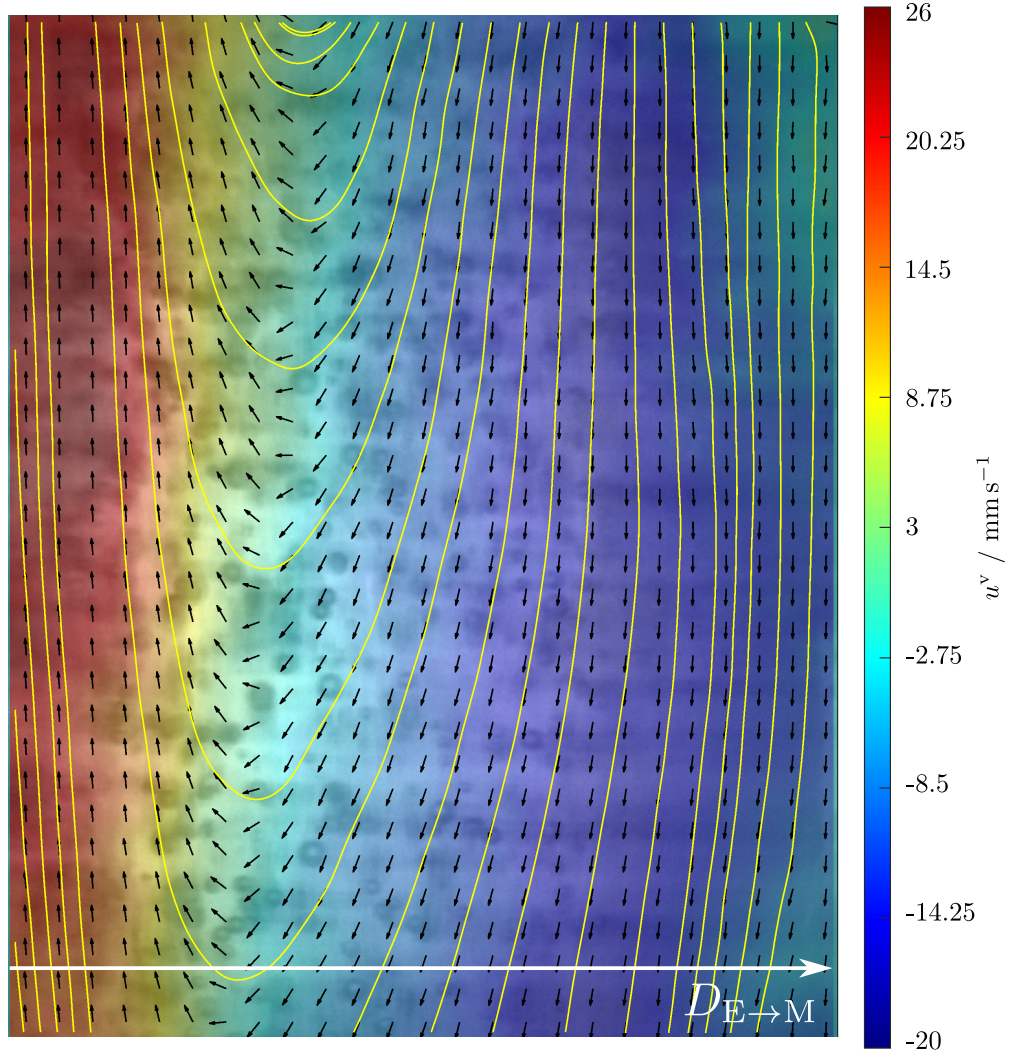


Figure 3.37.: Illustration of the averaged PIV measurement over 1 s at $i=0.1 \text{ A cm}^{-2}$, $u_{\text{el}}^0=0 \text{ mm s}^{-1}$, and the top viewing panel with the color legend on the right. Streamlines are indicated by yellow lines. The white line illustrates the poly-line along which the vertical velocity is evaluated in the following from the electrode ($D_{\text{E} \rightarrow \text{M}}=0$) to the membrane.

integrating the up- and downwards flow at $i=0.05 \text{ A cm}^{-2}$ alongside $D_{\text{E} \rightarrow \text{M}}$, the positive and negative flow rate per unit width, q^+ and q^- , can be determined to $39.3 \text{ mm}^2 \text{ s}^{-1}$ and $-37.7 \text{ mm}^2 \text{ s}^{-1}$. By adding q^+ and q^- together and dividing the resulting value by the electrode-membrane gap, an average 'mixed' vertical velocity of 0.2 mm s^{-1} can be calculated that is very close to $u_{\text{el}}^0=0 \text{ mm s}^{-1}$ and fulfills the momentum balance. For $i=0.01$ and 0.1 A cm^{-2} the average 'mixed' vertical velocity amount 2.2 mm s^{-1} and -2.1 mm s^{-1} , showing a small deviation from u_{el}^0 .

When a forced circulation of $u_{\text{el}}^0=20 \text{ mm s}^{-1}$ is applied, the flow field of the anolyte and spatial distribution of bubble drastically changes: Figure 3.38 depicts the course of u_{m}^v along $D_{\text{E} \rightarrow \text{M}}$ for the three current densities of 0.01 , 0.05 , and 0.1 A cm^{-2} . By pushing electrolyte through the electrolyzer, the backflow of the electrolyte is completely suppressed, which is

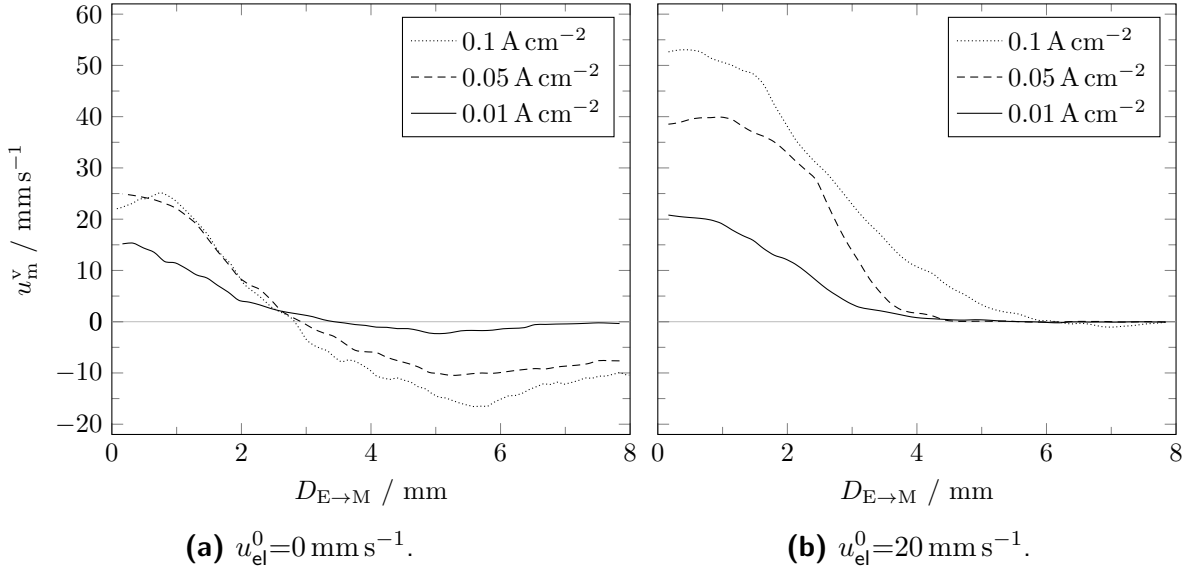


Figure 3.38.: Course of u_m^v along $D_{E \rightarrow M}$ for $i=0.01, 0.05$, and 0.1 A cm^{-2} , and **(a)** $u_{el}^0=0$ and **(b)** 20 mm s^{-1} obtained by the PIV algorithm at the top viewing panel.

indicated by exclusively positive values of u_m^v at all three current densities. Instead of a regime with downwards flow, the region outside the bubble curtain is now stagnant with velocities close or equal to 0 mm s^{-1} . Though, dependent on i , the value of u_m^v at the electrode surface and the range of the upward flow increases. At $i=0.01 \text{ A cm}^{-2}$, u_m^v and the bubble curtain width amounts to 20.8 mm s^{-1} and 3 mm , respectively. These values for u_m^v and the bubble curtain width increase to 38.5 mm s^{-1} and 3.5 mm , and 53 mm s^{-1} and 6 mm for, respectively, $i=0.05$ and 0.1 A cm^{-2} . Due to an increase in \dot{V}_g , a higher number and larger bubbles detach from the electrode surface, leading to a greater acceleration of the electrolyte. Further, the bubble curtain width is increased due to the greater collision rate.

Figure 3.39 showcases the effect of different u_{el}^0 on u_m^v for the two current densities of 0.01 A cm^{-2} in Figure 3.39 (a) and 0.1 A cm^{-2} Figure 3.39 (b). At $i=0.01 \text{ A cm}^{-2}$ the differences in u_m^v are only minimal. Though, a small backflow of -2.3 mm s^{-1} is present at $D_{E \rightarrow M}=5 \text{ mm}$ and $u_{el}^0=0 \text{ mm s}^{-1}$. In addition, the width of the bubble curtain slightly increases along with u_{el}^0 . The measured course for u_m^v at $u_{el}^0=10$ and 20 mm s^{-1} is inaccurate as an increase of u_{el}^0 should result in an increase of u_m^v , especially in the absence of large gas phase volumes. This observed contradiction indicates that the illumination of the tracer particle is inadequate due to the low number of reflecting gas bubbles and that u_m^v is closer to u_b^v . For the same operating conditions of $i=0.01 \text{ A cm}^{-2}$ and $u_{el}^0=0, 10$, and 20 mm s^{-1} , the PTV algorithm determines values for \bar{u}_b^v of respectively $27.6, 19.8$ and 25 mm s^{-1} , which are a little above the corresponding values from the PIV measurements ($15.2, 21$, and 20.8 mm s^{-1}). This slight deviation is appropriate, since the bubble experience buoyancy

forces.

At $i=0.1 \text{ A cm}^{-2}$, u_m^v increases from 22.3, 46.2, and 53 mm s^{-1} at respectively $u_{el}^0=0, 10$, and 20 mm s^{-1} . Due to the higher value of \dot{V}_g the bubble-induced backflow reaches values of 16.5 mm s^{-1} at $u_{el}^0=0 \text{ mm s}^{-1}$. Though, even at $u_{el}^0=10$ and 20 mm s^{-1} , smaller sections of negative values for u_m^v exist with minima of -1.4 mm s^{-1} and -1.1 mm s^{-1} . Here, at the higher current density, the effect of u_{el}^0 on the bubble curtain becomes more visible. The width of the bubble curtain increases from 3 mm at $u_{el}^0=0 \text{ mm s}^{-1}$ to 5 and 6 mm at $u_{el}^0=10$ and 20 mm s^{-1} , respectively.

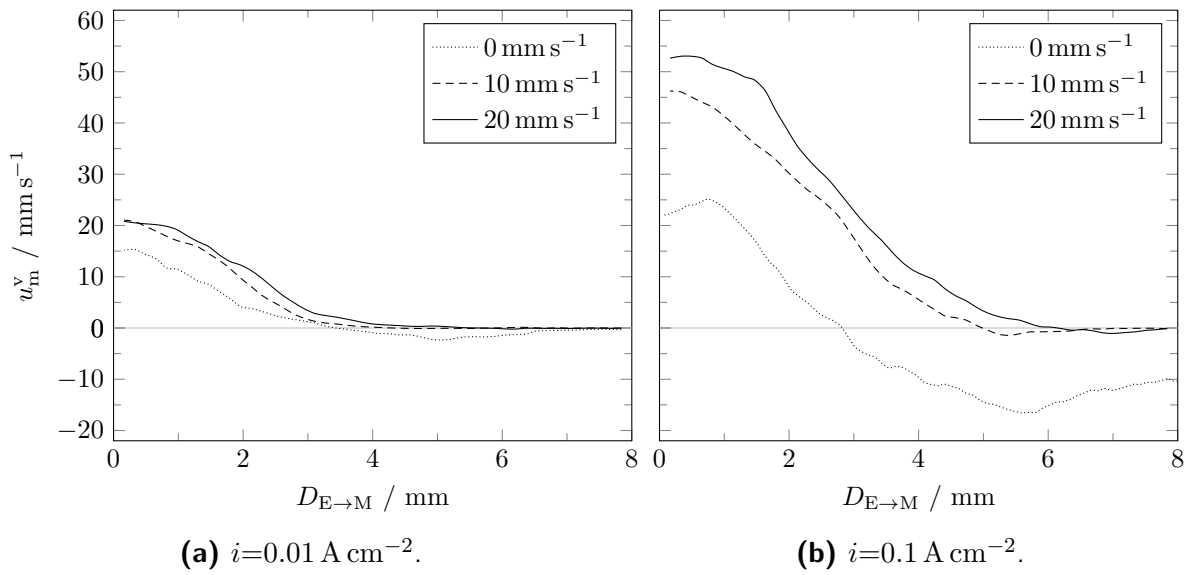


Figure 3.39.: Course of u_m^v along $D_{E \rightarrow M}$ for $u_{el}^0=0, 10$, and 20 mm s^{-1} , and **(a)** $i=0.01$ and **(b)** 0.1 A cm^{-2} obtained by the PIV algorithm at the top viewing panel.

The relation between u_m^v and u_{el}^0 is contradictory to u_b^v and u_{el}^0 : While shown and discussed in the previous section 3.4.4, an increase of u_{el}^0 leads to decreased values for u_b^v . As a possible cause for this, the spreading of the bubble curtain was discussed, which is confirmed by the presented course of u_b^v in Figure 3.39. The spreading of the bubble curtain increases the accelerated area of the electrolyte and, thus, the bubble-induced momentum is redistributed over a greater electrolyte volume. As a result of this wider momentum distribution, \bar{u}_b^v is reduced as the momentum and gas phase fraction in the proximity of the electrode is reduced. Further, through the use of tracer particles, u_m^v measured by the PIV algorithm accounts for both the velocity of the electrolyte and bubbles, whereas the PTV solely measures the u_b . Therefore, the positive correlation between u_m^v and u_{el}^0 is reasonable.

3.6.2. Flow field across different viewing panels

In addition to the measurement at the top panel, the PIV algorithm is also applied to image data at the bottom of the parallel plate electrolyzer. Here, the flow is still developing and the gas phase fraction is significantly lower than at the top of the cell. This lower gas phase fraction and thereby linked buoyant induced convection leads to decrease of u_m^v along the poly-line. Figure 3.40 depicts the course of u_m^v against for the three current densities of $i=0.01, 0.05$, and 0.1 A cm^{-2} at $u_{el}^0=0 \text{ mm s}^{-1}$ (a) and $u_{el}^0=20 \text{ mm s}^{-1}$ (b), similar to Figure 3.39 in the previous section. Regardless of the operating conditions, u_m^v is smaller at the bottom viewing panel compared to the top one. At $u_{el}^0=0 \text{ mm s}^{-1}$ and $i=0.1 \text{ A cm}^{-2}$, the width of the bubble curtain roughly amounts to 1.4 mm and the velocity at the electrode amounts to about 15 mm s^{-1} . Noticeably, the PIV measurement was unsuccessful to measure any velocity vectors close to the membrane for values of $D_{E \rightarrow M} > 6 \text{ mm}$. This shortcoming of the measurement close to the membrane could result from the insufficient illumination of the tracer particle and absence of bubbles and tracer particle in this region. When u_{el}^0 is set to 20 mm s^{-1} , u_m^v increases, and the backflow regime vanishes. Compared to the top viewing panel, u_m^v at the electrode is smaller by an almost constant offset of $15.2 \pm 1.5 \text{ mm s}^{-1}$.

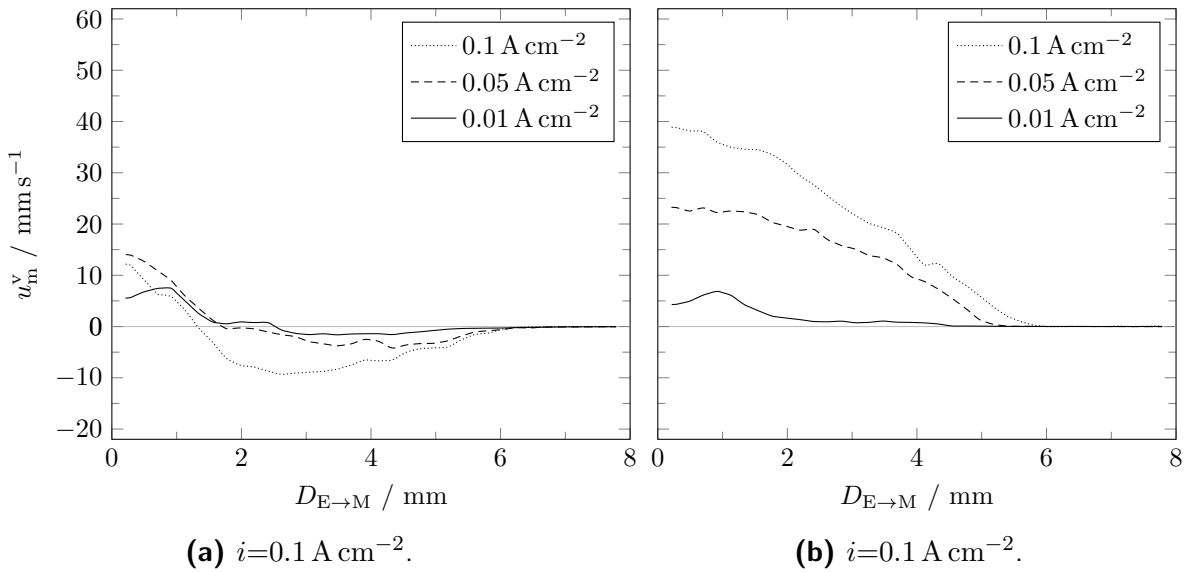


Figure 3.40.: Course of u_m^v along $D_{E \rightarrow M}$ for $i=0.01, 0.05$, and 0.1 A cm^{-2} and (a) $u_{el}^0=0 \text{ mm s}^{-1}$ and (b) 20 mm s^{-1} at the bottom viewing panel obtained by the PIV algorithm.

For better comparison, Figure 3.41 directly plots the course of u_m^v against $D_{E \rightarrow M}$ for the top and bottom viewing panels at $i=0.1 \text{ A cm}^{-2}$ and $u_{el}^0=0 \text{ mm s}^{-1}$ (a), and $i=0.1 \text{ A cm}^{-2}$ and $u_{el}^0=20 \text{ mm s}^{-1}$ (b). Here, the difference becomes apparent: At $i=0.1 \text{ A cm}^{-2}$ and $u_{el}^0=0 \text{ mm s}^{-1}$, the width of the bubble increases from 1.4 mm at the bottom to 3 mm at the top. In addition, the value and position of the minima of the backflow changes from

-9.3 mm s^{-1} and 2.6 mm at the bottom to -16.5 mm s^{-1} and 5.7 mm . As the backflow regime stretches all the way to the membrane at the top, the flow velocity amounts to 0 mm s^{-1} at the membrane on the bottom. These differences in the backflow regime arise due to the accumulation of the gas phase along the electrode. In opposition to this, the courses of u_m^v only diverge during the first 3 mm from the electrode into the bulk electrolyte. In this section, u_m^v is greater at the top compared to the bottom viewing panel reaching a maximum difference of 13.7 mm s^{-1} at the electrode.

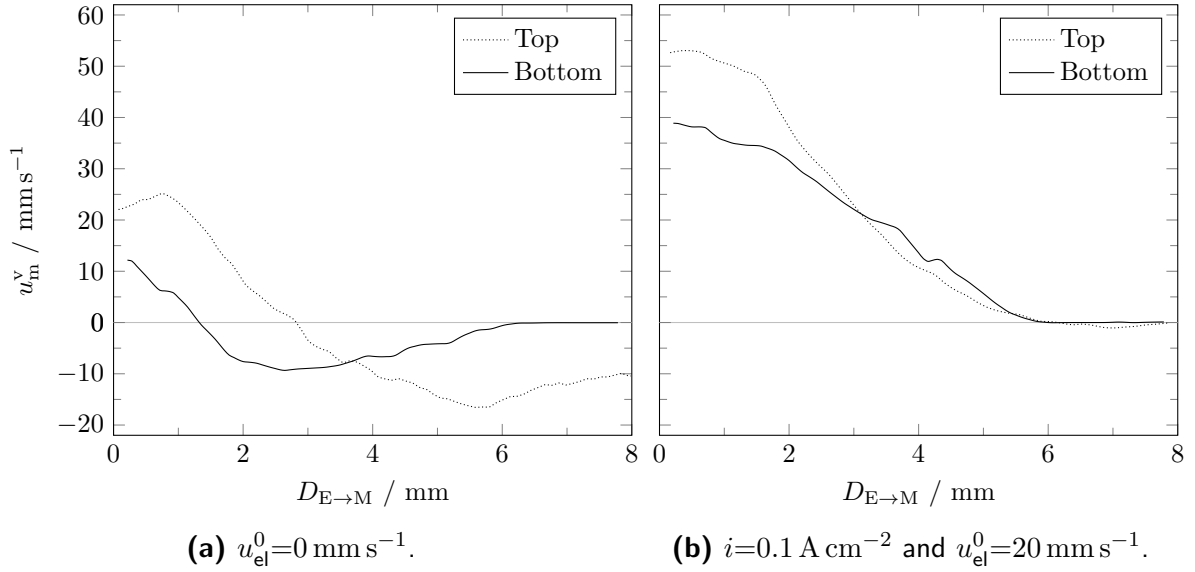


Figure 3.41.: Comparison of the course of u_m^v along $D_{E \rightarrow M}$ at the bottom and top viewing panels at $i = 0.1 \text{ A cm}^{-2}$ and **(a)** $u_{el}^0 = 0 \text{ mm s}^{-1}$ and **(b)** 20 mm s^{-1} .

Figure 3.42 shows the whole corresponding anolyte flow fields from the previous Figure 3.43 (b) at $i = 0.1 \text{ A cm}^{-2}$ and $u_{el}^0 = 20 \text{ mm s}^{-1}$ at the top and bottom viewing panel. In the proximity of the electrode, the number of bubbles on the top viewing panels exceeds the number on the bottom. Even though the differences in actual bubble velocity determined by the PTV only amounts to 3.9 mm s^{-1} , the sheer number of bubbles leads to the differences in u_m^v obtained from the PIV measurement. As the PIV algorithm determines the velocity for 200 frames and subsequently averages over all frames, the number of bubbles has a significant impact on u_m^v . Nonetheless, a similar effect is to be expected when using Euler-Euler modeling approaches for the modeling of the gas-liquid flow.

3.6.3. Impact of electrode-membrane gap

Narrowing the electrode-membrane gap from 8 to 6 mm concentrates the momentum due to the circulation of the electrolyte and bubble-induced buoyancy to a smaller cross-section. This change in the momentum distribution is illustrated in Figure 3.40 that shows the anolyte flow pattern for the 6 (a) and 8 mm (b) gaps at $i = 0.05 \text{ A cm}^{-2}$ and $u_{el}^0 = 0 \text{ mm s}^{-1}$.

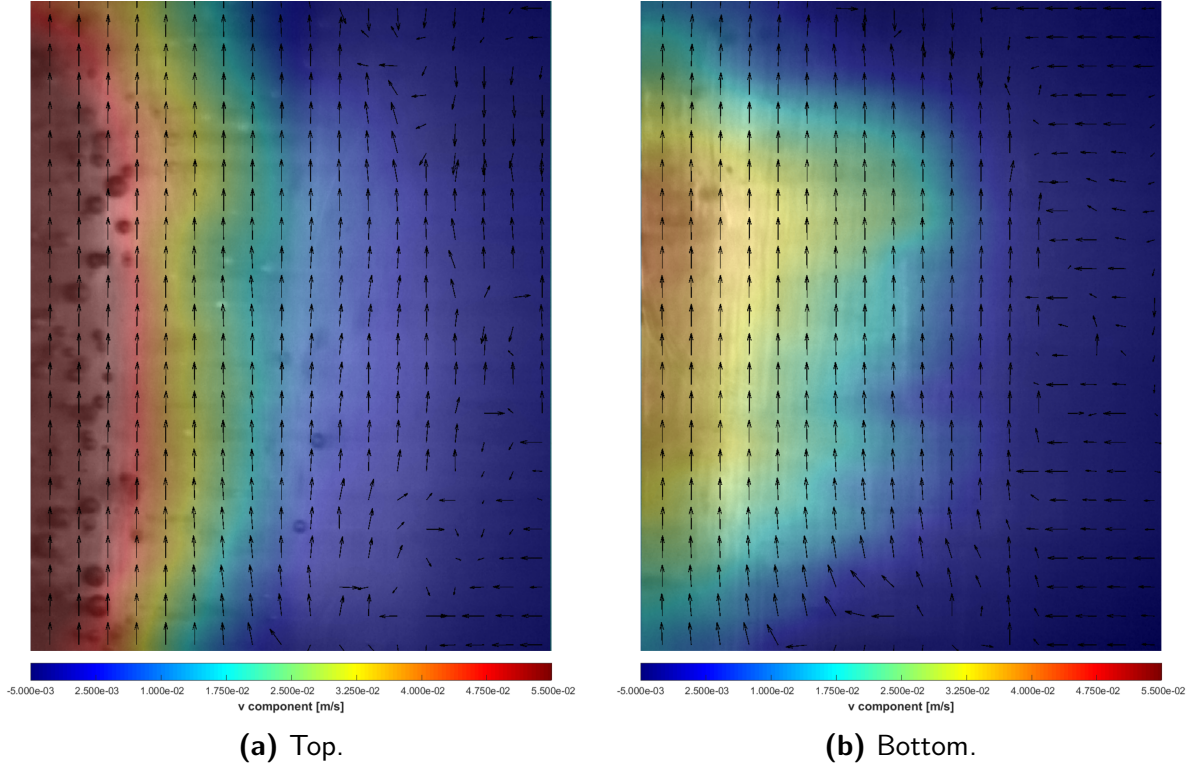


Figure 3.42.: Anolyte flow field at the **(a)** top and **(b)** bottom viewing panel at $u_{\text{el}}^0 = 20 \text{ mm s}^{-1}$ and $i = 0.1 \text{ A cm}^{-2}$.

Whereas a large backflow regime is present for a gap of 8 mm, the smaller gap results in a higher u_{m}^{v} at the electrode and the vanishing of the backflow flow regime. Hence, the electrode-membrane gap influences the present velocities of both phases along with the in Figure 2.12 introduced flow pattern.

Figure 3.44 depicts the course of u_{m}^{v} along $D_{\text{E} \rightarrow \text{M}}$ for an electrode-membrane gap of 6 mm and the three current densities of 0.01, 0.05, and 0.1 A cm^{-2} at $u_{\text{el}}^0 = 0$, and the top viewing panel. At $i = 0.01 \text{ A cm}^{-2}$ the course is comparable to that with a gap of 8 mm. u_{m}^{v} amounts to 15 mm s^{-1} at the electrode and intersects the x-axis at 3 mm. Here, the measured width of the upward flow section is equal for both electrode-membrane gaps. Afterwards, for $D_{\text{E} \rightarrow \text{M}} > 3 \text{ mm}$, a marginal backflow is measured. For the medium value of i , the value of u_{m}^{v} at the electrode is 45 mm s^{-1} and triples the corresponding value for $i = 0.01 \text{ A cm}^{-2}$. At this operating conditions, the upward flow regime increases further and the backflow is further diminished. When increasing i to 0.1 A cm^{-2} , the present flow pattern changes to 'pseudo-turbulent' and positive values in between 22 and 5 mm s^{-1} with an average of are measured for u_{m}^{v} . Here, the upward motion of the bubbles spans over the entire 6 mm long membrane-electrode.

Next, Figure 3.45 depicts the course of u_{m}^{v} at operating conditions of $i = 0.1 \text{ A cm}^{-2}$, and $u_{\text{el}}^0 = 0 \text{ mm s}^{-1}$ at the bottom and top for the two different electrode-membrane gaps of 6 and

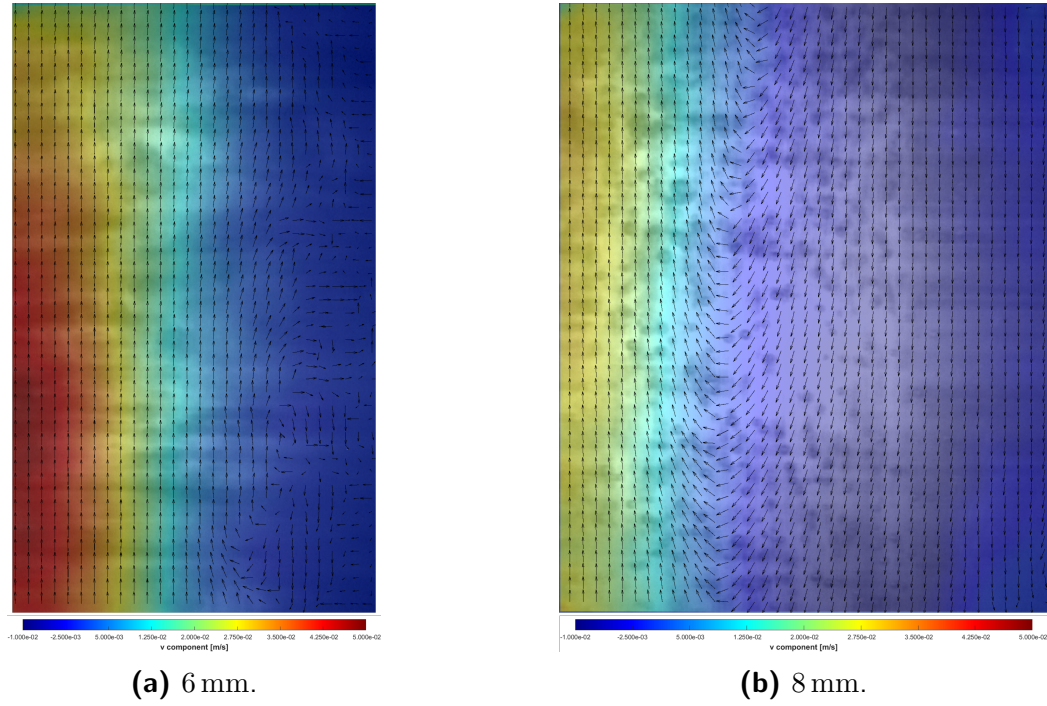


Figure 3.43.: Anolyte flow field for electrode-membrane gaps of **(a)** 6 mm and **(b)** 8 mm at $u_{\text{el}}^0 = 0 \text{ mm s}^{-1}$, and $i = 0.05 \text{ A cm}^{-2}$.

8 mm. At the smaller gap and the bottom panel, the two flow regimes are still visible and at $D_{\text{E} \rightarrow \text{M}} = 4 \text{ mm}$, u_{m}^v equals -3 mm s^{-1} . As depicted in Figure 3.43 (a) and discussed in the previous section 3.6.2 for an 8 mm gap, the bubble curtain spreads towards the membrane with increasing active electrode height. With the smaller 6 mm electrode-membrane gap, not only does the bubble curtain spread, but the flow pattern also fundamentally changes

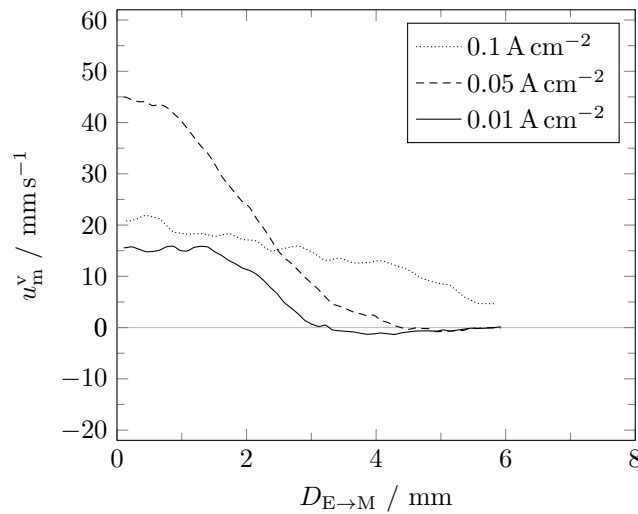


Figure 3.44.: Course of u_{m}^v along $D_{\text{E} \rightarrow \text{M}}$ for $i = 0.01, 0.05$, and 0.1 A cm^{-2} , $u_{\text{el}}^0 = 0$, and a electrode-membrane gap of 6 mm

from two segregated flows at the bottom to a completely dispersed gas-liquid flow at the top viewing panel.

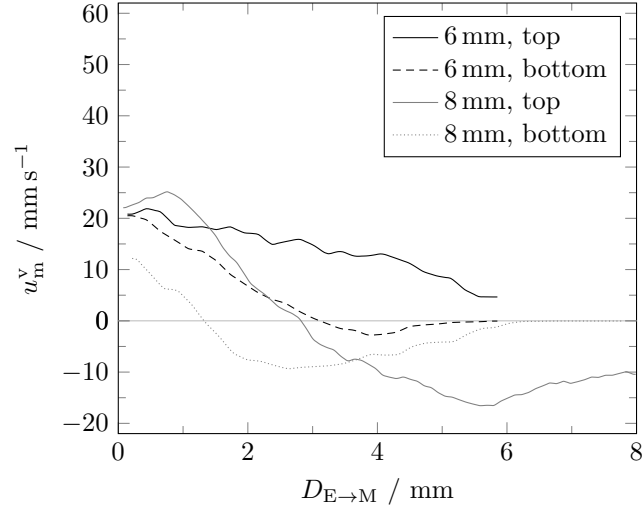


Figure 3.45.: Comparison of the course of u_m^v along $D_{E \rightarrow M}$ at the bottom and top viewing panels, $i=0.1 \text{ A cm}^{-2}$, and $u_{el}^0=0 \text{ mm s}^{-1}$ recorded for electrode-membrane gaps of 6 and 8 mm.

3.7. Summary of experimental findings

Modeling and describing the gas-liquid flow in electrolyzers requires precise knowledge and experimental data. Especially the bubble size and motion dictates the dimension of the bubble curtain and the bulk flow inside electrolyzers [94]. The developed and presented experimental setup along with suitable post-processing algorithms that partially employ CNN enable the (i) object detection, (ii) size determination, and (iii) velocity determination of bubbles as well as (iv) a PIV measurement of a defined section of the gas-liquid flow. Concluding this chapter, the key findings can be summarized as follows:

- (i) The custom-made, semi-transparent parallel plate electrolyzer represents the first membrane-separated electrochemical flow cell setup to study the oxygen and hydrogen bubble size distribution for current densities up to $i=0.2 \text{ A cm}^{-2}$ and $i=0.1 \text{ A cm}^{-2}$, respectively. Applying the Mask R-CNN algorithm on acquired images throughout different experiments enables the successful detection of bubbles event at technical relevant i of 0.1 A cm^{-2} . The obtained values for $\bar{d}_{b,0}$ for detached oxygen bubbles exceed that of commonly used literature [58, 59, 87, 88, 90, 108, 186] by factors between two and four. Here, the results presented in this thesis and in Görtz et al. [54] address the lack of data regarding the size distribution of electrogenerated oxygen bubbles in parallel plate electrolyzers that was also discussed in the simulation studies of Rajora and Haverkort [138] and Colli and Bisang [74]. The recorded larger bubbles impose a greater drag on the electrolyte and introduce local velocity fluctuation, also referred to as pseudo-turbulence compared to smaller bubbles with $d_b < 50 \mu\text{m}$.
- (ii) The investigation of the operating parameters, i , u_{el} , c_{Na^+} , impact and measurement height on the bubble size exhibits that i and thus the gas generation \dot{V}_g outweighs all other varied operating conditions and has the greatest impact on the size distribution. Further, simple equations of the correlation between the volume-weighted and number-weighted average bubble size and i are developed that enable the interpolation between the measuring points used for fitting. Aside from the i , the investigation also revealed a strong dependence of the present electrode surface and its topology. A weak linkage between \bar{d}_b and Θ that was also measured in a simple membrane-less setup could be established. Though, this correlation should be subject of future investigations. Variations of both c_{Na^+} and u_{el} caused only a small change of the bubble size distribution, except for a technically irrelevant value of $c_{\text{Na}^+}=0.05 \text{ mol L}^{-1}$.
- (iii) A PTV algorithm from Vukasinovic et al. [110] was further developed that relies on the frame number, bubble position and size obtained by the Mask R-CNN algorithm. The PTV algorithm analyzes the bubble velocity based on the bubble position and

size in four frames - the base, one frame backward alongside the one and two-frame forward - and was applied on image data acquired at different operating conditions on the top, middle, and bottom viewing panel of the custom made electrolyzer. By using the bubble size and position, the results obtained allow for the first time an in-depth analysis of the velocity distribution of different bubble size ranges inside electrolyzers. In comparison to other works [88, 90], the superimposition of the bubble velocity by the bubble size can be avoided by the presented approach.

- (iv) Independent of the operating conditions, \bar{u}_b^v of the different size bins asymptotically increases with respect to d_b . This progression indicates that due to the presence of larger bubbles the small bubbles are accelerated and, vice versa, large bubbles are decelerated by smaller bubbles. For oxygen bubbles, the relative difference in u_b^v between the three viewing panel becomes at larger bubble sizes above $150\ \mu\text{m}$ and on average, \bar{u}_b^v increases by roughly 15 % between each viewing panel for each individual bubble size bin.
- (v) Similar to d_b , an increase \dot{V}_g also triggers greater \bar{u}_b^v . For hydrogen and oxygen, this link between \dot{V}_g and \bar{u}_b^v is illustrated in Figure 3.46. The courses of \bar{u}_b^v for hydrogen and oxidation also capture the fact that twice as much gas is released in the hydrogen evolution reaction. Here, \bar{u}_b^v of hydrogen exceeds the value for oxygen by an average of $87 \pm 9.7\%$, despite \bar{d}_b of oxygen bubbles doubling the corresponding value of hydrogen ones.

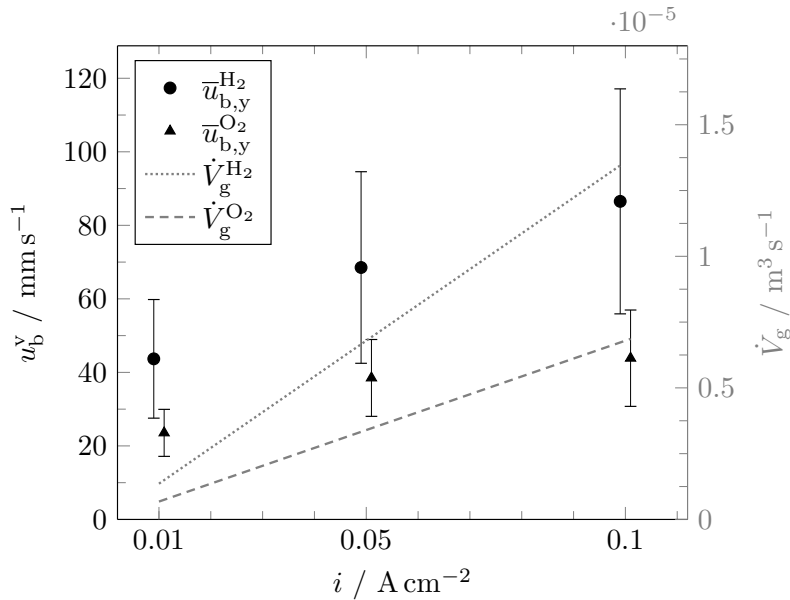


Figure 3.46.: \bar{u}_b^v and $\zeta_0(u_b^v)$ of hydrogen and oxygen bubbles for $i=0.01, 0.05$, and $0.1\ \text{A cm}^{-2}$ at $u_{\text{el}}^0=0\ \text{mm s}^{-1}$. On the left y-axis and in gray dotted and dashed lines, \dot{V}_g for hydrogen and oxygen is respectively plotted.

- (vi) If the operation mode is switched to forced convection by peristaltic pumping, the movement of the electrolyte affects u_b and the width of the bubble curtain: Counterintuitively, an increase in u_{el}^0 results in a reduction of u_b^v for all studied current densities. At $u_{el}^0=20$ and 30 mm s^{-1} , \bar{u}_b^v equals the respective values for u_{el}^0 . This observation indicates the spreading of the bubble curtain that leads to a reduction of u_b and is inline with the results from the PIV measurement of the anolyte chamber. By extending the bubble curtain, the acceleration due to buoyancy is expanded over a larger volume, resulting in a reduction of the local electrolyte and bubble velocity.
- (vii) By applying a PIV algorithm on image data from the anode-membrane gap, the buoyancy-induced backflow of the electrolyte at $u_{el}^0=0 \text{ mm s}^{-1}$ could be visualized for all three current densities alongside the two flow regimes (see Figure 2.12). When applying an electrolyte flow, the width of the bubble curtain increases alongside i . In addition, the results from the PIV algorithm also depict the spreading of the bubble curtain alongside the electrode height from the bottom to the top viewing panel.

The obtained results form a solid basis for evaluating CFD models depicting the gas-liquid flow in electrolyzers. Using the determined bubble sizes as a model input, the PTV and PIV measurements allow for an in-depth, three-dimensional comparison of the results. The next chapter introduces the chosen multiphase modeling approach, selected models for the momentum exchange, model assumptions, and computational domains.

4. Euler-Lagrange multiphase model for pH shift electrolyzers

This chapter introduces the CFD multi-phase model that depicts the gas-liquid flow and multi-phase interaction inside (pH shift) electrolyzers. To enable a comprehensive comparison of bubble size, velocity, trajectory and gas phase fraction, an Euler-Lagrange algorithm is selected. The algorithm, often referred to as *solver*, is based on the OpenFOAM v9 framework and upon the standard solver *denseParticleFoam*. For an overview and explanation of the italic printed descriptors, e.g. *face*, *faceCells*, *volScalarFields*, used within the following model description, the reader is referred to the OpenFOAM documentation. Section B.2 in the appendix contains an overview of the structure of the *solver* and overview of used preexisting OpenFOAM libraries.

Figure 4.1 depicts employed algorithm and initially, Section 4.1 introduces the assumptions and simplification of the Euler-Lagrangian model. During the calculation of each time step, the algorithm starts by calculating the Lagrangian phase and the derived fields from it. The therefore implemented model equations, momentum exchange, Lagrangian-Euler mapping are presented in Section 4.2. Subsequently, the procedure for solving the general continuum equations of the Eulerian phase are described in Section 4.3. In addition, this chapter also depicts the inserted momentum due to bubble nucleation, the mass transport model, system of equation for the calculation of the pH value, speciation, and supersaturation of mono- and diprotic acids.

Lastly, a method for the determination of the residence time distribution of the electrolyte and solid (crystal) phase is implemented in Section 4.4. In closing, the final Section 4.5 presents the simulation setups that comprise of the computational domains boundary conditions, studied operating parameters and general simulation settings. Here, two different geometries for the anode chamber are meshed and simulated: The first matches the geometry of the custom-made electrolyzer depicted in Figure that is employed for the experimental study of the gas-liquid flow. Thus, the simulation enables a comparison between experimental and simulated velocities of the disperse and continuous phase. The second computational domain maps the novel prototype of Kocks et al. [17] for the electrochemical pH-shift crystallization of succinic acid.

Parts of the following sections are also published in

Sander, K. „Modeling of Gas-Liquid Flow Fields in Electrolysis Cells Using Computational Fluid Dynamics“, Master thesis, RWTH Aachen University (2023) [149].

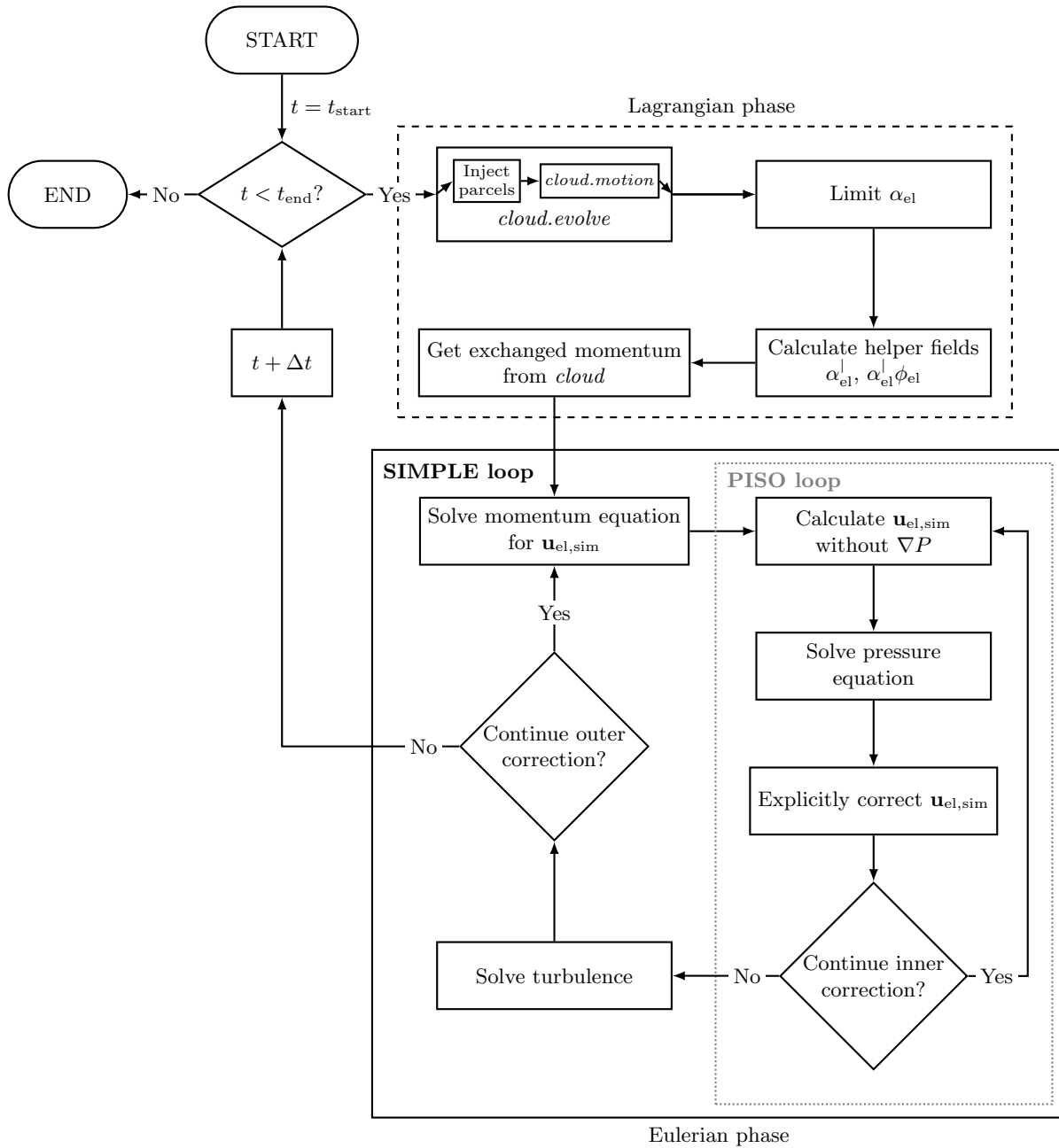


Figure 4.1.: Overview of the employed Euler-Lagrange model for the calculation of the gas-liquid flow.

4.1. Model assumptions

To model the gas-electrolyte flow in electrolyzers using the Euler-Lagrangian approach, the following assumptions and simplifications are made:

- The electrolyte phase can be considered as an incompressible, Newtonian, continuous Eulerian phase.

In general, liquid phases can be regarded as incompressible and the gas phase fraction of the electrolyte usually does not exceed 45 % [75]. Hence, the assumption of a dispersed gaseous phase in an continuous electrolyte phase holds.

- $\rho_{\text{el}}, \nu_{\text{el}}, \sigma_{\text{el} \leftrightarrow \text{b}} = \text{constant}$.

The density and kinematic viscosity of the electrolyte phase as well as interfacial tension are considered to be independent of the concentration of solutes in each volume cell. This simplification greatly reduces the computational cost. Nonetheless, due to the high concentration of the electrolyte ($c_{\text{Na}_2\text{SA}} = 0.3 \text{ mol L}^{-1}$) little changes of both quantities are to be expected.

- The computational domain depicts the electrolyte.

The computational domain only maps the volume of the electrolyzer that is filled with electrolyte. Hence, the air above the liquid level is not considered and the pressure on top of the electrolyte is at atmospheric pressure.

- Oxygen bubbles are considered to be perfect spheres and spawn without any momentum.

As depicted in Figure 2.10, this simplification is reasonable for particles with low Eotvös numbers ($< 3 \cdot 10^{-3}$) or low bubble Reynolds numbers of $< 2 \cdot 10^{-1}$. The validity of this assumption will be checked after simulation. Additionally, it is assumed that $\mathbf{u}_b = 0 \text{ mm s}^{-1}$ post the nucleation of a bubble, since the initial velocity of after its detachment is unknown.

- $\rho_g^{\text{O}_2} = 1.429 \text{ km}^{-3} = \text{constant}$.

The density of the oxygen bubbles is assumed to equals that of oxygen at standard conditions [187]. This assumption follows the electrolyte phase that regards the top of the simulation domain to be at atmospheric pressure. Further, the impact of the oxygen density on the simulation is limited, since the density difference between continuous and disperse phase is determining the active bubble forces.

- $\Delta z \geq \tilde{d}_{\text{max}}, V_{\text{cell}} \geq \pi \frac{\tilde{d}_{\text{max}}^3}{6} \cdot 10$:

The minimal grid size in the z-direction, Δz , has to be greater than the maximal value of the bubble size distribution [188, 189]. In addition, the cell volume has to be at least one order of magnitude larger than the volume of the bubble with the maximum diameter [189].

- The current and, hence, the gas generation is distributed equally alongside the anode: Even though, this assumption is erroneous, as demonstrated by both experimental and numerical works [73, 89, 130, 134, 190, 191], it is nonetheless chosen for the simplification of the model. In general, a greater value of i is to be expected at the bottom of the electrode.

4.2. Disperse gaseous Lagrangian phase

The disperse gas phase is modeled as a Lagrangian phase that comprises of a *cloud* of Lagrangian parcels. Each Lagrangian parcel p resembles a single or number of bubbles, n_p that are treated as a mass point with a distinct set of properties like, e.g., position \mathbf{x}_j , velocity \mathbf{u}_p , or density ρ_p , N_p . During each time step Δt , the new position of the parcel p at t_{i+1} is calculated based on the parcel's current velocity that is obtained by solving Newton's second law of motion as introduced in equations (2.40) and (2.41).

As shown in flow chart in Figure 4.1, the calculation of the Lagrangian phase can be divided into five different steps: (i) Injection of new parcels, (ii) motion of the Lagrangian cloud, (iii) Lagrange-Euler mapping, (iv) calculation of helper fields, (v) and momentum exchange between the Lagrangian and Eulerian phase. The algorithm and distribution used for the injection is introduced in Section 4.2.1. Subsequently, Figure 4.4 and sections 4.2.2 and 4.2.3 present the calculation procedure within the *cloud.move* function, the implemented acting forces, and collision model. Next, the Lagrange-Euler mapping and the creation of helper fields is described in Section 4.2.4 and in closing, the interphase coupling is depicted in Section 4.2.5.

4.2.1. Parcel injection

During the evolution of the Lagrangian cloud illustrated in Figure 4.1, new parcels are inserted into the numerical domain alongside the anode at each time step. Therefore, parcel are introduced using an algorithm that is depicted in Figure 4.2, and includes the following steps:

Using Faraday's law (2.40) the injected gas volume $V_{\text{inj},j}$ for a time step j and time step size Δt can be calculated depending on i . Additionally, the remaining volume of the previous time step, $V_{\text{inj},j-1}^*$, is added to $V_{\text{inj},j}$. Next, the algorithm determines the average bubble volume \bar{V}_b using the mean \bar{d}_3 , $\min d_{b,\min}, d_{b,\max}$. According to Görtz et al. [54], the bubble sizes follow a normal distribution, and, for a more robust implementation, a truncated normal distribution is employed. Truncated normal distributions are based upon normal distribution, but truncate the distribution at a minimum $d_{b,\min}$ and maximum $d_{b,\max}$ value. Using the normal probability (PDF_N) and cumulative distribution functions

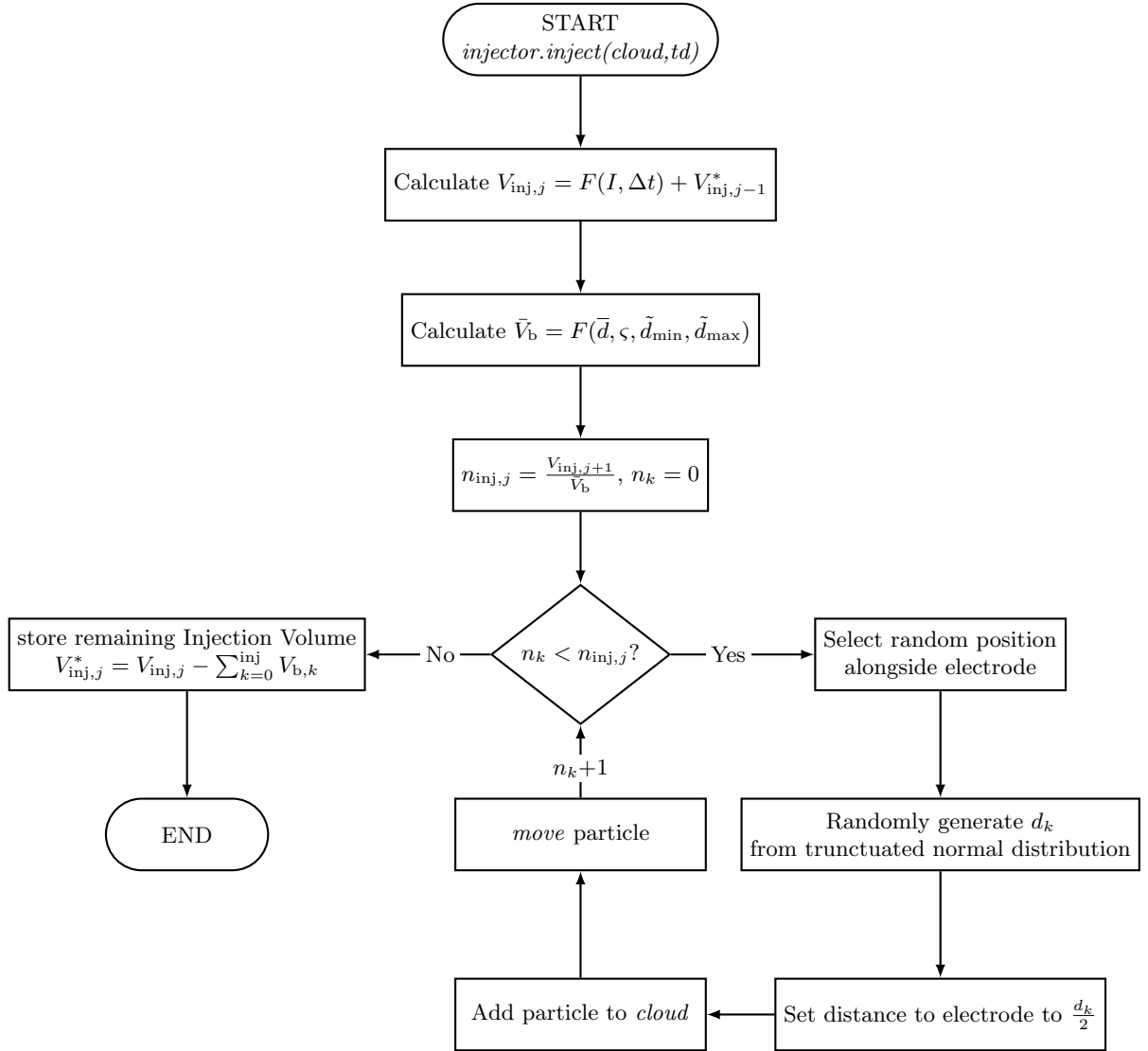


Figure 4.2.: Algorithm for the injection of bubbles during a timestep j .

(CDF_N), the probability density function of a truncated normal distribution PDF_T for a bubble size writes as

$$PDF_T(d_b | \bar{d}_b, \varsigma_b, d_{b,max}, d_{b,min}) = \frac{PDF_N\left(\frac{d_b - \bar{d}_b}{\varsigma_b}\right)}{\varsigma_b \cdot \left[CDF_N\left(\frac{d_{b,max} - \bar{d}_b}{\varsigma_b}\right) - CDF_N\left(\frac{d_{b,min} - \bar{d}_b}{\varsigma_b}\right) \right]}, \quad (4.1)$$

with \bar{d}_b and ς_b representing the mean bubble size and standard deviation, respectively [192]. Exemplary, Figure 4.3 shows both normal and truncated normal probability density distributions.

Dividing $V_{inj,j}$ by \bar{V}_b yields the number of parcels $n_{inj,j}$ that will be injected during the time step j . Next, for each parcel to be injected, the system randomly generates

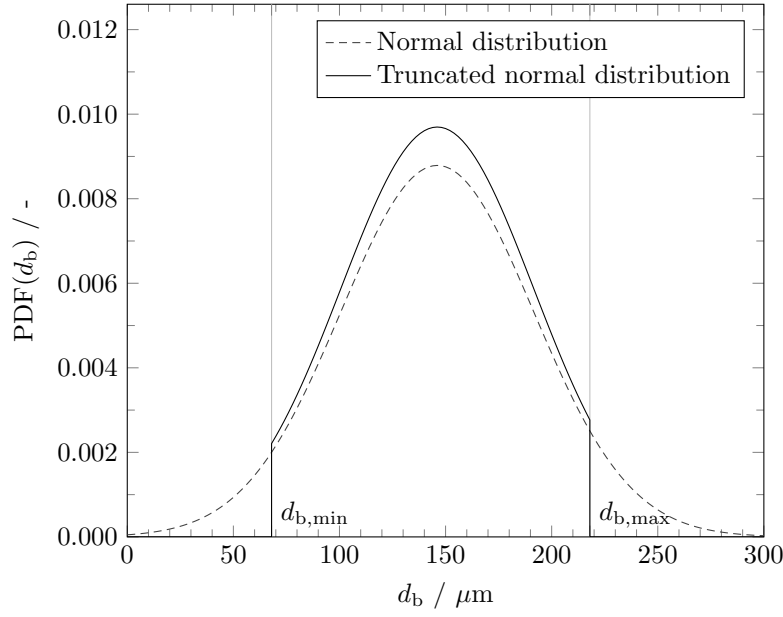


Figure 4.3.: Illustration of the PDF for a normal and truncated normal distribution. The latter is employed for determine the injection bubble size.

a position inside all *faceCells* of the *face* anode and bubble size $d_{b,k}$ using the PDF_T . Subsequently, the z -coordinate of the injection position is corrected such that the center position is one bubble radius away from the anode. Thus, the positions represents a freshly detached bubble. Afterwards, the parcel is created and added to the *cloud*. To model a continuous injection, the injection time $t_{\text{inj},k}$ of each parcel p increases linearly between t_j and t_{j+1} . Finally, each created parcel moves for the remaining time interval $t_{j+1} - t_{\text{inj},k}$. This procedure is repeated until the number of created parcels n_k exceeds $n_{\text{inj},k}$.

After the injection of all parcels, the algorithm sums all injected parcel volumes and subtracts them from $V_{\text{inj},j}$ to calculate $V_{\text{inj},j}^*$ that will be accounted for in the next injection at time step $j + 1$.

4.2.2. Parcel forces

The evolution of the *cloud* displayed in Figure 4.4 starts by calculating the number of move-collision subcycles. If a collision model is selected, $n_{\text{subcycles}}$ is obtained by

$$n_{\text{subcycles}} = \frac{\Delta t}{\Delta t_{\text{coll}}} . \quad (4.2)$$

Otherwise, $n_{\text{subcycles}}$ is equal to one. During each move-collision cycle, the velocity of each particle $u_{p,j}$ is updated based upon $\mathbf{F}_{\text{sum},i}$ from the previous time step and $0.5 \cdot t_{\text{coll}}$, and with that velocity, the particle moves for t_{coll} . Thereafter, the force balance $\mathbf{F}_{\text{sum},i+1}$ and cell occupancy of the parcel are calculated and updated. Subsequently, all parcels are

checked for collision and, finally, $u_{p,j}$ is updated based on $\mathbf{F}_{\text{sum},i+1}$ for half of the collision time step.

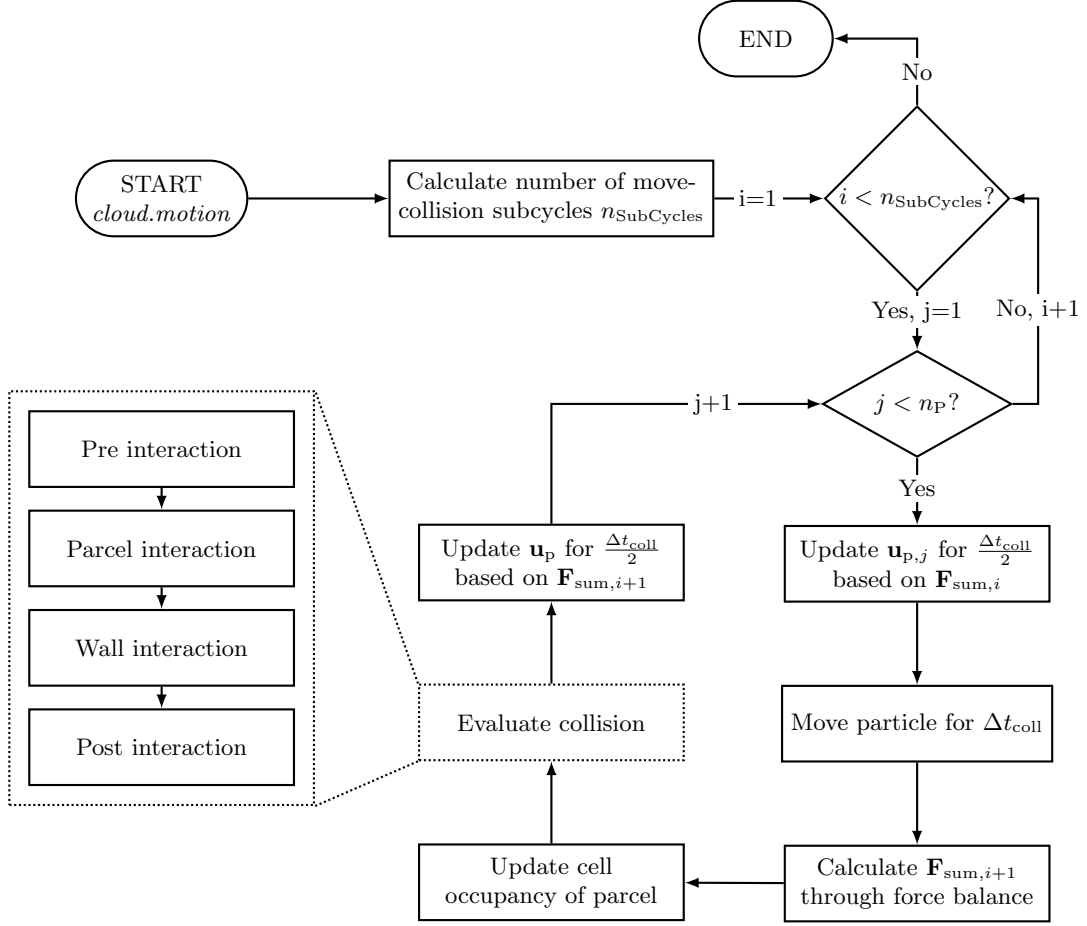


Figure 4.4.: Flow chart of the algorithm for evolving the *Parcel/Cloud*.

For the calculation of the force balance, the drag \mathbf{F}_{Drag} , buoyancy $\mathbf{F}_{\text{Bouyancy}}$, virtual mass $\mathbf{F}_{\text{Virtual mass}}$, and wall lubrication force $\mathbf{F}_{\text{Wall lubrication}}$ are considered in this thesis and the sum of all parcel forces is obtained by

$$\mathbf{F}_{\text{sum},p} = \mathbf{F}_{\text{Drag}} + \mathbf{F}_{\text{Bouyancy}} + \mathbf{F}_{\text{Gravity}} + \mathbf{F}_{\text{Virtual mass}} + \mathbf{F}_{\text{Wall lubrication}}. \quad (4.3)$$

Using both the densities of the electrolyte and gas phase in relation, $\mathbf{F}_{\text{Bouyancy}}$ and $\mathbf{F}_{\text{Gravity}}$ can simply be expressed by

$$\mathbf{F}_{\text{Bouyancy}} + \mathbf{F}_{\text{Gravity}} = m_k \mathbf{g} \left(1 - \frac{\rho_{\text{el}}}{\rho_{\text{g}}} \right). \quad (4.4)$$

For the other acting forces, different calculation models can be implemented. In the following, the model choice and model equations are briefly introduced.

Drag force

Table 2.2 lists a variety of drag models that have been applied to model the experienced drag of bubbles inside an electrolyzer. Though, the models can be grouped into two classes:

- (i) **Schiller and Naumann [142] based models.** All of the models proposed by Morsi and Alexander [144], Grace et al. [147], Ishii and Zuber [151], Tomiyama et al. [152] exhibit the same kernel for small, spherical bubbles in the viscous regime ($0 < \text{Re}_b \leq 100$, $\text{Eo} < 0.5$), namely

$$C_D = \frac{24}{\text{Re}_b} (1 + 0.15 \text{Re}_b^{0.687}) . \quad (4.5)$$

The implementation of any of those models would lead to exactly the same result for the drag coefficient and, thus, bubble motion.

- (ii) **Hadamard and Rybczński [146] based models.** The originally proposed hard sphere model by Hadamard and Rybczński is only valid for $\text{Re}_b \geq 1$. Lain et al. [143] conducted experiments to propose a model with exact the same values for $\text{Re}_b \geq 1$, but extended the model validity up to a Re_b of 1500.

As a result, one drag model is implemented out of each group to discuss the suitability and impact on the simulation of the gas-liquid flow. Here, from the two model groups, Schiller and Naumann [142] and Lain et al. [143] are chosen.

Virtual mass

To account for the added virtual mass, $m_{p,k}$ in equation (2.40) can be substituted by the effective mass

$$m_{p,k,\text{eff}} = m_{p,k} + m_{p,k,\text{added}} \quad (4.6)$$

of the particle. According to [193], the added mass of a sphere is defined by

$$m_{p,k,\text{added}} = \underbrace{C_{\text{vm}}}_{0.5} \frac{m_{p,k}}{\rho_g} \rho_{\text{el}} \quad (4.7)$$

that is used within this thesis to investigate the effect of added virtual mass on the simulation of the gas-liquid flow.

Wall lubrication force

Lastly, the model accounts for the additional friction imposed by a nearby wall on a moving parcel. Here, the friction force is calculated using equation (2.54) introduced by Goldman et al. [164]. For simplification, the wall lubrication force is calculated within the latter, in

Section 4.2.3, described collision model due to the availability of the wall distance of each parcel.

4.2.3. Collision Model

When activating a collision model for the simulation, a list is created during initialization of the model that contains an array of all neighboring cells for each cell of the computational domain within an interaction distance L_{interact} and is similar to the latter described Lagrange-Euler mapping in Section 4.2.4. When evaluating the collision after updating the cell occupancy (see Figure 4.4), four different sub-steps are performed for each parcel:

Pre collision

First, the collision record data from the previous move-collide time step is erased. In addition, \mathbf{F}_{sum} and an eventually stored torque moments are set to zero for all parcels.

Parcel collision

For a parcel k in the owner cell i , a parcel list is created that contains all parcels that are in the same owner cell i or in neighboring cells. The neighboring cells are determined by using the array list that was created during initialization. Afterwards, the algorithm loops through all parcels of the parcel lists and determines if the parcel centers of the initial parcel, $\mathbf{x}_{p,k}$, and the current parcel from the list, $\mathbf{x}_{p,j}$ are within the distance L_{interact} . If yes, the equation (2.48) is used to calculate the distance deficit $\delta_{j \leftrightarrow k}$ based on the positions $\mathbf{x}_{p,j}$ and $\mathbf{x}_{p,k}$, and parcel diameters, $d_{p,k}$ and $d_{p,k}$ as well as h_{gap} . Subsequently, the approaching velocity between the two parcels $\mathbf{u}_{k \rightarrow j}^n$ is obtained by

$$\mathbf{u}_{k \rightarrow j}^n = \mathbf{u}_{k \rightarrow j}^{\text{rel}} \cdot \mathbf{e}_{k \rightarrow j}^n, \quad (4.8)$$

using the normal vector between the two parcels

$$\mathbf{e}_{k \rightarrow j}^n = \frac{\mathbf{x}_{p,j} - \mathbf{x}_{p,k}}{|\mathbf{x}_{p,k} - \mathbf{x}_{p,k}|} \quad (4.9)$$

and the relative inter-parcel velocity

$$\mathbf{u}_{k \rightarrow j}^{\text{rel}} = \mathbf{u}_{p,j} - \mathbf{u}_{p,k}. \quad (4.10)$$

With $\mathbf{u}_{k \rightarrow j}^n$, $\delta_{j \leftrightarrow k}$, h_{gap} , $\sigma_{\text{el} \leftrightarrow b}$, μ_{el} , and $r_{\text{eq},kj}$, the equations for the elastic and viscous normal forces, $\mathbf{F}_{\text{elastic}}^n$ and $\mathbf{F}_{\text{viscous}}^n$ can be calculated respectively with equations (2.51) and (2.52)-(2.53). Here, as described in Section 2.3.1, the model differentiates two different

cases for the normal viscous force:

$$\mathbf{F}_{\text{viscous}}^n = \begin{cases} \text{eq. (2.52)} & \text{if } (\mathbf{x}_{p,j} - \mathbf{x}_{p,k}) \cdot \mathbf{e}_{j \rightarrow k}^n > h_{\text{gap}} + r_{\text{eq},kj} \\ \text{eq. (2.53)} & \text{if } (\mathbf{x}_{p,j} - \mathbf{x}_{p,k}) \cdot \mathbf{e}_{j \rightarrow k}^n \leq h_{\text{gap}} + r_{\text{eq},kj} . \end{cases} \quad (4.11)$$

Further, two different averaging methods are available to calculate $r_{\text{eq},kj}$ from the two parcel diameters:

$$r_{\text{eq},kj} = \begin{cases} \frac{d_{p,k}d_{p,j}}{2} & \text{(arithmetic mean)} \\ \frac{d_{p,k}d_{p,j}}{d_{p,k}+d_{p,j}} & \text{(harmonic mean)} \end{cases} \quad (4.12)$$

The Young-Laplace equation on which the collision model is based upon and the work of Liu et al. [194] suggest that the harmonic mean is more suitable. However, both methods are implemented, used for a simulation and their impact on the results will be discussed. In the appendix, Figure B.18 displays the difference in $r_{\text{eq},kj}$ between the arithmetic and harmonic mean. At $i=0.1 \text{ A cm}^{-2}$ and the extreme case of two bubbles colliding with the maximum and minimum size, the arithmetic mean yields a value for $r_{\text{eq},kj}=120.5 \mu\text{m}$. This exceeds the corresponding value obtained by the harmonic mean ($73.81 \mu\text{m}$) by 38.7%.

Wall collision

The calculation of a possible collision of a parcel k with a wall w follows a similar procedure to the previously described parcel parcel collision. First, the algorithm checks if the distance of the cell center of the owner cell and a wall is within L_{interact} . In case that this condition is true, an algorithm determines the nearest wall site \mathbf{x}_w . Similar to equation (4.9), $\mathbf{e}_{w \rightarrow p}^n$ can be obtained by

$$\mathbf{e}_{w \rightarrow p}^n = \frac{\mathbf{x}_{p,k} - \mathbf{x}_w}{|\mathbf{x}_w - \mathbf{x}_{p,k}|} . \quad (4.13)$$

Next, the approaching velocity of a parcel normal to the wall $\mathbf{u}_{p \rightarrow w}^n$ is calculated by

$$\mathbf{u}_{p \rightarrow w}^n = -\mathbf{u}_{p,k} \cdot \mathbf{e}_{w \rightarrow p}^n , \quad (4.14)$$

enabling the computation of $\mathbf{F}_{\text{elastic}}^n$ and $\mathbf{F}_{\text{viscous}}^n$ with $\delta_{k \leftrightarrow w}$. In addition, the wall lubrication force, $\mathbf{F}_{\text{viscous}}^t$, is calculated and added to the parcel forces within the wall collision routine. This procedure saves computational time, since the required slip velocity tangential to the wall, $\mathbf{u}_{j,\text{slip}}$, can easily be calculated by the closing condition

$$\mathbf{u}_{j,\text{slip}}^{\text{tang}} = \mathbf{u}_{p,k} - \mathbf{u}_{b \rightarrow w}^{\text{app}} . \quad (4.15)$$

Post collision

Finally, after computing the parcel-parcel and parcel-wall collision, the data from the collision is stored. This data contains properties like a boolean showing if the parcel did collide during the timestep, the particle number of the colliding parcel and its processor number.

4.2.4. Lagrange-Euler mapping

By default, the gas phase fraction of each cell is simply calculated by the volume of all parcels whose center position is within the cell. This procedure is the easiest technique to map Lagrangian properties to the Euler mesh. However, this method leads to the emerging of cells with extremely high hold ups in the proximity of the electrode, since parcels spawn on the surface and intersect each other. In addition, the gas phase fraction close to the electrode is highly dependent on the mesh size when using the default approach and attributing the whole volume of a parcel to its owner cell. Commonly, this problem is solved by simply introducing a maximum Lagrangian or minimum Eulerian phase fraction $\alpha_{\text{el,min}}$ and the specific value has to be chosen by the user before the start of the simulation. After each movement of the cell, the α_{el} is corrected according to

$$\tilde{\alpha}_{\text{el}} = \max(\alpha_{\text{el}}, \alpha_{\text{el,min}}) . \quad (4.16)$$

Another, more sophisticated method is to check if each parcel overlaps the faces of the owner cell after its motion and to split its volume with the intersecting neighboring cells. Therefore, different method have been presented to improve the Lagrangian-Euler mapping: Hoomans et al. [195] was the first to publish a tow-dimensional averaging method for the local phase fraction of the Lagrangian properties. Based on that averaging method, Wu et al. [196] further developed a method that represents the spherical particle by a cube and, subsequently, distributes his in a three-dimensional domain using an algorithm from Tomiyama et al. [197]. Unfortunately, none of this algorithm is readily available in the employed simulation software OpenFOAM v9.

Similar to the work of Wu et al. [196], an algorithm is implemented that approximates the sphere by a cube, checks for any overlap with the faces of the owner cells and subsequently calculates the neighbor overlap distances in the positive and negative Cartesian directions $\lambda_{x|y|z}^+$, $\lambda_{x|y|z}^-$. In order to enable a efficient calculation, a *labelList* is created within the initialization of the solver that contains a list of all the indices of the up to 26 neighboring cells alongside a *vectorList* that contains the the geometric cell width in all three spatial directions. The numbering of the owner cell (13) and neighboring cells is depicted in Figure 4.5. By using the two lists, the six neighbor overlap distances in a three-dimensional domain

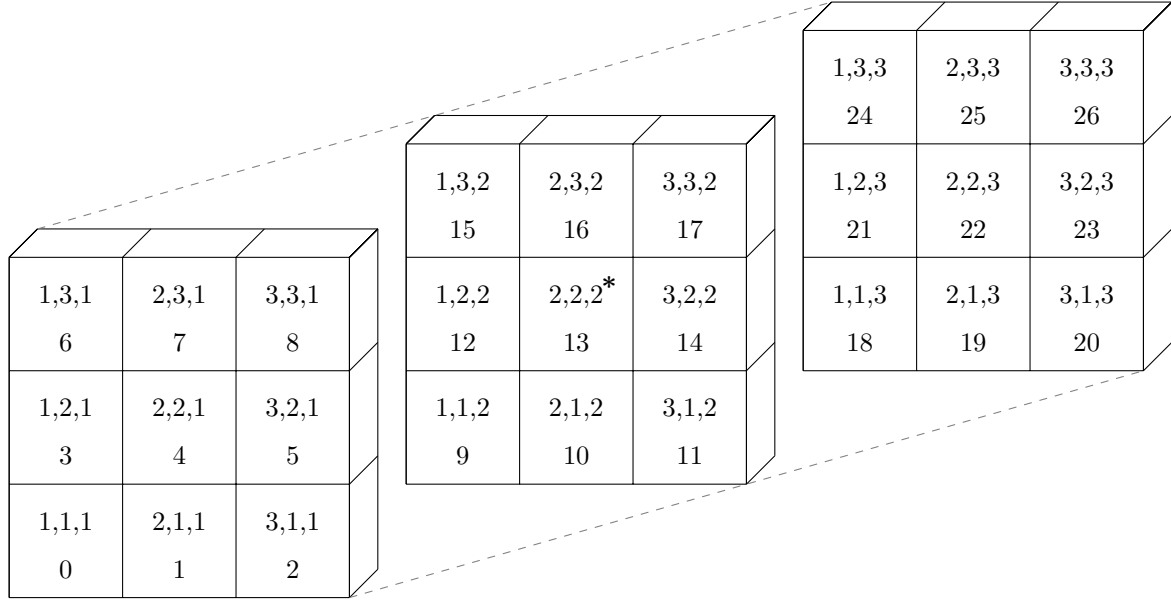


Figure 4.5.: Visualization of neighboring cells for distributing the bubble volume. The bubble center containing cell (2, 2, 2) is marked with *.

can be calculated by

$$\lambda_i^+ = \max \left[0, \mathbf{x}_{i,p}^0 + \tilde{d}_p - (\mathbf{x}_{i,G}^0 + \Delta x) \right] \text{ and} \quad (4.17)$$

$$\lambda_i^- = \max \left[0, \mathbf{x}_{i,G}^0 - \mathbf{x}_{i,p}^0 \right] \text{ for } i \in \{x, y, z\}. \quad (4.18)$$

Here, $\mathbf{x}_{i,G}^0$ and $\mathbf{x}_{i,p}^0$ represents the first point of the cell and cube representation with the smallest global value for x, y , and z . For a better visualization of equations (4.17) and (4.18), Figure 4.6 depicts a schematic, two-dimensional representation of three overlapping bubbles alongside the corresponding lengths for λ_x^+ , λ_y^+ , λ_x^- , and λ_y^- . Depending on the number of cube intersection, the volume of the cube representing the parcel volume has to be split either into two, four or eight cells. Therefore, an algorithm is developed that calculates and stores the volume fractions for each parcel based on the *labelList* for the neighboring cell indices, *vectorList* for $\Delta x, \Delta y$, and Δz , $\lambda_{x|y|z}^{+|-}$, $\mathbf{x}_{i,G}^0$, $\mathbf{x}_{i,p}^0$, and \tilde{d}_p . Since a maximum of three intersection is considered, the algorithm only functions in a structured, cuboid mesh and the bubble size must not exceed any of $\Delta x, \Delta y$, and Δz of the mesh.

4.2.5. Interphase Coupling

Section 2.3.1 and Figure 2.13 depicted the different available coupling mechanisms for Euler-Lagrangian simulation that are based on the phase fraction of the disperse phase

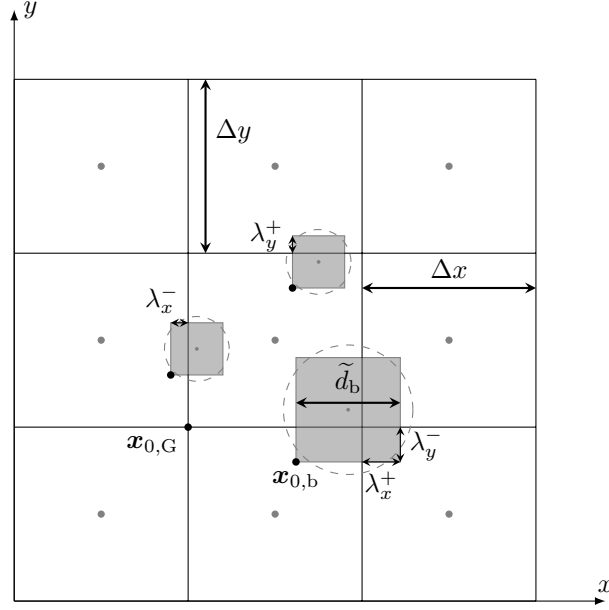


Figure 4.6.: 2D-Visualization of the calculation according to equations (4.17) and (4.18) for $\lambda_{x|y}^{+|-}$ for three bubbles that intersect with neighboring cells. The gray area illustrates the corresponding area through the cubic approximating of the bubble volume.

in the computational domain. Depending on the employed multiphase model, different simulative works determined gas phase fraction in parallel-plate electrolyzers from low single digits up to 70 % [73, 94, 121]. Hence, according to Elghobashi [159], a four-way coupling model has to be introduced that accounts for parcel-parcel interaction and momentum exchange between the Lagrangian and Euler phase. A suitable model has been introduced previously in Section 4.2.3.

When evaluating the change in velocity of a parcel k for a new time step t_{i+1} , Newton's second law (eq. (2.40)) is rewritten to

$$\frac{\partial \mathbf{u}_{p,k}}{\partial t} = a_{\text{non-coupled}} + a_{\text{coupled}} - b_{\text{coupled}} \cdot \mathbf{u}_{p,k}. \quad (4.19)$$

Here, \mathbf{F}_{sum} is divided into coupled and non-coupled forces and acceleration terms by introducing

$$a_{\text{non-coupled}} = \frac{\mathbf{F}_{\text{non-coupled}} + \mathbf{S}_{\mathbf{u}_b}}{m_{p,\text{eff}}}, \quad (4.20)$$

$$a_{\text{coupled}} = \frac{\mathbf{F}_{\text{coupled}} \cdot \mathbf{u}_{\text{el,sim}} + \mathbf{F}_{\text{asdf}}}{m_{p,\text{eff}}}, \quad (4.21)$$

and

$$b_{\text{coupled}} = \frac{\mathbf{F}_{\text{coupled}}}{m_{p,\text{eff}}} \quad (4.22)$$

allowing an implicit integration of $\frac{\partial \mathbf{u}_{p,k}}{\partial t}$. Here, the term *coupled* and *non-coupled* refers to either an exchange of the momentum of the Lagrangian particle with the continuous phase or no momentum exchange. Finally, an Euler-implicit integration scheme can be applied to equation (4.19) resulting in

$$\Delta \mathbf{u}_{p,\text{sim}}(t_i) = \underbrace{\int_{t_i}^{t_{i+1}} a_{\text{non-coupled}} dt}_{\Delta \mathbf{u}_{p,\text{non-coupled},\text{sim}}} + \underbrace{\int_{t_i}^{t_{i+1}} (a_{\text{coupled}} - \mathbf{u}_p(t) \cdot b_{\text{coupled}}) dt}_{\Delta \mathbf{u}_{p,\text{coupled},\text{sim}}} . \quad (4.23)$$

Out of the five different presented forces in Section 4.2.2, solely the drag force is computed as a coupled force, as the other forces are independent of the local electrolyte velocity and $u_{p,k}(t_i)$. In addition, forces arising from collisions that are presented in the next section are also added as a non-coupled force.

By using this Euler-implicit integration scheme, the numerical procedure accounts for change in parcel velocity during $t_{i+1}-t_i$. The splitting of the acceleration term also simplifies the calculation of the momentum exchange with the continuous Euler-phase. Therefore, the second term, $\Delta \mathbf{u}_{p,\text{coupled},\text{sim}}$ is used to calculate the momentum transfer term $\mathbf{S}_{\mathbf{U},\text{Transfer}}(t_{i+1})$. Here, the momentum of each parcel is distributed between the owner and neighboring cells in accordance to the volumetric contribution determined by the algorithm presented in Section 4.2.4. The first contribution, $\Delta \mathbf{u}_{b,\text{non-coupled},\text{sim}}$, is solely used to calculate the change in bubble velocity, but has no affect on the continuous, electrolyte phase. Consecutively, the exchanged momentum is calculated by

$$\mathbf{S}_{\mathbf{U},\text{Transfer}}(t_{i+1}) = \mathbf{S}_{\mathbf{U},\text{Transfer}}(t_i) - \Delta \mathbf{U}_{b,\text{coupled}} \cdot m_{b,\text{eff}} . \quad (4.24)$$

Since the global time step is divided into a number of move-collide substeps, the equation accounts for the accumulation of the momentum across the number of substeps. At the beginning of each new global time step, $\mathbf{S}_{\mathbf{U},\text{Transfer}}(t_{i+1})$ is reset to zero. Lastly, the updated velocity for the new time step is defined by

$$\mathbf{u}_{p,\text{sim}}(t_{i+1}) = \mathbf{u}_{p,\text{sim}}(t_i) + \Delta \mathbf{u}_{p,\text{sim}}(t_i) \quad (4.25)$$

4.3. Continuous electrolyte Euler phase

The electrolyte phase is treated as the continuous Eulerian phase and can be described by the Navier-Stokes equations for continuity (2.21) and momentum (2.22) for a multiphase flow presented in Section 2.3.1. Based on the literature survey listed in Table 2.1, the electrolyte phase is either considered to be turbulent or laminar. In order to model areas with high gas phase fraction and, hence, velocity fluctuations, the k- ω SST model with

standard coefficients is selected as turbulence model. This turbulence model is suitable to also depict areas of both low Reynolds flow [140] and Colli and Bisang [130] demonstrated that is an excellent choice for the modeling of electrolyzers.

For solving the Eulerian phase, the standard Euler-Lagrangian solver uses a *PIMPLE* coupling algorithm that merges the Semi-Implicit Method for Pressure Linked Equations with a Pressure Implicit with Splitting Operators algorithm as depicted in Figure 4.1.

First, within the outer SIMPLE-loop, the momentum equation for the continuous phase is discretized as *fvVectorMatrix* inside the file '*UcEqn.H*' according to equation (2.22). In addition, a source term, $\text{Sp}\left(\frac{\partial \alpha_{\text{el}}}{\partial t} + \nabla \cdot (\alpha_{\text{el}} \phi_{\text{el}}), \mathbf{u}_{\text{el}}\right)$, for the implicit treatment of contributions that arise from the coupling of α_{el} with $u_{\text{el, sim}}$ is introduced on the right side of the equation. Sp stabilizes the numerical solution and captures the momentum redistribution due to phase fraction changes. Next, the *fvVectorMatrix* is relaxed to stabilize the solution and boundary constraints are applied.

Subsequently, reciprocal coefficient volume fields $r_{\text{D}_{\mathbf{u}_{\text{el}}}}$ and $r_{\text{D}_{\text{Sp}\mathbf{u}_{\text{el}}}}$, are setup to aid the iterative solution by

$$r_{\text{D}_{\mathbf{u}_{\text{el}}}} = \frac{1}{\text{D}_{\mathbf{u}_{\text{el}}}} \quad \text{and} \quad r_{\text{D}_{\text{Sp}\mathbf{u}_{\text{el}}}} = \frac{1}{\text{D}_{\mathbf{u}_{\text{el}}} - \frac{\mathbf{S}_{\mathbf{u}, \text{Transfer}}}{\rho_{\text{el}}}}, \quad (4.26)$$

where $\text{D}_{\mathbf{u}_{\text{el}}}$ represents the diagonal coefficient matrix for \mathbf{U}_{el} . By interpolating the volume field $r_{\text{D}_{\text{Sp}\mathbf{u}_{\text{el}}}}$ and mapping it into the cell faces, the face field $r_{\text{D}_{\text{Sp}\mathbf{u}_{\text{el}}f}}$ is created and the surface flux contributions from explicit source terms, $\Phi_{\text{el}}^{\text{SUSu}}$ and $\Phi_{\text{el}}^{\text{SUSp}}$, are expressed by

$$\Phi_{\text{el}}^{\text{SUSu}} = \nabla \cdot \left(\frac{r_{\text{D}_{\text{Sp}\mathbf{u}_{\text{el}}}} \mathbf{S}_{\text{Uu}}}{\rho_{\text{el}}} \right) + r_{\text{D}_{\text{Sp}\mathbf{u}_{\text{el}}f}} (\mathbf{g} \cdot \mathbf{S}_f), \quad (4.27)$$

$$\Phi_{\text{el}}^{\text{SUSp}} = \nabla \cdot \left(\frac{r_{\text{D}_{\text{Sp}\mathbf{u}_{\text{el}}}} \mathbf{S}_{\text{Up}}}{\rho_{\text{el}}} \right), \quad (4.28)$$

where \mathbf{S}_f denotes the face areas. Finally, the algorithm enters the PISO loop and predicts the momentum (\mathbf{u}_{el}) by

$$\mathbf{u}_{\text{el}} = \frac{\Phi_{\text{el}}^{\text{SUSu}} + \Phi_{\text{el}}^{\text{SUSp}}}{r_{\text{D}_{\text{Sp}\mathbf{u}_{\text{el}}}}} - \nabla \cdot P \cdot |\mathbf{S}_f| + \frac{1}{\rho_{\text{el}}} (\text{Sp}(\mathbf{S}_{\text{Up}}, \mathbf{u}_{\text{el}}) - \mathbf{S}_{\text{Up}} \mathbf{u}_{\text{el}}). \quad (4.29)$$

Here, the explicit contribution of the Lagranigan cloud are treated implicitly by $\text{Sp}(\mathbf{S}_{\text{Up}}, \mathbf{u}_{\text{el}})$. After the momentum prediction, the algorithm enters '*pEqn.H*' to solve the pressure equation and explicitly correct \mathbf{u}_{el} . Therefore, a helper field is computed first by

$$\mathbf{H}/A_{\text{Sp}} = \frac{r_{\text{D}_{\text{Sp}\mathbf{u}_{\text{el}}}}}{r_{\text{D}_{\mathbf{u}_{\text{el}}}}} \quad (4.30)$$

that represents the velocity flux divided by the diagonal coefficient matrix that is also

constrained based on the p , u_{el} , and $r_{\text{D}_{\text{u}_{\text{el}}}}$ fields. Next, the surface flux $\phi_{H/A_{\text{Sp}}}$ is computed as

$$\phi_{H/A_{\text{Sp}}} = \nabla \cdot (\mathbf{H}_{\text{Sp}}/A) + \phi_{\alpha_{\text{el}}} \left(\frac{\partial \mathbf{u}_{\text{el}}}{\partial t} + \nabla \cdot (\phi_{\text{el}} \mathbf{u}_{\text{el}}) \right). \quad (4.31)$$

The source contributions are then added by

$$\phi_{H/A_{\text{Sp}}} += \phi_{\text{el}}^{\text{SUSu}} \quad (4.32)$$

to complete the calculation of the surface flux. Next the pressure equation is solved iteratively to address non-orthogonality. Here, the employed governing equation for pressure correction is

$$\nabla \cdot (\alpha_{\text{el}} f_{\text{D}_{\text{Sp}} \mathbf{u}_{\text{el}}} \nabla P) = \frac{\partial \alpha_{\text{el}}}{\partial t} + \nabla \cdot (\alpha_{\text{el}} f_{\text{D}_{\text{Sp}} \mathbf{u}_{\text{el}}} \phi_{H/A_{\text{Sp}}}), \quad (4.33)$$

accounting for the pressure diffusivity weighted by the phase fraction α_{el} and the adjusted flux including the source terms from the previous equation (4.32). Boundary constrained are applied and the equation is solved. Thereafter, the fluxes of the continuous phase are corrected by

$$\phi_{\text{el}} = \phi_{H/A_{\text{Sp}}} - \frac{\nabla \cdot P}{\phi_{\alpha_{\text{el}}}}, \quad (4.34)$$

the pressure is relaxed, and the velocity field is finally updated explicitly using the pressure corrections

$$\mathbf{u}_{\text{el}} = r_{\text{D}_{\text{u}_{\text{el}}}} \cdot \nabla \cdot \left(\frac{\Phi_{\text{el}}^{\text{SUSu}} + \Phi_{\text{el}}^{\text{SUSp}} \phi_{\text{el}} - \frac{\nabla P}{\phi_{\alpha_{\text{el}}}}}{r_{\text{D}_{\text{Sp}} \mathbf{u}_{\text{el}}}} \right). \quad (4.35)$$

and the same boundary corrections than used in equation (4.30). The whole procedure within the PISO-loop is repeated until convergence as depicted in Figure 4.1. Thereafter, the turbulence model that is presented in the next section is evaluated. Afterwards, depending on the number of outer correction loops, the PIMPLE loop starts again by the momentum predictor or the simulation of the current time step is finished and the solver proceeds to the next time step.

4.3.1. Turbulence model

For the modeling of the (bubble-induced) turbulence inside the electrolyzer, the $k - \omega$ Shear Stress Transport (SST) turbulence model is implemented using the model equations introduced in Section 2.3.1. Default model coefficients for the standard $k - \omega$ equations and blending functions are selected according to Menter et al. [141] alongside the formulas for

the calculation of the inlet values for k_{inlet} , ω_{inlet} , and $\nu_{t,\text{inlet}}$:

$$k_{\text{inlet}} = \frac{3}{2} (|\mathbf{u}_{\text{el,sim}}| \cdot I)^2 , \quad (4.36)$$

$$\omega_{\text{inlet}} = \frac{\sqrt{k}}{\beta^* \cdot L_t} , \text{ and} \quad (4.37)$$

$$\nu_{t,\text{inlet}} = k_{\text{inlet}} \cdot \omega_{\text{inlet}}^{-1} . \quad (4.38)$$

4.3.2. Volume displacement due to bubble nucleation

When bubbles nucleate, a volume of the electrolyte corresponding to the bubble volume is displaced. Due to this displacement, a momentum is generated that has to be considered in the simulation. Euler-Euler approaches like, e.g., Colli and Bisang [74], Alexiadis et al. [122] implicitly introduce the momentum due to bubble nucleation by the boundary condition of the disperse phase on the electrodes. Dependent on an arbitrarily chosen α_g on the electrode and \dot{V}_g , an inlet velocity for the introduced gas phase is calculated as a boundary conditions of electrode.

As described in Section 4.2.1, the introduction of bubbles is handled differently in Euler-Lagrangian compared to the Euler-Euler modeling. By default, the volume displacement is neglected and the bubbles simply spawn inside the domain. In order to account for the volume displacement during bubble nucleation, an expression is developed that considers the growth of a half sphere on the electrode and calculates the volume displacement in all three directions of space. Therefore, all normal vectors over the surface of the half sphere have to be integrated at all area elements of the surface. Using the volume growth

$$dV = \xi^2 \sin(\theta) d\theta d\Theta d\xi , \quad (4.39)$$

and multiplying it with each normal vector, \mathbf{e}^n , of the infinitesimal volume element in the following way

$$\int \int \int_S \mathbf{e}^n dV . \quad (4.40)$$

the growth of the half sphere can be described. Here, θ and Θ represent the polar and azimuthal angle, and ξ the the incremental radius of the sphere that increases upon growth. Figure 4.7 illustrates the assumed growth of an attached bubble in z -direction away from the electrode. Further, \mathbf{e}^n is defined as the position vector \mathbf{R} divided by the bubble radius $0.5 \cdot d_b$:

$$\mathbf{e}^n = \frac{2\mathbf{R}}{d_b} = \begin{bmatrix} \sin(\theta) \cos(\Theta) \\ \sin(\theta) \sin(\Theta) \\ \cos(\Theta) \end{bmatrix} . \quad (4.41)$$

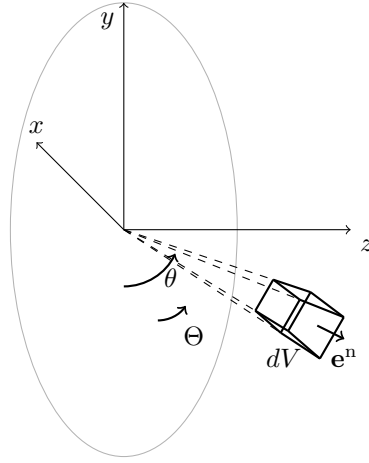


Figure 4.7.: Illustration of the assumed three dimensional volume displacement of a half sphere representing a growing bubble prior to detachment.

Inserting equations (4.39-4.41) in (4.40) yields

$$\int_{r_b}^{r_b+dr_b} \int_0^{2\pi} \int_0^{\frac{1}{2}\pi} \begin{bmatrix} \sin(\theta) \cos(\phi) \\ \sin(\theta) \sin(\phi) \\ \cos(\phi) \end{bmatrix} \xi^2 \sin(\theta) d\theta d\phi d\xi = \begin{bmatrix} 0 \\ 0 \\ \frac{1}{3}\pi ((r_b + dr_b)^3 - r_b^3) \end{bmatrix} \quad (4.42)$$

for the half-sphere. From the solution of equation (4.42), it follows that a quarter of the volumetric expansion of a half sphere is in the direction away from the wall. In addition, from the derivation also follows that the displacement due to the growth cancels itself out in in x and y directions. Hence, a time-constant momentum source is added to all face cells of the boundary field of the anode:

$$\mathbf{u}_{\text{el,disp}} = \left(0, 0, \frac{\dot{V}_{\text{O}_2}^g}{4 \cdot A_{\text{electrode}}} \right) \quad (4.43)$$

4.3.3. Mass transfer and electrolyte composition

This subsection describes the algorithm for the calculation of the mass transfer, speciation, supersaturation of target component S_{TC} , and conductivity within the continuous electrolyte phase. The flow chart, Figure 4.8, displays the calculation procedure to obtain the concentration, supersaturation, and conductivity fields. First, the α_{el} and $u_{\text{el,sim}}$ fields are read from a previous solved gas-liquid flow mass and are assumed to be constant. In addition, the name, charge, and diffusion coefficient R_i of all active Ions are read from a user-defined dictionary *speciesDict* alongside the *reactionDict* containing the included dissociation reactions, with educts, products, pKa values, and forward reaction rate k^{\rightarrow} .

For each time step, the transfer of an ionic species i within the continuous electrolyte

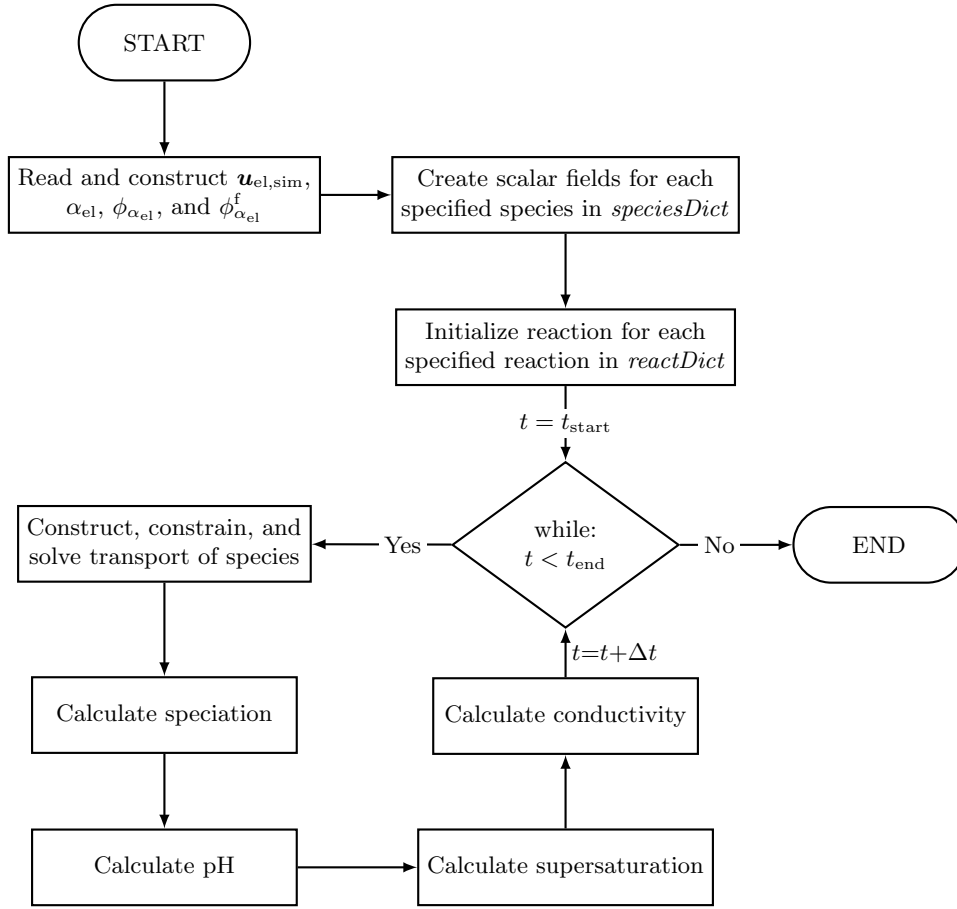


Figure 4.8.: Flow chart of the OpenFOAM solver *pHConcentrationFoam* for the calculation of mass transfer, speciation, supersaturation, and conductivity of the continuous electrolyte phase.

phase is described and solved by modifying equation (2.60) to

$$\frac{\partial (\alpha_{el} c_i)}{\partial t} - \nabla \cdot (D_i \alpha_{el}^f \nabla c_i) + \nabla \cdot (\alpha_{el} c_i) = R_i, \text{ with } i \in \{H, HA, H_2A, \dots\}. \quad (4.44)$$

Here, the contribution due to electromigration is neglected as its impact is comparably low at single digits voltages [35]. R_i equals zero, except for H^+ , where is it calculated by

$$R_H = \tilde{R}_H \cdot \frac{\alpha_{el}}{\bar{\alpha}_{el}}. \quad (4.45)$$

Upon initialization, \tilde{R}_H is calculated for all neighboring cells of the anode with the face area A_{cell}^f and $z = 1$ according to Faraday's Law:

$$\tilde{R}_H = \frac{A_{cell}^f i}{F} \quad (4.46)$$

The fraction $\frac{\alpha_{el}}{\bar{\alpha}_{el}}$ in equation (4.45) distributes the reaction based on the local gas phase

fraction of each cell. Thus, this implementation leads to a constant volumetric reaction rate in each cell at the anode.

After solving the transport equation, the speciation is calculated. Therefore, the dissociation reaction (2.8) and (2.9) are transferred into an ordinary differential equation (ODE) system similar to the scheme presented in [198]. Here, a sub-time step for the chemical reaction $\Delta t_{\text{chemical}}$ can be selected for explicitly solving the ODE. For each dissociation reaction the forward K_d^{\rightarrow} and backwards K_d^{\leftarrow} reaction rates are calculated by

$$K_d^{\rightarrow} = k_d^{\rightarrow} \cdot c_{e,d} \text{ and} \quad (4.47)$$

$$K_d^{\leftarrow} = k_d^{\leftarrow} \cdot c_{p1,d} c_{p2,d}, \quad (4.48)$$

where k_d^{\rightarrow} and k_d^{\leftarrow} represents the forward and backwards reaction rate, respectively [199, 200]. $c_{e,d}$, $c_{p1,d}$, and $c_{p2,d}$ represent the specified species concentration fields of the educt and the two products of the dissociation reaction. Here, k_d^{\leftarrow} is calculated using

$$k_d^{\leftarrow} = \frac{k_d^{\rightarrow}}{10^{-K_{a,d}}}. \quad (4.49)$$

$K_d^{\rightarrow} \cdot \Delta t_{\text{chemical}}$ and $K_d^{\leftarrow} \cdot \Delta t_{\text{chemical}}$ are then added or subtracted from the respective species in accordance to Schell et al. [198] and Hlawitschka et al. [199]. This step is repeated until the number of iterations equals the maximal number, $i_{\text{max}} = \frac{\Delta t_{\text{sim}}}{\Delta t_{\text{chemical}}}$, or the residual $(1 - \left| \frac{K_d^{\rightarrow}}{K_d^{\leftarrow}} \right|)$ is lower than a user-specified res_d . Afterwards, the pH value is computed based on c_{H^+} and S_{TC} is calculated after

$$S_{\text{TC}} = \frac{c_{\text{TC}}}{c_{\text{TC}}^*}. \quad (4.50)$$

Lastly, the conductivity of each cell can be computed by Bruggeman's law according to equation (2.17).

4.4. Determination of the residence time distribution

Once the simulation of the gas-liquid flow is finished, the flow fields can be averaged over a distinct time span. Subsequently, the flow fields can be analyzed and the RTD of phases can be studied. The average residence time of bubbles in the computational domain can directly be extracted from the fluid flow simulation by evaluating the age of the parcels leaving the domain at the outlet. For simulating the RTD of the continuous and, in electrochemical pH shift crystallization units present, solid phase, a Lagrangian approach is implemented that inserts particles at the inlet and measures the number of particles leaving the outlet. Thereafter, the procedure described in Section 2.3.4 can be applied

on the in- and outlet data and the RTD can be obtained. Compared to the procedure for the calculation of the disperse gaseous Lagrangian phase (Section 4.2), the calculation of the Lagrangian particle motion is greatly simplified. For the simulation of the RTD, only one-way coupling is considered as the tracer parcels shall act as *fluid* particles. In the following, the simulation parameters for the electrolyte and crystal phase are briefly introduced.

4.4.1. Electrolyte phase

As default, the fluid parcels are modeled as Lagrangian parcels with $n_p=1$, $\rho_p = \rho_{el}$, and $d_p = 50 \mu\text{m}$. They are introduced without any momentum ($\mathbf{u}_{p,0} = 0 \text{ mm s}^{-1}$) at the inlet as a step injection with a frequency f_p of 10,000 parcels per second. To study the effect of d_p and f_p on the RTD, initial simulations are conducted that vary d_p and f_p by an order of magnitude.

4.4.2. Crystal phase

Similar to the RTD determination of the electrolyte phase, Lagrangian parcels are used to depict the RTD of particles. Here, the crystal phase is chosen according to the work of Kocks et al. [17] to be H_2SA and, hence, $\rho_p = \rho_{\text{H}_2\text{SA}}$. When simulating the RTD of the crystal phase, d_p strongly impacts the results. Here, two different sieve fractions containing 0-200 μm and 200-400 μm are chosen and are implemented with a truncated normal distribution as depicted in Section 4.2.1.

4.5. Simulation Setups

This section presents the implemented electrolyte properties, the different studied computational domains alongside boundary conditions, and simulated operating conditions of the partially-transparent electrolyzer and a novel prototype for the electrochemical pH shift crystallization from Kocks et al. [17]. The simulations are run for 50 s and every 0.25 s, the current pressure, velocity, phase fraction, k , ω fields are written alongside with the parcels within the cloud and particles that escaped through the outlet.

4.5.1. Electrolyte properties

For the simulation of the gas-liquid flow, the implemented values for the electrolyte properties are either taken from literature or measured using the benchtop density meter DMA 4100M. In accordance to the PTV and PIV measurements, the electrolyte phase is considered to consist of deionized water with $c_{\text{Na}^+} = 0.6 \text{ mol L}^{-1}$ and $c_{\text{SA}^{2-}} = 0.3 \text{ mol L}^{-1}$ and

to be Newtonian. Table 4.1 presents the values alongside its reference or measurement method.

Table 4.1.: Electrolyte properties for the simulation of the gas-liquid flow.

Property	Value	Reference
σ	0.069 N m^{-1}	[201, 202]
ρ_{el}	$1\,027.5 \text{ kg m}^{-3}$	DMA 4100M
ν_{el}	$0.001\,042 \text{ kg m}^{-1} \text{ s}$	DMA 4100M

4.5.2. Computational domains and boundary conditions

The investigated computational domains in this thesis can be grouped in two categories: First, the sensitivity and suitability of the Euler-Lagrange model are simulated and compared to experimental data from the partially transparent electrolyzer that is depicted in Section 3.1.2. Therefore, the anode chamber geometry is meshed without the membrane holder in OpenFOAM using the *blockMesh* functionality. Here, two separate geometries are used to simulate either NNF or FCF conditions that are depicted in Figure B.2. For the NNF conditions, shown in Figure B.2 (b), no in- or outlet through the hose nozzles are modeled and a *fixedValue* (Dirichlet) boundary condition with a value of zero is chosen at the bottom. The electrolyte-air interface on the top is considered to have *zeroGradient* (Neumann boundary condition). Contrarily, the computational domain for FCF conditions features two patches for the in- and outlet hose nozzles. Here, the Dirichlet condition of $\mathbf{u}_{\text{el,sim}}$ at the inlet is calculated by dividing the chosen volume flow by the inner cross section of the hose nozzle. The outlet condition remains unchanged. The height of the computational domain is selected in accordance with experimental observations and the free electrolyte-air interface (called top) is modeled using a slip condition. Inlet values for the turbulence model are calculated according to the equations presented in Section 4.3.1.

Secondly, the electrochemical crystallization prototype from Kocks et al. [17] is mapped. Based on the stereolithography (STL) file used for the fused deposition modeling of the prototype and a block mesh *snappyHexMesh* is used to generate a mesh representation of the prototype. This procedure was repeated for the three different prototypes with electrode-membrane widths of 6, 8, and 10 mm. Exemplary, Figure B.3 shows a representation of the 6 and 10 mm prototypes. For the simulation of the gas-liquid flow, similar boundary conditions are applied as for the previous FCF conditions of the partially transparent electrolyzer. Though, the free air-electrolyte surface is non-existent in this computational domain.

For the $k\text{-}\omega\text{-SST}$ model, the boundary conditions are calculated according to Menter et al. [141]. Here, a turbulent intensity of 5% is assumed representing a low to moderate

turbulence [140]. A complete description of all the employed boundary conditions of all required fields is given in the appendix.

4.5.3. Simulation of the partially transparent electrolyzer

First, to analyze and discuss the simulation results, suitable averaging techniques, model parameters, and coupling methods have to be determined. Therefore, a base case is defined that uses the highest value for i (0.1 A cm^{-2}) and NNF conditions. For the mesh size in electrode-membrane direction Δz , n_p , virtual mass, drag model, coupling method, and the collision model parameters ($\delta_{j \leftrightarrow k, \max}$, Δt_{coll} , $r_{\text{eq}, kj}$, r_{coll}) default values are selected based on either literature [162, 189] or being the most realistic, e.g., $n_p=1$. Based on these default values, the parameters are varied to study their effect on the resulting $u_{b, \text{sim}}^v$, $u_{el, \text{sim}}^v$, α_g , flow regimes, and required core hour per simulated second (CPS). Table 4.2 lists the used default values alongside its variation for the parameters and model choices for the Euler-Lagrangian model.

Table 4.2.: Overview of the used default parameter for the base case and their variation for the sensitivity analysis of the Euler-Lagrangian model.

Value, Model	Default value	Variation(s)
Δz (mm)	0.4	0.67, 0.8, 1.0
n_p (-)	1	2, 5, 10
Drag model	Schiller and Naumann [142]	Lain et al. [143]
Virtual mass	No	Yes
Coupling method	Four-way	Two-way
$\delta_{j \leftrightarrow k, \max}$ (-)	10 %	5 %, 20 %
Δt_{coll} (ms)	1	0.5, 2
$r_{\text{eq}, kj}$	$r_{\text{eq}, kj}^{\text{arithm}}$	$r_{\text{eq}, kj}^{\text{harm}}$
r_{coll} (mm)	1	0.5

On the basis of the sensitivity study, parameters and models are selected that represent a good compromise between accuracy and computational effort. These settings are then used to simulate the NNF and FCF conditions within the partially transparent electrolyzer with their respective computational domains. The simulated operating conditions equal those used for the PIV and PTV measurements that are presented in Table 3.6.

4.5.4. Simulation of a novel prototype for electrochemical crystallization

Next, the parameterized Euler-Lagrangian model is applied to analyze the prototype for the electrochemical crystallization of succinic acid from Kocks et al. [17]. Three different

modifications with three different widths ($D_{E \rightarrow M}$) of 6, 8, and 10 mm are proposed and studied by Kocks [172]. In accordance to the studies of Kocks [17, 172], the three geometries are meshed using the selected resolution from the previous mesh sensitivity study and simulated for different electric currents and volumetric flow rates. Here, the previously selected model parameters are implemented and Table 4.3 displays the conditions applied to the simulation of each of the three prototypes. Depending on the simulated value for i , the experimentally determined bubble size distribution, introduced in Section 3.2, is applied for the nucleation of oxygen bubbles.

Table 4.3.: Overview of simulated operating condition within the 6, 8, and 10 mm-wide prototypes from Kocks [172].

$i \setminus V_{el,in} \text{ (mL min}^{-1}\text{)}$	6 mm		8 mm		10 mm	
	50	500	50	500	50	500
0 A cm ⁻²	6_50_0	6_500_0	8_50_0	8_500_0	10_50_0	10_500_0
0.01 A cm ⁻²	6_50_1	6_500_1	8_50_1	8_500_1	10_50_1	10_500_1
0.1 A cm ⁻²	6_50_10	6_500_10	8_50_10	8_500_10	10_50_10	10_500_10
0.2 A cm ⁻²			8_500_20			

Each simulation case is run for 25 s and afterwards, the flow field is used to determine the RTD of the electrolyte and solid, crystalline phase. The crystalline phase is regarded as succinic acid with $\rho_{H_2SA} = 1572 \text{ kg m}^{-3}$ [202] and two experimentally determined size distributions are implemented. Using the Vibratory Sieve Shaker AS 200 from RETSCH GmbH (Haan, Germany), two different fractions, 0-200 μm and 200-400 μm were generated and the distribution is measured using the Camsizer v2 from RETSCH GmbH. Thereby, the smaller size fraction corresponds to fine particles due to nucleation and the larger fraction to the larger portion a electrochemically crystallized particles [172]. Figure 4.9 shows the measured particle size distribution and a fitted normal distribution that is used for the tracer particle size distribution of the crystal phase. Table 4.4 lists the obtained parameters for the truncated normal distribution of the two different sieve fractions. Here, the fraction of crystals $< 100 \mu\text{m}$ are neglected for the fitting of the larger size distribution, since they do not have an impact on the q_3 distribution displayed in Figure 4.9 (b).

To study the local supersaturation profile within the novel prototype, the 8 mm version of the prototype is further studied as its being used in Kocks et al. [17]. Therefore, the results from the simulations 8_500_20, 8_500_10, and 8_500_1 are simulated for another 0.1 s with higher inner (4) and outer (4) PIMPLE correctors to minimize the error within the continuity equation to obtain the final flow field.

For the study of the supersaturation profile, the three carboxylic acids, SA, furan-2,5-

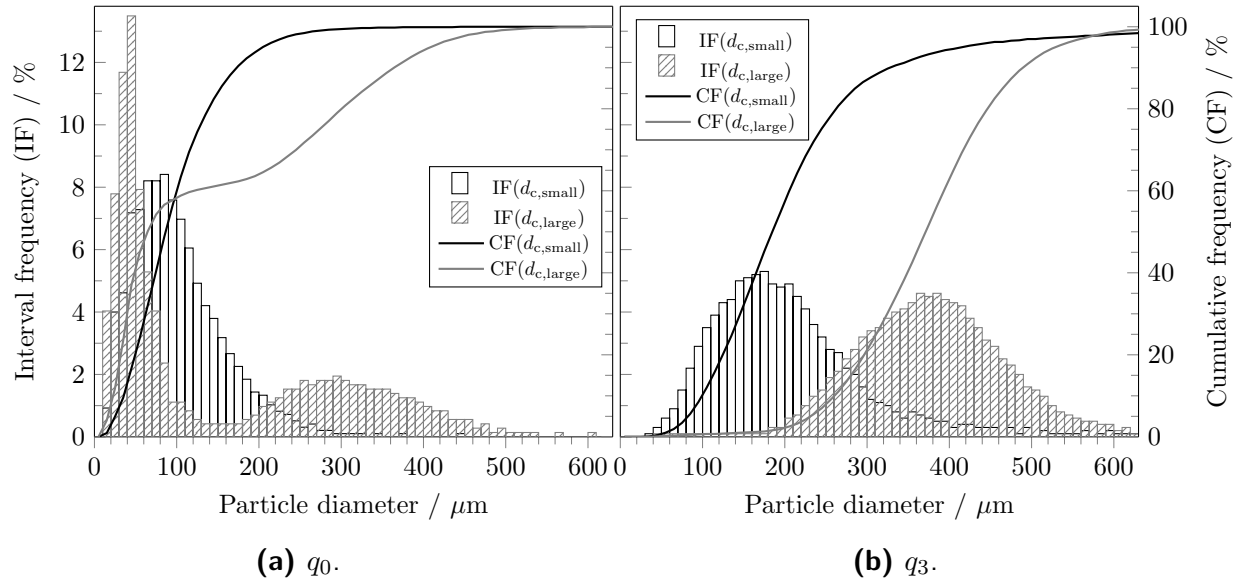


Figure 4.9.: Experimentally measured number-based (a) and volume-weighted (b) crystal size distribution and fitted normal distribution of the two small and large sieve fractions.

Table 4.4.: \bar{d}_c , $\varsigma(d_c)$, $d_{c,\min}$, and $d_{c,\max}$ of the small and large sieve fractions used for the truncated normal distribution.

Fraction	\bar{d}_c (μm)	$\varsigma(d_c)$ (μm)	$d_{c,\min}$ (μm)	$d_{c,\max}$ (μm)
Small	102.2	56.6	20	200
Large	300.7	95.8	200	400

dicarboxylic acid (FDCA) and terephthalic acid (TA), are studied. The three acids are listed with decreasing intrinsic solubility and, hence, greater local supersaturation are to be expected for TA compared to SA. The initial condition for the species concentrations of the simulation domain are selected either on experimental work [17] or on the pK_a values of the acid. Here, the speciation of the initial concentrations is in equilibrium. Table 4.5 displays the different examined operating conditions that will be simulated using *pHConcentrationFoam* introduced in Section 4.3.3. The concentration for the FDCA and TA are chosen based on the recent work by Harhues et al. [7] and the maximum solubility of Na_2TA [203]. The $pK_{a,1}$ and $pK_{a,2}$ values for SA, FDCA, and TA are assumed to be 4.18 and 5.55 [204], 2.04 and 3.44 [205], and 3.54 and 4.46 [204], respectively.

4.6. Criteria for comparison of simulation results

In order to compare the simulation results with each other and with experimental data, the following criteria are defined. First, the average number of bubbles in the computational

Table 4.5.: Simulated initial concentrations, i , $\dot{V}_{\text{el,in}}$, and pH values for the 8 mm prototype.

Case	$c_{\text{H}_2\text{A}}$ (mol L ⁻¹)	c_{HA^-} (mol L ⁻¹)	$c_{\text{A}^{2-}}$ (mol L ⁻¹)	pH (-)	i (A cm ⁻²)	$\dot{V}_{\text{el,in}}$ (L min ⁻¹)
Succinic acid (SA)						
SA-1	0.10	0.72	0.18	5	0.01	0.5
SA-2	0.10	0.72	0.18	5	0.1	0.5
SA-3	0.10	0.72	0.18	5	0.2	0.5
SA-3	0.0	0.05	0.63	3	0.1	0.5
Furan-2,5-dicarboxylic acid (FDCA)						
FDCA-1	0.0	0.0	0.9	7	0.1	0.5
FDCA-2	0.0	0.0	0.9	12	0.1	0.5
Terephthalic acid (TA)						
TA-1	0.0	0.0	0.63	7	0.1	0.5
TA-2	0.0	0.0	0.63	7	0.1	0.5

domain \bar{n}_b and computational core hours per simulated second CHPS by calculating the average value for the last 50 written time steps (12.5 s). Next, the velocity over the lines in the bottom, middle, and top viewing panel are extracted at the positions presented in Figure 3.8 from the PIV measurement. The specific coordinates of the lines are given in the appendix. Further, by calculating the average of cell values for $\overline{u_{\text{el,sim}}^x}$ and $\overline{\alpha_g^x}$ along the x -axis, the plot over line can be transferred to a plot over area. Figure 4.10 illustrates this post-processing that is conducted in Python using the *pandas*-library.

Based on the calculated averaged cell center data, the absolute difference of a quantity, e.g. $u_{\text{el,error}}^v$, between simulations can be obtained by

$$\overline{\Delta u_{\text{el,error}}^v} = \frac{\sum_{i=1}^{n_z} |u_{\text{el,sim},i} - u_{\text{el,exp},i}|}{n_z} \quad (4.51)$$

Using the 10 μm -spaced size bins, $\overline{\Delta u_{\text{b,error}}^v}$ and $\overline{\varsigma(u_{\text{b,error}}^v)}$ can be calculated after the same calculation scheme of above equation (4.51). Since the injection model also introduces bubbles at occupied positions, the collision model can lead to unphysical high bubble velocity. Thus, bubbles with vertical velocities outside $-100 \text{ mm s}^{-1} \leq u_{\text{b,sim}}^v \leq 200 \text{ mm s}^{-1}$ are excluded from the evaluation. Hence, the fraction of discarded bubbles $f_{\text{b}}^{\text{discarded}}$ is introduced that denotes the percentage of bubbles with vertical velocity outside the specified range.

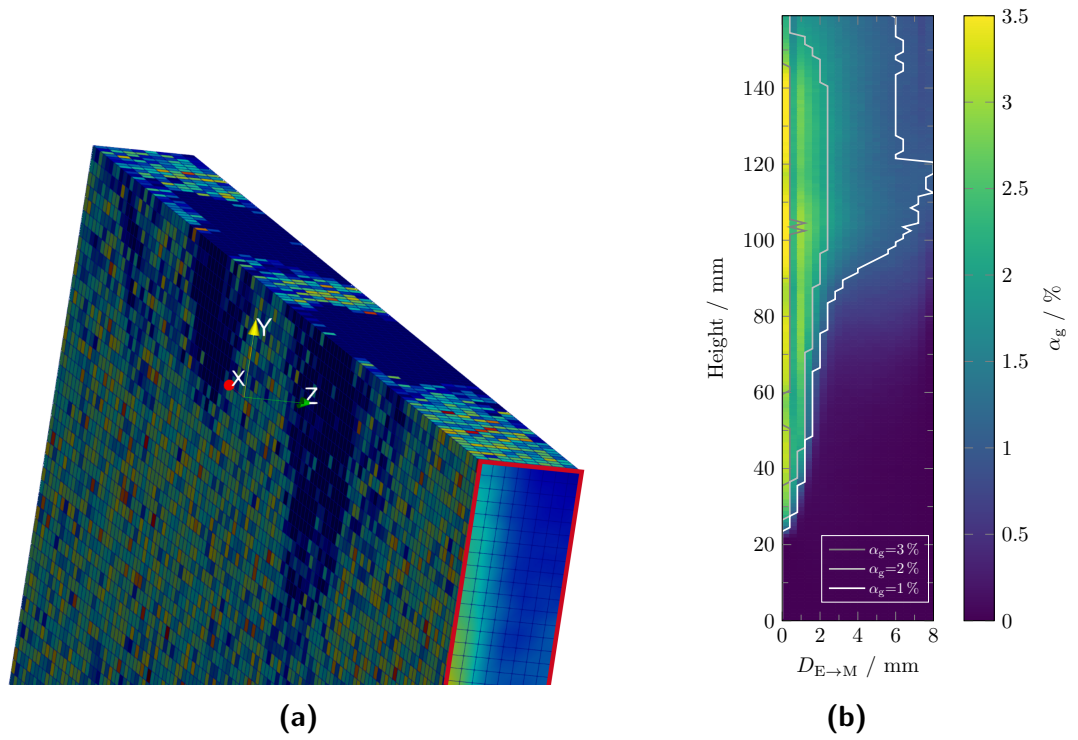


Figure 4.10.: Illustration of the averaging of the whole domain (a) along the x -axis during post-processing of the numerical results to obtain a two dimensional zy -plot of, e.g., the gas phase fraction (b).

5. Evaluation of the Euler-Lagrangian model for gas-liquid flows in electrolyzers

This chapter presents the sensitivity of the Euler-Lagrange Model to different simulation parameters, mesh sizes, and model choices in Section 5.1. Based on the results of the sensitivity analysis suitable, values are selected. Using the determined values for the parameters, Section 5.2 depicts the simulation results for the gas-liquid flow inside the tailor-made, partially transparent electrolyzer at different operating conditions and compares them with experimental data from Chapter 3.

5.1. Sensitivity analysis of simulation parameters

Appropriate simulation parameters must be determined before comparing simulation results with experimental data. Therefore, using $u_{\text{el}}^{\text{v}}=0 \text{ mm s}^{-1}$ and $i=0.1 \text{ A cm}^{-2}$ as base case, suitable time and spatial averaging methods for the transient simulation are discussed and selected in section 5.1.1. Next, the impact of a different number of cells between electrode and membrane on $u_{\text{b},\text{sim}}^{\text{v}}$, $u_{\text{el},\text{sim}}^{\text{v}}$, and the flow regimes are presented, and a suitable value for Δz is selected in section 5.1.2. Subsequently, sections 5.1.3, 5.1.4, 5.1.5, and 5.1.6, respectively, show the simulation results alongside the selected values for different n_{p} , drag models, coupling methods, and parameters for the collision model. Implementing the virtual mass force produced unphysical results and is discarded from the force balance.

5.1.1. Influence of averaging technique

The Euler-Lagrangian model presented in Chapter 4 uses a transient PIMPLE algorithm for the solution of the gas-liquid flow. As a result, the simulations do not result in a steady-state solution. Further, the flow field is constantly changing due to the random bubble injection at the electrode. The PIV measurement also captured this temporary and spatial variation in Section 3.6. For the base case of $u_{\text{el}}^{\text{v}}=0 \text{ mm s}^{-1}$ and $i=0.1 \text{ A cm}^{-2}$, Figure 5.1 displays the fluctuation of number of bubbles N_{b} inside the computational

domain against simulated time. In addition, the impact of different time intervals for the averaging on $\bar{u}_{b,\text{sim}}^v$ for different size bins is illustrated in Figure 5.1. Averaging over ten

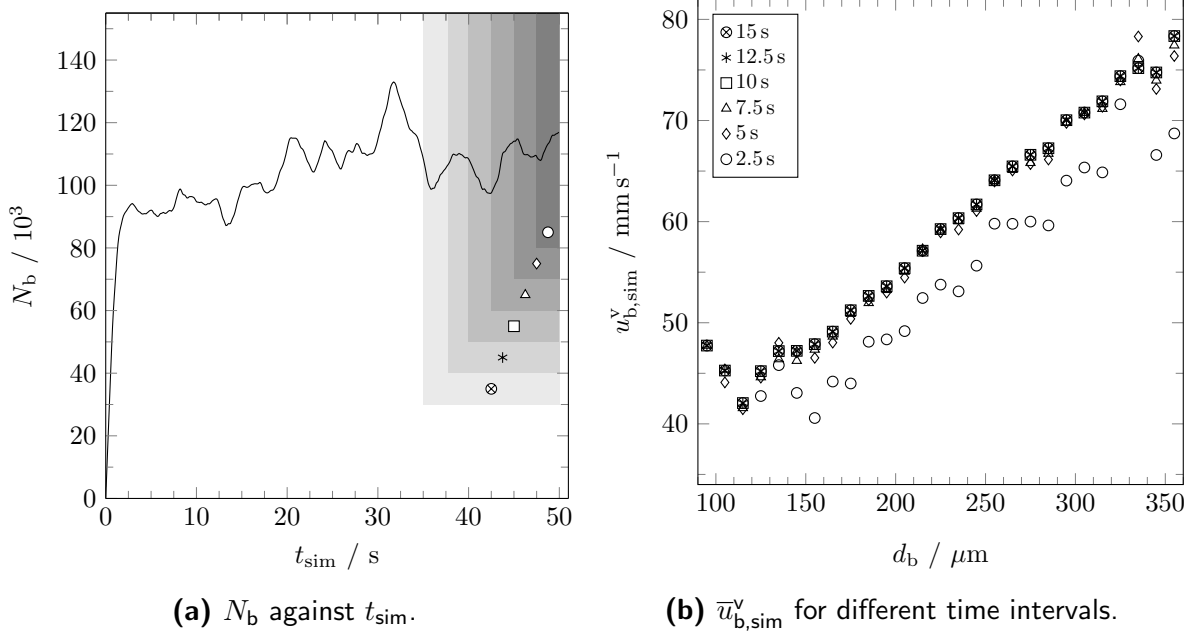


Figure 5.1.: Course of N_b in the computational domain over (a) the course of 50 s and (b) impact of different averaging time intervals on $\bar{u}_{b,\text{sim}}^v$ in the middle viewing panel.

time steps ($\equiv 2.5$ s) leads to a significant deviation of up to 12 mm s^{-1} compared to larger time periods. Using periods of 5 and 7.5 s for averaging the results leads to barely visible deviations, and between even longer time spans, the deviations approach zero. Hence, all following results will be presented based on a 10 s period of time that comprises out of the last 40 written time steps.

Next, the impact of plotting along a line versus a plane is depicted in Figure 5.2. The fluctuations of $u_{\text{el},\text{sim}}^v$ of the time-averaged base case along a single line more than double that of the corresponding plane. The difference between these two methods arises from the emergence of larger backflows of the transient simulation that lead to large negative local vertical velocities. The minimum displayed in Figure 5.2 (a) comprehensively captures the occurrence of larger backflows during the evaluated time interval. Hence, the plot over plane is selected for all following comparisons between simulation results because of its more minor variance.

5.1.2. Mesh size

Next, the effect of different discretization schemes of the gap between electrode and membrane on $u_{b,\text{sim}}^v$ and $u_{\text{el},\text{sim}}^v$ are studied using the previously determined time and spatial-averaging. Therefore, Δz is varied between 0.4 and 1 mm, and the resulting values for

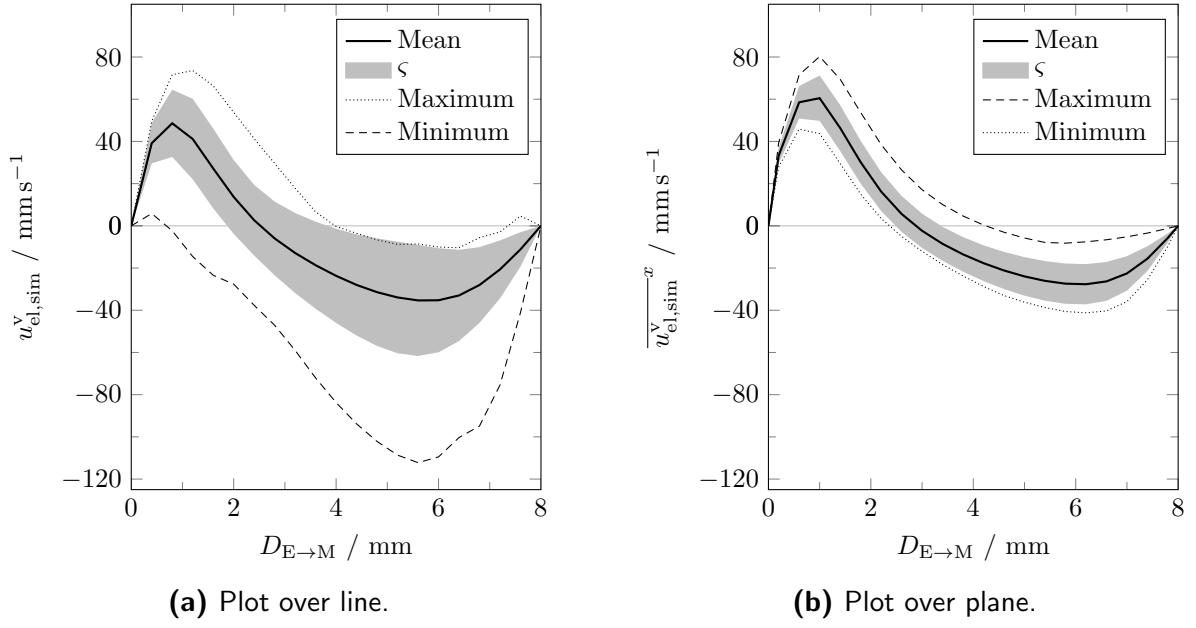


Figure 5.2.: Mean value, standard deviation, as well as minimal and maximal values for $u_{el,sim}^v$ plotted over (a) a line versus over (b) a plane against the distance from the electrode to membrane.

$u_{b,sim}^v$ in the middle viewing panel are plotted against the different bubble size bins in Figure 5.3. Here, the largest mesh size of $\Delta z = 1$ mm results in the lowest mean bubble

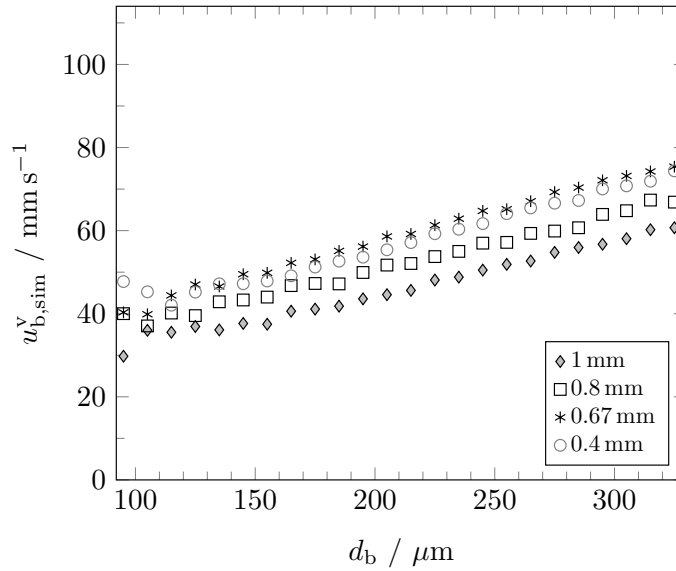


Figure 5.3.: Comparison of $u_{b,sim}^v$ for different bubble size bins and different values of Δz .

velocities. Compared to $\Delta z = 1$ mm, the average increase of the mean velocity of all size bins amounts to 5.4 mm s^{-1} for $\Delta z = 0.8$ mm and 12.8 mm s^{-1} for $\Delta z = 0.67$ mm. Further increasing the number of cells between electrode and membrane introduces only a slight deviation from the mean bubble velocities at $\Delta z = 0.67$ mm. A value of 0.4 mm for Δz

reduces the mean bubble velocity by an average of 2.0 mm s^{-1} . In relation to the average velocity of all evaluated bubbles at the middle viewing panel, this equals a relative difference of 3 %.

Figure 5.4 displays the impact of Δz on the flow field of the electrolyte averaged along the x -axis. In general, the flow field is not very sensible to changes in Δz , except for the maximum value of $\Delta z=1 \text{ mm}$. This quasi-grid independence exhibits the advantage of the Euler-Lagrangian approach over other studies that studied grid independence using Euler-Euler approaches [128]. The position and quantity of the maximum and minimum of

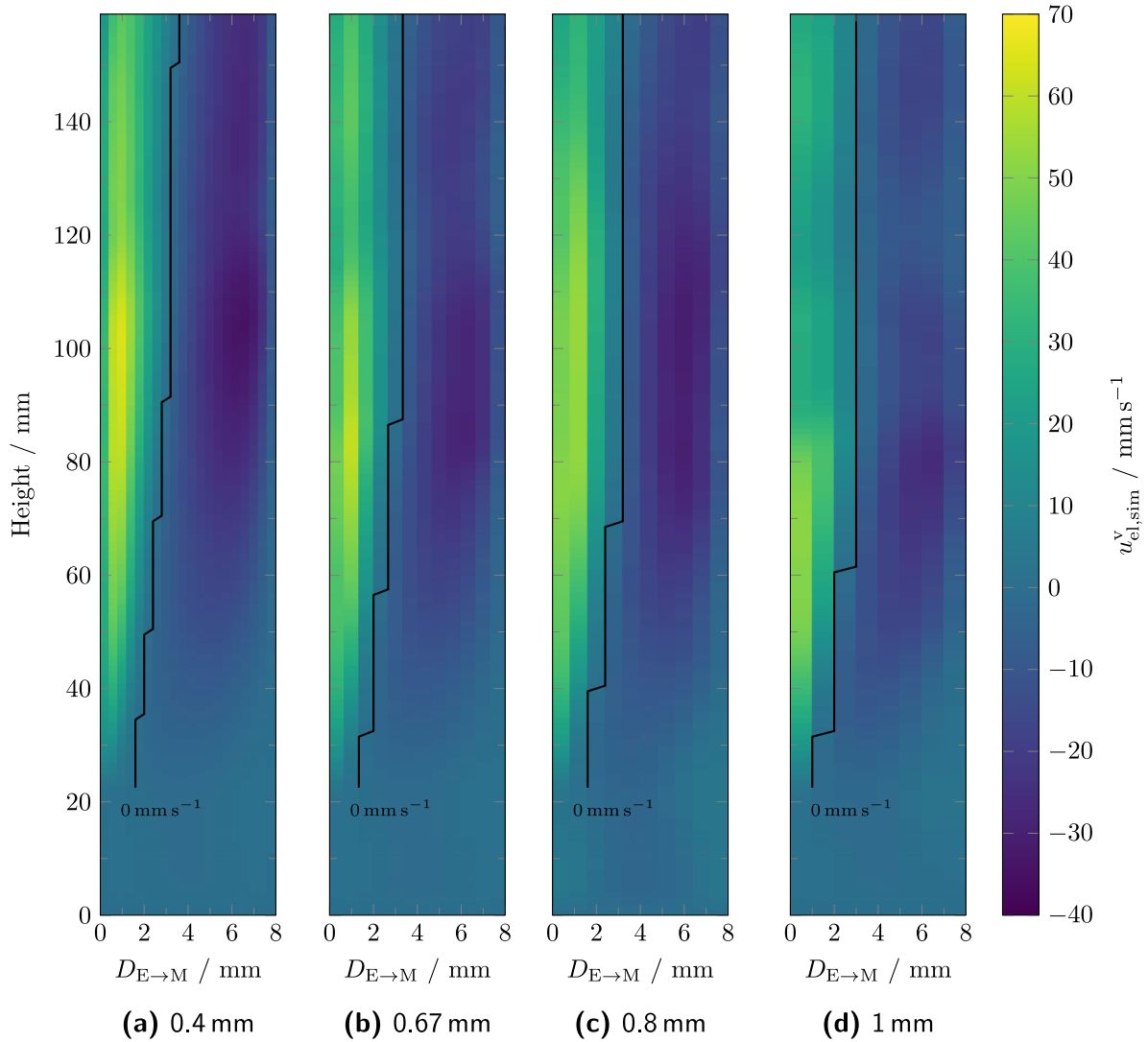


Figure 5.4.: Comparison of the flow fields for different mesh sizes between $0.4 \text{ mm} \geq \Delta z \geq 1 \text{ mm}$. The black line illustrates the border between the upward and downward directed flow regimes.

$\overline{u_{\text{el,sim}}^v}^x$ remain constant at a height and $D_{\text{E} \rightarrow \text{M}}$ of circa 80 to 100 mm and 1 mm, respectively. With increasing Δz , this area shifts downward, and the maximum value of $\overline{u_{\text{el,sim}}^v}^x$ diffuses due to the larger cell volumes. Though, the borderline between the upward and downward

flow regimes sketched in Figure 2.12 and marked by the black line in Figure 5.4 remains almost independent of Δz .

For a quantitative comparison, Figure 5.5 depicts $\overline{u_{\text{el},\text{sim}}^v}^x$ at the middle (a) and bottom (b) viewing panels. Similar to $u_{\text{b},\text{sim}}^v$, only the simulation results for $\Delta z=1$ mm deviate significantly from the other simulations. Here, the maximum value at the middle viewing panel increases from 39.6 mm s^{-1} for $\Delta z=1$ mm to 52.5, 60.2, and 60.5 mm s^{-1} for $\Delta z=0.8$, 0.67, and 0.4 mm, respectively. At the bottom panel, no major differences in $\overline{u_{\text{el},\text{sim}}^v}^x$ against $D_{\text{E} \rightarrow \text{M}}$ are apparent for different mesh sizes. Further, the intersection at which the electrolyte flow transition from upward ($u_{\text{el},\text{sim}}^v > 0 \text{ mm s}^{-1}$) to downward remains constant at $D_{\text{E} \rightarrow \text{M}}=3$ and 2 mm for the middle and bottom viewing panels, respectively. This finding is in good accordance with the gray borderline between the two flow regimes displayed in Figure 5.4.

Because there are no significant differences regarding $u_{\text{b},\text{sim}}^v$, $\overline{u_{\text{el},\text{sim}}^v}^x$, and also the computational costs (3.3 vs. $3.8 \text{ h s}_{\text{sim}}^{-1}$) between $\Delta z=0.67$ and 0.4 mm, $\Delta z=0.4$ mm is selected for all further simulations. This selection helps to depict better the concentration gradient in the electrode membrane gap in the final simulations.

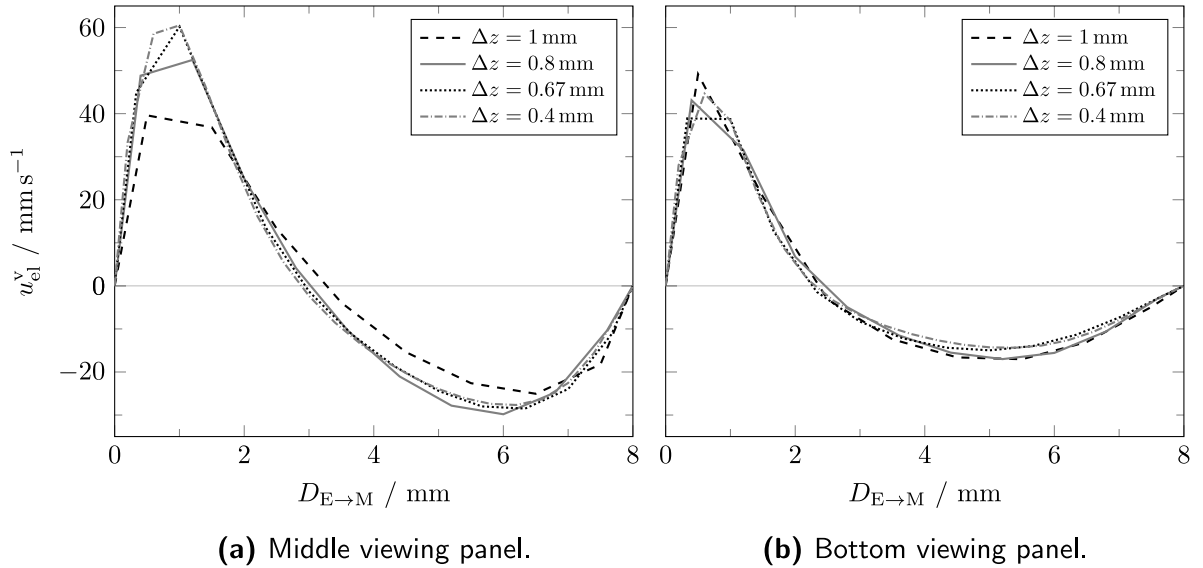


Figure 5.5.: $\overline{u_{\text{el},\text{sim}}^v}^x$ of the base case plotted at the (a) top and (b) bottom viewing panel for $\Delta z=0.4, 0.67, 0.8$ and 1 mm.

5.1.3. Number of bubbles per parcels

To reduce the computational costs of Euler-Lagrangian models, n_p is introduced to combine multiple dispersed objects into one computational parcel with the corresponding mass. Figure 5.6 shows the resulting flow fields for simulation in which two, five, and ten bubbles are aggregated into one parcel. For comparison, the base case with $n_p=1$ is also added

to Figure 5.6. When combining multiple bubbles into one parcel, the number of injected parcels is reduced by n_p different. This reduction of injected parcels leads to a smaller number of parcels in the simulation domain and, hence, a smaller computational cost that is illustrated in the appendix in Figure B.20. However, the reduced number of parcels also impacts the collision frequency and results in a different behavior bubble curtain spreading. Figure 5.6 illustrates this change in the bubble curtain behavior: As soon as

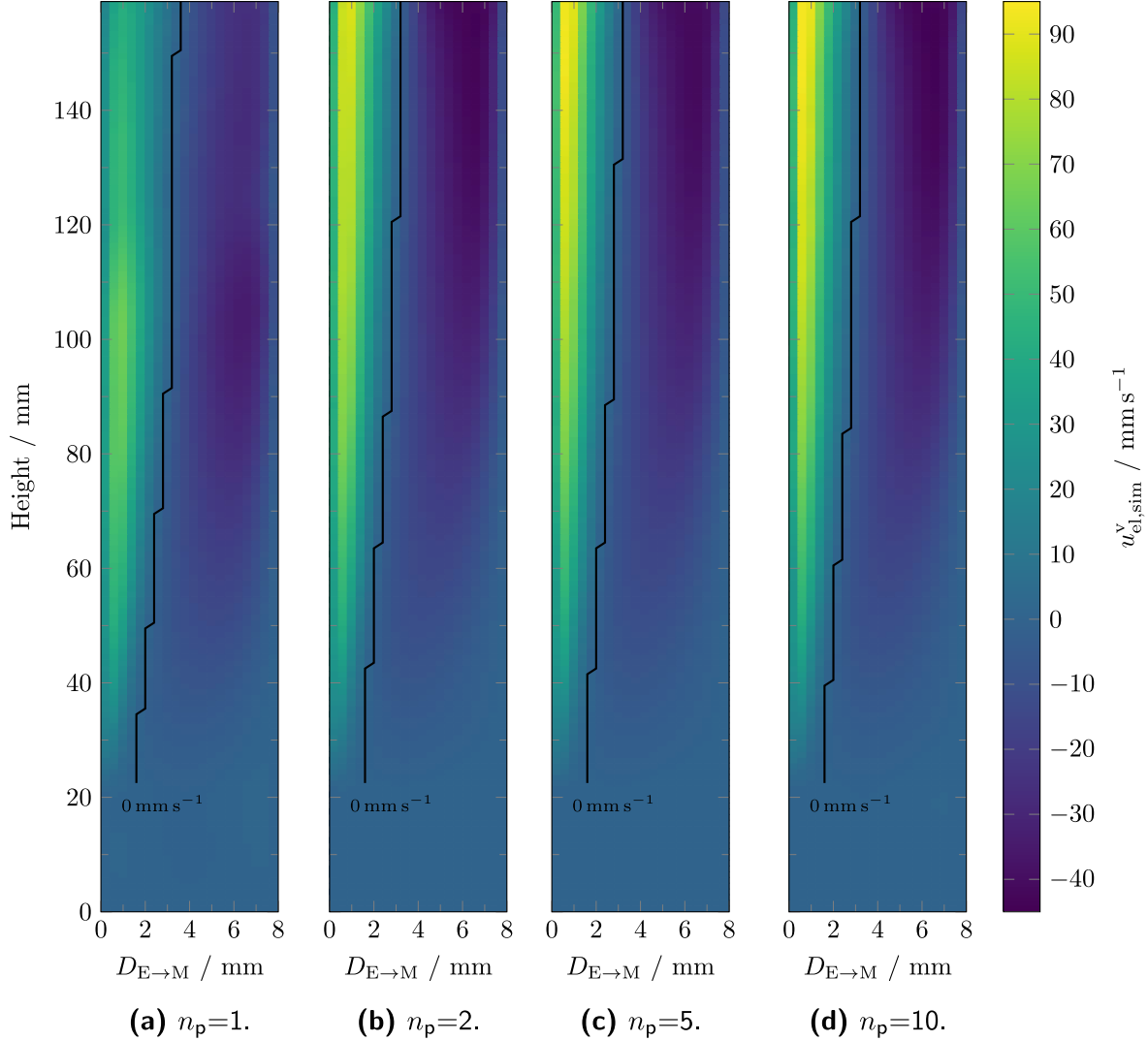


Figure 5.6.: Comparison of the flow fields at different values for n_p . The black line illustrates the border between the upward and downward directed flow regimes.

two bubbles are combined into a parcel, $\overline{u_{el,sim}^v}^x$ close to the electrode increases due to the greater buoyancy of the electrolyte through a more dense bubble curtain. This effect becomes more pronounced at heights above 100 mm. Surprisingly, simulations with $n_p=2$, 5, and 10 behave very similarly and hardly any difference can be identified. Figure 5.7 depicts $\overline{u_{el,sim}^v}^x$ at the top (a) and middle (b) viewing panel and quantitatively confirms the observations from Figure 5.6: For each of the two viewing panels, the average deviations

of $\overline{u_{\text{el},\text{sim}}^v}^x$ between simulations run with at least $n_p=2$ are below 1 mm s^{-1} . Simulating each bubble individually (n_p) does affect the spreading of the bubble curtain, especially at the top of the simulation domain. Here, the width of the bubble curtain decreases by roughly 1 mm when combining multiple bubbles into one parcel. Calculating an equivalent bubble radius based on $V_b \cdot n_p$ and using it for the calculation of forces and collision did not result in any changes in the simulation results. Subsequently, $n_p=1$ is chosen for all following simulations, since it presents the most physically-motivated setting. Nonetheless, the average number of parcels in the domain is reduced by 65, 86, and 94% for $n_p=2$, 5, and 10, speeding up the simulation by factors of roughly 3, 5, and 6.

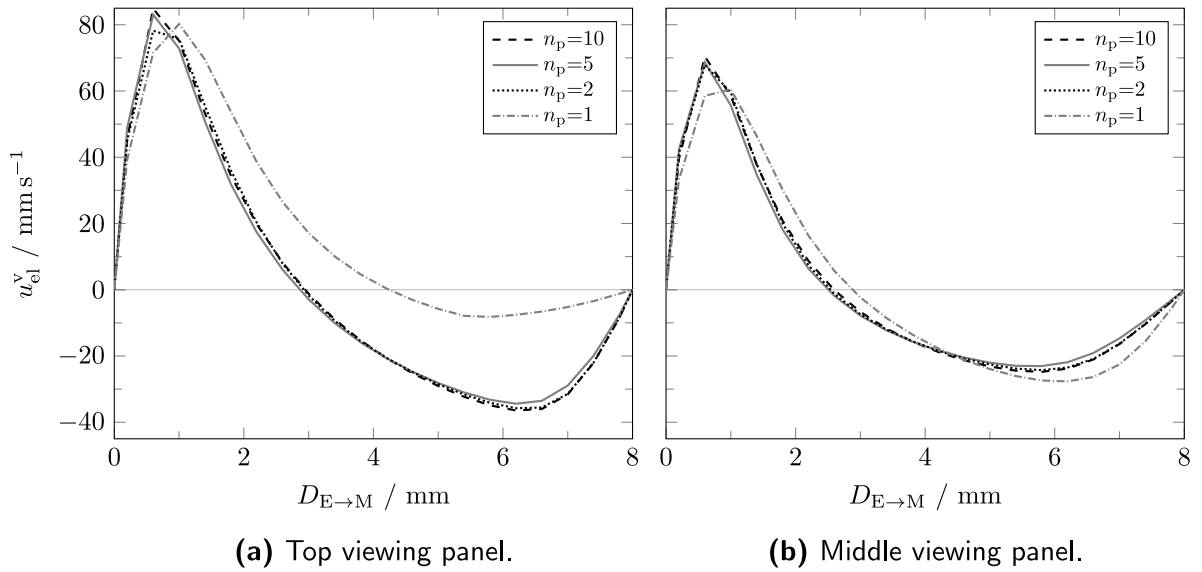


Figure 5.7.: $\overline{u_{\text{el},\text{sim}}^v}^x$ for the base case and different values for n_p at the (a) top and (b) middle viewing panel.

5.1.4. Drag model

Next, the simulation results of the base case with the rigid-bubble [142] drag model are compared with the corresponding case using the fluid-sphere [143] model. Figure 5.8 depicts the distributions of $u_{\text{b},\text{sim}}^v$ along the height of the electrolyzer for bubbles of all sizes and the two drag models. The first bubbles spawn at the beginning of the electrode (22.5 mm), and at this height, $u_{\text{b},\text{sim},50}^v$ respectively amount to 25.9 and 24 mm s^{-1} for the rigid-bubble and fluid-sphere model. In addition, the IQV and span of both distributions are $10.2 \pm 0.1 \text{ mm s}^{-1}$ and $30.6 \pm 0.2 \text{ mm s}^{-1}$. These small deviations show that both drag models predict a similar vertical bubble velocity distribution at the bottom of the electrode. This minimal change in the distribution remains up to a height of about 94 mm. Here, the span of the vertical velocity distribution of the rigid-bubble model exceeds that of the fluid-sphere model by 10.7 mm s^{-1} . In addition, $u_{\text{b},\text{sim},50}^v$ of the fluid-sphere model is 65 mm s^{-1}

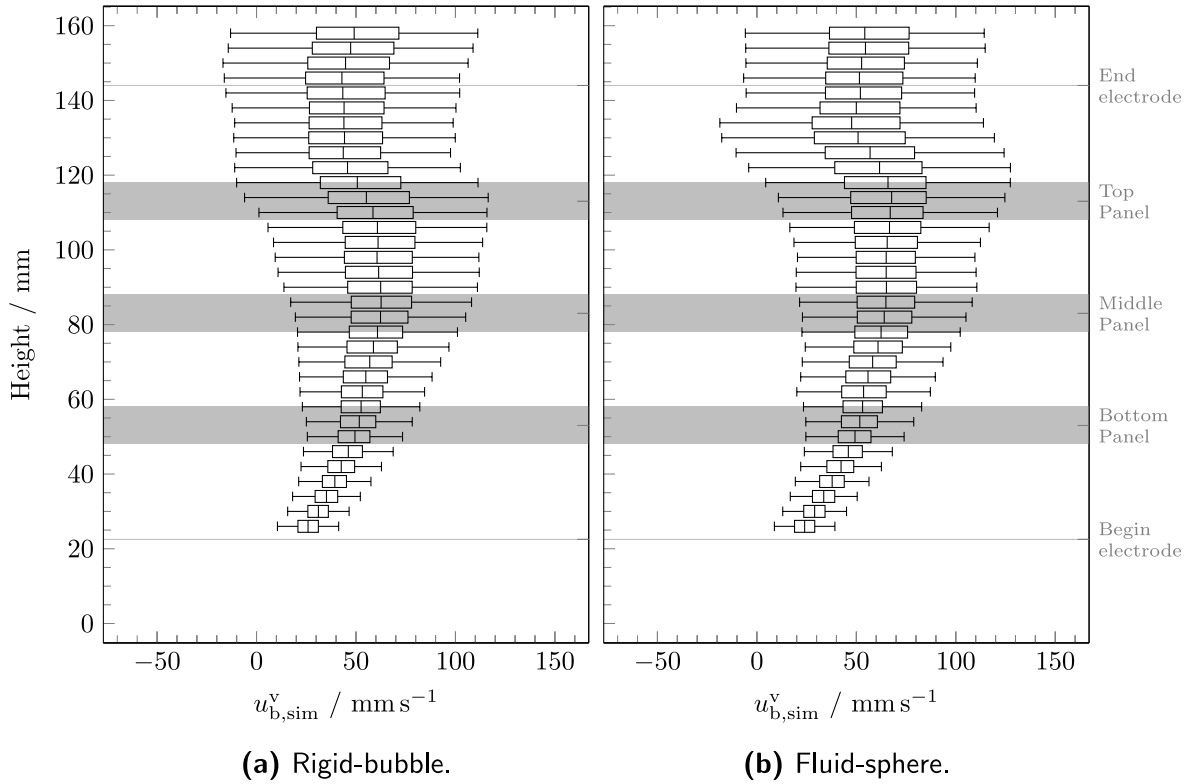


Figure 5.8.: Distribution of $u_{b,sim}^v$ along the height of the electrolyzer for the full bubble size range using the **(a)** rigid-bubble and **(b)** fluid-sphere drag models for the base case. The gray areas represent the respective viewing panels and the lines the begin and end of the electrode.

and greater than the corresponding value of the rigid-bubble model, 61.4 mm s^{-1} . From that point on, the differences between the distributions first widen and before converging again above the end of the electrode:

At heights of 106, 122, and 146 mm, $u_{b,sim,50}^v$ of the fluid-sphere model exceeds the corresponding value simulated with the rigid-bubble model by 5.9 , 15.9 , and 8.6 mm s^{-1} . Simultaneously, the difference in the IQR and span of the vertical velocity distribution between the rigid-bubble and fluid-sphere model changes from 3.2 and 9.8 mm s^{-1} to -6 and -18.1 mm s^{-1} and finally to 0.6 and 1.9 mm s^{-1} at the three heights.

For an in-depth analysis, Figure 5.9 visualizes $u_{b,sim,50}^v$ for three distinct size bins of 150-160 mm (a), 220-230 mm (b), and 270-280 mm (c) along the height of the electrolyzer for the two drag models. For comparison, the vertical velocity distribution for each size bin and height is calculated from experimental data and added as a box plot to Figure 5.9. Comparably to Figure 5.8, the only minor deviation between $u_{b,sim,50}^v$ between the two drag models exists up to the end of the middle viewing panel. Thereafter, between the middle and top viewing panel, the rigid-bubble model predicts a slight decrease of $u_{b,sim,50}^v$, whereas the fluid-sphere model leads to a minor increase for all size bins. Above the top viewing panel, both models predict a decrease for $u_{b,sim,50}^v$ of the three size bins.

Compared with the experimental data, both models predict $u_{b,\text{sim},50}^v$ of the bottom viewing panel well. Solely, the simulated vertical velocity of the bubbles with sizes between 290-300 μm surpasses the experimental data by an average of 5 mm s^{-1} . At the middle viewing panel, the two simulations slightly overestimate the vertical bubble velocity. However they are able to reflect the increase in vertical bubble velocity between the bottom and middle viewing panels. Further, the rigid-bubble model almost perfectly maps the $u_{b,\text{exp},50}^v$ of the upper part of the middle viewing panel. The comparison with experimental data in the top viewing panel exhibits a two-part picture: The vertical bubble velocities in the lower 5 mm of the viewing panel are better reflected by the simulation with the rigid-bubbles model than with the fluid-sphere model. However, this observation flips at the top of the upper viewing panel.

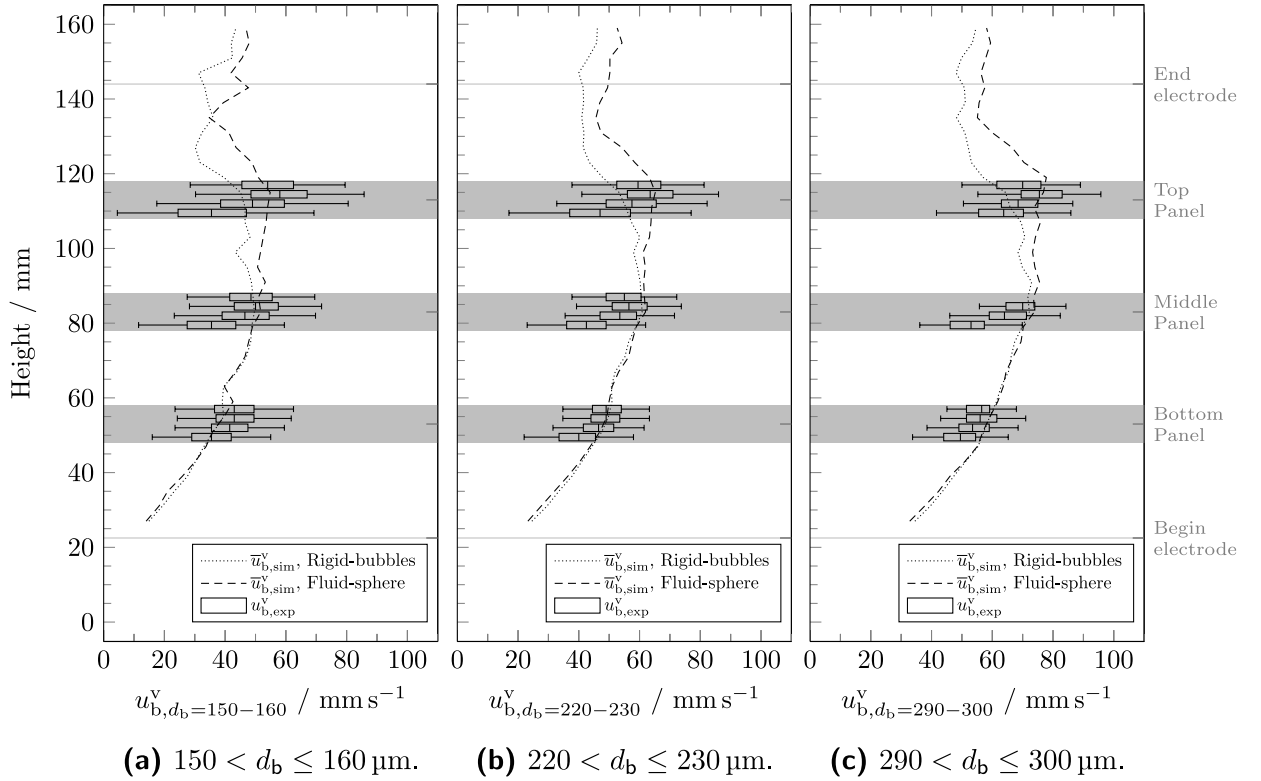


Figure 5.9.: Comparison of $u_{b,\text{sim},50}^v$ and $u_{b,\text{exp},50}^v$ for different bubble size bins of (a) 150-160 μm , (b) 220-230 μm , and (c) 270-280 μm along the height of the electrolyzer.

Based on the comparison between the simulation results and the experimental data for the three size bins, both drag models can reasonably predict the experimental data. The fluid-sphere model is selected since the underlying experimental data points at the start of each viewing panel are sparse compared to the upper section and because there is an overall more minor deviation from the numerical and experimental vertical bubble velocity.

5.1.5. Two-way vs. four-way coupling

Apart from the theoretical requirement to include bubble-bubble interactions [159], the impact and necessity of the introduced four-way coupling model are studied. Figure 5.10 (a) depicts the flow field and numerical values for $u_{\text{el,sim}}^v$ from the base case simulation of with two-way coupling. In comparison to the results depicted in Figure 5.4 obtained with

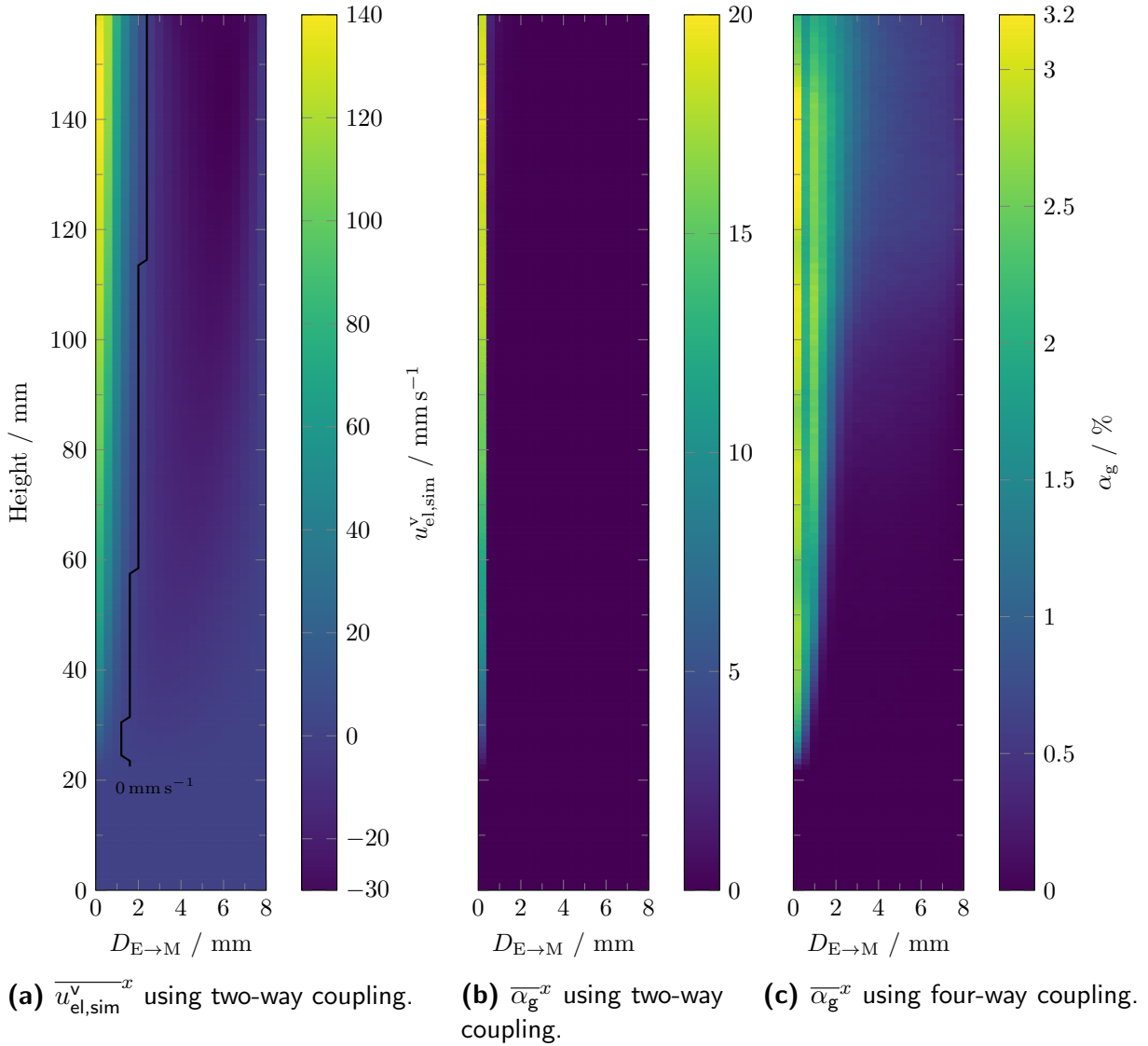


Figure 5.10.: x -averaged flow fields for the (a) base case and two-way coupling. The black line illustrates the border between the upward and downward directed flow regimes. (b) and (c) display the distribution of the gas phase fraction $\overline{\alpha_g^x}$ for two-way and four-way coupling, respectively.

four-way coupling, the upward regime close to the electrode narrows, and the maximal velocity balloons to 140 mm s^{-1} compared to roughly 70 mm s^{-1} with the collision model. These differences between the two coupling mechanisms arise from the local distribution

of the oxygen bubbles: Without modeling bubble-wall and bubble-bubble collisions, the bubbles remain in direct proximity to the walls, and the bubble curtain spreading does not occur. Figure 5.10 (b) and (c) depict this phenomenon, respectively, showing the gas phase fraction using two- and four-way coupling. In Figure 5.10 (b) the x -averaged gas phase $\overline{\alpha_g^x}$ is only present in the cell next to the electrode or wall. Here, it reaches phase fractions of up to 20 %. Contrarily, the four-way model ideally predicts the experimentally measured spreading of the bubble curtain. Figure 5.10 (c) depicts the distribution of $\overline{\alpha_g^x}$, and the classic behavior of the bubble curtain growing along the height of the electrolyzer can be observed. Here, $\overline{\alpha_g^x}$ in the partially transparent electrolyzer is capped at 3.2 %.

The comparison between the two coupling methods unambiguously yields that a two-way phase coupling is inadequate for modeling the gas-electrolyte flow within an electrolyzer. This limitation regarding the bubble curtain also arises in Euler-Euler simulations that usually do not depict the interplay between dispersed particles. Instead, semi-physical models such as turbulent dispersion [74] or purely empirical transversal forces that act perpendicular to the electrode [73, 133] are added. The implemented four-way model from [162] showcases the potential of the Euler-Lagrangian approach for the simulation of electrolyzers and does not introduce any new model parameters. Solely, numerical limiters were introduced, whose sensitivity will be discussed in the next section.

5.1.6. Sensitivity study of the collision model parameter

The implemented numerical limiters for the collision model include the maximal overlap $\delta_{j \leftrightarrow k, \max}$, time increment of the collision Δt_{coll} , the calculation of the middle diameter of two colliding bubbles $\bar{d}_{j,k}$, and finally the maximal distance for which the collision model is evaluated r_{coll} . Table 4.2 lists their default values and simulated variations. The sensitivity of the base case results to the parameter variations are tabulated in Table 5.1.

Limiting the overlap of spawning bubbles, $\delta_{j \leftrightarrow k, \max}$ to 5 % leads to an average increase in vertical bubble velocity over all size bins of 5.2 mm s^{-1} while also decreasing the standard deviation by 6 mm s^{-1} . Permitting a greater overlap has little impact on the averaged vertical bubble velocity but does affect the x -averaged electrolyte velocity at the middle viewing panel. However, this variation is within the standard fluctuation of the transient simulation. Changing $\delta_{j \leftrightarrow k, \max}$ has no effect on $f_b^{\text{discarded}}$ that arises while calculating collisions. As a consequence, the value of 20 % is selected and this numerical limiter could also be dropped in future implementations.

Reducing t_{coll} by 50 % increases the computational costs by 60 % as the resolution of the collision event becomes even more time-consuming. Au contraire, doubling t_{coll} reduces the CPS by 40 %. However, $t_{\text{coll}}=200 \mu\text{s}$ impacts the simulation results and increases the fraction of discarded bubbles to 1.15 %. As a compromise, $t_{\text{coll}}=100 \mu\text{s}$ is chosen due to

Table 5.1.: Sensitivity of the simulation results of the base case to the variation in parameters $\delta_{j \leftrightarrow k, \max}$, Δt_{coll} , $\bar{d}_{j,k}$, and r_{coll} .

Varied Parameter		\bar{n}_b (10^3)	CPS ($\text{h s}_{\text{sim}}^{-1}$)	$\overline{\Delta u_b^v} /$ (mm s^{-1})	$\overline{\varsigma(u_b^v)}$ (mm s^{-1})	$\overline{\Delta u_{\text{el}}^{v,x}}$ (mm s^{-1})	$f_b^{\text{discarded}}$ (-)
Base case		112	3.8	-	-	-	0.73%
$\delta_{j \leftrightarrow k, \max}$	5%	115 (+3%)	3.7 (-3%)	5.2	-6.0	2.7	0.74%
	20%	96 (-14%)	3.8 (-1%)	0.6	-4.8	4.0	0.74%
Δt_{coll}	50 μs	87 (-22%)	6.1 (+60%)	0.6	1.4	0.9	0.36%
	200 μs	116 (+4%)	2.2 (-41%)	-6.8	-2.4	1.1	1.15%
$\bar{d}_{j,k}^{\text{har}}$		119 (+6%)	4.1 (+7%)	3.9	-5.4	1.1	0.68%
r_{coll}	0.5 mm	95 (+4%)	2.0 (-48%)	2.1	-2.1	0.8	0.8%

the minor computational cost. Changing the computational scheme for $\bar{d}_{j,k}$ leads to an increase in average vertical bubble velocity of the size bins and $\overline{\Delta u_{\text{el}}^{v,x}}$ of 1.1 and 4 mm s^{-1} , respectively. Out of simplicity, the previous sections' standard option (arithmetic mean) is kept. Finally, halving r_{coll} to 0.5 mm drastically reduces the computational cost and almost halves the required CPS. Since the impact on the computational results is small and r_{coll} is often chosen around the maximal parcel diameter, r_{coll} is set to 0.5 mm for all following simulations.

5.2. Simulation of partially transparent electrolyzer

After discussing and selecting adequate simulation parameters, this Section simulates different operating conditions of the partially transparent electrolyzer and compares them to experimental data. First, Section 5.2.1 presents the results for the NNF configuration. Thereafter, the comparison of the forced flow configuration is depicted in Section 5.2.2 to conclude the evaluation of the Euler-Lagrangian model.

5.2.1. No net flow configuration

Foremost, Figure 5.11 depicts the time-averaged Re_{el} and electrolyte flow direction of the NNF-base case at $i=0.1 \text{ A cm}^{-2}$ in the partially transparent electrolyzer. Figure 5.11 (a) depicts the flow field and Re_{el} in the xy -plane 1 mm away from the electrode and (b) the x -averaged flow field and Re_{el} in the zy -plane. Across the entire xy -plane, the flow of the electrolyzer is directed upward due to the buoyancy of the electrogenerated bubbles. In the area around the viewing panels, a maximum Reynolds number of 1,000 is obtained that falls below the values at the right and left sides of the computational domain. This difference in Re_{el} originates from the reduced active electrode area due to the carved-in viewing panels in the middle of the domain. Further, an increase of Re_{el} alongside

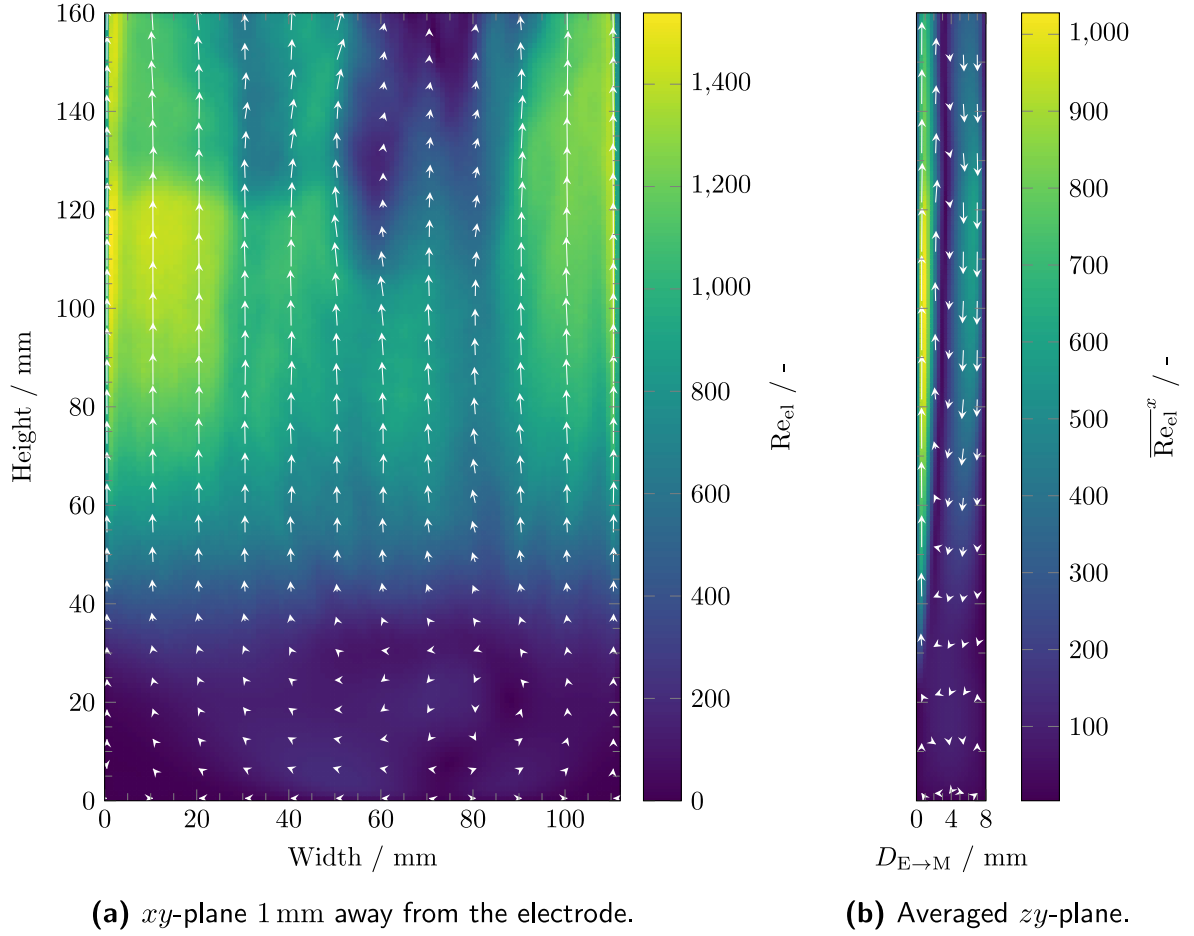


Figure 5.11.: $\overline{Re_{el}}$, and direction of flow in the xy (a) and yz plane (b).

the height of the electrolyzer depicts the increased gas phase fraction and thereby linked acceleration of the electrolyte. In the xy -plane at $D_{E \rightarrow M} = 1$ mm, the maximum value of Re_{el} equals circa 1,500, indicating the presence of a laminar flow regime. The spreading of the bubble curtain alongside the electrolyzer height is highlighted in the x -averaged flow field and Re_{el} in the zy -plane displayed in Figure 5.11 (b). Here, the two flow regimes are present, and due to their different width, the arithmetic mean of $\overline{Re_{el}^x}$ amounts, on average, 800 and 500 for the up- and downward flow regimes, respectively.

To examine the assumption proposed in Section 4.1 that the bubbles can be regarded to be spherical, Figure 5.12 shows the distribution of the Re_b , Eo_b , and We_b as box plots. On average, Re_b , Eo_b , and We_b average to 3.6 , $6.2 \cdot 10^{-3}$, and $9.7 \cdot 10^{-4}$, respectively. Further, $\tilde{Re}_{b,max}$ and $Re_{b,75}$ are equal to 6.6 and 11.2 . Comparing these obtained values with the different bubble shapes depicted in Figure 2.10, the assumption of spherical bubbles is justified.

Next, Figure 5.13 displays the x -averaged vertical velocity of the electrolyte $u_{el,sim}^v$ and gas phase fraction α_g at $i = 0.01$ (a+d), 0.05 (b+e), and 0.1 A cm $^{-2}$ (c,f) and NNF conditions, allowing for a comparison of the three different current densities. Independent of i ,

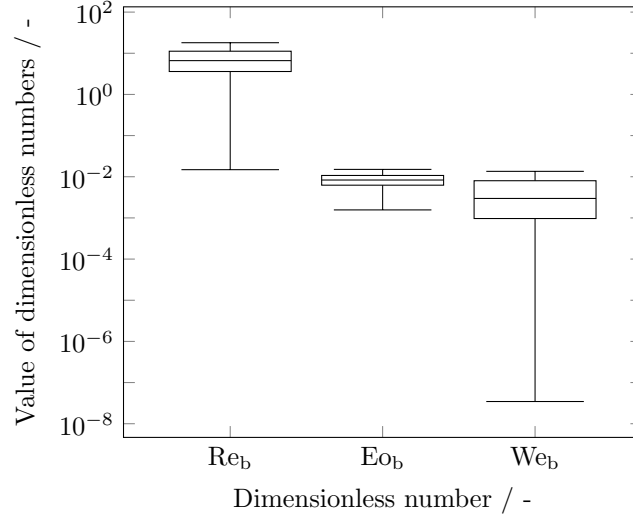


Figure 5.12.: Re_b , Eo_b , and We_b of all simulated bubbles in the computational domain for the base case.

the width of the upward flow regime stays almost constant along the height of the electrolyzer. However, due to the amount of produced oxygen gas, the maximum of $\overline{u_{el,sim}^v}^x$ at the middle viewing panel increases from roughly 23 mm s^{-1} at $i=0.01$ and $i=0.05 \text{ A cm}^{-2}$ to 62.6 mm s^{-1} at $i=0.1 \text{ A cm}^{-2}$ in the upflow regime. Simultaneously, the magnitude of the downward flow increases in the backflow regime. The cause of the same upward velocities at the middle viewing panel at $i=0.01$ and $i=0.05 \text{ A cm}^{-2}$ arises from the different distributions of the gas phase fraction depicted in Figure 5.13 (d,e). Whereas the majority of generated bubbles stay within the bubble curtain close to the electrode at $i=0.01$ and 0.1 A cm^{-2} , the backflow at $i=0.05 \text{ A cm}^{-2}$ pulls gas bubbles out of the bubble curtain. Thereby, the segregated flow is disturbed, resulting in the complete break up of the bubble curtain. Opposed to the curtain breaking up at $i=0.05 \text{ A cm}^{-2}$, a greater current density of 0.1 A cm^{-2} results in the presence of a clear two-regime flow. This different behavior originates from (a) the different bubble size distribution and (b) the amount of oxygen produced. The larger bubbles at $i=0.1 \text{ A cm}^{-2}$ ascend faster and are less likely to be pulled out of the bubble curtain. In addition, generating a larger and simply higher number of generated bubbles leads to greater acceleration and circulatory flow of the electrolyte, thereby reducing the residence time of the bubbles. The width of the upward flow regime dz_1 alongside the value and position of the maximum vertical velocity of the electrolyte $u_{el,max}^v$ and $z(u_{el,max}^v)$ at the three viewing panels is tabulated in Table 5.2.

Using the data published in Görtz et al. [86], the simulation results can be compared to experimental data acquired within the partially transparent electrolyzer. Figure 5.14 (a) presents the distribution of u_b^v of the base case at the middle viewing panel and (b) the development of the simulated distribution from the bottom to the top viewing panel. At

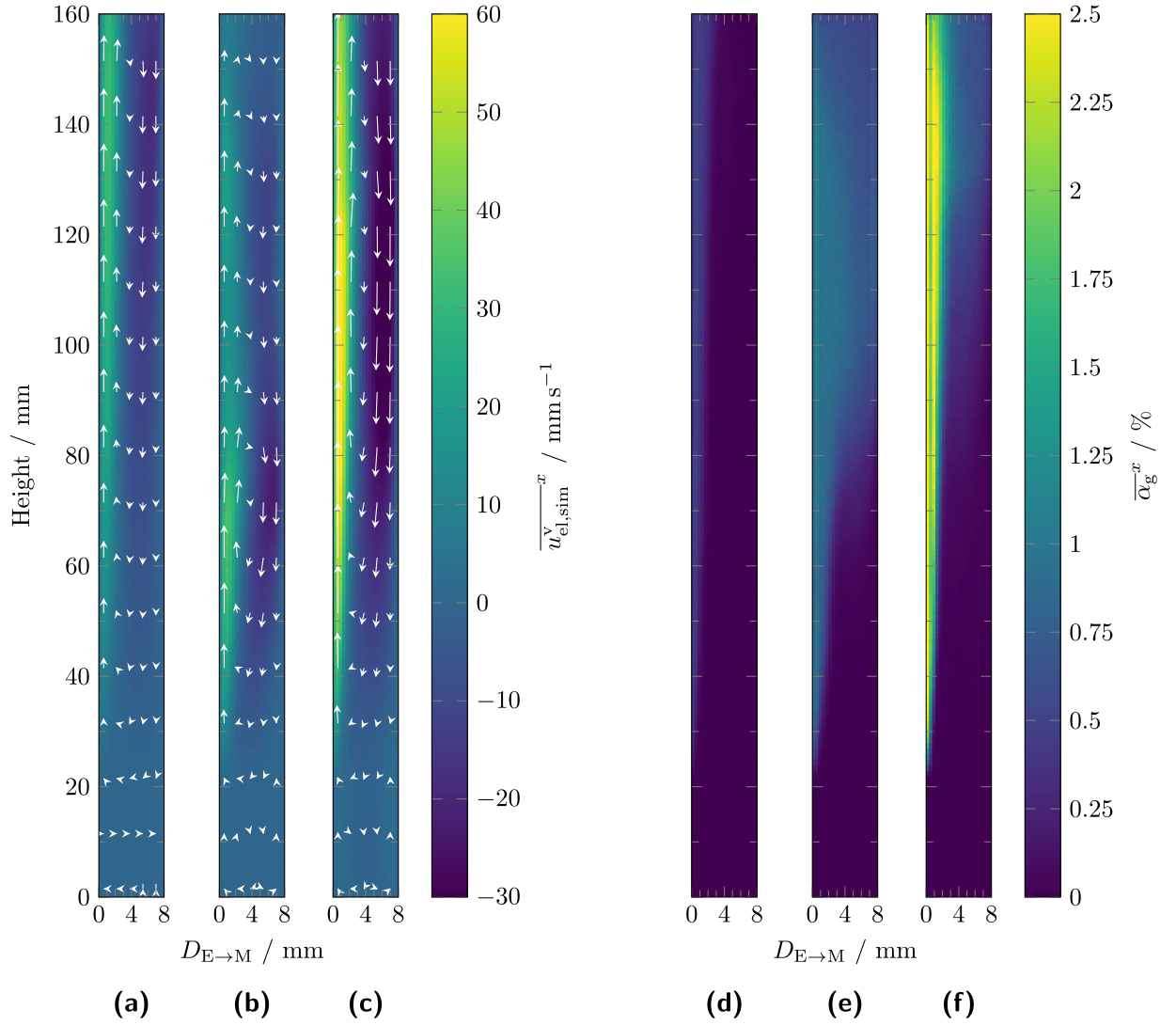


Figure 5.13.: Simulated x -averaged vertical velocity at NNF and **(a)** $i=0.01$, **(b)** 0.05 , and **(c)** 0.1 A cm^{-2} and gas phase fraction fields at **(d)** $i=0.01$, **(e)** 0.05 and **(f)** 0.1 A cm^{-2} in the partially transparent electrolyzer.

the middle viewing panel, the simulated distribution of u_b^v is wider and exhibits a larger mean value of 63 mm s^{-1} compared to the experimental data measured using the PTV algorithm [86]. Hence, it can be concluded that the bubble velocity is slightly overestimated in the middle viewing panel at $i=0.1 \text{ A cm}^{-2}$. Comparing the simulation results across different viewing panels (Figure 5.14 (b)), $\overline{u_{b,sim}^v}$ changes from 52.5 mm s^{-1} at the bottom to 63.0 mm s^{-1} at the middle and 59.0 mm s^{-1} at the top viewing panel. This development of $\overline{u_{b,sim}^v}$ along the height is already discussed in Section 3.4.3 and mainly stems from the increase in greater buoyancy due to the growing gas phase fraction.

For a more in-depth analysis, u_b^v is classified into different size bins and Figure 5.17 displays the resulting experimental and simulation data of $\overline{u_b^v}$ against different bubble sizes for the three different current densities at the middle viewing panel (a) and all view-

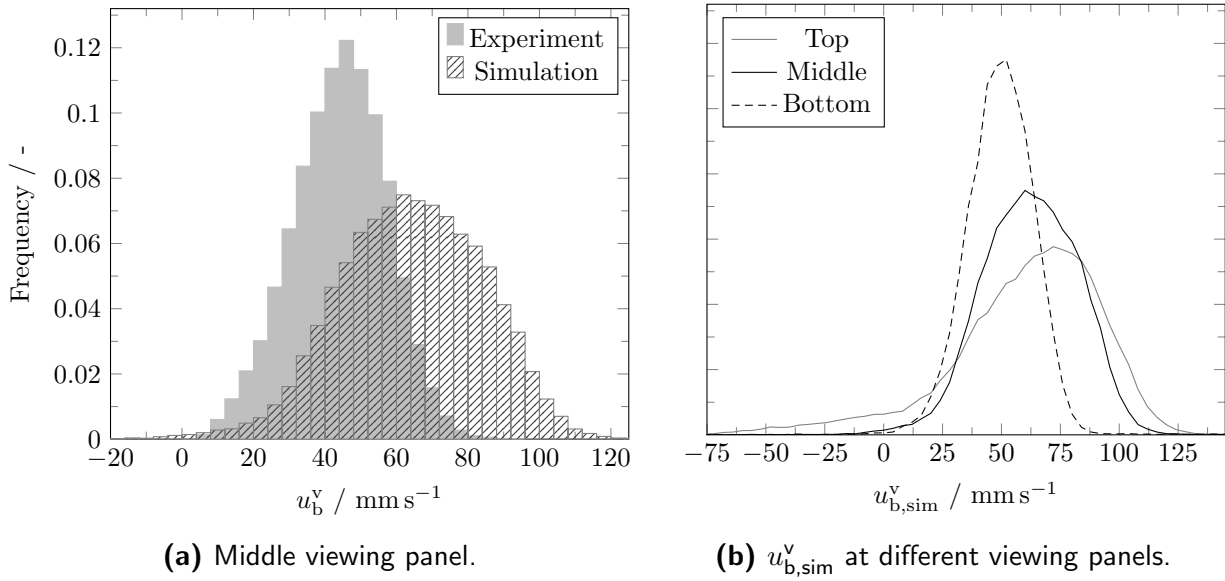
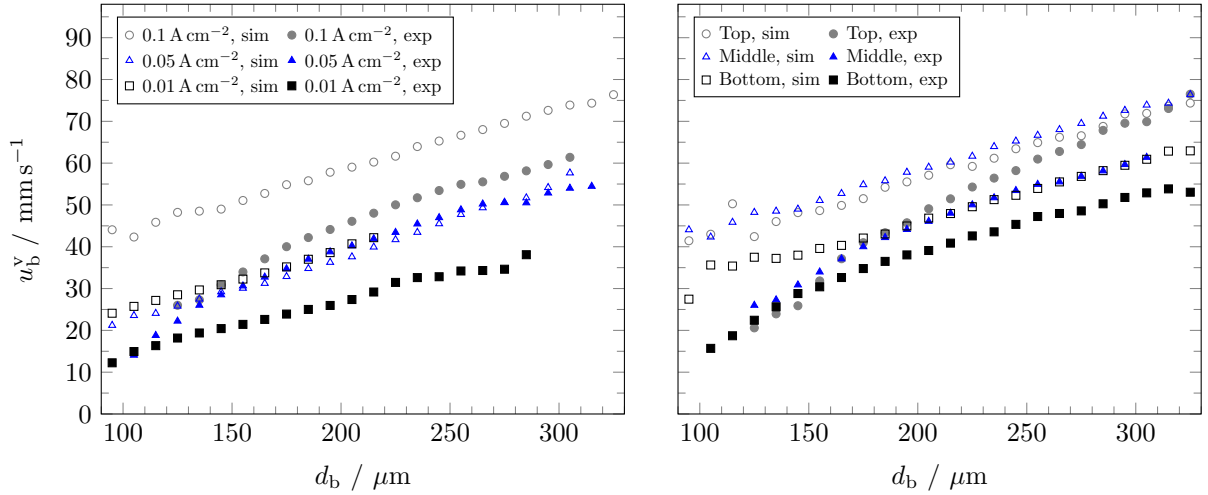


Figure 5.14.: (a) Distribution of simulated values for u_b^v and comparison with data from Görtz et al. [86] and (b) distribution of $u_{b,sim}^v$ at the three viewing panels at NNF conditions and $i=0.1 \text{ A cm}^{-2}$.

ing panels at $i=0.1 \text{ A cm}^{-2}$ (b). Comparing the simulation results for the three different current densities with experimental data from Görtz et al. [86], the middle current density of $i=0.05 \text{ A cm}^{-2}$ shows an excellent agreement over the whole range of bubble sizes. Under these operating conditions, the error is estimated to be 1.9 mm s^{-1} on average. Contrarily, the differences at $i=0.01$ and 0.1 A cm^{-2} between the experimental and numerical results are significantly larger and exhibit a constant offset of about 11.4 and 14.4 mm s^{-1} , respectively. The varying performance of the model can be explained by the difference in gas phase distribution in the computational domain displayed in Figure 5.13. At $i=0.05 \text{ A cm}^{-2}$, the gas phase is almost homogeneously dispersed along the width of the electrolyzer, resulting in generally low gas phase fractions. For the other two current densities, the bubble curtain formed at the electrode leads to greater gas phase fraction and acceleration of the electrolyte. The comparison suggests that the bubble velocity must be damped through, e.g., a swarm model. In addition, the bubble size distribution recorded by the LRHSC system could be overestimating the bubble size. This discrepancy between the two camera systems was already discussed in Section 3.2.6.

The course of $u_{b,sim}^v$ against d_b at $i=0.1 \text{ A cm}^{-2}$ and the three viewing panels also differs from $u_{b,exp}^v$. Whereas, the experimental data follows more a horizontal asymptote, the simulation result resembles a linear correlation between $u_{b,sim}^v$ and d_b . This trend leads to larger differences at lower bubble sizes. For the larger bubbles at the top viewing panel, the data shows good agreement. At the bottom and middle viewing panels, the offset between the simulation and experiments amounts to 9.2 and 13.7 mm s^{-1} , respectively.



(a) Comparison of different i at the middle viewing panel.

(b) Comparison of the different viewing panels at $i=0.1 \text{ A cm}^{-2}$.

Figure 5.15.: Comparison of simulated and experimentally measured values of u_b^v for $10 \mu\text{m}$ size bins at NNF, (a) the middle viewing panel and $i=0.01, 0.05$, and 0.1 A cm^{-2} and (b) at $i=0.1 \text{ A cm}^{-2}$ and all three viewing panels.

To examine the validity of the Euler-Lagrangian model, the simulated flow profile at NNF conditions is compared with the data obtained from the PIV measurement. However, as mentioned in sections 3.1.5 and 3.6.2, the comparison between the simulated vertical electrolyte velocity and 'mixed' vertical velocity is limited. Thus, the following will focus on (a) the width of the upward flow regime dz_I , (b) the value and position of maximal upward and downward velocity u_{\max}^v , u_{\min}^v , $z(u_{\max}^v)$, and $z(u_{\min}^v)$, (c) the ratio between maximal upward and minimal downward velocity $|u_{\max}^v (u_{\min}^v)^{-1}|$, and (d) the relative deviation of the experimentally and numerically determined positions of the flow regime width alongside the maxima and minima of the vertical velocity Δdz_I , $\Delta z(u_{\min}^v)$, and $\Delta z(u_{\max}^v)$. For a better discussion, the latter is also divided by $D_{E \rightarrow M}$ to relate it to the membrane-electrode gap. All determined experimental and simulated values for the nine different operating conditions are listed in Table 5.2.

Figure 5.16 displays the course of $\overline{u_{\text{el},\text{sim}}^v}^x$ and $\overline{u_{\text{m},\text{exp}}^v}^x$ against $D_{E \rightarrow M}$ at the bottom and top viewing panels at $i=0.1 \text{ A cm}^{-2}$ (a) and $i=0.01 \text{ A cm}^{-2}$ (b). At the bottom viewing panel, the PIV data and the simulation results reveal an increase in the maximum vertical velocity alongside a shift of the maxima position away from the electrode. In addition, the width of the upward flow regime also increases. At $i=0.1 \text{ A cm}^{-2}$, the experimental and simulation results quantify the increase of bubble curtain width to bet from 1.3 to 2.7 mm and 2.3 to 3.3 mm, respectively. Further, the relative difference between the experiments and simulation of the maxima and minima positions, $\Delta z(u_{\max}^v) D_{E \rightarrow M}^{-1}$ and $\Delta z(u_{\min}^v) D_{E \rightarrow M}^{-1}$ respectively amounts 5 %, 0 % at the bottom and 4 % and 14 % at the top viewing panel.

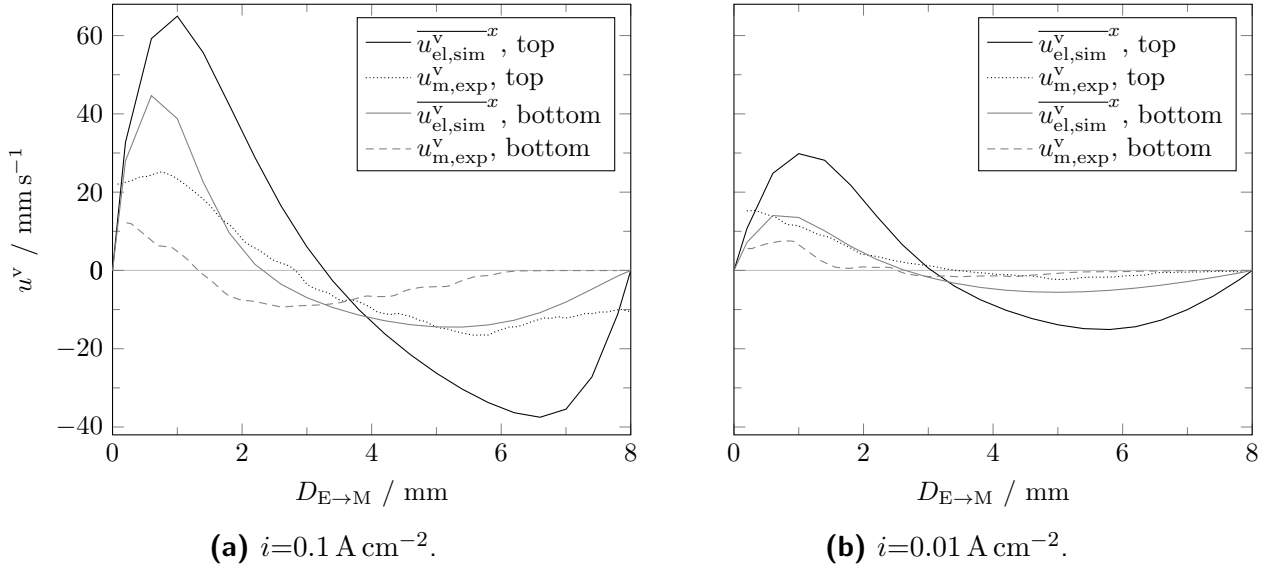


Figure 5.16.: Comparison of $\overline{u_{\text{el,sim}}^v}^x$ and $u_{\text{m,exp}}^v$ obtained by the PIV measurement at NNF conditions and either **(a)** $i=0.1 \text{ A cm}^{-2}$ or **(b)** $i=0.1 \text{ A cm}^{-2}$ in the partially transparent electrolyzer.

Whereas the comparison between $u_{\text{m,exp}}^v$ from experimental data and $u_{\text{el,sim}}^v$ from the simulation reveals larger discrepancies at the bottom panel, the data show excellent agreement at the top viewing panel for all three studied current densities: The average errors for the width of the upflow regime Δdz_1 , and minimum and maximum position, are 0.37, 0.6, and 0.6 mm. Further, the relation between the maximal and minimal velocity, $|u_{\text{max}}^v (u_{\text{min}}^v)^{-1}|$, is in the same order of magnitude. At $i=0.01$, 0.05, and 0.1 A cm^{-2} , the experimental and numerical values for $|u_{\text{max}}^v (u_{\text{min}}^v)^{-1}|$ amount 6.7 and 5.3, 2.4 and 1.6, 1.5 and 1.7, respectively. These results show that the position is within 1.5 times the z -distance of the computational grid.

In general, the measured values for $u_{\text{el,sim}}^v$ exceed the experimentally measured counterpart of $u_{\text{m,exp}}^v$. Besides uncertainties of the PIV algorithm and the simulation, this divergence also arises because the 'mixed' velocity is averaged over 1 s and relies heavily on present bubbles. As mentioned in Section 3.1.5, the illumination of the tracer particle is poor compared to that of the bubbles. However, the PIV measurements allow for a qualitative comparison and underline the validity and capability of the Euler-Lagrangian model for the gas-liquid flow inside the electrolyzer at NNF conditions.

5.2.2. Forced flow configuration

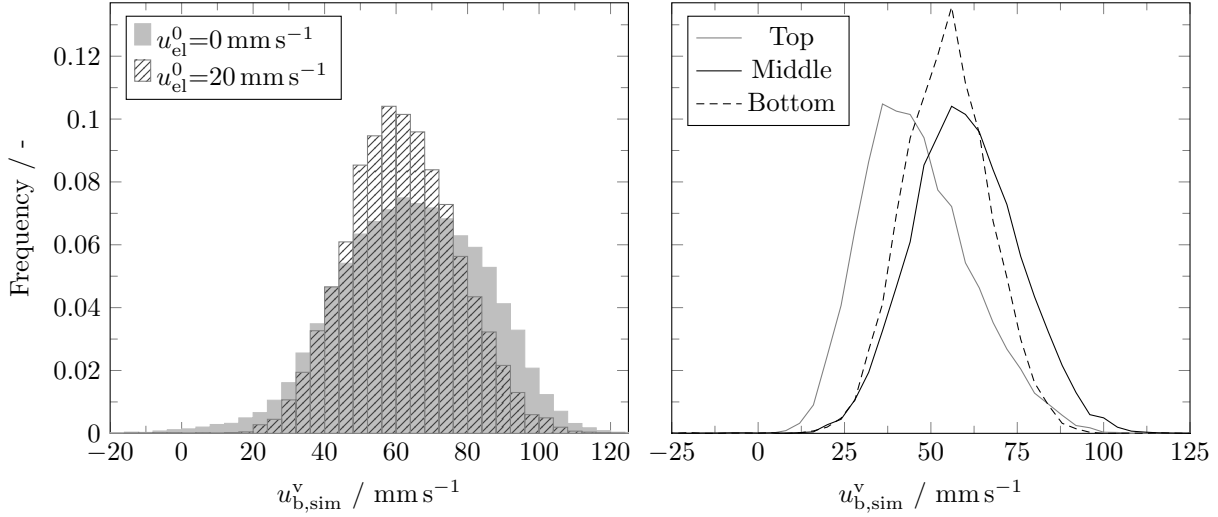
Finally, the evaluation of the Euler-Lagrangian model for the gas-liquid flow inside electrolyzers concludes with a presentation, discussion, and comparison of the simulation results for the FFC. To showcase the impact of the forced circulation on $u_{\text{b,sim}}^v$, Figure 5.17

Table 5.2.: Tabulation of key parameters dz_I , Δdz_I , u_{\max}^v , u_{\min}^v , $|u_{\max}^v (u_{\min}^v)^{-1}|$, $\Delta z(u_{\max}^v) (: D_{E \rightarrow M})$, $\Delta z(u_{\min}^v) (: D_{E \rightarrow M})$, $z(u_{\max}^v)$, and $z(u_{\min}^v)$ for the electrolyte flow at NNF conditions and $i=0.01, 0.05$, and 0.1 A cm^{-2} .

Variable	Unit	Viewing panel	Data					
i	(A cm^{-2})		0.01		0.05		0.1	
Data type	(-)		exp	sim	exp	sim	exp	sim
dz_I	(mm)	Bottom	2.5	2.6	1.7	2.5	1.3	2.3
$\Delta dz_I (: D_{E \rightarrow M})$	(mm)		0.1 (1%)		0.8 (10%)		1 (13%)	
u_{\max}^v	(mm s^{-1})		7.6	14	14	31	12.2	44.7
u_{\min}^v	(mm s^{-1})		-1.6	-15.1	-4.2	-15.4	-9.3	-14.8
$ u_{\max}^v (u_{\min}^v)^{-1} $	(-)		4.8	0.9	3.3	2.0	1.3	3.0
$z(u_{\max}^v)$	(mm)		0.9	0.6	0.2	1	0.2	0.6
$\Delta z(u_{\max}^v) (: D_{E \rightarrow M})$	(mm)		0.3 (4%)		0.8 (10%)		0.4 (5%)	
$z(u_{\min}^v)$	(mm)		2.5	5.8	4.4	5.4	5.4	5.4
$\Delta z(u_{\min}^v) (: D_{E \rightarrow M})$	(mm)		3.3 (41%)		1 (13%)		0 (0%)	
dz_I	(mm)	Middle	2.8		2.6		2.9	
$\Delta dz_I (: D_{E \rightarrow M})$	(mm)		-		-		-	
u_{\max}^v	(mm s^{-1})		23.3		23		62.6	
u_{\min}^v	(mm s^{-1})		-10.3		-17.5		-30.2	
$ u_{\max}^v (u_{\min}^v)^{-1} $	(-)		2.3		1.3		2.1	
$z(u_{\max}^v)$	(mm)		1		1.4		1	
$\Delta z(u_{\max}^v) (: D_{E \rightarrow M})$	(mm)		-		-		-	
$z(u_{\min}^v)$	(mm)		5.4		6.6		6.2	
$\Delta z(u_{\min}^v) (: D_{E \rightarrow M})$	(mm)		-		-		-	
dz_I	(mm)	Top	3.4	3	2.9	2.8	2.7	3.3
$\Delta dz_I (: D_{E \rightarrow M})$	(mm)		0.4 (5%)		0.1 (1%)		0.6 (8%)	
u_{\max}^v	(mm s^{-1})		15.3	29.8	25	17	25.2	65
u_{\min}^v	(mm s^{-1})		-2.3	-5.6	-10.5	-10.9	-16.5	-37.5
$ u_{\max}^v (u_{\min}^v)^{-1} $	(-)		6.7	5.3	2.4	1.6	1.5	1.7
$z(u_{\max}^v)$	(mm)		0.3	1	0.2	1	0.7	1
$\Delta z(u_{\max}^v) (: D_{E \rightarrow M})$	(mm)		0.7 (9%)		0.8 (10%)		0.3 (4%)	
$z(u_{\min}^v)$	(mm)		5.1	5	5.2	5.8	5.5	6.6
$\Delta z(u_{\min}^v) (: D_{E \rightarrow M})$	(mm)		0.1 (1%)		0.6 (8%)		1.1 (14%)	

(a) depicts the change in the distribution at $i=0.1 \text{ A cm}^{-2}$ and $u_{\text{el}}^0=0$ and 20 mm s^{-1} and the evolution of the distribution along the height of the electrolyzer (b). Comparing the distributions displayed in Figure 5.17 (a), the NNF condition results in a broader distribution $\varsigma(u_{\text{bv}})=20.0 \text{ mm s}^{-1}$ and slightly greater $\bar{u}_{\text{b, sim}}^v$ of 63.0 mm s^{-1} compared to FFC (16.2 and 63.0 mm s^{-1}). In addition, no bubbles with downward velocity are present at FFC since the forced upward flow of the electrolyte inhibits the formation of a downward flow

[86]. When comparing Figure 5.17(b) to Figure 5.14(b), the difference in flow pattern also becomes apparent: Whereas a steady increase in $\bar{u}_{b,\text{sim}}^v$ can be observed from bottom to top through the increase in α_g at NNF conditions, $\bar{u}_{b,\text{sim}}^v$ first increases from bottom to the middle before collapsing towards the exit of the electrolyzer. Through the constant addition of oxygen and forced flow of the electrolyte, the segregated flow breaks down towards a more homogeneously dispersed flow [86, 122].



(a) $u_{el}^0 = 0$ and 20 mm s^{-1} , middle viewing panel. (b) $u_{el}^0 = 20 \text{ mm s}^{-1}$ at different viewing panels.

Figure 5.17.: Comparison of (a) the distribution of $u_{b,\text{sim}}^v$ at $u_{el}^0 = 0$ and 20 mm s^{-1} and the middle viewing panel and $i = 0.1 \text{ A cm}^{-2}$ and (b) at different viewing panels for $u_{el}^0 = 20 \text{ mm s}^{-1}$ and $i = 0.1 \text{ A cm}^{-2}$.

Figure 5.18 presents the simulated flow fields and distribution of gas phase fraction at $i = 0.1 \text{ A cm}^{-2}$ for $u_{el}^0 = 0, 10$, and 20 mm s^{-1} and highlights the change in the flow pattern. Whilst a segregated flow and intact bubble curtain are present at $u_{el}^0 = 0 \text{ mm s}^{-1}$ in Figure 5.18 (a) and (d), the forced flow leads to a more equally distributed gas phase fraction. As a consequence of this more homogeneous gas phase fraction, the electrolyte flow also becomes uniform. However, the height at which the flow is homogeneous is subject to u_{el}^0 . As the electrolyte is introduced at $D_{E \rightarrow M} = 0 \text{ mm}$, it is redirected from the opposing wall. Through the gas evolution at the electrode, the electrolyte flows towards this region close to the electrode, where the electrolyte is accelerated due to buoyancy. Afterwards, the flow requires an additional distance before homogenization. At $u_{el}^0 = 10 \text{ mm s}^{-1}$, the height at which the flow is homogeneous along $D_{E \rightarrow M}$ is at 80 mm . Further increasing u_{el}^0 to 20 mm s^{-1} also enlarges this distance to 125 mm . The phase fraction fields in Figure 5.18(e) and (f) emphasize the connection between the electrolyte flow and α_g since a homogeneous flow requires a prior homogenization of the distribution of α_g . Furthermore, all three flow fields also affirm the existence of significant back-mixing in the regions where

the segregated two-regime flows are present. For $u_{\text{el}}^0=0, 10$, and 20 mm s^{-1} , these regions are roughly within heights of 30 to 160 mm, 50 to 70 mm, and 70 to 110 mm, respectively.

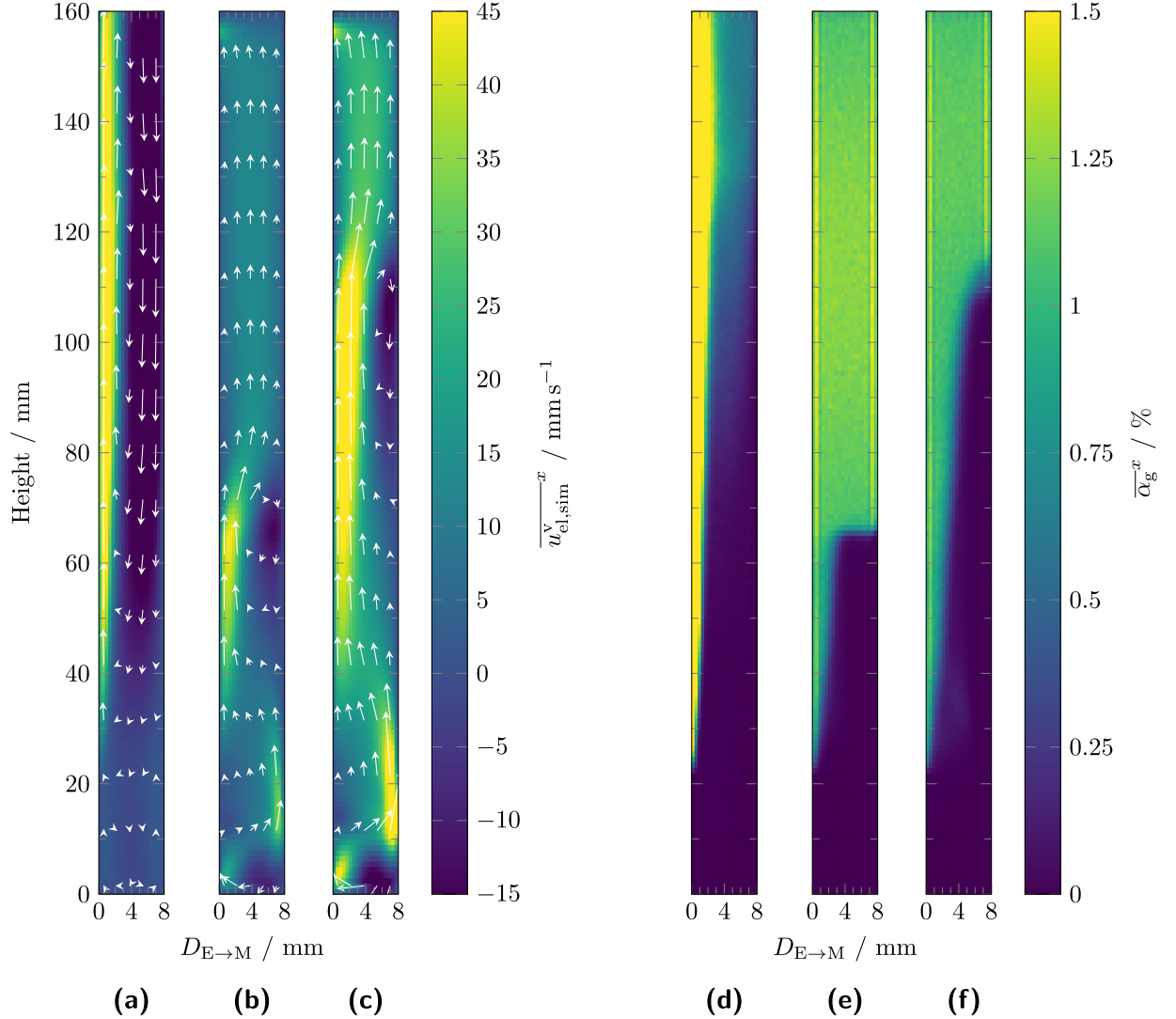


Figure 5.18.: Simulated x -averaged vertical velocity at $i=0.1 \text{ A cm}^{-2}$ and **(a)** $u_{\text{el}}^0=0$, **(b)** 10, and **(c)** 20 mm s^{-1} and gas phase fraction fields at **(d)** $u_{\text{el}}^0=0$, **(e)** 10, and **(f)** 20 mm s^{-1} in the partially transparent electrolyzer.

Furthermore, Figure 5.19 displays the impact of the different flow regimes on $\overline{u_{\text{el,sim}}^v}^x$ at $i=0.1 \text{ A cm}^{-2}$ and $u_{\text{el}}^0=20 \text{ mm s}^{-1}$. At the bottom viewing panel that is located X mm above the inlet, the electrolyte flows upward over the whole length of $D_{\text{E} \rightarrow \text{M}}$. Upon closer inspection; two segments can be identified: Close to the electrode, between $D_{\text{E} \rightarrow \text{M}}=0$ and 3 mm, the electrolyte is accelerated due to buoyancy and afterwards, the electrolyte pumped into the electrolyzer leads to positive values of $\overline{u_{\text{el,sim}}^v}^x$. At the middle viewing panel, the maximum of $\overline{u_{\text{el,sim}}^v}^x$ shifts towards the center of the channel and increases by 18 mm s^{-1} . Further, the flow profile trends towards the typical two-regime scheme, also reported in the previous Section 5.2.1 for NNF conditions, reveal a small backflow region

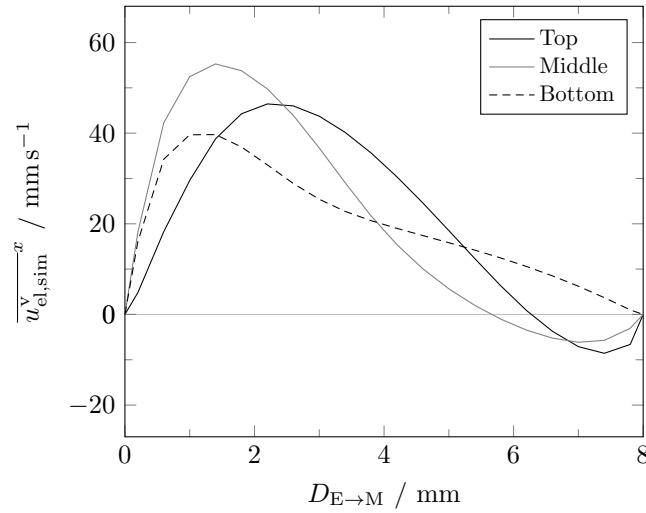


Figure 5.19.: Evolution of $\overline{u_{el,sim}^v}^x$ from the bottom to the top viewing panel at $i=0.1 \text{ A cm}^{-2}$ and $u_{el}^0=20 \text{ mm s}^{-1}$.

close to the membrane. This trend of the position of the maximum of $\overline{u_{el,sim}^v}^x$ shifting towards the center continues at the top viewing panel. Here, the backflow regime is smaller than 2 mm, and the flow profile gravitates toward a plug flow that is ultimately reached at a height of 130 mm (see Figure 5.18(c)).

Next, the observed flow profiles at the bottom and top viewing panels are compared to the corresponding values for $u_{m,exp}^v$ obtained by the PIV measurement from Section 3.6.2). Figure 5.20 compares $u_{el}^0=20 \text{ mm s}^{-1}$ with $i=0.01$ (a) and 0.1 A cm^{-2} (b). At $i=0.1 \text{ A cm}^{-2}$ and the bottom panel, the PIV measurement shows good accordance with the simulation results. However, the PIV measurement reports $u_{m,exp}^v=0 \text{ mm s}^{-1}$ close to the membrane at the two viewing panels, which contradicts the results from the simulation. Nevertheless, the discrepancy most likely arises from the poor illumination of the region close to the membrane. Nonetheless, the PIV measurement also reports a small backward flow at the top at $D_{E \rightarrow M}=7 \text{ mm}$. For the lower current density of 0.01 A cm^{-2} , the experimental flow profiles do not match the ones obtained by the simulation. Solely, the absence of the backflow regime is reported by both methods. The difficulty of carrying out suitable PIV measurement inside electrolyzers that has already been discussed by Hreiz et al. [94] and becomes apparent here: Since u_{el}^0 equals 20 mm s^{-1} , the average of $u_{m,exp}^v$ should ideally equal that value. However, the experimental data in Figure 5.20(b) does not reflect this closure condition.

Besides the electrolyte flow profile, the FC condition also impacts u_b^v , and Figure 5.21 depicts $\overline{u_b^v}$ at the middle (a) and top viewing panel (b) for different operating conditions. At the middle viewing panel displayed in Figure 5.21 (a), $\overline{u_b^v}$ remains constant for $i=0.01 \text{ A cm}^{-2}$ and only reveals a small impact of u_{el}^0 on $u_{b,sim}^v$ at $i=0.1 \text{ A cm}^{-2}$. Instead of the superposition of u_b^v and u_{el}^0 , $\overline{u_{b,sim}^v}$ of bubbles with $d_b < 250 \mu\text{m}$ decreases

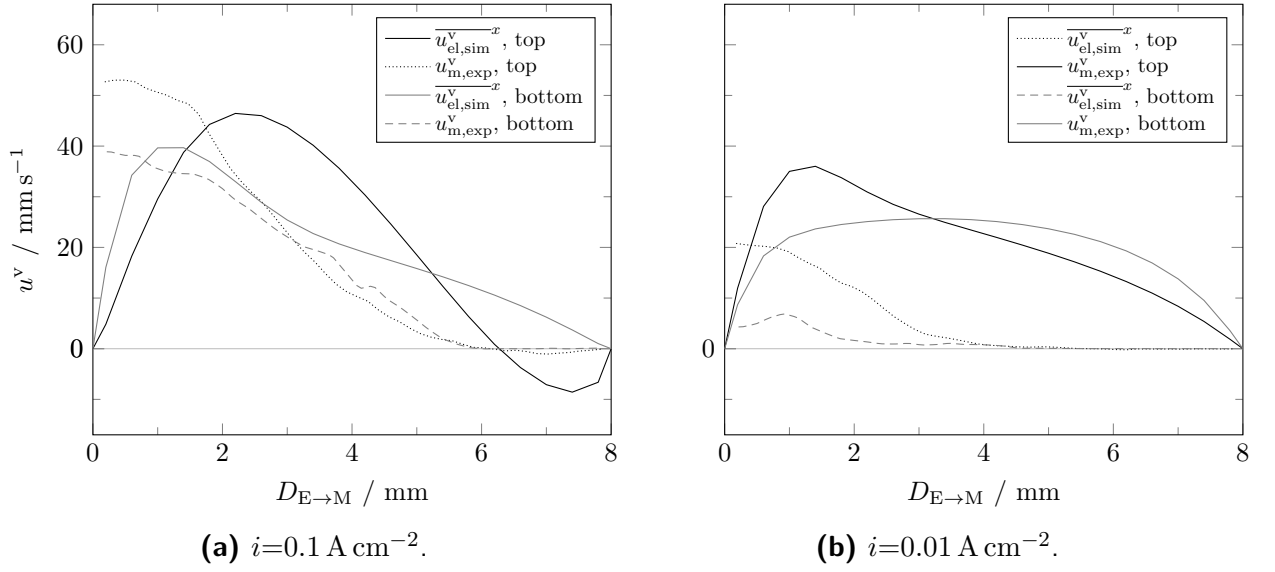


Figure 5.20.: Comparison of $\overline{u_{\text{el,sim}}^x}$ and $u_{\text{m,exp}}^v$ obtained by the PIV measurement at $u_{\text{el}}^0 = 20 \text{ mm s}^{-1}$ and either **(a)** $i = 0.1 \text{ A cm}^{-2}$ or **(b)** $i = 0.01 \text{ A cm}^{-2}$ in the partially transparent electrolyzer.

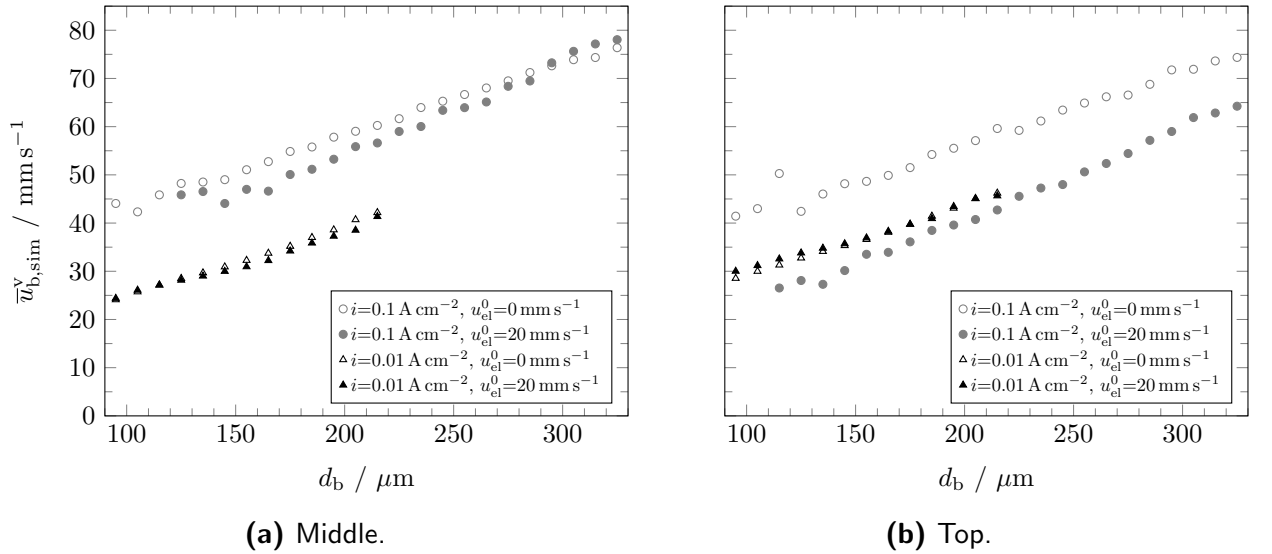


Figure 5.21.: Comparison of simulated values of $u_{b,\text{sim}}^v$ for $10 \mu\text{m}$ size bins at FC ($u_{\text{el}}^0 = 20 \text{ mm s}^{-1}$) and NNF conditions at the **(a)** middle and **(b)** top viewing panel and $i = 0.01$, and 0.1 A cm^{-2} .

at $i = 0.1 \text{ A cm}^{-2}$ and $u_{\text{el}}^0 = 20 \text{ mm s}^{-1}$ compared to NNF conditions. At the top viewing panel, the change in the flow pattern and the homogenization of the gas phase fraction (see Figure 5.18(c,f)) leads to a substantially slower rising velocity of the gas bubbles at $i = 0.1 \text{ A cm}^{-2}$. This offset is more or less constant over the whole range of d_b and amounts, on average, 12.1 mm s^{-1} . This decrease in $\overline{u_{b,\text{sim}}^v}$ at $u_{\text{el}}^0 = 20 \text{ mm s}^{-1}$ highlights the dependence of the bubble velocity on the present flow pattern within the electrolyzer.

To compare the simulation results with the data from the PTV measurements, Fig-

ure 5.22 presents the simulated and experimentally measured values for \bar{u}_b^v of bubbles with sizes between $220 \leq d_b \leq 230 \mu\text{m}$. Despite $\bar{u}_{b,\text{sim}}^v$ exceeding the values of $\bar{u}_{b,\text{exp}}^v$ by an offset of 12 mm, both methods reveal a similar trend of \bar{u}_b^v against u_{el}^0 . At $i=0.01 \text{ A cm}^{-2}$, the

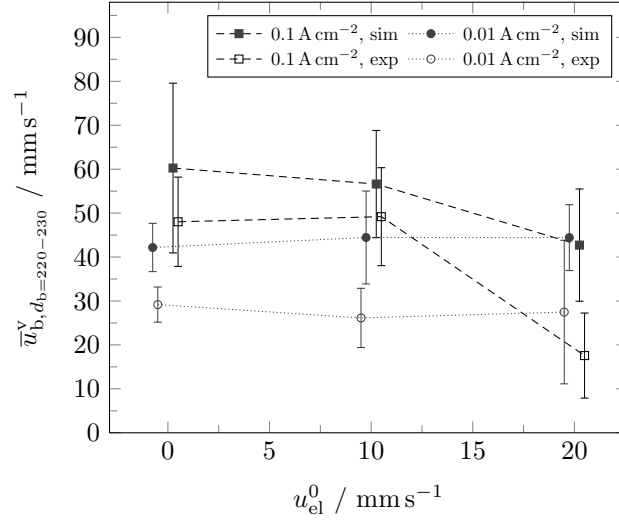


Figure 5.22.: Comparison of simulated and experimentally measured [86] values for \bar{u}_b^v of bubbles with sizes between 220-230 μm in the top viewing panel at $i=0.01$, and 0.1 A cm^{-2} and $u_{\text{el}}^0=0$, 10, and 20 mm s^{-1} .

impact of u_{el}^0 on \bar{u}_b^v is only marginal as $\bar{\alpha}_g$ is generally low, and the forced flow does not impact the flow pattern and spatial bubble distribution. In contrast, Figure 5.18 shows the break up of the segregated flow with the increase of u_{el}^0 at $i=0.1 \text{ A cm}^{-2}$. This breakup of the segregated flow and bubble curtain widening distributes the buoyancy force of the gas volume over a greater cross-section. As a consequence, the homogeneous distribution causes a reduction of u_{el}^v within the DOF of the viewing panel and, ultimately, decreases of \bar{u}_b^v . At $u_{\text{el}}^0=20 \text{ mm s}^{-1}$, this phenomenon becomes apparent as the simulated and experimentally measured vertical bubble velocity at $i=0.1 \text{ A cm}^{-2}$ collapses towards the values obtained at $i=0.01 \text{ A cm}^{-2}$. This conformity of observed effects in both experimental measurements and simulation results showcases the capability of the Euler-Lagrangian model for the gas-liquid flow within electrolyzers.

5.3. Summary of model evaluation

Chapter 5 presented a sensitivity analysis and evaluation of the implemented Euler-Lagrangian Model for the simulation of the gas-liquid flows within electrolyzers derived in Chapter 4. First, this chapter systematically examines how different simulation parameters and averaging methods affect the model outcomes. An averaging period of 10 s was found to be sufficient to minimize the time deviation of the results introduced by the

transient simulation. In addition, plane-based plotting of the electrolyte velocity is preferred over line-based due to reduced variance in capturing backflow effects. Different mesh sizes Δz between the anode and membrane are analyzed, showing quasi-grid independence except at larger mesh sizes, which affected the mean bubble velocities and only slightly reducing computational costs. Therefore, the smallest mesh size of $\Delta z=0.4\text{ mm}$ is chosen for further simulations to enhance the spatial resolution of the concentration gradients of the latter simulations. Further, the simulation results with four-way coupling show superior prediction of bubble curtain spread compared to two-way coupling. By incorporating bubble-bubble and bubble-wall collisions, the Euler-Lagrangian model is able to predict key aspects of the experimentally measured gas-liquid flow presented in Chapter 3. The necessity of depicting the collision was further underlined when varying n_p . The results demonstrated that aggregating multiple bubbles into one Lagrangian parcel impairs the performance of the model. Out of the two different groups of drag models, the fluid-sphere model by Lain et al. [143] was selected due to its closer alignment with experimental data across the three viewing panels.

Simulating the partially-transparent electrolyzer with the selected simulation parameters at NNF conditions revealed the influence of i on the flow regimes at $i=0.01, 0.05$, and 0.1 A cm^{-2} . Through the generation of larger bubbles and gas volumes at higher currents, the buoyancy-induced acceleration close to the electrode increases, and more liquid is displaced, creating segregated flow regions within the electrolyzer. Comparisons with experimental data from the PIV and PTV measurement suggest a slight overestimation in simulated bubble velocities. However, the model predicted the width of the upward regime well with an average deviation of 6.3%. The simulation results with FCC highlight the forced circulation's impact on the gas-liquid flow patterns: By suppressing the backflow of the electrolyte, the gas phase distribution is homogenized, and the vertical electrolyte velocities are altered compared to NNF conditions. Despite small discrepancies, both simulations and experiments reflect similar trends under forced flow conditions, validating the Euler-Lagrangian approach and showcasing its capability to model electrolyzer dynamics accurately for the studied operating conditions and electrolyzer design.

6. Study of the gas-liquid-solid flow inside a novel electrochemical crystallizer

This chapter demonstrates the application of the Euler-Lagrangian model presented and discussed in the two previous chapters to a model-based study of a novel prototype for electrochemical crystallization. Therefore, the previously published prototypes by Kocks [17, 172] are studied for different operating conditions according to section 4.5.4. First, section 6.1 displays the resulting gas-liquid flow inside the prototypes alongside experimentally measured [172] and simulated residence time distributions of the electrolyte. Next, section 6.2 introduces the algorithm and results of a CNN-based method for the determination of the RTD of the crystal phase. In closing, section 6.3 showcases the calculated local pH distribution alongside the supersaturation profiles for the prototype with $D_{E \rightarrow M}=8$ mm. Here, the linkages between the fluid flow, gas phase fraction, and pH gradients are discussed.

6.1. Gas-liquid flow inside a novel prototype for the electrochemical crystallization

This section presents the impact of different operating conditions, i and u_{el}^0 , on the gas-liquid flow and distribution of the gas phase inside the novel electrochemical crystallizer. Thereafter, the influence of the electrode-membrane gap on the flow pattern is illustrated and discussed. For this purpose, the flow and gas phase fraction fields are averaged over the x and z coordinates. Due to the variable xz cross area along the height of the prototype, u_{el}^0 also changes with respect to y inside the prototype, and, hence, \dot{V}_{el} will be used in the following.

The medium-sized prototype ($D_{E \rightarrow M}=8$ mm) is chosen along with $i=0.1$ A cm⁻² and $\dot{V}_{el,in}=0.5$ L min⁻¹ as the base case. Figure 6.1 illustrates the scaled vertical volume flow and flow direction in the xy (a) and zy -plane (b) at those conditions. The electrolyte is introduced at the inlet at the bottom, resulting in $\overline{\phi}_{el}^{vz}$ and $\overline{\phi}_{el}^{vx}$ of 25 mL min⁻¹ and 70 mL min⁻¹, respectively. The differences arise from the different inlet dimensions in x

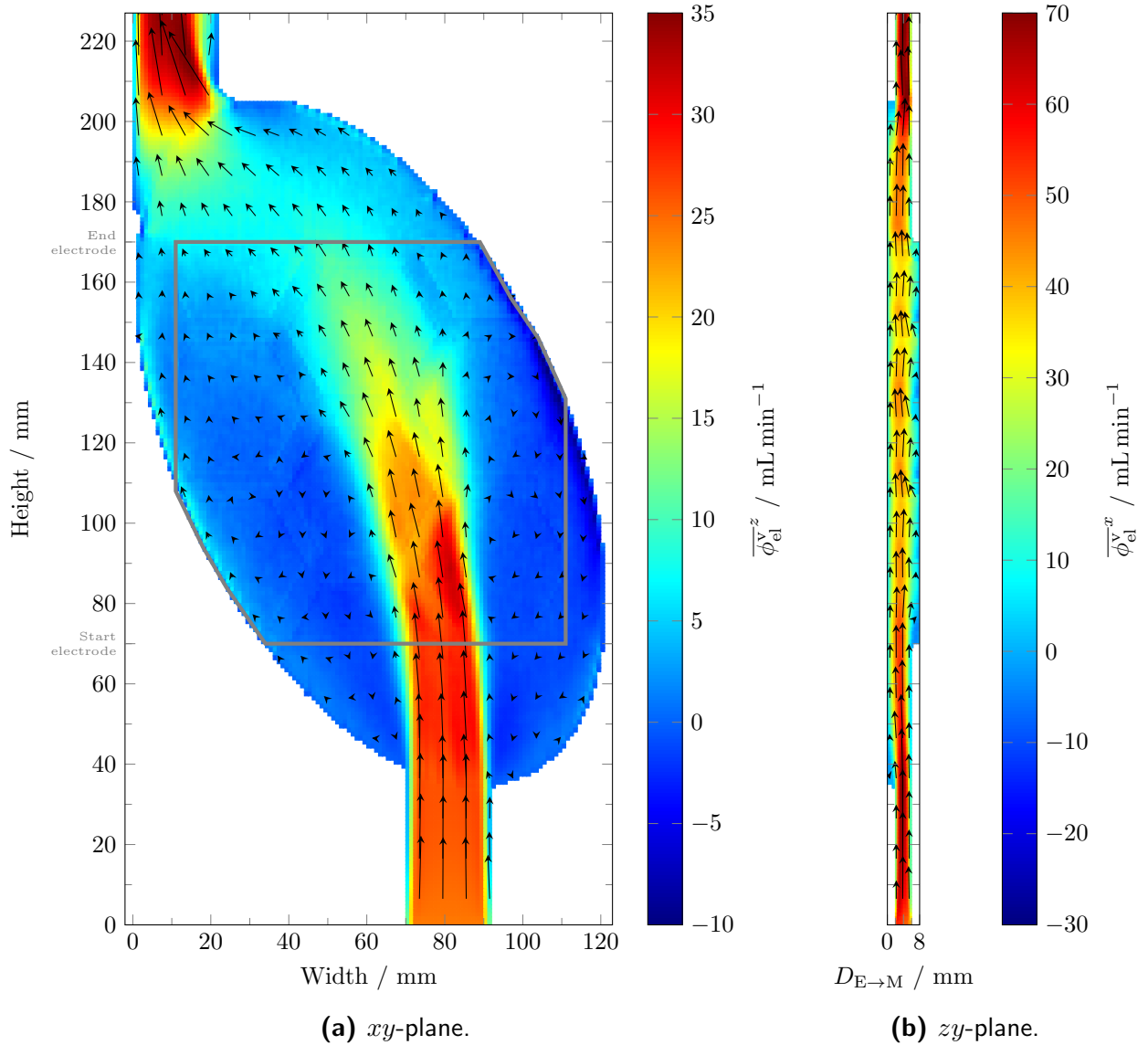


Figure 6.1.: $\overline{\phi_{el}^v}$, and direction of flow in the $D_{E \rightarrow M}=8 \text{ mm}$ prototype at $i=0.1 \text{ A cm}^{-2}$ and $\dot{V}_{el,in}=0.5 \text{ L min}^{-1}$ in the *xy* (a) and *yz*-plane (b).

(18 mm) and z (4 mm) direction used for calculating of ϕ_{el}^v . In the *xy*-plane displayed in Figure 6.1 (a), the limitation of the deficiencies of the prototype becomes apparent: Since no flow baffles are present, the momentum of the inflowing - electrolyte is not distributed over the width of the electrolyte - instead, a narrow channel forms at the lower section of the prototype. In addition, the flow channel induces a recirculation of the electrolyte on both sides of the flow channel between heights of 40 and 70 mm. As soon as the main flow enters the gas-evolving region by the active electrode, the buoyancy force of the electrogenerated bubbles widens and homogenizes the flow. However, the flow distribution requires the whole length of the electrode. At the top, the flow is forced towards the outlet, where it exits the computational domain at higher velocities than at the inlet. This discrepancy

arises from the introduced gas volume and its momentum. The zy -plane in Figure 6.1(b) depicts the flow field between electrode and membrane, almost resembling a plug flow. Merely, the honeycomb structured membrane holder introduces velocity fluctuations in the z -direction. By design, small dead zones form above and below the electrode.

6.1.1. Impact of superficial electrolyte velocity

To study the impact of $\dot{V}_{\text{el, in}}$ on the gas-liquid flow, Figure 6.2 presents the time and x -averaged vertical volume flow and α_g profiles of the 8 mm prototype at $i=0.1 \text{ A cm}^{-2}$ and $\dot{V}_{\text{el, in}}=0.05 \text{ L min}^{-1}$ (a,c), and 0.5 L min^{-1} (b,d). Since the smaller electrolyte inlet flow rate

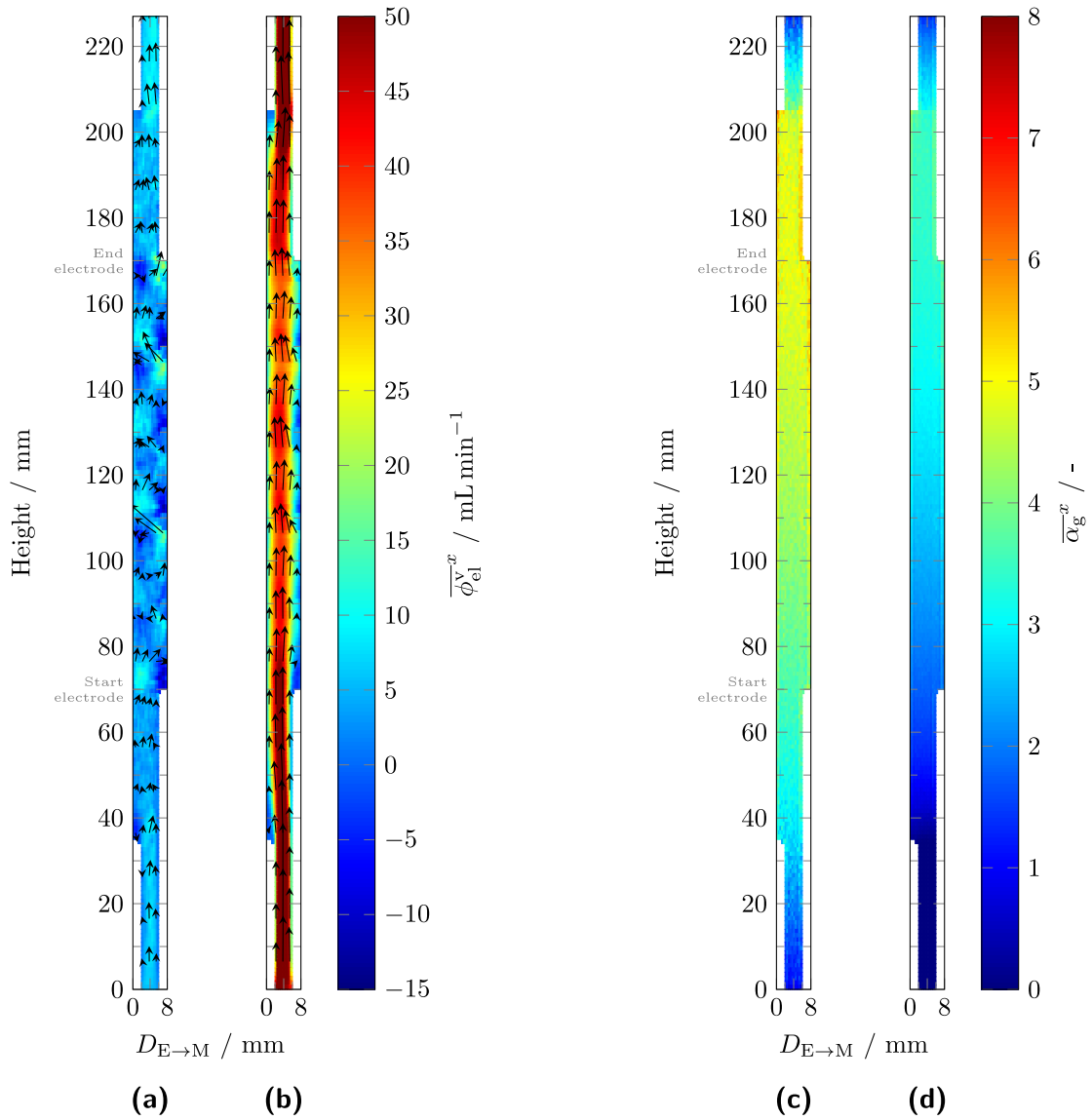


Figure 6.2.: $\overline{\phi_{\text{nel}}^v}$ and direction of flow at (a) $\dot{V}_{\text{el, in}}=0.05$ and (b) 0.5 L min^{-1} along with the distributions of $\overline{\alpha_g}$ at (c) $\dot{V}_{\text{el, in}}=0.05$ and (d) 0.5 L min^{-1} in the $D_{E \rightarrow M}=8 \text{ mm}$ prototype at $i=0.1 \text{ A cm}^{-2}$ in the yz -plane.

of $\dot{V}_{\text{el, in}}=0.05 \text{ L min}^{-1}$ results in smaller vertical electrolyte velocities inside the anode chamber, the effect of the inserted momentum of oxygen bubbles on the flow field in Figure 6.2 (a) is more pronounced compared to the corresponding flow field for $\dot{V}_{\text{el, in}}=0.5 \text{ L min}^{-1}$ (b). The combination of buoyancy forces close to the electrode and the circulations induced by the almost 2 mm thick honeycomb membrane support structure prevents the formation of an straight upward flow. Ultimately, this effect and the smaller vertical velocity results in an average gas phase fraction of 4.2 % inside the anode chamber. The average gas phase fraction of the entire simulation domain almost doubles the corresponding value of 2.6 % obtained for $\dot{V}_{\text{el, in}}=0.5 \text{ L min}^{-1}$. A similar trend can be observed for the 6 mm prototype with $\bar{\alpha}_{\text{g}}$ equaling 5.8 and 3.4 %, respectively. Due to the broader cross-section, the 10 mm prototype behaves differently and exhibits only a small deviation of $\bar{\alpha}_{\text{g}}$ between 7.5 % at $\dot{V}_{\text{el, in}}=0.05 \text{ L min}^{-1}$ and 6.8 % at 0.5 L min^{-1} . According to Bruggeman's law [79], the discrepancy in $\bar{\alpha}_{\text{g}}$ between the 8 and 10 mm prototypes lead to a reduction of the mixed conductivity τ_{m} of 4 % and 12 %, highlighting the impact of the gas phase distribution of different prototypes on the power consumption. All the flow fields in the xy and zy plane for the three prototypes and studied operating conditions are depicted in the appendix.

6.1.2. Impact of current density

Next, Figure 6.3 displays the effect of different current densities of $i=0, 0.01$, and 0.1 A cm^{-2} on $\overline{V_{\text{el, sim}}^z}$ and the flow profile (a,b,c) and the averaged gas phase fraction (e,f) in the zy -plane inside the 8 mm prototype at a constant $\dot{V}_{\text{el, in}}=0.5 \text{ L min}^{-1}$. Without bubble evolution ($i=0 \text{ A cm}^{-2}$, (a)), the flow resembles a plug flow with slight deviation at the membrane holder, end of the inlet, and the start of the outlet. The maximum flow velocity is within the center ($D_{\text{E} \rightarrow \text{M}}=3.8 \text{ mm}$) of the domain. Through the evolution of bubbles at the electrode, a current density as low as 0.01 A cm^{-2} already changes the flow pattern in the zy -plane shown in Figure 6.3 (b). After entering the domain centered through the inlet, the electrolyte flows upward until it reaches the start of the electrode at a height of 70 mm. The maximum upward flow trends towards the electrode over the entire length along which the electrolyte passes the electrode, and $\dot{V}_{\text{el, sim}}$ increases along the height. Opposed to the electrode, a backward or stagnant flow regime forms close to the membrane. This two-regime flow is similar to the NNF conditions in section 5.2.1 and the findings of Alexiadis et al. [104]. Similar to the results for the NNF condition, the areas of great vertical velocities are congruent with those of high gas phase fraction (see Figure 6.3(d)). Further increasing i to 0.1 A cm^{-2} leads to a breakup of the segregated flow and a homogeneously distributed gas phase fraction depicted in Figure 6.3(c) and (e). As a result, the maximum of $\overline{u_{\text{el, sim}}^x}$ decreases and shifts towards the center of the channel. Examining the average gas phase fraction over the entire simulation domain, a tenfold increase of i leads to a

15-time increase of $\bar{\alpha}_g$ from 0.17 % at $i=0.01 \text{ A cm}^{-2}$ to 2.6 % at 0.1 A cm^{-2} . This non-linear behavior is despite of $\bar{d}_{3,b}$ of the electrogenerated oxygen bubbles at $i=0.1 \text{ A cm}^{-2}$ exceeding the corresponding value at $i=0.01 \text{ A cm}^{-2}$ by 68 % (see section 3.2.2). Typically, smaller values for d_b decrease the rising velocity, leading to larger residence times of the bubbles in the electrolyte and, hence, larger gas phase fractions. This discrepancy also matches the experimental findings of the PTV measurements and simulation results of the partially transparent electrolyzer in sections 3.4.4 and 5.2, respectively.

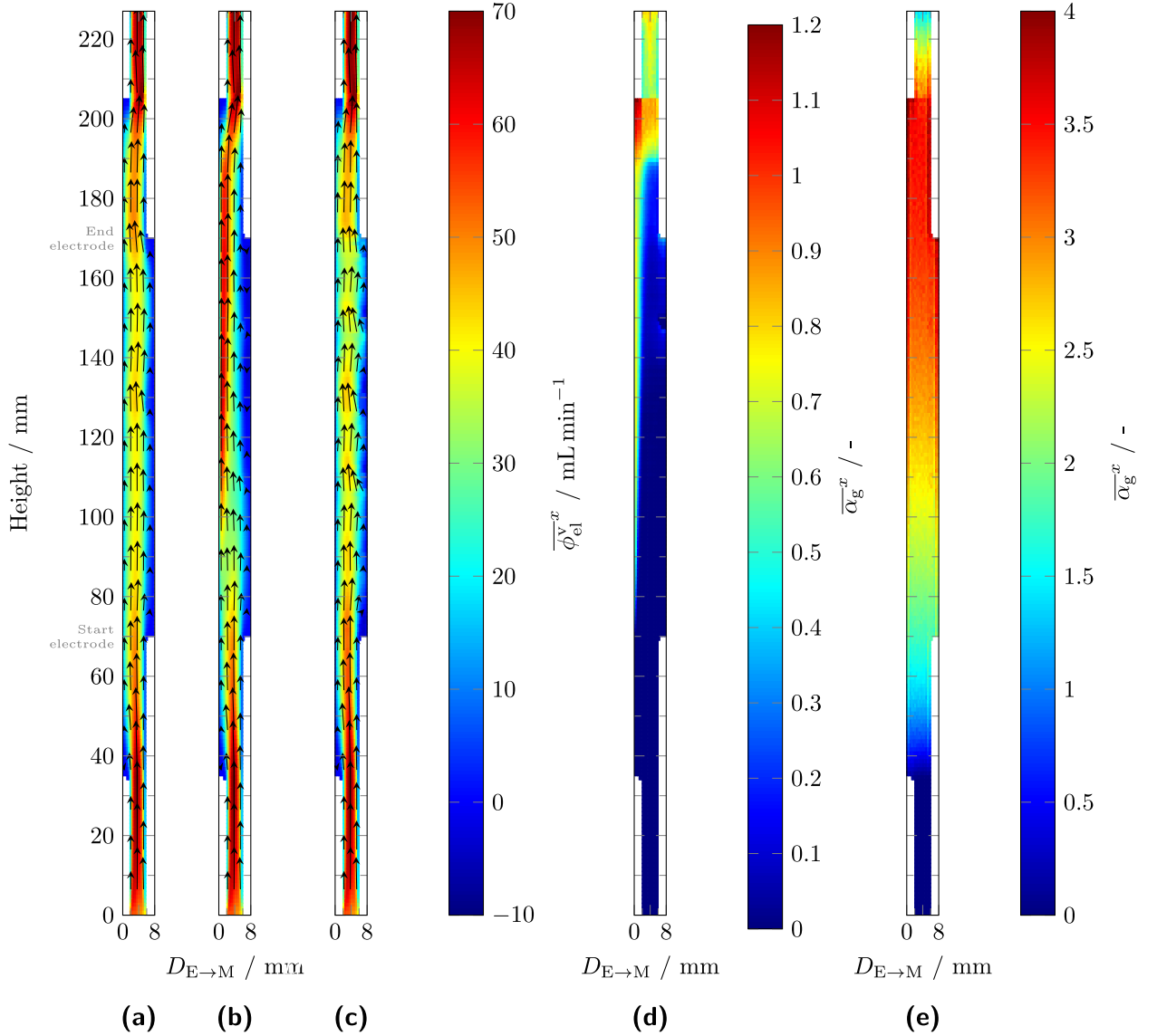


Figure 6.3.: $\overline{\phi_{el}^v}^z$ and direction of flow at $i=(\text{a}) 0$, $(\text{b}) 0.01$, and $(\text{c}) 0.1 \text{ A cm}^{-2}$ along with the distributions of $\bar{\alpha}_g^x$ at $(\text{d}) i=0.01$ and $(\text{e}) 0.1 \text{ A cm}^{-2}$ in the $D_{E \rightarrow M}=8 \text{ mm}$ prototype at $\dot{V}_{el,in}=0.5 \text{ L min}^{-1}$ in the yz -plane.

To better depict the vertical velocity instead of the volumetric flow, Figure 6.4 plots $\overline{u_{el,sim}^v}^x$ against $D_{E \rightarrow M}$ for $i=0.01, 0.1$, and 0.2 A cm^{-2} at a height of 133 mm. The lowest current density of 0.01 A cm^{-2} features a different flow pattern than the higher current

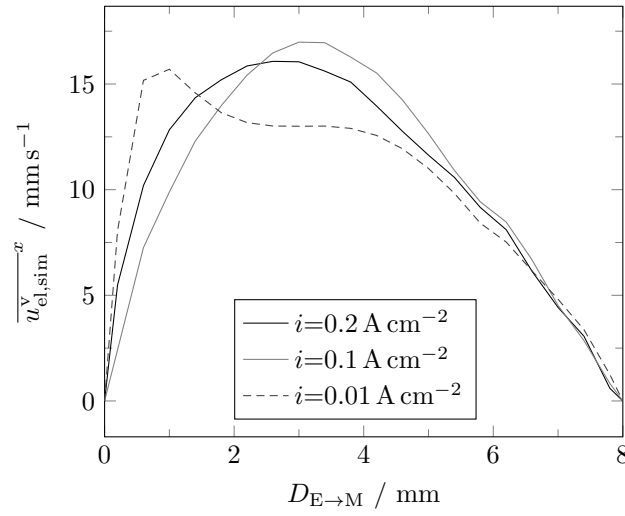


Figure 6.4.: x -averaged vertical velocity at different current densities at a height of 133 mm.

densities of 0.1 and 0.2 A cm⁻². Whereas only minor changes exist between the two higher current densities, the smallest current density deviates from them, exhibiting a maximum close to the electrode at $D_{E→M}=1$ mm. This maximum of $\overline{u_{el,sim}^v}^x=15.4$ mm s⁻¹ is within the range of the corresponding values for the higher current densities. These reported differences in the maximum with respect to the current density are despite the fact that only 10 or 5 % of the gas volume is produced at the electrode at $i=0.01$ A cm⁻².

6.1.3. Impact of electrode-membrane gap

For the design of electrolyzers, the electrode-membrane gap plays a crucial role as it drastically influences the voltage. However, $D_{E→M}$ also heavily impacts the fluid dynamic inside the electrolyte chamber. To prevent the blockage with particles, Kocks [172] chose $D_{E→M}$ of 6, 8, and 10 mm. Figure 6.5 depicts the respective flow fields (a-c) and gas phase fractions (d-f) in the zy plane within the 6, 8, and 10 mm prototypes. With the increasing cross-section, the x -averaged vertical volume flow increases from a maximum of about 70 mL min⁻¹ at $D_{E→M}=6$ mm to circa 40-50 and finally 30 mL min⁻¹ for the $D_{E→M}=8$ and 10 mm prototypes, respectively. Further, with increasing $D_{E→M}$, the center of the upward flow shifts away from the electrode towards the center of the respective channel. Simultaneously, the velocity fluctuations in the z direction decrease from a standard deviation across all cells of the computational domain of 4.8 to 3.1 mm s⁻¹ before more than doubling to 8.7 mm s⁻¹ in the 6, 8, and 10 mm prototypes, respectively. This change in the fluctuation of the z -velocity proceeds in the same way as the average gas phase fraction in the simulation domain. $\overline{\alpha_g}^x$ is depicted in Figure 6.5 (d-e) and $\overline{\alpha_g}$ of the whole domain respectively amounts 3.4, 2.6, and 6.8 %. Weighting these values with the different volumes of the prototypes, gas volumes of 3.2, 2.8, and 9.1 mL are obtained, highlighting the

increased amount of present oxygen gas in the 10 mm prototype.

To further analyze the different gas phase fractions, Figure 6.6 presents $\overline{u_{\text{el},\text{sim}}^x}$ (a) and $\overline{\alpha_g^x}$ (b) at a height of 130 mm across $D_{\text{E} \rightarrow \text{M}}$ of the 6, 8, and 10 mm prototypes. Examining

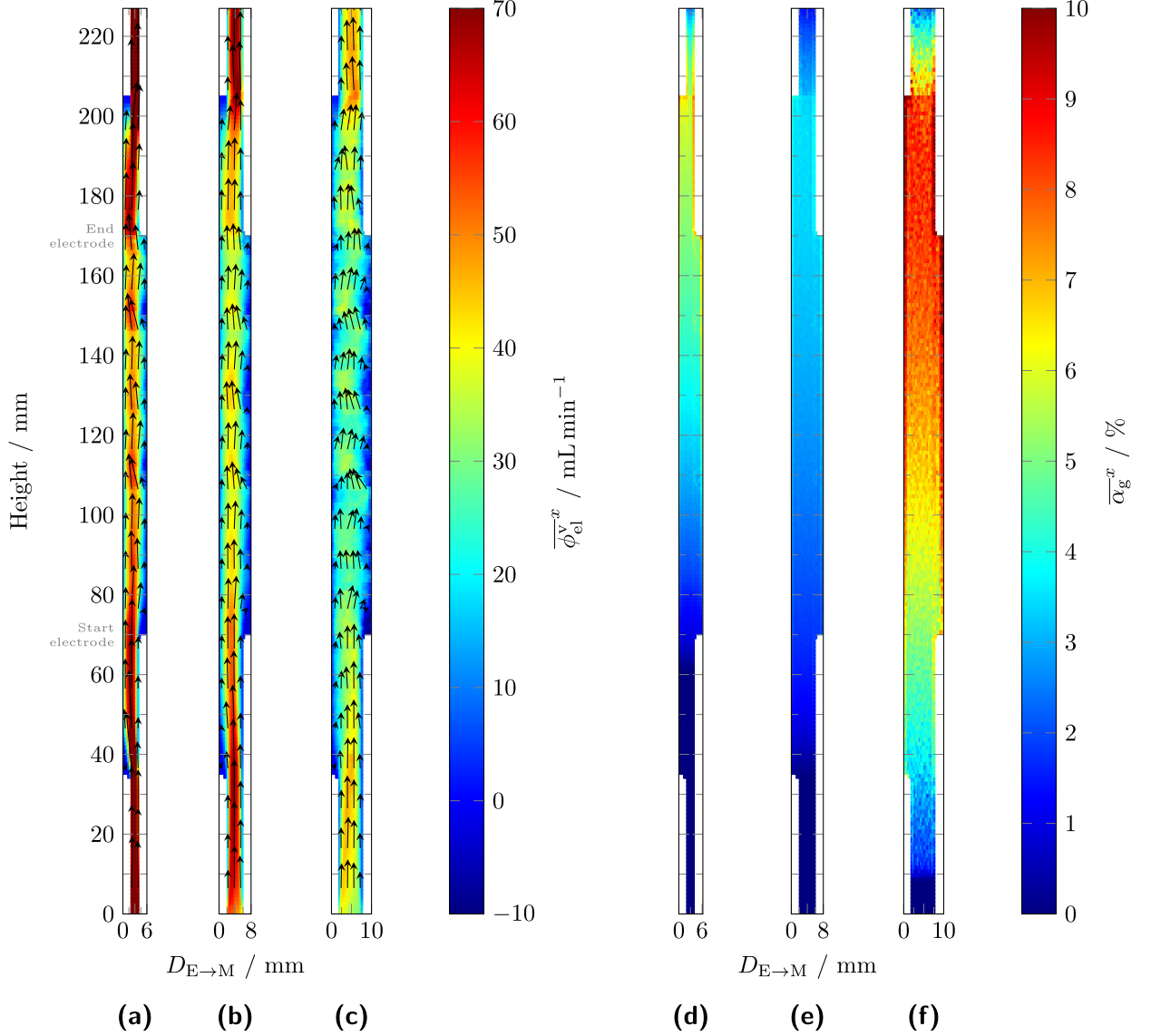


Figure 6.5.: $\overline{\phi_{\text{el}}^{vz}}$ and direction of flow in the (a) $D_{\text{E} \rightarrow \text{M}}=6$, (b) 8 and (c) 10 mm prototype along with the distributions of $\overline{\alpha_g^z}$ in the (d) $D_{\text{E} \rightarrow \text{M}}=6$, (e) 8 and (f) 10 mm prototypes at $\dot{V}_{\text{el},\text{in}}=0.5 \text{ L min}^{-1}$ and $i=0.1 \text{ A cm}^{-2}$ in the yz -plane.

$\overline{u_{\text{el},\text{sim}}^x}$ in Figure 6.6(a), the change in the z -direction and the thereby accompanied difference in the cross area lead to a reduction in the upward flow velocity. The maximum of the vertical flow velocity respectively increases from 11.9 to 17.0 and finally to 21.5 mm s^{-1} for $D_{\text{E} \rightarrow \text{M}}=10, 8$, and 6 mm. Despite the quantitative differences in $\overline{u_{\text{el},\text{sim}}^x}$, the course of $\overline{u_{\text{el},\text{sim}}^x}$ along the relative distance between electrode and membrane $D_{\text{E} \rightarrow \text{M}} D_{\text{E} \rightarrow \text{M},\text{max}}^{-1}$ resembles a typical plug flow. In addition, $\overline{\alpha_g^x}$ for the 6 and 8 mm prototypes is also almost congruent. Solely, the 10 mm prototype shows significant deviations from the two smaller

ones and the membrane and electrode exhibit local gas phase fractions of about 2 %. The

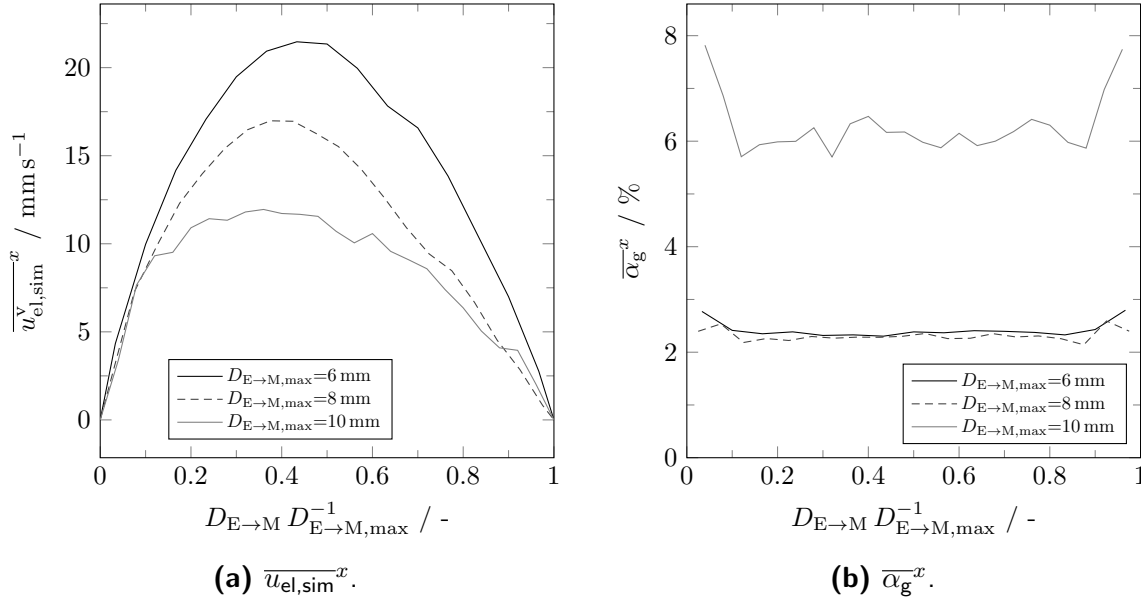


Figure 6.6.: Comparison of (a) $\overline{u_{el,sim}^x}$ and (b) $\overline{\alpha_g^x}$ at a height of 130 mm across $D_{E \rightarrow M}$ of the 6, 8, and 10 mm prototypes.

distinctive distance between the 10 mm prototype and the other two is also reflected in the velocity components of the gaseous phase, which is listed in Table 6.1. Whereas only minor differences exist between the velocity components in the 6 and 8 mm prototype, the large standard deviation in all three spatial directions for $D_{E \rightarrow M, \max} = 10$ indicates the formation of large vortices. Here, the standard deviation of $u_{b,sim}^y$ doubles while the standard deviations of $u_{b,sim}^x$ and $u_{b,sim}^z$ even quadruple.

Table 6.1.: Mean values and standard deviation of the three velocity components of oxygen bubbles at $i=0.1 \text{ A cm}^{-2}$, $\dot{V}_{el,in}=0.5 \text{ L min}^{-1}$ in the three different prototypes.

Velocity component	$D_{E \rightarrow M, \max}$		
	6 mm	8 mm	10 mm
$u_{b,sim}^x \text{ (mm s}^{-1}\text{)}$	-6.0 ± 10.5	-4.7 ± 12.0	-0.5 ± 44.8
$u_{b,sim}^y \text{ (mm s}^{-1}\text{)}$	39.3 ± 18.7	37.0 ± 19.5	45.0 ± 39.3
$u_{b,sim}^z \text{ (mm s}^{-1}\text{)}$	0.13 ± 6.3	0.2 ± 8.6	1.9 ± 44.8

6.1.4. Simulated residence time distribution of the electrolyte and comparison with experimental data

Besides the spatial distribution of the electrolyte flow, the determination of the RTD of the electrolyte allows to abstract the reactor and has already been experimentally determined by Kocks [172]. By using a step increase of Na_2SO_4 at the inlet, the conductivity is

measured at the outlet, and subsequently, t_M , $F(\theta)$ and the characteristic values θ_5 , θ_{50} , θ_{95} are calculated. As described in Section 4.4, the simulation introduces fluid tracer particles and uses the amount of particles leaving the domain to calculate the above parameters. For illustration, Figure 6.7 (a) and (b) respectively display the simulated and experimentally determined course of $F(\theta)$ and comparison of the characteristic RTD values θ_5 , θ_{50} , and θ_{95} . To better visualize the differences between the different operating conditions and

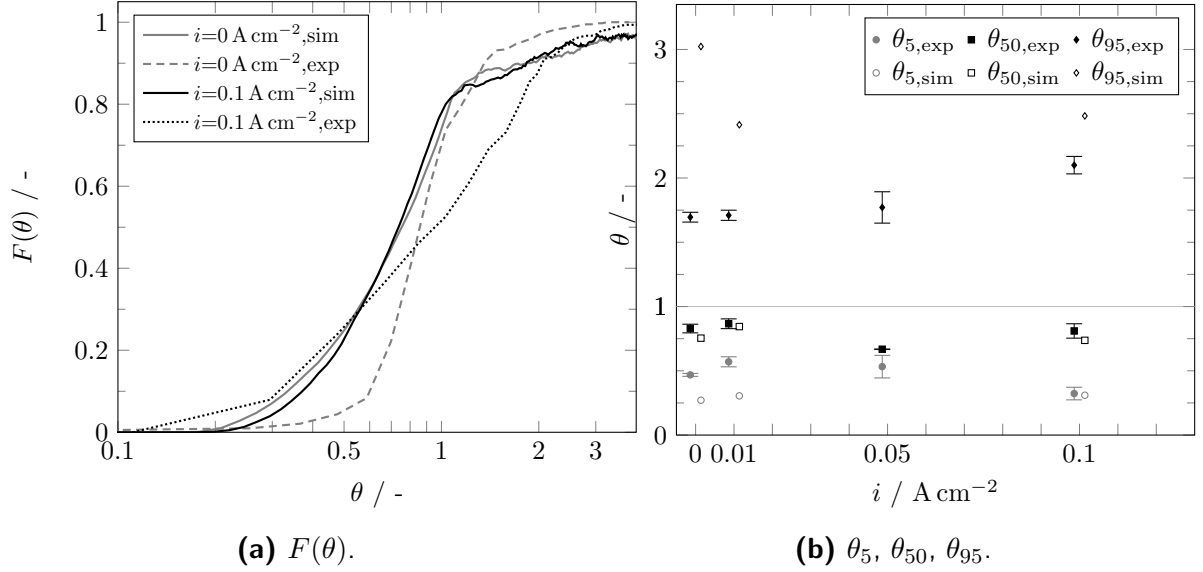


Figure 6.7.: Comparison of simulation results and experimental data [172] for **(a)** the dimensionless $F(\theta)$ and **(b)** characteristic values of θ_5 , θ_{50} , θ_{95} of the electrolyte RTD for the 8mm-wide prototype, $\dot{V}_{\text{el,in}}=0.5 \text{ L min}^{-1}$ and different current densities. The data in (a) is plotted with a logarithmic x -axis.

the simulated and experimental results, the x -axis in Figure 6.7 is logarithmic. At the beginning of $F(\theta)$ and at $i=0.1 \text{ A cm}^{-2}$, the simulation overestimates the amount of tracer particles leaving the domain resulting in $\theta_{5,\text{sim}} = 0.27 < \theta_{5,\text{exp}} = 0.57$. Further, θ_{50} only shows a minor deviation of 0.08 before the simulation reports a value of 3 for $\theta_{95,\text{sim}}$ exceeding the experimentally determined value of $\theta_{95,\text{exp}}=1.7$. This discrepancy might arise from the fluctuation of the parcels leading the computational domain and resulting in $F(\theta)$ falling below the 95 % mark. The simulated mean residence time $t_{M,\text{sim}}$ equals 16.8 s and is in the range of the experimental measurements ($t_{M,\text{exp}} = 19.5 \pm 1.5 \text{ s}$).

At $i=0.1 \text{ A cm}^{-2}$, $\dot{V}_{\text{el,in}}=0.5 \text{ L min}^{-1}$, and $D_{\text{E} \rightarrow \text{M}} = 8 \text{ mm}$, the experimentally determined and simulated course of $F(\theta)$ converges, and the characteristic values depicted in Figure 6.7(b) also show an excellent agreement between experiments and the simulation. The respective differences between experimental and simulated values for θ_5 , θ_{50} , and θ_{95} are 0.01, 0.07, and 0.38. Besides, $t_{M,\text{sim}}$ almost equals $t_{M,\text{exp}}$ with values of 20.4 and $19.2 \pm 0.4 \text{ s}$, respectively. The comparison of key RTD parameters between experiments and simulation at $i=0.01 \text{ A cm}^{-2}$ also yields similar offset obtained for $i=0.1 \text{ A cm}^{-2}$.

To further compare the simulated with the experimentally determined RTDs, Figure 6.8 displays the key parameters of the RTD at $\dot{V}_{\text{el,in}}=0.5 \text{ L min}^{-1}$ and different i in the 6 mm (a) and 10 mm (b) prototypes. The smallest prototype with $D_{\text{E} \rightarrow \text{M}}=6 \text{ mm}$ reveals a similar trend as presented in Figure 6.7(b): The deviations between the experimentally determined and simulated values of the key parameters at $i=0$ or 0.01 A cm^{-2} exhibit larger deviations compared to the ones recorded at $i=0.1 \text{ A cm}^{-2}$ that show excellent accordance. The obtained key parameters of the RTD for the largest prototype feature the largest disparities between the experimental and simulated data. Contrarily to the other two prototypes, the difference at $i=0$ and 0.01 A cm^{-2} , and $\dot{V}_{\text{el,in}}=0.5 \text{ L min}^{-1}$ are smaller compared to $i=0.1 \text{ A cm}^{-2}$. However, the experimental data at the highest current density also includes an error through the change in conductivity through the electrolysis, contributing to the difference in θ_{10} .

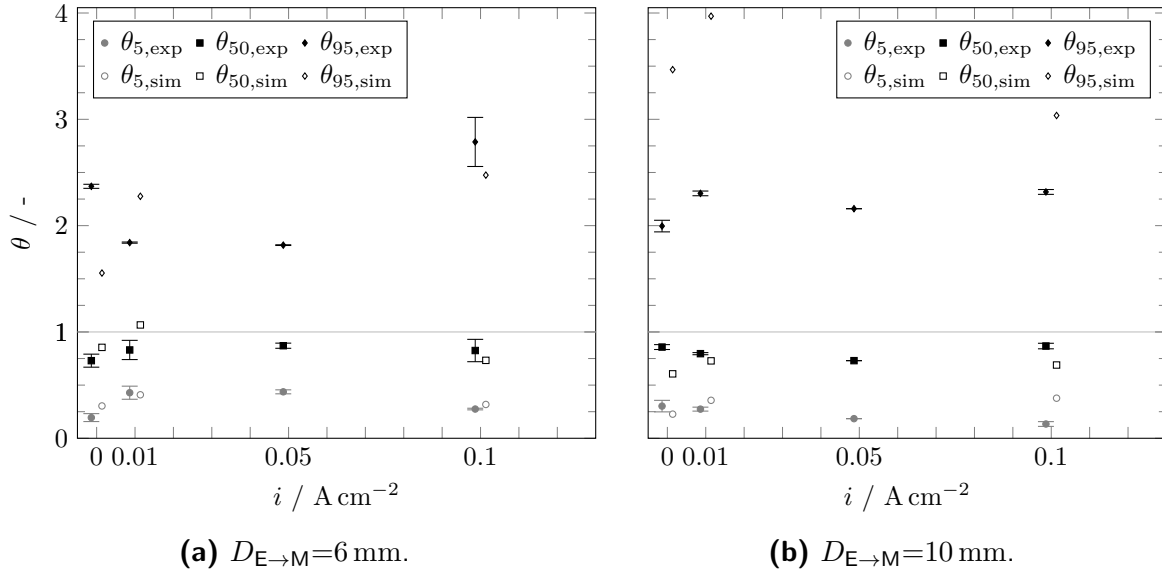


Figure 6.8.: Comparison of simulation results and experimental data [172] for characteristic values of θ_5 , θ_{50} , θ_{95} of the electrolyte RTD in the (a) 6 mm and (b) 10 mm wide prototype at $\dot{V}_{\text{el,in}}=0.5 \text{ L min}^{-1}$ and different current densities.

Concluding the comparison of the experimentally measured and simulated RTD, Table 6.2 comprises the values for t_{M} , θ_5 , θ_{50} , and θ_{95} , at different operating conditions and $D_{\text{E} \rightarrow \text{M}}$. When comparing the experimental and simulated data, it is noticeable that $\theta_{95,\text{sim}}$ is greatly overestimated at $i=0$ and 0.01 A cm^{-2} for the 6 and 10 mm prototypes. Hence, the simulation setting, e.g., number of tracer particles, could be adjusted to limit the fluctuations of escaping tracer particles. At the smaller volume flow rate of 0.05 L min^{-1} , the deviation between the simulation and the experiments enlarges and is depicted in the appendix. The deviation between experiments and simulations could be due to the disparity between the simulation domain and the real volume at which the RTD is experimentally

determined. For example, the simulation does not account for the redirection of the flow at both the in- and outlet. Further, the inductive probe for experimentally measuring the conductivity at the outlet is submerged in a 30 mL glass container that both possess inertia impacting the RTD measurement. Besides, the produced oxygen gas most likely alters the dead time of the system that is experimentally measured without the presence of a gas [172]. However, the results tabulated in Table 6.2 demonstrate the capability of the Euler-Lagrangian model to predict the RTD inside anode prototypes.

Table 6.2.: Simulated and experimentally measured [172] key values of the RTD, t_M , θ_5 , θ_{50} , and θ_{95} for the electrolyte in the three different prototypes at $i=0$, 0.01, and 0.1 A cm⁻² and $\dot{V}_{el,in}=0.05$ and 0.5 L min⁻¹.

\dot{V}_{el} (L min ⁻¹)	i (A cm ⁻²)	t_{M} (s)		θ_5 (-)		θ_{50} (-)		θ_{95} (-)	
		exp	sim	exp	sim	exp	sim	exp	sim
$D_{\text{E} \rightarrow \text{M}} = 6 \text{ mm}$									
0.05	0	120.2 ± 4.9	71.4	0.72	0.65	0.94	0.97	1.36	1.60
0.05	0.01	122.5 ± 2.0	85.6	0.60	0.64	0.96	0.93	1.59	1.80
0.05	0.1	196.6 ± 0.8	139.2	0.34	0.49	0.85	0.88	2.19	1.90
0.5	0	10.2 ± 0.3	19.8	0.19	0.30	0.73	0.86	2.37	1.55
0.5	0.01	15.4 ± 1.1	11.3	0.43	0.41	0.83	1.07	1.84	2.28
0.5	0.1	16.1 ± 1.7	13.8	0.27	0.32	0.83	0.73	2.79	2.48
$D_{\text{E} \rightarrow \text{M}} = 8 \text{ mm}$									
0.05	0	201.2 ± 0.8	143.7	0.86	0.52	0.98	0.52	1.19	2.18
0.05	0.01	173.4 ± 2.4	111	0.62	0.44	0.99	0.44	1.71	2.42
0.05	0.1	164.7 ± 1.9	116.5	0.34	0.49	0.82	0.49	2.29	1.83
0.5	0	19.5 ± 1.5	16.8	0.47	0.27	0.83	0.75	1.7	3.02
0.5	0.01	21.1 ± 0.7	17.2	0.57	0.31	0.87	0.84	1.71	2.41
0.5	0.1	19.2 ± 0.4	20.4	0.32	0.31	0.81	0.74	2.10	2.48
$D_{\text{E} \rightarrow \text{M}} = 10 \text{ mm}$									
0.05	0	211.6 ± 2.4	127.8	0.56	0.56	0.85	0.89	1.88	2.06
0.05	0.01	192.1 ± 3.5	139.2	0.53	0.48	0.87	0.88	1.92	2.03
0.05	0.1	179.8 ± 6.4	303.5	0.34	0.49	0.82	0.49	2.29	1.83
0.5	0	19.0 ± 0.2	22.9	0.30	0.23	0.86	0.61	2.00	3.47
0.5	0.01	19.5 ± 0.2	30.9	0.27	0.36	0.80	0.73	2.30	3.97
0.5	0.1	22.0 ± 0.1	34	0.13	0.38	0.87	0.69	2.32	3.04

6.2. Residence time distribution of the crystal phase

In addition to the RTD of the electrolyte phase, the movement and suspension of the crystals is of central interest in guaranteeing the stable operation of electrochemical crystallization units. Therefore, Section 6.2.1 describes the setup and the employed Mask R-CNN detection algorithm. Afterwards, the results are presented and compared with

simulation results in Sections 6.2.2 and 6.2.3, respectively.

6.2.1. Experimental measurement

Figure 6.9 presents the setup, which is used to perform step-out experiments. The setup is similar to the one published by Kocks [172] to study the RTD of the electrolyte experimentally. However, the setup had to be modified to be eligible to record the residence time of crystals within the system. First, the initial feed contains a suspension with 2.5 wt-% of SA particles that a pump circulates through the system for 2 min to guarantee a good distribution of particles in the system. In addition, to check for a consistent suspension of particles in the system and later obtain images of the multiphase flow, a custom-made flow-through cell is designed and inserted close to the outlet of the electrolyte chamber. The flow-through cell consists of a 3D-printed body from ABS paired with two microscope support glass plates glued to the back and front. The flow within the flow-through cell is redirect into a channel with only 2 mm depth to match the DOF of the HRHPC setup that is used for image acquisition. A white LED is placed behind the back glass plate to illuminate the gas-liquid-solid flow, enabling a shutter speed as low as 39 μ s.

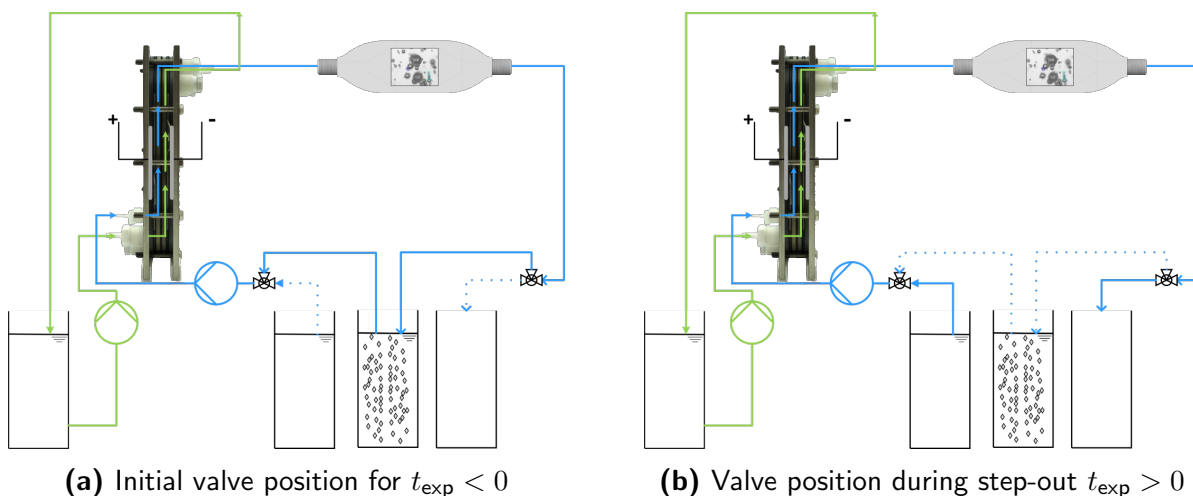


Figure 6.9.: Illustration of the experimental setup for the RTD determination of the crystal phase. To perform a step-out experiment, the valve is in position **(a)** until the experiment starts and the three-way valve is switched towards **(b)** the feed container without solids.

After the distribution of the suspension has entered a steady state, the three-way valve is switched towards a saturated SA solution to elute and flush out the particles within the anode chamber. The time at which the valve is turned is taken as the start of the experiment, and the camera system starts to record images with a frame rate of 30 fps. Next, images from various operating conditions are selected to train the Mask R-CNN algorithm for detecting particles in the gas-liquid-solid flow. The procedure to obtain the new weights for the CNN follows the procedure presented in section 3.1.3.

6.2.2. Experimental result

Using the trained algorithm, the dead time of the tubing system and the flow-through cell is determined by short-circuiting the electrolysis cell and measuring the time until the number of particles averaged over 1 s becomes constant. Table 6.3 lists the obtained deadtimes for particles of the small and large sieve fraction (see Figure 4.9) at $\dot{V}_{\text{el}}=0.75$ and 1 L min^{-1} . At $\dot{V}_{\text{el}}=0.75 \text{ L min}^{-1}$, the deadtime of the larger particles (26.6 s) more than doubles compared to the value for the smaller ones (11.8 s). This difference indicates that larger particles are on the verge of being fluidized by the electrolyte at $\dot{V}_{\text{el}}=0.75 \text{ L min}^{-1}$. The greater volume flow rate of 1 L min^{-1} greatly reduces the deadtime of the larger particles to 9.6 s and the difference to the smaller particles to 1 s.

Table 6.3.: Experimentally measured deadtimes at $\dot{V}_{\text{el}}=0.75$ and 1 L min^{-1} for particles of the small and large sieve fractions.

\dot{V}_{el} (L min^{-1})	i (A cm^{-2})	size (-)	t_{Dead} (s)
0.75	0	large	26.6
0.75	0	small	11.8
1	0	large	9.6 ± 0.5
1	0	small	8.6

After obtaining the deadtimes, the RTD of the particle phase can finally be measured. Therefore, the experimental time is corrected by the respective deadtime to obtain and the averaged particle counts can be evaluated and post-processed to assess the deadtime. To visualize the raw data obtained from the camera system, Figure 6.10 displays image data analyzed by the Mask R-CNN algorithm that was obtained at different corrected experimental times of 0, 5, 20, and 40 s. As the experimental time progresses, the number of particles in the images decreases showing the dilution through the insertion of the solid-free inlet solution. Here, clusters of colored rectangles represent intersecting rectangles that are marked as potential agglomerate. This information was not further used for the determination of the RTD, but could be used for future analysis of electrochemical crystallization experiments.

Despite extensive training of the CNN algorithm, Figure 6.10 depicts that bubbles are falsely detected and counted as particles. Therefore, both a minimum that resembles the noise through false detections and maximum threshold are calculated and used to normalize the particle counts. The minimum is determined by calculating the arithmetic mean of the number of identified objects during the last 10 s of the total experimental duration (120 s). The maximum was defined by taking the arithmetic mean of all analyzed images for a duration equal to the respective deadtime. Figure 6.11 presents the resulting normalized residence time function for the smaller-sized particles at $i=0.1 \text{ A cm}^{-2}$ and $\dot{V}_{\text{el,in}}=1 \text{ L min}^{-1}$

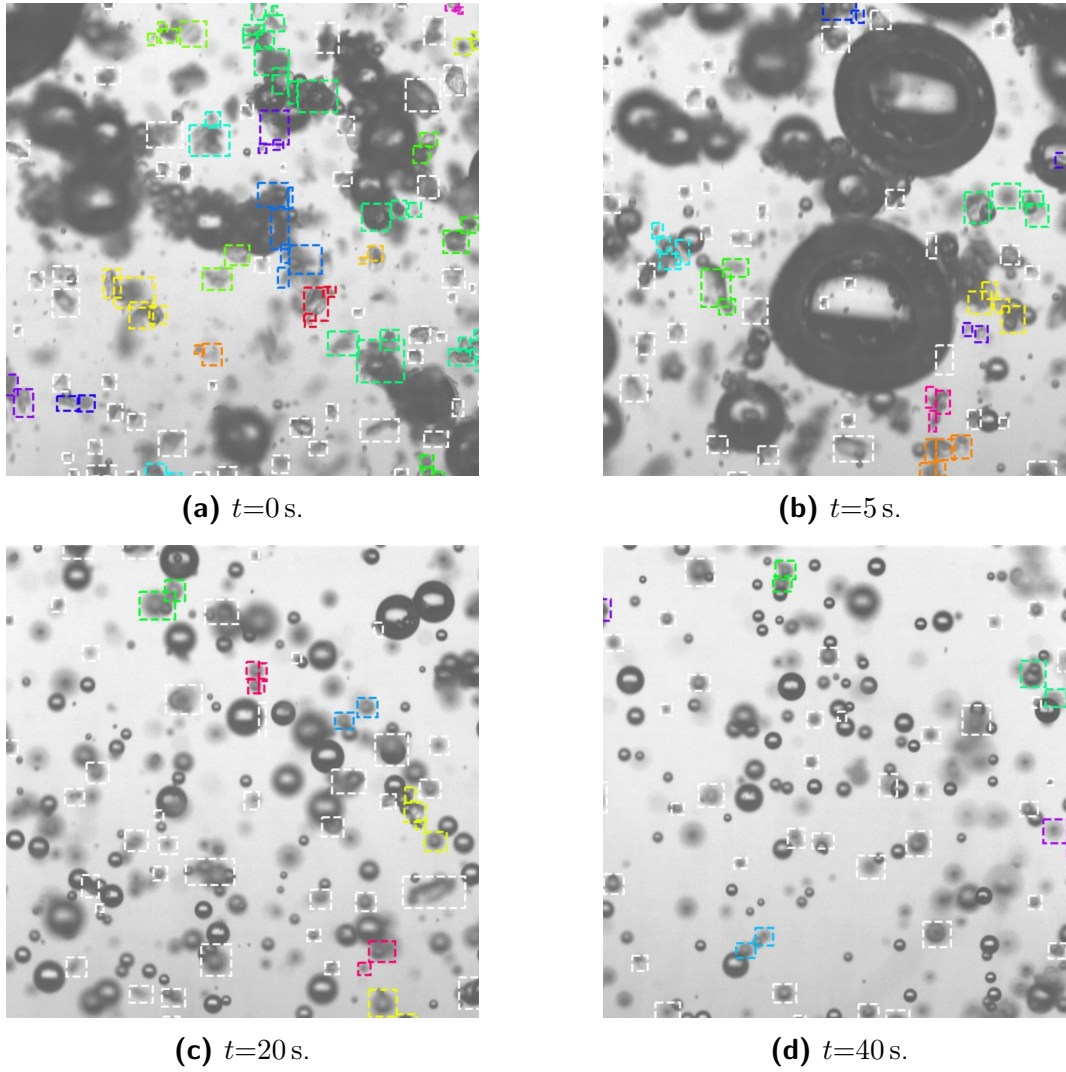


Figure 6.10.: Raw image data at different times from an RTD experiment with particles of the larger sieve fraction (0-200 μm) at $i=0.1 \text{ A cm}^{-2}$ and $\dot{V}_{\text{el,in}}=1 \text{ L min}^{-1}$. Colored clusters indicate a possible formation of an agglomerate.

for two different experimental runs. The two runs exhibit good reproducibility for the first 10 s of the experiments. Thereafter, the first run measured an increase in counts, whereas the second run further declined. At $t_{\text{exp}}=30$ s, both experiments reach normalized counts close to 0. The differences between 20 and 40 s also result in a rather large standard deviation of the key parameters of the RTD. t_M , θ_5 , θ_{50} , and θ_{95} are respectively determined to be 4 ± 2.3 s, 0.33 ± 0.24 , 0.84 ± 0.44 , and 1.98 ± 1.15 . With the same conditions except $i=0 \text{ A cm}^{-2}$, the standard deviations of the four parameters decrease to 0.7 s, 0.08, 0.06, and 0.06. This showcases the introduced velocity fluctuations within the electrochemical reactor that were also previously depicted in Section 5.1.1.

Figure 6.12 plots the obtained RTD parameters for the larger and smaller particle sieve fraction alongside the corresponding ones for the electrolyte phase from [172] at

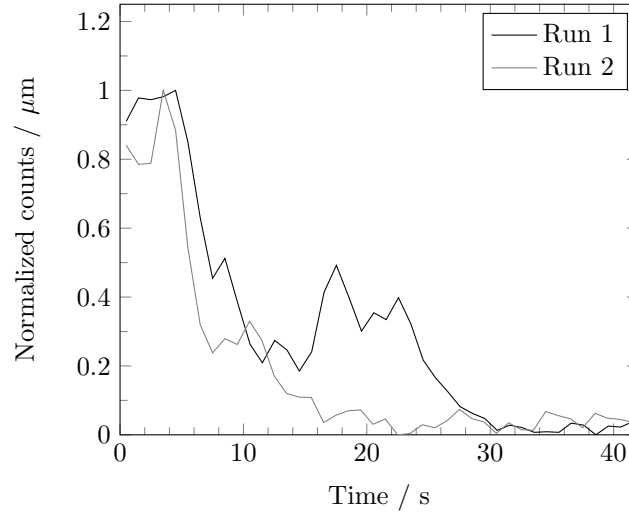


Figure 6.11.: $F(t)$ of two runs for particles with d_p of 0-200 μm at 0.1 A cm^{-2} and $\dot{V}_{\text{el,in}}=1 \text{ L min}^{-1}$.

$\dot{V}_{\text{el,in}}=0.1 \text{ L min}^{-1}$ and $i=0, 0.05$, and 0.1 A cm^{-2} . In general, the measured values for θ_5 ,

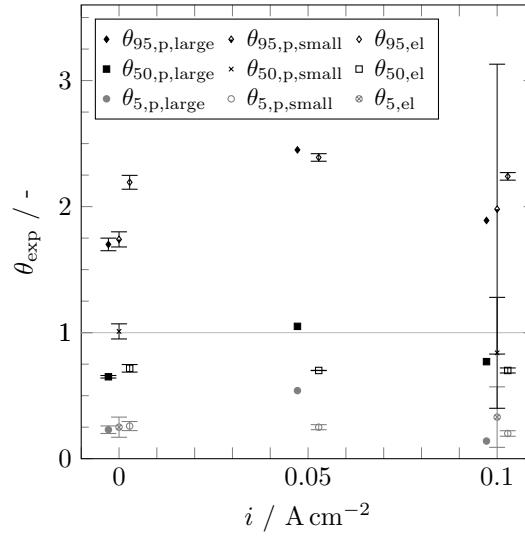


Figure 6.12.: Visualization of the experimentally determined RTD of small and large crystals, and the electrolyte [172] at $\dot{V}_{\text{el,in}}=1 \text{ L min}^{-1}$ and different i in the 8 mm prototype.

θ_{50} , and θ_{95} exhibit good agreement between the three different phases. Especially at the highest current density of 0.1 A cm^{-2} , the comparison yields only minor deviations between the three phases. It demonstrates that the motion of particles and the electrolyte is closely linked at these operating conditions. Furthermore, the key parameters of the RTD are also almost identical for $i=0 \text{ A cm}^{-2}$, with the exception of $\theta_{50,p,\text{small}}$ and $\theta_{50,\text{el},\text{small}}$. At these conditions, t_M for the small and large particles, and the electrolyte equals 13.1 ± 0.7 , 13.5 ± 1.1 , and 12.1 ± 0.3 . Due to the slight differences in t_M , the experimental results demonstrate a good fluidization of the solids in the electrochemical crystallizer and that

the solids do not accumulate within the anode chamber.

6.2.3. Simulation result and comparison

Besides the experimental RTD determination, the movement of particles through the anode chamber is also simulated. The complete results of the experiments and simulations are tabulated in Table 6.4. Similar to the results for the electrolyte phase depicted in section 6.1.4, the Euler-Lagrangian model predicts the RTD of the particulate phase significantly better for the gas-liquid flow than for the single-phase, electrolyte flow. Without the presence of the gas phase, the experimentally measured t_M of the particles at least triples the corresponding ones obtained by the simulation. This deviation is unexpected since one-phase CFD simulation are regarded to be more reliable than multi-phase simulations [158]. As a consequence, θ_5 also exhibits significant differences. On the contrary, a current density of 0.1 A cm^{-2} features good agreements at $\dot{V}_{\text{el, in}}=0.75 \text{ L min}^{-1}$ for the larger and smaller size fractions of $t_{M, \text{exp}}=6.5 \text{ s}$ and $t_{M, \text{sim}}=7.4 \text{ s}$, and $t_{M, \text{exp}}=5.9 \text{ s}$ and $t_{M, \text{sim}}=8.5 \text{ s}$. Increasing $\dot{V}_{\text{el, in}}$ to 1 L min^{-1} still yields good agreements between the larger and smaller fractions with corresponding values of $t_{M, \text{exp}}=6.5 \text{ s}$ and $t_{M, \text{sim}}=3.4 \text{ s}$, and $t_{M, \text{exp}}=4.3 \text{ s}$ and $t_{M, \text{sim}}=4.0 \text{ s}$, respectively.

Table 6.4.: Simulated and experimentally measured RTD [172] of the electrolyte in the three different prototypes at $i=0, 0.01$, and 0.1 A cm^{-2} and $\dot{V}_{\text{el, in}}=0.05$ and 0.5 L min^{-1} .

\dot{V}_{el} (L min^{-1})	i (A cm^{-2})	t_M (s)		θ_5 (-)		θ_{50} (-)		θ_{95} (-)	
		exp	sim	exp	sim	exp	sim	exp	sim
large fraction (200 – 400 μm)									
0.75	0	15.4 \pm 1.7	4	0.07 \pm 0.04	0.65	1.68 \pm 0.59	1.01	3.13 \pm 0.37	5.22
0.75	0.1	6.5	7.4	0.14	0.43	0.56	0.69	2.46	2.51
1	0	13.5 \pm 1.1	2.6	0.23 \pm 0.03	0.78	0.65 \pm 0.01	1.31	1.76 \pm 0.05	1.89
1	0.05	11.2		0.54		1.05		3.45	
1	0.1	6.5	3.4	0.14	0.64	0.77	1.09	1.89	2.16
small fraction (0 – 200 μm)									
0.75	0.1	5.9	8.5	0.31	0.33	0.78	0.57	1.53	3.04
1	0	13.1 \pm 0.7	3.9	0.25 \pm 0.08	0.49	1.01 \pm 0.06	0.89	1.74 \pm 0.06	1.62
1	0.1	4 \pm 2.3	4	0.33 \pm 0.24	0.41	0.84 \pm 0.44	0.82	1.98 \pm 1.15	1.09

Figure 6.13 plots the simulated and experimentally measured values for $\theta_{5, \text{p}}$, $\theta_{50, \text{p}}$, and $\theta_{95, \text{p}}$ against different current densities for the small (a) and large (b) sieve fractions and $\dot{V}_{\text{el, in}}=1 \text{ L min}^{-1}$. At $i=0$ and 0.1 A cm^{-2} , the small particles show good accordance of all three key parameter between simulation and experiments, except for $\theta_{95, \text{p}}$ at $i=0.1 \text{ A cm}^{-2}$. Here, $\theta_{95, \text{p}}$ equals 1.09, which is atypical and might be an artifact from averaging particles leaving the domain. The simulation of larger particles does not match the experimental data well. This deviation between the simulation and experiment could be due to the

greater noise within the measurement of the larger particles that arise from the fixed weight fraction of crystals in the solution. The different means of the two sieve fractions result in approximately 27 times the number of particles in the small sieve fraction compared to the larger fraction. The presence of electrogenerated oxygen bubbles greatly reduces t_M of the particles regardless of size and $\dot{V}_{el,in}$. However, no substantial change in the key parameter RTD of the particle with different current densities can be observed.

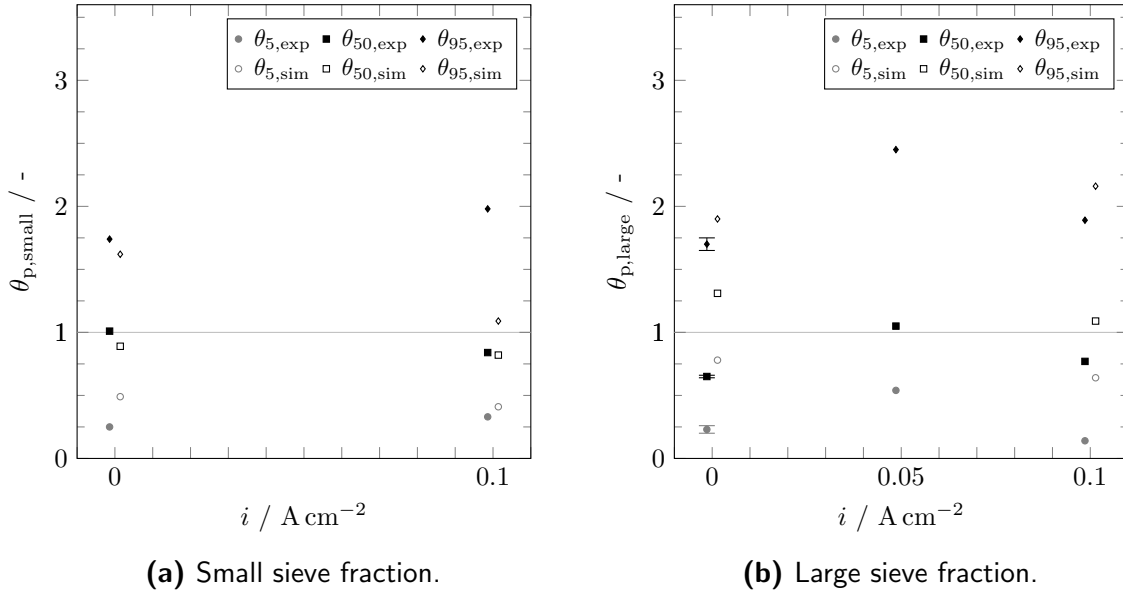


Figure 6.13.: Visualization of the key parameters, θ_5 , θ_{50} , and θ_{95} , of the experimental and simulated RTD for **(a)** the small and **(b)** large particle sieve fractions at $\dot{V}_{el,in}=1 \text{ L min}^{-1}$ and different i in the 8 mm prototype.

6.3. Local pH and supersaturation

Finally, based on the previous experimental and simulative results, the concentration and pH gradients can be calculated and are discussed for the electrochemical crystallization of SA, FDCA, and TA alongside different operating conditions for the $D_{E \rightarrow M}=8 \text{ mm}$ prototype.

6.3.1. Succinic acid

Starting with the most predominantly electrochemically crystallized organic acid, Figure 6.14 displays the local pH averaged along the (a) z - and (b) x -coordinate for SA for an inlet pH value of 5, $c_{SA}=1 \text{ mol L}^{-1}$, $i=0.1 \text{ A cm}^{-2}$, $\dot{V}_{el,in}=0.5 \text{ L min}^{-1}$ and after an electric charge of 1 kC (case SA-2, Table 4.5). Similar to the flow profile presented in Figure 6.1, the pH of the main flow remains almost constant throughout the inlet area and until pass-

ing half of the height of the electrode. Thereafter, the breakup of the flow results in a reduction of upward flow velocity, which also leads to a decrease in the local pH value of about 0.4. Further, the interplay of the local pH and electrolyte flow becomes apparent. Especially in the stagnant and recirculation zones of the prototype, the simulation reports local pH values of as low as 4.1. Exhibiting the zy -plane close to the electrode, the lowest pH values are registered close to the electrode, and the pH decreases along with $D_{E \rightarrow M}$. However, it has to be noted that due to the use of constant ('frozen') velocity and gas phase fraction fields, the minima and maxima might be overestimated, since the gradient cannot disintegrate through changes in bubble motion and distribution.

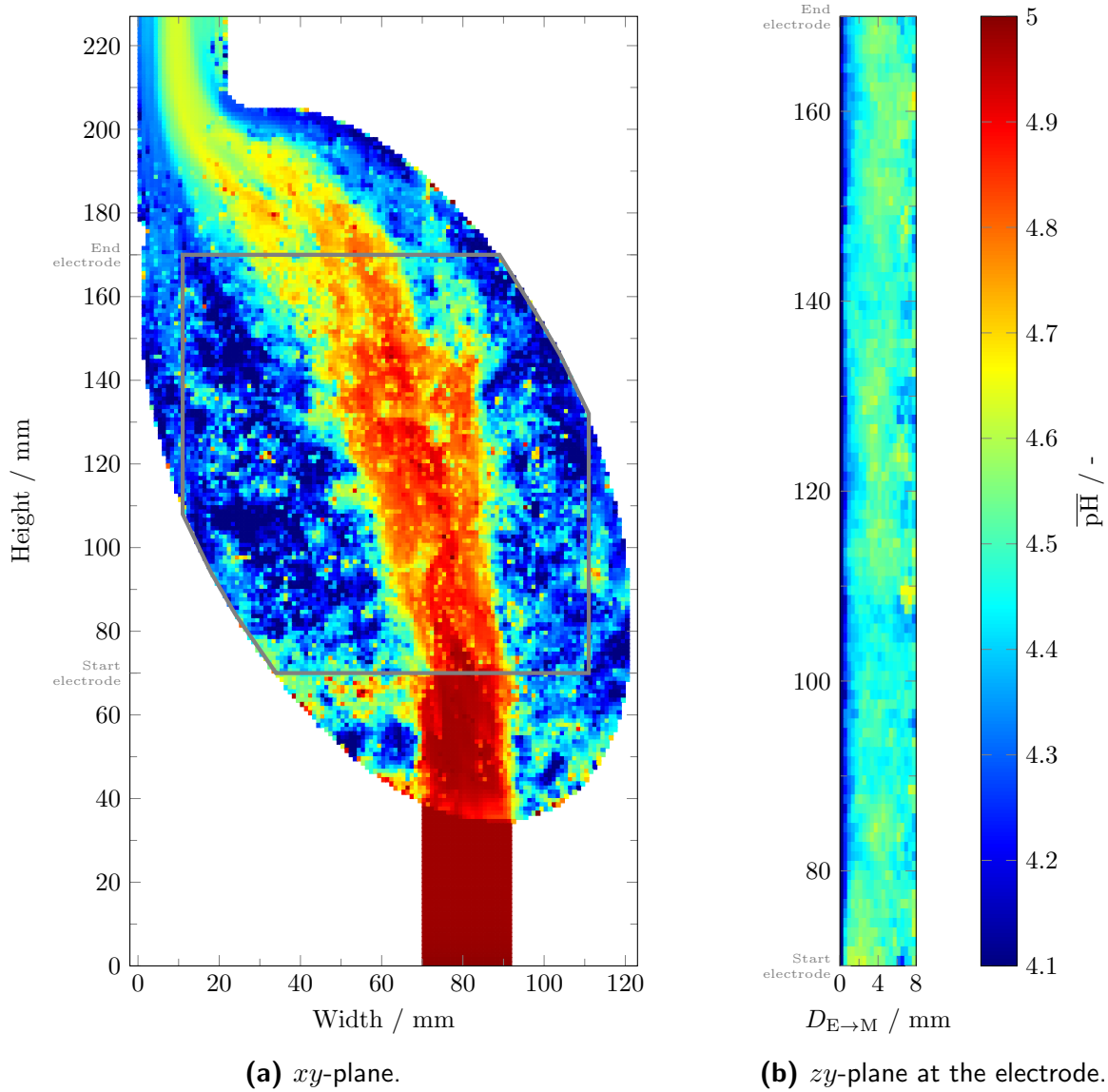


Figure 6.14.: (a) \overline{pH}^z , and (b) \overline{pH}^x of the electrochemical crystallization of succinic acid in the $D_{E \rightarrow M}=8$ mm prototype at $i=0.1$ A cm $^{-2}$, $\dot{V}_{el,in}=0.5$ L min $^{-1}$, $c_{SA}=1$ mol L $^{-1}$, and $pH_{Inlet}=5$ after an electric charge of 1 kC.

Besides the pH gradients, the computational model also calculates the local concentrations of the acid species and, subsequently, the supersaturation S of the protonated acid species. Figure 6.15 depicts the z and x -averaged local supersaturations in the xy - (a) and zy -plane (b). Close to the electrode and in the areas of no or even backward volume flows, local supersaturations as high as 1.4 are calculated. In contrast the supersaturation in the main flow stays close to 0.2-0.3. For reference, the inlet supersaturation amounts to roughly 0.2.

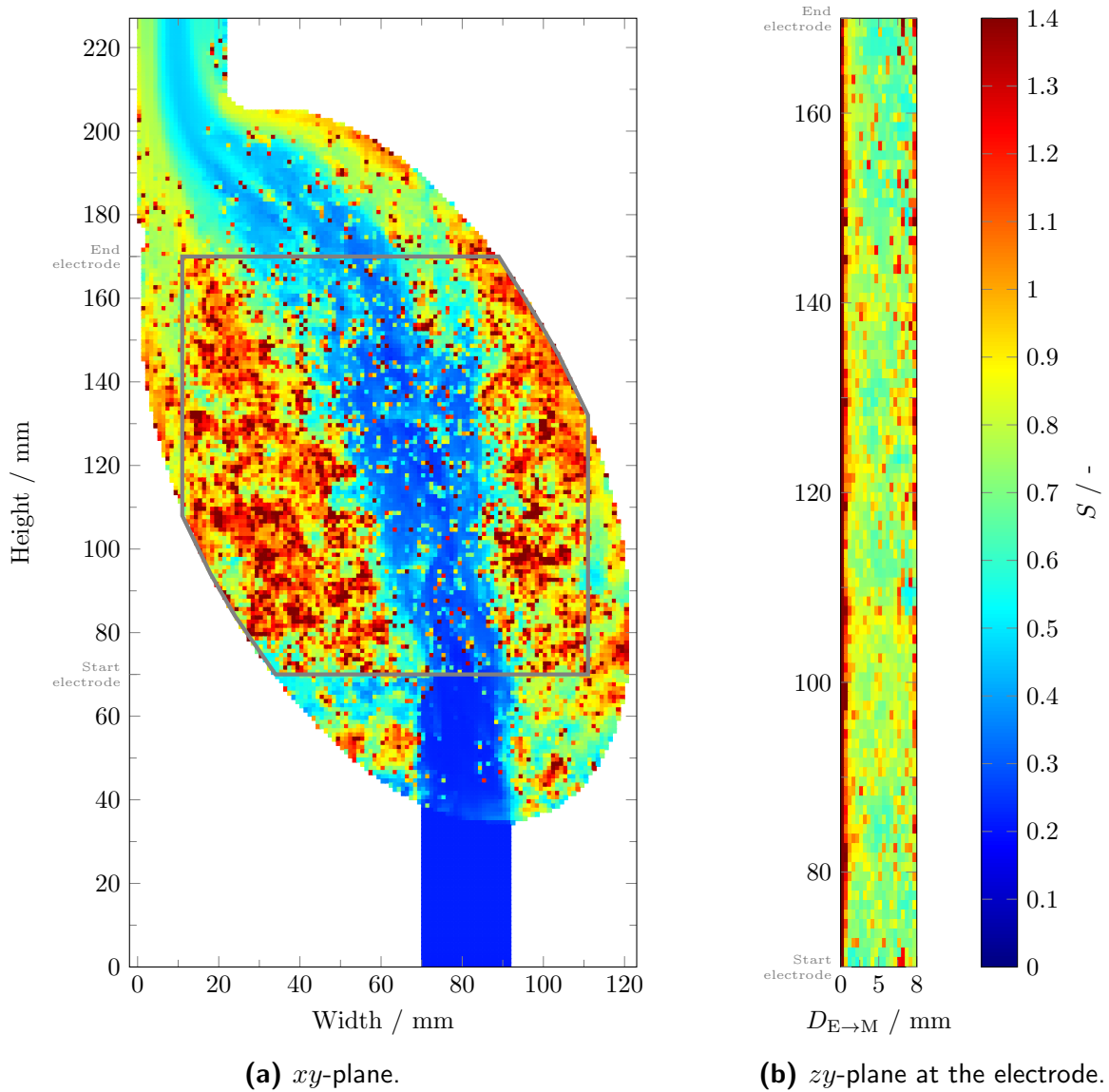


Figure 6.15.: (a) \bar{S}^z , and (b) \bar{S}^x of the electrochemical crystallization of SA in the $D_{E \rightarrow M}=8$ mm prototype at $i=0.1$ A cm $^{-2}$, $\dot{V}_{el,in}=0.5$ L min $^{-1}$, $c_{SA}=1$ mol L $^{-1}$, and pH $_{Inlet}=5$ after an electric charge of 1 kC.

To compare the impact of different current densities on the local pH after 1 kC, Figure 6.16 depicts the z -averaged pH at a height of $y=133$ mm (a) and for different heights

for $i=0.1 \text{ A cm}^{-2}$ (b) against $D_{E \rightarrow M}$. Assessing the different current densities at $y=133 \text{ mm}$, the simulation for $i=0.1 \text{ A cm}^{-2}$ results in lower pH values and a smaller pH gradient close to the electrode when compared against simulations for $i=0.2 \text{ A cm}^{-2}$. From $D_{E \rightarrow M}=1 \text{ mm}$ to the cell closest to the electrode, the pH receptively reduces from 4.4 to 4 and 4.6 to 4.4 for $i=0.1$ and 0.2 A cm^{-2} . This counterintuitive behavior arises from (i) the larger size of electrogenerated bubbles, (ii) the larger volume of produced oxygen gas that increases the upward flow velocity, and (iii) the more homogeneous flow field that is a direct result of (a) and (b) resolving parts of the limitation of the prototype design.

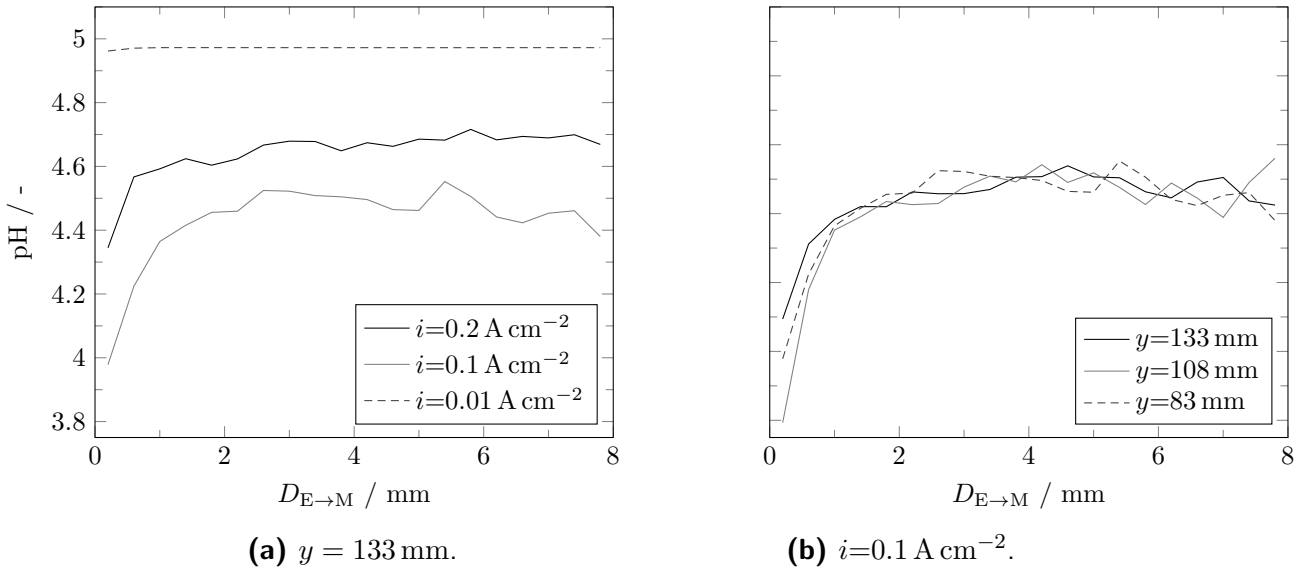


Figure 6.16.: $\overline{\text{pH}}^x$ after 1 kC at (a) $i=0.01, 0.1$, and 0.2 A cm^{-2} at a height of $y = 133 \text{ mm}$ and (b) at different heights at $i=0.1 \text{ A cm}^{-2}$. $\dot{V}_{\text{el,in}}$ and pH_{Inlet} equals 0.5 L min^{-1} and 5, respectively.

Even though the electric charge is held constant, the lowest current density of 0.01 A cm^{-2} leads to a minimal pH change within the entire computational domain. Besides the ten times smaller amperage per volume flow, the flow profile depicted in Figure 6.4 shows the highest vertical velocity close to the electrode for $i=0.01 \text{ A cm}^{-2}$. This higher velocity close to the electrode increases the upward advection of H^+ ions, reducing the local pH. Studying the pH against $D_{E \rightarrow M}$ at different heights within the prototype, the pH course and gradient stay almost constant. This pH course is in accordance with Figure 6.1 and highlights the agitation through the gas bubbles alongside the circulation through the honeycomb structure. Further, this finding also excellently matches the experimental findings of Kocks [172], who also reported a behavior close to an ideal stirred tank of the electrolyte within the prototype. The difference in the local supersaturation between $i=0.1$ and 0.2 A cm^{-2} is further depicted in Figure 6.17. Here, the respective distributions of cell values for S throughout the whole computational domain are shown. Whereas the majority

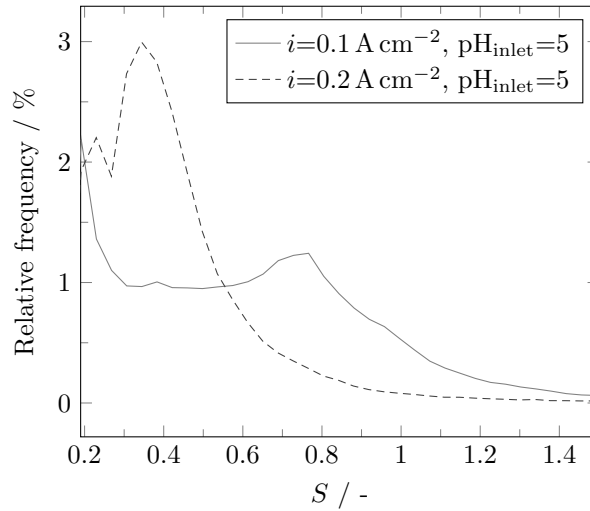


Figure 6.17.: Distribution of S across all cell values of the computational domain for $D_{E \rightarrow M}=8$ mm, $i=0.1$ A cm $^{-2}$, $\dot{V}_{el,in}=0.5$ L min $^{-1}$, $c_{SA}=1$ mol L $^{-1}$, and $pH_{inlet}=5$ after an electric charge of 1 kC. S_{inlet} corresponds to 0.19.

of cells exhibit values between 0.2 and 0.6 for $i=0.1$ A cm $^{-2}$ that almost follow a normal distribution, the percentage of cells in that range is significantly smaller for $i=0.2$ A cm $^{-2}$. Instead, the distribution of the supersaturations is shifted towards higher values with smaller relative frequencies. This representation further underlines the better mixing at the higher current density, resulting in a greater frequency of cells with supersaturations above 1.

6.3.2. 2,5-furandicarboxylic acid

Besides SA, FDCA is a promising new building block for novel (bio-)polymers that can be crystallized by shifting the pH. Due to the low solubility of the protonated acid species of FDCA (0.7 g L $^{-1}$ [205]), the local fluctuations of the pH result in areas with larger supersaturation. Adjusting the pH of a process solution from Harhues et al. [7] with $c_{FDCA} = 0.9$ mol L $^{-1}$ to a value of 7 and feeding it through the anode chamber results in a substantially higher supersaturation than the previous ones for SA presented in Figure 6.14. Figure 6.18 depicts the corresponding local supersaturation profile for FDCA within the anode chamber at $i=0.1$ A cm $^{-2}$ and $\dot{V}_{el,in}=0.5$ L min $^{-1}$ after an electric charge of 1 kC. Due to the inhomogeneous distribution of the upward flow, the \bar{S}^z equals up to 8 in the areas with low upward or backward flow velocities that are in the proximity of the electrode. Hence, the spontaneous nucleation of crystals is expected in those areas due to the large local oversaturation [16]. This nucleation event of FDCA crystals at times where the bulk solution is still undersaturated, was also observed in unpublished proof of concept experiments within the research project *ZeTA*. After its formation, the nuclei

dissolves again in the storage tank, which enables the anolyte to be multipassed through the anode, as mapped in Figure B.19. This formation and dissolution directly result from the simulated concentration gradients within the anode chamber that generated a local supersaturation while the bulk is still highly undersaturated. The corresponding pH profile at $i=0.1 \text{ A cm}^{-2}$ and $\dot{V}_{\text{el,in}}=0.5 \text{ L min}^{-1}$ is depicted in the appendix alongside the pH and S profiles for a pH_{in} of 12 in Figure B.22, B.23, and B.27.

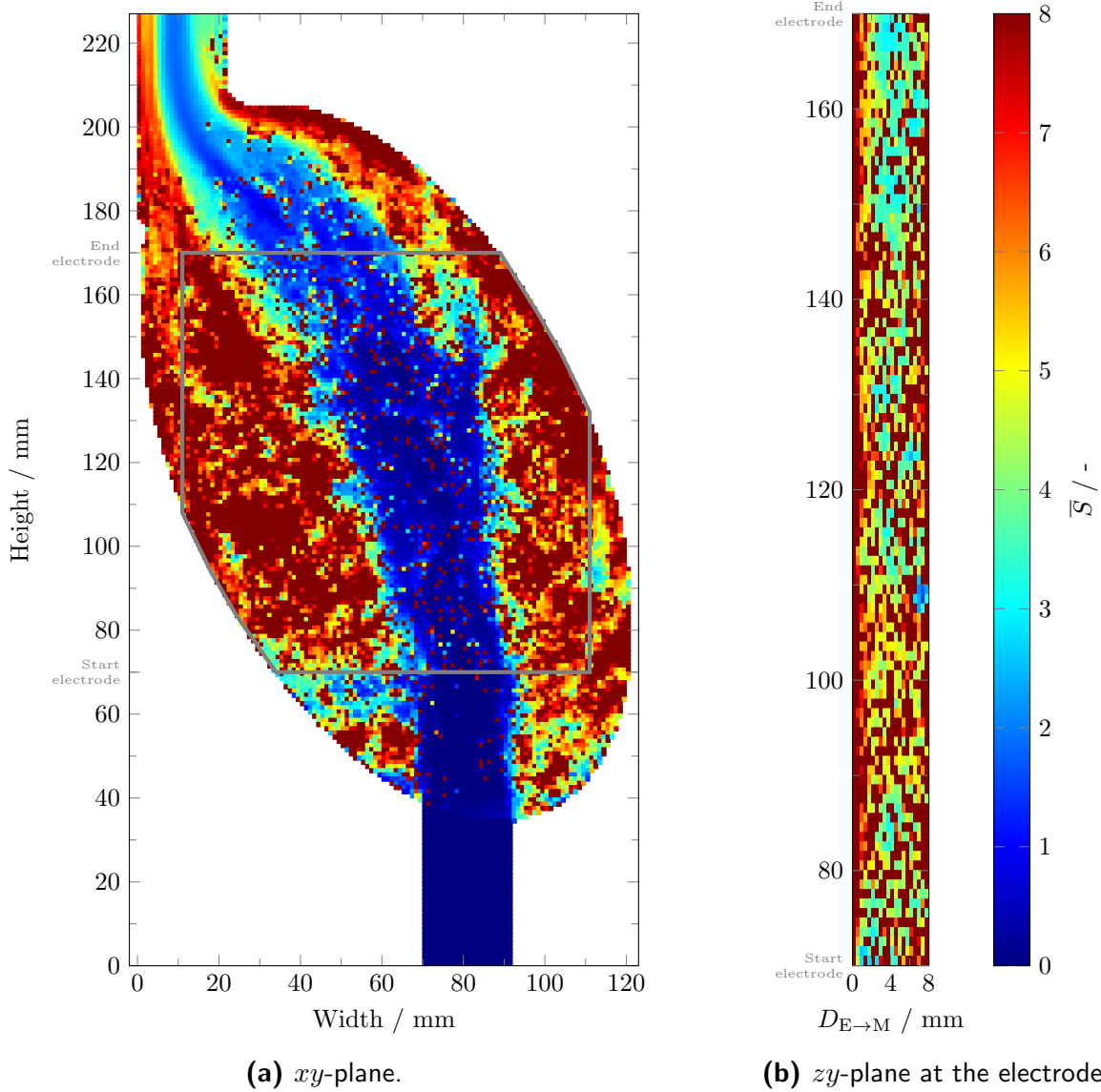


Figure 6.18.: (a) \bar{S}^z , and (b) \bar{S}^x of the electrochemical crystallization of TA in the $D_{\text{E} \rightarrow \text{M}}=8 \text{ mm}$ prototype at $i=0.1 \text{ A cm}^{-2}$, $\dot{V}_{\text{el,in}}=0.5 \text{ L min}^{-1}$, $c_{\text{FDCA}}=0.9 \text{ mol L}^{-1}$, and $\text{pH}_{\text{Inlet}}=7$.

Based on the displayed supersaturation profile, different designs could be derived: (i) A design incorporating large concentration gradients to trigger the nucleation and growth of crystals paired with a solid-liquid separation directly at the outlet of the anode chamber.

This process concept would be beneficial for *in situ* process concepts already described in [12, 17, 22], since it would circumvent the protonation of the whole anolyte volume and enable the separation of the target molecule at a bulk supersaturation $\ll 1$. Exploiting the areas of large local supersaturation can significantly boost the efficiency of the electrochemical crystallization as the share of protons that go into the crystallized product exceeds the theoretical yield in an ideal mixed system. In addition, the counter-reaction at the cathode would also require a smaller pH-shift of the catholyte that goes back to a potential upstream, e.g., fermentation. (ii) On the contrary, the inlet section of the anode chamber could be modified to be homogeneously distributed before it enters the area of gas evolution. This homogeneous distribution would result in significantly smaller concentration gradients and the reduction of the maximum supersaturation. Hence, a more homogeneous flow design could significantly reduce the crystal nucleation rate, favor crystal growth, and, thus, lead to a larger crystal size distribution.

6.3.3. Terephthalic acid

Conventional alkaline hydrolysis approaches for the recovery of TA from recycling polyethyleneterephthalat streams require extensive use of pH agents. Thus, applying electrochemical pH-shift crystallization for TA can greatly reduce the amount of required pH agents and also reduce salt waste. This concept was also recently filed for patent [15].

In comparison with FDCA, the intrinsic solubility of the protonated species of TA is 17 mg L^{-1} [203] and almost zero. As a direct consequence, the supersaturation profile for $i=0.1 \text{ A cm}^{-2}$, $\dot{V}_{\text{el,in}}=0.5 \text{ L min}^{-1}$, $c_{\text{TA}}=0.63 \text{ mol L}^{-1}$, and $\text{pH}_{\text{inlet}}=7$ depicted in Figure 6.19 exhibits values of $\bar{S} \gg 100$. Through the presence of areas with great supersaturation, high nucleation rates of the target molecules are expected. However, the maximum nucleation rates are located close to the electrode and outside the main electrolyte flow. This observation demonstrates that the presence of areas with low upward flow velocity poses two substantial problems for the operability of electrochemical crystallization units for highly insoluble target components. Not only does the oversaturation profile exhibit the greatest values in these areas, but the transport of the nuclei through convection is also limited. Consequently, this combination can lead to the blockade of the respective area through the formation of solids. The patent Thauront et al. [206] even describes the formation of up to 10 mm thick solid formation around the anode through the electrochemical acidification of a sodium terephthalate solution. In the appendix, Figure B.24, B.25, and B.28 display the obtained pH profile at $i=0.1 \text{ A cm}^{-2}$ and $\dot{V}_{\text{el,in}}=0.5 \text{ L min}^{-1}$ alongside the pH and S profiles for a pH_{inlet} of 12 and $c_{\text{TA}}=0.63 \text{ mol L}^{-1}$.

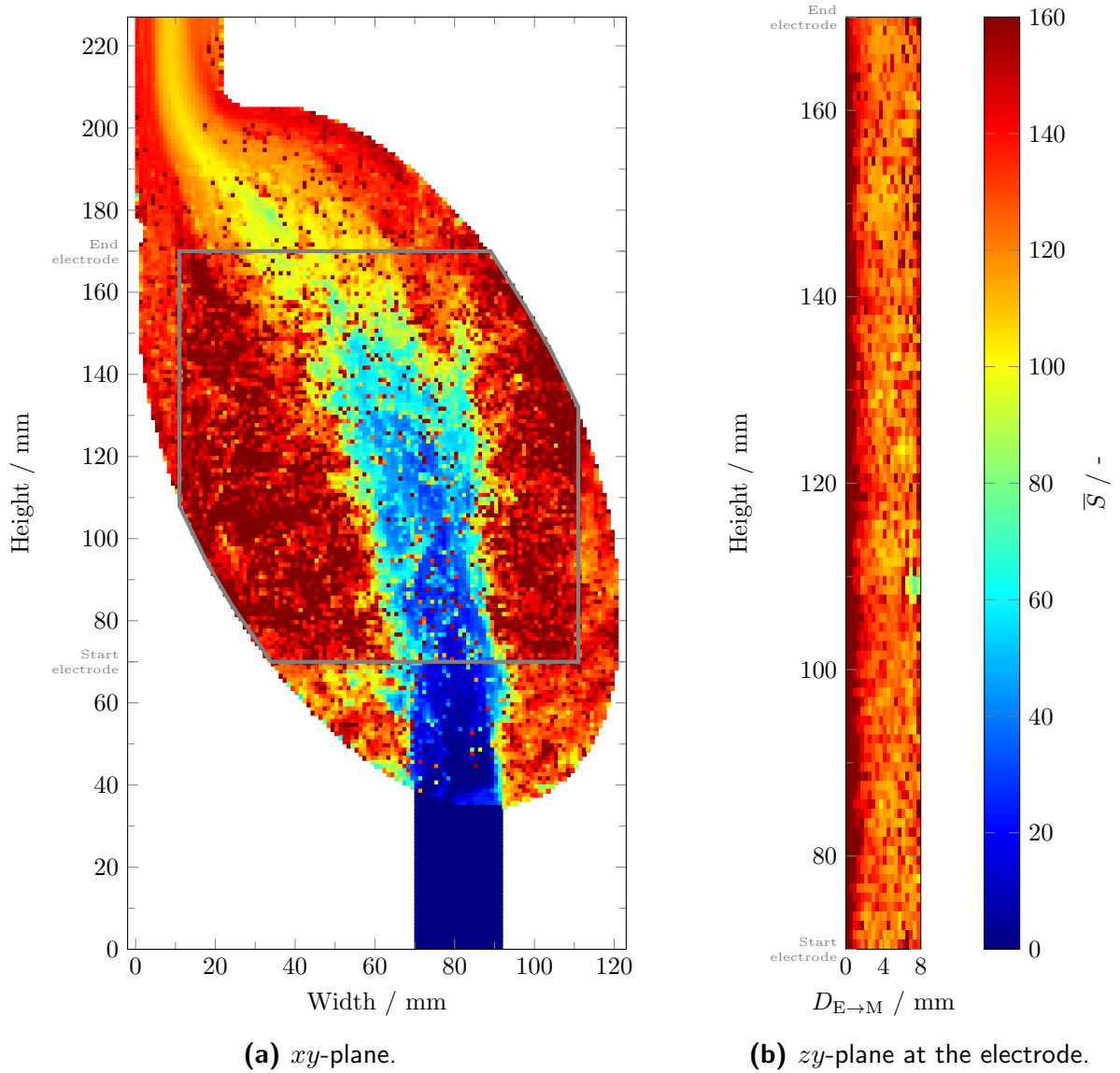


Figure 6.19.: (a) \overline{S}^z , and (b) \overline{S}^x of the electrochemical crystallization of TA in the $D_{E \rightarrow M} = 8$ mm prototype at $i = 0.1 \text{ A cm}^{-2}$, $\dot{V}_{\text{el, in}} = 0.5 \text{ L min}^{-1}$, $c_{\text{TA}} = 0.63 \text{ mol L}^{-1}$, and $\text{pH}_{\text{Inlet}} = 7$.

6.4. Summary of reactor study

This chapter focused on the application of the Euler-Lagrangian model to investigate a novel prototype for electrochemical crystallization proposed by Kocks [17, 172]. Examining the gas-liquid flow inside the prototypes revealed that lowering $\dot{V}_{\text{el, inlet}}$ from 0.5 to 0.05 L min^{-1} roughly doubles the average gas phase fraction in the reactor. The simulation results depict the effect of i on the flow profile and gas phase distribution, demonstrating that higher current densities promote a more homogeneous flow and greater gas phase fractions. However, the $\overline{\alpha}_g$ does not linearly scales with i . Further, varying electrode-

membrane gap impacted the gas-liquid flow in different ways: Reducing $D_{E \rightarrow M}$ from 8 to 6 mm at identical operating conditions increases $\bar{\alpha}_g$ through the reduction of the reactor volume. Within the $D_{E \rightarrow M}=10$ mm prototype, large circular flows were present that resulted in a substantial increase of $\bar{\alpha}_g$.

Comparing the key parameter from simulated RTDs with experimentally determined ones [172] show the capability of the Euler-Lagrangian model to predict the flow characteristic at different operating conditions. The simulation results for the solid crystal phase exhibit larger deviations between the simulation and experimental measurements compared to the liquid phase. However, for the highest value of $i=0.1 \text{ A cm}^{-2}$, the model predicted similar RTD key parameters than the experimental Mask R-CNN-based measurement.

Finally, this chapter presents local pH gradients and supersaturation levels during electrochemical crystallization processes for three different organic acids: SA, FDCA, and TA. The findings showcase the influence of current density and electrolyte flow rates on the local pH levels and supersaturation profiles within the electrochemical crystallizer. The simulation results show decreased local pH levels at the electrode due to buoyancy-induced mixing. Nonetheless, the simulation revealed large levels of local supersaturation for all three studied acids. For SA, FDCA, and TA, the maximum local supersaturation was as high as 1.4, 8, and 160, respectively.

7. Conclusion and Outlook

The emergence of novel, sustainable process routes within the chemical industry, like the production of either biotechnological building blocks or monomer recovery from polymer waste streams, relies on innovative new techniques for processing aqueous solutions. By electrifying the pH shift required at several stages in those novel processes, neutral salt emissions and liquid discharge can be substantially reduced, boosting the feasibility and sustainability of the processes. By realizing this novel technique, the increasing supply of renewable energy resources can be incorporated into novel process concepts to compete with established, fossil-based production processes. In particular, the process intensification achieved with the electrochemical crystallization of carboxylic acid inside a parallel plate electrolyzer constitutes a promising novel separation unit.

7.1. Summary of findings

This thesis aims to generate new insights into the electrochemical pH shift technology by depicting, measuring, and modeling the local phenomena occurring inside pH shift electrolyzers. Based on the results obtained with the proposed fluid dynamic model, novel prototypes and electrochemical apparatuses can be designed and examined. For this purpose, the state of the art regarding the electrochemical pH shift and separation units and their use in the context of biotechnological processes is presented in the second Chapter. Furthermore, the key aspects that determine the economic efficiency and operability of electrochemical pH shift separation units are highlighted, in addition to the omnipresent influence of gas bubble evolution on the operation. Hereinafter, available optical methods for studying the flow of the electrolyte and the electrogenerated bubbles inside electrolyzers are presented along with their results, and limiting factors for the different optical methods are critically discussed. Following the overview of available experimental optical methods, different literature-based computational fluid dynamic model approaches are introduced and assessed for depicting the gas-liquid flow insight parallel plate electrolyzers. In particular, the advantages and disadvantages of the most commonly used Euler-Euler approach in comparison with the Euler-Lagrangian and other approaches are examined. Here, the dependence of the Euler-Euler model on boundary conditions at the electrode

has to be emphasized since the *a priori* selection of the gas phase fraction at the electrode significantly impacts the simulation results.

The third Chapter comprises the experimental study of the bubble motion and electrolyte flow pattern within a parallel plate electrolyzer. The centerpiece of this study is the specially developed semi-transparent electrolyzer that enables a novel perspective on the gas-liquid flow. By introducing viewing panels that are machined into the electrode, the overlapping of bubbles is significantly reduced compared to state-of-the-art methods that only exhibit the small inter-electrode gap. Paired with a specifically trained Mask R-CNN algorithm, the presented approach enables the recording of the combination of bubble size and velocity for different operating conditions of both oxygen and hydrogen bubbles. Inside this setup, which is deducted from a commercially available 100 cm² electrolyzer, the measured average bubble sizes surpass corresponding ones obtained using artificial electrolyzers by factors between two and three. The impact of i and u_{el}^0 on the bubble size distribution is comparable to the literature and the size distribution is almost solely dependent on i . Besides the size, varying i also heavily impacts $u_{\text{b,exp}}^v$. Based on the gas phase fraction and the thereby linked acceleration of the electrolyte due to buoyancy, $\bar{u}_{\text{b,exp}}^v$ increases with the amount of electrogenerated gas regardless of the size of the bubbles. Counterintuitively, changing u_{el}^0 from 0 to 20 mm s⁻¹ reduces $\bar{u}_{\text{b,exp}}^v$ significantly for $i=0.05$ and 0.1 A cm⁻². Through the forced convection of the electrolyte, the bubble curtain breaks apart, the gas bubbles are distributed, and the gas phase fraction within the viewing panels at which $\bar{u}_{\text{b,exp}}^v$ is recorded reduces. This effect is exceptionally high for $i=0.1$ A cm⁻². Applying a PIV measurement to the gap between electrode and membrane, the change in flow pattern depending on u_{el}^0 was also qualitatively verified. Whereas at $u_{\text{el}}^0=0$ mm s⁻¹, the flow is segregated and consists of an upward and downward flow regime, the downward flow regime disappears when the electrolyte is pumped through the electrolyzer.

Next, an Euler-Lagrangian framework developed in OpenFOAM v9 for modeling the gas-liquid flow is described in Chapter 4. Therein, the assumptions made are listed, and the algorithm used to calculate the gas-liquid flow is depicted. Next, modifications from the standard Lagrangian library from OpenFOAM v9 are described to depict the behavior of the dispersed gas bubble. In particular, the position of the injected bubbles is modified to be equal to its radius, and the implemented forces are introduced. Moreover, a dedicated algorithm is developed and implemented that distributes bubbles that intersect multiple cells according to their position and intersection lengths. Most importantly, a dedicated collision model for bubble-bubble collisions is implemented in the Lagrangian library. Here, different limiters are introduced to dampen the collision between injected and bubbles that happen to be at the injection position. Lastly, the deployed interphase coupling between the Lagrangian and Eulerian phases and the governing equations of the Eulerian phase are described. To model the mass transfer, an algorithm is developed that calculates

multi-phase mass transport alongside the dissociation reaction of the dicarboxylic acids. In closing, a procedure for calculating the residence time distribution is implemented.

The Euler-Lagrangian model is then used to successfully simulate the experimentally examined partially-transparent parallel plate electrolyzer in Chapter 5. First, in a sensitivity analysis, suitable simulation parameters are investigated. As a result, Δz was chosen to be equal to 0.4 mm allowing for a good depiction of the gradients between electrode and membrane. Further, the shortcomings of the commonly used Euler-Lagrangian models without bubble-bubble collision are depicted and the excellent prediction of the proposed model is highlighted through comparison with experimental data from Chapter 3. The simulation results are able to reasonably predict the changes in u_b^v and u_{el}^v due to variation of the operating conditions. The model highlights its capability to depict the growth of the bubble curtain along the electrode height and its breakup due to forced convection of the electrolyte or through high current densities.

Finally, the validated model is applied to study a novel prototype in three different $D_{E \rightarrow M}$ for the electrochemical pH shift crystallization of SA in the sixth Chapter. Depending on \dot{V}_{el} and i , the simulation results reveal the presence of either a segregated flow profile or a homogeneously dispersed gas phase. Besides, the present flow profile and gas phase fraction also depend on the distance between electrode and membrane. Here, the medium-sized prototype with $D_{E \rightarrow M}=8$ mm exhibits the lowest gas phase fraction and best overall performance. In addition, the Euler-Lagrangian model can also predict the key characteristics of the RTD of both electrolyte and solid phases reasonably well.

In closing, the algorithm to calculate the electrochemical reaction, mass transfer, and dissociation is applied to the 8 mm for SA, FDCA, and TA solutions. The model shows that through the impact of the gas motion, the local supersaturation is lower at $i=0.2$ A cm⁻² compared to $i=0.1$ A cm⁻². As a result of the simulation, the impact of the inadequate electrolyte's flow distribution along the width of the prototype on the supersaturation profile is illustrated. For saturated solutions containing SA at a $pH_{Inlet}=5$ and $c_{SA}=1$ mol L⁻¹, FDCA at $pH_{Inlet}=7$ and $c_{FDCA}=0.9$ mol L⁻¹, and TA at $pH_{Inlet}=7$ and $c_{TA}=0.63$ mol L⁻¹ local supersaturation of 1.4, 8, and 160 are determined for $i=0.1$ A cm⁻² and $\dot{V}_{el,in}=0.5$ L min⁻¹, respectively.

7.2. Future research question

To further develop the electrochemical pH shift crystallization towards higher technology readiness levels, different challenges have to be addressed in future works. While the current prototypes enable a steady operation to electrochemical pH shift multiple (di-)carboxylic acids, the required cell potential amounts about 10 V for $i=0.1$ A cm⁻², exceeding

the minimal potential for water-splitting electrolysis by almost one magnitude. The required cell potential dictates the operating costs of the electrochemical pH shift as it is directly proportional to the required electric energy demand. One of several options to reduce the energy demand of the electrochemical pH shift is the optimization of the electrolyte chamber geometry to generate a more uniform and faster vertical flow within the parallel plate electrolyzer. As showcased in this thesis, a faster and more homogeneous flow can significantly decrease the overall gas phase fraction and thus prevent the reduction in conductivity caused by the dielectric gas bubbles. Through the presence of large areas with stagnant flow, the fraction of the active electrode is further decreased since the local concentration gradients increase the diffusion layer and decrease the mass transport. Consequently, fewer bubbles are produced in these areas, further intensifying this effect.

To better depict the interplay of fluid dynamic and electrochemistry, the model derived in this thesis could be further extended to depict the required cell voltage based on the local concentrations, conductivity and gas phase fraction. By incorporating the interplay between fluid dynamics and electrochemistry, the model can account for the local current distribution, and the bubble can be injected based on the local current distribution. The complete model could then be used to improve the current density distribution and required cell voltage. Further, the Euler-Lagrangian simulations could be performed and directly compared to the status quo Euler-Euler modeling approach.

Appendix A.

Additional experimental settings and results

A.1. Illumination of PTV setup

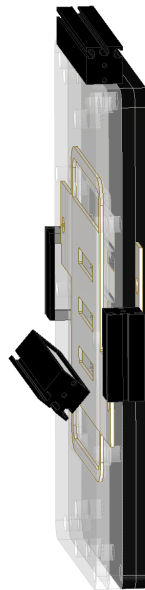


Figure A.1.: Illustration of the employed position of the LEDs for the illumination of the middle viewing panel. Depending on the studied viewing panel, the position of the front LEDs is adjusted.

A.2. Image results from the PIV measurement

8 mm gap, bottom panel and $i=0.1 \text{ A cm}^2$

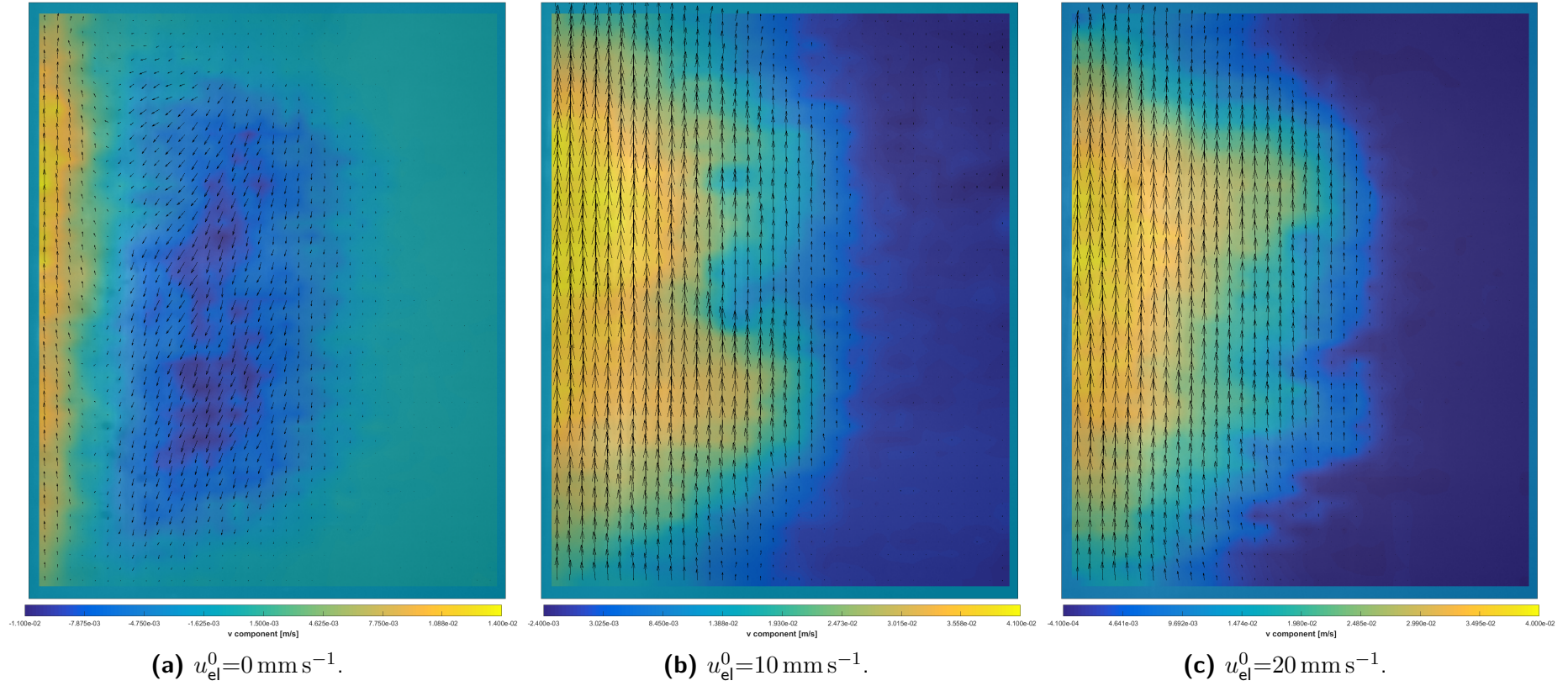


Figure A.2.: PIV measurement of electrode-membrane gap in the 8 mm prototype at $i=0.1 \text{ A cm}^{-2}$, bottom panel, and different superficial electrolyte velocities.

8 mm gap, bottom panel and $i=0.05 \text{ A cm}^{-2}$

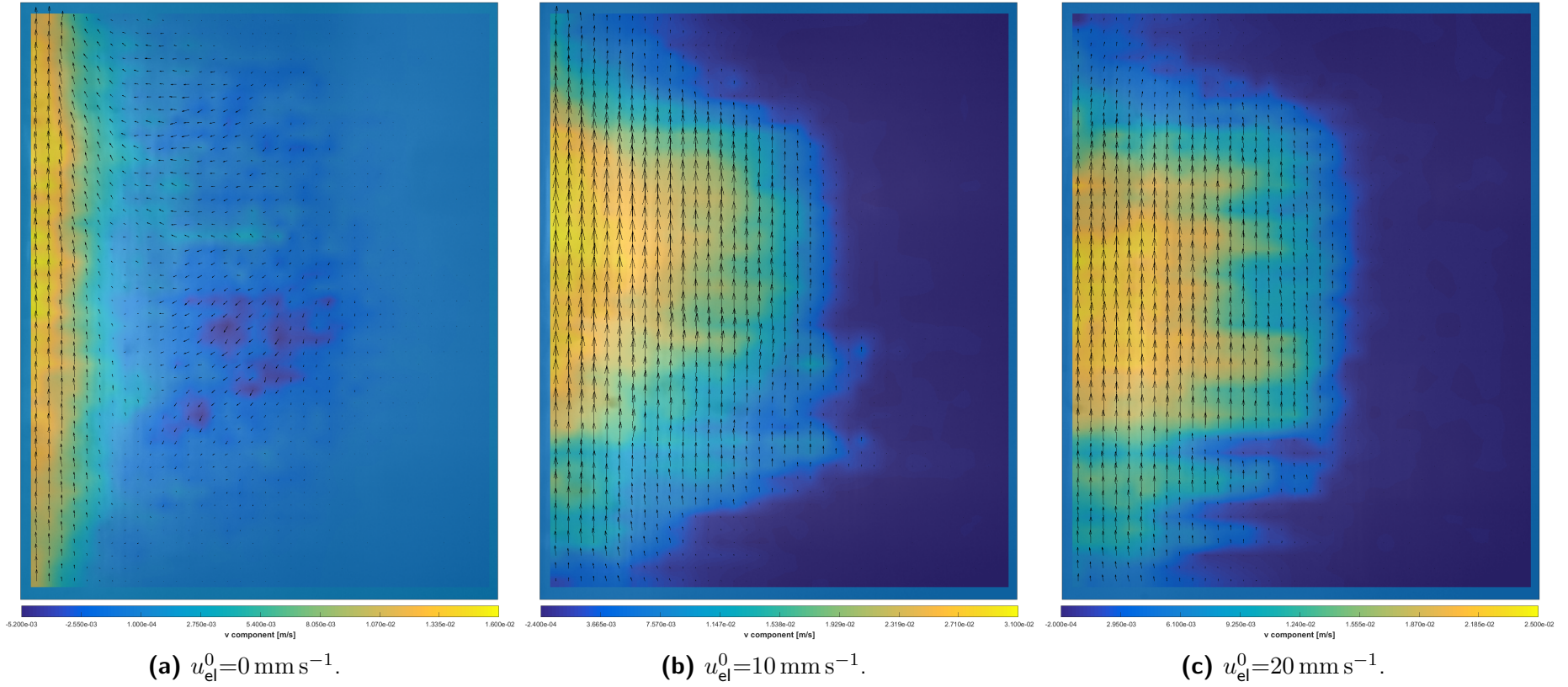


Figure A.3.: PIV measurement of electrode-membrane gap in the 8 mm prototype at $i=0.05 \text{ A cm}^{-2}$, bottom panel, and different superficial electrolyte velocities.

8 mm gap, bottom panel and $i=0.01 \text{ A cm}^2$

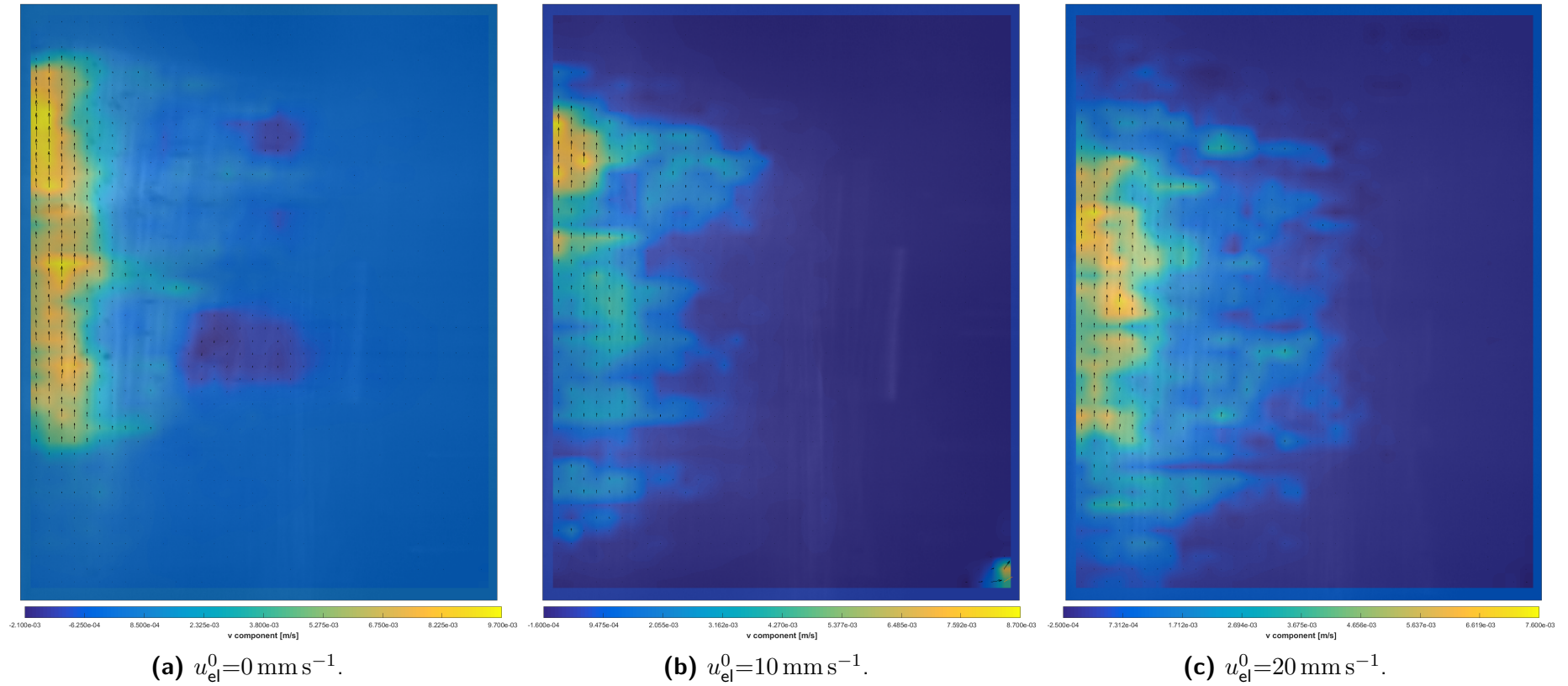


Figure A.4.: PIV measurement of electrode-membrane gap in the 8 mm prototype at $i=0.01 \text{ A cm}^{-2}$, bottom panel, and different superficial electrolyte velocities.

8 mm gap, top panel and $i=0.1 \text{ A cm}^2$

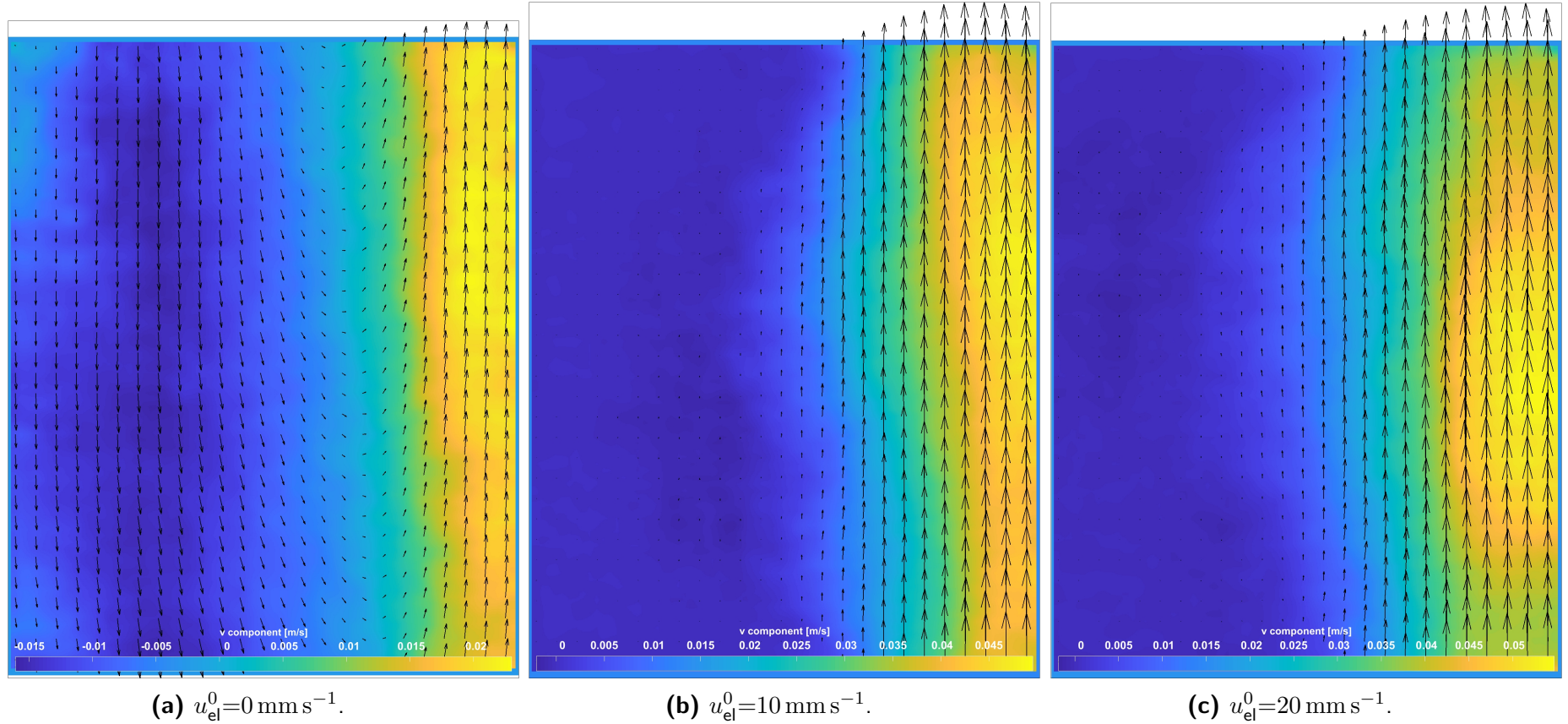


Figure A.5.: PIV measurement of electrode-membrane gap in the 8 mm prototype at $i=0.1 \text{ A cm}^{-2}$, top panel, and different superficial electrolyte velocities. The electrode is located at the right in this figure.

8 mm gap, top panel and $i=0.05 \text{ A cm}^{-2}$

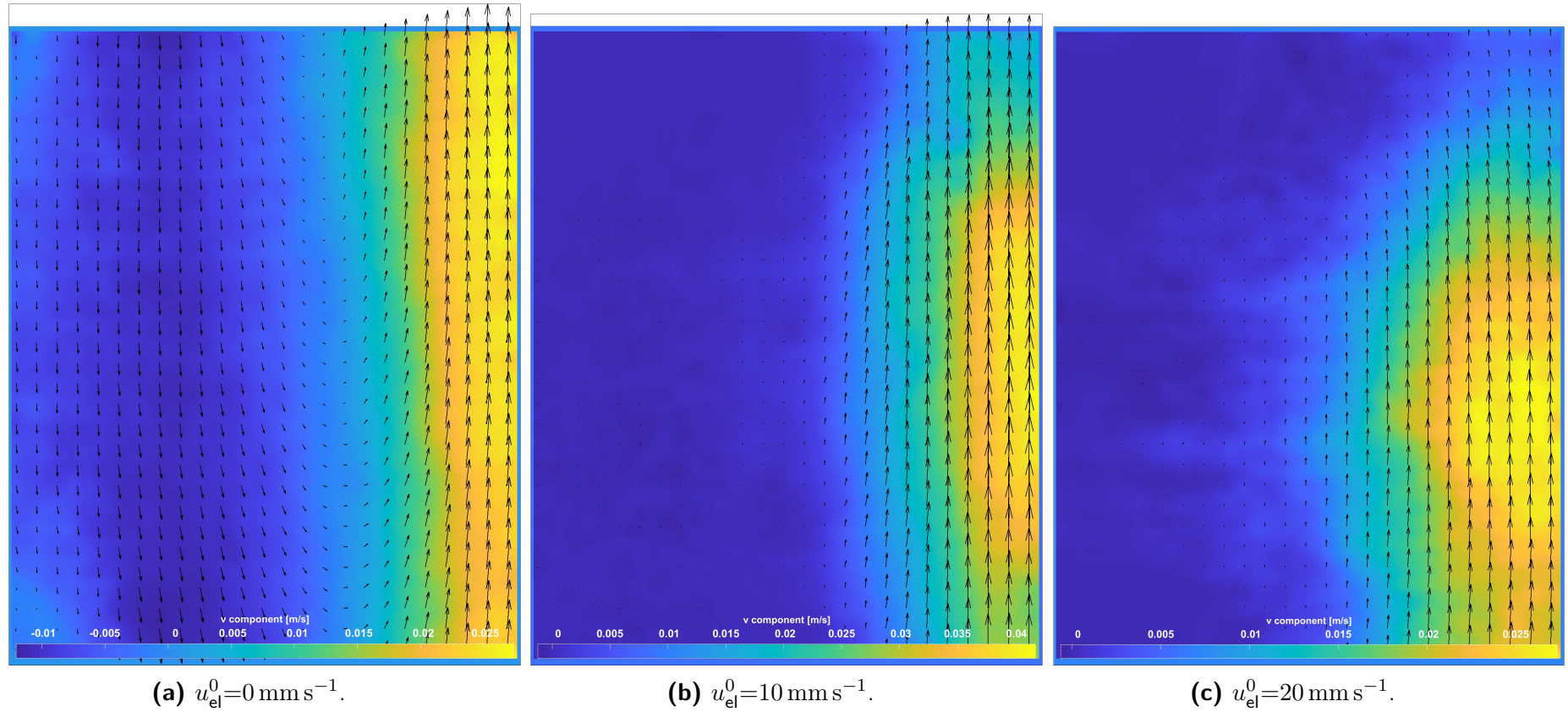


Figure A.6.: PIV measurement of electrode-membrane gap in the 8 mm prototype at $i=0.05 \text{ A cm}^{-2}$, top panel, and different superficial electrolyte velocities. The electrode is located at the right in this figure.

8 mm gap, top panel and $i=0.01 \text{ A cm}^2$

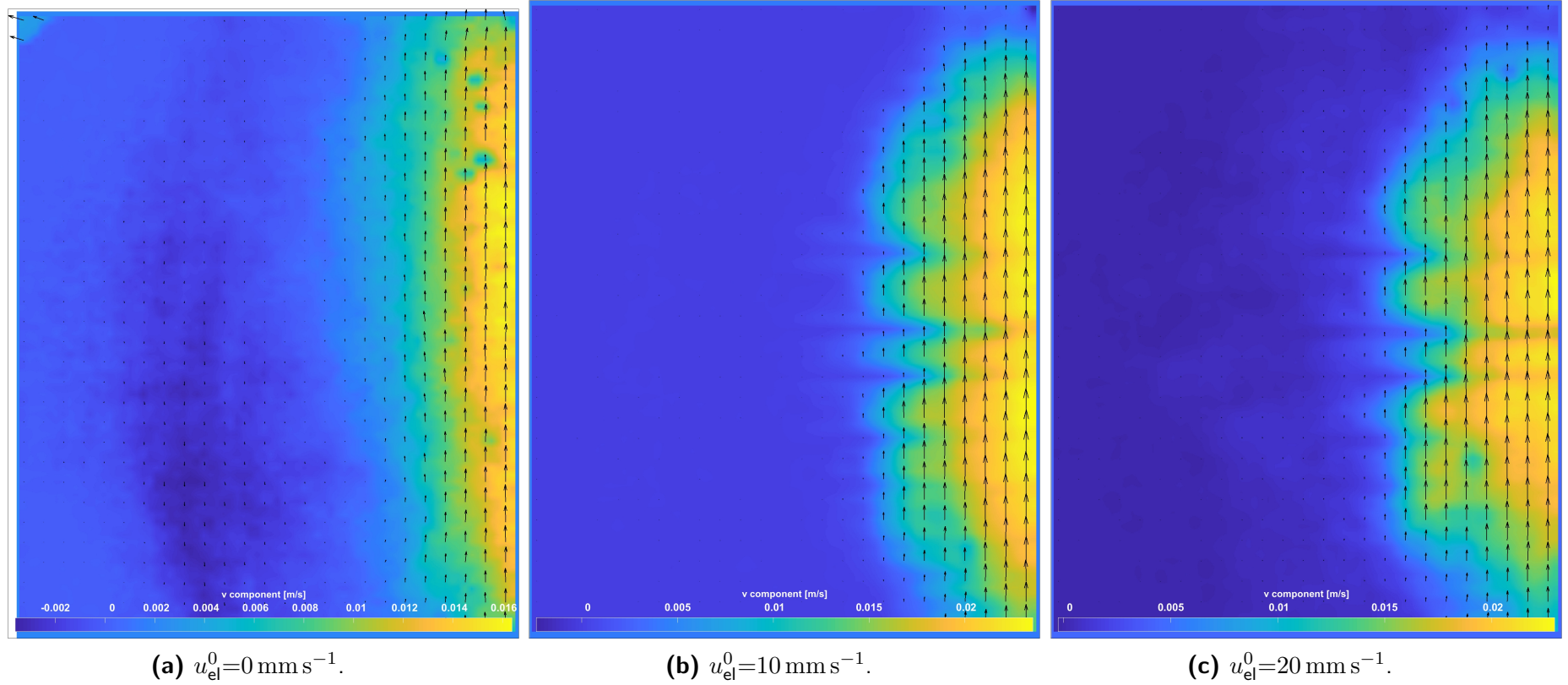


Figure A.7.: PIV measurement of electrode-membrane gap in the 8 mm prototype at $i=0.01 \text{ A cm}^{-2}$, top panel, and different superficial electrolyte velocities. The electrode is located at the right in this figure.

6 mm gap and $u_{\text{el}}^0 = 20 \text{ mm s}^{-1}$

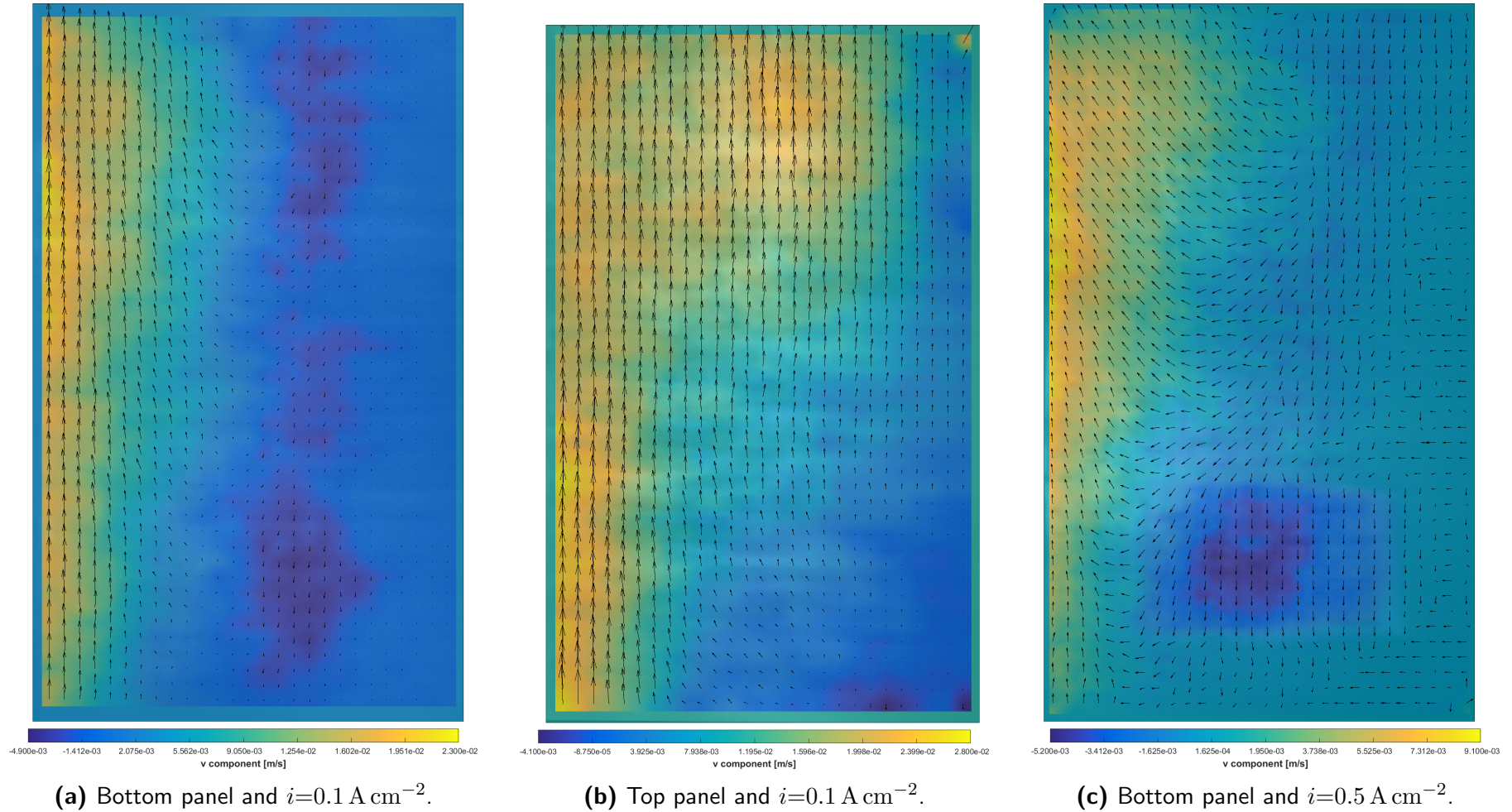


Figure A.8.: PIV measurement of electrode-membrane gap in the 6 mm prototype at NNF conditions, different current densities, and top and bottom panel.

Appendix B.

Additional simulation settings and results

B.1. Mesh description

Partially-transparent electrolyzer

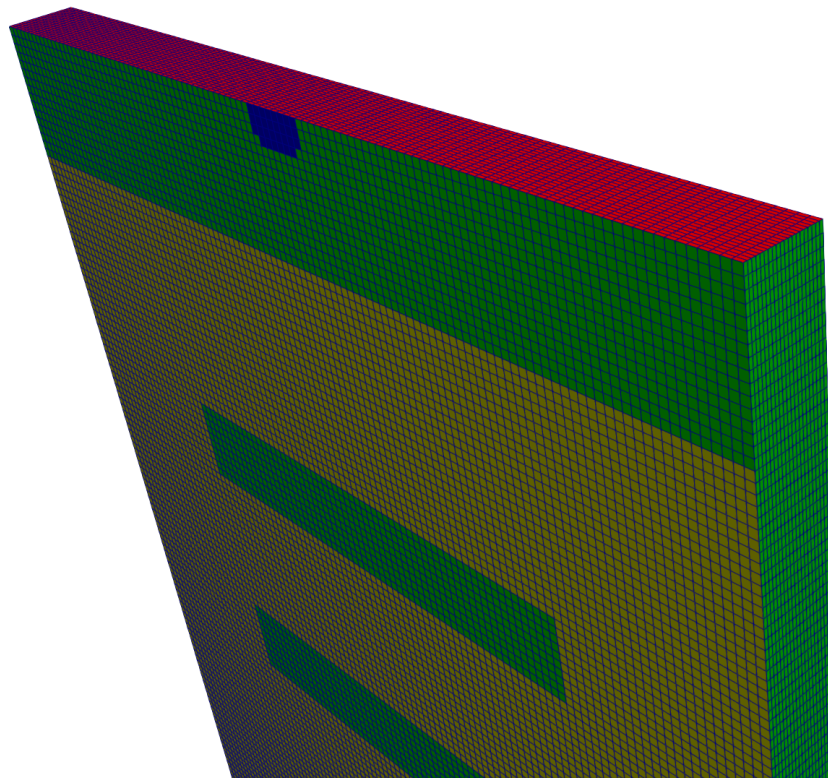


Figure B.1.: Close up of the mesh for the FC conditions. The blue, yellow, and red patches resemble the liquid outlet, electrode, and (fixed) liquid level, respectively.

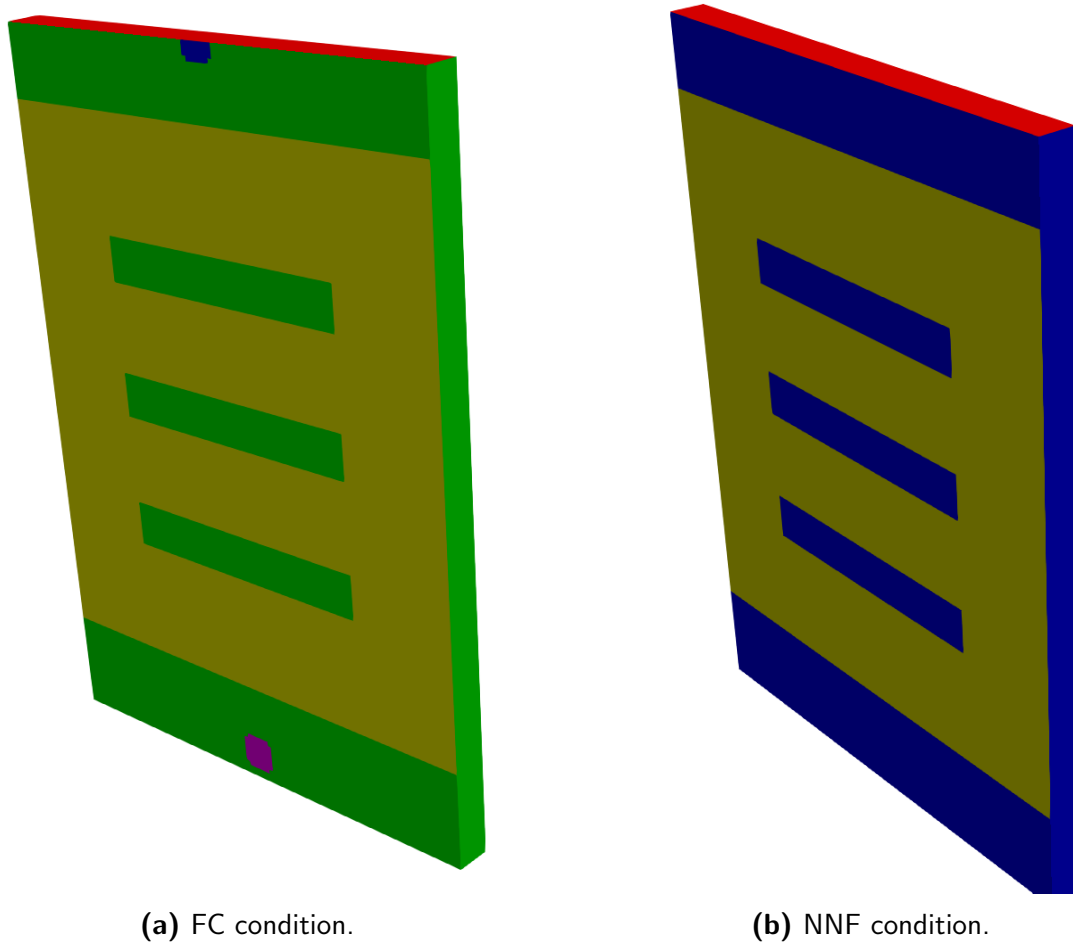
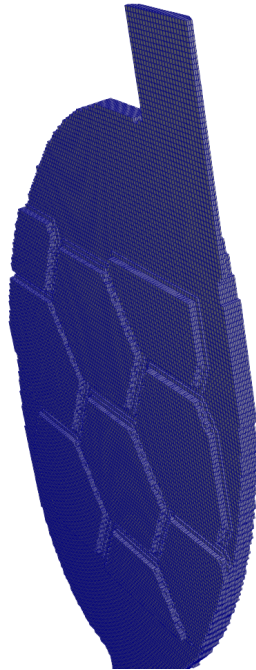
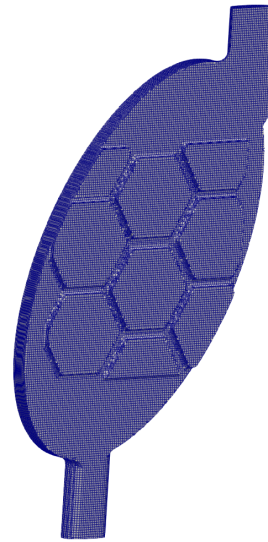


Figure B.2.: Illustration of the two meshes and geometries used for **(a)** FC and **(b)** NNF conditions. The blue, yellow, red, and pink patches resemble the liquid outlet, electrode, (fixed) liquid level, and inlet, respectively.

Electrochemical crystallizers



(a) 6 mm.



(b) 10 mm.

Figure B.3.: Meshed **(a)** 6 and **(b)** 10 mm prototype from Kocks [172] with 190,029 and 384,808 cells, respectively.

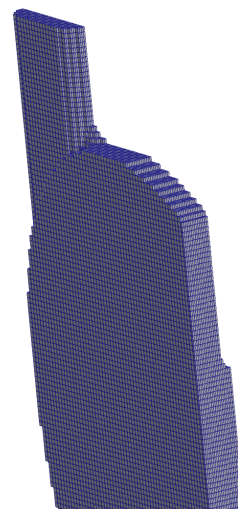
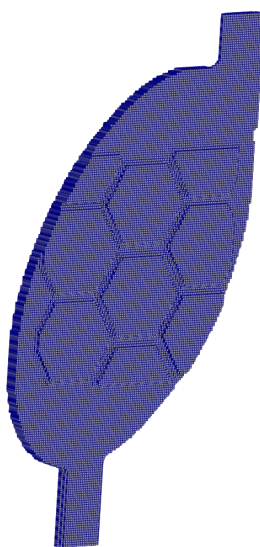


Figure B.4.: Mesh of the 8 mm prototype from Kocks [172] from with 269,055 cells

B.2. General Solver structure in OpenFOAM

As example, the solver structure of the Euler-Lagrangian solver is depicted in Figure B.5 (a). The required fields, e.g., pressure, α_{el} and cell/faceSets are initialized in *createFields.H* except the velocity field and helper fields for the calculation of the velocity. Those are introduced in *createUcF.H*. *alphaPrep.H* creates the matrices that are required for the splitting of the bubble volume inside the mesh. *pEqn.H* and *UcEqn.H* contain the algorithm for the calculation of the PIMPLE loop and *denseBubbleFoam.C* contains the main function of the solver including calculation sequence.

Figure B.5 (b) depicts the general structure of each simulation case. The folder *0* contains all the required boundary condition and initialization values. In *constant* the used mesh is stored alongside the Lagrangian settings in *cloudProperties*. The folder *system* contains three dictionaries that define the general parameter, interpolation/discretization schemes, and convergence criteria for the simulation.

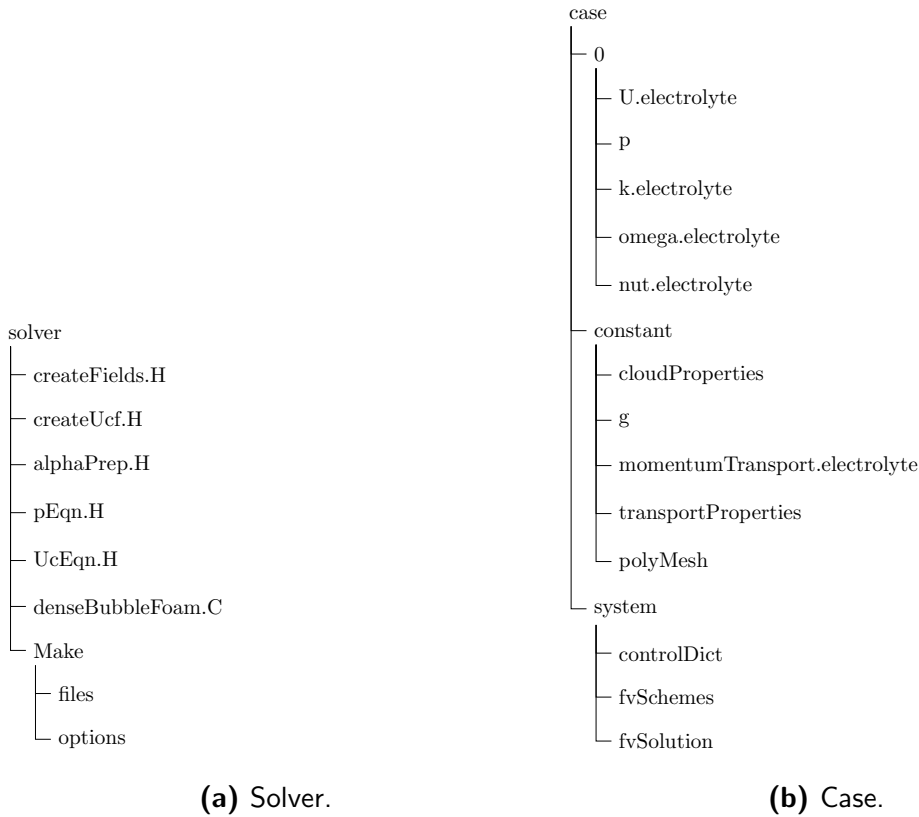


Figure B.5.: General structure of the Euler-Lagrangian (a) solver and of (b) a case.

B.3. Boundary conditions

Below in Tables B.1 and B.2 the boundary conditions for the NNF conditions of the partially transparent electrolyzer are listed. The values with * indicate that the values depend on the chosen value of \mathbf{u}_{el}^0 .

Boundary Patch	U.electrolyte		p	
	Type	Value	Type	Value
walls	noSlip	–	fixedFluxPressure	–
anode	noSlip	–	fixedFluxPressure	–
top	zeroGradient	–	fixedValue	0
bottom	fixedValue	(0 0 0)*	fixedFluxPressure	–

Table B.1.: Boundary conditions for \mathbf{u} and pressure p .

Boundary Patch	k.electrolyte		omega.electrolyte		nut.electrolyte	
	Type	Value	Type	Value	Type	Value
walls	fixedValue	1e-12	omegaWallFunction	1e9	nutWallFunction	0
anode	fixedValue	1e-12	omegaWallFunction	1e9	nutWallFunction	0
top	zeroGradient	–	zeroGradient	–	calculated	–
bottom	inletOutlet	1.5e-4*	inletOutlet	2e-4*	calculated	–

Table B.2.: Boundary conditions for k , ω , and ν_t .

B.4. Flow profiles of the prototypes in the xy and zy -plane

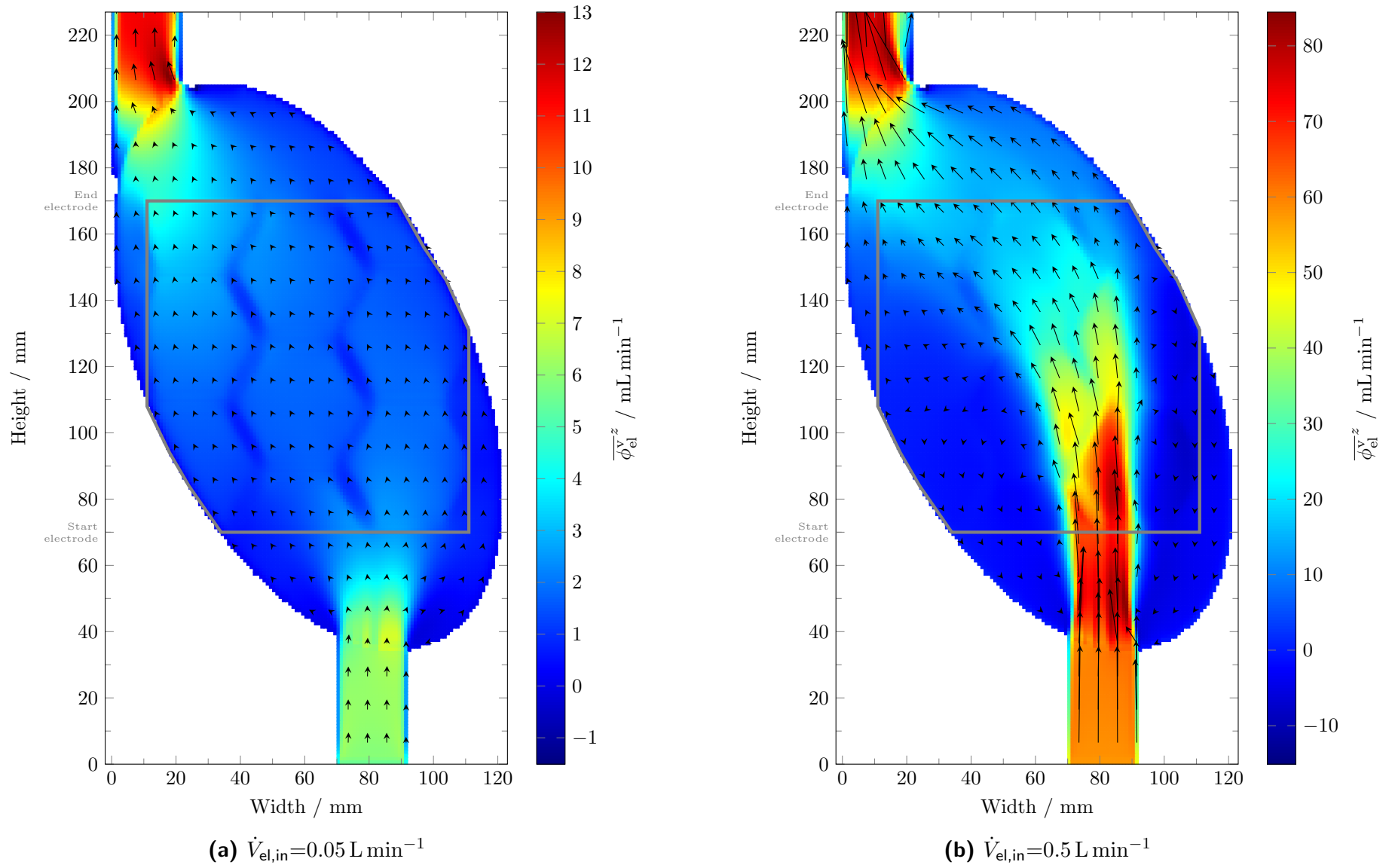


Figure B.6.: $\overline{\phi_{\text{el}}^{\text{v},z}}$, and direction of flow in the $D_{\text{E} \rightarrow \text{M}}=6 \text{ mm}$ prototype at $i=0 \text{ A cm}^{-2}$ and $\dot{V}_{\text{el},\text{in}}=0.05$ (a), and 0.5 L min^{-1} (b) in the xy -plane.

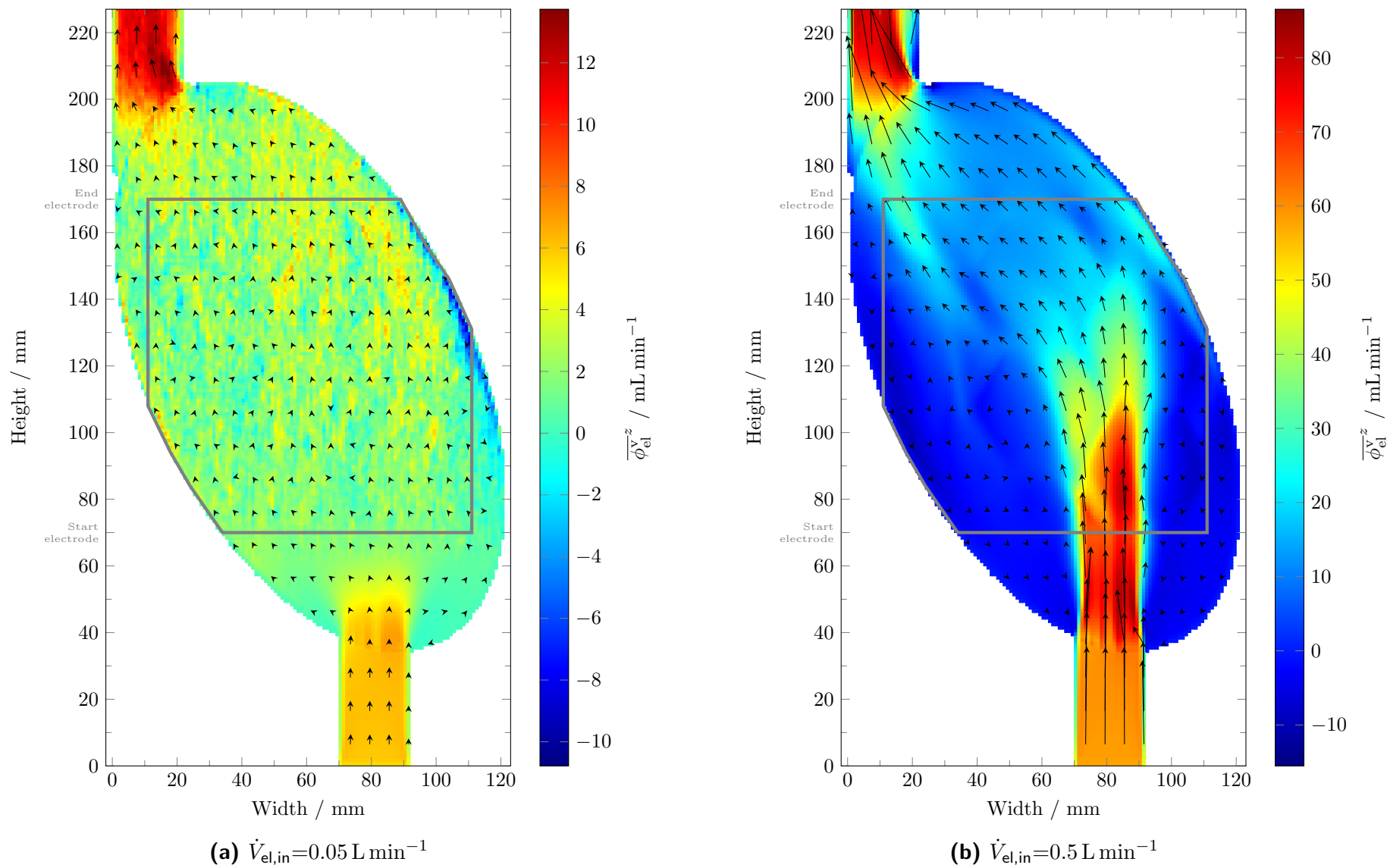


Figure B.7.: $\overline{\phi_{el}^{v,z}}$, and direction of flow in the $D_{E \rightarrow M}=6 \text{ mm}$ prototype at $i=0.01 \text{ A cm}^{-2}$ and **(a)** $\dot{V}_{el,in}=0.05$, and **(b)** 0.5 L min^{-1} in the xy -plane.

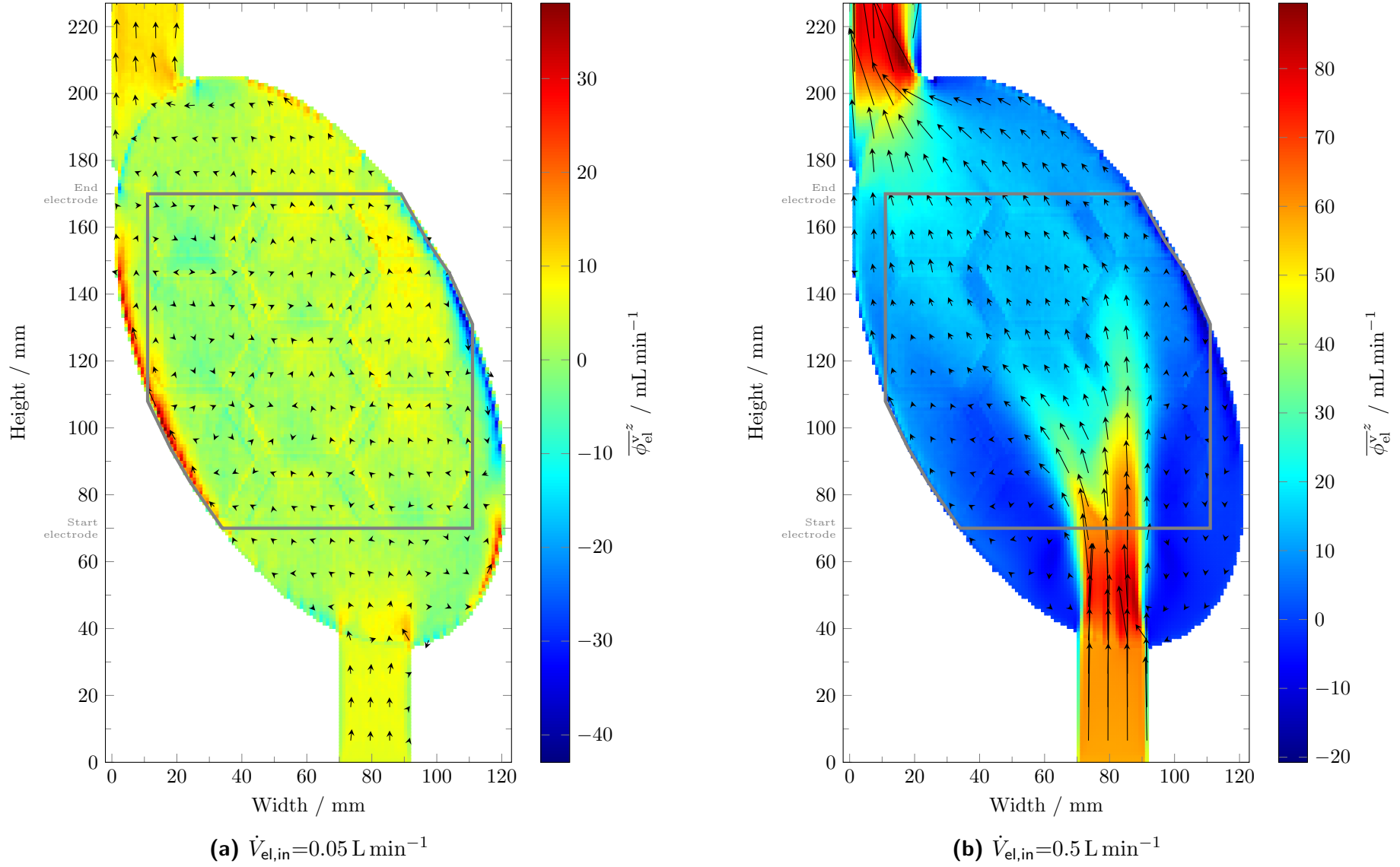
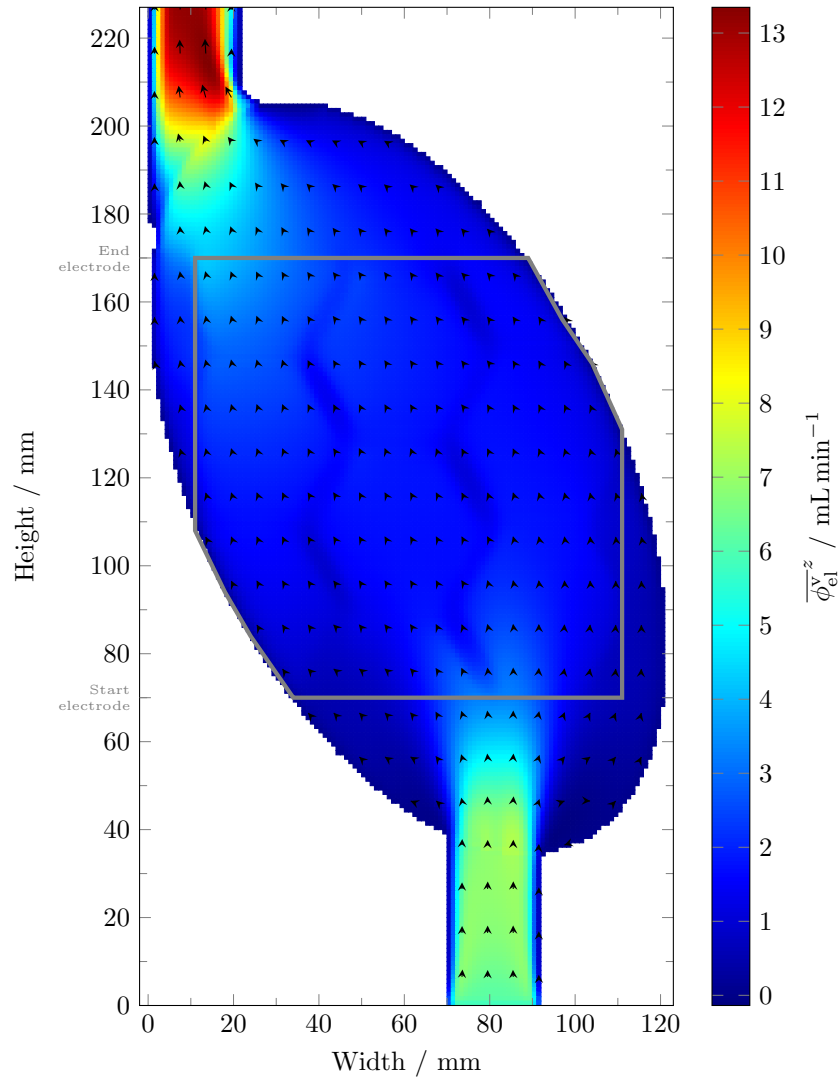
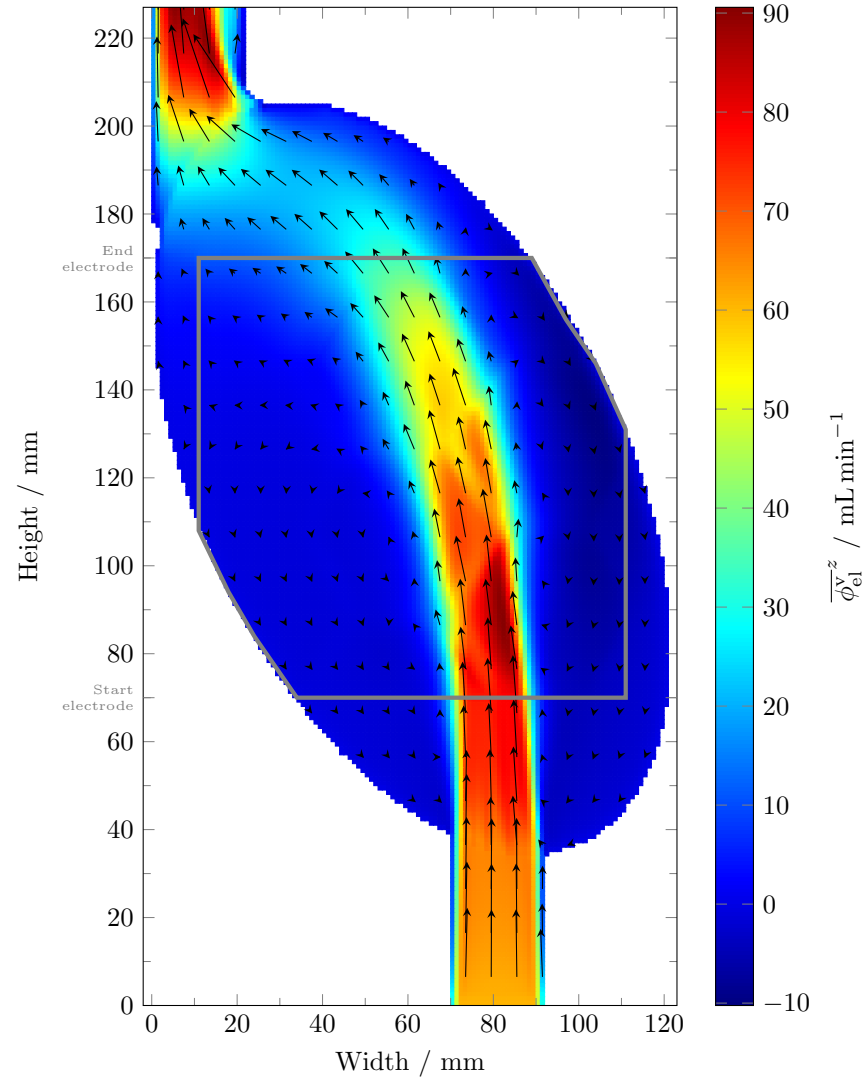


Figure B.8.: $\overline{\phi_{\text{el}}^{\text{V}z}}$, and direction of flow in the $D_{\text{E} \rightarrow \text{M}}=6 \text{ mm}$ prototype at $i=0.1 \text{ A cm}^{-2}$ and **(a)** $\dot{V}_{\text{el,in}}=0.05$, and **(b)** 0.5 L min^{-1} in the xy -plane.



(a) $\dot{V}_{\text{el},\text{in}}=0.05 \text{ L min}^{-1}$



(b) $\dot{V}_{\text{el},\text{in}}=0.5 \text{ L min}^{-1}$

Figure B.9.: $\overline{\phi_{\text{el}}^v}^z$, and direction of flow in the $D_{\text{E} \rightarrow \text{M}}=8 \text{ mm}$ prototype at $i=0 \text{ A cm}^{-2}$ and (a) $\dot{V}_{\text{el},\text{in}}=0.05$, and (b) 0.5 L min^{-1} in the xy -plane.

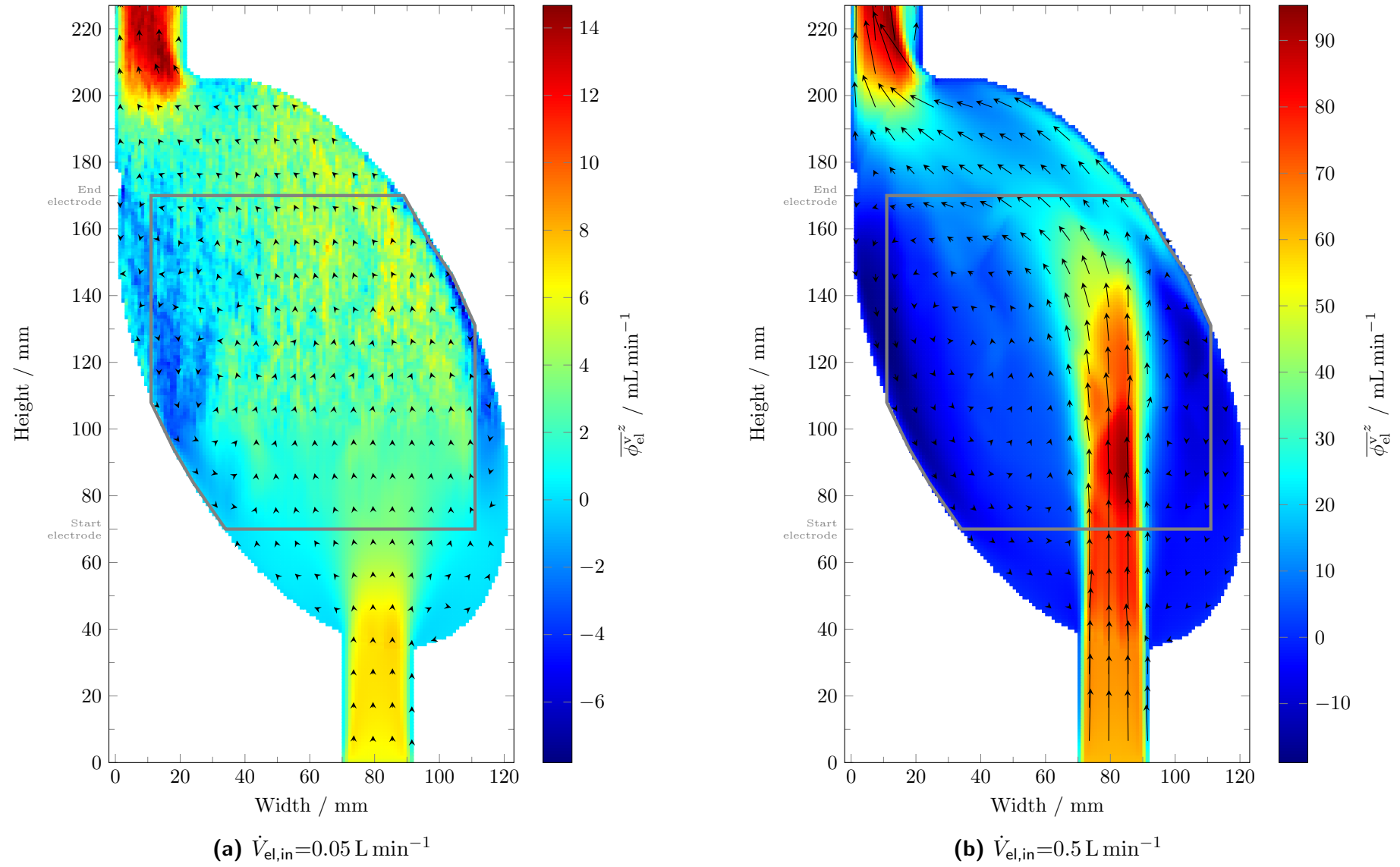
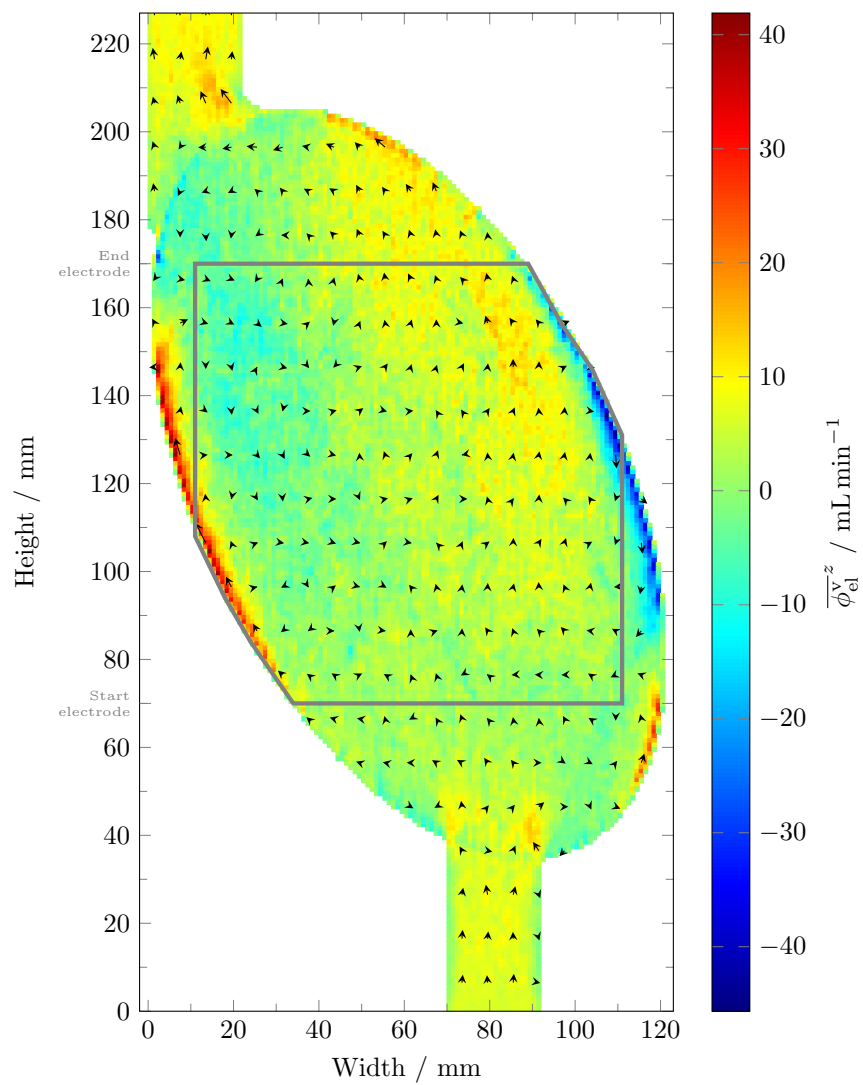
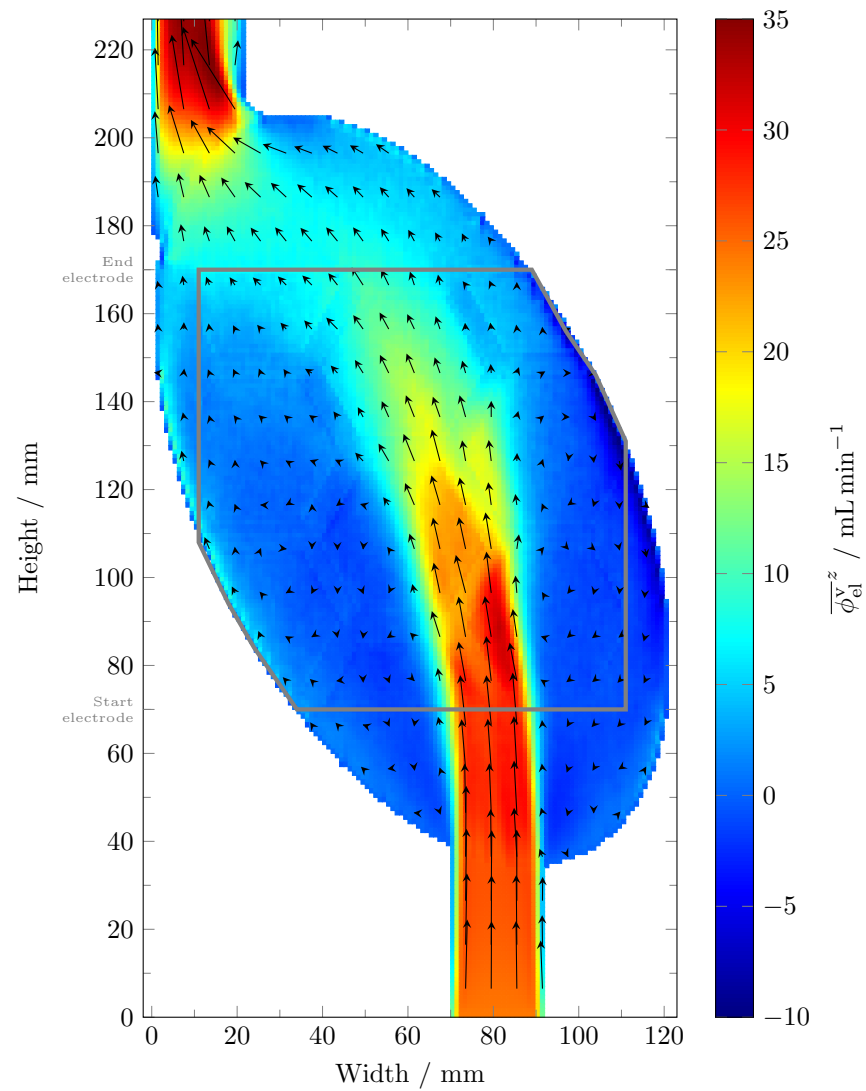


Figure B.10.: $\overline{\phi_{\text{el}}^{\text{v},z}}$, and direction of flow in the $D_{\text{E} \rightarrow \text{M}}=8 \text{ mm}$ prototype at $i=0.01 \text{ A cm}^{-2}$ and **(a)** $\dot{V}_{\text{el},\text{in}}=0.05$, and **(b)** 0.5 L min^{-1} in the xy -plane.



(a) $\dot{V}_{\text{el,in}}=0.05 \text{ L min}^{-1}$



(b) $\dot{V}_{\text{el,in}}=0.5 \text{ L min}^{-1}$

Figure B.11.: $\overline{\phi_{\text{el}}^{v,z}}$, and direction of flow in the $D_{\text{E} \rightarrow \text{M}}=8 \text{ mm}$ prototype at $i=0.1 \text{ A cm}^{-2}$ and **(a)** $\dot{V}_{\text{el,in}}=0.05$, and **(b)** 0.5 L min^{-1} in the xy -plane.

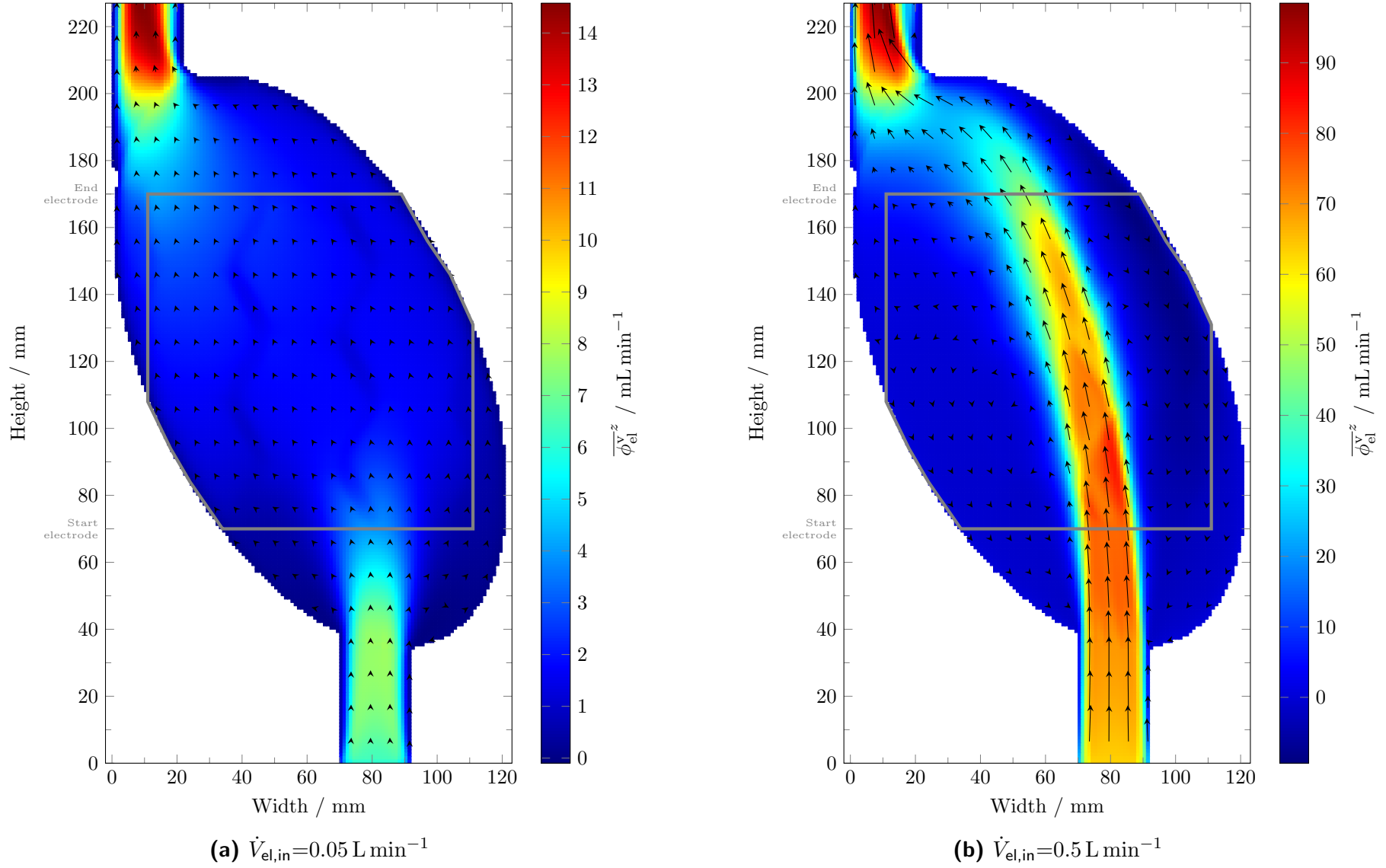


Figure B.12.: $\overline{\phi_{\text{el}}^{v,z}}$, and direction of flow in the $D_{\text{E} \rightarrow \text{M}} = 10 \text{ mm}$ prototype at $i = 0 \text{ A cm}^{-2}$ and (a) $\dot{V}_{\text{el,in}} = 0.05$, and (b) 0.5 L min^{-1} in the xy -plane.

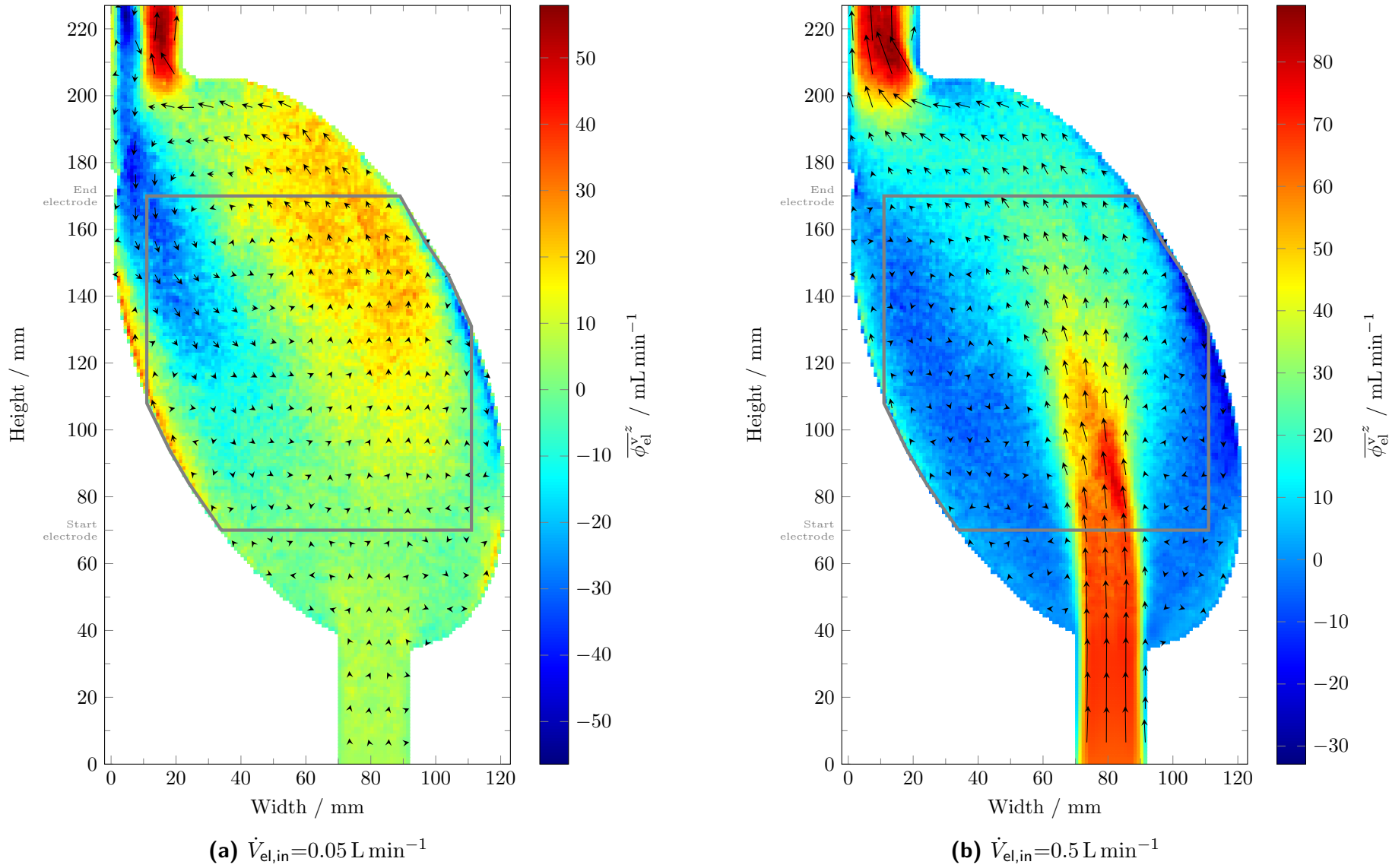


Figure B.13.: $\overline{\phi_{\text{el}}^{\text{v},z}}$, and direction of flow in the $D_{\text{E} \rightarrow \text{M}}=10 \text{ mm}$ prototype at $i=0.01 \text{ A cm}^{-2}$ and **(a)** $\dot{V}_{\text{el},\text{in}}=0.05$, and **(b)** 0.5 L min^{-1} in the xy -plane.

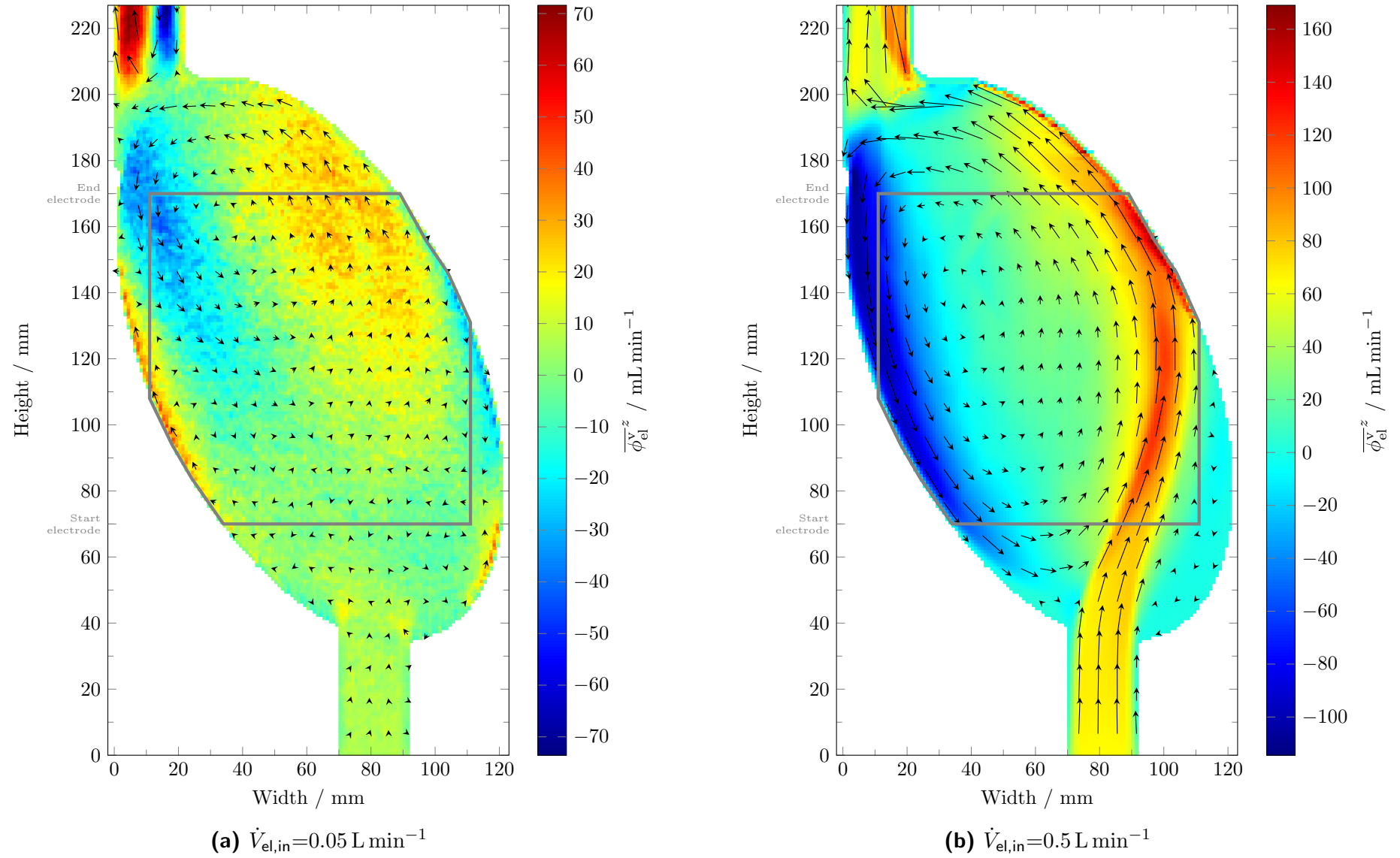


Figure B.14.: $\overline{\phi_{\text{el}}^{\text{v},z}}$, and direction of flow in the $D_{\text{E} \rightarrow \text{M}}=10 \text{ mm}$ prototype at $i=0.1 \text{ A cm}^{-2}$ and (a) $\dot{V}_{\text{el},\text{in}}=0.05$, and (b) 0.5 L min^{-1} in the xy -plane.

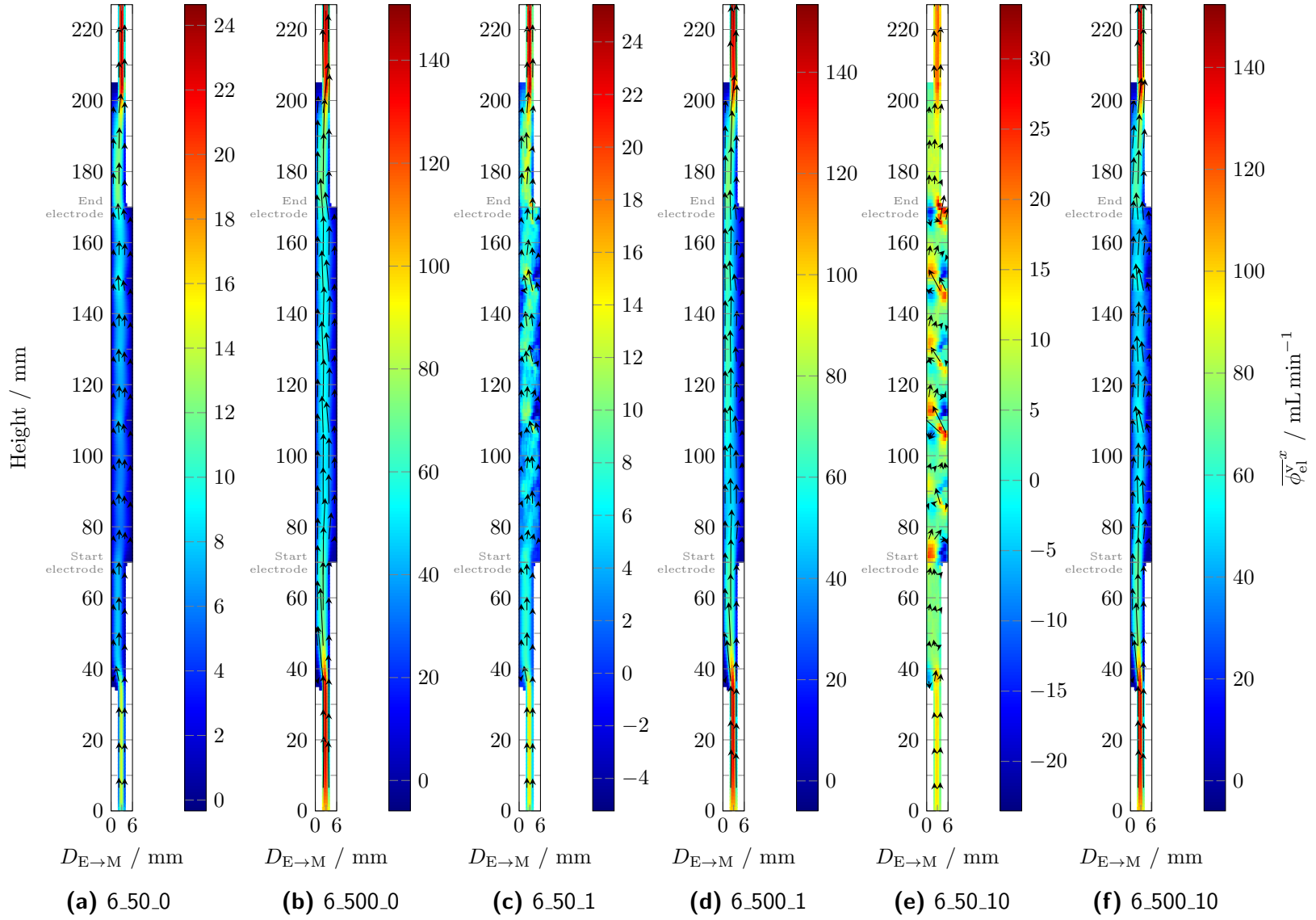


Figure B.15.: $\overline{\phi_{\text{el}}^v}^x$, and direction of flow in the $D_{E \rightarrow M}=10$ mm prototype for different simulation cases in the zy -plane.

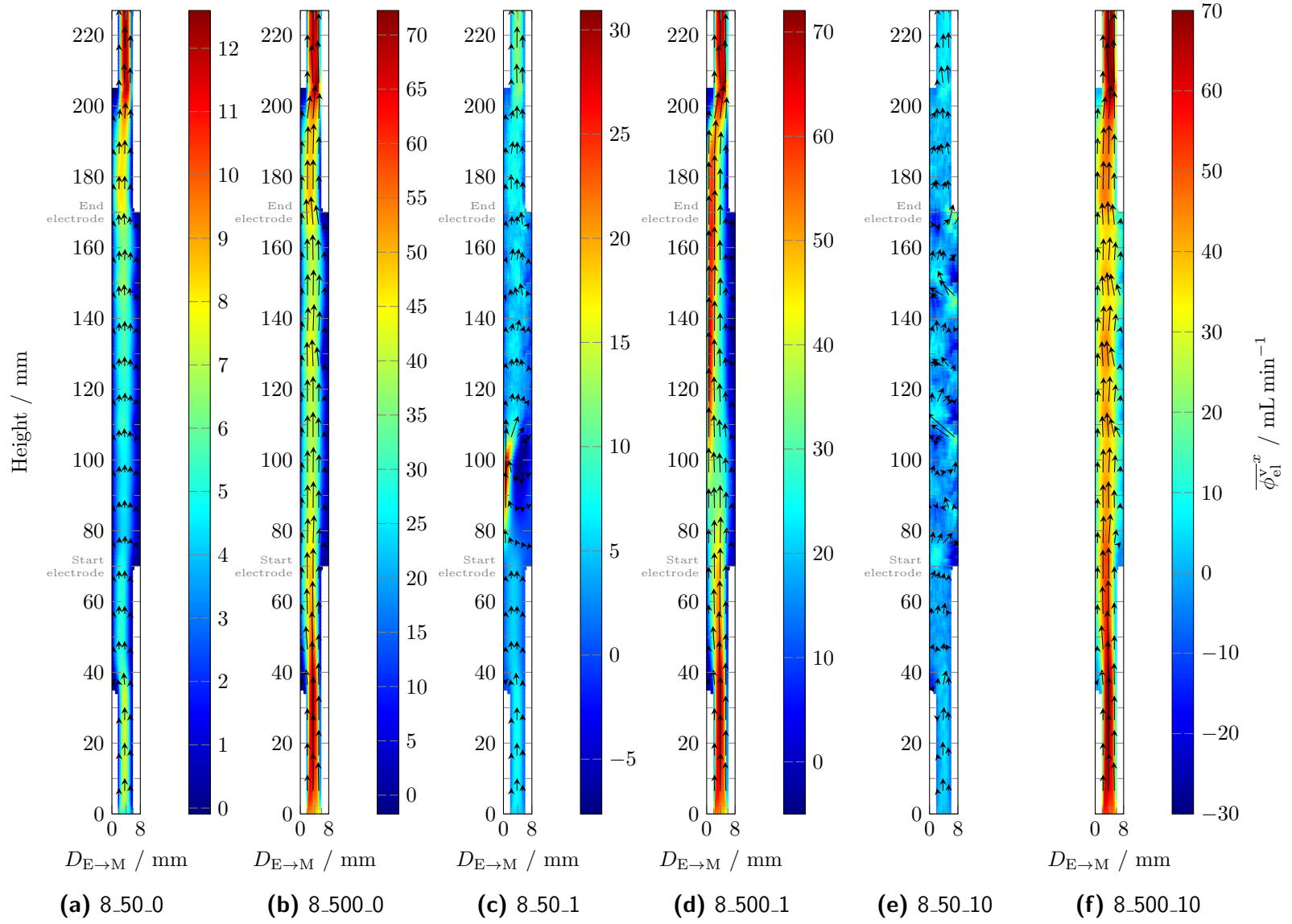


Figure B.16.: $\overline{\phi_{\text{el}}^{v,x}}$, and direction of flow in the $D_{E \rightarrow M} = 10$ mm prototype for different simulation cases in the zy -plane.

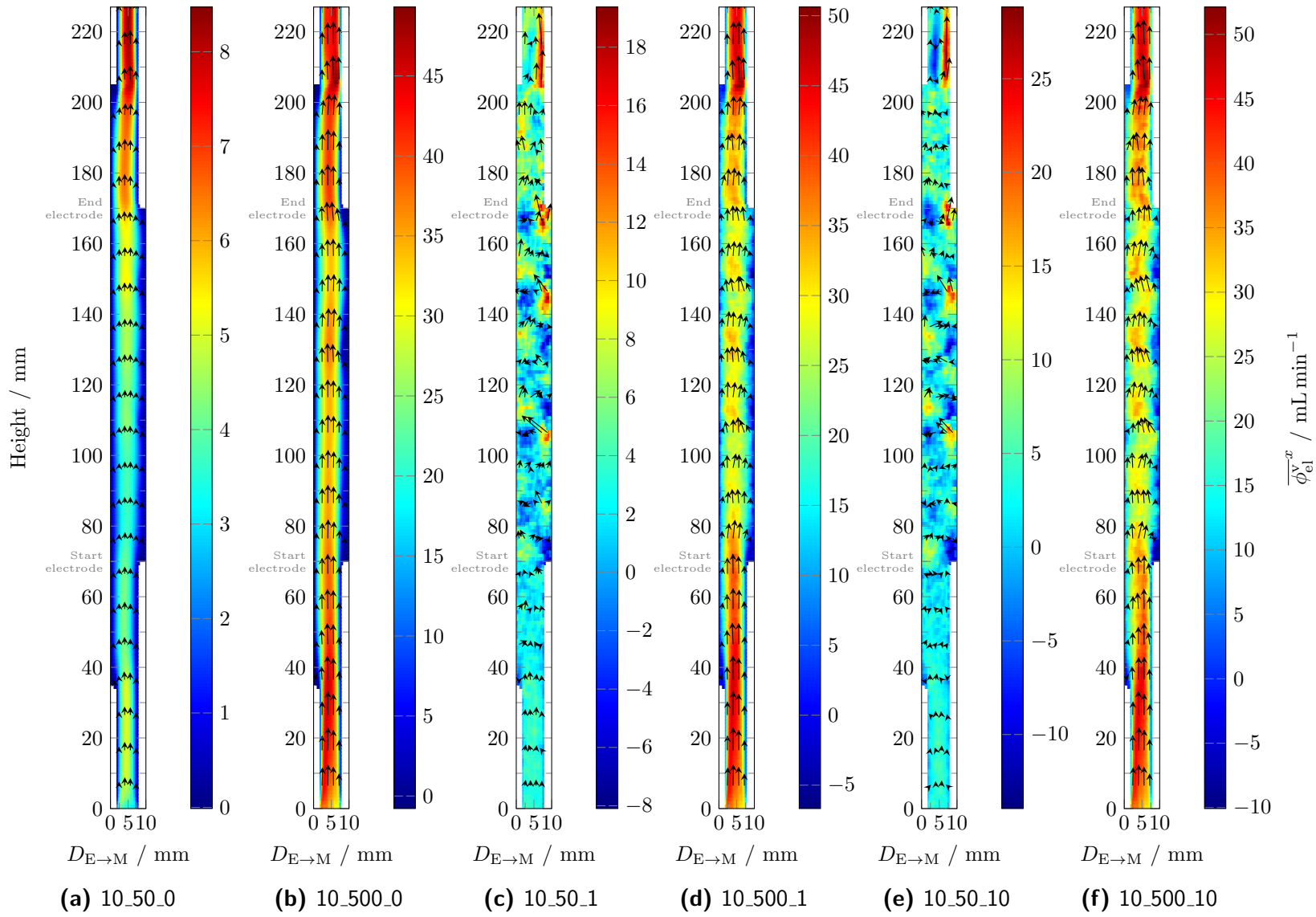


Figure B.17.: $\overline{\phi_{\text{el}}^v}^x$, and direction of flow in the $D_{E \rightarrow M}=10$ mm prototype for different simulation cases in the zy -plane.

B.5. Miscellaneous simulation settings results

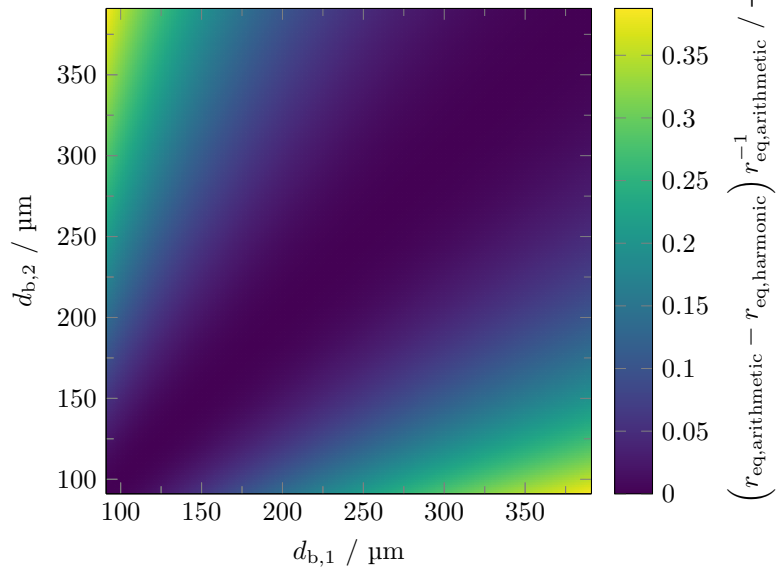


Figure B.18.: Comparison of the difference between harmonic and arithmetic mean for the calculateion of r_{eq} .

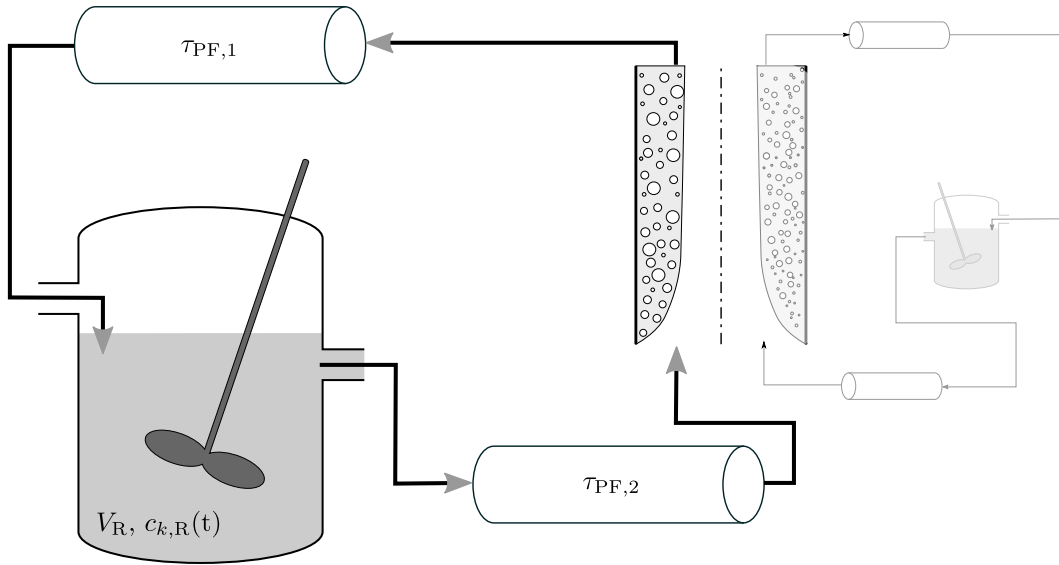


Figure B.19.: Reactor network of the simulation domain for the multi-pass electrochemical crystallization experiments from Kocks et al. [17] in the 8 mm prototype.

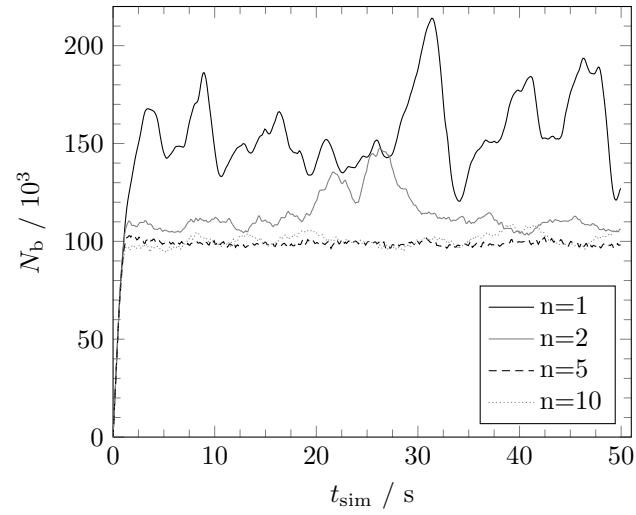


Figure B.20.: Comparison of the number of bubbles over the simulation time of 50 s for $n_b=1$, 2, 5, and 10.

B.6. pH profiles of the 8 mm prototype

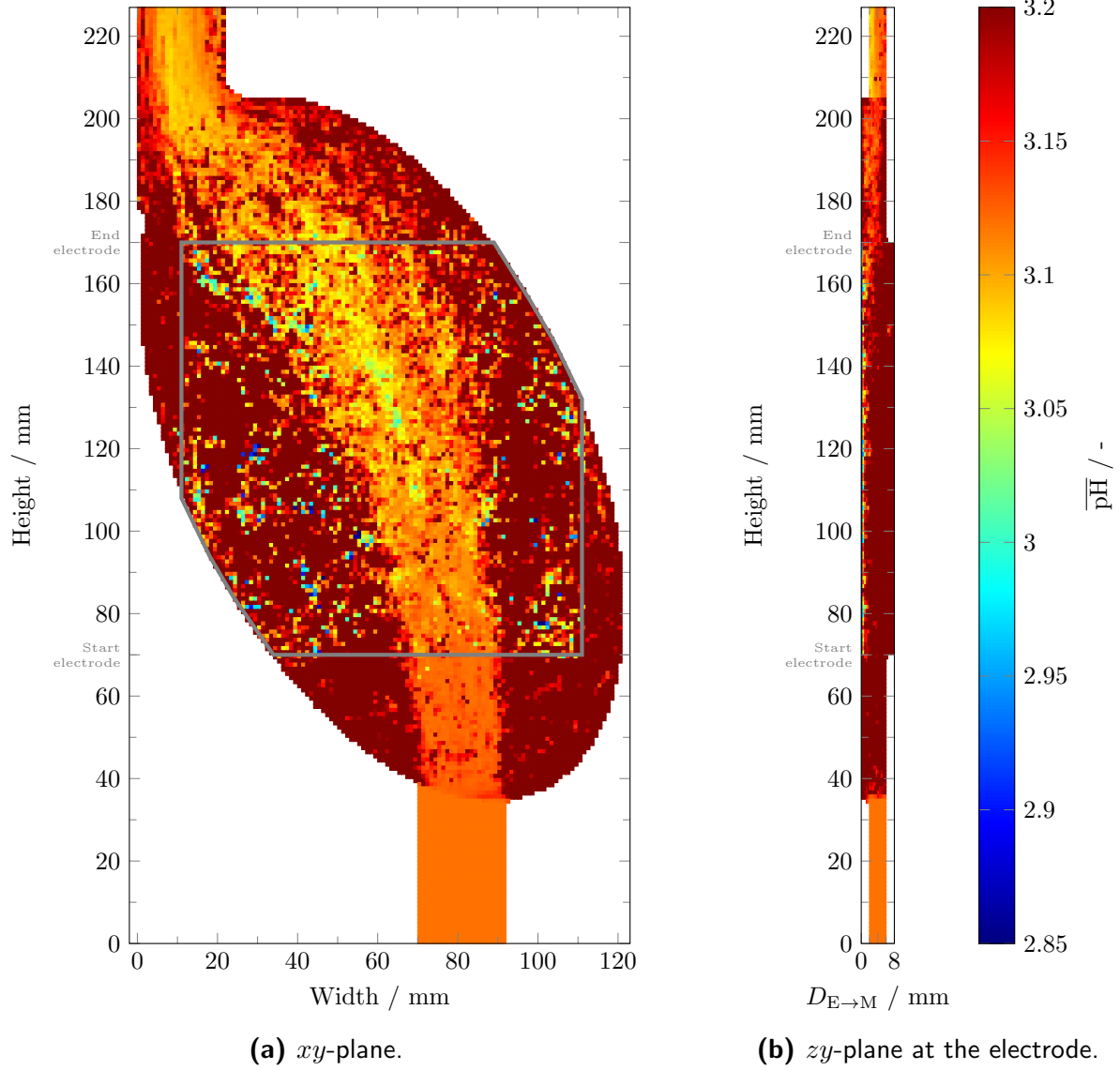


Figure B.21.: (a) \overline{pH}^z , and (b) \overline{pH}^x of the electrochemical crystallization of SA in the $D_{E \rightarrow M} = 8$ mm prototype at $i = 0.1 \text{ A cm}^{-2}$, $\dot{V}_{el} = 0.5 \text{ L min}^{-1}$, $c_{SA} = 1 \text{ mol L}^{-1}$, and $\text{pH}_{inlet} = 3.2$ after an electric charge of 1 kC.

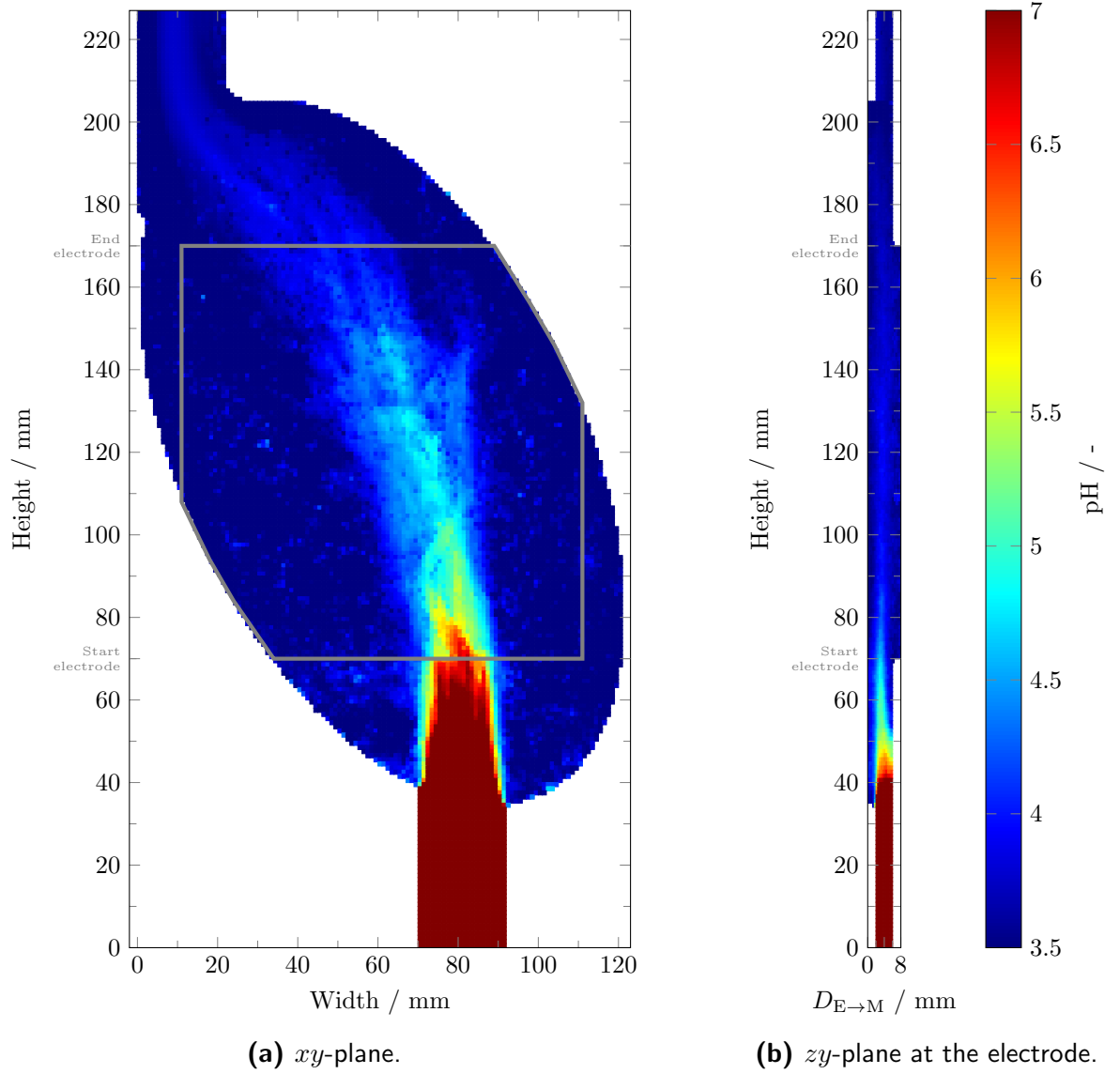


Figure B.22.: (a) $\overline{\text{pH}}^z$, and (b) $\overline{\text{pH}}^x$ of the electrochemical crystallization of FDCA in the $D_{E \rightarrow M}=8$ mm prototype at $i=0.1 \text{ A cm}^{-2}$, $\dot{V}_{\text{el}}=0.5 \text{ L min}^{-1}$, $c_{\text{FDCA}}=0.9 \text{ mol L}^{-1}$, and $\text{pH}_{\text{Inlet}}=7$ after an electric charge of 1 kC.

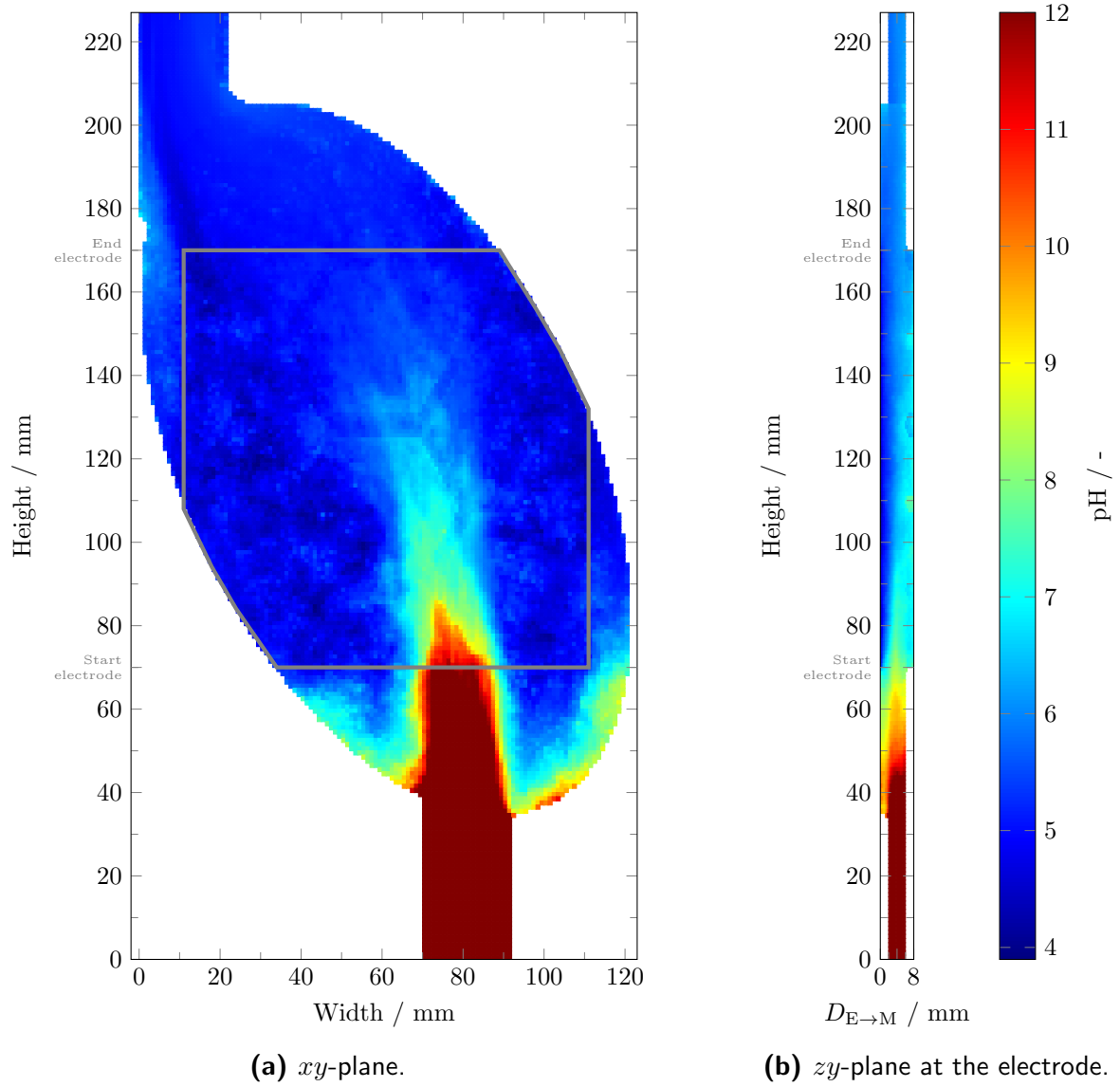


Figure B.23.: (a) $\overline{\text{pH}}^z$, and (b) $\overline{\text{pH}}^x$ of the electrochemical crystallization of FDCA in the $D_{E \rightarrow M}=8$ mm prototype at $i=0.1 \text{ A cm}^{-2}$, $\dot{V}_{\text{el}}=0.5 \text{ L min}^{-1}$, $c_{\text{FDCA}}=0.9 \text{ mol L}^{-1}$, and $\text{pH}_{\text{Inlet}}=12$ after an electric charge of 1 kC.

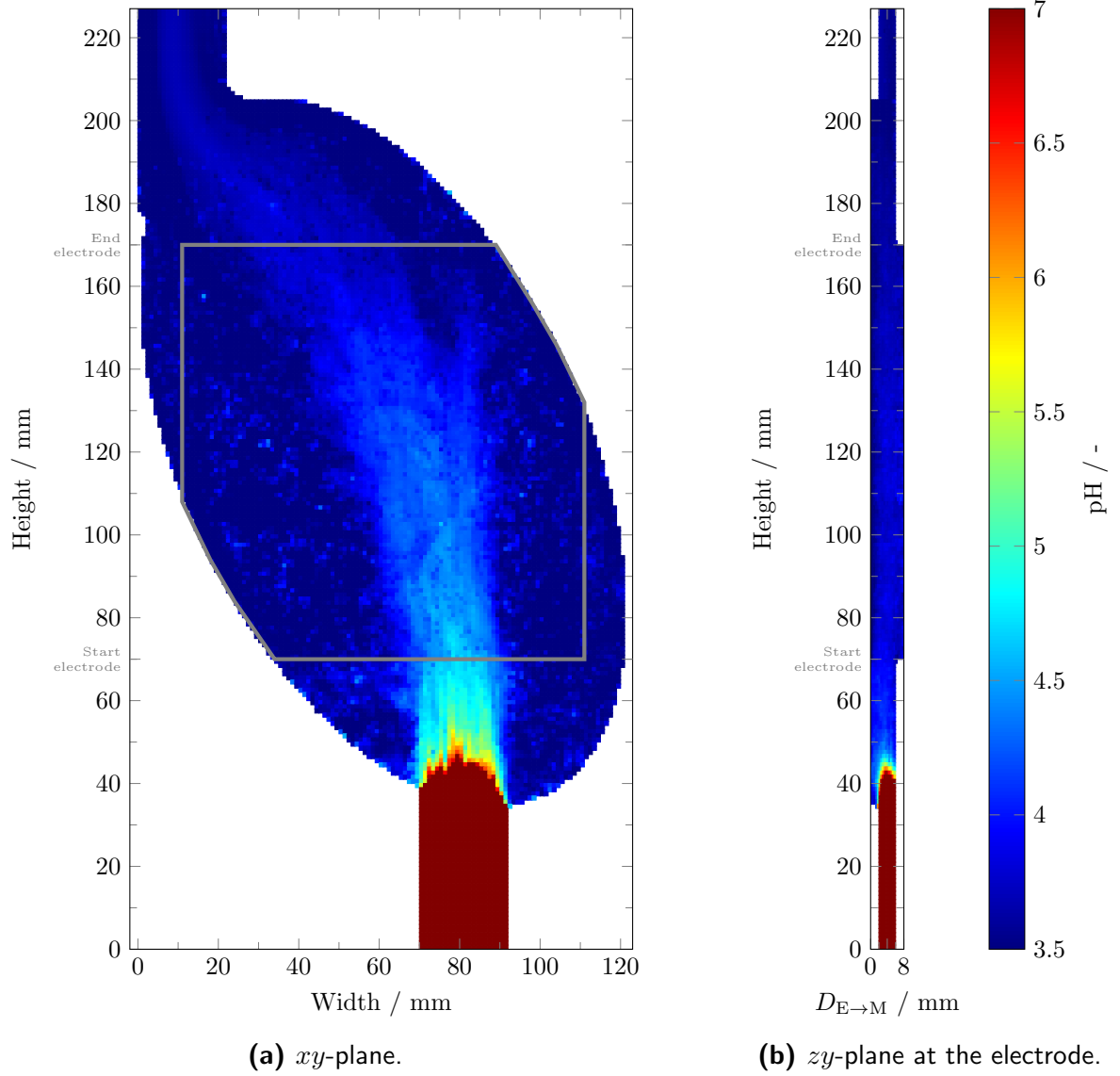


Figure B.24.: (a) $\overline{\text{pH}}^z$, and (b) $\overline{\text{pH}}^x$ of the electrochemical crystallization of TA in the $D_{E→M}=8$ mm prototype at $i=0.1 \text{ A cm}^{-2}$, $\dot{V}_{\text{el}}=0.5 \text{ L min}^{-1}$, $c_{\text{TA}}=0.63 \text{ mol L}^{-1}$, and $\text{pH}_{\text{Inlet}}=7$ after an electric charge of 1 kC.

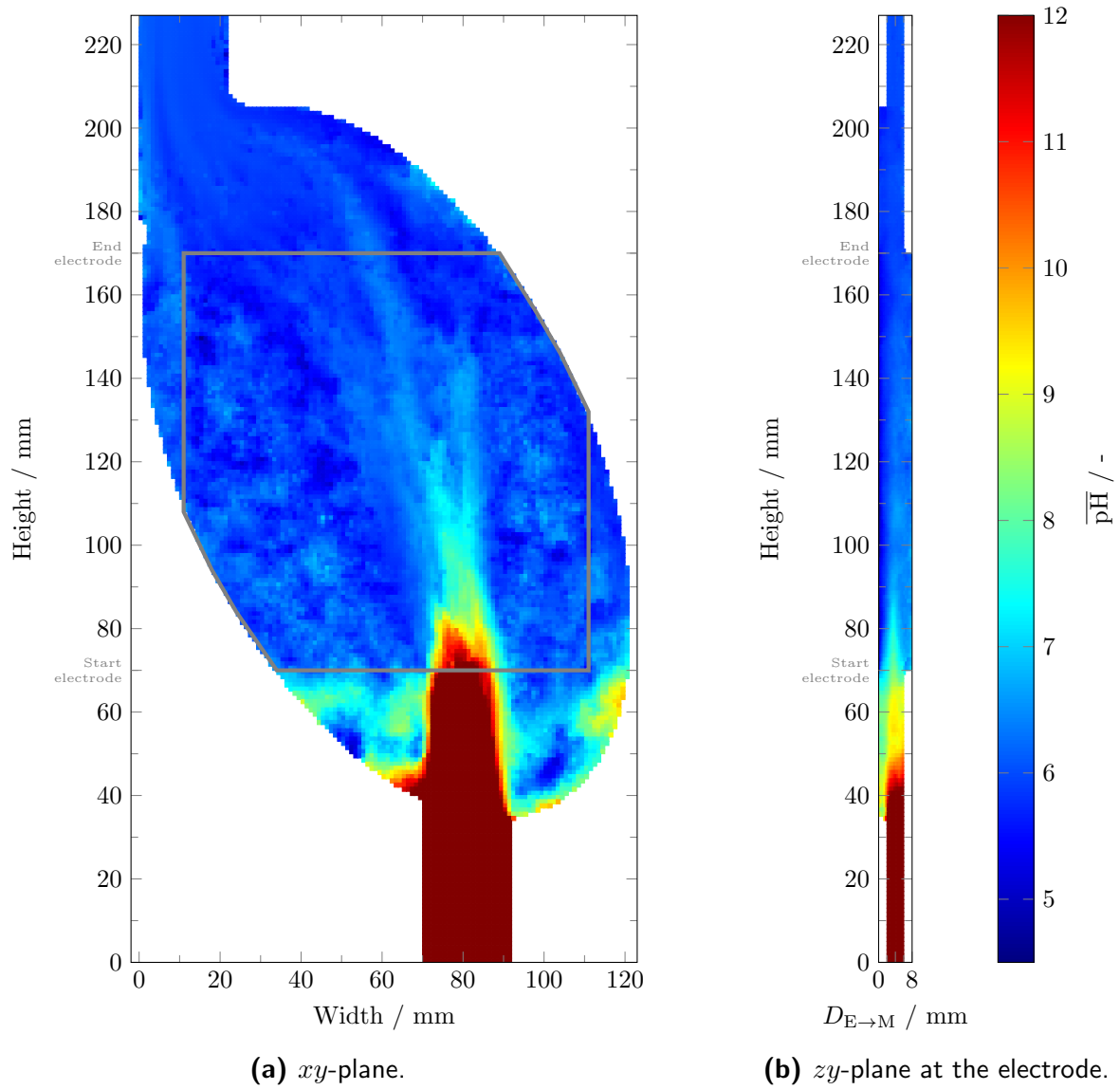


Figure B.25.: (a) $\overline{\text{pH}}^z$, and (b) $\overline{\text{pH}}^x$ of the electrochemical crystallization of TA in the $D_{E \rightarrow M}=8$ mm prototype at $i=0.1$ A cm $^{-2}$, $\dot{V}_{\text{el}}=0.5$ L min $^{-1}$, $c_{\text{TA}}=0.63$ mol L $^{-1}$, and $\text{pH}_{\text{Inlet}}=12$ after an electric charge of 1 kC.

B.7. Oversaturation profiles of the 8 mm prototype

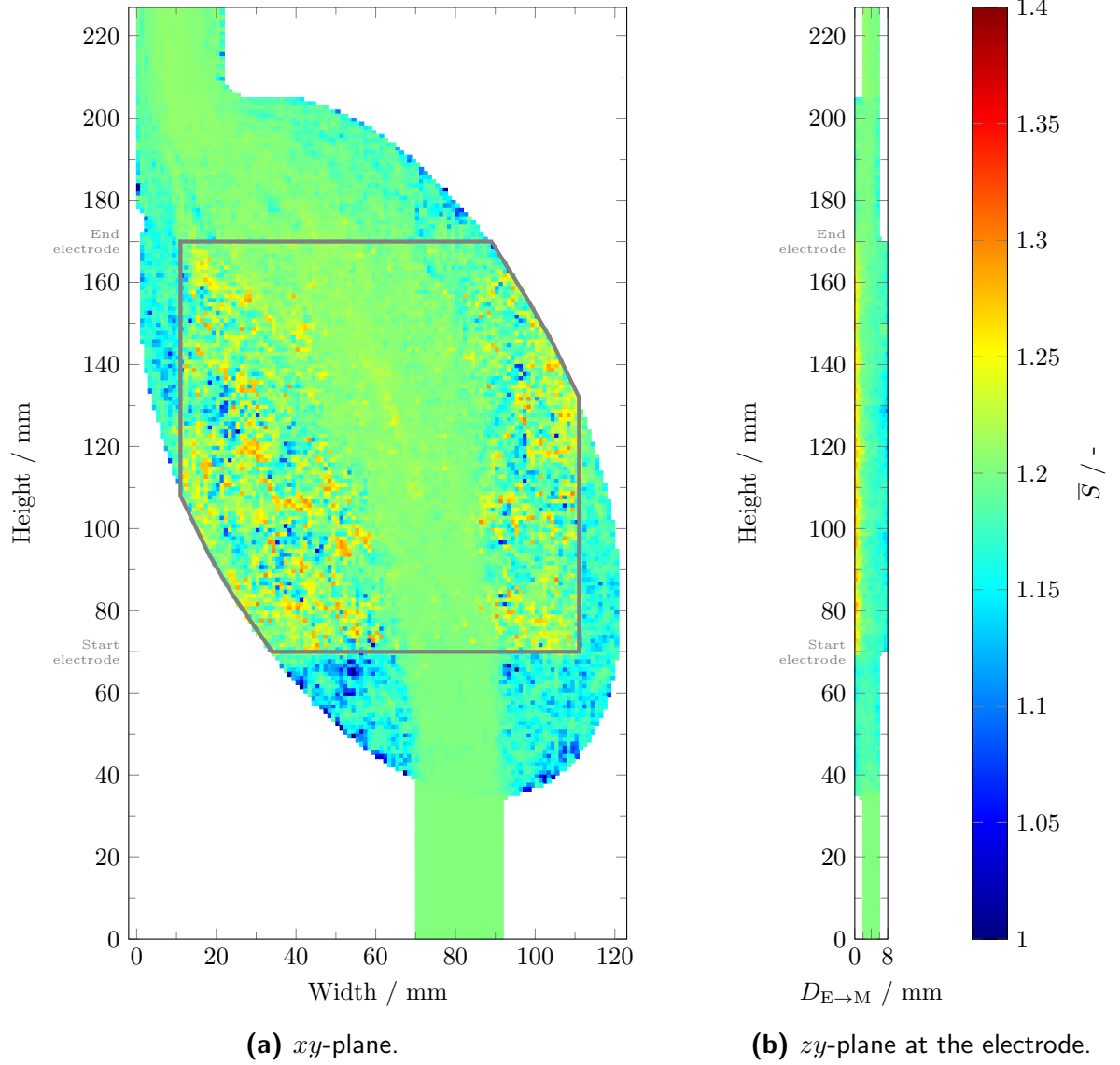


Figure B.26.: (a) \bar{S}^z , and (b) \bar{S}^x of the electrochemical crystallization of SA in the $D_{E \rightarrow M}=8$ mm prototype at $i=0.1$ A cm $^{-2}$, $\dot{V}_{el}=0.5$ L min $^{-1}$, $c_{SA}=1$ mol L $^{-1}$, and pH $_{Inlet}=3.2$ after an electric charge of 1 kC.

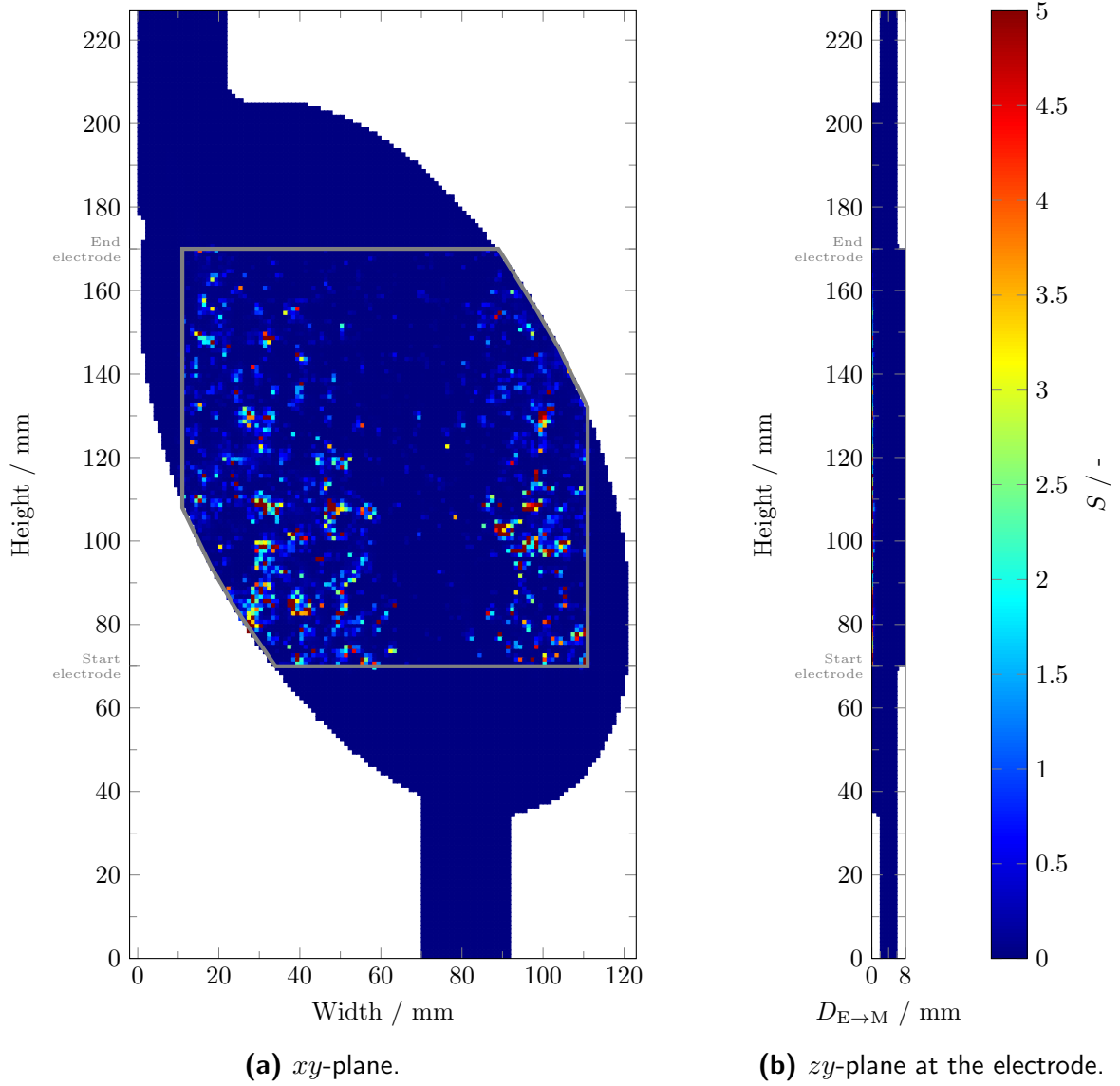


Figure B.27.: (a) \bar{S}^z , and (b) \bar{S}^x of the electrochemical crystallization of FDCA in the $D_{E \rightarrow M}=8$ mm prototype at $i=0.1$ A cm $^{-2}$, $\dot{V}_{el}=0.5$ L min $^{-1}$, $c_{FDCA}=0.9$ mol L $^{-1}$, and pH $_{Inlet}=12$ after an electric charge of 1 kC.

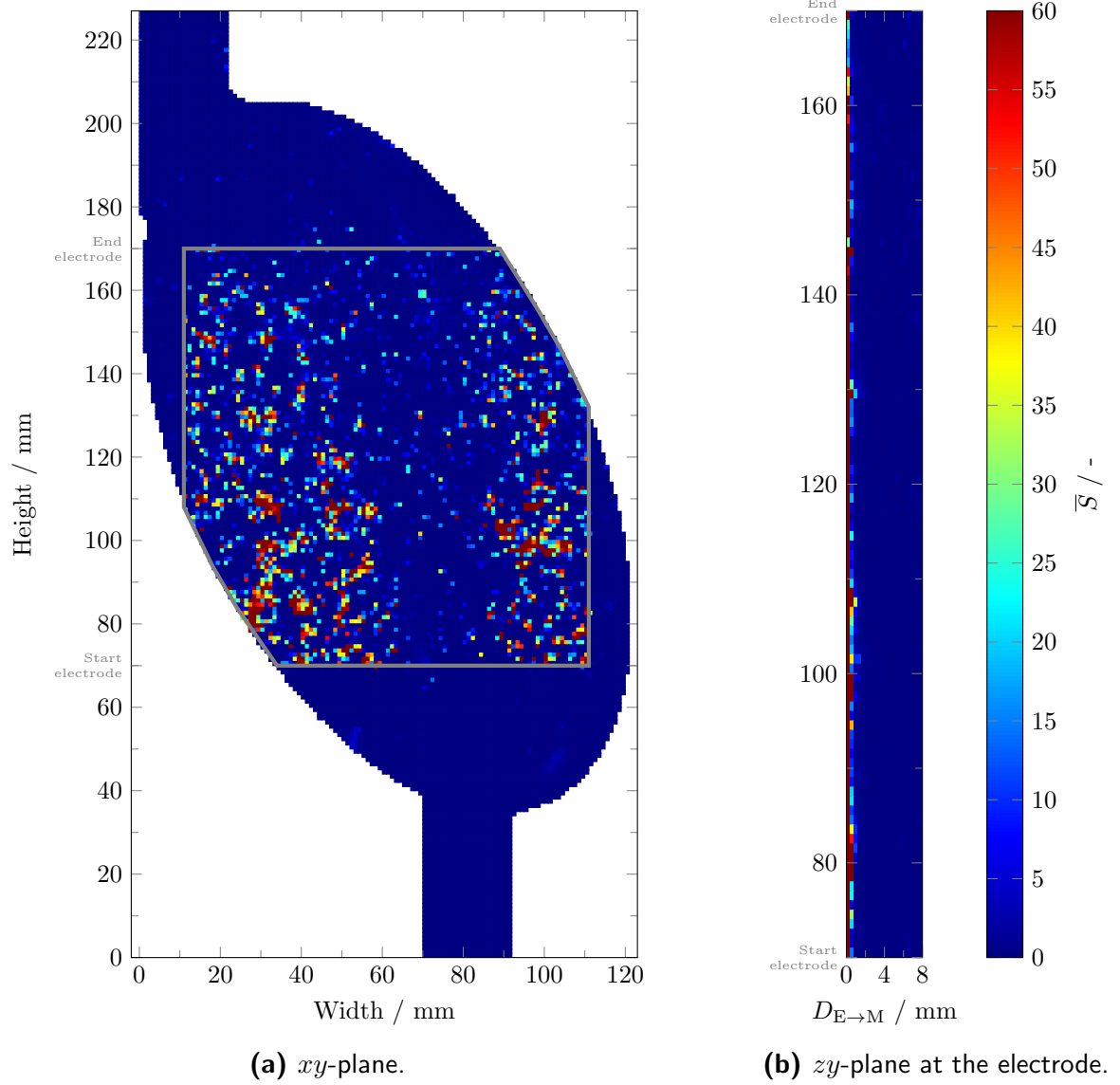


Figure B.28.: (a) \bar{S}^z , and (b) \bar{S}^x of the electrochemical crystallization of TA in the $D_{E \rightarrow M}=8$ mm prototype at $i=0.1$ A cm⁻², $\dot{V}_{el}=0.5$ L min⁻¹, $c_{TA}=0.63$ mol L⁻¹, and pH_{Inlet}=12 after an electric charge of 1 kC.

B.8. Comparison of experimental and simulated residence time distribution of the electrolyte

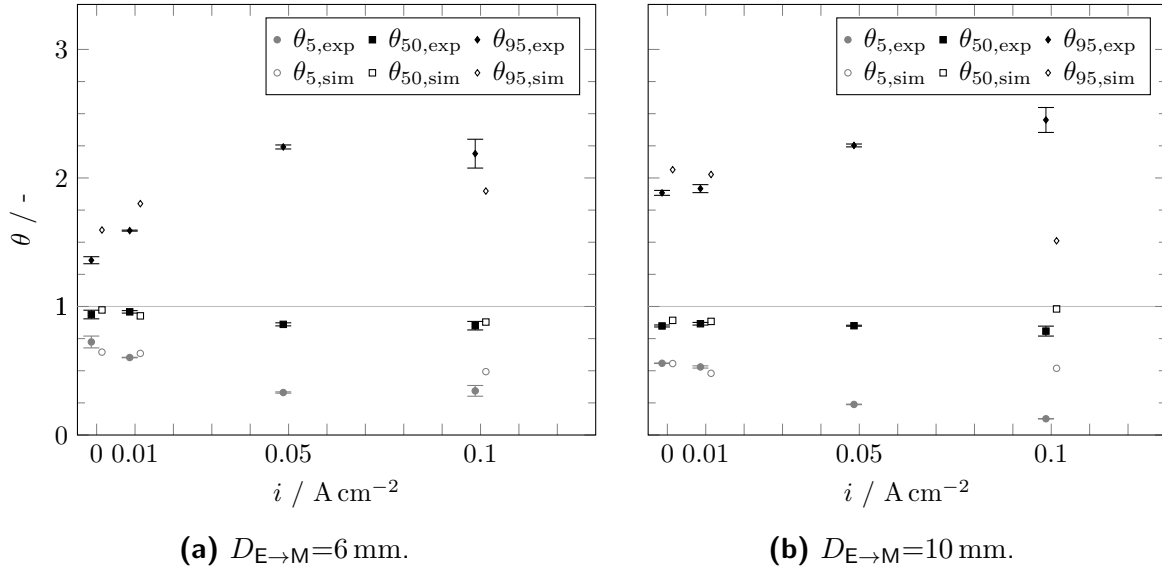


Figure B.29.: Comparison of simulation results and experimental data [172] for characteristic values of θ_5 , θ_{50} , θ_{95} of the electrolyte RTD in the (a) 6 mm and (b) 10 mm wide prototype at $\dot{V}_{\text{el,in}} = 0.05 \text{ L min}^{-1}$ and different current densities.

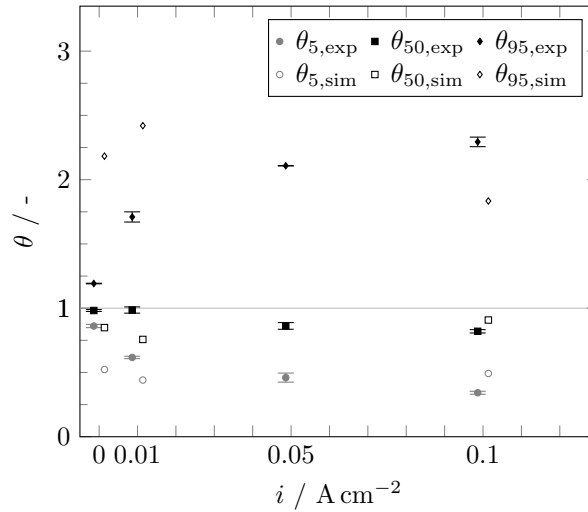


Figure B.30.: Comparison of simulation results and experimental data [172] for characteristic values of θ_5 , θ_{50} , θ_{95} of the electrolyte RTD in the 8 mm wide prototype at $\dot{V}_{\text{el,in}} = 0.05 \text{ L min}^{-1}$ and different current densities.

List of Figures

2.1. Insertion of electrochemical pH-shift electrolyzers in a biotechnological separation process for succinic acid [13]. Reprinted from <i>Separation and Purification Technology</i> , 240, M. Gausmann, C. Kocks, M. Doeker, A. Eggert, T. Maßmann, and A. Jupke, Recovery of succinic acid by integrated multi-phase electrochemical pH-shift extraction and crystallization, 116489, Copyright 2024, with permission from Elsevier.	6
2.2. Different physical phenomena in electrochemical parallel plate electrolyzer on macro-, meso- and molecular-scale.	7
2.3. Degrees of dissociation, $\beta_{\text{H}_2\text{SA}}$, β_{HSA^-} and $\beta_{\text{SA}^{2-}}$, of succinic acid with $\text{p}K_{\text{a},1} = 4.21$ and $\text{p}K_{\text{a},2} = 5.64$ [41] against the pH.	10
2.4. SLE data from Apelblat and Manzurola [42] and fitted Schröder-van-Laar equation of succinic acid for different temperatures.	11
2.5. Experimental data [43] and theoretical concentration of the different succinic acid species against different pH values at 25 °C. The black line corresponds to the total soluble amount of all succinic acid species. In the first (I) pH range, the protonated acid species, H_2SA , precipitates. The present solid states in equilibrium in the second (II) and third (III) pH range are NaHSA and $\text{Na}_2\text{SA} \cdot 10\text{H}_2\text{O}$, respectively. Adapted with permission from Lange et al. [43]. Copyright 2024 American Chemical Society.	12
2.6. Nucleation, growth, and coalescence of oxygen bubbles on an IrOMM-coated titanium electrode surface.	15
2.7. Bubble coverage on an IrOMM-anode during electrolysis in a parallel plate electrolyzer. The oxygen bubbles in focus are attached to the electrode, whereas the bubble with motion blur are detached bubbles.	17
2.8. Different models for the estimation of κ_{mixed} for the gas-liquid mixture for gas fractions between 0 and 50 %.	19
2.9. CNN classifier architecture for the detection of bubbles in a two-phase bubbly jet used in Poletaev et al. [97]. Image is taken from Poletaev et al. [97].	22

2.10. Modified illustration of the different shape regimes of gas bubbles for different Reynolds and Eötvös numbers based on the findings of Bhaga and Weber [145].	29
2.11. Drag coefficient C_D as proposed by Schiller and Naumann [142], Morsi and Alexander [144] and Lain et al. [143] for different Re_b	29
2.12. Schematic drawing of different electrolyte flow patterns based on i under no net flow conditions based on the works of Alexiadis et al. [104, 121, 122]. The dashed vectors indicate the reflux or pseudo-turbulence of the electrolyte due to the bubble motion. Figure is taken from [86].	33
2.13. Overview of the different phase coupling mechanisms between the Euler and Lagrangian phase. Figure is adapted with permission from Springer Nature from Elghobashi [159].	36
2.14. Illustration of the used slider-dash-pot model. Figure is adapted with permission from Elsevier from Tsuji et al. [161].	36
2.15. Illustration of the used slider-dash-pot model from Heitkam et al. [162]. Adapted with permission from IOP Publishing.	38
2.16. Visualization of the simplified collision process and two validity ranges of the calculation of the viscous force after either (2.52) or (2.53) after Heitkam et al. [162]. Adapted with permission from IOP Publishing.	39
2.17. Illustration of the normal and normalized RTD function $E(t)$, $E(\theta)$, summed RTD function $F(t)$, $F(\theta)$ and $E(t) \cdot t$ for artificial experimental data. Here, \bar{t} , $\bar{\sigma}_t$ and Bo amount 18.6 s, 7.3 s, and 14, respectively.	46
3.1. The developed novel parallel plate electrolyzer for the study of the gas-liquid flow. It consists of two PMMA lids, two PMMA electrolyte chambers and two customized electrodes. For clarity, the sealing chords and mats are not shown. The image is taken from Görtz et al. [54].	49
3.2. Drawing of the geometry of (a) the inserted custom-made electrodes and (b) representation of the electrolytes' flow through the electrolyzer. The gray shaded area indicates the point of view of the camera of the three viewing panels top, middle and bottom. Images are taken from [86].	50
3.3. Sample of the annotated images for the training of the CNN.	52
3.4. Combined loss and validation loss of the CNN during training against the epoch number [54].	52
3.5. Illustration of the developed PTV algorithm for the bubble velocity determination based on the implementation of Vukasinovic et al. [110].	54

3.6. Illustration of the further developed four-frames, forward-backward PTV algorithm from Vukasinovic et al. [110]. The indices indicate the frame number. $r_{1,\min}$ represents the threshold for the stuck particle detection and $r_{1,\max}$ for the maximal velocity. The image is taken from [86].	55
3.7. Sample of the introduced four-frames, forward-backward PTV algorithm applied to a series of four frames. Here, for the blue bubble (b) in the base frame, matching bubbles in the (a) backwards, (c) forward, (d) and two forward frames are found. Images are taken from [86].	56
3.8. Illustration of (a) the front and (b) side view of the modified illumination and the two viewing panels at which images are recorded for the PIV algorithm.	58
3.9. Flow chart of the evaluation process of the raw image data in the yz-plane.	59
3.10. Illustration of the three different interrogation areas used by the PIV algorithm on an exemplary image.	60
3.11. Setup for the measurement of the contact angle.	60
3.12. Exemplary determination of the contact angle Θ using the <i>Contact Angle</i> -plugin of the open-source software ImageJ on a RuOMM-coated electrode.	61
3.13. Exemplary bubble size distribution, \tilde{d}_{\min} , d_{25} , d_{50} , d_{75} , and \tilde{d}_{\max} for an IrOMM-coated titanium anode at $i=0.15 \text{ A cm}^{-2}$, $u_{\text{el}}^0=0 \text{ mm s}^{-1}$ and $c_{\text{Na}^+}=0.6 \text{ mol L}^{-1}$	65
3.14. Box plot diagram of the number-based distribution obtained with different evaluation frame rates at $i = 0.1 \text{ A cm}^{-2}$, $u_{\text{el}}^0=0 \text{ mm s}^{-1}$, $c_{\text{Na}^+}=0.6 \text{ mol L}^{-1}$ and IrOMM-coated titanium anode. The gray boxes represent the average number of detected bubbles in each frame.	65
3.15. Arithmetic mean size (\triangle) and box plot diagram of the volume-weighted size distribution of oxygen bubbles at $u_{\text{el}}^0=0, 4.65, 9.3, 13.95$ and 18.6 mm s^{-1} at $i=0.1 \text{ A cm}^{-2}$, $c_{\text{Na}^+}=0.6 \text{ mol L}^{-1}$ and an IrOMM-coated titanium anode. . .	66
3.16. Average oxygen bubble size and distribution for $i=0.01, 0.05, 0.1, 0.15$ and 0.2 A cm^{-2} at $u_{\text{el}}^0=0 \text{ mm s}^{-1}$, $c_{\text{Na}^+}=0.6 \text{ mol L}^{-1}$ and an IrOMM-coated titanium anode.	68
3.17. Average, volume-weighted oxygen bubble size and distribution for $i=0.01, 0.05, 0.1, 0.15$ and 0.2 A cm^{-2} at $u_{\text{el}}^0=0 \text{ mm s}^{-1}$, $c_{\text{Na}^+}=0.6 \text{ mol L}^{-1}$, an IrOMM-coated titanium anode and the middle and top viewing panel. . . .	70
3.18. Volume-based oxygen bubble size distribution and cell voltage for different electrolyte compositions between 0.05 and 0.5 mol L^{-1} Na^+ -ions at $i=0.15 \text{ A cm}^{-2}$, $u_{\text{el}}^0=9.3 \text{ mm s}^{-1}$ and an IrOMM-coated titanium anode. . .	70
3.19. Bubble size distribution for different anodic materials and current densities of $i=0.01, 0.05, 0.1, 0.15$ and 0.2 A cm^{-2} at $u_{\text{el}}^0=0 \text{ mm s}^{-1}$ and $c_{\text{Na}^+}=0.6 \text{ mol L}^{-1}$	72

3.20. Oxygen bubble size distribution for different anodic materials and current densities of $i=0.01, 0.05$ and 0.1 A cm^{-2} at $u_{\text{el}}^0=0 \text{ mm s}^{-1}$ and $c_{\text{Na}^+}=0.6 \text{ mol L}^{-1}$.	74
3.21. Determined contact angle of between 20 and 40 oxygen bubbles for each of the three different electrode catalysts, IrOMM, RuOMM, and titanium. The Figure is printed with permission from [54].	76
3.22. Comparison of the size distribution at $0.01, 0.05$ and 0.1 A cm^{-2} obtained by the two camera systems HRHSC with LM1119TC and LRHSC with 1X-WD110-1.1-NI. To enhance the readability, the box plots are shifted slightly to the left and right, respectively.	78
3.23. Exemplary (a) number- and (b) volume-weighted size distributions, \tilde{d}_{min} , d_{25} , d_{50} , d_{75} , and \tilde{d}_{max} of detached hydrogen bubble at $i=0.15 \text{ A cm}^{-2}$, $u_{\text{el}}^0=0 \text{ mm s}^{-1}$, $c_{\text{Na}^+}=0.6 \text{ mol L}^{-1}$ and a nickel cathode.	79
3.24. Average (a) number- and (b) volume-weighted hydrogen bubble size and distribution for $i=0.01, 0.05, 0.1, 0.15$ and 0.2 A cm^{-2} at $u_{\text{el}}^0=0 \text{ mm s}^{-1}$, $c_{\text{Na}^+}=0.6 \text{ mol L}^{-1}$, and for a nickel cathode. (*) indicates the compromise of the experimental data due to overlapping bubbles.	80
3.25. Exemplary detection of the hydrogen bubbles at $i=0.2 \text{ A cm}^{-2}$, $u_{\text{el}}^0=0 \text{ mm s}^{-1}$, $c_{\text{Na}^+}=0.6 \text{ mol L}^{-1}$. The white circles resemble bubbles with successful velocity determination using the PTV algorithm.	81
3.26. Distribution of vertical velocity of oxygen bubbles over all sizes at $i=0.1 \text{ A cm}^{-2}$, $u_{\text{el}}^0=0 \text{ mm s}^{-1}$, $c_{\text{Na}^+}=0.6 \text{ mol L}^{-1}$, and an IrOMM-coated anode. Figure is adapted from [86].	82
3.27. Calculated average acceleration for each bubble size bin at the middle viewing panel for $i=0.1 \text{ A cm}^{-2}$ and $u_{\text{el}}^0=0 \text{ mm s}^{-1}$. The gray area displays the 99 % confidence interval of the average acceleration. The right y-axis indicates the deviation between two subsequent trajectories of a tracked bubble in pixels. Figure is adapted from [86].	83
3.28. Distribution of u_{b}^v for different oxygen bubble size bins and cumulative bubble size distribution (blue) at the middle viewing panel at $i=0.1 \text{ A cm}^{-2}$ and $u_{\text{el}}^0=0 \text{ mm s}^{-1}$. For comparison, terminal velocities of single oxygen bubbles, measured by Brandon et al. [182] and Kelsall et al. [183], are added. Figure is adapted from [86].	83
3.29. Comparison of the average vertical velocity of oxygen bubbles at the middle viewing panels at different $i = 0.01, 0.5$ and 0.1 A cm^{-2} and $u_{\text{el}}^v=0 \text{ mm s}^{-1}$. Figure is adapted from [86].	85
3.30. Comparison of the average vertical velocity at the three different viewing panels, bottom, middle and top, at $i=0.1 \text{ A cm}^{-2}$ and $u_{\text{el}}^v=0 \text{ mm s}^{-1}$. Figure is adapted from [86].	86

3.31. Distribution of Λ of u_b at $u_{el}^0=0, 10$ and $u_{el}^0=20 \text{ mm s}^{-1}$. An angle of 0° corresponds to a straight vertical velocity trajectory. Figure is adapted from [86].	88
3.32. Impact of u_0^{el} on u_b^v of oxygen bubbles with different sizes at $i=0.1 \text{ A cm}^{-2}$. Figure is adapted from [86].	89
3.33. Comparison of \bar{u}_b^v for bubbles with a size between $210 \mu\text{m} < d_b < 220 \mu\text{m}$ at $i=0.01, 0.5$, and 0.1 A cm^{-2} , and $u_{el}^0=0, 10$ and 20 mm s^{-1} . For readability, the curves for $i=0.01$ and 0.01 A cm^{-2} are slightly displaced to the right and left, respectively. Figure is adapted from [86].	90
3.34. Distribution of vertical velocity of hydrogen bubbles over all sizes at $i=0.1 \text{ A cm}^{-2}$, $u_{el}^0=0 \text{ mm s}^{-1}$, $c_{Na^+}=0.6 \text{ mol L}^{-1}$, and nickel cathode.	91
3.35. Box plots of u_b^v for different hydrogen bubble size bins and cumulative bubble size distribution (blue) at the middle viewing panel at $i=0.1 \text{ A cm}^{-2}$ and $u_{el}^0=0 \text{ mm s}^{-1}$. For comparison, velocities of hydrogen bubbles measured by Davis et al. [87] are added.	92
3.36. Comparison of the average vertical velocity of hydrogen bubbles at the middle viewing panels at different $i = 0.01, 0.5$ and 0.1 A cm^{-2} and $u_{el}^0=0 \text{ mm s}^{-1}$	93
3.37. Illustration of the averaged PIV measurement over 1 s at $i=0.1 \text{ A cm}^{-2}$, $u_{el}^0=0 \text{ mm s}^{-1}$, and the top viewing panel with the color legend on the right. Streamlines are indicated by yellow lines. The white line illustrates the poly-line along which the vertical velocity is evaluated in the following from the electrode ($D_{E \rightarrow M}=0$) to the membrane.	95
3.38. Course of u_m^v along $D_{E \rightarrow M}$ for $i=0.01, 0.05$, and 0.1 A cm^{-2} , and (a) $u_{el}^0=0$ and (b) 20 mm s^{-1} obtained by the PIV algorithm at the top viewing panel.	96
3.39. Course of u_m^v along $D_{E \rightarrow M}$ for $u_{el}^0=0, 010$, and 20 mm s^{-1} , and (a) $i=0.01$ and (b) 0.1 A cm^{-2} obtained by the PIV algorithm at the top viewing panel.	97
3.40. Course of u_m^v along $D_{E \rightarrow M}$ for $i=0.01, 0.5$, and 0.1 A cm^{-2} and (a) $u_{el}^0=0 \text{ mm s}^{-1}$ and (b) 20 mm s^{-1} at the bottom viewing panel obtained by the PIV algorithm.	98
3.41. Comparison of the course of u_m^v along $D_{E \rightarrow M}$ at the bottom and top viewing panels at $i=0.1 \text{ A cm}^{-2}$ and (a) $u_{el}^0=0 \text{ mm s}^{-1}$ and (b) 20 mm s^{-1}	99
3.42. Anolyte flow field at the (a) top and (b) bottom viewing panel at $u_{el}^0=20 \text{ mm s}^{-1}$ and $i=0.1 \text{ A cm}^{-2}$	100
3.43. Anolyte flow field for electrode-membrane gaps of (a) 6 mm and (b) 8 mm at $u_{el}^0=0 \text{ mm s}^{-1}$, and $i=0.05 \text{ A cm}^{-2}$	101
3.44. Course of u_m^v along $D_{E \rightarrow M}$ for $i=0.01, 0.05$, and 0.1 A cm^{-2} , $u_{el}^0=0$, and a electrode-membrane gap of 6 mm	101

3.45. Comparison of the course of u_m^v along $D_{E \rightarrow M}$ at the bottom and top viewing panels, $i=0.1 \text{ A cm}^{-2}$, and $u_{el}^0=0 \text{ mm s}^{-1}$ recorded for electrode-membrane gaps of 6 and 8 mm.	102
3.46. \bar{u}_b^v and $\varsigma_0(u_b^v)$ of hydrogen and oxygen bubbles for $i=0.01, 0.05$, and 0.1 A cm^{-2} at $u_{el}^0=0 \text{ mm s}^{-1}$. On the left y-axis and in gray dotted and dashed lines, \dot{V}_g for hydrogen and oxygen is respectively plotted.	104
4.1. Overview of the employed Euler-Lagrange model for the calculation of the gas-liquid flow.	108
4.2. Algorithm for the injection of bubbles during a timestep j	111
4.3. Illustration of the PDF for a normal and truncated normal distribution. The latter is employed for determine the injection bubble size.	112
4.4. Flow chart of the algorithm for evolving the <i>ParcelCloud</i>	113
4.5. Visualization of neighboring cells for distributing the bubble volume. The bubble center containing cell (2, 2, 2) is marked with *.	118
4.6. 2D-Visualization of the calculation according to equations (4.17) and (4.18) for $\lambda_{x y}^{+ -}$ for three bubbles that intersect with neighboring cells. The gray area illustrates the corresponding area through the cubic approximating of the bubble volume.	119
4.7. Illustration of the assumed three dimensional volume displacement of a half sphere representing a growing bubble prior to detachment.	124
4.8. Flow chart of the OpenFOAM solver <i>pHConcentrationFoam</i> for the calculation of mass transfer, speciation, supersaturation, and conductivity of the continuous electrolyte phase.	125
4.9. Experimentally measured number-based (a) and volume-weighted (b) crystal size distribution and fitted normal distribution of the two small and large sieve fractions.	131
4.10. Illustration of the averaging of the whole domain (a) along the x -axis during post-processing of the numerical results to obtain a two dimensional zy -plot of, e.g., the gas phase fraction (b).	133
5.1. Course of N_b in the computational domain over (a) the course of 50 s and (b) impact of different averaging time intervals on $\bar{u}_{b,\text{sim}}^v$ in the middle viewing panel.	136
5.2. Mean value, standard deviation, as well as minimal and maximal values for $u_{el,\text{sim}}^v$ plotted over (a) a line versus over (b) a plane against the distance from the electrode to membrane.	137
5.3. Comparison of $u_{b,\text{sim}}^v$ for different bubble size bins and different values of Δz	137

5.4.	Comparison of the flow fields for different mesh sizes between $0.4 \text{ mm} \geq \Delta z \geq 1 \text{ mm}$. The black line illustrates the border between the upward and downward directed flow regimes.	138
5.5.	$\overline{u_{\text{el},\text{sim}}^v}^x$ of the base case plotted at the (a) top and (b) bottom viewing panel for $\Delta z=0.4, 0.67, 0.8$ and 1 mm	139
5.6.	Comparison of the flow fields at different values for n_p . The black line illustrates the border between the upward and downward directed flow regimes.	140
5.7.	$\overline{u_{\text{el},\text{sim}}^v}^x$ for the base case and different values for n_p at the (a) top and (b) middle viewing panel.	141
5.8.	Distribution of $u_{\text{b},\text{sim}}^v$ along the height of the electrolyzer for the full bubble size range using the (a) rigid-bubble and (b) fluid-sphere drag models for the base case. The gray areas represent the respective viewing panels and the lines the begin and end of the electrode.	142
5.9.	Comparison of $u_{\text{b},\text{sim},50}^v$ and $u_{\text{b},\text{exp},50}^v$ for different bubble size bins of (a) 150-160 μm , (b) 220-230 μm , and (c) 270-280 μm along the height of the electrolyzer.	143
5.10.	x -averaged flow fields for the (a) base case and two-way coupling. The black line illustrates the border between the upward and downward directed flow regimes. (b) and (c) display the distribution of the gas phase fraction $\overline{\alpha_g}^x$ for two-way and four-way coupling, respectively.	144
5.11.	$\overline{\text{Re}_{\text{el}}}$, and direction of flow in the xy (a) and yz plane (b)	147
5.12.	Re_b , Eo_b , and We_b of all simulated bubbles in the computational domain for the base case.	148
5.13.	Simulated x -averaged vertical velocity at NNF and (a) $i=0.01$, (b) 0.05 , and (c) 0.1 A cm^{-2} and gas phase fraction fields at (d) $i=0.01$, (e) 0.05 and (f) 0.1 A cm^{-2} in the partially transparent electrolyzer.	149
5.14.	(a) Distribution of simulated values for u_b^v and comparison with data from Görtz et al. [86] and (b) distribution of $u_{\text{b},\text{sim}}^v$ at the three viewing panels at NNF conditions and $i=0.1 \text{ A cm}^{-2}$	150
5.15.	Comparison of simulated and experimentally measured values of u_b^v for $10 \mu\text{m}$ size bins at NNF, (a) the middle viewing panel and $i=0.01, 0.05$, and 0.1 A cm^{-2} and (b) at $i=0.1 \text{ A cm}^{-2}$ and all three viewing panels. . . .	151
5.16.	Comparison of $\overline{u_{\text{el},\text{sim}}^v}^x$ and $u_{\text{m},\text{exp}}^v$ obtained by the PIV measurement at NNF conditions and either (a) $i=0.1 \text{ A cm}^{-2}$ or (b) $i=0.1 \text{ A cm}^{-2}$ in the partially transparent electrolyzer.	152
5.17.	Comparison of (a) the distribution of $u_{\text{b},\text{sim}}^v$ at $u_{\text{el}}^0=0$ and 20 mm s^{-1} and the middle viewing panel and $i=0.1 \text{ A cm}^{-2}$ and (b) at different viewing panels for $u_{\text{el}}^0=20 \text{ mm s}^{-1}$ and $i=0.1 \text{ A cm}^{-2}$	154

5.18. Simulated x -averaged vertical velocity at $i=0.1 \text{ A cm}^{-2}$ and (a) $u_{\text{el}}^0=0$, (b) 10, and (c) 20 mm s^{-1} and gas phase fraction fields at (d) $u_{\text{el}}^0=0$, (e) 10, and (f) 20 mm s^{-1} in the partially transparent electrolyzer.	155
5.19. Evolution of $\overline{u_{\text{el, sim}}^v}^x$ from the bottom to the top viewing panel at $i=0.1 \text{ A cm}^{-2}$ and $u_{\text{el}}^0=20 \text{ mm s}^{-1}$	156
5.20. Comparison of $\overline{u_{\text{el, sim}}^v}^x$ and $u_{\text{m, exp}}^v$ obtained by the PIV measurement at $u_{\text{el}}^0=20 \text{ mm s}^{-1}$ and either (a) $i=0.1 \text{ A cm}^{-2}$ or (b) $i=0.01 \text{ A cm}^{-2}$ in the partially transparent electrolyzer.	157
5.21. Comparison of simulated values of u_b^v for $10 \mu\text{m}$ size bins at FC ($u_{\text{el}}^0=20 \text{ mm s}^{-1}$) and NNF conditions at the (a) middle and (b) top viewing panel and $i=0.01$, and 0.1 A cm^{-2}	157
5.22. Comparison of simulated and experimentally measured [86] values for $\overline{u_b^v}$ of bubbles with sizes between $220\text{-}230 \mu\text{m}$ in the top viewing panel at $i=0.01$, and 0.1 A cm^{-2} and $u_{\text{el}}^0=0$, 10, and 20 mm s^{-1}	158
6.1. $\overline{\phi_{\text{el}}^v}$, and direction of flow in the $D_{\text{E} \rightarrow \text{M}}=8 \text{ mm}$ prototype at $i=0.1 \text{ A cm}^{-2}$ and $\dot{V}_{\text{el, in}}=0.5 \text{ L min}^{-1}$ in the xy (a) and yz -plane (b).	162
6.2. $\overline{\phi_{\text{nel}}^v}^z$ and direction of flow at (a) $\dot{V}_{\text{el, in}}=0.05$ and (b) 0.5 L min^{-1} along with the distributions of $\overline{\alpha_g^z}$ at (c) $\dot{V}_{\text{el, in}}=0.05$ and (d) 0.5 L min^{-1} in the $D_{\text{E} \rightarrow \text{M}}=8 \text{ mm}$ prototype at $i=0.1 \text{ A cm}^{-2}$ in the yz -plane.	163
6.3. $\overline{\phi_{\text{el}}^v}^z$ and direction of flow at $i=\textbf{(a)}$ 0, (b) 0.01, and (c) 0.1 A cm^{-2} along with the distributions of $\overline{\alpha_g^z}$ at (d) $i=0.01$ and (e) 0.1 A cm^{-2} in the $D_{\text{E} \rightarrow \text{M}}=8 \text{ mm}$ prototype at $\dot{V}_{\text{el, in}}=0.5 \text{ L min}^{-1}$ in the yz -plane.	165
6.4. x -averaged vertical velocity at different current densities at a height of 133 mm .166	
6.5. $\overline{\phi_{\text{el}}^v}^z$ and direction of flow in the (a) $D_{\text{E} \rightarrow \text{M}}=6$, (b) 8 and (c) 10 mm prototype along with the distributions of $\overline{\alpha_g^z}$ in the (d) $D_{\text{E} \rightarrow \text{M}}=6$, (e) 8 and (f) 10 mm prototypes at $\dot{V}_{\text{el, in}}=0.5 \text{ L min}^{-1}$ and $i=0.1 \text{ A cm}^{-2}$ in the yz -plane.167	
6.6. Comparison of (a) $\overline{u_{\text{el, sim}}^v}^x$ and (b) $\overline{\alpha_g^x}$ at a height of 130 mm across $D_{\text{E} \rightarrow \text{M}}$ of the 6, 8, and 10 mm prototypes.	168
6.7. Comparison of simulation results and experimental data [172] for (a) the dimensionless $F(\theta)$ and (b) characteristic values of θ_5 , θ_{50} , θ_{95} of the electrolyte RTD for the 8 mm -wide prototype, $\dot{V}_{\text{el, in}}=0.5 \text{ L min}^{-1}$ and different current densities. The data in (a) is plotted with a logarithmic x -axis. . . .	169
6.8. Comparison of simulation results and experimental data [172] for characteristic values of θ_5 , θ_{50} , θ_{95} of the electrolyte RTD in the (a) 6 mm and (b) 10 mm wide prototype at $\dot{V}_{\text{el, in}}=0.5 \text{ L min}^{-1}$ and different current densities.	170

6.9. Illustration of the experimental setup for the RTD determination of the crystal phase. To perform a step-out experiment, the valve is in position (a) until the experiment starts and the three-way valve is switched towards (b) the feed container without solids.	172
6.10. Raw image data at different times from an RTD experiment with particles of the larger sieve fraction (0-200 μm) at $i=0.1 \text{ A cm}^{-2}$ and $\dot{V}_{\text{el,in}}=1 \text{ L min}^{-1}$. Colored clusters indicate a possible formation of an agglomerate.	174
6.11. $F(t)$ of two runs for particles with d_p of 0-200 μm at 0.1 A cm^{-2} and $\dot{V}_{\text{el,in}}=1 \text{ L min}^{-1}$	175
6.12. Visualization of the experimentally determined RTD of small and large crystals, and the electrolyte [172] at $\dot{V}_{\text{el,in}}=1 \text{ L min}^{-1}$ and different i in the 8 mm prototype.	175
6.13. Visualization of the key parameters, θ_5 , θ_{50} , and θ_{95} , of the experimental and simulated RTD for (a) the small and (b) large particle sieve fractions at $\dot{V}_{\text{el,in}}=1 \text{ L min}^{-1}$ and different i in the 8 mm prototype.	177
6.14. (a) $\overline{\text{pH}}^z$, and (b) $\overline{\text{pH}}^x$ of the electrochemical crystallization of succinic acid in the $D_{\text{E} \rightarrow \text{M}}=8 \text{ mm}$ prototype at $i=0.1 \text{ A cm}^{-2}$, $\dot{V}_{\text{el,in}}=0.5 \text{ L min}^{-1}$, $c_{\text{SA}}=1 \text{ mol L}^{-1}$, and $\text{pH}_{\text{Inlet}}=5$ after an electric charge of 1 kC.	178
6.15. (a) \overline{S}^z , and (b) \overline{S}^x of the electrochemical crystallization of SA in the $D_{\text{E} \rightarrow \text{M}}=8 \text{ mm}$ prototype at $i=0.1 \text{ A cm}^{-2}$, $\dot{V}_{\text{el,in}}=0.5 \text{ L min}^{-1}$, $c_{\text{SA}}=1 \text{ mol L}^{-1}$, and $\text{pH}_{\text{Inlet}}=5$ after an electric charge of 1 kC.	179
6.16. $\overline{\text{pH}}^x$ after 1 kC at (a) $i=0.01, 0.1$, and 0.2 A cm^{-2} at a height of $y = 133 \text{ mm}$ and (b) at different heights at $i=0.1 \text{ A cm}^{-2}$. $\dot{V}_{\text{el,in}}$ and pH_{Inlet} equals 0.5 L min^{-1} and 5, respectively.	180
6.17. Distribution of S across all cell values of the computational domain for $D_{\text{E} \rightarrow \text{M}}=8 \text{ mm}$, $i=0.1 \text{ A cm}^{-2}$, $\dot{V}_{\text{el,in}}=0.5 \text{ L min}^{-1}$, $c_{\text{SA}}=1 \text{ mol L}^{-1}$, and $\text{pH}_{\text{Inlet}}=5$ after an electric charge of 1 kC. S_{inlet} corresponds to 0.19.	181
6.18. (a) \overline{S}^z , and (b) \overline{S}^x of the electrochemical crystallization of TA in the $D_{\text{E} \rightarrow \text{M}}=8 \text{ mm}$ prototype at $i=0.1 \text{ A cm}^{-2}$, $\dot{V}_{\text{el,in}}=0.5 \text{ L min}^{-1}$, $c_{\text{FDCA}}=0.9 \text{ mol L}^{-1}$, and $\text{pH}_{\text{Inlet}}=7$	182
6.19. (a) \overline{S}^z , and (b) \overline{S}^x of the electrochemical crystallization of TA in the $D_{\text{E} \rightarrow \text{M}}=8 \text{ mm}$ prototype at $i=0.1 \text{ A cm}^{-2}$, $\dot{V}_{\text{el,in}}=0.5 \text{ L min}^{-1}$, $c_{\text{TA}}=0.63 \text{ mol L}^{-1}$, and $\text{pH}_{\text{Inlet}}=7$	184
A.1. Illustration of the employed position of the LEDs for the illumination of the middle viewing panel. Depending on the studied viewing panel, the position of the front LEDs is adjusted.	191

A.2. PIV measurement of electrode-membrane gap in the 8 mm prototype at $i=0.1 \text{ A cm}^{-2}$, bottom panel, and different superficial electrolyte velocities. .	192
A.3. PIV measurement of electrode-membrane gap in the 8 mm prototype at $i=0.05 \text{ A cm}^{-2}$, bottom panel, and different superficial electrolyte velocities.	193
A.4. PIV measurement of electrode-membrane gap in the 8 mm prototype at $i=0.01 \text{ A cm}^{-2}$, bottom panel, and different superficial electrolyte velocities.	194
A.5. PIV measurement of electrode-membrane gap in the 8 mm prototype at $i=0.1 \text{ A cm}^{-2}$, top panel, and different superficial electrolyte velocities. The electrode is located at the right in this figure.	195
A.6. PIV measurement of electrode-membrane gap in the 8 mm prototype at $i=0.05 \text{ A cm}^{-2}$, top panel, and different superficial electrolyte velocities. The electrode is located at the right in this figure.	196
A.7. PIV measurement of electrode-membrane gap in the 8 mm prototype at $i=0.01 \text{ A cm}^{-2}$, top panel, and different superficial electrolyte velocities. The electrode is located at the right in this figure.	197
A.8. PIV measurement of electrode-membrane gap in the 6 mm prototype at NNF conditions, different current densities, and top and bottom panel. . .	198
B.1. Close up of the mesh for the FC conditions. The blue, yellow, and red patches resemble the liquid outlet, electrode, and (fixed) liquid level, respectively.	199
B.2. Illustration of the two meshes and geometries used for (a) FC and (b) NNF conditions. The blue, yellow, red, and pink patches resemble the liquid outlet, electrode, (fixed) liquid level, and inlet, respectively.	200
B.3. Meshed (a) 6 and (b) 10 mm prototype from Kocks [172] with 190,029 and 384,808 cells, respectively.	201
B.4. Mesh of the 8 mm prototype from Kocks [172] from with 269,055 cells . . .	201
B.5. General structure of the Euler-Lagrangian (a) solver and of (b) a case. . .	202
B.6. $\overline{\phi}_{\text{el}}^{v,z}$, and direction of flow in the $D_{\text{E} \rightarrow \text{M}}=6 \text{ mm}$ prototype at $i=0 \text{ A cm}^{-2}$ and $\dot{V}_{\text{el, in}}=0.05$ (a), and 0.5 L min^{-1} (b) in the xy -plane.	204
B.7. $\overline{\phi}_{\text{el}}^{v,z}$, and direction of flow in the $D_{\text{E} \rightarrow \text{M}}=6 \text{ mm}$ prototype at $i=0.01 \text{ A cm}^{-2}$ and (a) $\dot{V}_{\text{el, in}}=0.05$, and (b) 0.5 L min^{-1} in the xy -plane.	205
B.8. $\overline{\phi}_{\text{el}}^{v,z}$, and direction of flow in the $D_{\text{E} \rightarrow \text{M}}=6 \text{ mm}$ prototype at $i=0.1 \text{ A cm}^{-2}$ and (a) $\dot{V}_{\text{el, in}}=0.05$, and (b) 0.5 L min^{-1} in the xy -plane.	206
B.9. $\overline{\phi}_{\text{el}}^{v,z}$, and direction of flow in the $D_{\text{E} \rightarrow \text{M}}=8 \text{ mm}$ prototype at $i=0 \text{ A cm}^{-2}$ and (a) $\dot{V}_{\text{el, in}}=0.05$, and (b) 0.5 L min^{-1} in the xy -plane.	207
B.10. $\overline{\phi}_{\text{el}}^{v,z}$, and direction of flow in the $D_{\text{E} \rightarrow \text{M}}=8 \text{ mm}$ prototype at $i=0.01 \text{ A cm}^{-2}$ and (a) $\dot{V}_{\text{el, in}}=0.05$, and (b) 0.5 L min^{-1} in the xy -plane.	208

B.11.	$\overline{\phi_{\text{el}}^{\text{v}}{}^z}$, and direction of flow in the $D_{\text{E} \rightarrow \text{M}}=8 \text{ mm}$ prototype at $i=0.1 \text{ A cm}^{-2}$ and (a) $\dot{V}_{\text{el, in}}=0.05$, and (b) 0.5 L min^{-1} in the xy -plane.	209
B.12.	$\overline{\phi_{\text{el}}^{\text{v}}{}^z}$, and direction of flow in the $D_{\text{E} \rightarrow \text{M}}=10 \text{ mm}$ prototype at $i=0 \text{ A cm}^{-2}$ and (a) $\dot{V}_{\text{el, in}}=0.05$, and (b) 0.5 L min^{-1} in the xy -plane.	210
B.13.	$\overline{\phi_{\text{el}}^{\text{v}}{}^z}$, and direction of flow in the $D_{\text{E} \rightarrow \text{M}}=10 \text{ mm}$ prototype at $i=0.01 \text{ A cm}^{-2}$ and (a) $\dot{V}_{\text{el, in}}=0.05$, and (b) 0.5 L min^{-1} in the xy -plane.	211
B.14.	$\overline{\phi_{\text{el}}^{\text{v}}{}^z}$, and direction of flow in the $D_{\text{E} \rightarrow \text{M}}=10 \text{ mm}$ prototype at $i=0.1 \text{ A cm}^{-2}$ and (a) $\dot{V}_{\text{el, in}}=0.05$, and (b) 0.5 L min^{-1} in the xy -plane.	212
B.15.	$\overline{\phi_{\text{el}}^{\text{v}}{}^x}$, and direction of flow in the $D_{\text{E} \rightarrow \text{M}}=10 \text{ mm}$ prototype for different simulation cases in the zy -plane.	213
B.16.	$\overline{\phi_{\text{el}}^{\text{v}}{}^x}$, and direction of flow in the $D_{\text{E} \rightarrow \text{M}}=10 \text{ mm}$ prototype for different simulation cases in the zy -plane.	214
B.17.	$\overline{\phi_{\text{el}}^{\text{v}}{}^x}$, and direction of flow in the $D_{\text{E} \rightarrow \text{M}}=10 \text{ mm}$ prototype for different simulation cases in the zy -plane.	215
B.18.	Comparison of the difference between harmonic and arithmetic mean for the calculateion of r_{eq}	216
B.19.	Reactor network of the simulation domain for the multi-pass electrochemical crystallization experiments from Kocks et al. [17] in the 8 mm prototype. .	216
B.20.	Comparison of the number of bubbles over the simulation time of 50 s for $n_{\text{b}}=1, 2, 5$, and 10	217
B.21.	(a) $\overline{\text{pH}}^z$, and (b) $\overline{\text{pH}}^x$ of the electrochemical crystallization of SA in the $D_{\text{E} \rightarrow \text{M}}=8 \text{ mm}$ prototype at $i=0.1 \text{ A cm}^{-2}$, $\dot{V}_{\text{el}}=0.5 \text{ L min}^{-1}$, $c_{\text{SA}}=1 \text{ mol L}^{-1}$, and $\text{pH}_{\text{Inlet}}=3.2$ after an electric charge of 1 kC	218
B.22.	(a) $\overline{\text{pH}}^z$, and (b) $\overline{\text{pH}}^x$ of the electrochemical crystallization of FDCA in the $D_{\text{E} \rightarrow \text{M}}=8 \text{ mm}$ prototype at $i=0.1 \text{ A cm}^{-2}$, $\dot{V}_{\text{el}}=0.5 \text{ L min}^{-1}$, $c_{\text{FDCA}}=0.9 \text{ mol L}^{-1}$, and $\text{pH}_{\text{Inlet}}=7$ after an electric charge of 1 kC	219
B.23.	(a) $\overline{\text{pH}}^z$, and (b) $\overline{\text{pH}}^x$ of the electrochemical crystallization of FDCA in the $D_{\text{E} \rightarrow \text{M}}=8 \text{ mm}$ prototype at $i=0.1 \text{ A cm}^{-2}$, $\dot{V}_{\text{el}}=0.5 \text{ L min}^{-1}$, $c_{\text{FDCA}}=0.9 \text{ mol L}^{-1}$, and $\text{pH}_{\text{Inlet}}=12$ after an electric charge of 1 kC	220
B.24.	(a) $\overline{\text{pH}}^z$, and (b) $\overline{\text{pH}}^x$ of the electrochemical crystallization of TA in the $D_{\text{E} \rightarrow \text{M}}=8 \text{ mm}$ prototype at $i=0.1 \text{ A cm}^{-2}$, $\dot{V}_{\text{el}}=0.5 \text{ L min}^{-1}$, $c_{\text{TA}}=0.63 \text{ mol L}^{-1}$, and $\text{pH}_{\text{Inlet}}=7$ after an electric charge of 1 kC	221
B.25.	(a) $\overline{\text{pH}}^z$, and (b) $\overline{\text{pH}}^x$ of the electrochemical crystallization of TA in the $D_{\text{E} \rightarrow \text{M}}=8 \text{ mm}$ prototype at $i=0.1 \text{ A cm}^{-2}$, $\dot{V}_{\text{el}}=0.5 \text{ L min}^{-1}$, $c_{\text{TA}}=0.63 \text{ mol L}^{-1}$, and $\text{pH}_{\text{Inlet}}=12$ after an electric charge of 1 kC	222
B.26.	(a) \overline{S}^z , and (b) \overline{S}^x of the electrochemical crystallization of SA in the $D_{\text{E} \rightarrow \text{M}}=8 \text{ mm}$ prototype at $i=0.1 \text{ A cm}^{-2}$, $\dot{V}_{\text{el}}=0.5 \text{ L min}^{-1}$, $c_{\text{SA}}=1 \text{ mol L}^{-1}$, and $\text{pH}_{\text{Inlet}}=3.2$ after an electric charge of 1 kC	223

B.27.(a) \bar{S}^z , and (b) \bar{S}^x of the electrochemical crystallization of FDCA in the $D_{E \rightarrow M}=8$ mm prototype at $i=0.1$ A cm ⁻² , $\dot{V}_{el}=0.5$ L min ⁻¹ , $c_{FDCA}=0.9$ mol L ⁻¹ , and pH _{Inlet} =12 after an electric charge of 1 kC.	224
B.28.(a) \bar{S}^z , and (b) \bar{S}^x of the electrochemical crystallization of TA in the $D_{E \rightarrow M}=8$ mm prototype at $i=0.1$ A cm ⁻² , $\dot{V}_{el}=0.5$ L min ⁻¹ , $c_{TA}=0.63$ mol L ⁻¹ , and pH _{Inlet} =12 after an electric charge of 1 kC.	225
B.29.Comparison of simulation results and experimental data [172] for characteristic values of θ_5 , θ_{50} , θ_{95} of the electrolyte RTD in the (a) 6 mm and (b) 10 mm wide prototype at $\dot{V}_{el,in}=0.05$ L min ⁻¹ and different current densities.	226
B.30.Comparison of simulation results and experimental data [172] for characteristic values of θ_5 , θ_{50} , θ_{95} of the electrolyte RTD in the 8 mm wide prototype at $\dot{V}_{el,in}=0.05$ L min ⁻¹ and different current densities.	226

List of Tables

2.1. Overview of different simulation domains, multiphase models, and turbulence models for gas-liquid flows in electrochemical reactors (extended from Hreiz et al. [94]).	26
2.2. Comparison of different drag coefficient correlations for spherical bubbles in the viscous region ($0 \geq Re_b \geq 1000$) that have been used for the modeling of gas-liquid flows in electrolyzers. Table is adapted from Mühlbauer et al. [148] and Sander [149].	30
3.1. Characteristics of the camera setups used for the study of the gas-liquid flow.	51
3.2. Chosen parameter for the minimal, and maximal search radii and maximal size deviation s_{\max} for the four-frame, forward-backward PTV algorithm. .	56
3.3. Parameters and settings of the PIV algorithm	59
3.4. Varied operating parameter to study the effect of u_{el}^0 , i , c_{Na^+} , viewing panel, and electrode material on the size distribution of detached oxygen bubbles. The table is adapted from [54].	63
3.5. Varied operating parameter to study the effect of i on the size distribution of hydrogen bubbles with a Ni-electrode.	63
3.6. Experimental matrix for the PTV and PIV measurements inside the parallel plate electrolyzer. The anolyte consists of $c_{\text{Na}^+} = 0.6 \text{ mol L}^{-1}$ and $c_{\text{SA}^{2-}} = 0.3 \text{ mol L}^{-1}$. PTV measurements are carried out in all three viewing panels, whereas the PIV algorithm is only applied to images of the top and bottom viewing panel. * denotes only PTV measurement	64
3.7. $\bar{d}_{b,0}$, $\varsigma(d_{b,0})$, Min, Max, N_b and outliers for different evaluated frame rates at $i = 0.1 \text{ A cm}^{-2}$, $u_{\text{el}}^0 = 0 \text{ mm s}^{-1}$, $c_{\text{Na}^+} = 0.6 \text{ mol L}^{-1}$ and IrOMM-coated titanium anode.	66
3.8. Results for the surface roughness analysis of the IrOMM-, RuOMM-coated and plain titanium electrode. Table is taken from [54].	73
3.9. Images from microscopy, topology measurements, FESEM, and from the EDS analysis of the three different catalyst materials IrOMM, RuOMM and plain titanium. Parts of the pictures are taken from [54].	75

3.10. Composition of the IrOMM-, RuOMM-coated and plain titanium electrode from Magneto [®] obtained by EDS analysis. Table is adapted from [54].	77
3.11. \bar{u}_b^v and $\varsigma_0(\bar{u}_b^v)$ for the vertical bubble velocity distribution at the three different viewing panels at $i=0.01, 0.05$ and 0.1 A cm^{-2} and $u_{\text{el}}^0=0 \text{ mm s}^{-1}$	87
4.1. Electrolyte properties for the simulation of the gas-liquid flow.	128
4.2. Overview of the used default parameter for the base case and their variation for the sensitivity analysis of the Euler-Lagrangian model.	129
4.3. Overview of simulated operating condition within the 6, 8, and 10 mm-wide prototypes from Kocks [172].	130
4.4. \bar{d}_c , $\varsigma(d_c)$, $d_{c,\text{min}}$, and $d_{c,\text{max}}$ of the small and large sieve fractions used for the truncated normal distribution.	131
4.5. Simulated initial concentrations, i , $\dot{V}_{\text{el, in}}$, and pH values for the 8 mm prototype.	132
5.1. Sensitivity of the simulation results of the base case to the variation in parameters $\delta_{j \leftrightarrow k, \text{max}}$, Δt_{coll} , $\bar{d}_{j,k}$, and r_{coll}	146
5.2. Tabulation of key parameters dz_{I} , Δdz_{I} , u_{max}^v , u_{min}^v , $ u_{\text{max}}^v (u_{\text{min}}^v)^{-1} $, $\Delta z(u_{\text{max}}^v) (: D_{\text{E} \rightarrow \text{M}})$, $\Delta z(u_{\text{min}}^v) (: D_{\text{E} \rightarrow \text{M}})$, $z(u_{\text{max}}^v)$, and $z(u_{\text{min}}^v)$ for the electrolyte flow at NNF conditions and $i=0.01, 0.05$, and 0.1 A cm^{-2}	153
6.1. Mean values and standard deviation of the three velocity components of oxygen bubbles at $i=0.1 \text{ A cm}^{-2}$, $\dot{V}_{\text{el, in}}=0.5 \text{ L min}^{-1}$ in the three different prototypes.	168
6.2. Simulated and experimentally measured [172] key values of the RTD, t_{M} , θ_5 , θ_{50} , and θ_{95} for the electrolyte in the three different prototypes at $i=0, 0.01$, and 0.1 A cm^{-2} and $\dot{V}_{\text{el, in}}=0.05$ and 0.5 L min^{-1}	171
6.3. Experimentally measured deadtimes at $\dot{V}_{\text{el}}=0.75$ and 1 L min^{-1} for particles of the small and large sieve fractions.	173
6.4. Simulated and experimentally measured RTD [172] of the electrolyte in the three different prototypes at $i=0, 0.01$, and 0.1 A cm^{-2} and $\dot{V}_{\text{el, in}}=0.05$ and 0.5 L min^{-1}	176
B.1. Boundary conditions for \mathbf{u} and pressure p	203
B.2. Boundary conditions for k , ω , and ν_t	203

Bibliography

- [1] T. Werpy and G. Petersen. Top Value Added Chemicals from Biomass: Volume I – Results of Screening for Potential Candidates from Sugars and Synthesis Gas. Technical Report DOE/GO-102004-1992, 15008859, August 2004. URL <http://www.osti.gov/servlets/purl/15008859/>.
- [2] R. D. Noble and R. Agrawal. Separations Research Needs for the 21st Century. *Ind. Eng. Chem. Res.*, 44(9):2887–2892, April 2005. ISSN 0888-5885, 1520-5045. doi: 10.1021/ie0501475. URL <https://pubs.acs.org/doi/10.1021/ie0501475>.
- [3] A. Eggert, T. Maßmann, D. Kreyenschulte, M. Becker, B. Heyman, J. Büchs, and A. Jupke. Integrated in-situ product removal process concept for itaconic acid by reactive extraction, pH-shift back extraction and purification by pH-shift crystallization. *Separation and Purification Technology*, 215:463–472, May 2019. ISSN 13835866. doi: 10.1016/j.seppur.2019.01.011. URL <https://linkinghub.elsevier.com/retrieve/pii/S1383586618339327>.
- [4] M. Okabe, D. Lies, S. Kanamasa, and E. Y. Park. Biotechnological production of itaconic acid and its biosynthesis in *Aspergillus terreus*. *Appl Microbiol Biotechnol*, 84(4):597–606, September 2009. ISSN 0175-7598, 1432-0614. doi: 10.1007/s00253-009-2132-3. URL <http://link.springer.com/10.1007/s00253-009-2132-3>.
- [5] N. Nghiem, S. Kleff, and S. Schwegmann. Succinic Acid: Technology Development and Commercialization. *Fermentation*, 3:26, June 2017. doi: 10.3390/fermentation3020026.
- [6] N. Tenhaef, A. Hermann, M. F. Müller, J. Görtz, J. Marienhagen, M. Oldiges, W. Wiechert, M. Bott, A. Jupke, L. Hartmann, S. Herres-Pawlis, and S. Noack. From Microbial Succinic Acid Production to Polybutylene Bio-Succinate Synthesis. *Chemie Ingenieur Technik*, 95(4):587–595, April 2023. ISSN 0009-286X, 1522-2640. doi: 10.1002/cite.202200163. URL <https://onlinelibrary.wiley.com/doi/10.1002/cite.202200163>.

- [7] T. Harhues, S. Fischer, M. Wessling, and R. Keller. Membrane Matters in Paired Electrolysis: Synthesis of 2,5-Furandicarboxylic Acid and 2-Butanone. *ACS Sustainable Chem. Eng.*, 12(45):16603–16612, November 2024. ISSN 2168-0485, 2168-0485. doi: 10.1021/acssuschemeng.4c04754. URL <https://pubs.acs.org/doi/10.1021/acssuschemeng.4c04754>.
- [8] M. Labib, J. Görtz, C. Brüsseler, N. Kallscheuer, J. Gätgens, A. Jupke, J. Marienhagen, and S. Noack. Metabolic and process engineering for microbial production of protocatechuate with *Corynebacterium glutamicum*. *Biotech & Bioengineering*, 118(11):4414–4427, November 2021. ISSN 0006-3592, 1097-0290. doi: 10.1002/bit.27909. URL <https://onlinelibrary.wiley.com/doi/10.1002/bit.27909>.
- [9] M. T. Allaart, G. R. Stouten, D. Z. Sousa, and R. Kleerebezem. Product Inhibition and pH Affect Stoichiometry and Kinetics of Chain Elongating Microbial Communities in Sequencing Batch Bioreactors. *Front. Bioeng. Biotechnol.*, 9:693030, June 2021. ISSN 2296-4185. doi: 10.3389/fbioe.2021.693030. URL <https://www.frontiersin.org/articles/10.3389/fbioe.2021.693030/full>.
- [10] N. Klos, O. Osterthun, H. G. Mengers, P. Lanzerath, W. Graf Von Westarp, G. Lim, M. Gausmann, J.-D. Küsters-Spöring, J. Wiesenthal, N. Guntermann, L. Lauterbach, A. Jupke, W. Leitner, L. M. Blank, J. Klankermayer, and D. Rother. Concatenating Microbial, Enzymatic, and Organometallic Catalysis for Integrated Conversion of Renewable Carbon Sources. *JACS Au*, 4(12):4546–4570, December 2024. ISSN 2691-3704, 2691-3704. doi: 10.1021/jacsau.4c00511. URL <https://pubs.acs.org/doi/10.1021/jacsau.4c00511>.
- [11] A. Barredo, A. Asueta, I. Amundarain, J. Leivar, R. Miguel-Fernández, S. Arnaiz, E. Epelde, R. López-Fonseca, and J. I. Gutiérrez-Ortiz. Chemical recycling of monolayer PET tray waste by alkaline hydrolysis. *Journal of Environmental Chemical Engineering*, 11(3):109823, June 2023. ISSN 22133437. doi: 10.1016/j.jece.2023.109823. URL <https://linkinghub.elsevier.com/retrieve/pii/S2213343723005626>.
- [12] C. Kocks, J. Görtz, A. Holtz, M. Gausmann, and A. Jupke. Electrochemical Crystallization Concept for Succinic Acid Reduces Waste Salt Production. *Chemie Ingenieur Technik*, 92(3):221–228, March 2020. ISSN 0009-286X, 1522-2640. doi: 10.1002/cite.201900088. URL <https://onlinelibrary.wiley.com/doi/10.1002/cite.201900088>.
- [13] M. Gausmann, C. Kocks, M. Doeker, A. Eggert, T. Maßmann, and A. Jupke. Recovery of succinic acid by integrated multi-phase electrochemical pH-shift extraction and crystallization. *Separation and Purification Technology*, 240:116489,

- June 2020. ISSN 13835866. doi: 10.1016/j.seppur.2019.116489. URL <https://linkinghub.elsevier.com/retrieve/pii/S1383586619322427>.
- [14] M. Gausmann, C. Kocks, and A. Jupke. Elektrochemische pH-T-swing Extraktion von biobasierter Itaconsäure. *Chemie Ingenieur Technik*, 92(9):1211–1212, September 2020. ISSN 0009-286X, 1522-2640. doi: 10.1002/cite.202055117. URL <https://onlinelibrary.wiley.com/doi/10.1002/cite.202055117>.
- [15] M. Gausmann, J. Görtz, W. Graf von Westarp, A. Jupke, A. Becker, and T. Gries. Method for producing a monomer from the polymer comprising the monomer. *World Intellectual Property Organization*, (WO2024013254A1), 2023.
- [16] C. Kocks, C. M. Krekel, M. Gausmann, and A. Jupke. Determination of the Metastable Zone Width and Nucleation Parameters of Succinic Acid for Electrochemically Induced Crystallization. *Crystals*, 11(9):1090, September 2021. ISSN 2073-4352. doi: 10.3390/cryst11091090. URL <https://www.mdpi.com/2073-4352/11/9/1090>.
- [17] C. Kocks, D. Wall, and A. Jupke. Evaluation of a Prototype for Electrochemical pH-Shift Crystallization of Succinic Acid. *Materials*, 15(23):8412, November 2022. ISSN 1996-1944. doi: 10.3390/ma15238412. URL <https://www.mdpi.com/1996-1944/15/23/8412>.
- [18] T. Nasrollahnejad, J. Urbanus, J. H. Ter Horst, D. Verdoes, and C. P. Roelands. Electrochemically Induced Crystallization as a Sustainable Method for Product Recovery of Building Block Chemicals: Techno-Economic Evaluation of Fumaric Acid Separation. *Industrial Biotechnology*, 8(3):133–151, June 2012. ISSN 1550-9087, 1931-8421. doi: 10.1089/ind.2011.0012. URL <http://www.liebertpub.com/doi/10.1089/ind.2011.0012>.
- [19] S. J. Andersen, T. Hennebel, S. Gildemyn, M. Coma, J. Desloover, J. Berton, J. Tsukamoto, C. Stevens, and K. Rabaey. Electrolytic Membrane Extraction Enables Production of Fine Chemicals from Biorefinery Sidestreams. *Environ. Sci. Technol.*, 48(12):7135–7142, June 2014. ISSN 0013-936X, 1520-5851. doi: 10.1021/es500483w. URL <https://pubs.acs.org/doi/10.1021/es500483w>.
- [20] S. J. Andersen, P. Candry, T. Basadre, W. C. Khor, H. Roume, E. Hernandez-Sanabria, M. Coma, and K. Rabaey. Electrolytic extraction drives volatile fatty acid chain elongation through lactic acid and replaces chemical pH control in thin stillage fermentation. *Biotechnol Biofuels*, 8(1):221, December 2015. ISSN 1754-6834. doi:

- 10.1186/s13068-015-0396-7. URL <http://www.biotechnologyforbiofuels.com/content/8/1/221>.
- [21] Andersen, Stephen. *Electrochemical extraction, recovery and valorization of carboxylic acids from biorefineries*. PhD Thesis, Ghent University, 2016. ISBN: 9789059899360.
- [22] M. Gausmann, C. Kocks, J. Pastoors, J. Büchs, N. Wierckx, and A. Jupke. Electrochemical pH-T-Swing Separation of Itaconic Acid for Zero Salt Waste Downstream Processing. *ACS Sustainable Chem. Eng.*, 9(28):9336–9347, July 2021. ISSN 2168-0485, 2168-0485. doi: 10.1021/acssuschemeng.1c02194. URL <https://pubs.acs.org/doi/10.1021/acssuschemeng.1c02194>.
- [23] L. Fu, X. Gao, Y. Yang, F. Aiyong, H. Hao, and C. Gao. Preparation of succinic acid using bipolar membrane electrodialysis. *Separation and Purification Technology*, 127:212–218, April 2014. ISSN 13835866. doi: 10.1016/j.seppur.2014.02.028. URL <https://linkinghub.elsevier.com/retrieve/pii/S1383586614001294>.
- [24] D. Arslan, Y. Zhang, K. Steinbusch, L. Diels, H. Hamelers, C. Buisman, and H. De Wever. In-situ carboxylate recovery and simultaneous pH control with tailor-configured bipolar membrane electrodialysis during continuous mixed culture fermentation. *Separation and Purification Technology*, 175:27–35, March 2017. ISSN 13835866. doi: 10.1016/j.seppur.2016.11.032. URL <https://linkinghub.elsevier.com/retrieve/pii/S1383586616310826>.
- [25] M. Szczygiełda, J. Antczak, and K. Prochaska. Separation and concentration of succinic acid from post-fermentation broth by bipolar membrane electrodialysis (EDBM). *Separation and Purification Technology*, 181:53–59, June 2017. ISSN 13835866. doi: 10.1016/j.seppur.2017.03.018. URL <https://linkinghub.elsevier.com/retrieve/pii/S1383586617304628>.
- [26] J. Urbanus, R. Bisselink, K. Nijkamp, J. Ter Horst, D. Verdoes, and C. Roelands. Integrated product removal of slightly water-soluble carboxylates from fermentation by electrochemically induced crystallization. *Journal of Membrane Science*, 363(1-2): 36–47, November 2010. ISSN 03767388. doi: 10.1016/j.memsci.2010.07.030. URL <https://linkinghub.elsevier.com/retrieve/pii/S037673881000582X>.
- [27] J. Urbanus, C. P. M. Roelands, J. Mazurek, D. Verdoes, and J. H. Ter Horst. Electrochemically induced co-crystallization for product removal. *CrystEngComm*, 13(8):2817–2819, 2011. ISSN 1466-8033. doi: 10.1039/C0CE00284D. URL <https://xlink.rsc.org/?DOI=C0CE00284D>.

-
- [28] J. Urbanus, C. Roelands, D. Verdoes, and J. Ter Horst. Intensified crystallization in complex media: Heuristics for crystallization of platform chemicals. *Chemical Engineering Science*, 77:18–25, July 2012. ISSN 00092509. doi: 10.1016/j.ces.2012.02.019. URL <https://linkinghub.elsevier.com/retrieve/pii/S0009250912001157>.
- [29] N. Kim, J. Jeon, R. Chen, and X. Su. Electrochemical separation of organic acids and proteins for food and biomanufacturing. *Chemical Engineering Research and Design*, 178:267–288, February 2022. ISSN 02638762. doi: 10.1016/j.cherd.2021.12.009. URL <https://linkinghub.elsevier.com/retrieve/pii/S0263876221005104>.
- [30] U. Seeliger, W. F. Mueller, F. Heimann, G. Huber, W. Habermann, H. Voss, and H. Siegel. Method for the simultaneous preparation of dicarboxylic acids and diamines by decomposing polyamides into their constituent monomers, October 1998. URL <https://patents.google.com/patent/EP0646106B1/en#patentCitations>.
- [31] T. Muddemann, D. Haupt, M. Sievers, and U. Kunz. Elektrochemische Reaktoren für die Wasserbehandlung. *Chemie Ingenieur Technik*, 91(6):769–785, June 2019. ISSN 0009-286X, 1522-2640. doi: 10.1002/cite.201800193. URL <https://onlinelibrary.wiley.com/doi/10.1002/cite.201800193>.
- [32] K. Zeppenfeld. Electrochemical removal of calcium and magnesium ions from aqueous solutions. *Desalination*, 277(1-3):99–105, August 2011. ISSN 00119164. doi: 10.1016/j.desal.2011.04.005. URL <https://linkinghub.elsevier.com/retrieve/pii/S0011916411003286>.
- [33] V. M. Schmidt. *Elektrochemische Verfahrenstechnik: Grundlagen, Reaktionstechnik, Prozeßoptimierung*. Wiley-VCH, Weinheim, 2003. ISBN 978-3-527-29958-4 978-3-527-62362-4.
- [34] S. Geitmann. *Wasserstoff & Brennstoffzellen: die Technik von morgen*. Hydrogeit-Verl, Kremen, neuaufl. edition, 2004. ISBN 978-3-937863-04-7.
- [35] T. F. Fuller and J. N. Harb. *Electrochemical engineering*. Wiley, Hoboken, NJ, USA, first edition edition, 2018. ISBN 978-1-119-44658-3 978-1-119-44659-0.
- [36] P. Debye and E. Hückel. Zur Theorie der Elektrolyte. *Physikalische Zeitschrift*, 24(9):185–206, 1923.
- [37] H. Davis and U. Commission. *Introduction to Nonlinear Differential and Integral Equations*. Dover books on advanced mathematics. Dover Publications, 1962. ISBN 978-0-486-60971-3. URL <https://books.google.de/books?id=RgbWowrjKd4C>.

- [38] K. S. Pitzer. *Activity coefficients in electrolyte solutions*. CRC, Boca Ratob Ann Arbor Boston [etc.], 2nd ed edition, 1991. ISBN 978-0-8493-5415-1.
- [39] L. F. Cameretti, G. Sadowski, and J. M. Mollerup. Modeling of Aqueous Electrolyte Solutions with Perturbed-Chain Statistical Associated Fluid Theory. *Ind. Eng. Chem. Res.*, 44(9):3355–3362, April 2005. ISSN 0888-5885, 1520-5045. doi: 10.1021/ie0488142. URL <https://pubs.acs.org/doi/10.1021/ie0488142>.
- [40] C. Held, L. F. Cameretti, and G. Sadowski. Modeling aqueous electrolyte solutions Part 1. Fully dissociated electrolytes. *Fluid Phase Equilibria*, 2008.
- [41] Y. K. Hong and W. H. Hong. Extraction of succinic acid with 1-octanol/ n-heptane solutions of mixed tertiary amine. *Bioprocess Engineering*, 23(5):535–538, November 2000. ISSN 16157591. doi: 10.1007/s004499900193. URL <http://link.springer.com/10.1007/s004499900193>.
- [42] A. Apelblat and E. Manzurola. Solubility of oxalic, malonic, succinic, adipic, maleic, malic, citric, and tartaric acids in water from 278.15 to 338.15 K. *The Journal of Chemical Thermodynamics*, 19(3):317–320, March 1987. ISSN 00219614. doi: 10.1016/0021-9614(87)90139-X. URL <https://linkinghub.elsevier.com/retrieve/pii/002196148790139X>.
- [43] L. Lange, K. Lehmkemper, and G. Sadowski. Predicting the Aqueous Solubility of Pharmaceutical Cocrystals As a Function of pH and Temperature. *Crystal Growth & Design*, 16(5):2726–2740, May 2016. ISSN 1528-7483, 1528-7505. doi: 10.1021/acs.cgd.6b00024. URL <https://pubs.acs.org/doi/10.1021/acs.cgd.6b00024>.
- [44] J. W. Mullin. *Crystallization*. Butterworth-Heinemann, Oxford, 4. ed., repr edition, 2004. ISBN 978-0-7506-4833-2.
- [45] W. Beckmann, editor. *Crystallization: basic concepts and industrial applications*. Wiley-VCH, Weinheim, Germany, 2013. ISBN 978-3-527-32762-1. OCLC: ocn841250907.
- [46] A. Mersmann, M. Kind, and J. Stichlmair. *Thermische Verfahrenstechnik: Grundlagen und Methoden*. Verfahrenstechnik. Springer, Berlin Heidelberg New York, 2., wesentlich erw. und aktualis. aufl edition, 2005. ISBN 978-3-540-23648-1.
- [47] A. M. Holtz. *Modellbasierte Untersuchung der Prozessführung von pH-shift Kristallisationen von Itaconsäure*. PhD thesis, RWTH Aachen University, 2023. URL <https://publications.rwth-aachen.de/record/960420>. Artwork Size: pages

- Online-Ressource : Illustrationen, Diagramme Pages: pages Online-Ressource : Illustrationen, Diagramme Publication Title: Dissertation Volume: Rheinisch-Westfälische Technische Hochschule Aachen.
- [48] S. Ben Moussa, G. Maurin, C. Gabrielli, and M. Ben Amor. Electrochemical Precipitation of Struvite. *Electrochem. Solid-State Lett.*, 9(6):C97, 2006. ISSN 10990062. doi: 10.1149/1.2189222. URL <https://iopscience.iop.org/article/10.1149/1.2189222>.
- [49] Q. Chen, R. Ranaweera, and L. Luo. Hydrogen Bubble Formation at Hydrogen-Insertion Electrodes. *J. Phys. Chem. C*, 122(27):15421–15426, July 2018. ISSN 1932-7447, 1932-7455. doi: 10.1021/acs.jpcc.8b03770. URL <https://pubs.acs.org/doi/10.1021/acs.jpcc.8b03770>.
- [50] J. Manthey, M. Guesmi, R. Schab, S. Unz, and M. Beckmann. A sensitivity analysis on the bubble departure diameter for bubble growth due to oxygen super-saturation in highly purified water. *International Journal of Thermofluids*, 18:100327, May 2023. ISSN 26662027. doi: 10.1016/j.ijft.2023.100327. URL <https://linkinghub.elsevier.com/retrieve/pii/S2666202723000460>.
- [51] J. Dukovic and C. W. Tobias. The Influence of Attached Bubbles on Potential Drop and Current Distribution at Gas-Evolving Electrodes. *J. Electrochem. Soc.*, 134(2): 331–343, February 1987. ISSN 0013-4651, 1945-7111. doi: 10.1149/1.2100456. URL <https://iopscience.iop.org/article/10.1149/1.2100456>.
- [52] X. Zhao, H. Ren, and L. Luo. Gas Bubbles in Electrochemical Gas Evolution Reactions. *Langmuir*, 35(16):5392–5408, April 2019. ISSN 0743-7463, 1520-5827. doi: 10.1021/acs.langmuir.9b00119. URL <https://pubs.acs.org/doi/10.1021/acs.langmuir.9b00119>.
- [53] S. F. Jones, G. M. Evans, and K. P. Galvin. Bubble nucleation from gas cavities ? a review. 1999.
- [54] J. Görtz, J. Seiler, P. Kolmer, and A. Jupke. Raising the curtain: Bubble size measurement inside parallel plate electrolyzers. *Chemical Engineering Science*, 286: 119550, March 2024. ISSN 00092509. doi: 10.1016/j.ces.2023.119550. URL <https://linkinghub.elsevier.com/retrieve/pii/S0009250923011065>.
- [55] J. Eigeldinger and H. Vogt. The bubble coverage of gas-evolving electrodes in a flowing electrolyte. *Electrochimica Acta*, 45(27):4449–4456, September 2000. ISSN 00134686. doi: 10.1016/S0013-4686(00)00513-2. URL <https://linkinghub.elsevier.com/retrieve/pii/S0013468600005132>.

- [56] H. Vogt and R. Balzer. The bubble coverage of gas-evolving electrodes in stagnant electrolytes. *Electrochimica Acta*, 50(10):2073–2079, March 2005. ISSN 00134686. doi: 10.1016/j.electacta.2004.09.025. URL <https://linkinghub.elsevier.com/retrieve/pii/S001346860400948X>.
- [57] C. P. Sillen. The effect of gas bubble evolution on the energy efficiency in water electrolysis. 1983. doi: 10.6100/IR40592. URL <https://research.tue.nl/en/publications/the-effect-of-gas-bubble-evolution-on-the-energy-efficiency-in-water-electrolysis/>.html. Publisher: Technische Hogeschool Eindhoven.
- [58] J. Chin Kwie Joe, L. Janssen, S. van Strelen, J. Verbunt, and W. Sluyter. Bubble parameters and efficiency of gas bubble evolution for a chlorine-, a hydrogen- and an oxygen-evolving wire electrode. *Electrochimica Acta*, 33(6):769–779, June 1988. ISSN 00134686. doi: 10.1016/S0013-4686(98)80006-6. URL <https://linkinghub.elsevier.com/retrieve/pii/S0013468698800066>.
- [59] L. Janssen, C. Sillen, E. Barendrecht, and S. van Stralen. Bubble behaviour during oxygen and hydrogen evolution at transparent electrodes in KOH solution. *Electrochimica Acta*, 29(5):633–642, May 1984. ISSN 00134686. doi: 10.1016/0013-4686(84)87122-4. URL <https://linkinghub.elsevier.com/retrieve/pii/0013468684871224>.
- [60] B. Kabanow and A. Frumkin. Über die Grösse elektrolytisch entwickelter Gasblasen. *Zeitschrift für Physikalische Chemie*, 165A(1):433–452, June 1933. ISSN 2196-7156, 0942-9352. doi: 10.1515/zpch-1933-16539. URL <https://www.degruyter.com/document/doi/10.1515/zpch-1933-16539/html>.
- [61] Z. Zhang, W. Liu, and M. L. Free. Phase-Field Modeling and Simulation of Gas Bubble Coalescence and Detachment in a Gas-Liquid Two-Phase Electrochemical System. *J. Electrochem. Soc.*, 167(1):013532, January 2020. ISSN 0013-4651, 1945-7111. doi: 10.1149/2.0322001JES. URL <https://iopscience.iop.org/article/10.1149/2.0322001JES>.
- [62] J. Glas and J. Westwater. Measurements of the growth of electrolytic bubbles. *International Journal of Heat and Mass Transfer*, 7(12):1427–1443, December 1964. ISSN 00179310. doi: 10.1016/0017-9310(64)90130-9. URL <https://linkinghub.elsevier.com/retrieve/pii/0017931064901309>.
- [63] V. S. J. Craig, B. W. Ninham, and R. M. Pashley. The effect of electrolytes on bubble coalescence in water. *J. Phys. Chem.*, 97(39):10192–10197, September 1993.

- ISSN 0022-3654, 1541-5740. doi: 10.1021/j100141a047. URL <https://pubs.acs.org/doi/abs/10.1021/j100141a047>.
- [64] F. Sepahi, N. Pande, K. L. Chong, G. Mul, R. Verzicco, D. Lohse, B. T. Mei, and D. Krug. The effect of buoyancy driven convection on the growth and dissolution of bubbles on electrodes. *Electrochimica Acta*, 403:139616, January 2022. ISSN 00134686. doi: 10.1016/j.electacta.2021.139616. URL <http://arxiv.org/abs/2109.14515>. arXiv:2109.14515 [physics].
- [65] J. L. Trompette, H. Vergnes, G. Hébrard, and P. Bamrungsri. Characteristic Aspects of Bubble Coalescence during Electrolysis of Ammonium Salt Solutions. *J. Phys. Chem. C*, 111(13):5236–5243, April 2007. ISSN 1932-7447, 1932-7455. doi: 10.1021/jp0684426. URL <https://pubs.acs.org/doi/10.1021/jp0684426>.
- [66] L. Janssen. Mass transfer at gas evolving electrodes. *Electrochimica Acta*, 23(2): 81–86, February 1978. ISSN 00134686. doi: 10.1016/0013-4686(78)80101-7. URL <https://linkinghub.elsevier.com/retrieve/pii/0013468678801017>.
- [67] G. Wosiak, J. d. Silva, S. S. Sena, E. B. Carneiro-Neto, M. C. Lopes, and E. Pereira. Investigation of the influence of the void fraction on the energy consumption of a vertical electrolyser under natural convection. *Journal of Environmental Chemical Engineering*, 10(3):107577, June 2022. ISSN 22133437. doi: 10.1016/j.jece.2022.107577. URL <https://linkinghub.elsevier.com/retrieve/pii/S221334372200450X>.
- [68] D. Zhu, L. Xu, X. Su, B. Hu, T. Jia, and L. Mi. Experimental study of the effect of mechanical vibration and water velocity on bubble management in PEM electrolysis cell. *International Journal of Hydrogen Energy*, 49:390–403, January 2024. ISSN 03603199. doi: 10.1016/j.ijhydene.2023.08.063. URL <https://linkinghub.elsevier.com/retrieve/pii/S0360319923040193>.
- [69] K. M. Cho, P. Deshmukh, and W. G. Shin. Hydrodynamic behavior of bubbles at gas-evolving electrode in ultrasonic field during water electrolysis. *Ultrasonics Sonochemistry*, 80:105796, December 2021. ISSN 13504177. doi: 10.1016/j.ultsonch.2021.105796. URL <https://linkinghub.elsevier.com/retrieve/pii/S1350417721003382>.
- [70] A. Rajora and J. Haverkort. An analytical model for the velocity and gas fraction profiles near gas-evolving electrodes. *International Journal of Hydrogen Energy*, 48(71):27450–27463, August 2023. ISSN 03603199. doi: 10.1016/j.ijhydene.2023.03.154. URL <https://linkinghub.elsevier.com/retrieve/pii/S0360319923012247>.

- [71] J. F. Thorpe, J. E. Funk, and T. Y. Bong. Void Fraction and Pressure Drop in a Water Electrolysis Cell. *Journal of Basic Engineering*, 92(1):173–182, March 1970. ISSN 0021-9223. doi: 10.1115/1.3424926. URL <https://asmedigitalcollection.asme.org/fluidsengineering/article/92/1/173/396649/Void-Fraction-and-Pressure-Drop-in-a-Water>.
- [72] J. M. Bisang. Theoretical and experimental studies of current distribution in gas-evolving electrochemical reactors with parallel-plate electrodes. *J Appl Electrochem*, 21(9):760–766, September 1991. ISSN 0021-891X, 1572-8838. doi: 10.1007/BF01402811. URL <http://link.springer.com/10.1007/BF01402811>.
- [73] P. Mandin, J. Hamburger, S. Bessou, and G. Picard. Modelling and calculation of the current density distribution evolution at vertical gas-evolving electrodes. *Electrochimica Acta*, 51(6):1140–1156, November 2005. ISSN 00134686. doi: 10.1016/j.electacta.2005.06.007. URL <https://linkinghub.elsevier.com/retrieve/pii/S0013468605006201>.
- [74] A. N. Colli and J. M. Bisang. Current and Potential Distribution in Two-Phase (Gas Evolving) Electrochemical Reactors by the Finite Volume Method. *J. Electrochem. Soc.*, 169(3):034524, March 2022. ISSN 0013-4651, 1945-7111. doi: 10.1149/1945-7111/ac5d90. URL <https://iopscience.iop.org/article/10.1149/1945-7111/ac5d90>.
- [75] G. Kreysa and M. Kuhn. Modelling of gas evolving electrolysis cells. I. The gas voidage problem. *J Appl Electrochem*, 15(4):517–526, July 1985. ISSN 0021-891X, 1572-8838. doi: 10.1007/BF01059293. URL <http://link.springer.com/10.1007/BF01059293>.
- [76] L. Rayleigh. LVI. *On the influence of obstacles arranged in rectangular order upon the properties of a medium*. *The London, Edinburgh, and Dublin Philosophical Magazine and Journal of Science*, 34(211):481–502, December 1892. ISSN 1941-5982, 1941-5990. doi: 10.1080/14786449208620364. URL <https://www.tandfonline.com/doi/full/10.1080/14786449208620364>.
- [77] J. C. Maxwell. *Treatise on electricity and magnetism. 1*. Oxford University Press, Oxford, repr., unabridged 3. ed., [clarendon press, oxford 1891] edition, 2002. ISBN 978-0-19-850373-6.
- [78] P. Delahay and C. Tobias. *Advances in Electrochemistry and Electrochemical Engineering*. Number Bd. 1 in Advances in Electrochemistry and Electrochemical Engineering. Wiley, 1961. URL <https://books.google.de/books?id=X0YMAQAIAAJ>.

-
- [79] D. A. G. Bruggeman. Berechnung verschiedener physikalischer Konstanten von heterogenen Substanzen. I. Dielektrizitätskonstanten und Leitfähigkeiten der Mischkörper aus isotropen Substanzen. *Annalen der Physik*, 416(7):636–664, January 1935. ISSN 0003-3804, 1521-3889. doi: 10.1002/andp.19354160705. URL <https://onlinelibrary.wiley.com/doi/10.1002/andp.19354160705>.
- [80] S. Prager. Viscous Flow through Porous Media. *The Physics of Fluids*, 4(12):1477–1482, December 1961. ISSN 0031-9171. doi: 10.1063/1.1706246. URL <https://doi.org/10.1063/1.1706246>.
- [81] D. Pyle and D. Harrison. The rising velocity of bubbles in two-dimensional fluidised beds. *Chemical Engineering Science*, 22(4):531–535, April 1967. ISSN 00092509. doi: 10.1016/0009-2509(67)80036-8. URL <https://linkinghub.elsevier.com/retrieve/pii/0009250967800368>.
- [82] L. Sigrist, O. Dossenbach, and N. Ibl. Mass transport in electrolytic cells with gas sparging. *International Journal of Heat and Mass Transfer*, 22(10):1393–1399, October 1979. ISSN 00179310. doi: 10.1016/0017-9310(79)90201-1. URL <https://linkinghub.elsevier.com/retrieve/pii/0017931079902011>.
- [83] L. Sigrist, O. Dossenbach, and N. Ibl. On the conductivity and void fraction of gas dispersions in electrolyte solutions. *J Appl Electrochem*, 10(2):223–228, March 1980. ISSN 0021-891X, 1572-8838. doi: 10.1007/BF00726089. URL <http://link.springer.com/10.1007/BF00726089>.
- [84] D. Nicklin. Two-phase bubble flow. *Chemical Engineering Science*, 17(9):693–702, September 1962. ISSN 00092509. doi: 10.1016/0009-2509(62)85027-1. URL <https://linkinghub.elsevier.com/retrieve/pii/0009250962850271>.
- [85] J. Richardson and W. Zaki. The sedimentation of a suspension of uniform spheres under conditions of viscous flow. *Chemical Engineering Science*, 3(2):65–73, April 1954. ISSN 00092509. doi: 10.1016/0009-2509(54)85015-9. URL <https://linkinghub.elsevier.com/retrieve/pii/0009250954850159>.
- [86] J. Görtz, J. Seiler, and A. Jupke. Bubble up: Tracking down the vertical velocity of oxygen bubbles in parallel plate electrolyzers using CNN. *International Journal of Multiphase Flow*, 177:104849, July 2024. ISSN 03019322. doi: 10.1016/j.ijmultiphaseflow.2024.104849. URL <https://linkinghub.elsevier.com/retrieve/pii/S0301932224001277>.
- [87] J. T. Davis, D. E. Brown, X. Pang, and D. V. Esposito. High Speed Video Investigation of Bubble Dynamics and Current Density Distributions in Membraneless

- Electrolyzers. *J. Electrochem. Soc.*, 166(4):F312–F321, 2019. ISSN 0013-4651, 1945-7111. doi: 10.1149/2.0961904jes. URL <https://iopscience.iop.org/article/10.1149/2.0961904jes>.
- [88] P. Boissonneau and P. Byrne. An experimental investigation of bubble-induced free convection in a small electrochemical cell. *Journal of Applied Electrochemistry*, 30(7):767–775, 2000. ISSN 0021891X. doi: 10.1023/A:1004034807331. URL <http://link.springer.com/10.1023/A:1004034807331>.
- [89] C.-L. Liu, Z. Sun, G.-M. Lu, X.-F. Song, and J.-G. Yu. Experimental and numerical investigation of two-phase flow patterns in magnesium electrolysis cell with non-uniform current density distribution. *Can. J. Chem. Eng.*, 93(3):565–579, March 2015. ISSN 00084034. doi: 10.1002/cjce.22135. URL <https://onlinelibrary.wiley.com/doi/10.1002/cjce.22135>.
- [90] L. Abdelouahed. Conception optimale de l’anode d’une cellule de production de fer par voie électrochimique. page 7, 2013.
- [91] P. Kierkegaard. A method for detection of circular arcs based on the Hough transform. *Machine Vision and Applications*, 5(4):249–263, 1992. doi: 10.1007/BF01212714.
- [92] L. Liu, W. Cai, Y. Chen, and Y. Wang. Fluid Dynamics and Mass Transfer Study of Electrochemical Oxidation by CFD Prediction and Experimental Validation. *Ind. Eng. Chem. Res.*, 57(18):6493–6504, 2018. ISSN 0888-5885. doi: 10.1021/acs.iecr.7b04226.
- [93] P. Chandran, S. Bakshi, and D. Chatterjee. Study on the characteristics of hydrogen bubble formation and its transport during electrolysis of water. *Chemical Engineering Science*, 138:99–109, December 2015. ISSN 00092509. doi: 10.1016/j.ces.2015.07.041. URL <https://linkinghub.elsevier.com/retrieve/pii/S0009250915005278>.
- [94] R. Hreiz, L. Abdelouahed, D. Fünfschilling, and F. Lapique. Electrogenated bubbles induced convection in narrow vertical cells: A review. *Chemical Engineering Research and Design*, 100:268–281, August 2015. ISSN 02638762. doi: 10.1016/j.cherd.2015.05.035. URL <https://linkinghub.elsevier.com/retrieve/pii/S0263876215001963>.
- [95] K. He, X. Zhang, S. Ren, and J. Sun. Deep Residual Learning for Image Recognition, December 2015. URL <http://arxiv.org/abs/1512.03385>. arXiv:1512.03385 [cs].

-
- [96] J. Ilonen, R. Juránek, T. Eerola, L. Lensu, M. Dubská, P. Zemčík, and H. Kälviäinen. Comparison of bubble detectors and size distribution estimators. *Pattern Recognition Letters*, 101:60–66, January 2018. ISSN 01678655. doi: 10.1016/j.patrec.2017.11.014. URL <https://linkinghub.elsevier.com/retrieve/pii/S0167865517304282>.
- [97] I. Poletaev, M. P. Tokarev, and K. S. Pervunin. Bubble patterns recognition using neural networks: Application to the analysis of a two-phase bubbly jet. *International Journal of Multiphase Flow*, 126:103194, May 2020. ISSN 03019322. doi: 10.1016/j.ijmultiphaseflow.2019.103194. URL <https://linkinghub.elsevier.com/retrieve/pii/S0301932219305701>.
- [98] I. Goodfellow, Y. Bengio, and A. Courville. *Deep learning*. Adaptive computation and machine learning. The MIT Press, Cambridge, Massachusetts, 2016. ISBN 978-0-262-03561-3.
- [99] S. Sibirtsev, S. Zhai, M. Neufang, J. Seiler, and A. Jupke. Mask R-CNN based droplet detection in liquid–liquid systems, Part 2: Methodology for determining training and image processing parameter values improving droplet detection accuracy. *Chemical Engineering Journal*, 473:144826, October 2023. ISSN 13858947. doi: 10.1016/j.cej.2023.144826. URL <https://linkinghub.elsevier.com/retrieve/pii/S138589472303557X>.
- [100] S. Sibirtsev, S. Zhai, M. Neufang, J. Seiler, and A. Jupke. Mask R-CNN based droplet detection in liquid-liquid systems. Part 1: A proof of concept. *Proceedings of International Solvent Extraction Conference*, pages 133–139, 2023. doi: 10.5281/zenodo.7907607. URL <http://media.isec2022.com/2023/05/Final-collected-Proceedings-ISEC-2022.pdf>.
- [101] K. He, G. Gkioxari, P. Dollár, and R. Girshick. Mask r-cnn. In *Proceedings of the IEEE international conference on computer vision*, pages 2961–2969, 2017.
- [102] W. Abdulla. Mask R-CNN for object detection and instance segmentation on Keras and TensorFlow, 2017. URL https://github.com/matterport/Mask_RCNN. Publication Title: GitHub repository.
- [103] S. Sibirtsev, S. Zhai, and A. Jupke. Mask R-CNN based droplet detection in liquid–liquid systems, Part 3: Model generalization for accurate processing performance independent of image quality. *Chemical Engineering Research and Design*, 202:161–168, February 2024. ISSN 02638762. doi: 10.1016/j.cherd.2023.12.005. URL <https://linkinghub.elsevier.com/retrieve/pii/S0263876223007979>.

- [104] A. Alexiadis, M. Dudukovic, P. Ramachandran, A. Cornell, J. Wanngård, and A. Bokkers. Liquid–gas flow patterns in a narrow electrochemical channel. *Chemical Engineering Science*, 66(10):2252–2260, May 2011. ISSN 00092509. doi: 10.1016/j.ces.2011.02.046. URL <https://linkinghub.elsevier.com/retrieve/pii/S0009250911001412>.
- [105] S. Charton, P. Rivalier, D. Ode, J. Morandini, and J. P. Caire. Hydrogen production by the Westinghouse cycle: modelling and optimization of the two-phase electrolysis cell. pages 11–22, Bologna, Italy, June 2009. doi: 10.2495/ECOR090021. URL <http://library.witpress.com/viewpaper.asp?pcode=ECOR09-002-1>.
- [106] R. Hreiz, L. Abdelouahed, D. Fünfschilling, and F. Lapique. Electrogenenerated bubbles induced convection in narrow vertical cells: PIV measurements and Euler–Lagrange CFD simulation. *Chemical Engineering Science*, 134:138–152, September 2015. ISSN 00092509. doi: 10.1016/j.ces.2015.04.041. URL <https://linkinghub.elsevier.com/retrieve/pii/S0009250915003024>.
- [107] R. J. Goldstein, editor. *Fluid mechanics measurements*. Taylor & Francis, Washington, DC, 2. ed edition, 1996. ISBN 978-1-56032-306-8.
- [108] I. Kuroda, A. Sakakibara, T. Sasaki, Y. Murai, N. Nagai, and F. Yamamoto. PIV Study on Buoyant Bubble Flows in a Small Electrolytic Cell. *JAPANESE JOURNAL OF MULTIPHASE FLOW*, 22(2):161–174, 2008. ISSN 1881-5790, 0914-2843. doi: 10.3811/jjmf.22.161. URL http://www.jstage.jst.go.jp/article/jjmf/22/2/22_2_161/_article.
- [109] W. Cheng, Y. Murai, T. Sasaki, and F. Yamamoto. Bubble velocity measurement with a recursive cross correlation PIV technique. *Flow Measurement and Instrumentation*, 16(1):35–46, March 2005. ISSN 09555986. doi: 10.1016/j.flowmeasinst.2004.08.002. URL <https://linkinghub.elsevier.com/retrieve/pii/S0955598604000597>.
- [110] B. Vukasinovic, M. K. Smith, and A. Glezer. Spray characterization during vibration-induced drop atomization. *Physics of Fluids*, 16(2):306–316, February 2004. ISSN 1070-6631, 1089-7666. doi: 10.1063/1.1632907. URL <http://aip.scitation.org/doi/10.1063/1.1632907>.
- [111] L. Abdelouahed, R. Hreiz, S. Poncin, G. Valentin, and F. Lapique. Hydrodynamics of gas bubbles in the gap of lantern blade electrodes without forced flow of electrolyte: Experiments and CFD modelling. *Chemical Engineering Science*, 111:255–265, May

2014. ISSN 00092509. doi: 10.1016/j.ces.2014.01.028. URL <https://linkinghub.elsevier.com/retrieve/pii/S0009250914000384>.
- [112] W. Thielicke and R. Sonntag. Particle Image Velocimetry for MATLAB: Accuracy and enhanced algorithms in PIVlab. *Journal of Open Research Software*, 9(1):12, May 2021. doi: 10.5334/jors.334. URL <https://doi.org/10.5334/jors.334>. Publisher: Ubiquity Press, Ltd.
- [113] S. Van Damme, P. Maciel, H. Van Parys, J. Deconinck, A. Hubin, and H. Deconinck. Bubble nucleation algorithm for the simulation of gas evolving electrodes. *Electrochemistry Communications*, 12(5):664–667, May 2010. ISSN 13882481. doi: 10.1016/j.elecom.2010.03.001. URL <https://linkinghub.elsevier.com/retrieve/pii/S1388248110000901>.
- [114] H. Peng, G. R. Birkett, and A. V. Nguyen. Progress on the Surface Nanobubble Story: What is in the bubble? Why does it exist? *Advances in Colloid and Interface Science*, 222:573–580, August 2015. ISSN 00018686. doi: 10.1016/j.cis.2014.09.004. URL <https://linkinghub.elsevier.com/retrieve/pii/S0001868614002516>.
- [115] K. Aldas. Application of a two-phase flow model for hydrogen evolution in an electrochemical cell. *Applied Mathematics and Computation*, 154(2):507–519, 2004. ISSN 00963003. doi: 10.1016/S0096-3003(03)00731-8.
- [116] M. Mat. A two-phase flow model for hydrogen evolution in an electrochemical cell. *International Journal of Hydrogen Energy*, 29(10):1015–1023, August 2004. ISSN 03603199. doi: 10.1016/j.ijhydene.2003.11.007. URL <https://linkinghub.elsevier.com/retrieve/pii/S036031990300329X>.
- [117] M. Mat and K. Aldas. Application of a two-phase flow model for natural convection in an electrochemical cell. *International Journal of Hydrogen Energy*, 30(4):411–420, March 2005. ISSN 03603199. doi: 10.1016/j.ijhydene.2004.04.002. URL <https://linkinghub.elsevier.com/retrieve/pii/S036031990400179X>.
- [118] K. Aldas, N. Pehlivanoglu, and M. Mat. Numerical and experimental investigation of two-phase flow in an electrochemical cell. *International Journal of Hydrogen Energy*, 33(14):3668–3675, July 2008. ISSN 03603199. doi: 10.1016/j.ijhydene.2008.04.047. URL <https://linkinghub.elsevier.com/retrieve/pii/S0360319908004734>.
- [119] S. Charton, J. Janvier, P. Rivalier, E. Chaînet, and J.-P. Caire. Hybrid sulfur cycle for H₂ production: A sensitivity study of the electrolysis step in a filter-press cell. *International Journal of Hydrogen Energy*, 35(4):1537–1547, Febru-

- ary 2010. ISSN 03603199. doi: 10.1016/j.ijhydene.2009.12.046. URL <https://linkinghub.elsevier.com/retrieve/pii/S0360319909019740>.
- [120] A. Alexiadis, M. P. Dudukovic, P. Ramachandran, A. Cornell, J. Wanngård, and A. Bokkers. On the electrode boundary conditions in the simulation of two phase flow in electrochemical cells. *International Journal of Hydrogen Energy*, 36(14):8557–8559, 2011. ISSN 03603199. doi: 10.1016/j.ijhydene.2011.04.149.
- [121] A. Alexiadis, M. P. Dudukovic, P. Ramachandran, A. Cornell, J. Wanngård, and A. Bokkers. Transition to pseudo-turbulence in a narrow gas-evolving channel. *Theor. Comput. Fluid Dyn.*, 26(6):551–564, December 2012. ISSN 0935-4964, 1432-2250. doi: 10.1007/s00162-011-0248-4. URL <http://link.springer.com/10.1007/s00162-011-0248-4>.
- [122] A. Alexiadis, M. P. Dudukovic, P. Ramachandran, and A. Cornell. On the stability of the flow in multi-channel electrochemical systems. *J Appl Electrochem*, 42(9):679–687, September 2012. ISSN 0021-891X, 1572-8838. doi: 10.1007/s10800-012-0426-0. URL <http://link.springer.com/10.1007/s10800-012-0426-0>.
- [123] L. Abdelouahed, G. Valentin, S. Poncin, and F. Lapique. Current density distribution and gas volume fraction in the gap of lantern blade electrodes. *Chemical Engineering Research and Design*, 92(3):559–570, March 2014. ISSN 02638762. doi: 10.1016/j.cherd.2013.10.003. URL <https://linkinghub.elsevier.com/retrieve/pii/S0263876213003997>.
- [124] M. Dreoni, F. Balduzzi, G. Ferrara, and A. Bianchini. Accuracy Assessment of the Eulerian Two-phase Model for the CFD Simulation of Gas Bubbles Dynamics in Alkaline Electrolyzers. *J. Phys.: Conf. Ser.*, 2385(1):012040, December 2022. ISSN 1742-6588, 1742-6596. doi: 10.1088/1742-6596/2385/1/012040. URL <https://iopscience.iop.org/article/10.1088/1742-6596/2385/1/012040>.
- [125] J. Rodríguez and E. Amores. CFD Modeling and Experimental Validation of an Alkaline Water Electrolysis Cell for Hydrogen Production. *Processes*, 8(12):1634, December 2020. ISSN 2227-9717. doi: 10.3390/pr8121634. URL <https://www.mdpi.com/2227-9717/8/12/1634>.
- [126] S. Zhan, J. Yang, Z. Wang, R. Zhao, J. Zheng, and J. Wang. CFD Simulation of Effect of Interphase Forces and Turbulence Models on Gas-Liquid Two-Phase Flows in Non-Industrial Aluminum Electrolysis Cells. *JOM*, 69(9):1589–1599, September 2017. ISSN 1047-4838, 1543-1851. doi: 10.1007/s11837-017-2327-5. URL <http://link.springer.com/10.1007/s11837-017-2327-5>.

-
- [127] A. Zarghami, N. G. Deen, and A. W. Vreman. CFD modeling of multiphase flow in an alkaline water electrolyzer. *Chemical Engineering Science*, 227:115926, December 2020. ISSN 0009-2509. doi: 10.1016/j.ces.2020.115926. URL <https://www.sciencedirect.com/science/article/pii/S0009250920304589>.
- [128] D. Le Bideau, P. Mandin, M. Benbouzid, M. Kim, M. Sellier, F. Ganci, and R. Inguanta. Eulerian Two-Fluid Model of Alkaline Water Electrolysis for Hydrogen Production. *Energies*, 13(13):3394, July 2020. ISSN 1996-1073. doi: 10.3390/en13133394. URL <https://www.mdpi.com/1996-1073/13/13/3394>.
- [129] A. Colli and J. Bisang. Current and potential distribution in electrochemical reactors with activated or resistive electrodes. A multiregion and open source approach. *Electrochimica Acta*, 290:676–685, November 2018. ISSN 00134686. doi: 10.1016/j.electacta.2018.09.121. URL <https://linkinghub.elsevier.com/retrieve/pii/S0013468618321170>.
- [130] A. N. Colli and J. M. Bisang. Editors’ Choice—Coupling k Convection-Diffusion and Laplace Equations in an Open-Source CFD Model for Tertiary Current Distribution Calculations. *J. Electrochem. Soc.*, 167(1):013513, 2020. ISSN 0013-4651, 1945-7111. doi: 10.1149/2.0132001JES. URL <https://iopscience.iop.org/article/10.1149/2.0132001JES>.
- [131] A. N. Colli and J. M. Bisang. Considerations about the gas fraction in two-phase electrochemical reactors by using a rigorous hydrodynamic model. *Chemical Engineering Science*, 276:118699, July 2023. ISSN 0009-2509. doi: 10.1016/j.ces.2023.118699. URL <https://www.sciencedirect.com/science/article/pii/S0009250923002555>.
- [132] A. N. Colli and J. M. Bisang. A two-phase model to predict the enhanced mass transfer by bubble-induced convection in parallel-plate electrochemical reactors. *Electrochimica Acta*, 498:144606, September 2024. ISSN 0013-4686. doi: 10.1016/j.electacta.2024.144606. URL <https://www.sciencedirect.com/science/article/pii/S0013468624008466>.
- [133] E. Karimi-Sibaki, A. Vakhrushev, M. Wu, J. Bohacek, and A. Kharicha. A numerical study on effects of current density distribution, turbulence, and magnetohydrodynamics (MHD) on electrolytic gas flow with application to alkaline water electrolysis (AWE). *Chemical Engineering Research and Design*, 208:731–739, August 2024. ISSN 02638762. doi: 10.1016/j.cherd.2024.07.042. URL <https://linkinghub.elsevier.com/retrieve/pii/S0263876224004349>.

- [134] A. A. Dahlkild. Modelling the two-phase flow and current distribution along a vertical gas-evolving electrode. *J. Fluid Mech.*, 428:249–272, February 2001. ISSN 0022-1120, 1469-7645. doi: 10.1017/S0022112000002639. URL https://www.cambridge.org/core/product/identifier/S0022112000002639/type/journal_article.
- [135] R. Wedin and A. A. Dahlkild. On the Transport of Small Bubbles under Developing Channel Flow in a Buoyant Gas-Evolving Electrochemical Cell. *Ind. Eng. Chem. Res.*, 40(23):5228–5233, November 2001. ISSN 0888-5885, 1520-5045. doi: 10.1021/ie001073u. URL <https://pubs.acs.org/doi/10.1021/ie001073u>.
- [136] N. Ipek, M. Vynnycky, and A. Cornell. A Coupled Electrochemical and Hydrodynamical Two-Phase Model for the Electrolytic Pickling of Steel. *J. Electrochem. Soc.*, 155(4):P33, 2008. ISSN 00134651. doi: 10.1149/1.2835224. URL <https://iopscience.iop.org/article/10.1149/1.2835224>.
- [137] H. Van Parys, S. Van Damme, P. Maciel, T. Nierhaus, F. Tomasoni, A. Hubin, H. Deconinck, and J. Deconinck. Eulerian-Lagrangian model for gas-evolving processes based on supersaturation. pages 109–118, Bologna, Italy, June 2009. doi: 10.2495/ECOR090111. URL <http://library.witpress.com/viewpaper.asp?pcode=ECOR09-011-1>.
- [138] A. Rajora and J. Haverkort. An analytical multiphase flow model for parallel plate electrolyzers. *Chemical Engineering Science*, 260:117823, October 2022. ISSN 00092509. doi: 10.1016/j.ces.2022.117823. URL <https://linkinghub.elsevier.com/retrieve/pii/S0009250922004079>.
- [139] T. Nierhaus, D. Vanden Abeele, and H. Deconinck. Direct numerical simulation of bubbly flow in the turbulent boundary layer of a horizontal parallel plate electrochemical reactor. *International Journal of Heat and Fluid Flow*, 28(4):542–551, August 2007. ISSN 0142727X. doi: 10.1016/j.ijheatfluidflow.2007.03.005. URL <https://linkinghub.elsevier.com/retrieve/pii/S0142727X07000355>.
- [140] B. Andersson, editor. *Computational fluid dynamics for engineers*. Cambridge University Press, Cambridge ; New York, 2012. ISBN 978-1-107-01895-2. OCLC: ocn751752493.
- [141] F. R. Menter, M. Kuntz, R. Langtry, and others. Ten years of industrial experience with the SST turbulence model. *Turbulence, heat and mass transfer*, 4(1):625–632, 2003.
- [142] L. Schiller and A. Naumann. Über die grundlegenden Berechnungen bei der Schwerkraftaufbereitung. *Zeitschrift des Vereins Deutscher Ingenieure*, 77:318–321, 1935.

-
- [143] S. Lain, D. Bröder, and M. Sommerfeld. Experimental and numerical studies of the hydrodynamics in a bubble column. *Chemical Engineering Science*, 54(21):4913–4920, November 1999. ISSN 00092509. doi: 10.1016/S0009-2509(99)00212-2. URL <https://linkinghub.elsevier.com/retrieve/pii/S0009250999002122>.
- [144] S. A. Morsi and A. J. Alexander. An investigation of particle trajectories in two-phase flow systems. *J. Fluid Mech.*, 55(02):193, September 1972. ISSN 0022-1120, 1469-7645. doi: 10.1017/S0022112072001806. URL http://www.journals.cambridge.org/abstract_S0022112072001806.
- [145] D. Bhaga and M. E. Weber. Bubbles in viscous liquids: shapes, wakes and velocities. *J. Fluid Mech.*, 105(-1):61, April 1981. ISSN 0022-1120, 1469-7645. doi: 10.1017/S002211208100311X. URL http://www.journals.cambridge.org/abstract_S002211208100311X.
- [146] W. Rybczyński. Über die fortschreitende Bewegung einer flüssigen Kugel in einem zähen Medium. *Bull. Acad. Sci. Cracovie A*, 1:40–46, 1911.
- [147] J. Grace, T. Wairegi, and T. Nguyen. Shapes and velocities of single drops and bubbles moving freely through immiscible liquids. *Trans Inst Chem Eng*, 54(3): 167 – 173, 1976. URL <https://www.scopus.com/inward/record.uri?eid=2-s2.0-0016978161&partnerID=40&md5=de5d078841fb99ee42292a36801814f2>. Type: Article.
- [148] A. Mühlbauer, M. W. Hlawitschka, and H.-J. Bart. Models for the Numerical Simulation of Bubble Columns: A Review. *Chemie Ingenieur Technik*, 91(12):1747–1765, December 2019. ISSN 0009-286X, 1522-2640. doi: 10.1002/cite.201900109. URL <https://onlinelibrary.wiley.com/doi/10.1002/cite.201900109>.
- [149] K. M. Sander. Modeling of Gas-Liquid Flow Fields in Electrolysis Cells Using Computational Fluid Dynamics. Master’s thesis, RWTH Aachen University, Aachen, August 2023.
- [150] T. Nierhaus, H. Van Parys, S. Dehaeck, J. Van Beeck, H. Deconinck, J. Deconinck, and A. Hubin. Simulation of the Two-Phase Flow Hydrodynamics in an IRDE Reactor. *J. Electrochem. Soc.*, 156(9):P139, 2009. ISSN 00134651. doi: 10.1149/1.3155423. URL <https://iopscience.iop.org/article/10.1149/1.3155423>.
- [151] M. Ishii and N. Zuber. Drag coefficient and relative velocity in bubbly, droplet or particulate flows. *AIChE J.*, 25(5):843–855, September 1979. ISSN 0001-1541, 1547-5905. doi: 10.1002/aic.690250513. URL <https://onlinelibrary.wiley.com/doi/10.1002/aic.690250513>.

- [152] A. Tomiyama, I. Kataoka, I. Zun, and T. Sakaguchi. Drag Coefficients of Single Bubbles under Normal and Micro Gravity Conditions. *JSME Int. J., Ser. B*, 41(2):472–479, 1998. ISSN 1340-8054, 1347-5371. doi: 10.1299/jsmeb.41.472. URL http://www.jstage.jst.go.jp/article/jsmeb1993/41/2/41_2_472/_article.
- [153] P. Mandin, A. A. Aissa, H. Roustan, J. Hamburger, and G. Picard. Two-phase electrolysis process: From the bubble to the electrochemical cell properties. *Chemical Engineering and Processing: Process Intensification*, 47(11):1926–1932, 2008. ISSN 02552701. doi: 10.1016/j.cep.2007.10.018.
- [154] M. R. Maxey and J. J. Riley. Equation of motion for a small rigid sphere in a nonuniform flow. *The Physics of Fluids*, 26(4):883–889, April 1983. ISSN 0031-9171. doi: 10.1063/1.864230. URL <https://pubs.aip.org/pfl/article/26/4/883/816404/Equation-of-motion-for-a-small-rigid-sphere-in-a>.
- [155] R. Clift, J. Grace, and M. Weber. *Bubbles, Drops, and Particles*. Dover Civil and Mechanical Engineering Series. Dover Publications, 2005. ISBN 978-0-486-44580-9. URL <https://books.google.de/books?id=UUrOmD8niUQC>.
- [156] C. W. Tobias. Effect of Gas Evolution on Current Distribution and Ohmic Resistance in Electrolyzers. *J. Electrochem. Soc.*, 106(9):833, 1959. ISSN 00134651. doi: 10.1149/1.2427506. URL <https://iopscience.iop.org/article/10.1149/1.2427506>.
- [157] F. Hine and K. Murakami. Bubble Effects on the Solution IR Drop in a Vertical Electrolyzer Under Free and Forced Convection. *J. Electrochem. Soc.*, 127(2):292–297, February 1980. ISSN 0013-4651, 1945-7111. doi: 10.1149/1.2129658. URL <https://iopscience.iop.org/article/10.1149/1.2129658>.
- [158] G. H. Yeoh and J. Tu. *Computational techniques for multi-phase flows: basics and applications*. Butterworth-Heinemann Elsevier, Oxford, 2010. ISBN 978-0-08-046733-7.
- [159] S. Elghobashi. On predicting particle-laden turbulent flows. *Appl. Sci. Res.*, 52(4):309–329, June 1994. ISSN 0003-6994, 1573-1987. doi: 10.1007/BF00936835. URL <http://link.springer.com/10.1007/BF00936835>.
- [160] P. A. Cundall and O. D. L. Strack. A discrete numerical model for granular assemblies. *Géotechnique*, 29(1):47–65, March 1979. ISSN 0016-8505, 1751-7656. doi: 10.1680/geot.1979.29.1.47. URL <https://www.icevirtuallibrary.com/doi/10.1680/geot.1979.29.1.47>.

-
- [161] Y. Tsuji, T. Tanaka, and T. Ishida. Lagrangian numerical simulation of plug flow of cohesionless particles in a horizontal pipe. *Powder Technology*, 71(3):239–250, 1992. ISSN 0032-5910. doi: [https://doi.org/10.1016/0032-5910\(92\)88030-L](https://doi.org/10.1016/0032-5910(92)88030-L). URL <https://www.sciencedirect.com/science/article/pii/003259109288030L>.
- [162] S. Heitkam, A.-E. Sommer, W. Drenckhan, and J. Fröhlich. A simple collision model for small bubbles. *J. Phys.: Condens. Matter*, 29(12):124005, March 2017. ISSN 0953-8984, 1361-648X. doi: 10.1088/1361-648X/aa56fc. URL <https://iopscience.iop.org/article/10.1088/1361-648X/aa56fc>.
- [163] R. Manica, E. Klaseboer, R. Gupta, M. H. W. Hendrix, C.-D. Ohl, and D. Y. C. Chan. Modelling Film Drainage of a Bubble Hitting and Bouncing Off a Surface. 2012.
- [164] A. Goldman, R. Cox, and H. Brenner. Slow viscous motion of a sphere parallel to a plane wall—I Motion through a quiescent fluid. *Chemical Engineering Science*, 22(4):637–651, April 1967. ISSN 00092509. doi: 10.1016/0009-2509(67)80047-2. URL <https://linkinghub.elsevier.com/retrieve/pii/0009250967800472>.
- [165] E. Adam, J. Venczel, and E. Schalch. Stofftransport bei der Elektrolyse mit Gasrührung. *Chemie Ing. Techn.*, 43(4):202–215, February 1971. ISSN 0009-286X, 1522-2640. doi: 10.1002/cite.330430418. URL <https://onlinelibrary.wiley.com/doi/10.1002/cite.330430418>.
- [166] A. N. Colli and J. M. Bisang. A CFD Study with Analytical and Experimental Validation of Laminar and Turbulent Mass-Transfer in Electrochemical Reactors. *J. Electrochem. Soc.*, 165(2):E81–E88, 2018. ISSN 0013-4651, 1945-7111. doi: 10.1149/2.0971802jes. URL <https://iopscience.iop.org/article/10.1149/2.0971802jes>.
- [167] J. S. Newman and K. E. Thomas-Alyea. *Electrochemical systems*. J. Wiley, Hoboken, N.J, 3rd ed edition, 2004. ISBN 978-0-471-47756-3.
- [168] H. Vogt. The actual current density of gas-evolving electrodes—Notes on the bubble coverage. *Electrochimica Acta*, 78:183–187, September 2012. ISSN 00134686. doi: 10.1016/j.electacta.2012.05.124. URL <https://linkinghub.elsevier.com/retrieve/pii/S0013468612009437>.
- [169] S. Shadpoor, A. Pirouzi, H. Hamze, and D. Mazaheri. Determination of Bodenstein number and axial dispersion of a triangular external loop airlift reactor. *Chemical Engineering Research and Design*, 165:61–68, January 2021. ISSN 02638762. doi:

- 10.1016/j.cherd.2020.10.018. URL <https://linkinghub.elsevier.com/retrieve/pii/S0263876220305244>.
- [170] R. Güttel and T. Turek. *Chemische Reaktionstechnik*. Lehrbuch. Springer Spektrum, Berlin [Heidelberg], 2021. ISBN 978-3-662-63149-2. doi: 10.1007/978-3-662-63150-8.
- [171] W. Dahmen and A. Reusken. *Numerik für Ingenieure und Naturwissenschaftler*. Springer-Lehrbuch. Springer, Berlin Heidelberg, 2., korrigierte aufl edition, 2008. ISBN 978-3-540-76492-2.
- [172] C. U. Kocks. *Entwicklung und Charakterisierung eines Reaktors für die elektrochemische pH-Shift Kristallisation von biotechnologisch hergestellter Bernsteinsäure*. PhD thesis, RWTH Aachen University, Aachen, 2024.
- [173] G. Aparicio-Mauricio, F. A. Rodríguez, J. J. Pijpers, M. R. Cruz-Díaz, and E. P. Rivero. CFD modeling of residence time distribution and experimental validation in a redox flow battery using free and porous flow. *Journal of Energy Storage*, 29: 101337, June 2020. ISSN 2352152X. doi: 10.1016/j.est.2020.101337. URL <https://linkinghub.elsevier.com/retrieve/pii/S2352152X19318638>.
- [174] S. Sibirtsev. MRCNN Particle Detection, 2023. URL <https://git.rwth-aachen.de/avt-fvt/public/mrcnn-particle-detection>. Publication Title: GitHub repository.
- [175] H. A. Sturges. The choice of a class interval. *Journal of the american statistical association*, 21(153):65–66, 1926. Publisher: New York.
- [176] Y. Feng, J. Goree, and B. Liu. Errors in particle tracking velocimetry with high-speed cameras. *Review of Scientific Instruments*, 82(5):053707, May 2011. ISSN 0034-6748, 1089-7623. doi: 10.1063/1.3589267. URL <http://aip.scitation.org/doi/10.1063/1.3589267>.
- [177] C. A. Schneider, W. S. Rasband, and K. W. Eliceiri. NIH Image to ImageJ: 25 years of image analysis. *Nat Methods*, 9(7):671–675, July 2012. ISSN 1548-7091, 1548-7105. doi: 10.1038/nmeth.2089. URL <https://www.nature.com/articles/nmeth.2089>.
- [178] G. Lamour, A. Hamraoui, A. Buvailo, Y. Xing, S. Keuleyan, V. Prakash, A. Eftekhari-Bafrooei, and E. Borguet. Contact Angle Measurements Using a Simplified Experimental Setup. *J. Chem. Educ.*, 87(12):1403–1407, December 2010. ISSN 0021-9584, 1938-1328. doi: 10.1021/ed100468u. URL <https://pubs.acs.org/doi/abs/10.1021/ed100468u>.

- [179] R. Wüthrich, C. Comninellis, and H. Bleuler. Bubble evolution on vertical electrodes under extreme current densities. *Electrochimica Acta*, 50(25-26):5242–5246, September 2005. ISSN 00134686. doi: 10.1016/j.electacta.2004.12.052. URL <https://linkinghub.elsevier.com/retrieve/pii/S0013468605005608>.
- [180] H. G. Möller. Elektrolytische Vorgänge an der Elektrodenoberfläche. überspannung und Elektrokapillarität. *Zeitschrift für Physikalische Chemie*, 65U(1):226–254, December 1909. ISSN 2196-7156, 0942-9352. doi: 10.1515/zpch-1909-6515. URL <https://www.degruyter.com/document/doi/10.1515/zpch-1909-6515/html>.
- [181] G. Jones and W. A. Ray. The Surface Tension of Solutions of Electrolytes as a Function of the Concentration. III. Sodium Chloride. *J. Am. Chem. Soc.*, 63(12): 3262–3263, December 1941. ISSN 0002-7863, 1520-5126. doi: 10.1021/ja01857a007. URL <https://pubs.acs.org/doi/abs/10.1021/ja01857a007>.
- [182] N. P. Brandon, G. H. Kelsall, S. Levine, and A. L. Smith. Interfacial electrical properties of electrogenerated bubbles. *J Appl Electrochem*, 15(4):485–493, July 1985. ISSN 0021-891X, 1572-8838. doi: 10.1007/BF01059289. URL <http://link.springer.com/10.1007/BF01059289>.
- [183] G. H. Kelsall, S. Tang, A. L. Smith, and S. Yurdakul. Measurement of rise and electrophoretic velocities of gas bubbles. *Faraday Trans.*, 92(20):3879, 1996. ISSN 0956-5000, 1364-5455. doi: 10.1039/ft9969203879. URL <http://xlink.rsc.org/?DOI=ft9969203879>.
- [184] Y. Tanaka, K. Kikuchi, Y. Saihara, and Z. Ogumi. Bubble visualization and electrolyte dependency of dissolving hydrogen in electrolyzed water using Solid-Polymer-Electrolyte. *Electrochimica Acta*, 50(25-26):5229–5236, September 2005. ISSN 00134686. doi: 10.1016/j.electacta.2005.01.062. URL <https://linkinghub.elsevier.com/retrieve/pii/S001346860500558X>.
- [185] K. Bar-Eli. The peristaltic effect on chemical oscillations. *J. Phys. Chem.*, 89(13): 2852–2855, June 1985. ISSN 0022-3654, 1541-5740. doi: 10.1021/j100259a029. URL <https://pubs.acs.org/doi/10.1021/j100259a029>.
- [186] C. Schneider. Gas fraction, velocity and bubble size distributions in a model of alkaline chlorine electrolysis cells. *Institute of Safety Research*, page 41, 2000.
- [187] M. J. O’Neil. *The Merck index: an encyclopedia of chemicals, drugs, and biologicals*. RSC Publishing, 2013.

- [188] L. Lu, A. Konan, and S. Benyahia. Influence of grid resolution, parcel size and drag models on bubbling fluidized bed simulation. *Chemical Engineering Journal*, 326:627–639, October 2017. ISSN 13858947. doi: 10.1016/j.cej.2017.06.002. URL <https://linkinghub.elsevier.com/retrieve/pii/S1385894717309531>.
- [189] B. Vreman, B. J. Geurts, N. G. Deen, J. A. M. Kuipers, and J. G. M. Kuerten. Two- and Four-Way Coupled Euler–Lagrangian Large-Eddy Simulation of Turbulent Particle-Laden Channel Flow. *Flow Turbulence Combust*, 82(1):47–71, January 2009. ISSN 1386-6184, 1573-1987. doi: 10.1007/s10494-008-9173-z. URL <http://link.springer.com/10.1007/s10494-008-9173-z>.
- [190] W. El-Askary, I. Sakr, K. Ibrahim, and A. Balabel. Hydrodynamics characteristics of hydrogen evolution process through electrolysis: Numerical and experimental studies. *Energy*, 90:722–737, October 2015. ISSN 03605442. doi: 10.1016/j.energy.2015.07.108. URL <https://linkinghub.elsevier.com/retrieve/pii/S0360544215010038>.
- [191] R. S. Jupudi, H. Zhang, G. Zappi, and R. Bourgeois. Modeling Bubble Flow and Current Density Distribution in an Alkaline Electrolysis Cell. *The Journal of Computational Multiphase Flows*, 1(4):341–347, December 2009. ISSN 1757-482X, 1757-4838. doi: 10.1260/1757-482X.1.4.341. URL <http://journals.sagepub.com/doi/10.1260/1757-482X.1.4.341>.
- [192] C. P. Robert. Simulation of truncated normal variables. *Stat Comput*, 5(2):121–125, June 1995. ISSN 0960-3174, 1573-1375. doi: 10.1007/BF00143942. URL <http://link.springer.com/10.1007/BF00143942>.
- [193] C. E. Brennen. A review of added mass and fluid inertial forces. *Naval Civil Engineering Laboratory*, 1982. Publisher: Citeseer.
- [194] B. Liu, R. Manica, Q. Liu, Z. Xu, E. Klaseboer, and Q. Yang. Nanoscale Transport during Liquid Film Thinning Inhibits Bubble Coalescing Behavior in Electrolyte Solutions. *Phys. Rev. Lett.*, 131(10):104003, September 2023. ISSN 0031-9007, 1079-7114. doi: 10.1103/PhysRevLett.131.104003. URL <https://link.aps.org/doi/10.1103/PhysRevLett.131.104003>.
- [195] B. Hoomans, J. Kuipers, W. Briels, and W. Van Swaaij. Discrete particle simulation of bubble and slug formation in a two-dimensional gas-fluidised bed: A hard-sphere approach. *Chemical Engineering Science*, 51(1):99–118, January 1996. ISSN 00092509. doi: 10.1016/0009-2509(95)00271-5. URL <https://linkinghub.elsevier.com/retrieve/pii/0009250995002715>.

- [196] C. Wu, J. Zhan, Y. Li, K. Lam, and A. Berrouk. Accurate void fraction calculation for three-dimensional discrete particle model on unstructured mesh. *Chemical Engineering Science*, 64(6):1260–1266, March 2009. ISSN 00092509. doi: 10.1016/j.ces.2008.11.014. URL <https://linkinghub.elsevier.com/retrieve/pii/S0009250908006258>.
- [197] A. Tomiyama, I. Žun, H. Higaki, Y. Makino, and T. Sakaguchi. A three-dimensional particle tracking method for bubbly flow simulation. *Nuclear Engineering and Design*, 175(1-2):77–86, November 1997. ISSN 00295493. doi: 10.1016/S0029-5493(97)00164-7. URL <https://linkinghub.elsevier.com/retrieve/pii/S0029549397001647>.
- [198] J. Schell, E. Zars, C. Chicone, and R. Glaser. Simultaneous Determination of All Species Concentrations in Multiequilibria for Aqueous Solutions of Dihydrogen Phosphate Considering Debye–Hückel Theory. *J. Chem. Eng. Data*, 63(6):2151–2161, June 2018. ISSN 0021-9568, 1520-5134. doi: 10.1021/acs.jced.8b00146. URL <https://pubs.acs.org/doi/10.1021/acs.jced.8b00146>.
- [199] M. Hlawitschka, P. Kováts, K. Zähringer, and H.-J. Bart. Simulation and experimental validation of reactive bubble column reactors. *Chemical Engineering Science*, 170:306–319, October 2017. ISSN 00092509. doi: 10.1016/j.ces.2016.12.053. URL <https://linkinghub.elsevier.com/retrieve/pii/S0009250916307187>.
- [200] M. Hlawitschka. *Multi-scale Investigations of Reactive Bubbly Flows*, in: *Reactive Bubbly Flows: Final Report of the DFG Priority Program 1740*, pages 459–478. Springer International Publishing, Cham, 2021. ISBN 978-3-030-72361-3. doi: 10.1007/978-3-030-72361-3_19. URL https://doi.org/10.1007/978-3-030-72361-3_19.
- [201] J. Vanhanen. Ternary solution of sodium chloride, succinic acid and water; surface tension and its influence on cloud droplet activation. *Atmos. Chem. Phys.*, 2008.
- [202] A.-P. Hyvärinen, H. Lihavainen, A. Gaman, L. Vairila, H. Ojala, M. Kulmala, and Y. Viisanen. Surface Tensions and Densities of Oxalic, Malonic, Succinic, Maleic, Malic, and *cis* -Pinonic Acids. *J. Chem. Eng. Data*, 51(1):255–260, January 2006. ISSN 0021-9568, 1520-5134. doi: 10.1021/je050366x. URL <https://pubs.acs.org/doi/10.1021/je050366x>.
- [203] J. L. Ellingboe and J. H. Runnels. Solubilities of Disodium Terephthalate in Aqueous Solutions of Sodium Carbonate and Sodium Bicarbonate. *J. Chem. Eng. Data*, 11

- (2):185–187, April 1966. ISSN 0021-9568, 1520-5134. doi: 10.1021/je60029a017. URL <https://pubs.acs.org/doi/abs/10.1021/je60029a017>.
- [204] Z. Rappoport, editor. *CRC handbook of tables for organic compound identification*. CRC Press, Boca Raton, Fla, 3. ed., 14. print edition, 1985. ISBN 978-0-8493-0303-6.
- [205] H. B. Rose, T. Greinert, C. Held, G. Sadowski, and A. S. Bommarius. Mutual Influence of Furfural and Furancarboxylic Acids on Their Solubility in Aqueous Solutions: Experiments and Perturbed-Chain Statistical Associating Fluid Theory (PC-SAFT) Predictions. *J. Chem. Eng. Data*, 63(5):1460–1470, May 2018. ISSN 0021-9568, 1520-5134. doi: 10.1021/acs.jced.7b01039. URL <https://pubs.acs.org/doi/10.1021/acs.jced.7b01039>.
- [206] J. Thauront, S. Durecu, J.-P. Wiaux, and B.-T. Lam. Formation terephthalic acid by electrochemical acidification of a sodium terephthalate solution. *World Intellectual Property Organization*, (US6312582B1), 1997.